Cilt 4 Sayı 2 Aralık 2023
Volume 4 Number 2 December 2023

ISSN: 2717-8811(Online)

JOURNAL

Materials and Mechatronics:A

2023

JOURNAL

Materials

and

Mechatronics: A

e-ISSN: 2717-8811

Cilt: 4 Sayı: 2 Aralık 2023

Volume:4 Number: 2 December 2023

2023

JOURNAL of
MATERIALS and MECHATRONICS:A

JOURNAL of
MATERIALS and MECHATRONICS:A

JOURNAL of
MATERIALS and MECHATRONICS:A

JOURNAL of
MATERIALS and MECHATRONICS:A

JOURNAL of
MATERIALS and MECHATRONICS:A

JOURNAL of
MATERIALS and MECHATRONICS:A

JOURNAL of
MATERIALS and MECHATRONICS:A

JOURNAL of
MATERIALS and MECHATRONICS:A

e-ISSN 2717-8811
JournalMM, 2023, 4(2), 355-372
https://doi.org/10.55546/jmm.1295748

Araştırma Makalesi / Research Article

Taguchi Yöntemiyle Sağlamlık Oranının Dikey Eksenli Rüzgâr Türbini Performansına Etkisinin Sayısal Olarak İncelenmesi

Himmet Erdi TANÜRÜN

Kahramanmaraş İstiklal Üniversitesi, Elbistan Mühendislik Fakültesi, Enerji Sistemleri Mühendisliği Bölümü, Kahramanmaraş, Türkiye,
ORCID ID: https://orcid.org/0000-0001-7814-7043, erdi.tanurun@istiklal.edu.tr

Geliş/ Received: 11.05.2023; **Kabul / Accepted:** 25.07.2023

ÖZET: Son dönemde, Dikey Eksenli Rüzgâr türbinlerinin (DERT) kullanımı kentsel alan uygulamalarında artmasından dolayı, DERT performansının geliştirilmesi üzerine pasif kontrol çalışmaları yaygınlaşmaktadır. Bu çalışmada, DERT'in güç katsayısı (C_P) performansını geliştirmek için sağlamlık oranı optimizasyonu gerçekleştirmiştir. Optimizasyon, Taguchi metodu sayesinde elde edilmiştir. Türbin kanat sayısı (N), türbin kanadı veter uzunluğu (v), türbin çapını (D) içeren 3 kontrol faktörü ile çalışmalar yürütülmüştür. Belirlenen faktörler ile $L_9(3^3)$ ortogonal dizisi dizayn edilmiştir. Tüm modeller 2.62 kanat uç hız oranı (λ) ile hesaplamalı akışkanlar dinamiği (HAD) kullanılarak elde edilmiştir. Varyans analizi (ANOVA) yöntemiyle her bir kontrol faktörünün performansa olan katkı miktarları elde edilmiştir. Daha sonra Regresyon analiziyle, kontrol faktörlerini içeren lineer denklem oluşturularak, DERT'in tahmini C_P değerleri geliştirilmiştir. Sonuçlarda, sistem performansının optimal olmasını sağlayan parametre konfigürasyon N=2, v=60 mm, D=1.2 m, olarak elde edilmiştir. Optimal modelin C_P değeri, geleneksel DERT'e göre %9.96 daha yüksek olduğu tespit edilmiştir. ANOVA yöntemiyle parametrelerin DERT'in C_P'ye olan katkı sıralaması D>N>v olarak elde edilmiştir. Bu sonuçlara, göre D parametresi, %62.11 ile en majör etkiyi, v parametresi ise %1.73 ile en az etkiyi sağlamıştır. Doğrulama testi ile regresyon analizinden (RA) elde edilen tahmini sonuçlardaki mutlak yüzdelik değişimi (R^2) değerleri sırasıyla 0.995697 ve 0.971835, istatiksel hata miktarı (İHM) değerleri ise sırasıyla 0.000296 ve 0.001187 olmasından dolayı, doğrulama testi ile RA elde edilen sonuçlar ile nümerik sonuçlar oldukça uyumlu olduğu gözlemlenmiştir.

Anahtar Kelimeler: Dikey Eksenli Rüzgâr Türbini (DERT), Sağlamlık Oranı, Optimizasyon, HAD, Güç katsayısı (C_P), Varyans Analizi (ANOVA)

*Sorumlu yazar / Corresponding author: erdi.tanurun@istiklal.edu.tr

Bu makaleye atıf yapmak için /To cite this article

Tanürün, H.E. (2023). Taguchi Yöntemiyle Sağlamlık Oranının Dikey Eksenli Rüzgâr Türbini Performansına Etkisinin Sayısal Olarak İncelenmesi. Journal of Materials and Mechatronics: A (JournalMM), 4(2), 355-372.

Numerical Investigation of the Effect of Solidity on Vertical Axis Wind Turbine Performance by Taguchi Method

ABSTRACT: Recently, since the use of Vertical Axis Wind Turbines (VAWT) has increased in urban applications, passive control studies on improving VAWT performance have become widespread. In this study, solidity optimization was performed to improve the power coefficient (C_P) performance of VAWT. Optimization was achieved by the Taguchi method. Studies were carried out with 3 control factors including turbine blade number (N), turbine blade chord length (v), turbine diameter (D). The L9 (3^3) orthogonal array was designed with the determined factors. All models are obtained using computational fluid dynamics (CFD) with a blade tip speed ratio (λ) of 2.62. The contribution amounts of each control factor to the performance were obtained by the analysis of variant (ANOVA) method. Then, the estimated C_P of VAWT were developed by creating a linear equation containing control factors with Regression analysis. In the results, parameter configuration N=2, v=60 mm, D=1.2 m, which ensures optimal system performance, was obtained. The C_P value of the optimal model was found to be 9.96% higher than the traditional DERT. With the ANOVA method, the contribution order of the parameters DERT to C_P was obtained as D>N>v. According to these results, the D parameter had the most major effect with 62.11%, and the v parameter had the least effect with 1.73%. Since the absolute percentage change (R^2) values in the estimated results obtained from the validation test and regression analysis (RA) were 0.995697 and 0.971835, respectively, and the statistical error amount (RMSE) values were 0.000296 and 0.001187, respectively, it was observed that the results obtained from the validation test and RA were in good agreement with the numerical results.

Keywords: Vertical axis wind turbine (VAWT), Solidity, Optimization, CFD, Power Coefficient (C_P), Analysis of Variance (ANOVA)

1. GİRİŞ

Son yıllarda, fosil yakıtların hızlı bir şekilde tükenmesine ek olarak fosil yakıtlardan kaynaklanan sera gazı salınımının çevreye verdiği ciddi zararlar, yenilenebilir enerji teknolojilerinin gelişimi hızlı bir şekilde artırmaktadır (Chen ve ark., 2017; Tanürün ve ark., 2020). Rüzgâr enerjisi, diğer yenilebilir enerji kaynaklarının sahip olduğu avantajların yanı sıra daha ucuz olmasından dolayı dünyada yenilenebilir enerji alanında en hızlı büyüyen teknoloji durumunadır (Bhutta ve ark., 2012). Rüzgâr enerji genellikle dönüş yönüne göre dikey eksenli rüzgâr türbini (DERT) ve yatay eksenli rüzgâr türbini (YERT) olmak üzere 2 gruba ayrılmaktadır (Du ve ark., 2019). YERT'in yüksek veriminden kaynaklı, hem kıyıdan uzak hem de karadaki ticari uygulamalardaki kullanımı DERT'e göre daha yaygındır (Wang ve ark., 2016). Kıyıdan uzak bölgelerde, rüzgâr yönündeki anlık değişkenlik sınırlıdır ancak yüksek binalara sahip yerleşim yerlerinde rüzgâr yönü anlık olarak sürekli değişkenlik göstermektedir. Bu yüzden, DERT'in, YERT'e göre en önemli avantajlarından biri olan sapma mekanizmasına gerek kalmadan rüzgârı her bölgeden alabilme özelliği ve şehir merkezlerinde binalardaki çatı tipine kurulum uygunluğundan dolayı, DERT'in yakın gelecekteki kullanım alanının hızlı bir şekilde gelişeceği öngörülmektedir (Wang ve ark., 2018; Wang ve ark., 2018). Son dönemde uygulama alanın yaygınlaşması dolayı bilim insanların DERT'in performansı üzerinde çalışmalarını hızlandırmaktadır.

DERT'in güç performansı (C_P) üzerinde sağlamlık oranının (σ) dikkate değer bir etkisi olduğu literatürde birçok çalışmada tespit edilmiştir. Jiang ve ark. (2007) H tipi DERT'lerde σ'nın artması, maksimum C_P değerinin daha düşük kanat uç hız oranında (λ) gerçeklemesine sebep olduğunu

belirlemişlerdir. Howell ve ark. (2010) σ ve türbin kanat pürüzlülüğünün kanat uç girdaplarının oluşumuna ve buna bağlı olarak DERT'in performansı üzerine olan etkisini 3 boyutlu sayısal çalışmalarda incelemişlerdir. Li ve Li (2010) düz kanatlı DERT'lerde farklı kanat veter uzunluğu (v) ve sayısına (N) bağlı olarak elde edilen 2 farklı σ'nın C_P üzerine olan etkisini sayısal olarak incelemişlerdir. Bedon ve ark. (2012) DERT'in düşük σ değerlerinde yüksek üretim ve daha kontrol edilebilir bir türbin elde edildiğini belirlemişlerdir. Marco ve ark. (2012) DERT'in bir tam tur dönüşü sırasında Tork (T) varyasyonlarını sayısal olarak incelemişlerdir. Sonuçlarda türbin N'sinin artması, maksimum C_P değerini azalttığı ve aynı zamanda maksimum C_P değerini daha düşük λ'da gerçekleştiğini tespit etmişlerdir. Benzer sonuçlar Tangler'in (2000) çalışmasında görülmektedir. Roh ve ark. (2013) 0.5 ve 0.8 σ aralığındaki sayısal analizlerinde, σ'nın artmasıyla eliptik DERT'in, H-tipi DERT'e göre güç (P) eğrisi grafiğinde farklılıklar oluştuğunu tespit etmişlerdir. Joo ve ark. (2015) DERT'lerde σ'nın azalması, blokaj ve girdapların olumsuz etkisini azalttığını ayrıca düşük λ'larda negatif T oluşumunu azaltarak ilk uyartı probleminin çözümlenmesine olanak sağladığını tespit etmişlerdir. Lee ve Lim (2015) DERT'in v, rotor çapı, eğim açısı (β) ve helis açısı parametrelerinin P ve T performansına olan etkisini deneysel ve sayısal olarak incelemişlerdir. Sonuçlarda, küçük λ aralığında düşük rotor çapı ve yüksek v'ye bağlı olarak oluşan yüksek σ değerlerinde C_P'nin geliştiğini gözlemlemişlerdir. Aksine yüksek λ aralığında, yüksek rotor çapı ve düşük v'ye bağlı olarak elde edilen düşük σ'nın daha yüksek performansa sahip olduğunu tespit etmişlerdir. Abu-El-Yazied ve ark. (2015) DERT'lerde v ve N etkisini sayısal olarak incelemişlerdir. Sonuçlarda v'nin artışı belirli bir noktaya kadar C_P üzerinde olumlu etki sağladığını, belirli bir noktadan sonra verim üzerinde olumsuz etkisi olduğunu tespit etmişlerdir. Li ve ark. (2015) NACA 0021 kanat modeline sahip DERT'lerde, N etkisinin türbin performansına olan etkisini incelemişlerdir. N'nin artması C_P'yi azalttığını gözlemlemişlerdir. Senqupta ve ark. (2016), düşük rüzgâr hızı DERT'lerde ilk uyartı özelliklerini inceleyerek, enerji verim potansiyellerini anlamadaki önemli bir boşluğu ele almışlardır. Üç tip kanada sahip türbin modellerini kullanılarak yapılan deneyler sonucunda, simetrik olmayan veya yüksek σ sahip asimetrik kanatların kullanılmasının H-Darrieus rotorlarının hem ilk uyartı hem de C_P iyileştirebileceği tespit etmişlerdir. Özellikle, simetrik olmayan S815 kanatlı rotor, muadillerine göre daha yüksek bir dinamik tork ve C_P sergileyerek, düşük rüzgâr koşullarında performans artışı için umut verici bir potansiyel olduğunu belirlemişlerdir. Delafin ve ark. (2016) aynı v'ye sahip farklı kanat sayılarındaki Φ-DERT'lerin T, itki ve yanal kuvvet performanslarını deneysel olarak incelemişlerdir. Sonuçlarda, 3 kanatlı türbinin 2 kanatlıya göre T, itki ve yanal kuvvetlerdeki dalgalanmanın daha az olduğunu tespit etmişlerdir. Parra ve ark. (2018) H-tipi DERT'lerde σ'ın azalması ilk uyartı probleminin çözümlenmesine ve P üretimde λ aralığının genişlemesine katkı sağladığını tespit etmişlerdir. Liang ve ark. (2018) 0.2-1.28 σ aralığında H-tipi DERT'in performansını incelemişlerdir. Sonuçlarda, 0.2-0.6 σ aralığında optimal sonuçları elde etmişlerdir. Kaya ve ark. (2022) yarıçapa bağlı σ'nın, H-tipi DERT'in C_P'si üzerine olan etkisini incelemişlerdir. Sonuçlarda, düşük λ değerlerinde σ'nın artması, yüksek λ değerlerinde ise σ'nın azalması türbin veriminin performansını geliştirdiğini belirlemişlerdir.

Son yıllarda, güçlü dizayn metodolojisinden dolayı Taguchi metoduna olan ilgi mühendislik uygulamalarında artmaktadır (Athreya ve Venkatesh, 2012). Taguchi sistemi en iyi veriminin elde edilmesi için farklı bağımsız değişkenlerin belli bir algoritma altında analizini sağlayan istatiksel bir yöntem olmasından dolayı birçok farklı DERT uygulamalarında kullanılmaktadır. Hu ve Rao (2011) YERT'lerde optimal performansı Taguchi metoduyla gerçekleştirmiştir. Wang ve ark. (2018) farklı genlik ve dalga boyuna sahip tüberkül yapılı hücum kenarı ile sarmal kanatlı yapıları DERT'lerde pasif kontrol yöntemiyle uygulamışlardır. Bu 3 değişkenin optimizasyon algoritması Taguchi metodu

sayesinde elde edilmiştir. Sonuçlarda en efektif tüberkülün dalga boyu ve genliği sırasıyla v'nin %2.5'i ve %16.6'sı kadar olduğunu gözlemlemişlerdir. Ek olarak optimal verim kanat burkulma açısının 60° olduğu durumda elde etmişlerdir. Bu parametreler kullanılarak elde edilen optimal DERT, geleneksel DERT'den %18.3 daha yüksek verime sahip olduğu gözlemlemişlerdir. Qasemi ve ark. (2020) DERT'in akış yönü bölgesinin alt tarafına düz engel yerleştirerek, türbin performansına olan etkisini nümerik olarak incelemişlerdir. 5 farklı değişkenin DERT'in P performansına olan etkisini Taguchi metodu kullanarak optimize etmişlerdir. Sonuçlarda en optimal düz engel ile güçlendirilmiş DERT'in, geleneksel DERT'e göre verimi %16.42 daha yüksek olduğunu belirlemişlerdir. Hassanpour ve Azadani (2021) çift Darrieus DERT'in C_P performansını üç boyutlu sayısal çalışmalar ile analiz etmişlerdir. 3 farklı parametreden oluşan çift Darrieus DERT konfigürasyonu Taguchi metodu sayesinde elde edilmiştir. Optimal çift Darrieus DERT konfigürasyonu, geleneksel Darriues DERT'in performansını %26.6 geliştirdiğini tespit etmişlerdir. Detaylı literatür çalışması incelendiğinde, DERT'lerde σ analizi üzerine çalışmaların yoğun bir şekilde yapıldığı gözlemlenmiştir. Ancak Taguchi metodu kullanılarak DERT'in σ optimizasyonuna ve buna ek olarak ANOVA ile DERT'in σ'yı etkileyen parametrelerin katkı miktarını ve doğrulama testlerini içeren sayısal bir çalışmaya literatürde rastlanmamıştır.

Bu çalışmanın ana amacı, DERT'in güç performansı üzerinde dikkate değer bir etkiye sahip olan σ'yı içeren parametrelerden oluşan ortogonal dizayndaki denemeleri sayısal olarak incelemektir. Türbin kanat sayısı (N) , türbin kanat veter uzunluğu (v), türbin çapını (D) içeren bu dizayn parametreleri Taguchi metodu ile tasarlanmıştır. Taguchi metodu ile oluşturulan dizilerden elde edilen σ optimizesi yapılmış DERT'in güç katsayısı (C_P) çıktısı açısında geleneksel DERT ile karşılaştırılmıştır. Ek olarak σ'yı oluşturan N, v ve D parametrelerin DERT'in C_P'ye olan katkı sıralamaları, ANOVA yöntemiyle elde edilmiştir. Ardından Regresyon analizi ile testler için lineer bir denklem oluşturulup, doğrulama testleri gerçekleştirilmiştir. Son olarak σ optimizasyonu ile desteklenmiş DERT'in detaylı akış karakteristiği incelenmiştir.

2. MATERYAL VE YÖNTEM

2.1 Geometri

Bu çalışmada, literatürdeki aerodinamik çalışmalarda (Şahin ve Acır, 2015; Tanürün ve Acır, 2019; Tanürün ve ark., 2021; Kaya, 2023) yaygın olarak kullanılan 4 rijitli NACA 0021 kanat modeline sahip DERT'in güç performansı elde edilmiştir. Türbin modelinde doğrulamada kullanılan v ve D sırasıyla 85.8 ve 1030 mm olarak belirlenmiştir (Castelli ve ark., 2011). Bu v ve D değerlerine bağlı olarak σ değeri 0.5 olarak elde edilmiştir. Türbinin dönme esnasında dikey eksenli kanatların hareket simülasyonunu elde etmek için dönen bir iç bölge oluşturulmuştur. İç bölgeler içinde, her kanadı ayrı ayrı çevreleyen kontrol çember1 ($kç_1$), kontrol çember2 ($kç_2$), kontrol çember3 ($kç_3$) alanları oluşturarak her bir kanadın sayısal olarak daha iyi çözümlenmesi amaçlanmıştır. Akış hacmi, akış performansı üzerinde herhangi bir etki oluşturmaması için ideal boyutlar belirlenmiştir. Bu kapsamda diğer çalışmalara (Hao ve ark., 2021) dayanarak, Şekil 1'deki türbin merkezinin giriş, çıkış, alt ve üst yüzeylere olan uzaklığı sırasıyla 6D, 12D ve 5D olarak belirlenmiştir. Bölgeler arasında akış sürekliliğin oluşması için her bir bölge arasına ara yüzler oluşturulmuştur. Çalışmada havanın girişteki serbest akış hızı (U_0) 9 m/s olarak ayarlanmıştır. Çıkış sınır koşulu, atmosferik basınç olarak seçilmiştir. Yanal alt ve üst sınır simetri ve kaymaz koşul olarak belirlenmiştir. Türbülans şiddeti (Tİ) ve yoğunluk (ρ) değerleri sırasıyla %1 ve 1.225 kg/m^3'dür. Çizelge 1'de, geleneksel DERT'in fiziksel özelliklerini gösterilmektedir.

Çizelge 1. Doğrulama modeli için oluşturulan geleneksel türbin karakteristiği

Parametre	Değer
Türbin çapı (D)	1030 mm
Türbin yüksekliği (H) (iki boyutlu)	1m
Kanat veter uzunluğu (v)	85.8 mm
Kanat profili	NACA 0021
Kanat sayısı (N)	3
Türbin Göbek-Kanat bağlantı noktası	0.5c

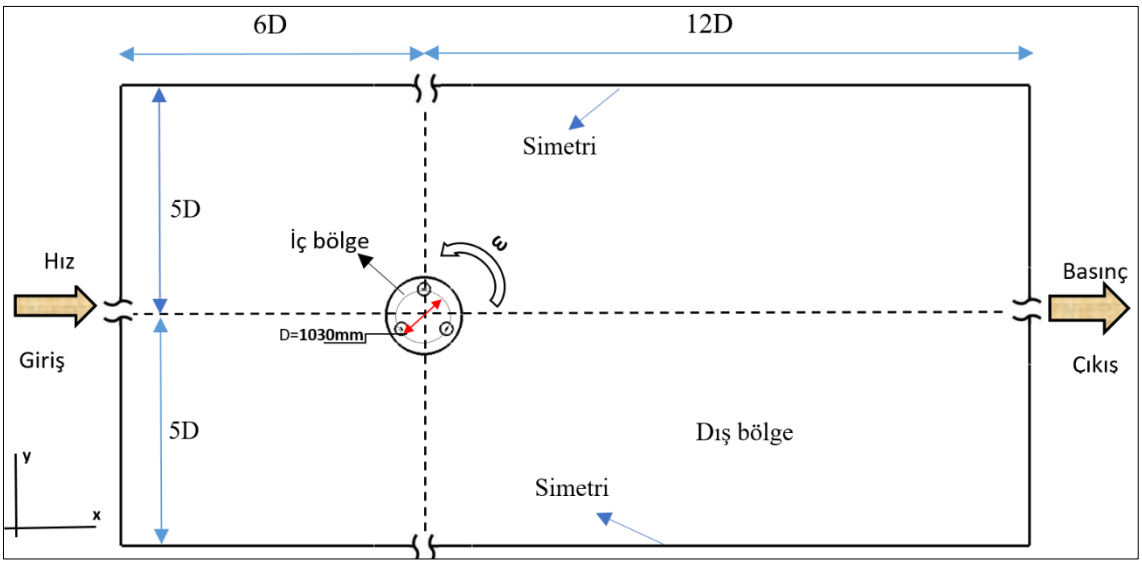

Şekil 1. Akış hacminin şematik diyagramı

2.2 Sayısal Metot

DERT'in rüzgâr türbini etrafındaki akış karakteristiğini URANS (Unsteady Reynolds Averaged Navier–Stokes) yöntemi ile modellenmiştir. URANS denklemleri, süreklilik ve Navier–Stokes denklemlerine, Reynolds (Re) ayrışımı ve ortalaması uygulanarak elde edilir ve şu şekilde verilir:

$$\frac{\partial \bar{u}_i}{\partial \bar{x}_i} = 0 \tag{1}$$

$$\frac{\partial \bar{u}_i}{\partial t} + \bar{u}_j \frac{\partial \bar{u}_i}{\partial \bar{x}_j} = -\frac{1}{p}\frac{\partial \bar{p}}{\partial \bar{x}_i} + v\frac{\partial^2}{\partial \bar{x}_i \partial \bar{x}_j} + \frac{\partial}{\partial \bar{x}_j}\left(\overline{-u_i' u_j'}\right) + \bar{f}_i \tag{2}$$

$\bar{u}_i, u_i'$ ve $\bar{f}_i$ sırasıyla ortalama hız, hız dalgalanması ve ortalama cisim kuvveti olarak tanımlanmaktadır. v ve $\overline{-u_i' u_j'}$ ise sırasıyla kinematik viskozite ve Re gerilme tensörüdür. SST $k-\omega$ modeli, $k-\omega$'nın iç sınır tabaka akış üzerindeki yeteneği (Wilcox, 1998) ile $k-\varepsilon$ modelinin serbest akış üzerindeki yeteneğinin (Jones ve Launder, 1973) birleştirmekte ve yüzey akış ayrışmalarını (Dar'oczy ve ark., 2015) uygun bir şekilde çözümlemektedir. Ayrıca bu çalışmada da kullanılan SST $k-\omega$ türbülans modeli güçlü girdap akışlarında olumlu sonuçlar vermesinden dolayı literatürdeki birçok çalışmada kullanılmıştır (Elkhoury ve ark., 2015; Balduzzi ve ark., 2016; Zuo ve ark., 2016).

DERT'e gelen akış, Eşitlik 3. de gösterildiği üzere türbin kanatlarında T'nin oluşmasına neden olmaktadır (Kaya ve ark., 2022).

$$T = \frac{1}{2} C_T \rho A R U_0^2 \quad (3)$$

Burada C_T ve ρ sırasıyla tork katsayısı ve yoğunluktur. Ayrıca $A\ ve\ R$ sırasıyla süpürme alanı ve türbin çapı olarak ifade edilmektedir. DERT'in performansını incelemek için, C_P olarak ifade edilen güç performansı katsayısı tanımlanmıştır. C_P değeri Eşitlik 4. de ifade edildiği üzere C_T'den türetilmiştir. C_P, bu çalışmada oluşturulan modeller arasındaki performansın karşılaştırılmasında kullanılmıştır (Tanürün ve Acır, 2022).

$$C_p = C_T * \lambda \quad (4)$$

Buradaki λ, kanat uç hız oranı (TSR) olarak tanımlanmaktadır ve aşağıda denklemde verilmiştir:

$$\lambda = \frac{R\omega}{U_0} \quad (5)$$

Buradaki R, ω ve U_0 sırasıyla türbin yarıçapı, açısal hız ve serbest rüzgâr akış hızı olarak tanımlanmaktadır.

$$\sigma = \frac{Nv}{D} \quad (6)$$

Eşitlik 6. da gösterilen σ, kanatların toplam alanının, türbinin süpürdüğü alana oranı olarak tanımlanmaktadır ki bu çalışmanın temel etken parametresini oluşturmaktadır.

Çalışmada doğrulama için kullanılan DERT'in ağ örgüsü dağılımı Şekil 2'de gösterilmiştir. Düşük ağ örgüsü boyutları, doğru çözümü ulaşmayı kolaylaştırırken yüksek hesaplama süreleri oluşturmaktadır. Bu yüzden, düşük hesaplama süresinde ve yüksek doğrulukta ağ örgüsü boyutları belirlenmesi son derece önemlidir. Akış hacminde, türbin kanatlarından giriş, çıkış ve dış duvara doğru ağ örgüsü boyutları büyümektedir. Bunun sebebi türbin civarında daha hassas çözüm gerekmesinden kaynaklanmaktadır. $kç_1$, $kç_2$ ve $kç_3$ bölgelerinde "Ansys-meshing" kullanarak üçgen ağ örgüsü uygulanırken, hesaplama alanının diğer bölgelerimde kare ağ örgüsü yöntemi uygulanmıştır. Türbinin kanat yüzeyinin yakın bölgelerinde akış karakteristiğindeki değişkenliğin yüksek olmasından dolayı çözüm süresini uzamasına rağmen doğru çözüm elde edilebilmesi için üçgen yapısı uygulanmıştır. Şekil 2'de görüldüğü üzere kanat yüzeyindeki sınır tabakada, laminerden türbülansa geçişin olduğu oldukça karmaşık bir akış olayı gerçekleşmektedir. Bu akış olayının doğru bir şeklide çözümlenebilmesi için kanat yüzeyine ağ örgüsü sınır tabakaları oluşturulurmuştur. Kanat yüzeyindeki sınır tabaka geçiş kalitesini denetleyen ve daha önceki çalışmalarda bahsedilmiş olan (Liu ve ark., 2020) kanat yüzeyindeki ilk sınır tabakaya y^+ denilmekte ve genel olarak dış akış uygulamalarında bu değerin 1'den küçük olması amaçlanmaktadır. Bu çalışmada, y^+ değerinin, ilk sınır tabaka yüksekliği ve büyüme oranı sırasıyla 0.29 mm ve 1.2 olacak şekilde 12 sınır tabakadan olarak oluşturularak, 1'den küçük olması planlanmıştır. Tüm bu ağ bileşeni içerikleri doğrultusunda geleneksel DERT modelinin ağ örgüsü sayısı 144 958 olarak elde edilmiştir. Belirlenen bu mesh sayısı, literatürdeki doğrulama yapılacak deneysel çalışmadan elde edilen C_P grafiği ile uyumlu olmasından dolayı kabul edilmiştir. Geleneksel model haricindeki 9 modelin boyut farklılıklarından kaynaklı ağ örgüsü sayısındaki küçük değişiklikler olmasına rağmen, tüm modellerin ağ örgüsü ile geleneksel DERT'in ağ örgüsü sayısı arasında %1'den daha düşük bir farklılık olduğu tespit

edilmiştir. Ağ örgüsü yapısının, elaman kalitesi, ortogonal kalite ve çarpıklık gibi parametreler ile de kalitesi değerlendirilmektedir. Eleman ve ortogonal kalitenin 1'e yakın, çarpıklık değerinin ise sıfıra yakın olması ağ örgüsü kalitesinin yüksek olduğu anlamına gelmektedir. Bu çalışmada eleman kalite, ortogonal kalite ve çarpıklık değeri sırasıyla, 0.845, 0.878 ve 0.194 olarak elde edilmiştir. Bu değerleri yüksek ağ örgüsü kalitesinin elde edildiğinin göstermektedir.

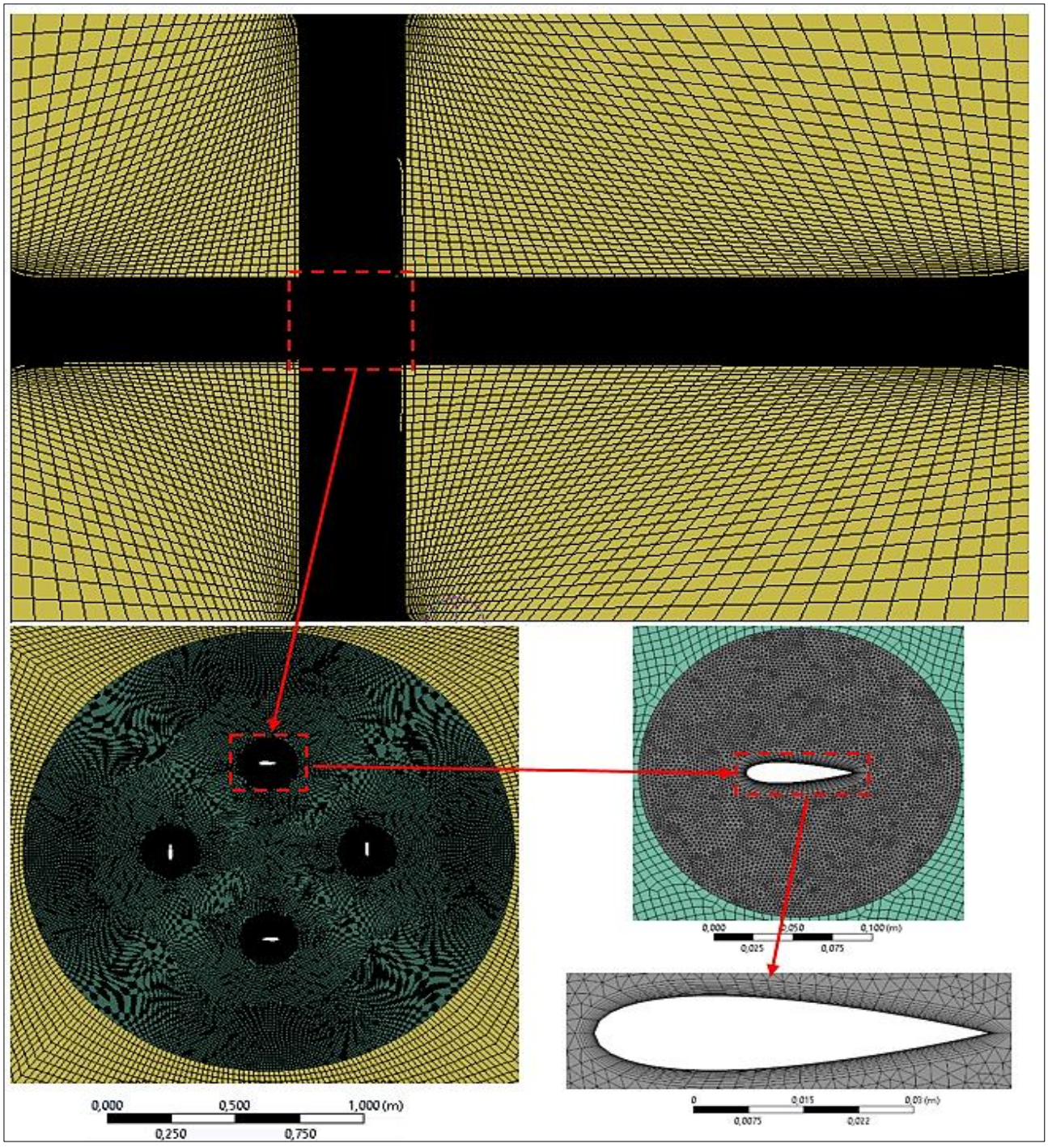

Şekil 2. Genel ve bölgesel alanlardaki ağ örgüsü

2.3 Model Doğrulaması

Nümerik çalışmalar güvenilirliği için deneysel çalışmalar ile doğrulama yapılması gerekmektedir. Bu çalışmada, Şekil 3'de görüldüğü üzere Castelli'nin (Castelli ve ark., 2011)

yürüttüğü deneysel ve sayısal çalışmalar ile doğrulama yapılmıştır. Sonuçlar incelendiğinde, tüm λ değerlerinde mevcut çalışma ile Ref. (Castelli ve ark., 2011)'nın deneysel sonuçları arasında iyi bir uyuşma gözlemlenmiştir. Özellikle maksimum C_P değerinin oluştuğu 2.62 λ değerinde deneysel çalışma ile oldukça benzer bir sonuç elde edilmiştir.

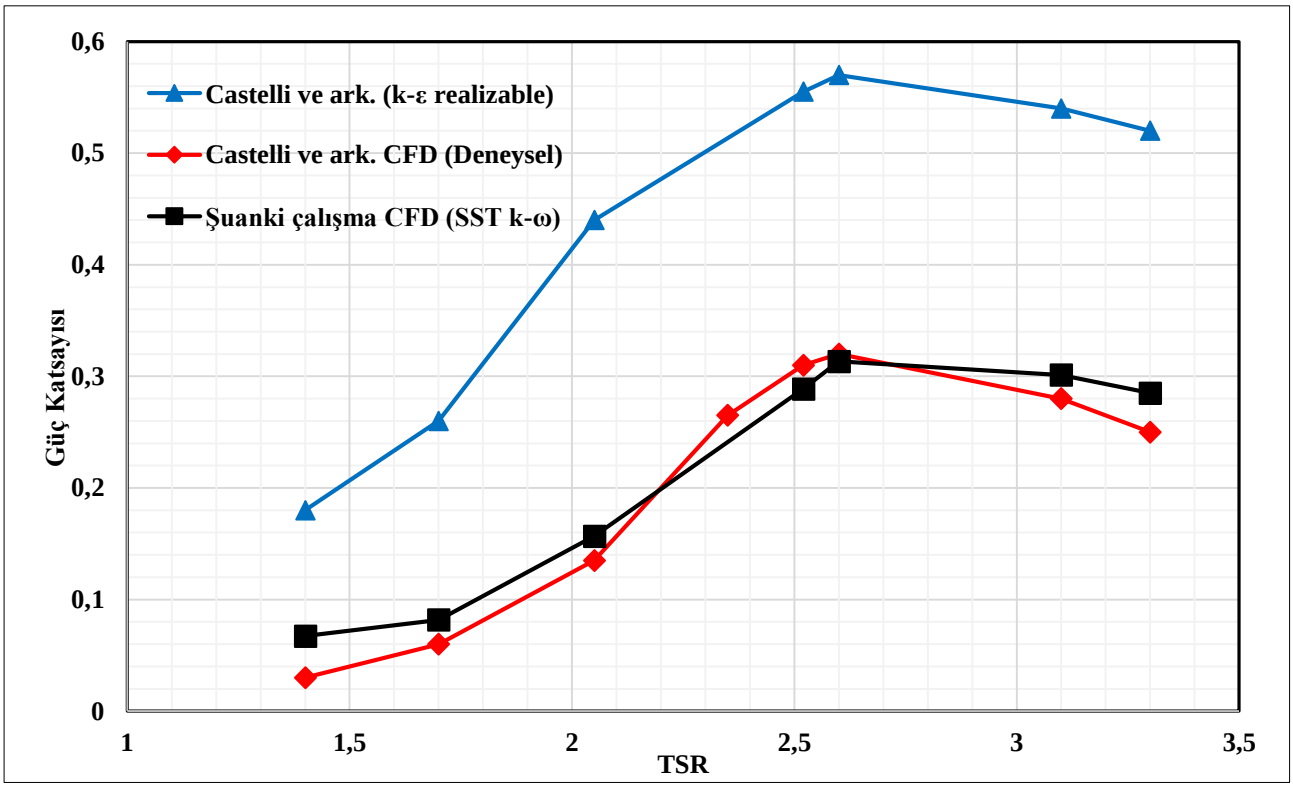

Şekil 3. Ref. (Castelli ve ark., 2011)'un nümerik ve deneysel çalışması ile mevcut çalışmanın güç katsayısı açısında karşılaştırılması

3. TAGUCHİ METOT

Rüzgâr türbini performansı üzerinde kanat aerodinamiğinin büyük etkisi bulunmaktadır. Rüzgâr türbini performansını etkileyen σ parametrelerini optimize etmek için Şekil 4'de akış şeması gösterilen Taguchi yöntemi kullanılmaktadır.

Bu çalışmada literatürde kullanılan ve kanat performansı üzerinde dikkate değer bir etkisi olan σ'yı oluşturan parametrelerin etkisi incelenmiştir. Şekil 5'de NACA 0021 kanat modelinde türbin yarıçapı ve türbin kanat veter uzunluğuna sahip 3 kanatlı bir DERT türbini gösterilerek σ'yı oluşturan parametreler ifade edilmiştir. Taguchi metodu, rüzgâr türbin performansını etkileyen parametrelerin optimize edilmesi için kullanılmaktadır. Taguchi metodu temelde amaç fonksiyonu tanımlanması, dizayn parametrelerinin belirlenmesi ve sinyal-gürültü yoğunluk oranı (S/N) analizlerine bağlı olarak optimal dizayn parametresinin elde edilmesi için sayısal denemelerin sonuçlarının kullanılması olmak üzere 3 ana unsuru içermektedir. Çizelge 2'de, N, v ve D olacak şekilde σ'yı oluşturan parametreler kullanarak belirlenen faktörler ile amaç fonksiyonu oluşturulmuştur. Amaç fonksiyonunda N, v ve D faktörleri A, B ve C olarak temsil edilmiştir. Taguchi metodunun en önemli adımlarından birisi de ortogonal dizisinin elde edilmesidir. 3 faktör ve her bir faktörün 3 seviyesi için, Çizelge 3'de L_9 (3^3) ortogonal dizisi oluşturularak, 9 sayısal deneme ile hem optimal parametre konfigürasyonu hem de parametrelerin etkilerinin belirlenmesi amaçlanmıştır.

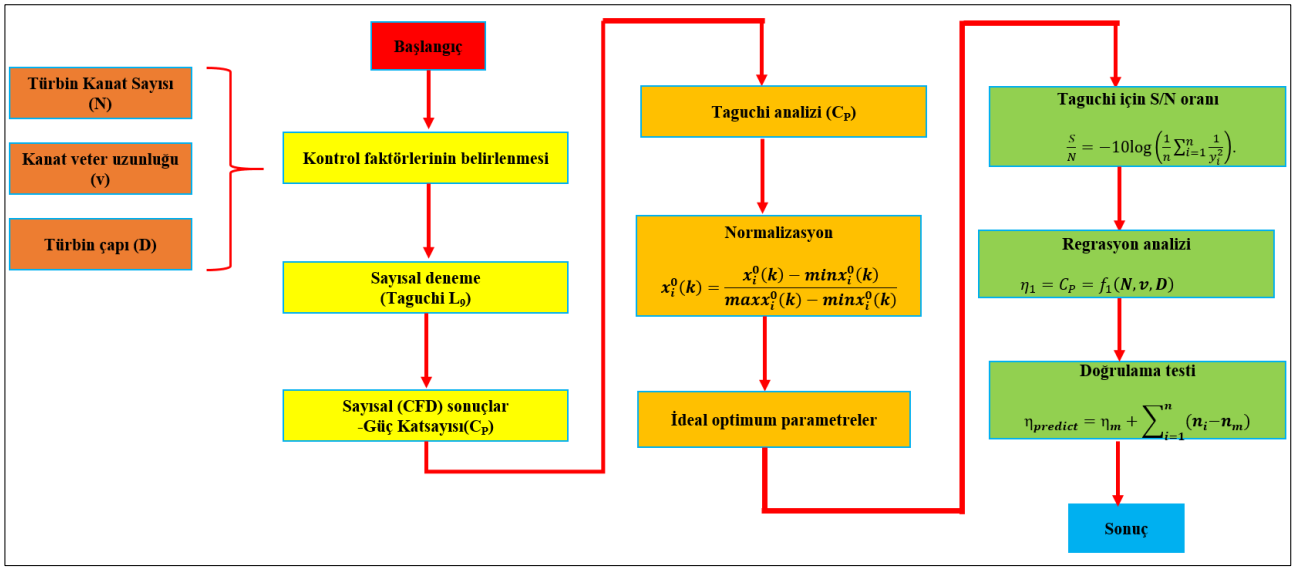

Şekil 4. Taguchi metodunun şematik gösterimi

Eşitlik 7. ile ifade edilen S/N amaç fonksiyonu parametrelerinin kalite ölçümünün bir göstergesi olarak tanımlanmaktadır. En yüksek C_P değerine sahip DERT'in σ faktörleri, optimal parametreler olarak belirlenmesinden dolayı Eşitlik 7. de "larger-the-better" modülü S/N oranıdır (Çakıroğlu ve ark., 2023; Evran ve Yıldır, 2023).

$$\frac{S}{N} = -10\log\left(\frac{1}{n}\sum_{i=1}^{n}\frac{1}{y_i^2}\right) \tag{7}$$

Buradaki n ve y_i ifadeleri sırasıyla sayısal deneme sayısı ve rüzgâr türbininden elde edilen C_P değeri anlamına gelmektedir.

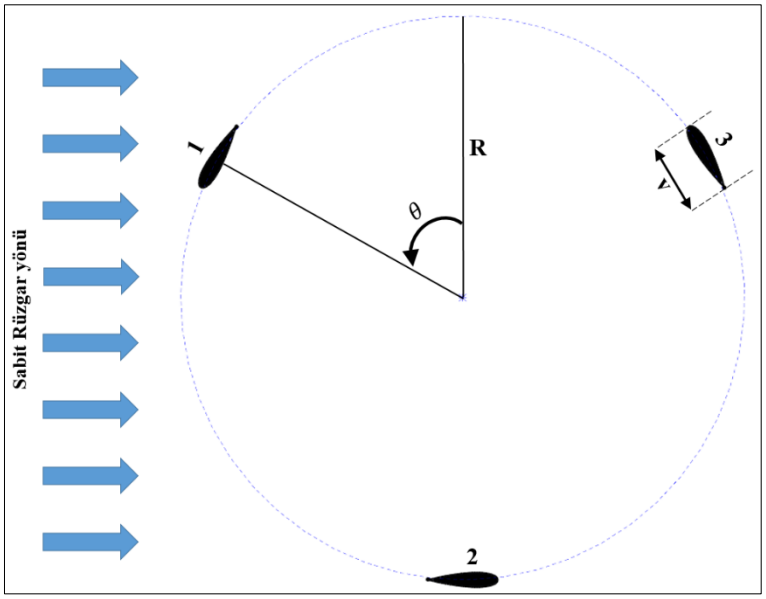

Şekil 5. 3 kanatlı azimut açısında DERT'in şematik gösterimi

Çizelge 2. Taguchi yöntemi faktör ve seviyeleri

	Kontrol Faktör	Seviyeler		
		1	**2**	**3**
A	Türbin kanat sayısı (N)	2	3	4
B	Kanat veter uzunluğu (v)	0.6 m	0.8 m	0.1 m
C	Türbin çapı (D)	0.8 m	1 m	1.2 m

Çizelge 3. Taguchi yöntemine dayalı sayısal deneme ortogonal dizaynı

Deneme	**Seviye**			
	N	**V (mm)**	**D (m)**	**σ**
1	2	60	0.8	0.30
2	2	80	1	0.32
3	2	100	1.2	0.33
4	3	60	1	0.36
5	3	80	1.2	0.40
6	3	100	0.8	0.75
7	4	60	1.2	0.40
8	4	80	0.8	0.80
9	4	100	1	0.80

4. BULGULAR VE TARTIŞMA

4.1 DERT'in Faktör ve S/N Etkileri

Temel DERT'in maksimum C_P değeri 2.62 λ olmasından dolayı Çizelge 3'de gösterilen 9 sayısal denemenin tamamı bu TSR değerinde gerçekleştirilmiştir. Çizelge 4'de, geleneksel DERT ve 9 denemenin C_P, S/N oranı ve güç artışı (%) gösterilmiştir. Geleneksel DERT'in C_P değeri 0.313 olarak elde edilmiştir. S/N "Larger is better" modülü olarak düzenlenmesinden dolayı yüksek S/N oranı değeri sahip modellerin yüksek C_P değerine de sahip olduğu görülmektedir. 3. ve 5. deneme tasarımlarının DERT'in performansını sırasıyla %9.158 ve %7.042 geliştirdiğini belirlenmiştir. Ortogonal diziye oluşturulan diğer 7 modelin DERT'in performansına olumsuz bir etki oluşturulduğu gözlemlenmiştir. Sonuçlarda σ'yı oluşturan parametrelerin C_P değeri üzerinde önemli bir etkiye sahip olduğu tespit edilmiştir.

Çizelge 5'dan türetilmiş olan Şekil 6'da gösterildiği üzere, 3 faktörün her bir seviyesinin etki seviyeleri S/N cinsinden ifade edilmiştir. Daha önceden de bahsedildiği üzere, S/N değerinin yüksek olması DERT'in performansına olumlu etkisi olmasından dolayı her bir faktöründeki maksimum S/N seviyeleri optimal σ parametrelerinin elde edilmesine imkân sağlamaktadır. Bu kapsamda, N, v ve D faktörlerinin en yüksek seviye değerleri sırasıyla 2 (A1), 60 mm (B1), 1.2 m (C3) olarak belirlenmiş ki bu değerler ile σ değeri 0.2 olarak elde edilmiştir. Çizelge 4 incelendiğinde, optimal σ parametrelerinden meydana gelen A1B1C3 modeli ortogonal dizi içinde yer almamaktadır. L_9'da belirlenmiş olan 9 sayısal denemeye ek olarak optimal modelinde sayısal analizi gerçekleştirilmiştir.

Çizelge 4. Ortalama güç katsayısı, S/N oranı için sayısal analiz sonuçları

Deneme	C_P	S/N oranı	Türbin Güç performans oranı (%)
Geleneksel DERT	0.313	-	-
1	0.265932	-11.5046	-15.0378
2	0.30796	-10.2301	-1.610
3	0.341665	-9.3280	**9.158**
4	0.296744	-10.5524	-5.194
5	0.33504	-9.4981	**7.042**
6	0.268197	-11.4309	-14.314
7	0.305259	-10.3066	-2.473
8	0.220638	-13.1264	-29.509
9	0.247401	-12.1320	-20.958

Çizelge 6'de, optimal modelin hesaplamalı akışkanlar dinamiği (HAD) analizinde elde edilen sayısal analiz sonucu ve MINITAB 22 programından elde edilen tahmini değer gösterilmiştir. Sonuçlar incelendiğinde, optimal modelin tahmini ile sayısal C_P değerleri sırasıyla 0.346522ve 0.344187 olarak elde edilmiş ki bu değerler birbirine oldukça yakındır. Orta model ise optimizasyon yapılmadan önce ortalama olarak belirlenen σ uygulanmış olduğu DERT'den elde edilen bulgulardır. Çizelge 6 incelendiğinde, optimal model, ortalama modele göre DERT'in C_P performansını %16.03 geliştirdiği gözlemlenmiştir. Ayrıca yine optimal modele sahip DERT'in, σ optimizasyonu yapılmamış olan geleneksel DERT'e (C_P=0.313 at 2.62 TSR) göre C_P performansını %9.96 daha yüksek olduğu tespit edilmiştir.

Çizelge 5. Güç katsayısı için S/N oranı

Seviye	Türbin kanat sayısı (N)	Kanat veter uzunluğu (V)	Türbin çapı (D) (m)
1	-10.354	-10.788	-12.021
2	-10.494	-10.952	-10.971
3	-11.855	-10.964	-9.711
Değişim	1.501	0.176	2.310
Etki Sırası	2	3	1

Çizelge 6. C_P için ortalama ve optimal parametrelerin tahmini ve sayısal sonuçları

	Ortalama parametre değerleri	Optimal parametre	
		Tahmini	Sayısal
Seviye	A2B2C2	A1B1C3	A1B1C3
$C_{P.max}$	0.296611	0.346522	0.344187
S N / oranı (dB)	-10,6148	-9,05097	-9.26411
S/N oranı performans artışı	1.35069 dB		
Tahmini hata (dB)	0.21314		

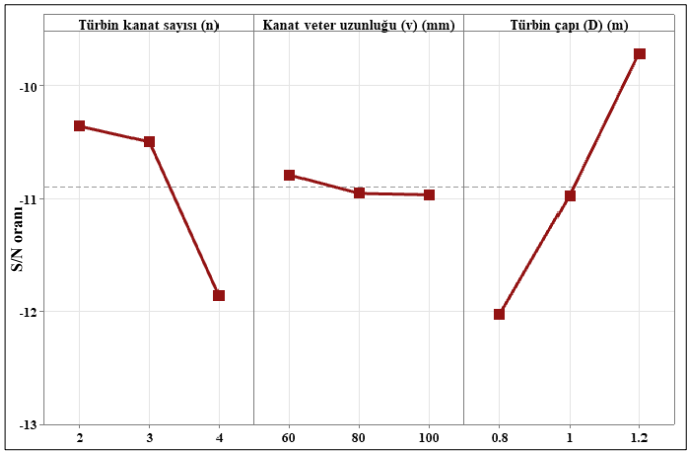

Şekil 6. Her seviyenin her bir faktörü için S/N oranı değerleri

4.2 Varyans analizi (ANOVA)

Bu bölüme kadar, Taguchi metodu yöntemiyle faktör ve seviyeleri kullanarak DERT'in optimal performansı elde edilmiştir. ANOVA yöntemi, sonucun üzerinde birden fazla değişkenin etkisi olduğu durumlarda kullanılır. ANOVA amaç fonksiyonunda belirlenmiş olan faktörlerin, DERT performansına olan katkı miktarlarının belirlenmesini sağlamaktadır. Yüzdelik katkı miktarı (YKM), Eşitlik 8. gösterildiği gibi hesaplanmaktadır. Çizelge 7'de 3 faktörün DERT üzerindeki katkı miktarları gösterilmiştir. DERT'in performansı üzerindeki majör etkiyi %62.11 ile D, en az etki ise %1.73 ile v faktörlerinde olduğunu tespit edilmiştir. N'nin ise etkisi %30.86 olarak elde edilmiştir. Ek olarak, hata miktarı değeri %8.75 olarak elde edilmiş ki bu değer oldukça düşük olup literatürde kabul edilebilir seviyededir (Çakıroğlu ve ark., 2023).

$$\%YKM = \frac{(SS_A - (v_e)(v_A))}{SS_T} * 100 \quad (8)$$

Çizelge 7. C_P için ANOVA sonuçları

Kaynak	DF	Seq SS	Adj MS	F	P	YKM(%)
N	2	4.1247	2.06234	15.1	0.062	30.86
v	2	0.0578	0.02891	0.21	0.825	1.73
D	2	8.0247	4.01237	29.38	0.033	62.11
Mutlak Hata	2	0.2731	0.13655			8.75
Toplam	8	12.4803				91.25

4.3 Korelasyon ve Doğrulama Testi

Korelasyon, Regresyon analizi (RA) sayesinde amaç fonksiyonundaki N, v ve D parametrelerine bağlı olarak oluşturulan lineer denklem ile C_P performansını geliştirilmesi sağlamaktır. Eşitlik 9. de C_P ile amaç fonksiyonu faktörleri arasındaki ilişki gösterilmiştir. Eşitlik 10. da korelasyon denklemiyle, amaç fonksiyonundaki faktör ve seviyeler ile oluşturulacak tüm modellerin analitik olarak çözümüne imkân sağlamaktadır. Doğrulama testinde elde edilen C_P değerleri, eğitim verisi ve test verisi olmak üzere iki parçaya ayrılmıştır. Eşitlik 10. da korelasyon denklemi için, doğrulama testi uygulanabilmesi için Çizelge 3'deki ortogonal dizaynda modellerinin tamamı dahil edilmeden eğitilmiştir. 9 sayısal denemenin 6'sı eğitim verisi olarak seçilip, korelasyon

denklemi oluşturulmasında kullanılmıştır. Diğer 3 model ise test verisi olarak seçilip, Eşitlik 10. daki korelasyon denkleminde uygulanarak doğrulama testleri gerçekleştirilmiştir. Şekil. 7'da, RA'yla oluşturulan Eşitlik 10. daki korelasyon denkleminden elde edilen eğitim verisi ve test verisi değerleri gösterilmiştir. Sonuçlar incelendiğinde RA analiziyle elde edilen eğitim ve test verileri birbirlerine oldukça yakın olduğu gözlemlenmiştir.

RA, eğitim ve test verisi olmak üzere iki aşamada yapılmıştır. İstatiksel analiz çözümün doğruluğunu denetlemek için eğitim verisi ve test verisi arasındaki hata miktarının belirlenmesini gerekmektedir. Eşitlik 11. ve 12. sırasıyla mutlak yüzdelik değişimi (R^2) ve istatiksel hata miktarı (İHM) ifadeleri tanımlanmıştır (Çakıroğlu ve ark., 2023). R^2 1'e, İHM ise 0'a yakın bir değer olması çalışmanın yüksek güvenilirlikte olduğunu göstermektedir. Çizelge 8'de RA'dan elde edilen eğitim verisi ve test verilerinin istatiksel analizleri gösterilmiştir. Sonuçlar incelediğimizde hem eğitim hem de test verisinin R^2 değerleri sırasıyla 0.995697 ve 0.971835, İHM değerlerinin ise sırasıyla 0.000296 ve 0.001187 olduğu görülmektedir. Bu değerler, nümerik çalışmanın, RA ile arasındaki güvenilirliği doğrular niteliktedir.

$$\eta_1 = C_p = f_1(N, c, D) \tag{9}$$

C_P için korelasyon denklemi

$$\eta_1 = 0.2528 - 0.02169\ (N) - 0.00507(v) + 0.04302(D) \tag{10}$$

$$R^2 = 1 - \left(\frac{\sum_{i=1}^{N}(t_i - o_i)^2}{\sum_{i=1}^{N} o_i^2}\right) \tag{11}$$

$$\text{İ}HM = 1 - \left(\frac{\sum_{i=1}^{N}(t_i - o_i)^2}{o_i}\right)^{0.5} \tag{12}$$

Çizelge 8. Regresyon analizinin istatiksel sonuçları

	RA	
	İHM	**R^2**
Eğitim	0.000296	0.995697
Test	0.001187	0.971835

Genel olarak değerlendirildiğinde, literatürde çalışmalarda σ'yı oluşturan N, v ve D parametrelerinin DERT'in C_P performansı üzerindeki etkisi ayrı ayrı incelemişlerdir. Bu çalışmada literatürden farklı olarak σ'yı oluşturan parametrelerin tamamının C_P performansı üzerindeki etkisi değerlendirilmiştir. Ayrıca σ'yı oluşturan her bir parametrenin C_P performansını ne oranda etkilediği tespit edilmiştir. Ek olarak σ'yı oluşturan tüm parametreler ve bu parametrelerin her bir seviyesini kapsayan sayısal analizler çok yüksek hesaplama süreleri oluşturmaktadır. Bu çalışmada, Taguchi metodu ile belirli bir algoritma tabanında geleneksel yönteme göre çok daha az sayısal deneme ile optimal model ve σ'yı oluşturan parametrelerin performansa olan katkı değerleri belirlenmesi sağlanmıştır.

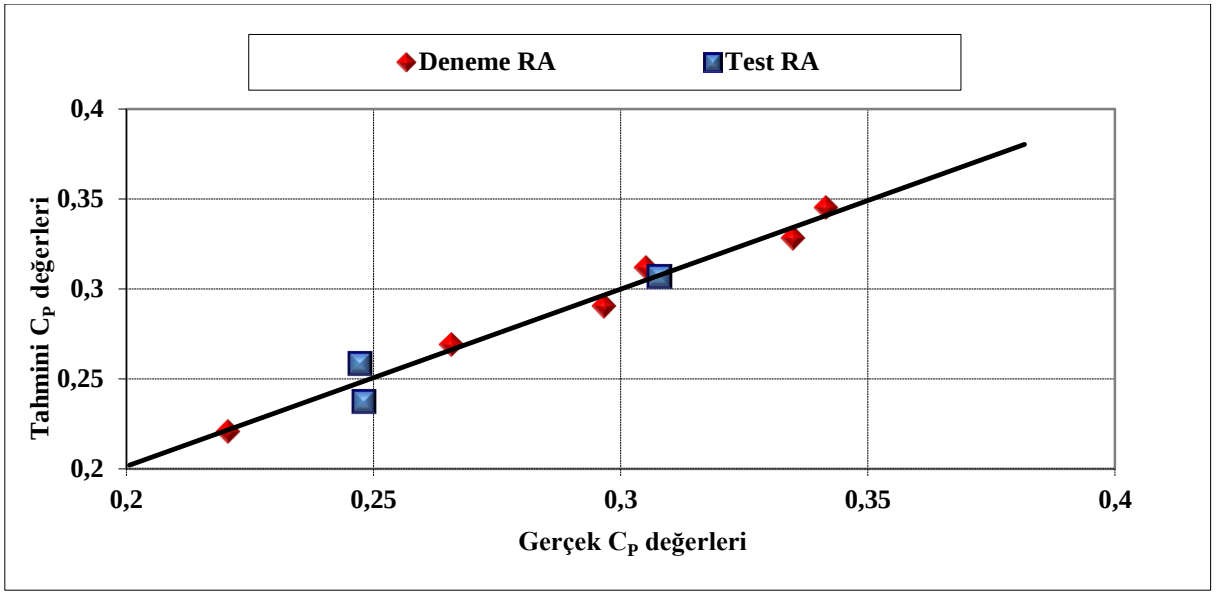

Şekil 7. σ optimizasyonu yapılmış DERT modellerinin C_P açısından RA ve sayısal sonuçlarının karşılaştırılması

σ'nın DERT performansı üzerinde etkisini fiziksel olarak anlamak ve aerodinamik açıdan da doğrulamak için anlık hız dağılım değerleri hesaplanmıştır. Şekil 8'da bir tam tur boyunca en düşük (Deneme 8) ile optimal DERT'in her bir kanadı için 30° azimut açısı aralığında hız dağılımları gösterilmiştir. Tüm azimut açılarında optimal modelin, deneme 8 modeline göre kanadın alt ve üst yüzeyindeki hız dağılım farklı belirgin şekilde daha yüksek olduğu görülmektedir. Özelliklede akışın kanat yüzeyine çarpma açısından kaynaklı en yüksek T'nin üretildiği 60-120° azimut açılarında, optimal modelin kanat yüzeyinde kırmızı renk ile tanımlanmış olan yüksek hızlar gözlemlenirken, deneme 8 modelinde yüksek hız değerlerine oldukça sınırlı alanlarda ulaşıldığı tespit edilmiştir. Bu durum iki kanat arasındaki T ve buna bağlı olarak oluşan güç katsayısı farkını kanıtlar niteliktedir.

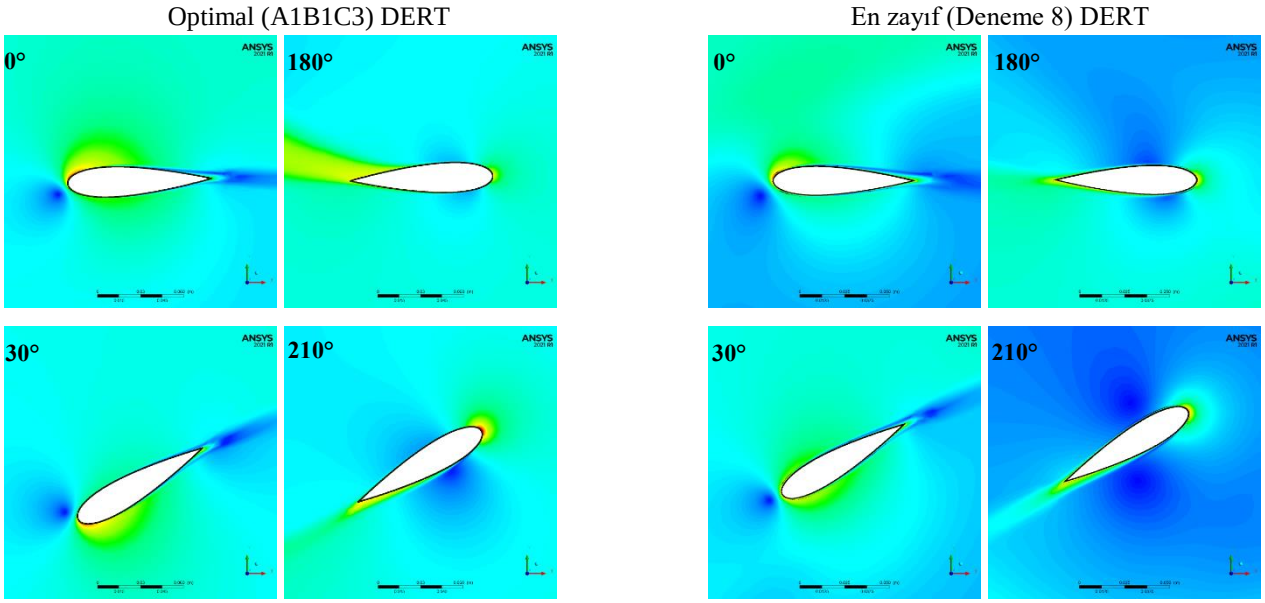

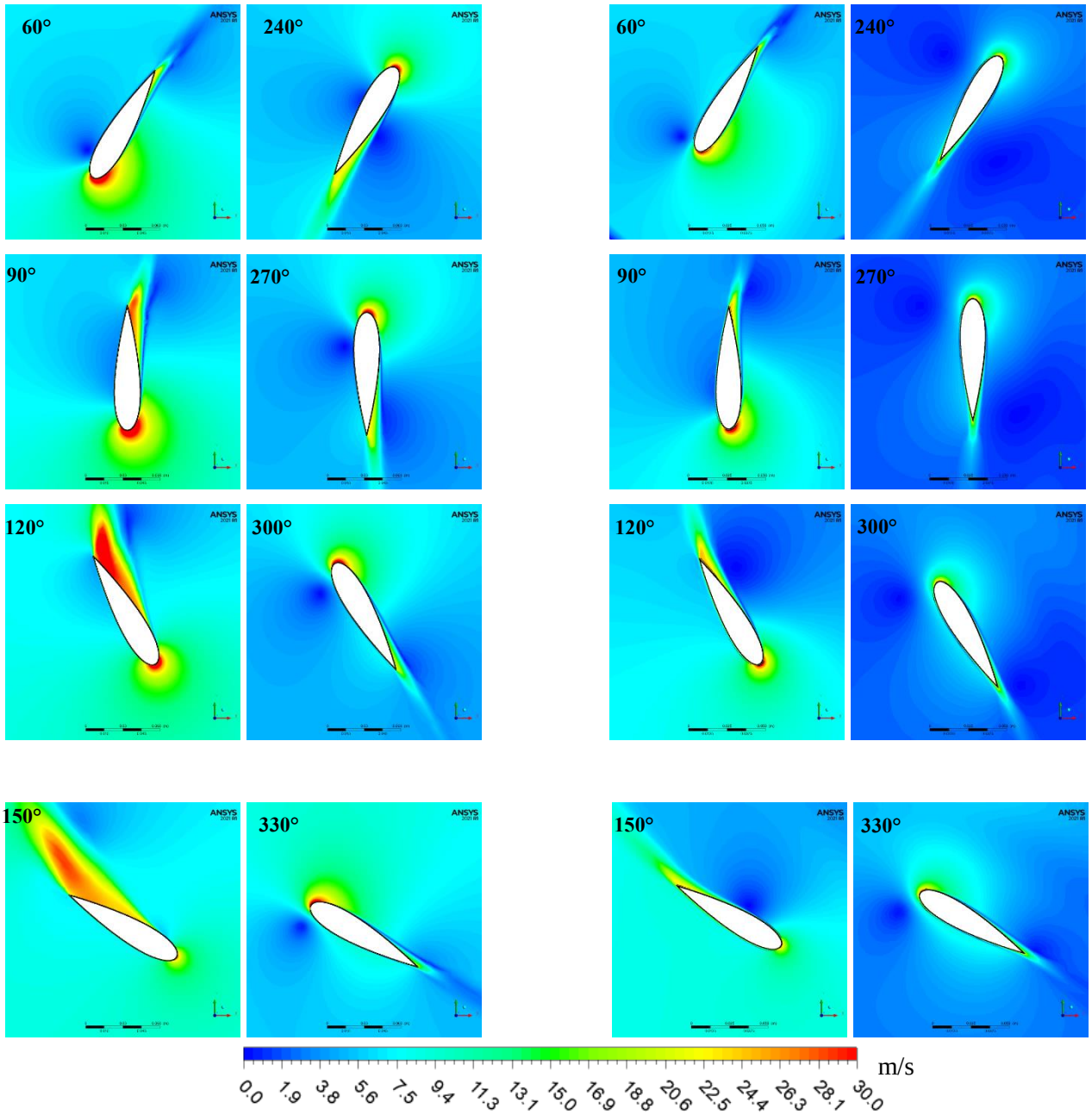

Şekil 8. Bir tam tur boyunca 30° azimut açısı aralığında tek bir türbin kanadının optimal ile deneme 8 DERT modellerinin anlık hız dağılımları

5. SONUÇ

Çeşitli σ konfigürasyonlarının DERT'in akış davranışı ve güç performansı üzerindeki etkileri, HAD ticari yazılımı olan ANSYS Fluent paket programı kullanılarak sayısal olarak gerçekleştirilmiştir. N, v ve D parametrelerini içeren σ'yı kullanılarak, DERT'in performansının optimal olması için Taguchi optimizasyon yönteminden faydalanılmıştır. Geleneksel DERT'in maksimum C_P değerinin 2.62 λ olmasın nedeniyle L_9 ortogonal dizisindeki tüm sayısal çalışmalar bu λ değerinde gerçekleştirilmiştir. Bu çalışmadaki önemli bulgular şu şekilde çizilmiştir:

- Taguchi methodu, DERT'in güç performansı üzerinde dikkate değer bir değişiklik sağlamasından dolayı, σ optimizasyonunda oldukça etkili bir yöntem olduğu tespit edilmiştir.

- Optimum parametreler N=2, v=60 mm, D=1.2 m ile A1B1C3 modelinde gerçekleşmiştir. Optimum σ parametrelerine sahip DERT modeli, geleneksel DERT'e göre performansı %9.96 geliştirmiştir.
- ANOVA sonuçlarına göre, DERT'in güç performansı üzerinde en majör etki %62.11 ile D faktöründe, en az etki ise %1.73 ile v faktöründe gerçekleşmiştir.
- İstatiksel yöntem ile test ve eğitim verilerinin R^2 değerleri sırasıyla 0.995697 ve 0.971835 elde edilmiştir ki bu da analizin oldukça doğru olduğunu kanıtlamaktadır.

6. ÇIKAR ÇATIŞMASI

Yazar, bilinen herhangi bir çıkar çatışması veya herhangi bir kurum/kuruluş ya da kişi ile ortak çıkar bulunmadığını onaylamaktadırlar.

7. KAYNAKLAR

Abu-El-Yazied T.G., Ali A.M., Al-Ajmi M.S, Hassan M.I., Effect of number of blades and blade chord length on the performance of Darrieus wind turbine. Journal of Mechanical Engineering and Automation 2(1), 16-25, 2015.

Athreya S., Venkatesh Y.D., Application of taguchi method for optimization of process parameters in improving the surface roughness of lathe facing operation. International Refereed Journal of Engineering and Science (IRJES) 1(3), 9-13, 2012.

Balduzzi F., Bianchini A., Maleci R., Ferrara G., Ferrari L., Critical issues in the CFD simulation of darrieus wind turbines. Renewable Energy 85, 419-435, 2016.

Bedon G., Castelli M.R., Benini E., Evaluation of the effect of rotor solidity on the performance of a H-Darrieus turbine adopting a blade element-momentum algorithm. World Academy of Science, Engineering and Technology International Journal of Aerospace and Mechanical Engineering 6(9), 1989-1194, 2012.

Bhutta M.M.A, Hayat N., Farooq A.U., Ali Z., Jamil S.R., Hussain Z. Vertical Axis Wind Turbine – A Review of Various Configurations and Design Techniques. Renewable and Sustainable Energy Reviews 16(4), 1926-1939, 2012.

Castelli M.R., Betta S.D., Benini E., Effect of blade number on a straight-bladed Vertical-Axis Darreius wind turbine. World Academy of Science, Engineering and Technology 61, 305-11, 2012.

Castelli M.R., Englaro A., Benini E., The Darrieus wind turbine: Proposal for a new performance prediction model based on CFD. Energy 36(8), 4919-4934, 2011.

Chen W.H., Chen C.Y., Huang C.Y., Hwang C.J., Power output analysis and optimization of two straight-bladed vertical-axis wind turbines. Applied Energy 185, 223-232, 2017.

Çakıroğlu, R., Tanürün, H.E., Acır, A., Üçgül, F., Olkun, S., Optimization of NACA 4412 augmented with a gurney flap by using grey relational analysis. Journal of the Brazilian Society of Mechanical Sciences and Engineering 45(3), 167, 2023.

Dar'oczy L., Janiga G., Petrasch K., Webner M., Th´evenin D. Comparative analysis of turbulence models for the aerodynamic simulation of H-Darrieus rotors. Energy 90(1), 680-690, 2015.

Delafin P.L., Nishino T., Wang L., Kolios A., Effect of the number of blades and solidity on the performance of a vertical axis wind türbine, The Science of Making Torque from Wind (TORQUE 2016), 753(2), October 4-7, 2016, pp. 1-8, Munih, Germany.

Du L., Ingram G., Dominy R.G., A review of H-Darrieus wind turbine aerodynamic research. Proceedings of the Institution of Mechanical Engineers, Part C: Journal of Mechanical Engineering Science 233(23-24), 7590-7616, 2019.

Elkhoury M., Kiwata T., Aoun E., Experimental and numerical investigation of a three-dimensional vertical-axis wind turbine with variable-pitch. Journal of Wind Engineering and Industrial Aerodynamics 139, 111–123, 2015.

Evran, S., Yıldır S.Z. Numerical and Statistical Aerodynamic Performance Analysis of NACA0009 and NACA4415 Airfoils. Journal of Polytechnic, 1-1, (2023). (Early view)

Hao W., Bashir M., Li C., Sun C.,Flow control for high-solidity vertical axis wind turbine based on adaptive flap. Energy Conversion and Management 249, 114845, 2021.

Hassanpour M., Azadani L.N., Aerodynamic optimization of the configuration of a pair of vertical axis wind turbines. Energy Conversion and Management 238, 114069, 2021.

Howell R., Qin N., Edwards J., Durrani N., Wind tunnel and numerical study of a small vertical axis wind turbine. Renewable. Energy 35(2), 412-422, 2010.

Hu Y., Rao S.S., Robust design of horizontal axis wind turbines using taguchi method. Journal of Mechanical Design 133(11), 111009, 2011.

Jiang Z.C, Doi Y., Zhang S.Y., Numerical investigation on the flow and power of small-sized multi-bladed straight Darrieus wind turbine. Journal of Zhejiang University-SCIENCE A 8(9), 1414-1421, 2007.

Jones W.P., Launder B.E. The calculation of low-Reynolds-number phenomena with a two-equation model of turbulence. International Journal of Heat and Mass Transfer 16(6), 1119–1130, 1973.

Joo S., Choi H., Lee J., Aerodynamic characteristics of two-bladed H-Darrieus at various solidities and rotating speeds. Energy 90, 439-451, 2015.

Kaya A.F., Tanürün H.E., Acır A., Numerical investigation of radius dependent solidity effect on H-type vertical axis wind turbines. Journal Of Polytechnic 25(3), 1007-1019, 2022.

Kaya, A.F., Investigation of a Rib Structure Effect on the Aerodynamic Performance of a Plain Flapped Symmetrical Airfoil. Journal of Polytechnic 1-1, 2023. (Eaerly view)

Lee Y.T., Lim H.C., Numerical study of the aerodynamic performance of a 500 W Darrieus-type vertical-axis wind turbine. Renewable Energy 83, 407-415, 2015.

Li Q., Maeda T., Kamada Y., Murata J., Furukawa K., Yamamoto M., Effect of number of blades on aerodynamic forces on a straight-bladed vertical axis wind türbine, Energy 90(1), 784-795, 2015.

Li S., Li Y., Numerical study on the performance effect of solidity on the straight-bladed vertical axis wind turbine. 2010 Asia-Pacific power and energy engineering conference (IEEE), March 28-31, 2010, pp. 1-4, Chengdu, China.

Liang C., Xi D., Zhang S., Yang Q., Effects of Solidity on Aerodynamic Performance of H-Type Vertical Axis Wind Turbine. 2nd International Symposium on Resource Exploration and Environmental Science 170(4), 042061, April 28-29, Ordos, China, 2018.

Liu, S., Ong M.C., Obhrai C., Gatin I., Vukcevic V., Influences of free surface jump conditions and different k-ω SST turbulence models on breaking wave modelling. Ocean Engineering 217, 107746, 2020.

Parra T., Uzarraga C., Gallegos A., Castro F., Influence of solidity on vertical Axis wind turbines. International Journal of Applied Mathematics, Electronics and Computers 3(3),215-207, 2015.

Qasemi K., Azadani L.N., Optimization of the power output of a vertical axis wind turbine augmented with a flat plate deflector. Energy 202:117745, 2020.

Roh S.C., Kang S.H., Effects of a blade profile, the Reynolds number, and the solidity on the performance of a straight bladed vertical axis wind turbine. Journal of Mechanical Science and Technology 27(11), 3299-3307, 2013.

Sengupta, A.R., Biswas, A., Gupta, R., Studies of some high solidity symmetrical and unsymmetrical blade H-Darrieus rotors with respect to starting characteristics, dynamic performances and flow physics in low wind streams. Renewable Energy 93:536-547, 2016.

Şahin İ., Acir, A., Numerical and experimental investigations of lift and drag performances of NACA 0015 wind turbine airfoil. International Journal of Materials, Mechanics and Manufacturing, 3: 22-25, (2015).

Tangler J.L., The evolution of rotor and blade design. Presented at the American Wind Energy Association WindPower 2000 April 30-May 4, 2000, California.

Tanürün H.E, Acır A., Modifiye edilmiş NACA-0015 kanat yapısında tüberkül etkisinin sayısal analizi, Politeknik Dergisi 22(1), 185-195, 2019.

Tanürün H.E., Acır A., Investigation of the hydrogen production potential of the H-Darrieus turbines combined with various wind-lens. International Journal of Hydrogen Energy 47(55), 23118-23138, 2022.

Tanürün H.E., Ata İ., Canlı M.E., Acır A., Farklı Açıklık Oranlarındaki NACA-0018 Rüzgâr Türbini Kanat Modeli Performansının Sayısal ve Deneysel İncelenmesi, Politeknik Dergisi 23(2), 371-381, 2020.

Tanürün, H.E., Akın A.G., Acır A., Rüzgâr Türbinlerinde Kiriş Yapısının Performansa Etkisinin Sayısal Olarak İncelenmesi, Politeknik Dergisi 24(3), 1219-1226, 2021.

Wang L., Tan A.C.C., Cholette M., Gu Y., Comparison of the effectiveness of analytical wake models for wind farm with constant and variable hub heights. Energy Conversion and Management 124:189-202, 2016.

Wang Z., Ozbay A., Tian W., Hu H., An Experimental study on the aerodynamic performances and wake characteristics of an innovative dual-rotor wind turbine. Energy 147, 94-109, 2018.

Wang Z., Tian W., Hu H., A comparative study on the aeromechanic performances of upwind and downwind horizontal-axis wind turbines. Energy Conversion and Management 163, 100–110, 2018.

Wang Z., Wang Y., Zhuanga M., Improvement of the aerodynamic performance of vertical axis wind turbines with leading-edge serrations and helical blades using CFD and Taguchi method. Energy Conversion and Management 177, 107-121, 2018.

Wilcox D.C., Reassessment of the scale-determining equation for advanced turbulence models. American Institute of Aeronautics and Astronautics (AIAA) 26(11), 1299–1310, 1998.

Zuo W., Wang X., Kang S., Numerical simulations on the wake effect of H-type vertical axis wind turbines. Energy 106, 691–700, 2016.

JOURNAL of
MATERIALS and MECHATRONICS:A

e-ISSN 2717-8811
JournalMM, 2023, 4(2), 373-383
https://doi.org/10.55546/jmm.1281984

Araştırma Makalesi / Research Article

Araçlarda Askı Koluna Etki Eden Yükler İçin Hesaplama Yönteminin Geliştirilmesi

Süleyman SOYDAŞ[1*], Talip ÇELİK[2], Halil İbrahim SARAÇ[3]

[1] Kocaeli Üniversitesi, Mühendislik Fakültesi, Makine Mühendisliği Bölümü, Kocaeli, Türkiye,
ORCID ID: https://orcid.org/0000-0002-3542-5805, suleyman.soydas@kocaeli.edu.tr
[2] Kocaeli Üniversitesi, Teknoloji Fakültesi, Biyomedikal Mühendisliği Bölümü, Kocaeli, Türkiye,
ORCID ID: https://orcid.org/0000-0003-0033-2454, talip.celik@kocaeli.edu.tr
[3] Kocaeli Üniversitesi, Mühendislik Fakültesi, Makine Mühendisliği Bölümü, Kocaeli, Türkiye,
ORCID ID: https://orcid.org/0000-0002-3414-3582, sarac@kocaeli.edu.tr

Geliş/ Received: 12.04.2023; **Kabul / Accepted:** 03.08.2023

ÖZET: Bu çalışmada araç konfor ve güvenliği için etkin bir rolü olan süspansiyon sisteminin denge konfigürasyonu kullanılarak analitik açıdan bir statik modeli oluşturulmuştur. Bazı literatür çalışmalarında aksın yük taşıdığı kabul edilirken bazılarında ise yük taşımadığı kabul edilmiştir. Bu nedenle matematiksel model iki durum için değerlendirilmiş, denklemler aksın yük taşıması ve taşımaması durumlarına göre ayrı ayrı incelenmiştir. Çalışmada süspansiyon sistemine ait statik denge şartları kapsamlı bir şekilde dikkate alınmış, analitik model genel bir formülle ifade edilmiştir. Bu sayede MacPherson süspansiyon sistemlerinde askı koluna etki eden yüklemeler ve askı kolu sınır şartları ortaya çıkarılmıştır. Sonuç olarak elde edilen denklemler ile MacPherson süspansiyon sisteminde askı koluna etki eden yükleri ortaya koymuştur. Bu çalışma ile bu tarz askı kolları üzerinde mukavemet analizi ve optimizasyon çalışmaları yapacak araştırmacılar için kullanılabilir denklemler ortaya çıkarılmıştır.

Anahtar Kelimeler: Askı Kolu, Optimizasyon, Yük ve Sınır Şartları, Aks.

*Sorumlu yazar / Corresponding author: suleyman.soydas@kocaeli.edu.tr

Bu makaleye atıf yapmak için /To cite this article

Soydaş, S., Çelik, T., Saraç, H.İ. (2023). Araçlarda Askı Koluna Etki Eden Yükler İçin Hesaplama Yönteminin Geliştirilmesi. Journal of Materials and Mechatronics: A (JournalMM), 4(2), 373-383.

Development of the Calculation Method for the Loads Acting on the Lower Control Arm in Vehicles

ABSTRACT: In this study, an analytical static model was created by using the balance configuration of the suspension system, which has an active role in vehicle comfort and safety. In some literature studies, it is accepted that the axle carries a load, while in others it is accepted that it does not carry a load. For this reason, the mathematical model was evaluated for two cases, and the equations were examined separately according to the axle load bearing and non-load bearing conditions. In the study, the static equilibrium conditions of the suspension system were taken into account in detail, and the analytical model was expressed with a general formula. In this way, the loadings affecting the suspension arm and the limit conditions of the suspension arm have been revealed in MacPherson suspension systems. With the resulting equations, MacPherson revealed the loads acting on the suspension arm in the suspension system. With this study, usable equations have been revealed for researchers who will carry out strength analysis and optimization studies on such suspension arms.

Keywords: Control Arm, Optimization, Load and Boundary Condition, Axle.

1. GİRİŞ

Günümüzde araç tasarımlarında yakıt tasarrufu sağlamak çok önemlidir. Ayrıca elektrikli araçlarda, aracın maksimum menzilini arttırabilmek için aracın hafif olması gerekir. Aynı zamanda hafiflikle birlikte dayanım da önemlidir. Aracın hem hafif olması hem de mukavemetli olması, güvenlik ve çevre kirliliği açısından olumlu sonuçlar verir. Bir aracın en önemli aksamlarından biri askı koludur (control arm). Süspansiyon sistemi için çok önemli parça olan askı kolunun yeterli mukavemeti yanında hafifliği de önemlidir (Wang and Chen, 2019; Tang ve ark., 2014; Carello and Airale, 2014). Araçlarda askı kolu parçası aracın stabilitesi açısından çok önemli parçalardan birisidir. Bu parçanın tasarımı yıllar içerisinde gelişmiş ve günümüzde malzeme teknolojisinin ve optimizasyon yöntemlerinin gelişmesi ile daha hafif ve mukavemetli parçalar haline gelmiştir (Song ve Zhao, 2017; Gillespie, 2021). Birçok çalışmada bu askı kolunun şekil, ölçü veya topoloji optimizasyonları yapılmıştır (Fuchs ve Salmon, 2011; Kutlak ve Uygur, 2014; Pachapuri ve ark., 2021; Song ve Zhao, 2017; Gadade, 2015; Tang ve ark., 2014). Ancak bu kapsamda yapılan sonlu elemanlar çalışmalarında askı koluna etki eden yükler basit hesaplamalar ile elde edilerek analize tanımlanmış ve bu şekilde optimizasyonlar yapılmıştır (Barton ve Fieldhouse; Yende ve Burande, 2020).

Askı kolu aparatı genellikle araçlara burç ve küresel mafsallar kullanılarak yerleştirilir. Bu sebepten dolayı askı kolunun serbestlik dereceli tasarıma bağlı olarak analizlere doğru tanımlanmalıdır (Kim ve ark., 2014). Bazı çalışmalarda burcun ve/veya küresel mafsalların bağlı olduğu noktadan rijit sabitleme verilmektedir (Yende ve Burande, 2020). Bu durum sonlu elemanlar çalışmalarının doğruluğunu etkiler. Çünkü sonlu elemanlar çalışmasında sınır şartları aynı gerçek ortamdaki gibi tanımlanmazsa elde edilen sonuçlar yanlış olacaktır. Diğer bir değişle gerçek ortam şartları simüle edilemeyecektir. Ayrıca, yanlış sınır şartlarının tanımlanması gereğinden fazla veya gereğinden az parça çıkarılmasına sebep olacak, bu durum da ya yetersiz mukavemete ya da etkin olmayan bir optimizasyona yol açacaktır. Literatürde optimizasyonun doğruluğunu arttırmak için farklı yaklaşımlar sunulmuştur (Alexandru, 2022; Pachapuri ve ark., 2021; Wang ve Chen, 2019). Tang Liang ve ve ark. (2014) yapmış oldukları optimizasyon çalışmasında plastik burç ve küresel mafsalları da dikkate almışlar ve buna göre daha doğru optimizasyon gerçekleştirdiklerini

belirtmişlerdir. Diğer bir çalışmada ticari bir aracın A tipi askı kolu tasarımı ve analizi gerçekleştirilmiştir (Gadade, 2015).

Askı kolu optimizasyon çalışmaları için diğer önemli bir nokta doğru kuvvet tanımlanmasıdır. Genellikle sonlu elemanlar çalışmalarında analizi basitleştirmek için askı kolu tek modellenir ve üzerine kuvvet ve sınır şartları uygulanarak çözümlemeye gidilir (Pachapuri ve ark., 2021; Song ve Zhao, 2017; Gadade, 2015; Tang ve ark., 2014). Askı koluna uygulanacak kuvveti de doğru hesaplamak gerekmektedir. Bir araç süspansiyon sisteminde askı koluna etki eden yükleri doğru hesaplamak ve her araç için ayrı ayrı hesap yapmak karmaşık ve zaman alıcı bir işlemdir (Heißing ve Ersoy, 2011). Bu sebeple aracın fiziksel ve tasarımsal özelliklerine bağlı olarak belirlenen noktaların koordinatlarından askı koluna etki eden yükü hesaplayan bir denklem çıkarmak hem optimizasyon çalışmalarında araştırmacılara kolaylık sağlayacak, hem de arge mühendisleri açısından yol gösterici olacaktır (Barton ve Fieldhouse, 2018).

Bu çalışmada askı kolu parçasının ve süspansiyon sisteminin şematik olarak tasarımı yapılmış ve buna bağlı olarak genel bir denklem çıkarılmıştır. Bu denklem sayesinde tekere etki eden kuvvete bağlı olarak askı koluna ve süspansiyon sistemine etki eden kuvvetler hesaplanmıştır. Bu çalışma ile askı kolu çalışması yapacak araştırmacıların askı koluna etki eden yükleri kolay bir şekilde hesaplamasını sağlayacak denklem ortaya çıkarılmıştır.

2. MATERYAL VE YÖNTEM

Araçlarda süspansiyon sistemi dikkate alındığında (Şekil 1) yük taşıyan sistemler amortisör ve askı koludur. Amortisör temel olarak düşey doğrultudaki yükü taşırken askı kolu yatay doğrultuda etki eden yükleri karşılamaktadır.

Araçlarda askı koluna gelen kuvvetleri etkileyen dinamik yol koşulları, araç ivmelenmesi vb. gibi bazı durumlar vardır (Putra ve Ikbal, 2021). Bunun yanı sıra Şekil 1'de araç teker bağlantı ve süspansiyon sistemine göre aks da belli bir yükü karşılamaktadır.

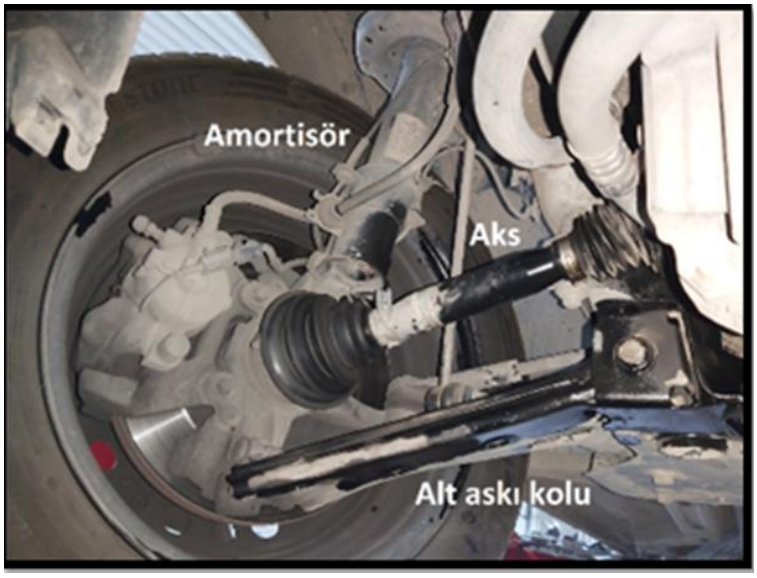

Şekil 1. Alt askı kolu, aks, yay ve ön teker bağlantısı

Bazı çalışmalarda aksın yük taşıdığı kabul edilirken bazılarında yük taşımadığı kabul edilmiştir (Kutlak ve Uygur, 2014). Bazı çalışmalarda ise aksın askı koluna etki eden yükün %50'ini taşıdığı

kabul edilmiştir (Khode ve ark., 2017) Bu durumda aksın yük taşıma durumuna göre askı koluna etkiyen yükler de önemli derecede değişebilmektedir. Ancak bu süspansiyon sistemlerinde aksın temel görevi yük taşımak olmadığı için bu çalışmada elde edilen denklemler aksın yük taşıması ve taşımaması durumlarına göre ayrı ayrı incelenmiştir ve buna göre tekere etkiyen yüke göre aksın da yük taşıma durumu değerlendirilmiştir.

2.1 Hafif Ticari Araç Süspansiyonu Matematiksel Modeli

Matematiksel modeli çıkarılacak aracın Şekil 2'de teker ve aksona etki eden yükleri vektörel olarak gösterilmiştir. D noktası tekere etki eden yükün merkezini, C noktası amortisör direğinin aksona bağlantısını, B noktası akson ile askı kolunun bağlantısını, E noktası aksın akson içinden geçtiği bölgenin merkezini ve A noktası ise askı kolunun araca bağlantısını göstermektedir. Şekil 2'de xy düzlemi yatay düzlemi, xz düzlemi ise düşey düzlemi ifade etmektedir. y ekseni ise aracın önünden arkasına doğru olan eksen olarak kabul edilmiştir.

Denklemlerin doğru bir şekilde çıkarılabilmesi için bağlantı noktalarının bağlantı şekilleri, yani serbestlik dereceleri çok iyi tanımlanmalıdır. Askı kolunun aksona bağlandığı noktada (B noktası) z eksenine göre kuvvet ve y eksenine göre moment oluşmaz. Çünkü tepki kuvvetinin oluşabilmesi için sınırlama olması gerekir. Askı kolunun hareketi incelendiğinde B noktasından yukarı etki eden kuvvete tepki oluşturmaz, çünkü A noktasından y eksenine göre dönme serbestliği vardır. Bu sebepten dolayı askı kolunun B noktasında x ve y eksenleri yönünde yük taşır, ancak z yönünde yük taşımaz. Tekere etki eden z yönündeki kuvvetler sebebi ile oluşan hareketi ise aksonun C noktasına bağlanan helezon yaylar engeller. Aynı şekilde E noktasından bağlanan akson, sadece x ekseninde yük taşır ve diğer yönlerde serbesttir.

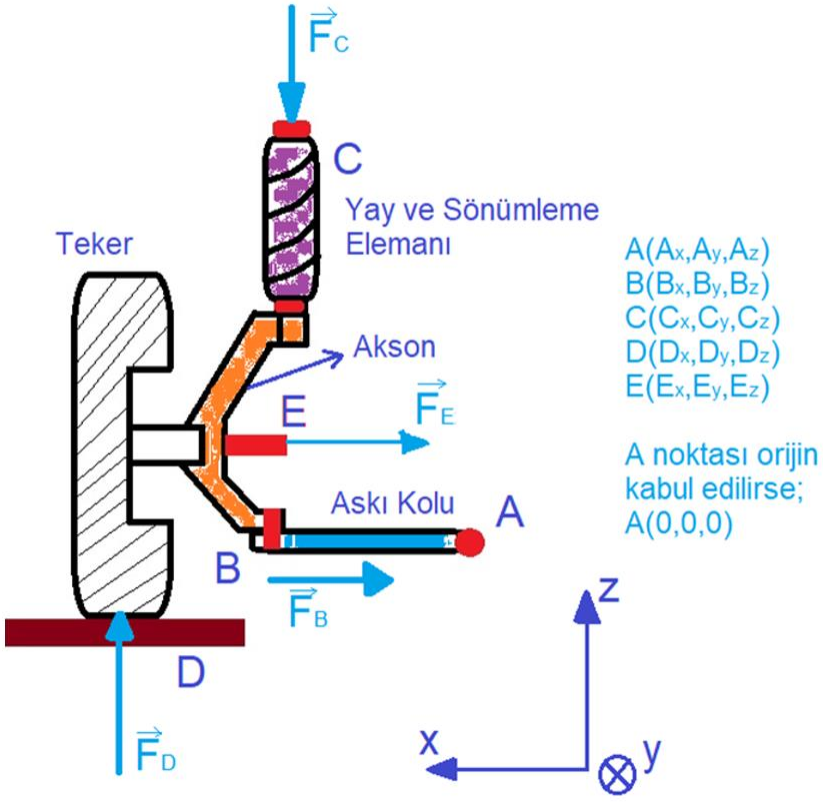

Şekil 2. Hafif ticari araç süspansiyonu matematiksel modeli

Bu bilgilere göre kuvvetleri vektörel olarak;

$$\vec{F}_{teker} = F_x\vec{\imath} + F_y\vec{j} + F_z\vec{k} \quad (1)$$

$$\vec{F}_c = F_{Cx}\vec{\imath} + F_{Cy}\vec{j} + F_{Cz}\vec{k} \quad (2)$$

$$\vec{F}_{aks} = F_{Ex}\vec{\imath} \quad (3)$$

$$\vec{F}_{askı} = F_{Bx}\vec{\imath} + F_{By}\vec{j} \quad (4)$$

Denklem (1), (2), (3) ve (4) şeklinde yazılabilir.

Sistem bağlantı noktaları dikkate alındığında vektörel olarak denge denklemleri:

$$\sum \vec{M}_c = 0 \quad (5)$$

$$\vec{r}_{CD} \text{ x } \vec{F}_{teker} + \vec{r}_{CE} \text{ x } \vec{F}_{aks} + \vec{r}_{CB} \text{ x } \vec{F}_{askı} + M_C = 0 \quad (6)$$

Denklem 5 ve 6'daki gibi yazılabilir. $\vec{r}$ yer vektörü olmak üzere vektörler yerine yazıldığında;

$$\left[(D_x - C_x)\vec{\imath} + (D_y - C_y)\vec{j} + (D_z - C_z)\vec{k}\right] x \left[F_x\vec{\imath} + F_y\vec{j} + F_z\vec{k}\right] + \left[(E_x - C_x)\right]\vec{\imath} + (E_y - C_y)\vec{j} + (E_z - C_z)\vec{k}]x[F_{Ex}\vec{\imath}] + \left[(B_x - C_x)\vec{\imath} + (B_y - C_y)\vec{j} + (B_z - C_z)\vec{k}\right]x\,[F_{Bx}\vec{\imath} + F_{By}\vec{j}] + [M_{Cx}\vec{\imath} + M_{Cy}\vec{j}] = 0 \quad (7)$$

Denklem 7 yazılabilir. Bu denklemde birinci kısım a, ikincisi b, üçüncüsü c ve moment kısmı d olarak alırsa a+b+c+d=0 formatında yazılır. Denklemdeki kısımlar ayrı ayrı çözümlenirse;

$$\text{a)}\quad \vec{r}_{CD} \text{ x } \vec{F}_{teker} = \begin{bmatrix} i & j & k \\ (D_x - C_x) & (D_y - C_y) & (D_z - C_z) \\ F_x & F_y & F_z \end{bmatrix} \begin{matrix} i & j \\ (D_x - C_x) & (D_y - C_y) \\ F_x & F_y \end{matrix} \quad (8)$$

Denklem 8 yazılır. Buradan;

$$\vec{r}_{CD} \text{ x } \vec{F}_{teker} = -F_x(D_y - C_y)\vec{k} - F_y(D_z - C_z)\vec{\imath} - F_z(D_x - C_x)\vec{j} + F_z(D_y - C_y)\vec{\imath} + F_x(D_z - C_z)\vec{j} + F_y(D_x - C_x)\vec{k} \quad (9)$$

elde edilir. Denklem 9'da değerler i, j ve k parantezinde toplanırsa;

$$\vec{r}_{CD} \text{ x } \vec{F}_{teker} = \left[F_z(D_y - C_y) - F_y(D_z - C_z)\right]\vec{\imath} + [F_x(D_z - C_z) - F_z(D_x - C_x)]\vec{j} + \left[F_y(D_x - C_x) - F_x(D_y - C_y)\right]\vec{k} \quad (10)$$

Denklem 10 oluşur. Denklem 7'nin ikinci kısmı (b) için;

$$\text{b) } \vec{r}_{CE} \text{ x } \vec{F}_{aks} = \begin{bmatrix} i & j & k \\ E_x - C_x & E_y - C_y & E_z - C_z \\ F_{Ex} & 0 & 0 \end{bmatrix} \begin{matrix} i & j \\ E_x - C_x & E_y - C_y \\ F_{Ex} & 0 \end{matrix} \quad (11)$$

Denklem 11 yazılır ve determinant açılırsa;

$$\vec{r}_{CE} \text{ x} \overrightarrow{F}_{aks} = F_{Ex}\,(E_z - C_z)j - F_{Ex}\big(E_y - C_y\big)k \tag{12}$$

Denklem 12 oluşur. Denklem 7'nin üçüncü kısmı (c) için;

$$\text{c)}\quad \vec{r}_{CB} \text{ x} \overrightarrow{F}_{askı} = \begin{bmatrix} i & j & k \\ B_x - C_x & B_y - C_y & B_z - C_z \\ F_{Bx} & F_{By} & 0 \end{bmatrix} \begin{matrix} i & j \\ B_x - C_x & B_y - C_y \\ F_{Bx} & F_{By} \end{matrix} \tag{13}$$

Denklem 13 yazılır ve determinant açılırsa;

$$\vec{r}_{CB} \text{ x} \overrightarrow{F}_{askı} = -F_{Bx}\,\big(B_y - C_y\big)k - F_{By}(B_z - C_z)i - 0 + 0 + F_{Bx}(B_z - C_z)j + F_{By}(B_x - C_x)k \tag{14}$$

Denklem 14 yazılır. i, j ve k'nın katsayıları aynı parantezde yazılırsa;

$$\vec{r}_{CB} \text{ x} \overrightarrow{F}_{askı} = [F_{Bx}(B_z - C_z)]j + [F_{By}(B_x - C_x) - F_{Bx}\,\big(B_y - C_y\big)]k - F_{By}(B_z - C_z)i \tag{15}$$

Denklem 15 elde edilir. Denklem 7'nin dördüncü kısmı (d) zaten moment olarak yazılmıştır. Denklem 7;

$$\text{a+b+c+d= 0} \tag{16}$$

formatında Denklem 16'daki gibi yazılmıştı. Buradan Denklem 10, 12 ve 15'de elde edilen eşitlikler yerine yazılır ve i, j ve k'nın katsayıları aynı parantezde yazılırsa;

$$\big[F_z\big(D_y - C_y\big) - F_y(D_z - C_z) - F_{By}(B_z - C_z) + M_{Cx}\big]\vec{\imath} + \big[F_x(D_z - C_z) - F_z(D_x - C_x) + F_{Ex}(E_z - C_z) + F_{Bx}(B_z - C_z) + M_{Cy}\big]\vec{\jmath} + [F_y(D_x - C_x) - F_x\big(D_y - C_y\big) - F_{Bx}\big(B_y - C_y\big) - F_{Ex}\big(E_y - C_y\big) + F_{By}(B_x - C_x)]\vec{k} = 0 \tag{17}$$

Denklem 17 oluşur. Buradan i, j ve k katsayıları 0'a eşittir. Bu sebepten dolayı;

$$F_z\big(D_y - C_y\big) - F_y(D_z - C_z) - F_{By}(B_z - C_z) + M_{Cx} = 0 \tag{18}$$

$$F_x(D_z - C_z) - F_z(D_x - C_x) + F_{Ex}(E_z - C_z) + F_{Bx}(B_z - C_z) + M_{Cy} = 0 \tag{19}$$

$$F_y(D_x - C_x) - F_x\big(D_y - C_y\big) - F_{Bx}\big(B_y - C_y\big) - F_{Ex}\big(E_y - C_y\big) + F_{By}(B_x - C_x) = 0 \tag{20}$$

Denklem 18, 19 ve 20'deki eşitlikler elde edilir. Askı koluna etki eden yükler olan F_{Bx} ve F_{By} değerlerini bulabilmek için yukarıdaki üç denklemden (Denklem 18, 19 ve 20) yararlanılır. Askı koluna etki edebilecek maksimum yükleri bulabilmek için Denklem 18 ve 19'da M_{Cx}ve M_{Cy} değerleri 0 kabul edilirse Denklem 18'den F_{By} değeri;

$$F_{By} = \frac{F_z\big(D_y - C_y\big) - F_y(D_z - C_z)}{(B_z - C_z)} \tag{21}$$

şeklinde Denklem 21'deki gibi elde edilir. Denklem 19'dan ise F_{Bx} ve F_{Ex} arasındaki ilişki bulunabilir. Denklem 19'dan;

$$F_{Bx}(B_z - C_z) = F_z(D_x - C_x) - F_x(D_z - C_z) - F_{Ex}(E_z - C_z) \quad (22)$$

$$F_{Bx} = \frac{F_z(D_x - C_x) - F_x(D_z - C_z) - F_{Ex}(E_z - C_z)}{(B_z - C_z)} \quad (23)$$

Denklem 22 bulunur ve bu denklemden de F_{Bx} yalnız bırakılarak Denklem 23 bulunur. Aksın yük taşımadığı kabul edildiğinde, yani F_{Ex} değeri 0 ise, F_{Bx} değeri;

$$F_{Bx} = \frac{F_z(D_x - C_x) - F_x(D_z - C_z)}{(B_z - C_z)} \quad (24)$$

Denklem 24'den elde edilir. Denklem 21 ve 23'den elde edilen değerler askı koluna etki eden maksimum değerler olacaktır. Çünkü aksın yük taşımadığı ve ayrıca süspansiyon sisteminin şasi bağlantı noktasındaki tepki momentlerinin de olmadığı kabul edilmiştir.

F_{Bx} değeri Denklem 20'de yerine yazılırsa F_{Ex} değeri bulunabilir. Diğer yandan Denklem 20'de F_{Ex} değerinin katsayısı olan $(E_y - C_y)$ sıfır değerine eşittir. Çünkü tasarım açısından incelendiğinde aksın bağlantı noktasının y ekseni ile süspansiyon sisteminin şasiye bağlantı noktasının y ekseni aynı hizadadır. Buradan Denklem 20;

$$F_y(D_x - C_x) - F_x(D_y - C_y) - F_{Bx}(B_y - C_y) + F_{By}(B_x - C_x) = 0 \quad (25)$$

Denklem 25'deki gibi yazılabilir. Diğer yandan literatürde (Khode ve ark., 2017) belirtildiği gibi aksın askı koluna etki eden kuvvetin %50'sini taşıdığı kabul edilirse;

$$F_{Ex} = \frac{(F_{Bx})}{2} \quad (26)$$

Denklem 26 oluşur. Denklem 23'de Denklem 26'daki F_{Bx} değeri yerine yazılırsa;

$$2.F_{Ex} = \frac{F_z(D_x - C_x) - F_x(D_z - C_z) - F_{Ex}(E_z - C_z)}{(B_z - C_z)} \quad (27)$$

Denklem 27 elde edilir. Buradan;

$$F_{Ex} = \frac{1}{3}\frac{[F_z(D_x - C_x) - F_x(D_z - C_z)]}{(B_z - C_z)} \quad (28)$$

Denklem 28 ile birlikte F_{Ex} değeri bulunabilir.

Bu denklemler Microsoft Excel programı kullanılarak, bu çalışma kapsamında dikkate alınan hafif ticari aracın askı koluna etki eden yüklemeler bulunmuştur. Öncelikle süspansiyon sistemindeki bağlantı noktalarının koordinatları süspansiyon sistemi üzerinden ölçümler alınarak belirlenmiştir. Buna göre askı koluna etki eden kuvvetlerin şiddeti ve yönü hesaplanabilmiştir.

3. BULGULAR VE TARTIŞMA

Bu çalışmada hafif bir ticari aracın süspansiyon sisteminin matematiksel modeli statik biliminin kuralları dikkate alınarak çıkarılmıştır. Özellikle askı koluna gelen yükü tayin etmek için çıkarılan bu denklemler, askı kolu üzerine düşen yükü doğru tayin etmeyi hedeflemiştir. Çünkü Mac Pherson süspansiyon sistemlerinde askı kolu optimizasyonu çalışmalarında sınır şartlarının farklı belirlendiği görülmüştür (Khode ve ark., 2017; Kim ve ark., 2014; Kutlak ve Uygur, 2014). Birçok çalışmada askı kolunun şasiye bağlantı noktaları ankastre bağlantı olarak kabul edilmiş ve askı kolunun hareketi her yönde kısıtlanmıştır (Khode ve ark., 2017; Yende ve Burande, 2020). Bu şekilde düşünüldüğünde askı koluna z ekseni yönünde çok yüksek kuvvetler uygulanmıştır ve bu sebeple ortaya çıkan optimizasyon askı kolu daha çok hafifleştirileceğine daha az ağırlık azaltılabilmiştir. Aslına bakıldığında askı kolu şasiye z yönünde hareket serbestliği verecek kapı menteşesi tipi bağlantı yapıldığı görülmektedir. Literatürdeki bu karmaşayı ortadan kaldırmak ve askı kolu optimizasyon çalışmalarında daha doğru ve etkili optimizasyon için bu çalışma gerçekleştirilmiştir.

Birçok çalışmada askı kolu optimizasyonlarında z yönünde yük uygulanmış ve sonuçlar buna göre değerlendirilmiştir. Ancak bu çalışmanın materyal metot bölümünde de bahsedildiği üzere bağlantı noktalarının serbestlik dereceleri, yani hareket kabiliyeti iyi tahmin edilmelidir. Eğer bir bağlantıda bir eksene göre dönme serbestisi varsa bu yönde tepki kuvveti oluşmamaktadır. Bu sebeple de bu çalışmada dikkate alınan Mac Pherson süspansiyon sistem tasarımlarında askı kolu z yönünde yük taşımaz ve bu tasarımlarda askı kolu z yönünde yük taşıması için tasarlanmamaktadır. Askı kolunun temel görevi tekerlerin dışa doğru hareketini ve tekerin öne veya arkaya hareketini engellemektir.

Günümüzde optimizasyon vazgeçilmez bir mühendislik konusu olmuştur. Çünkü, mukavemetten ödün vermeden parçaların hafifleştirilmesi hem maliyet hem de ağırlık açısından önemli kazançlar sunmaktadır. Bu sebepten dolayı özellikle araçlarda hem yakıt tasarrufu için hem de elektrikli araçlarda menzili arttırmak için çok sıklıkla kullanılabilmektedir. Ancak doğru hesaplamalar için mukavemet analizlerinde sınır şartları ve kuvvet durumları doğru tanımlanması çok önemlidir (Blundell ve Harty, 2004). Parçaların sınır şartları tanımlanırken gerçekteki hareket serbestisi durumları birebir analize tanımlanması elzemdir. Eğer bir parça sadece bir eksende dönme serbestliği varsa o serbestlik mutlaka analize tanımlanmalıdır. Yoksa olması gereken az veya çok parça azaltılmaları gerçekleşebilir ve bu sonuçlara göre elde edilen parçalar gerçek görevlerini yerine getiremeyebilir.

Bu çalışmada bazı eksik noktalar vardır. Bunlardan birincisi, sadece statik durumlar için geçerli olmasıdır. Diğeri ise, askı kolunun şasiye bağlandığı burç gibi elemanlarda plastik aksamlar bulunmaktadır ve bu aksamlar ister istemez hareket kısıtlılığı oluşturmaktadır. Ancak bu çalışmada en kötü durumlar dikkate alınarak askı koluna etki eden yükler değerlendirildiği için yeterli seviyede önemli sonuçlar vermektedir.

4. SONUÇ

Bu çalışmada dikkate alınan askı kolunda bağlantı noktalarının hareket serbestliğine göre sınır şartları Şekil 3'teki gibi olmalıdır. A ve F noktalarından şasiye bağlantı noktalarında oluşacak tepki kuvvetleri gösterilmiştir. A noktasında kapı menteşesi tarzı sabitleme vardır ve y ekseninde dönme serbestliği vardır. Bu sebepten dolay A noktasında rotasyon y tepkisi oluşmayacaktır. Ayrıca F noktasında da sadece lineer hareketler kısıtlanmıştır ve bu sebepten dolayı F noktasından da lineer yöndeki x, y ve z yönünde tepki oluşacaktır.

Askı kolu B noktasından aksona bağlıdır ve aksondan gelen x ve y yönündeki yükleri karşılar, fakat z yönünden gelen tekerlek kuvvetlerini A ve F noktalarının dönme serbestliği sebebiyle taşımaz. MacPherson süspansiyon sistemlerinde tekerlekten gelen dikey yükleri yay ve bununla birlikte çalışan sönümleme elemanı karşılar ve bu yükü araç şasisine iletir. Bu tarz süspansiyon sistemlerinde askı kolu analizlerinin sınır şartları Şekil 3'te belirtildiği gibi yapılmalıdır.

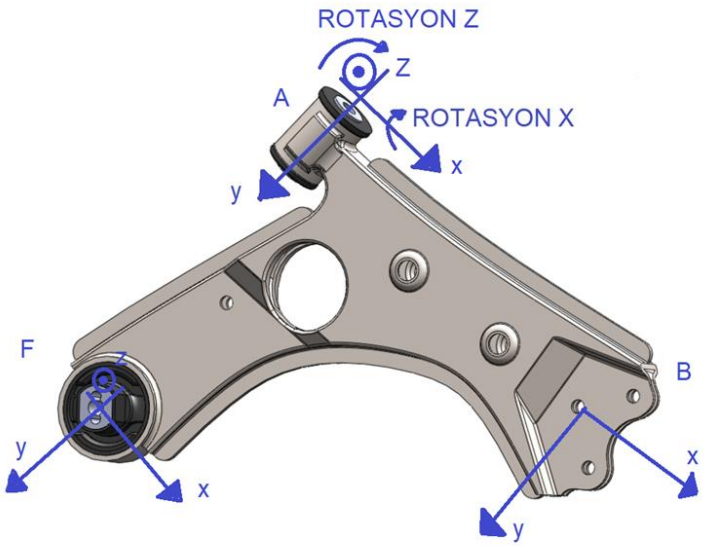

Şekil 3. MacPherson süspansiyon sisteminde askı kolu sınır şartları

Çizelge 1. Bir ticari araca ait süspansiyon sisteminin bağlantı noktaları koordinatları ve askı koluna etki eden kuvvet sonuçları

Nokta	x (cm)	y (cm)	z (cm)
A	0	0	0
B	30	5	0
C	25	0	70
D	35	0	-15
E	35	0	15
Kuvvetler (N)			
	F_{Bx}	F_{By}	F_{Ex}
Araç gross ağırlığında, duruyorken ve aks yük taşımadığı kabul edildiğinde	-528.57	0	0
Araç brüt ağırlığında, duruyorken ve aks yük taşımadığı kabul edildiğinde	-775.29	0	0
Araç gross ağırlığında, duruyorken ve aks yük taşıdığı kabul edildiğinde	-352.38	0	-176.2
Araç brüt ağırlığında, duruyorken ve aks yük taşıdığı kabul edildiğinde	-516.85	0	-258.43

*Aracın boş ağırlığı 14800 N ve Ön tekere gelen yükü 3700 N'dur

*Aracın brüt ağırlığı 21708 N ve ön tekere gelen yükü 5427 N'dur

Bu çalışmada dikkate alınan süspansiyon sistemi bir hafif ticari araca aittir. Bu aracın süspansiyon sistemi üzerinden alınan ölçülere göre koordinatlar Çizelge 1'de verilmiştir. Buna göre yukarıda çıkarılan denklemlere göre askı koluna etki eden yükler de Çizelge 1'de gösterilmiştir. Aracın boş ağırlığı 14800 N ve ön tekerlere gelen yük ise 3700 N'dur. Bu durumda aracın ön askı kolun etki eden yükler 528.27 N olarak hesaplanmıştır. Aracın brüt ağırlığında ise bu değer 775.29 N'a yükselmektedir. Bu değerler aksın yük taşımadığı kabul edildiğinde elde edilmektedir. Eğer aks yük taşıdığı kabul edilirse araç boş iken 352.38 N'a ve araç brüt ağırlığında ise 516.85 N'a düşmektedir. Aks ise maksimum 258.43 N olarak hesaplanmıştır. Tabi aracın farklı yol koşullarında tekere etkiyen yükler değiştikçe askı koluna etki eden yükler de değişecektir.

5. TEŞEKKUR

Bu makale Kocaeli Üniversitesi, Fen Bilimleri Enstitüsü, Makine Mühendisliği Anabilim Dalı'nda "Hafif ticari bir araçta kullanılan ön alt askı kolunun topoloji optimizasyonu" başlıklı doktora tezindeki veriler ve grafikler kullanılarak oluşturulmuştur.

6. ÇIKAR ÇATIŞMASI

Yazarlar, bilinen herhangi bir çıkar çatışması veya herhangi bir kurum/kuruluş ya da kişi ile ortak çıkar bulunmadığını onaylamaktadırlar.

7. YAZAR KATKISI

Süleyman Soydaş; çalışmanın modellenmesi, matematik modelinin çıkarılması ve veri analizi yönünden, Talip Çelik; matematik modelinin çıkarılması ve kontrolü, verilerin yorumlanması ve yazılması yönünden, Halil İbrahim Saraç; yazım kontrolü, sonuçların değerlendirilmesi, süreç takibi yönünden katkı sunmuştur.

8. KAYNAKLAR

Alexandru C., A Method for Finding the Static Equilibrium of the Non-steered Wheel Suspension Systems Used in Passenger Cars. Applied Sciences (Switzerland) 12 (14), 7122, 2022.

Barton D.C., Fieldhouse J.D., Steering systems, Automotive Chassis Engineering, Springer, First Edition, Germany, pp. 45-110, 2018.

Blundell M., Harty D., The Multibody Systems Approach to Vehicle Dynamics, Butterworth-Heinemann Publications, Germany, pp. 60-90, 2004. https://doi.org/10.1016/B978-0-7506-5112-7.X5000-3

Carello M., Airale A.G., Composite Suspension Arm Optimization for the City Vehicle XAM 2., Design and Computation of Modern Engineering Materials, Springer Link Publications, Germany, pp. 257-272, 2014.

Fuchs H., Salmon R, Lightweight MacPherson Strut Suspension Front Lower Control Arm Design Development. SAE International 01 (0562), 2011.

Gadade B., Design, analysis of A-type Front Lower Suspension Arm in Commercial Vehicle. International Research Journal of Engineering and Technology 2 (7), 759-766, 2015.

Gillespie T., Fundamental of Vehicle Dynamics, SAE International, Revised Edition, United State, pp. 50-250, 2021.

Heißing B., Ersoy M, The Chassis Handbook, Springer, First Edition, Germany, pp. 99-117, 2011.

Khode S.S., Patil P.A.N., Gaikwad P.A.B., Design Optimization of a Lower Control Arm of Suspension System in a LCV by Using Topological Approach. International Journal of Innovative Research in Science, Engineering and Technology, 6 (6), 11657-11665, 2017.

Kim D.H., Choi D.H., Kim H.S., Design Optimization of a Carbon Fiber Reinforced Composite Automotive Lower Arm. Composites Part B: Engineering, 58, 400-407, 2014.

Kutlak H., Uygur İ., Ticari Araç Sac Salıncak Düzeninin Sonlu Elemanlar Metodu ile Yorulma Analizi. Düzce Üniversitesi Bilim ve Teknoloji Dergisi, 2(1), 235-250, 2014.

Pachapuri M.S.A., Lingannavar R.G., Kelageri N.K., Phadate K.K., Design and Analysis of Lower Control Arm of Suspension System. Materials Today: Proceedings, 47, 2949-2956, 2021.

Putra T.E., Ikbal M, Heliyon Automotive Suspension Component Behaviors Driven on Flat and Rough Road Surfaces. Heliyon, 7, e07528, 2021.

Song Z., Zhao X., Research on Lightweight Design of Automobile Lower Arm Based on Carbon Fiber Materials. World Journal of Engineering and Technology, 05 (04), 730-742, 2017.

Tang L., Wu J., Liu J., Jiang C., Shangguan W. Bin., Topology Optimization and Performance Calculation for Control Arms of a Suspension. Advances in Mechanical Engineering, 6, 1-10, 2014.

Wang W., Chen X., Design Methodology for Wheel Corner Module Topology Based on Position and Orientation Characteristics. Mechanism and Machine Theory, 136 (4800), 122-140, 2019.

Yende S.V., Burande D.H., Static Structural Analysis and Topology Optimization of Lower Control Arm for LMV. The IUP Journal of Mechanical Engineering, 13 (2), 108-120, 2020.

e

JOURNAL of
MATERIALS and MECHATRONICS:A

e-ISSN 2717-8811
JournalMM, 2023, 4(2), 384-396
https://doi.org/10.55546/jmm.1309858

Araştırma Makalesi / Research Article

Evaluation of Mechanical Properties of PLA Auxetic Structures Produced by Additive Manufacturing

Ahu ÇELEBİ [1]*, Mustafa Mertcan İMANÇ[2]

[1] Manisa Celal Bayar Üniversitesi, Mühendislik Fakültesi, Metalurji ve Malzeme Mühendisliği Bölümü, Manisa, Türkiye, ORCID ID: https://orcid.org/0000-0003-0401-5384, ahu.celebi@cbu.edu.tr
[2] Manisa Celal Bayar Üniversitesi, Mühendislik Fakültesi, Metalurji ve Malzeme Mühendisliği Bölümü, Manisa, Türkiye, ORCID ID: https://orcid.org/0009-0004-7999-2096, mertcanimanc@icloud.com

Geliş/ Received: 05.06.2023; **Kabul / Accepted:** 08.08.2023

ABSTRACT: FDM (fused deposition modeling) is one of the most commonly used technologies in additive manufacturing. This technology is used to additively manufacture components from various polymer materials, mostly PLA (polylactic acid), etc. PLA filament is a widely used polymer for 3D printing due to its biodegradability, biocompatibility, and processability. In the study, PLA raw material and cellular auxetic structures were used in the design. Auxetic designs are called metamaterials, they are structures with advanced properties and can be obtained with various geometries. The auxetic designs used in the study are missing rib, re-entrant honeycomb and chiral. One of the biggest advantages of auxetic cellular materials is that it is not bulk material. Having a skeletal structure provides high strength at low density. Today, based on this mechanism, designs that can be used in engineering applications are being studied. It has an important place especially in the medical field, as well as in the areas where high precision and specific products are designed and produced. Considering its relationship with 3D printing technology, 3D printing enables the fabrication of auxetic structures for complex and personal designs. The novelty of auxetic structures comes from their topological features, which display counterintuitive response to the applied load. For the purpose of compare the properties of mechanical tensile, compression, surface roughness tests were applied. It is concluded that the presence of chiral structures improves mechanical performance. The chiral auxetic sample exhibited a maximum stress of 6.68 MPa, the missing-rib auxetic sample displayed a maximum stress of 2.26 MPa, and the re-entrant auxetic sample demonstrated a maximum stress of 3.68 MPa. These results obtained from the tests align well with the range reported in the literature, which falls between 1-12 MPa. The surface roughness of the all-auxtetic structure, perpendicular to the printing direction was higher than the measurements taken parallel to the printing direction.

Keywords: Additive Manufacturing, Fused Deposition Modeling, Auxetic design, PLA, Mechanical properties

*Sorumlu yazar / Corresponding author: ahu.celebi@cbu.edu.tr

Bu makaleye atıf yapmak için /To cite this article

Çelebi, A., İmanç, M.M. (2023). Evaluation of Mechanical Properties of PLA Auxetic Structures Produced by Additive Manufacturing. Journal of Materials and Mechatronics: A (JournalMM), 4(2), 384-396.

1. INTRODUCTION

The grater part of engineering materials exhibit a positive Poisson's ratio, but there are only a few materials that possess a negative Poisson's ratio. These materials are often called as auxetic materials (Anurag, 2010; Alderson, A. and Alderson, K.L, 2007; Baughman et al., 1998). The term auxetic is of Greek origin and comes from auxetikos and the meaning of the word tends to be extended. It was first used by Professor Ken Evans in 1991 (Evans, 1991). Unlike materials with positive poisson's ratio, auxetic materials expand as they are stretched and contract as they are pressed, an extraordinary property, as shown in Figure 1. (Luo, 2022). Although this feature has been known since the last century, its understanding as mechanics and logic and its application to materials started in the 1980s. For the first time, "foam" structures with negative Poisson ratio were published in Science by Rod Lakes in 1987 (Lakes, 1987).

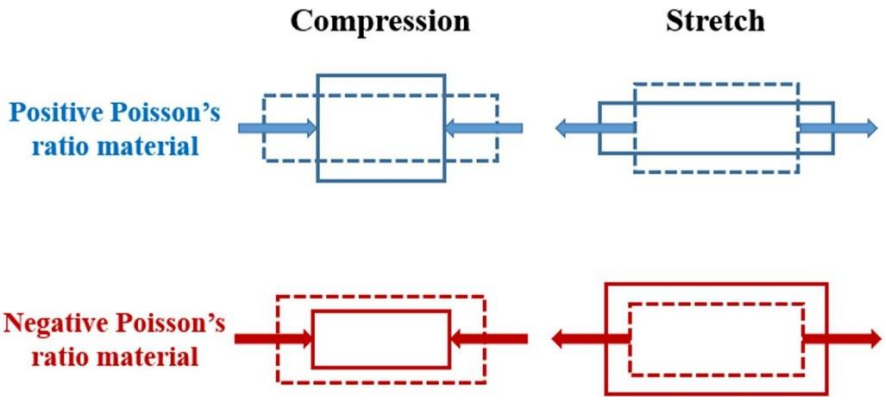

Figure 1. Deformation of conventional and auxetic materials (Luo, 2022)

Auxetic materials show an unusual feature by thickening when pulled, and there are some properties unique to these materials. This unique property makes them highly desirable for various industrial and biomedical applications. Auxetic materials are used in applications such as protective gear, smart textiles, impact-resistant materials, and tissue engineering (Joseph et al., 2021). Auxetic materials have a variety of distinct characteristics that render them extremely desirable in various applications. These characteristics include:

- Negative Poisson's ratio: Auxetic materials exhibit lateral expansion when subjected to stretching, making them highly effective in impact-resistant materials.
- High energy absorption: Auxetic materials can absorb high amounts of energy when subjected to impact, making them ideal for use in protective gear.
- High flexibility: Auxetic materials are highly flexible, making them ideal for use in smart textiles and wearable technologies.
- Biocompatibility: Auxetic materials are biocompatible, making them ideal for use in tissue engineering and medical implants.ibit acoustic behavior (Carneiro et al., 2013; Anurag, 2010; Guo et al., 2020).

Auxetic materials possess exceptional mechanical characteristics such as enhanced resistance to indentation, shear, fracture, and efficient energy absorption. Nonetheless, the stiffness of auxetic structures is generally lower than that of solid materials due to the presence of voids. Auxetic materials are used in various industrial and biomedical applications, including:

- Protective gear: Auxetic materials are used in applications such as body armor and helmets to absorb high amounts of energy during impacts.
- Smart textiles: Auxetic materials are used in smart textiles and wearable technologies to provide high flexibility and improved comfort.

- Impact-resistant materials: Auxetic materials are used in applications such as impact-resistant materials and cushioning.
- Tissue engineering: Auxetic materials are used in tissue engineering and medical implants due to their biocompatibility and flexibility (Mir et al., 2014; Dirrenberger et al., 2012; Liu et al., 2010).

Various methods have been searched and refined to achieve auxetic structures, aiming to create flexible, cost-effective, and time-saving processes. The production of auxetic structures typically involves modifications to foaming techniques and the combination of conventional processes like compression, heating, and cooling. Over time, several enhancements have been explored within this manufacturing process, including alterations to the mold's geometry or the use of pins for fabricating larger samples (Duncan et al., 2016). However, additive manufacturing can be a valuable solution to overcome these limitations, as it allows for the design of complex geometric structures in a cost-effective and rapid manner, even on a significant scale. Thus, additive manufacturing methods are currently intensively researched to produce components from various structural materials, i.e. superalloys, Al-alloys and stainless steels, in the industry (Çam, 2022; Günen et al, 2023a; Günen et al, 2023b; Ceritbinmez et al, 2023). The progress of additive fabrication has currently achieved a degree of adaptability that enables the creation and fine-tuning of architectures possessing an adverse Poisson's ratio and multifunctional capacities (Joseph et al., 2021). Among the various additive manufacturing techniques available, the optimal and flexible approach is the FDM process, which enables the manufacturing of polymer materials with negative Poisson ratios and various pattern types (Carton et al., 2019). FDM, as a unique material extrusion technique, offers several advantages in the realm of additive manufacturing. It enables the customization of personalized items, encourages design flexibility, and simplifies the production of complex elements for intricate parts, thereby minimizing expenses and lead times in product development. Additionally, FDM boasts other significant benefits, such as inexpensive and low-maintenance machines, as well as cost-effective stock materials compared to other additive manufacturing techniques. Moreover, it presents opportunities for modifying component characteristics and advancing materials inspired by nature's structures (Mocerino et al., 2023).

2. GEOMETRIC MODELLING

Depending on the required load and geometry, various topologies can be realized, as highlighted in Figure 2 (Liu et al., 2010). Numerous studies have examined different structures using various auxetic models, which can be categorized as re-entrant structures, rotating deformation models, and chiral structures (Guo, Y. et all., 2020; Duncan et al., 2016; Carneiro et al., 2013; Alderson, A 2007).

Re-entrant structures exhibit auxetic behavior by flexing diagonal ribs, resulting in an outward unfold under tension. This deformation mechanism provides the structure with its auxetic properties. On the other hand, rotating models consist of complex systems with rigid geometries (Alderson, A. and Alderson, K.L, 2007). Auxetic structures prove to be beneficial when specific mechanical properties need improvement. For instance, chiral structures demonstrate increased resistance to global and local buckling compared to conventional honeycomb structures (Miller et al., 2010; Spadoni et al., 2005). Negative Poisson ratio foams, on the other hand, exhibit higher energy absorption in dynamic impacts compared to conventional foams, resulting in improved stiffness (up to 4 times), indentation stiffness (up to 1.4 times), and energy absorption (up to 3 times) (Li et al., 2020; Lakes R.S. and Elms, K., 1993). They also exhibit enhanced indentation resilience and

hardness, increasing threefold compared to conventional materials under low-load conditions (Alderson et al., 2000; Chan, N. and Evans, K.E., 1998). Fracture toughness can experience an increase of up to 225% (Choi, J.B. and Lakes, R.S., 1996; Yang et al., 2017). The auxetic effect is further enhanced beyond the yield point (Dirrenberger et al., 2012).

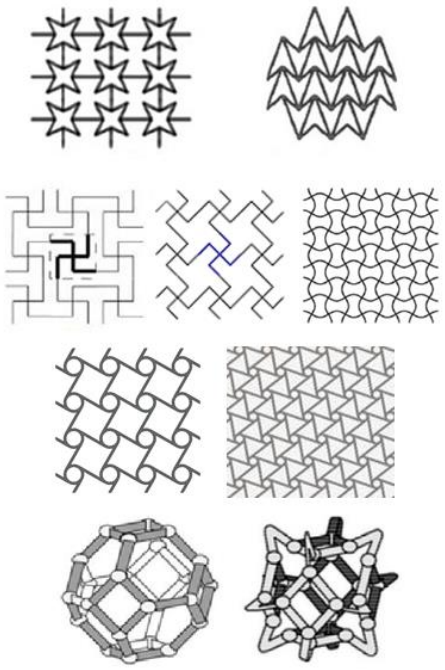

Figure 2. Different kind of auxetic topology reproduced from SAGE journals (Wang et al., 2001)

Moreover, the emergence of novel additive manufacturing (AM) techniques offers the potential to fabricate intricate shapes with fascinating mechanical properties, as well as multifunctional and smart attributes (Joseph et al., 2021). However, to fully exploit these opportunities, significant efforts are needed to address the existing processing challenges. Overcoming these technological limitations and developing scalable techniques for the production of auxetic structures with customized microstructures and properties, while transitioning from small-scale prototypes to industrial-grade products, requires substantial dedication and research.

In project, where we aim to achieve optimum performance from materials by altering the topology. Considering this literature, we decided to used in the study are missing rib, re-entrant honeycomb and chiral with the auxetic designs. For the purpose of compare the mechanical properties of the manufactured parts, mechanical tensile, compression, hardness and surface roughness tests were applied.

3. MATERIALS AND METHODS

3.1 Design of Auxetic Structure

Different programs are used to create designs for 3D printers. It is possible to create geometric designs with the CAD program, which is one of them. After the model is created, the file can be exported in formats that 3D printing programs can use. After the 3D model has been created, the Cura program is available for editing the necessary parameters for the printing process, separating them into layers and previewing the model. The Cura program to be used in the study is a software developed by Ultimaker, a leading 3D printer manufacturer. In this program, the layers required in

the production process of our model are sliced and the G codes of these layers are created. In addition, the Cura program notifies us if there are any problems in the structure of the model that may cause problems with the printing process. Auxetic designs of different 3 auxetic geometries [re-entrant (fig. 3.a), chiral (fig. 3.b), missing rib (fig. 3.c)], were made with CAD program. ASTM D638–14 standard is used for tensile test (fig.4) and ASTM-C365 standard is used for compression test (fig.5).

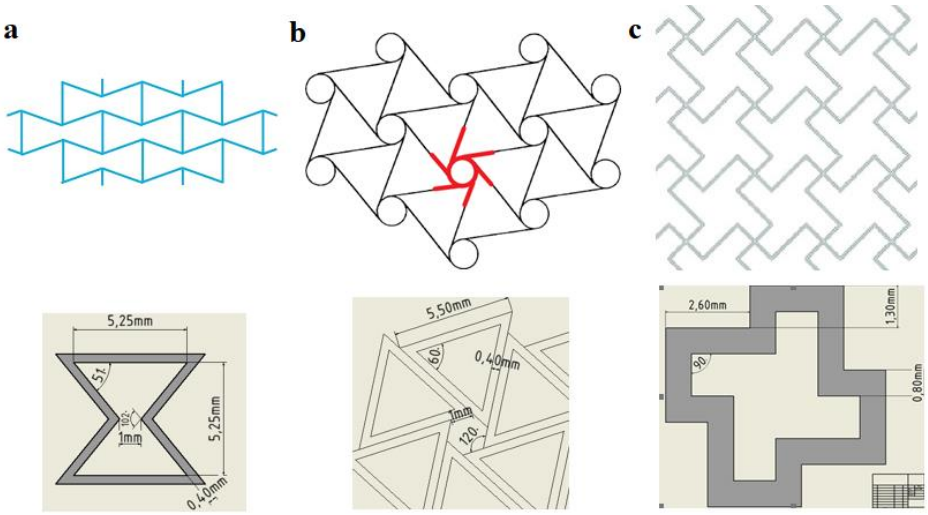

Figure 3. Different kinds of auxetic topology used in our research a. Re-entrant b. Chiral c. Missing-rib auxetic structure

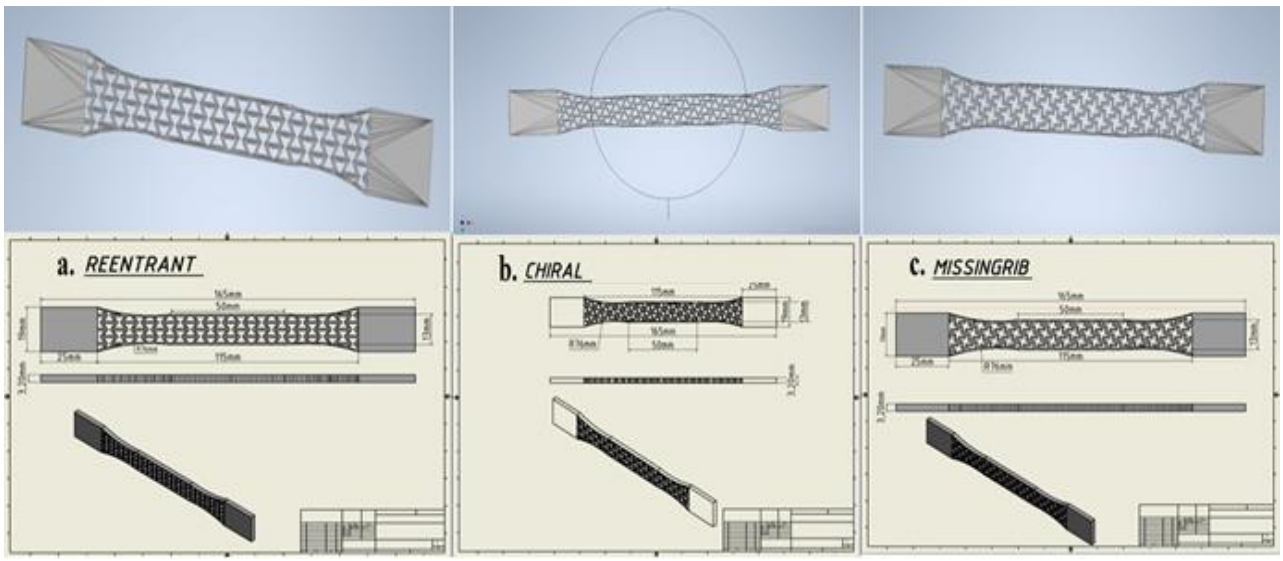

Figure 4. CAD drawings of tensile test specimens a. Re-entrant b. Chiral c. Missing-rib auxetic structure

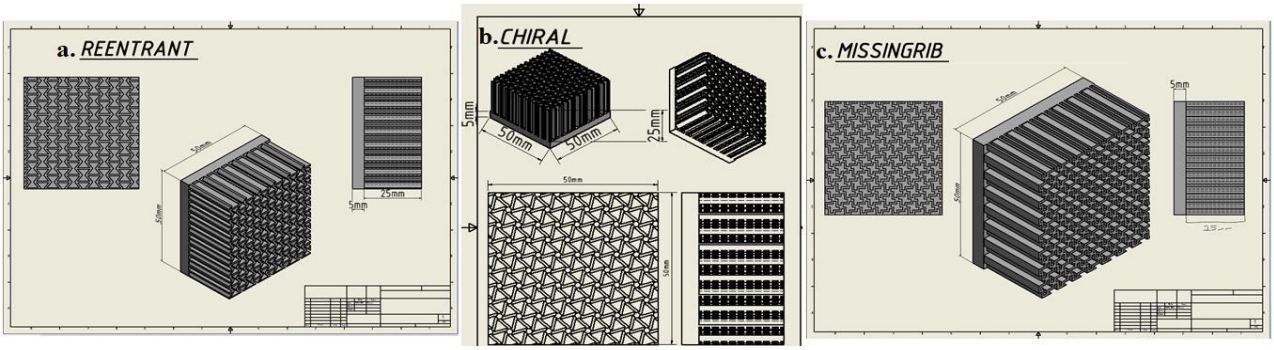

Figure 5. CAD drawings of comparision test specimens a. Re-entrant b. Chiral c. Missing-rib auxetic structure

The densities of different geometries were tried to be kept close to each other in order to make the comparisons of the data of the geometric patterns more reliable. Designs were made in such a way

that the dimensions and cell orientations of the unit cells in the tensile and compression test samples were the same. Surface area values calculated automatically through the drawing program are given in the Table 1.

Table 1. The surface area and weight values according to auxetic structure

Auxetic structure type	Surface area (mm^2)	Weight (gr)		
Chiral Auxetic Structure (Tensile Sample)	1636	6.37	6.35	6.36
Missing-rib Auxetic Structure (Tensile Sample)	1650	6.06	6.05	6.07
Re-entrant Auxetic Structure (Tensile Sample)	1650	5.86	5.88	5.89

3.2 Preparation of Sample

PLA, one of the most common polymers used in additive manufacturing methods, is an eco-friendly biopolymer and thermoplastic derived from corn starch and sugar cane, thus posing no risks to human health (Çelebi, 2022). This feature has made PLA widely used in the biomedical field. In addition, PLA is a biodegradable material and it can decompose in less than three months. Automotive, aerospace, biomedical, and robotics fields can be shown as the most extensive usage areas of PLA polymer (Taşdemir, 2022).

The structures for which the auxetic designs were created were printed by 3D FDM technology device using PLA filament raw material. The designs of the test samples were converted to STL file format and opened in the slicer program, and the models positioned on the virtual production table were sliced in layers with the Ultimaker Cura 4.4.1 program and became ready for production after the optimum manufacturing parameters were entered. The manufacturing parameters used are given in Table 2.

Table 2. The manufacturing parameters used in our study

Printer Type	Anycubic i3 Mega S
Filament type	PLA
Nozzle temprature	200 C
Build Platform temprature	65 C
Infill	% 100
Nozzle diameter	0,4 mm
Layer thickness	0,2 mm
Print speed	60mm/s
Print time (for tensile test)	32 dk

3.3 Tensile Test

Figure 6 depicts the complete auxetic tensile specimens. An AUTOGRAPH – AG-IS 100KN tensile strength machine was employed for conducting the experiments. Specimens are placed in the grips of the universal tester at a specified grip separation and pulled until failure. For ISO 527 the test speed is typically 5 or 50mm/min for measuring strength and elongation and 1mm/min for measuring modulus. The specimens were securely positioned between the lower and upper grips of the tensile apparatus and underwent a pulling procedure at a rate of 5.00 mm per minute according to ISO 527 standard. The tests were carried out at ambient temperature at room temperature and an average of 50% humidity. The performed examinations encompassed the evaluation of tensile potency, tensile elongation, and percentage elongation measurements for the specimens.

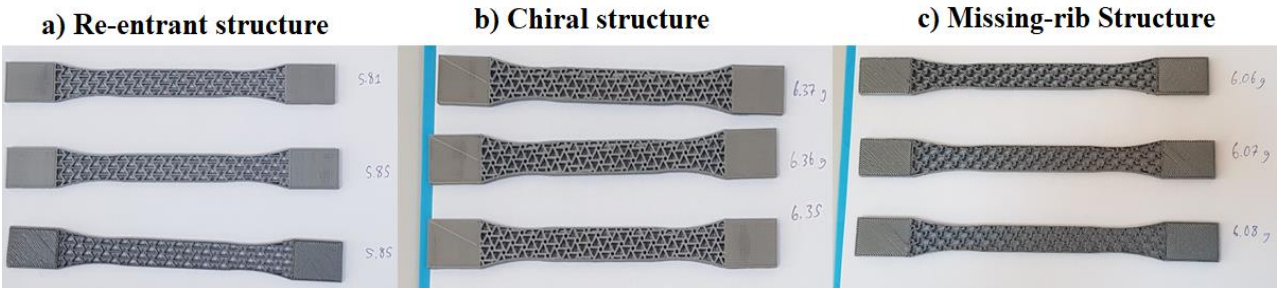

Figure 6. Tensile specimens a. Re-entrant b. Chiral c. Missing-rib auxetic structure

3.4 Compression Test

The fundamental aim of compression testing is to ascertain the characteristics and reaction of a material when exposed to a compressive load, through the measurement of essential parameters like stress and strain. The elastic modulus between the compressive force applied to pertaining to the material and the compressive resilience, yield resilience, ultimate resilience, elastic threshold, and other parameters of the material is determined. By comprehending these distinct variables and the corresponding values related to a specific material, it becomes evident whether the material is appropriate for specific applications or prone to failure under particular stress conditions. Uniaxial compression experiments were conducted utilizing a universal testing machine, AUTOGRAPH – AG-IS, with a measurement range of 10 kN and a precision of 0.001 N. The complete auxetic compression specimens are illustrated in Figure 7.

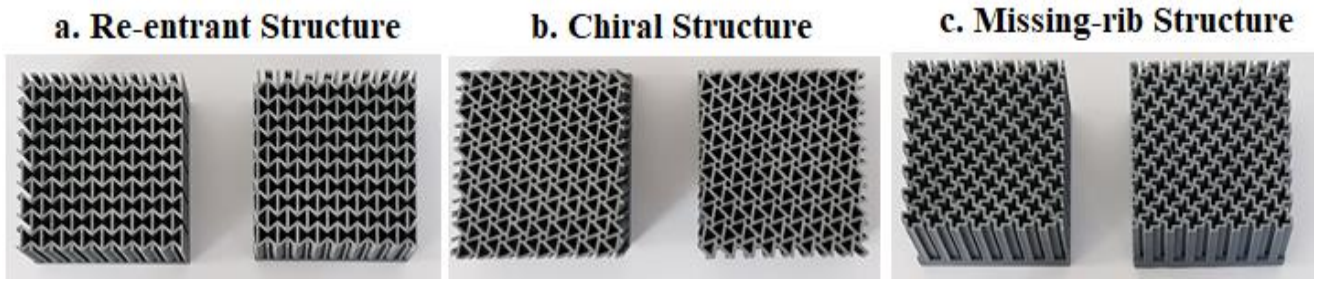

Figure 7. Compression specimens a. Re-entrant b. Chiral c. Missing-rib auxetic structure

3.5 Surface Roughness

The surface roughness of AM parts is typically measured with a profilometer to achieve an arithmetical mean of height of a line (Ra). However, the surface structure is dependent on the overlap of hatches and hatch strategy. Accurate quantitative analysis of surface roughness is therefore essential to qualify the functionality and appearance of a surface. and is thus important to quantify accurately. The direct measurement method with the device is the quantitative analysis method. In this method, a point-contact adapter is used and the surface roughness is determined numerically. The point-contact adapter moves over the surface of the part and the printouts are read on the device as an indicator. The principle is that the fine-tipped probe or point-contact adapter moves on the surface of the finished part. Vertical movements of the point-contact adapter due to surface irregularities are used to evaluate the roughness. The tip of the point-contact adapter is made of a diamond or similar hard material. As a result of the movement of the point-contact adapter, electrical signals are generated and these electrical signals are used as output. The standard for measuring surface roughness is TS EN ISO 21920-2: 2022. The roughness profile cutoff value (λc) is 0,8 mm and drive unit speed is 0,5 mm/s.

Taking into account the layer-by-layer forming process, each sample contains two sides with different surface roughness, and each side has two different surface roughness. 3 measurements perpendicular to the printing direction and 3 measurements parallel to the printing direction (Fig 8) were taken from each surface (bottom surface and upper surface) of the samples produced with using a 3D printer with SJ-210 Mitutoyo roughness tester and the Ra data obtained were compared.

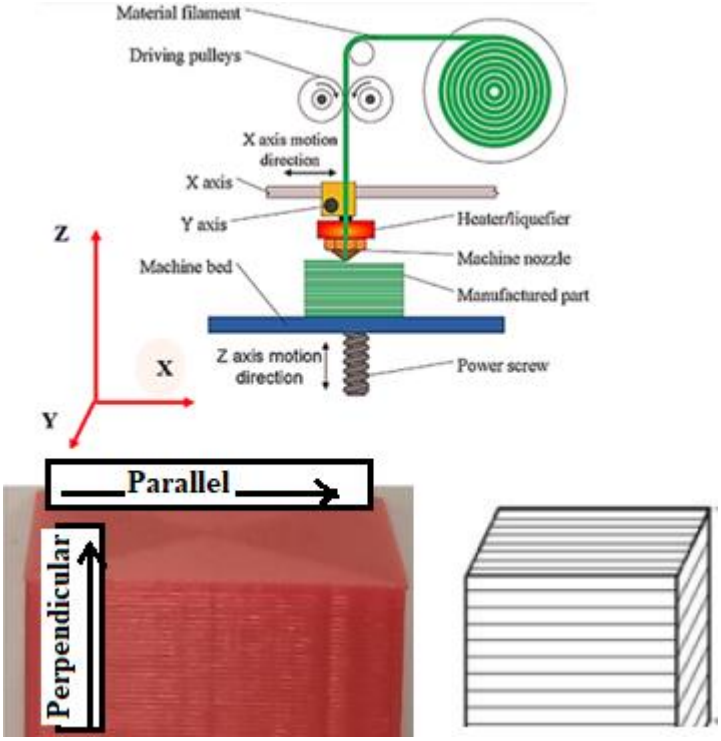

Figure 8. Measurements of Perpendicular and Parallel to the printing direction

4. RESULTS AND DISCUSSION

4.1 Tensile Test

Stress-displacement values were calculated based on the load-displacement data obtained from the Universal Testing Machine (UTM). For maximum stress (σ-N/mm^2), a total of 9 measurements were made for 3 different auxetic structures with three replicates. From Table 3 it can be seen that all of the experimentally determined values for the mechanical properties in different auxetic structures. Figure 9 illustrates the stress-displacement relationship of the tensile specimens fabricated with three distinct auxetic structures, as discussed in section 3.1. The presence of the auxetic structure had a significant impact on the overall performance of the specimens. The chiral auxetic sample exhibited a maximum stress of 6.68 MPa, the missing-rib auxetic sample displayed a maximum stress of 2.26 MPa, and the re-entrant auxetic sample demonstrated a maximum stress of 3.68 MPa. These results obtained from the tests align well with the range reported in the literature, which falls between 1-12 MPa (Berkay Ergene).

Table 3. Tensile testing values according to auxetic structure

Auxetic structure type	Maximum Stress (σ-N/mm^2)	Maximum Strain (%)	Maximum Displacement (mm)
Chiral	6.68	1.228	0.243
Auxetic	6.48	1.103	0.225
Structure	6.38	0.985	0.290
Missing-rib	2.26	0.654	-
Auxetic	2.07	0.510	0.235
Structure	1.69	0.647	0,225
Re-entrant	2.92	0.958	0.212
Auxetic	3.15	0.766	0.370
Structure	3.68	1.109	0.264

The walls within each distinct auxetic structure experienced failure, thereby reducing the load-carrying capacity of the structure. With further loading, the remaining auxetic cells fractured due to the conversion of the applied tensile load into shear load. In addition, it is seen that the re-antrant auxetic design has a strength between the two, while the missing rib auxetic structure has the lowest strength value.

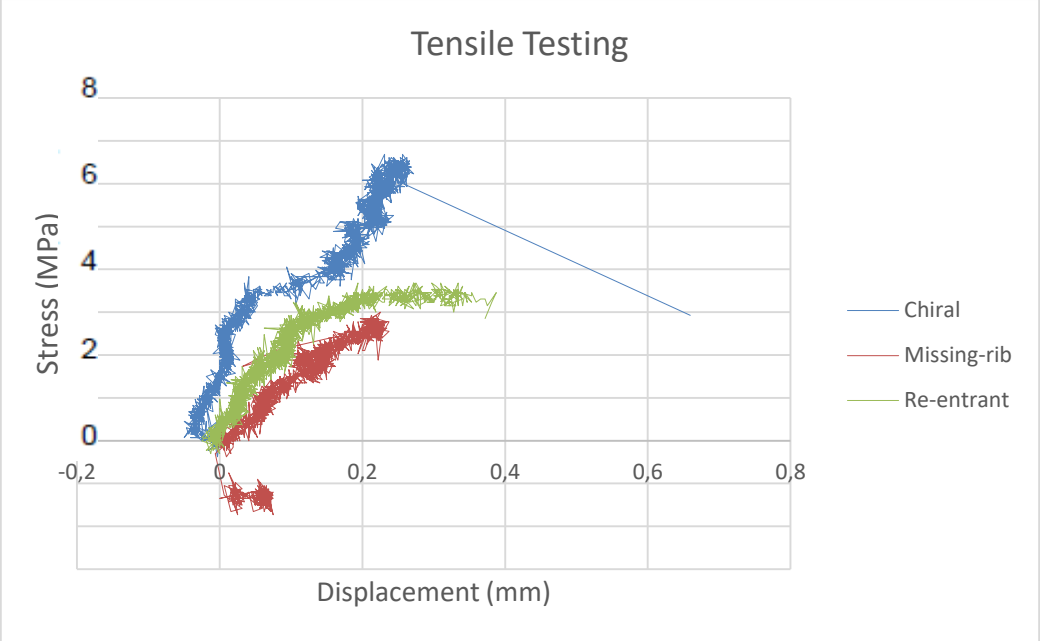

Figure 9. Stress-displacement curve of tensile samples

4.2 Compression Test

Stress-displacement obtained as a result of the compression test of all auxetic structures curves are presented in Figure 10. Compression test was repeated 3 times. As shown in Figure 10, the chiral auxetic structure has the highest compressive strength as the value in auxetic materials. The lowest compression value to failure was achieved with a re-entrant pattern in auxetic structures. However, the highest displacement value was achieved with a missing-rib pattern in auxetic structures which is the compression value between chiral and re-entrant auxetic.

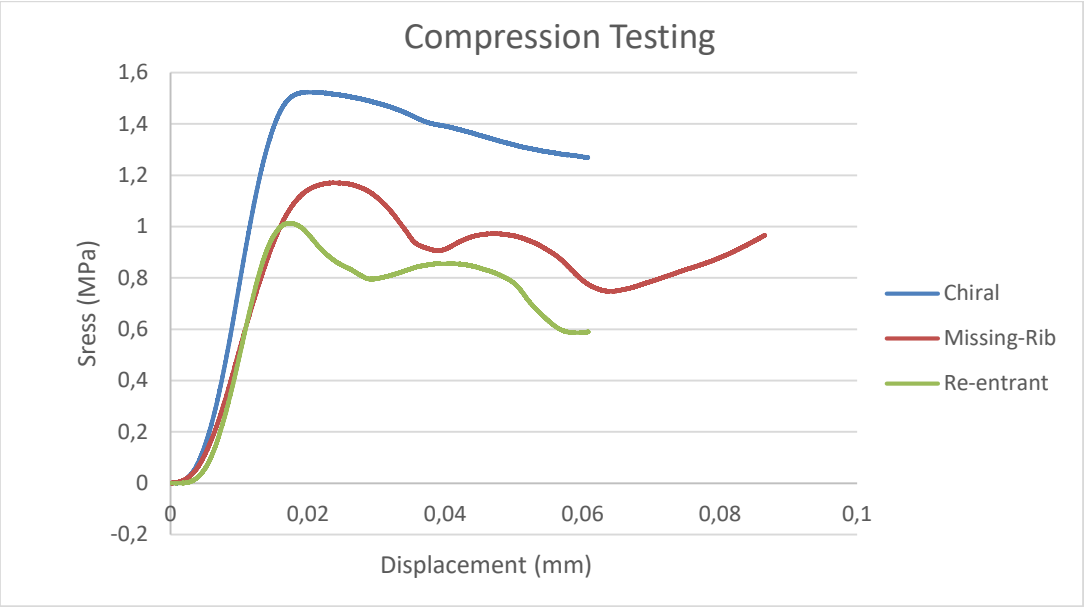

Figure 10. Outcomes obtained from compression test of 3 different auxetic structures

4.3 Surface Roughness

The surface roughness values of each auxetic design printed as a result of the studies, both parallel and perpendicular to the printing direction, are given in the Table 4. As a result of the comparisons, it was observed that the measurements taken perpendicular to the printing direction were higher than the measurements taken parallel to the printing direction. During the experiment, the surface treatment range was set as 4.60 mm.

Table 4. Surface roughness values according to printing direction

Auxetic structure type	Parallel to printing direction Ra (µm)	Perpendicular to printing direction Ra (µm)
Chiral Auxetic Structure	4.225	8.620
	4.328	7.327
	4.447	7.689
Missing-rib Auxetic Structure	7.573	9.097
	7.120	8.616
	7.290	8.956
Re-entrant Auxetic Structure	3.886	8.924
	4.251	7.849
	4.025	7.984

5. CONCLUSION

In this work, three types of auxetic structures were compared according to tensile, compression and surface rougness result. In order to make a correct comparison between different topologies, the specimen densities were kept close to each other for the three different geometries. The following conclusions can be drawn:

- It is concluded that the presence of chiral structures improves mechanical performance. The chiral structure exhibited larger stress than other auxetic structures.
- The chiral auxetic sample exhibited a maximum stress of 6.68 MPa, the missing-rib auxetic sample displayed a maximum stress of 2.26 MPa, and the re-entrant auxetic sample demonstrated a maximum stress of 3.68 MPa. These results obtained from the tests align well with the range reported in the literature, which falls between 1-12 Mpa.
- The surface roughness of the all-auxtetic structure, perpendicular to the printing direction was higher than the measurements taken parallel to the printing direction.

In project, where we aim to achieve optimum performance from materials by altering the topology, the tensile test revealed that the missingrib geometry exhibited the lowest performance. However, when the average of the maximum tensile stresses measured from three repeated tests was calculated, it was observed that the reentrant structure achieved approximately 60% higher pre-rupture maximum stress values compared to missingrib, while the chiral structure exhibited approximately 100% higher values. According to the compression test results, the reentrant structure exhibited the lowest performance, while the missingrib structure achieved approximately 20% higher maximum force values and the chiral structure reached approximately 40% higher maximum force values. In the compression test graph, the area under the graph, obtained by taking displacement data on the x-axis, provides a clue about the amount of energy absorbtion of the materials, and it is observed to be parallel to the performance values in the compression test.

The results provide new ideas for the design of novel metamaterials with superior mechanical properties in the future. However, it is also worth further research to design three-dimensional metamaterials based on unit cells with variable strength, such as variable structures. These auxetic metamaterials with different geometrical configurations could expand potential applications of auxetics in civil, medical and protective engineering.

This study indicates that the chiral structure is a promising energy absorbing structure subjected to quasi-static loading. However, in some applications, auxetic structures may be subjected to dynamic loading. Therefore, it will be interesting to examine the mechanical performance of the chiral structure under dynamic loading conditions. The auxetic cellular materials and structures show huge potential to become important light-weight structural materials of the future with further development of additive manufacturing technologies or with introduction of some new, more cost-effective manufacturing techniques.

6. CONFLICT OF INTEREST

Author(s) approve that to the best of their knowledge, there is not any conflict of interest or common interest with an institution/organization or a person that may affect the review process of the paper.

7. AUTHOR CONTRIBUTION

Ahu ÇELEBİ contributed determining the concept of the research and research management, Ahu ÇELEBİ and Mustafa Mertcan IMANÇ contributed design process of the research and research management, data analysis and interpretation of the results, critical analysis of the intellectual content, preparation of the manuscript, and final approval and full responsibility.

8. REFERENCES

Alderson, A.; Alderson, K.L. Auxetic materials. Proc. Inst. Mech. Eng. Part G J. Aerosp. Eng. 221, 565–575, 2007.

Alderson, K.L.; Fitzgerald, A.; Evans, K.E. The strain dependent indentation resilience of auxetic microporous polyethylene. J. Mater. Sci., 35, 4039–4047, 2000.

Anurag, C. K. Anvesh, and S. Katam, "Auxetic materials," Int. J. Research in Appl. Sci. Eng. Technol., 3, (4), 1176–1183, 2015.

Baughman, R.H.; Shacklette, J.M.; Zakhidov, A.A.; Stafström, S., Negative poisson's ratios as a common feature of cubic metals. Nature 1998, 392, 362–365. [CrossRef]

Çam G., Prospects of producing aluminum parts by wire arc additive manufacturing (WAAM), Materials Today: Proceedings, 62 (1), 77-85, 2022.

Carneiro, V.H.; Meireles, J.; Puga, H. Auxetic materials—A review. Mater. Sci. 31, 561–571, 2013.

Carton, M.A.; Ganter, M. Fast and simple printing of graded auxetic structures. In Proceedings of the 30th International Solid Freeform Fabrication–An Additive Manufacturing Conference SFF, University of Texas: Austin, TX, USA; pp. 2270–2279, 2019.

Çelebi, A., Experimental and statistical investigation of the bending and surface roughness properties on three-dimensional printing parts. Journal of Testing and Evaluation 50, no. 4, 2069–2082, 2022.

Ceritbinmez F., Günen A., Gürol U., Çam G., A comparative study on drillability of Inconel 625 alloy fabricated by wire arc additive manufacturing, Journal of Manufacturing Processes, 89, 150-169, 2023.

Chan, N.; Evans, K.E. Indentation resilience of conventional and auxetic foams. J. Cell. Plast. 34, 231–260, 1998.

Choi, J.B.; Lakes, R.S. Fracture toughness of re-entrant foam materials with a negative Poisson's ratio: Experiment and analysis. Int. J. Fract. 80, 73–83, 1996.

Dirrenberger, J.; Forest, S.; Jeulin, D. Elastoplasticity of auxetic materials. Comput. Mater. Sci. 64, 57–61, 2012.

Duncan, O.; Foster, L.; Senior, T.; Allen, T.; Alderson, A. A comparison of novel and conventional fabrication methods for auxetic foams for sports safety applications. Procedia Eng. 147, 384–389, 2016.

Ergene, B., Yalçın B., Eriyik yığma modelleme (EYM) ile üretilen çeşitli hücresel yapıların mekanikperformanslarının incelenmesi, Journal of the Faculty of Engineering and Architecture of Gazi University 38:1, 201-217, 2023.

Evans K.E., Nkansah M.A., Hutchison I.J., Rogers S.C., Molecular Network Design, Nature 353, 124, 1991.

Günen A., Gürol U., Koçak M., Çam G., A new approach to improve some properties of wire arc additively manufactured stainless steel components: Simultaneous homogenization and boriding, Surface & Coating Technology, 460, 129395, 2023b.

Günen A., Gürol U., Koçak M., Çam G., Investigation into the influence of boronizing on the wear behavior of additively manufactured Inconel 625 alloy at elevated temperature, Progress in Additive Manufacturing, 2023a.

Guo, Y.; Zhang, J.; Chen, L.; Du, B.; Liu, H.; Chen, L.; Li, W.; Liu, Y. Deformation behaviors and energy absorption of auxetic lattice cylindrical structures under axial crushing load. Aerosp. Sci. Technol. 98, 105662, 2020.

Hui Chen Luo, Xin Ren, Yi Zhang, Xiang Yu Zhang, Xue Gang Zhang, Chen Luo, Xian Cheng, Yi Min Xie, Mechanical properties of foam-filled hexagonal and re-entrant honeycombs under uniaxial compression, Composite Structures, Volume 280, 2022,

Joseph, A.; Mahesh, V.; Harursampath, D. On the application of additive manufacturing methods for auxetic structures: A review. Adv. Manuf. 9, 342–368, 2021.

Lakes R.S., Foam structures with a negative Poisson's ratio" Science, 235:1038–1040, 1997.

Lakes, R.S.; Elms, K. Indentability of conventional and negative poisson's ratio foams. J. Compos. Mater. 27, 1193–1202, 1993.

Li, T.; Liu, F.; Wang, L. Enhancing indentation and impact resistance in auxetic composite materials. Compos. Part B Eng. 198, 108229, 2020.

Liu, Y.; Hu, H. A review on auxetic structures and polymeric materials. Sci. Res. Essay, 5, 1052–1063, 2010.

Miller, W.; Smith, C.W.; Scarpa, F.; Evans, K.E. Flatwise buckling optimization of hexachiral and tetrachiral honeycombs. Compos. Sci. Technol. 70, 1049–1056, 2010.

Mir, M.; Ali, M.N.; Sami, J.; Ansari, U. Review of mechanics and applications of auxetic structures. Adv. Mater. Sci. Eng. 1–17, 2014.

Mocerino, D.; Ricciardi,M.R.; Antonucci, V.; Papa, I. Fused deposition modelling of polymeric auxetic structures: A Review. Polymers. 15, 1008, 2023.

Spadoni, A.; Ruzzene, M.; Scarpa, F. Global and local linear buckling behavior of a chiral cellular structure. Phys. Status Solidi. 242, 695–709, 2005.

Taşdemir M., Experimental and numerical investigation of mechanical properties of additively manufactured auxetic structures, Master Thesıs of Mıddle East Technıcal Unıversıty, Turkey, 2022.

Wang, Y.-C.; Lakes, R.; Butenhoff, A. Influence of cell size on re-entrant transformation of negative poisson's ratio reticulated polyurethane foams. Cell. Polym. 20, 373–385, 2001.

Yang, S.; Chalivendra, V.B.; Kim, Y.K. Fracture and impact characterization of novel auxetic Kevlar®/Epoxy laminated composites. Compos. Struct. 168, 120–129, 2017.

JOURNAL of
MATERIALS and MECHATRONICS:A

e-ISSN 2717-8811
JournalMM, 2023, 4(2), 397-408
https://doi.org/10.55546/jmm.1332369

Araştırma Makalesi / Research Article

Experimental Investigation of the Effects of Gasoline-Methyl Ethyl Ketone Fuel Blends on Engine Performance and Exhaust Emissions

Tolga KOCAKULAK[1], Ahmet UYUMAZ[2*], Emre ARABACI[3], Yusuf DAĞOĞLU[4], Celal ÇAMOĞLU[5]

[1] Burdur Mehmet Akif Ersoy University, Techical Sciences of High Vocational School, Hybrid and Electric Vehicles Program, Burdur, Turkey,
ORCID ID: https://orcid.org/0000-0002-1269-6370, tkocakulak@mehmetakif.edu.tr
[2] Burdur Mehmet Akif Ersoy University, Engineering Architecture Faculty, Department of Mechanical Engineering, Burdur, Turkey,
ORCID ID: https://orcid.org/0000-0003-3519-0935, auyumaz@mehmetakif.edu.tr
[3] Pamukkale University, Technology Faculty, Department of Automotive Engineering, Denizli, Turkey,
ORCID ID: https://orcid.org/0000-0002-6219-7246, earabaci@pau.edu.tr
[4] Burdur Mehmet Akif Ersoy University, Engineering Architecture Faculty, Department of Mechanical Engineering, Burdur, Turkey,
ORCID ID: https://orcid.org/0009-0007-1555-8751, dagogluyusuf@gmail.com.tr
[5] Burdur Mehmet Akif Ersoy University, Engineering Architecture Faculty, Department of Mechanical Engineering, Burdur, Turkey,
ORCID ID: https://orcid.org/0009-0007-0619-3092, celalcamoglu20@gmail.com

Geliş/ Received: 25.07.2023; **Kabul / Accepted:** 12.09.2023

ABSTRACT: Gasoline engines have been widely used because of operating with stoichiometric ratio and lower exhaust emissions compared to compression ignition engines. However, thermal efficiency is less than diesel engines due to lower compression ratio. In the present study, the influences of methyl ethyl addition were researched on engine performance, CO, CO_2 and HC emissions in a single cylinder spark ignition engine. For this purpose, the test engine was run at wide-open throttle, engine speeds of 2400, 2800, 3200, 3600, 4000 rpm and the variations of engine torque, effective power, specific fuel consumption (SFC), thermal efficiency, CO, CO_2 and HC emissions were investigated. It has been observed that engine power and torque increase and SFC decreases as methyl ethyl ketone is added to gasoline. It was observed that the thermal efficiency at 2800 rpm increased by 6.47%, 13.81% and 19.51%, respectively, with MEK20, MEK30 and MEK40 test fuels compared to gasoline. As the methyl ethyl ketone ratio in the blended fuels increased, HC and CO emissions reduced compared to gasoline. As a result, it was seen that methyl ethyl ketone additive can be utilized easily in a spark ignition engine without making any modification.

Keywords: Engine Performance, Exhaust Emissions, Methyl Ethyl Ketone, Gasoline.

*Sorumlu yazar / Corresponding author: auyumaz@mehmetakif.edu.tr

Bu makaleye atıf yapmak için /To cite this article

Kocakulak, T., Uyumaz, A., Arabacı, E., Dağoğlu, Y., Çamoğlu, C. (2023). Experimental Investigation of the Effects of Gasoline-Methyl Ethyl Ketone Fuel Blends on Engine Performance and Exhaust Emissions. Journal of Materials and Mechatronics: A (JournalMM), 4(2), 397-408.

1. INTRODUCTION

The depletion of petroleum-based fuels and the pollution of the atmosphere and nature by pollutants produced from combustion powered vehicles prompted researchers to conduct various studies on internal combustion engines. Compression ignition (diesel) engines have high thermal efficiency because of their high compression ratios and they are more economical than spark ignition (gasoline) engines in terms of fuel consumption because they work with excess air. However, sulfur content of diesel fuel, more harmful exhaust gases than gasoline engines and ignition delay time are some of its disadvantages. The inability to reduce NO_x and soot emissions simultaneously is another handicap in compression ignition engine. Extra cost is needed in order to reduce these emissions using exhaust gas aftertreatment systems. On the other hand, spark ignition engines have recently attracted attention with their reasonable thermal efficiency, considering the reduction of emissions and quieter operation. Pumping losses in the inlet line, the necessity of operating at stoichiometric air/fuel ratios due to the usage of a catalytic converter and lower thermal efficiency according to diesel engines owing to lower compression ratio are their shortcomings (Ackermann et al., 2021; Heywood, 1988; Jenkins et al., 2016; Magara et al., 2012; Majumdar et al., 2019; Oprescu et al., 2014; Prabhahar et al., 2017; Shah et al., 2009; Yang et al., 2016). At this point, improving the combustion process and flame development with different fuel additives come to the forefront in gasoline engines. At the same time, it is aimed to increase the thermal efficiency, which decreases due to the self-ignition characteristics (Heywood, 1988; Kumar et al., 2011; Nabi, 2010; Sarjovaara et al., 2013; Zhao, 2007).

It is predicted that methyl ethyl ketone, which has a high auto-ignition temperature, density and evaporation rate, can be used as an additive into gasoline. The organic solvent methyl ethyl ketone is a low toxic flammable liquid. Methyl ethyl ketone that can be produced from a renewable resource may present a solution on improving combustion in spark ignition engines. It can be also mentioned that high oxygen content of methyl ethyl ketone allows better oxidation reactions. So it is seen as promising fuel additive in spark ignition engines. (Ackermann et al., 2021; Hoppe et al., 2016; Jenkins et al., 2016; Kumar et al., 2011; Magnusson and Nilsson, 2011; Raj et al., 2008; Raj et al., 2010; Samoilov et al., 2020; Torres-Vinces et al., 2020). The general chemical formulation of methyl ethyl ketone is shown in Figure 1. Methyl ethyl ketone is widely used in industry. In some studies, it has been predicted that spark ignition engines provide better performance than gasoline according to certain indicators (Torres-Vinces et al., 2020).

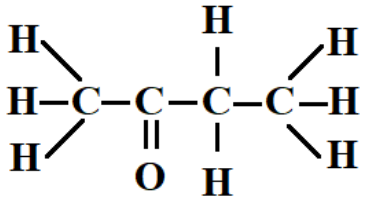

Figure 1. General chemical formula of methyl ethyl ketone (Kumar et al., 2011, Libretexts Chemistry, 2023)

The usage of ketone-ester-alcohol-alkane (KEAA) fuel mixture in a highly efficient spark-ignition engine has been investigated from the point of view of production cost, engine performance etc. It is seen that KEAA fuel provides high efficiency in a research engine. High resistance against auto ignition has also been observed (Ackermann et al., 2021). In a study conducted in a compression ignition engine, two glycerol derivatives were used as additives to diesel. In the experiments performed at full load between 1200-3700 rpm (2-ethyl-2-methyl-1,3-dioxolan-4-yl) methyl hexanoate has shown to be promising for smoke, HC and CO emissions. Reductions of 19.20%,

18.93% and 26.04% were detected in smoke, CO and HC emissions, respectively (Oprescu et al., 2014). A direct injection compression ignition turbocharged diesel engine was operated with diesel, biodiesel (B100) and 20% biodiesel+80% diesel (B20) fuels, and the variation of carbonyl emissions were investigated. Formaldehyde, acrolein + acetone, acetaldehyde, crotonaldehyde, propionaldehyde, and methyl ethyl ketone have more specific emissions with B20 and B100 compared diesel, and lower specific emissions with benzaldehyde and tolualdehyde. Total carbonyl emissions with B20 and B100 were found to be 8% and 32% higher than diesel respectively (Shah et al., 2009). The variation of carbonyl compounds and pollutants were investigated in an idling diesel engine. The changes in emissions were investigated with test fuels consisting of diesel, biodiesel and isobutanol mixtures. The largest carbonyls were found to be formaldehyde, acetaldehyde and acrolein, respectively. With the high rate of biodiesel in fuel blends, CO, NO_x and particulate matter emissions decreased by about 3.45%, 32.5%, and 38.5%, respectively (Yang et al., 2016). Warm three-way catalysts are used for the reduction of non-methane organic gases, NO_x and CO exhaust gases from spark ignition engines. Most emissions from gasoline engines are released under cold operating conditions when the catalyst is inactive. High performance fuel samples were investigated in a hydrothermal three-way warm catalytic converter with synthetic engine exhaust flow reactor system. Many fuel compositions have been studied, such as aromatic ethers, alcohols, alkanes, alkenes, esters, ketones, and oxygen-free aromatic hydrocarbons. It appears that short-chain acyclic oxygenates, including esters, ketones and alcohols tend to react at relatively low temperatures. On the other hand, alkenes, aromatics, and cyclic oxygenates tend to react at relatively high temperatures (Majumdar et al., 2019). Oxygen-containing fuels improve chemical oxygen reactions. In a study which changes in thermal efficiency, specific heat at constant pressure, adiabatic flame temperature, NO_x emissions for different oxygenated fuels were examined theoretically, it is shown that oxygen content of fuel is closely related to combustion parameters. It has been observed that decrease on NO_x is related to the adiabatic flame temperature of oxygenated fuels (Nabi, 2010). However, the usage of dual fuels to improve the combustion process is another method. In an engine used in a heavy-duty vehicle, ethanol was injected into the inlet manifold as the primary fuel, and diesel fuel was injected into the cylinder. The study showed that the concept of dual-fuel combustion with ethanol is feasible and has a lot of potential (Sarjovaara et al., 2013). The variations in aldehyde, ketone, HC, CO and NO_x emissions in a two-stroke chainsaw engine operating with fuels with high oxygen content were investigated. It was observed that the use of four oxygenated fuels (Ethyl tert butyl ether, ethanol, methanol and methyl tert butyl ether) resulted in higher (11, 11, 8.9 and 7.8 g/kWh) total carbonyl emissions compared to both aliphatic and normal gasoline usage (2.1 and 2.6 g/kWh), respectively (Magnusson and Nilsson, 2011). The main physical properties of eight different diol derivatives of gasoline mixture were investigated in a study. They observed that di-glycerol tert butyl ether was the most efficient octane booster (Samoilov et al., 2020). In another study, thermodynamic investigations of 2-methylfuran and methyl ethyl ketone fuels were performed in a spark ignition engine. Longer ignition delay was measured with methyl ethyl ketone than with ethanol and 2-methylfuran fuels. It was seen that the knock resistance increased using 2-methylfuran compared to gasoline under low loads and cold operating conditions. At the same time, it was observed that methyl ethyl ketone increased the combustion stability according to ethanol at low loads and under cold operation. However, compared to ethanol, methyl ethyl ketone and 2-methylfuran caused to increase NO_x. (Hoppe et al., 2016; Torres-Vinces et al., 2020). Methanol and methyl ethyl ketone fumigation can be applied to the intake manifold to improve the performance. An important decrease on the amount of smoke and NO_x was realized compared to diesel (Raj et al., 2008). In a similar study, the variations

on performance and emissions were researched by fumigation of methyl ethyl ketone, methanol, and liquefied petroleum gas (LPG) to the intake manifold in a diesel engine. It was found that there was a remarkable decrease on smoke and NO_x emissions with fumigation of all test fuels. But HC and CO increased. While the thermal efficiency increased by a maximum of 7% with methanol fumigation, it was increased by 3% with methyl ethyl ketone (Raj et al., 2010). In a study, 2%, 4%, 6% and 8% naphthalene were added to gasoline and it was observed that while engine performance improved, emissions increased. It was observed that the best fuel mixture was 6%, and it was seen that CO increased as the amount of naphthalene increased (Durgun and Alaçam, 2018).

In the present study, the influences of methyl ethyl ketone addition to gasoline on engine torque, engine power, specific fuel consumption, thermal efficiency, CO, CO_2 and HC emissions were experimentally investigated.

2. MATERIALS AND METHODS

2.1 Materials

Experimental study was carried out at Burdur Mehmet Akif Ersoy University Technical Sciences of High Vocational School Automotive Technology Laboratory. The schematic view of the test setup is seen in Figure 2. A single-cylinder, four-stroke spark ignition engine was utilized to investigate the effects of methyl ethyl ketone additive on engine performance and emissions (CO, CO_2 and HC). The engine specifications are given in Table 1.

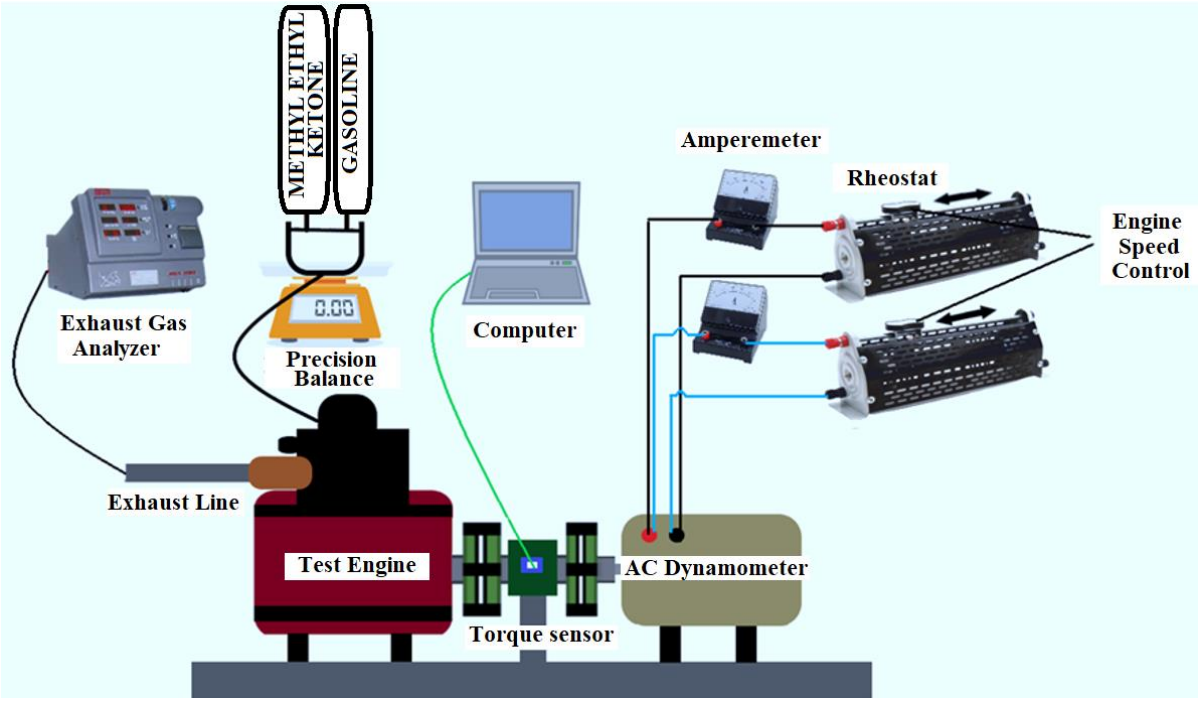

Figure 2. Schematic view of the test setup

Measurements were made after the test engine reached operating temperature in order to reduce experimental errors and to obtain more precise data. Measurements were carried out after stable operation was achieved. The test engine was run with gasoline, gasoline/methyl ethyl ketone fuel mixtures at wide open throttle and 2400, 2800, 3200, 3600 and 4000 rpm engine speeds. In the experiments, test fuels were obtained by mixing methyl ethyl ketone gasoline with 10%, 20%, 30%

and 40% by volume. The mixing ratios and names of the test fuels used in the experiments are shown in Table 2.

Table 1. Engine specifications

Model	Honda GX160
Bore x stroke [mm]	68x45
Cylinder volume [cm³]	163
Compression ratio	8.5:1
Maximum power BG@3600 d/d	5.5
Maximum Torque [Nm] @2500 d/d	10.78
Cooling system	Air cooled

Table 2. Test fuels and mixing ratios

Gasoline	%100 Gasoline
MEK10	%10 Methyl ethyl ketone + %90 Gasoline
MEK20	%20 Methyl ethyl ketone + %80 Gasoline
MEK30	%30 Methyl ethyl ketone + %70 Gasoline
MEK40	%40 Methyl ethyl ketone + %96 Gasoline

Some properties of the used test fuels are shown in Table 3.

Table 3. Properties of the test fuels (Methyl Ethyl Ketone-Cameo Chemicals,2023; Hoppe et al., 2016; Tüpraş, 2023)

	Gasoline	Methyl ethyl ketone
Density [kg/m^3]	746	805
Latent heat of vaporization [kJ/kg]	331.6	444
Flash point [℃]	-43	-9
Auto ignition temperature [℃]	257.2	505
Boiling point [℃]	30-225	79.6
Oxygen mass [%]	2.70	22.19
RON	95	117

2.2 Method

In order to obtain the full load speed characteristics of the spark ignition engine, the test engine was connected to the AC dynamometer as seen in Figure 2. With the gradual operation of the circuit elements (resistances) connected to the dynamometer output, the test engine operating at wide open throttle was loaded and operated at different speeds. In order to protect the resistances used during the loading of the test engine, the current passing through the circuit was measured with an ampere meter. In order to determine the fuel economy, PLT Power brand precision balance that can measure with 0.5 gr precision was used. Engine torque and engine speed were measured by the Burster 8661 brand torque sensor mounted between the AC dynamometer and the test engine. Measured engine speed and torque data were transferred to the computer via cable connection. Engine speed and torque data were continuously monitored and recorded with the Digivision interface. The properties of the torque sensor are shown in Table 4.

Table 4. Properties of the torque sensor

Model	Burster 8661
Nominal supply voltage range [V DC]	10-30
Nominal torque output voltage [V]	+10
Insulation resistance [MΩ]	> 5
-3 dB cutoff frequency [Hz]	200
Fluctuation [mV]	<50
Driver signal (K pin) [V DC]	10…30

SUN MGA1500 gas analyzer was utilized to determine CO, CO_2 and HC emissions. The technical properties of the exhaust gas analyzer are shown in Table 5.

Table 5. Technical properties of the exhaust gas analyzer

	Operating range	Accuracy
CO	% 0-14	% 0.001
HC	0-9999 ppm	1 ppm
NO_x	0-5000 ppm	1 ppm
CO_2	% 0-18	% 0.1
O_2	% 0-25	% 0.01
λ	0-4	0.001

3. RESULTS AND DISCUSSION

3.1 Engine Performance

The engine torque and engine power output values obtained by adding methyl ethyl ketone which is an organic solvent, to gasoline are seen in Figure 3. It is worth mentioning that engine test rig setup was by the authors and a partially worn and previosly used spark ignition engine was used as test engine. So, it was seen that the measured performance values are slightly less than the original performance values of the engine. Thus, maximum engine torque and power ouput were obtained at 2800 and 4000 rpm respectively. As seen in Figure 3-a, as a result of the experiments performed at full load and and different engine speeds, it was found that the engine torque decreased with MEK10 fuel. However, it is seen that engine torque increases with the increase of methyl ethyl ketone. It has been found that the maximum engine torque increased by 2.85% with MEK40 fuel at 2800 rpm compared to gasoline. As the engine speed increases, gas leakages and thermal losses for each stroke increase, and torque decreases for all test fuels. Although the thermal energy of methyl ethyl ketone is lower than gasoline (REF), its high oxygen content improves oxidation reactions. It can be also stated that higher octane number of methyl ethyl ketone resulted in higher in-cylinder gas pressure and temperature at the end of compression. Hence, in-cylinder pressure increases as a result of combustion. As shown in Figure 3-b, the effective engine power increases with all test fuels depending on engine speed. Power increase slows down due to the increase in mechanical and flow losses after the maximum power engine speed. Maximum engine power output was calculated at 4000 rpm for all fuels. With MEK10, the calculated effective power is reduced compared to gasoline. It is predicted that higher density and latent heat of vaporization of methyl ethyl ketone resulted in lower engine torque and power output with MEK10. Nevertheless, it was found that the effective engine power increased as methyl ethyl ketone is added. Chemical oxidation reactions are improved with methyl ethyl ketone additive with high oxygen content. At the same time, the high auto-ignition temperature may increase temperature and pressure of the charge mixture during the compression process. Besides, gas pressure and temperature increase as a result of combustion.

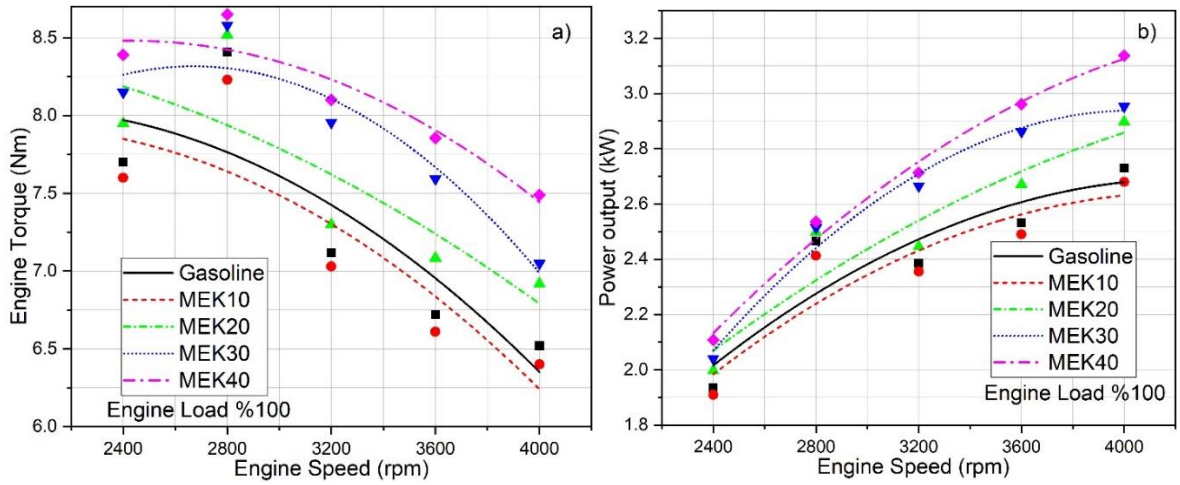

Figure 3. a) The variations of engine torque b) The variations of effective power

In Figure 4, the variations of SFC values versus engine speed are seen. The lowest SFC was calculated at 2800 rpm for all test fuels. Gas leakages and heat losses increase with higher engine speeds and SFC tends to increase. It is seen that the SFC decreases as the methyl ethyl ketone ratio increases in the fuel blends. Maximum SFC was determined with MEK10 fuel. Higher density of methyl ethyl ketone causes to increase SFC. But, higher octane number and oxygen content of methyl ethyl ketone improved the oxidation reactions. Hence, it was seen that SFC decreased and thermal efficiency increased with the increase of methyl ethyl ketone addition in the fuel blends. With MEK40, it was observed that SFC decreased by 5.78% at 2800 rpm compared to gasoline. Methyl ethyl ketone, which contains more oxygen in its chemical structure, improves oxidation reactions and increases the average gas temperature at the end of combustion. Oxidation conditions are thermodynamically improved in the combustion chamber and and fuel consumption decreases.

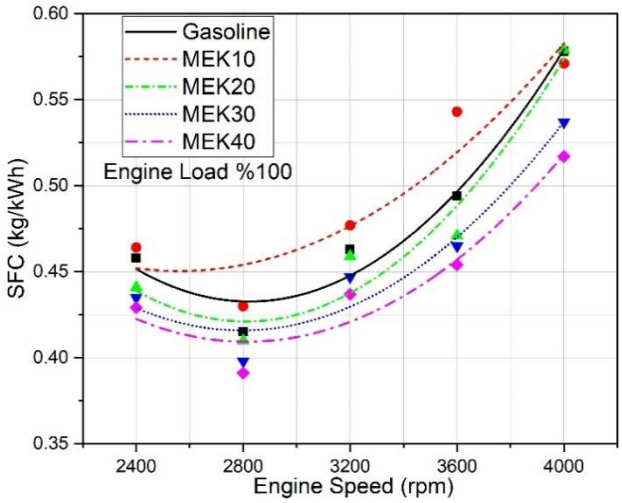

Figure 4. The influences of methyl ethyl ketone on SFC

Figure 5 shows the obtained thermal efficiency changes with the test fuels. Thermal efficiency, which expresses the conversion of obtained heat energy with fuel to the network, is an important performance parameter (Heywood, 1988). Maximum thermal efficiency was determined at 2800 rpm for all test fuels. It was determined that the thermal efficiency increased by approximately 19.51% with MEK40 fuel at 2800 rpm compared to gasoline. With high oxygen content fuel additive, oxygen molecules can be reacted more easily, and combustion reactions are improved. Since the engine speed

increases, the mechanical losses increase and the oxygen concentration decreases. So, combustion reactions slow down. Thus, thermal efficiency decreases.

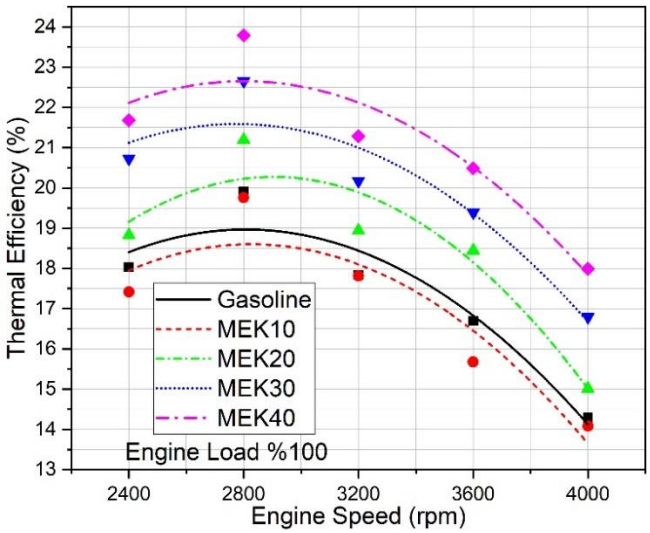

Figure 5. Thermal efficiency

3.2 Exhaust Emissions

Figure 6 depicts the variations of CO and CO_2 emissions. Insufficient temperature and oxygen causes to form CO which is incomplete combustion product. It is clearly presented that CO is reduced with the addition of methyl ethyl ketone. The methyl ethyl ketone additive increases the oxidation rate due to containing of high oxygen content and the formation of CO is reduced. The oxygen required for the oxidation of the fuel is provided by methyl ethyl ketone. As seen in Figure 6-a, CO emissions decrease as methyl ethyl ketone is added. With the increase of engine speed, the gas temperature after combustion increases and the formation of CO decreases. On the other hand, CO formation tends to increase due to insufficient oxygen intake into the cylinder at high engine speeds. With MEK40 test fuel at 4000 rpm, it is seen that CO emissions are reduced by 38.91% compared to gasoline. Figure 6-b exhibits the change of CO_2 with test fuels. It is possible to state that there is an inverse relationship between CO and CO_2 emissions. Oxidation reactions and CO_2 formation increases with fuel additive with high oxygen content. When Figure 6-b is examined, CO_2 emissions increase as the methyl ethyl ketone addition increases.

Due to the increase in pumping losses at high engine speeds and the decrease in the oxygen density in the combustion chamber, CO formation increases and CO_2 emissions decrease. It can be stated that methyl ethyl ketone with high auto-ignition temperature and octane number increases the temperature and pressure at the end of compression. In this case, in-cylinder gas temperature increases after combustion. Warmer combustion chamber causes the oxidation rate increase. As a result, CO_2 formation increases.

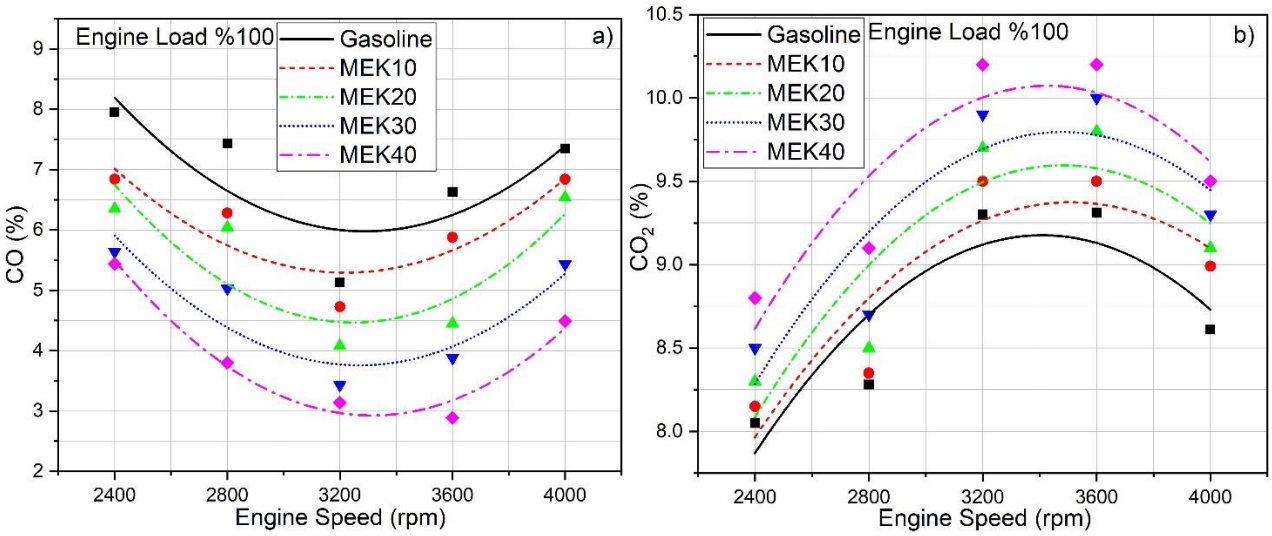

Figure 6. a) CO emissions b) CO_2 emissions

HC emissions are formed due to the inability to oxidize the remaining hydrocarbon molecules in the combustion chamber, in the hollow parts, on the edges of the pistons and rings. At the same time, the flame can go out when the flame front reaches to the cold cylinder walls after the combustion starts. In this case, the fuel remaining in the corners of the combustion chamber cannot react with the oxygen molecules and they are discharged from the cylinder. Figure 7 shows the effects of methyl ethyl ketone addition on HC emissions. It is seen that HC emissions decrease as the methyl ethyl ketone addition increases. Methyl ethyl ketone with high oxygen content causes to improve oxidation reactions and HC formation decreases. Minimum HC emissions were measured with MEK40 fuel. At 3600 rpm, HC emissions decreased by about 19.46% with MEK40 test fuel compared to gasoline. In cylinder gas temperature increases after combustion, and the heat losses per cycle decrease at high engine speeds. In the combustion chamber with a high temperature, the oxidation rate rises and the HC formation reduces. Because of the increase in mechanical and flow losses at high engine speeds, the volumetric efficiency decreases and the amount of oxygen that is delivered into the cylinder decreases. In this case, the fuel molecules cannot find enough oxygen for oxidation. As a result, HC formation begins to increase.

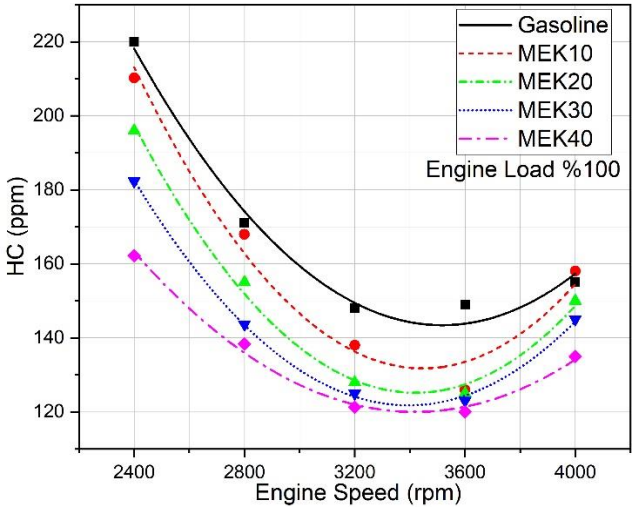

Figure 7. HC emissions

4. CONCLUSION

In this study, the influences of methyl ethyl ketone addition on engine performance and exhaust emissions were researched experimentally.

The changes in engine torque, effective power, SFC, thermal efficiency, CO, CO_2 and HC emissions were investigated at full load and at engine speeds of 2400, 2800, 3200, 3600 and 4000 rpm.

- It is found that the engine torque increases with the addition of methyl ethyl ketone. Engine torque increased by 1.30%, 2.02% and 2.85% with MEK20, MEK30 and MEK40 test fuels at 2800 rpm compared to gasoline, respectively.
- Engine power at 4000 rpm with MEK20, MEK30 and MEK40 test fuels increased by 6.11%, 8.12% and 14.86%, compared to gasoline, respectively.
- As the methyl ethyl ketone ratio increases in the fuel blends, SFC decreases. With MEK20, MEK30 and MEK40 test fuels, SFC decreased by 1.2%, 4.09% and 5.78% at 2800 rpm compared to gasoline, respectively.
- It was observed that the thermal efficiency decreased by 0.73% with MEK10 fuel at 2800 rpm compared to gasoline, and increased by 6.47%, 13.81% and 19.51%, respectively with MEK20, MEK30 and MEK40 test fuels compared to gasoline.
- HC and CO emissions were reduced with the addition of methyl ethyl ketone, and CO_2 emissions increased. It was found that CO emissions reduced by 6.93%, 11.02%, 26.12% and 38.91%, respectively, with MEK10, MEK20, MEK30 and MEK40 fuels at 4000 rpm according to gasoline. In addition, HC emissions decreased by 3.22%, 6.45% and 12.90% with MEK20, MEK30 and MEK40 fuels respectively at 4000 rpm compared to that of gasoline.
- Engine performance and exhaust emissions are improved with the addition of methyl ethyl ketone. However, it was found that CO_2 increased as the methyl ethyl ketone ratio increases in fuel blends.
- Engine performance and exhaust emissions can be investigated with different with alcohol-derived fuel additives based on different engine loads. The effects of methyl ethyl ketone on NO_x emissions can be also observed.
- As a result, it is seen that methyl ethyl ketone can be used as an additive in a spark ignition engine without any modification.

5. CONFLICT OF INTEREST

Authors approve that to the best of their knowledge, there is not any conflict of interest or common interest with an institution/organization or a person that may affect the review process of the paper.

6. AUTHOR CONTRIBUTION

Tolga KOCAKULAK: Determining the Concept and/or Design Processes of the Research, Preparation of the Manuscript, Data Collection, Final Approval and Full Responsibility

Ahmet UYUMAZ: Management of the Concept and/or Design Process of the Research, Determining of the Concept and/or Design Processes of the Research, Critical Analysis of the

Intellectual Content, Final Approval and Full Responsibility

Emre ARABACI: Management of the Concept and/or Design Process of the Research, Critical Analysis of Intellectual Content, Data Analysis and Interpretation of the Results, Final Approval and Full Responsibility

Yusuf DAĞOĞLU: Data Collection, Preparation of the Manuscript, Data Analysis and Interpretation of the Results, Final Approval and Full Responsibility

Celal ÇAMOĞLU: Data Analysis and Interpretation of the Results, Preparation of the Manuscript, Data Collection, Final Approval and Full Responsibility

7. REFERENCES

Ackermann P., Braun K.E., Burkardt P., Heger S., König A., Morsch P., Lehrheuer B., Surger M., Völker S., Blank L.M., Du M., Alexander Heufer K., Roß-Nickoll M., Viell J., Von der Aßen N., Mitsos A., Pischinger S., Dahmen M., Designed to Be Green, Economic, and Efficient: A Ketone-Ester-Alcohol-Alkane Blend for Future Spark-Ignition Engines. Chemistry-Sustainability-Energy- Materials, ChemSusChem, Chemistry Europe 14, 5254–5264, 2021.

Durgun O., Alaçam S. A., Benzin–Naftalin Karışımının Buji Ateşlemeli Motorun Performansına ve Eksoz Emisyonlarına Etkisinin Deneysel İncelenmesi. 2nd International Symposium on Innovative Approaches in Scientific Studies, Samsun, 3, 569-571, 2018.

Heywood, J., Internal Combustion Engines Fundamentals. McGraw-Hill, New York, 1988.

Hoppe F., Burke U., Thewes M., Heufer A., Kremer F., Pischinger S., Tailor-Made Fuels from Biomass: Potentials of 2-butanone and 2-methylfuran in direct injection spark ignition engines. Fuel 167, 106-117, 2016.

Jenkins R.W., Moore C.M., Semelsberger T.A., Chuck C.J., Gordon J.C., Sutton A.D., The Effect of Functional Groups in Bio-Derived Fuel Candidates. Chemistry-Sustainability-Energy-Materials, ChemSusChem, Chemistry Europe 9, 922-931, 2016.

Kumar S., Nayek M., Kumar A., Tandon A., Mondal P., Vijay P., Bhangale U.D., Tyagi D., Aldehyde, ketone and methane emissions from motor vehicle exhaust: a critical review. American Chemical Science Journal 1(1), 1-27, 2011.

Libretexts Chemistry, The Basics of GOB Chemistry, Nice CXOne, https://chem.libretexts.org/Bookshelves/Introductory_Chemistry/Basics_of_General_Organic_and_Biological_Chemistry_(Ball_et_al.)/00%3A_Front_Matter/03%3A_Table_of_Contents 2023, (Accessed on 04.08.2023).

Magara-Gomez K. T., Olson M. R., Okuda T., Walz K. A., Schauer J. J., Sensitivity of hazardous air pollutant emissions to the combustion of blends of petroleum diesel and biodiesel fuel. Atmospheric Environment 50, 307-313, 2012.

Magnusson R., Nilsson A. C., The influence of oxygenated fuels on emissions of aldehydes and ketones from a two-stroke spark ignition engine. Fuel 90(3), 1145-1154, 2011.

Majumdar S. S., Pihl J. A., Toops T. J., Reactivity of novel high-performance fuels on commercial three-way catalysts for control of emissions from spark-ignition engines. Applied Energy 255, 113640, 2019.

Methyl Ethyl Ketone-Cameo Chemicals, 1999, https://cameochemicals.noaa.gov/chris/MEK.pdf, June, 1999, (Accessed on 16.07.2023).

Nabi M. N., Theoretical investigation of engine thermal efficiency, adiabatic flame temperature, NO_x emission and combustion-related parameters for different oxygenated fuels. Applied Thermal Engineering 30(8-9), 839-844, 2010.

Oprescu E-E., Dragomir R.E., Radu E., Radu A., Velea S., Bolocan I., Stepan E., Rosca P., Performance and emission characteristics of diesel engine powered with diesel–glycerol derivatives blends. Fuel Processing Technology, 126, 460-468, 2014.

Prabhahar M., Sendilvelan S., Prakash S., Saravanakumar M., Investigation of pine oil methyl ester blends with diesel on a compression ignition engine to control oxides of nitrogen and soot particles. Rasayan Journal of Chemistry 10,4, 1075-1079, 2017.

Raj C. S., Arul S., Senthilvelan S., Some comparative performance and emission studies on DI diesel engine fumigated with methanol and methyl ethyl ketone using microprocessor controlled fumigator. The Open Fuels Energy Science Journal 1(1), 74-78, 2008.

Raj C. S., Arul S., Sendilvelan S., Saravanan C. G., A comparative assessment on performance and emissions characteristics of a diesel engine fumigating with methanol, methyl ethyl ketone, and liquefied petroleum gas. Energy Sources, Part A: Recovery, Utilization, and Environmental Effects 32(17), 1603-1613, 2010.

Samoilov V. O., Borisov R. S., Stolonogova T. I., Zarezin D. P., Maximov A. L., Bermeshev M. V., ... Kapustin V. M., Glycerol to renewable fuel oxygenates. Part II: Gasoline-blending characteristics of glycerol and glycol derivatives with C3-C4 alkyl (idene) substituents. Fuel 280, 118585, 2020.

Sarjovaara T., Alantie J., Larmi M., Ethanol dual-fuel combustion concept on heavy duty engine. Energy 63, 76-85, 2013.

Shah A. N., Yun-Shan G., Jian-wei T., Carbonyls emission comparison of a turbocharged diesel engine fuelled with diesel, biodiesel, and biodiesel-diesel blend. Jordan Journal of Mechanical and Industrial Engineering 3(2), 2009.

Torres-Vinces L., Contreras-Zarazua G., Huerta-Rosas B., Sánchez-Ramírez E., Segovia-Hernández J. G., Methyl ethyl ketone production through an intensified process. Chemical Engineering Technology 43(7), 1433-1441, 2020.

Tüpraş,2023.https://www.tupras.com.tr/uploads/Urunler_en/UNLEADED_MOTOR_GASOLINE_95_RON-243.pdf, (Accessed on 16.07.2023).

Yang P. M., Lin K. C., Lin Y. C., Jhang S. R., Chen S. C., Emission evaluation of a diesel engine generator operating with a proportion of isobutanol as a fuel additive in biodiesel blends. Applied Thermal Engineering 100, 628-635, 2016.

Zhao H., HCCI and CAI Engines for the Automotive Industry. Elsevier Science, 2007.

JOURNAL of
MATERIALS and MECHATRONICS:A

e-ISSN 2717-8811
JournalMM, 2023, 4(2), 409-423
https://doi.org/10.55546/jmm.1271191

Araştırma Makalesi / Research Article

Akıllı Üretim Sistemlerinde Kontrol ve Otomasyon Uygulamaları İçin Esnek Üretim Sistemi Deney Seti Geliştirilmesi

Yakup Yasin ŞAHİN[1*], Sezai TAŞKIN[2], Faruk KARTAL[3]

[1] Defaş Madencilik Sanayi ve Tic. A.Ş., Eynez-Soma, Manisa / Türkiye
ORCID ID: https://orcid.org/0000-0003-0944-4567, yasinyakupsahin@gmail.com
[2] Manisa Celal Bayar Üniversitesi, Mühendislik Fakültesi, Elektrik-Elektronik Mühendisliği Bölümü, Yunusemre, Manisa / Türkiye
ORCID ID: https://orcid.org/0000-0002-2763-1625, sezai.taskin@cbu.edu.tr
[3] Modül Modern Eğitim Teknolojileri A.Ş., Muradiye-Yunusemre, Manisa / Türkiye
ORCID ID: https://orcid.org/0009-0000-2070-955X, faruk.kartal@metdidactic.com.tr

Geliş/ Received: 26.03.2023 **Kabul / Accepted:** 14.08.2023

ÖZET: Akıllı üretim sistemlerinin geliştirilmesi sanayide yeni bir yaklaşımı ve değişimi başlatmıştır. Günümüzde, teknolojiyi kullanarak katma değer üretebilen ve bu teknolojilerin gerektirdiği teknik becerilere sahip çözümler sunabilen çalışanlar daha avantajlı hale gelmektedir. Bu nedenle mesleki teknik eğitimin niteliğini artırmaya yönelik çalışmaların odağında bireylerin yeni teknolojilere kolayca uyum sağlamalarını ve öğrenmeyi öğrenmelerini sağlayan modeller geliştirmenin önemi her geçen gün daha da artmaktadır. Bu çalışmada sunulan esnek üretim sistemi deney seti, ürün esnekliği ve istasyon sıralama esnekliği gibi yapılanma imkanı sunan bir fabrika otomasyon seti olarak tasarlanmıştır. Deney seti; endüstriyel otomasyon ve haberleşme, veri işleme, hareket kontrol sistemleri, basınç, boyut vb. fiziksel değişkenlerin ölçülmesi ve analizi, kestirimci bakım, durum izleme, görüntü işleme vb. birçok teknik ve güncel konuyu kapsayacak özelliklere sahip olarak geliştirilmiştir.

Anahtar Kelimeler: Esnek Üretim Sistemi Deney Seti, Akıllı Üretim Sistemleri, Kontrol ve Otomasyon, Durum İzleme.

*Sorumlu yazar / Corresponding author: yasinyakupsahin@gmail.com

Bu makaleye atıf yapmak için / to cite this article

Şahin, Y.Y., Taşkın, S., Kartal F. (2023). Akıllı Üretim Sistemlerinde Kontrol ve Otomasyon Uygulamaları İçin Esnek Üretim Sistemi Deney Seti Geliştirilmesi. Journal of Materials and Mechatronics: A (JournalMM), 4(2), 409-423.

Development of Flexible Manufacturing System Experimental Set for Control and Automation Applications in Smart Production Systems

ABSTRACT: The development of smart manufacturing systems has initiated a new approach and change in the industry. Employees who can add value by utilizing technology and providing solutions with the technical skills required by these technologies are at an advantage. Determining methods that simplify the adoption of new technologies by individuals and prevent them from becoming idle in the labor market is becoming increasingly crucial as part of efforts to improve the quality of vocational education. The experimental setup is designed to function as a factory automation system, offering options for product and station sequencing flexibility. The experimental setup is developed to encompass various technical topics including industrial automation and communication, data processing, motion control systems, measurement and analysis of physical variables such as pressure and dimensions, predictive maintenance, condition monitoring, image processing, and more.

Keywords: Flexible Manufacturing System Experimental Set, Smart Production Systems, Control and Automation, Condition Monitoring.

1. GİRİŞ

Üretim zincirinin her aşamasının dijitalleşmesi, makina-insan-altyapı etkileşiminin sağlanması ile akıllı üretim sistemlerinin geliştirilmesi sanayide yeni bir yaklaşımı ve değişimi başlatmıştır. Küresel öngörüler, yeni sanayi devrimi ile ilişkili teknolojilerin daha çok uygulama alanı bulacağını ve sürekli yükselen bir eğilim göstereceğini işaret etmektedir (Tübitak, 2016).

Gelişimin ve değişimin hızlı olduğu günümüz dünyasında işletmelerin verimliliklerinin artmasında teknolojik gelişmeleri takip etmek ve mümkün olabildiğince bu teknolojilerle desteklemek büyük önem taşımaktadır. Pazarın müşteriler tarafından belirlendiği ve müşteri taleplerinin sürekli değişim gösterdiği günümüzde klasik üretim sistemlerinin yeterli verimi sağlayamadığı görülmektedir. Bu nedenle esneklik kavramı üretim sistemlerinin temelini oluşturmaktadır. Endüstri 4.0 ile birlikte bireyselleşmiş üretim sistemlerinin yanında, değişime ayak uydurabilen, esnek üretim sistemleri daha fazla ön plana çıkmaya başlamıştır. Böylece klasik üretimin yerini akıllı otomasyona dayalı esnek üretim sistemleri almaya başlamıştır (Gönen ve Çelik, 2014; Bildstein ve Seidelmann, 2014). Buna bağlı olarak, aynı üretim hattında farklı ürünlerin üretilebilmesi rekabetin temelini oluşturmakta ve düşük üretim adetlerinde yüksek çeşitliliği mümkün kılmaktadır.

Esnek üretim sistemleri otomotiv, elektronik, tüketici ürünleri ve diğer birçok endüstriyel sektörde kullanılmaktadır. Esnek üretim sistemi, bir üretim ortamında ürünlerin seri üretimi için kullanılan otomasyon ve bilgisayar kontrollü bir sistem olup farklı ürünlerin aynı üretim hattında üretilmesine ve üretim süreçlerinin hızlı bir şekilde değiştirilmesine olanak tanır. Bu sistemlerde üretim hatları bilgisayar desteklidir (Erdil, 2021).

Akıllı üretim sistemleri, esnek üretim sistemlerinin bir bileşeni olarak ortaya çıkmıştır (Wang ve ark., 2020). Bu sistemler, yapay zeka, nesnelerin interneti ve büyük veri analitiği gibi teknolojileri kullanarak üretim süreçlerini optimize etmek için akıllı kararlar alır. Akıllı üretim sistemleri, veri analitiği ile üretim verimliliğini artırırken, otomasyon teknolojileri sayesinde hata oranını azaltır (Jin ve ark., 2021). Durum izleme ise üretim süreçlerinin gerçek zamanlı olarak takip edilmesini sağlar (Li ve ark., 2022). Sensörler ve veri toplama sistemleri kullanılarak üretim ekipmanlarının performansı ve durumu sürekli olarak izlenir. Bu bilgiler, anormal durumları tespit ederek hızlı müdahale ve plansız duruşların önüne geçmeyi sağlar.

Çalışma konusu ile ilgili olarak literatürde yapılan çalışmalar incelendiğinde, modüler üretim sistemi gerçek zamanlı ve uzaktan erişimli kontrolü (Taşkın, 2007), esnek üretim sistemi kontrolü için alternatif bir denetleyici tasarımı (Yabanova, 2011), mühendislik eğitimi için gerçekçi ve pratik öğrenme altyapısı sağlamak amacıyla Endüstri 4.0 öğrenme fabrikası konsepti (Sackey ve ark., 2017) ve öğrencilerin katılımını ve ilgisini arttırmak için bir akıllı üretim hattı (Wang ve ark., 2021) çalışmaları görülmektedir. Diğer benzer çalışmalar ise; bir esnek üretim sistemine ürünlerin sorunsuz taşınması için otonom transfer sistemi (Cronin ve ark., 2020), çok çeşitli üretime yönelik bir esnek üretim sistemi modeli (Alszer ve Krystek, 2018), dijital ikiz teknolojisinin modelleme yöntemi ile ilgili esnek üretim modeli prototipi (Zhang ve ark., 2021) olarak verilebilir.

Bu çalışmanın konusu olan akıllı ve esnek üretim sistemleri günümüzde orta ve büyük ölçekli birçok işletmede üretimin temelini oluşturmaktadır. Dolayısıyla bu sistemlerin kullanıldığı işletmelerde ciddi bir işgücü istihdam edilmektedir. Bu yüzden bu sistemlerde yer alan teknolojilerin öğrenilmesi, çalışma prensiplerinin ve işlevlerinin daha iyi anlaşılması gerekmektedir. Bu noktada çalışmada sunulan deney seti ile esnek üretim sistemlerindeki teorik bilginin uygulamalı pratik bilgiye dönüştürülmesi hedeflenmiştir. Deney seti sistem üzerinde ardışık yapıda işlemler gerçekleştiren iş parçaları üzerinde rulman çakma, kalite kontrol vb. uygulamaları gerçekleştiren 6 istasyondan ve 1 ana kontrol ünitesinden oluşacak şekilde tasarlanmıştır. Çalışmanın ana katkısı, sınırlı sayıda bulunan esnek üretim sistemleri deney setlerine yeni bir konfigürasyon ve açık mimaride bir tasarımın kazandırılmasıdır. Bu deney düzeneğinin kapsadığı teknolojiler kullanılarak uygulamalar gerçekleştirilmesi pratik deneyime önemli katkılar sağlayacak niteliktedir.

Çalışmanın ikinci kısmında materyal ve yöntem, üçüncü bölümünde esnek üretim sistemi deney setine ait bulgular, dördüncü bölümde ise elde edilen sonuçlara yer verilmiştir.

2. MATERYAL VE YÖNTEM

Esnek üretim sistemi deney seti için toplamda 8 farklı birimden oluşan bir uygulama düzeneği tasarlanmıştır. Tasarlanan sistem, biri transfer birimi olmak üzere altı adet istasyondan ve bir adet ana kontrol ünitesinden oluşmaktadır. Şekil 1'de tasarlanan sistemin katı model görüntüsü, Şekil 2'de ise haberleşme yapısına ait blok diyagram verilmiştir.

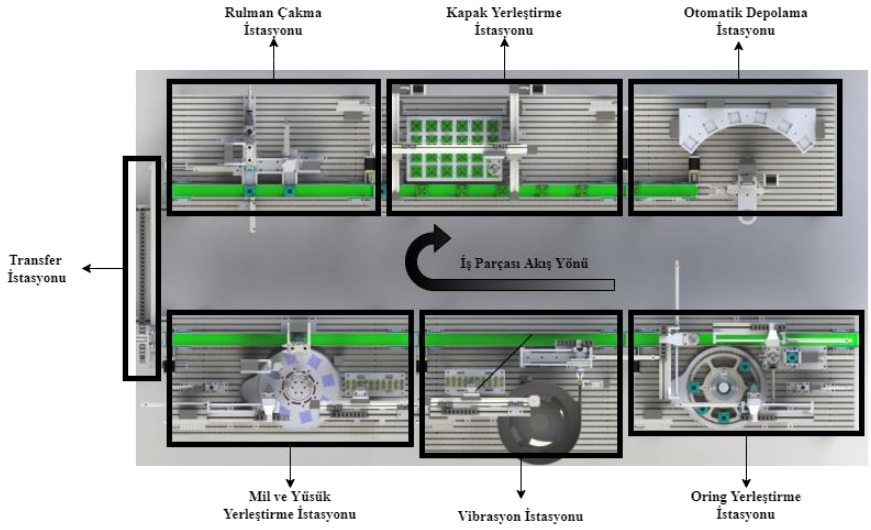

Şekil 1. İstasyonlar ve yerleşim planı

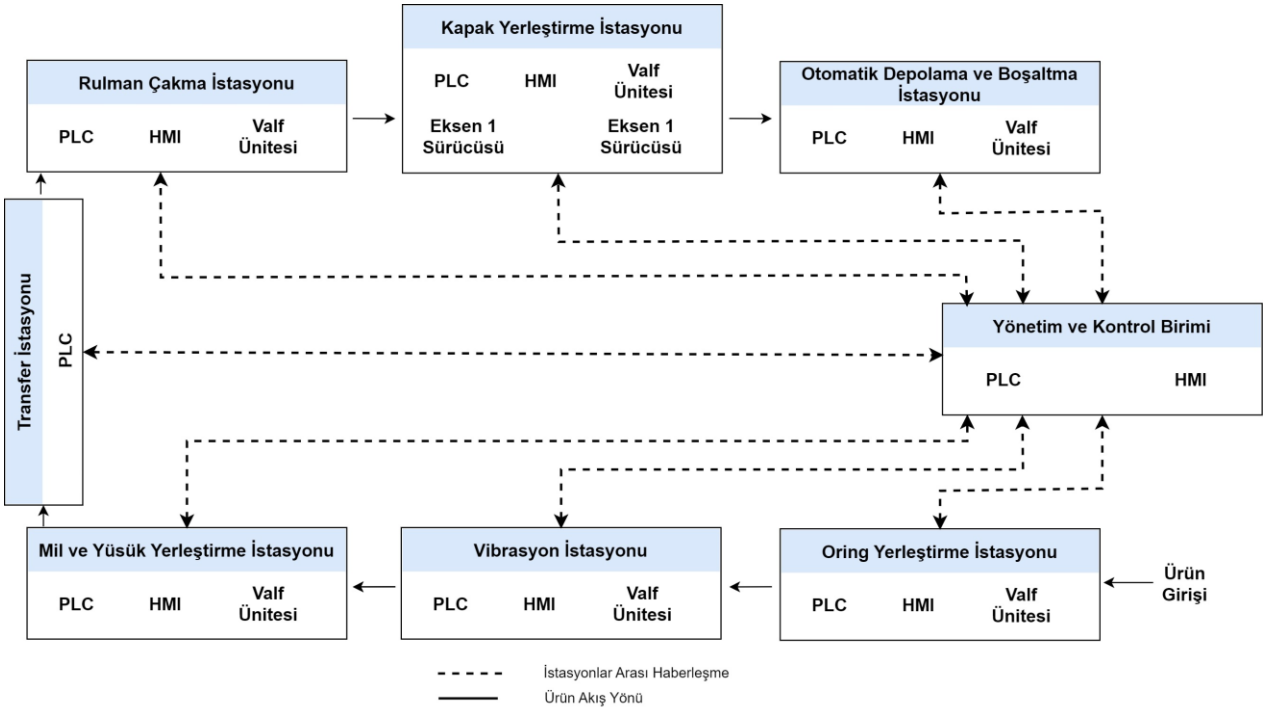

Şekil 2. İstasyonlar ile ana kontrol merkezi arası haberleşmesine ait blok diyagram

Bu istasyonlar dört farklı iş parçasının türüne ve şekline bağlı olarak işlemler gerçekleştirmek ve nihai bir ürün elde etmek üzerine planlanmıştır. İstasyonlarda işlenecek iş parçaları, kare/dairesel metal ve plastik yapıda olmak üzere dört farklı şekildedir. Şekil 3'de iş parçaları verilmiştir.

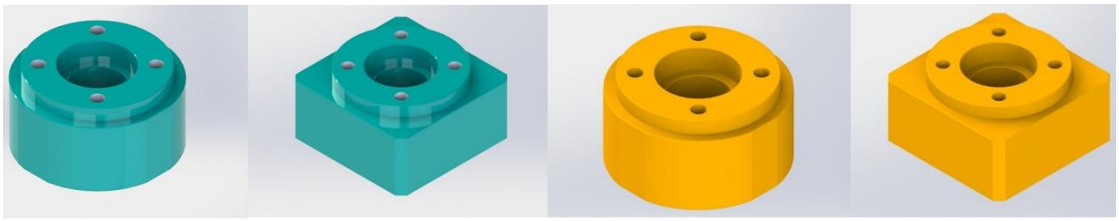

Şekil 3. Esnek üretim sisteminde kullanılan iş parçaları

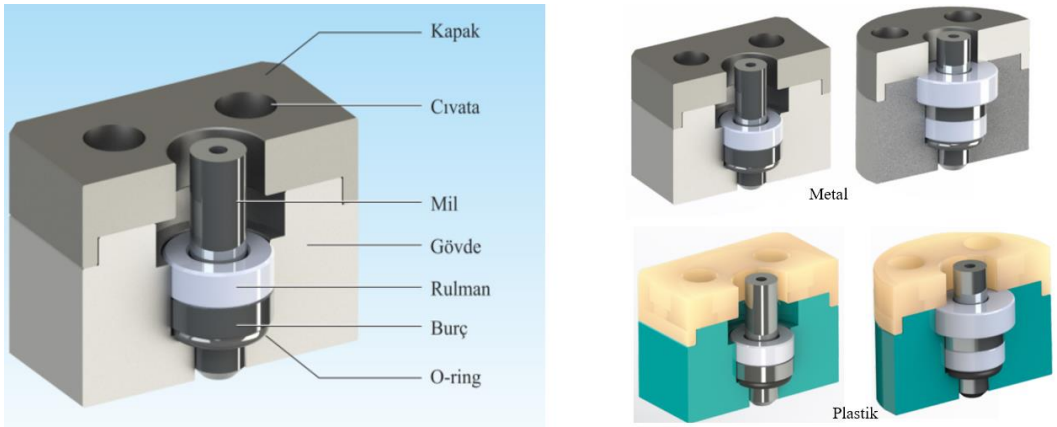

Şekil 4. Montaj işlemi bitmiş iş parçasının kesit görüntüsü

Şekil 4'te iş parçalarına montaj işleminde kullanılan ürünlerin iş parçası üzerindeki işlem sıralamasına ait görsel verilmiştir. İşlem sıralaması; (i) oring yerleşimi, (ii) mil yerleşimi, (iii) yüsük (burç) yerleşimi, (iv) rulman çakma işlemi, (v) kapak montajı şeklindedir.

2.1. Oring İstasyonu

Deney setinin ilk istasyonu olan oring istasyonu temel olarak 3 ana birimden oluşmaktadır. Bu birimlerden ilki otomatik besleme birimidir. Besleme biriminde çift etkili bir silindir yardımıyla şarjör mekanizması sayesinde sisteme ürün beslemesi otomatik olarak gerçekleşmektedir. İstasyona alınacak olan ürünler seçilir ve lineer çift etkili silindire bağlı olan vakum pistonu ile döner tablaya transfer edilir. İkinci birim olarak otomatik oring besleme birimi bulunmaktadır. Çift etkili silindir yardımıyla otomatik olarak beslenen oringler gripper tutucu yardımıyla merkezden tutularak iş parçasının içerisine yerleştirilir. Çift etkili lineer silindire bağlı olan vakum pistonu yardımıyla iş parçalarının konveyör banda transferi gerçekleştirilir. Böylece ilk istasyonda tüm işlemler tamamlanır ve bir sonraki istasyona iletilir. Şekil 5'te oring istasyon görüntüsü verilmiştir.

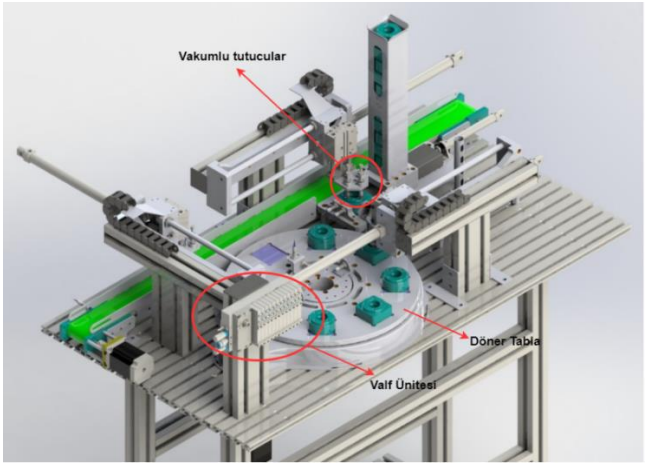

Şekil 5. Oring istasyonu

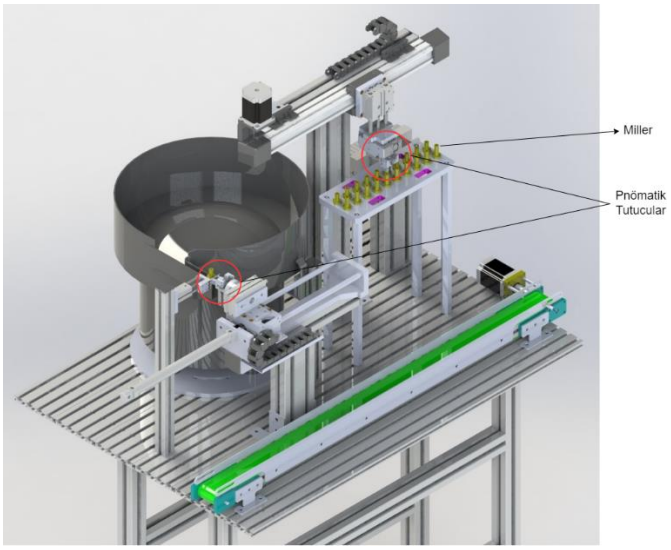

Şekil 6. Vibrasyon istasyonu

2.2 Vibrasyon İstasyonu

Vibrasyon kazanına karışık şekilde atılan miller titreşim sayesinde belirli bir düzende mil transfer birimine iletilmektedir. Çift etkili lineer silindir ve döner pnömatik tutucu ile alınan miller magazine dizilmek üzere mil dizme birimine iletilir. Step motor tarafından tahriki sağlanan bu eksen ile miller yerleri daha önceden belirlenen mil magazinine dizilir. Vibrasyon istasyonu Şekil 6'da verilmiştir.

2.3 Mil ve Yüsük Yerleştirme İstasyonu

İlk olarak istasyona alma işlemi lineer hareket eden çift etkili silindire bağlı olan döner silindirlerdeki iki adet gripper tutucu sayesinde gerçekleştirilir (Şekil 7, No 4). Magazine bir önceki istasyonda dizilmiş olan miller sırasıyla iş parçalarının içerisine yerleştirilir. Lineer actuator-eyleyici yardımıyla pozisyonlama yapılarak miller daha önceden belirlenen noktalardan gripper tutucu yardımıyla tutularak iş parçalarına yerleştirilir (Şekil 7, No 1). Lineer çift etkili silindire bağlı bulunan gripper yardımı ile yüsükler tutularak iş parçalarının içerisine yerleştirilir (Şekil 7, No 2). Yerleştirme işleminin ardından döner tabla 45 derece saat yönünde dönerek bir sonraki birime iş parçasını aktarır. Lineer silindirin iş parçası üzerine kapanması ile belirli süreli bir basınç sızdırmazlık testine tabi tutulur (Şekil 7, No 3). İşlem sonucunda hatalı montaj yapılmış olan ürünlerin ayrıştırılması sağlanır. Mil ve yüsük yerleştirme istasyonu Şekil 7'de verilmiştir.

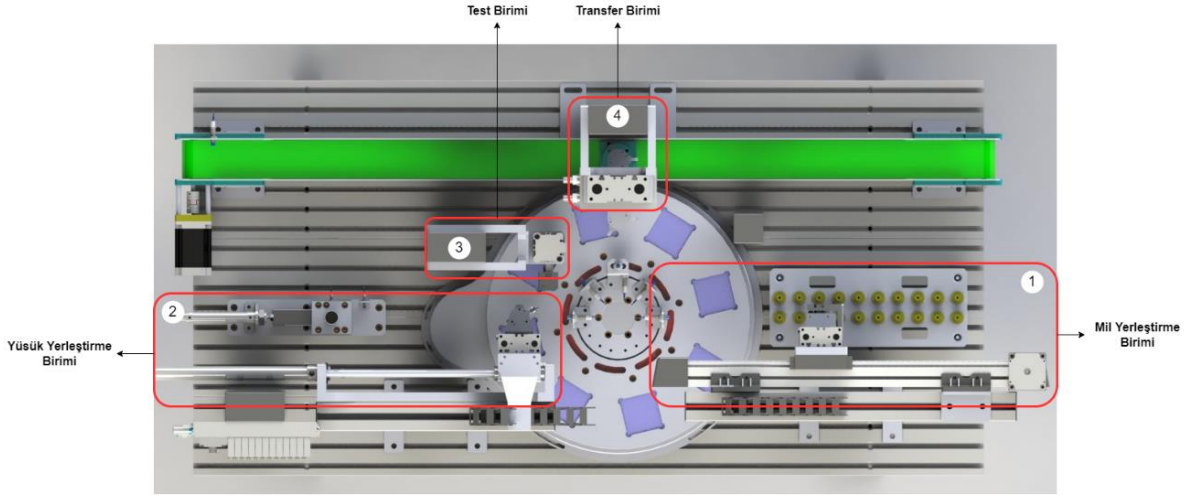

Şekil 7. Mil ve yüsük yerleştirme istasyonu

2.4 Rulman Çakma İstasyonu

Geliştirilen deney setinin dördüncü istasyonu olan rulman çakma istasyonunda iş parçalarındaki millere rulman geçirme ve baskı kuvvetiyle istenen ölçüde çakma işlemi gerçekleştirilir. Çift etkili silindir ile iş parçaları istasyona alınır. Döner silindire bağlı pnömatik tutucular ile rulman merkezdeki milin çevresine yerleştirilir. Ardından çift etkili lineer silindir ile üzerine baskı uygulanır. Uygulanan kuvvet yük hücresi ile kilogram cinsinden okunur ve oransal olarak ayarlanır. İstenen değerlerin dışında olan işlemler hatalı olarak sınıflandırılır. İşlem sonucu başarılı olan ürünler çift etkili silindir ile konveyör banda itilerek bir sonraki istasyona transfer edilir. Şekil 8'de geri beslemeli baskı kontrol sisteminin blok diyagramı, Şekil 9'da bu istasyonun akış şeması, Şekil 10'da ise istasyon görselinin üstten görünüşü verilmiştir.

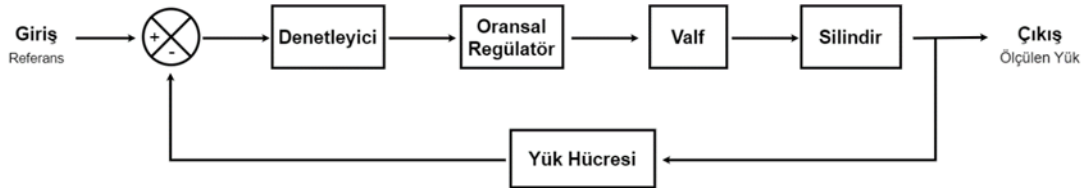

Şekil 8. Geri beslemeli baskı kontrol sisteminin blok diyagramı

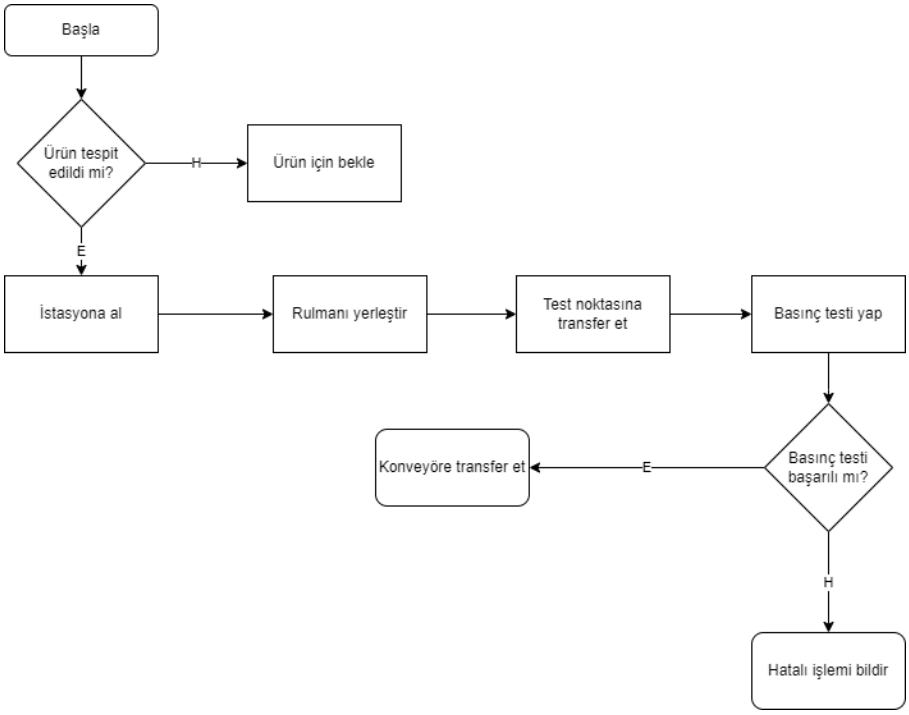

Şekil 9. Rulman çakma istasyonu akış şeması

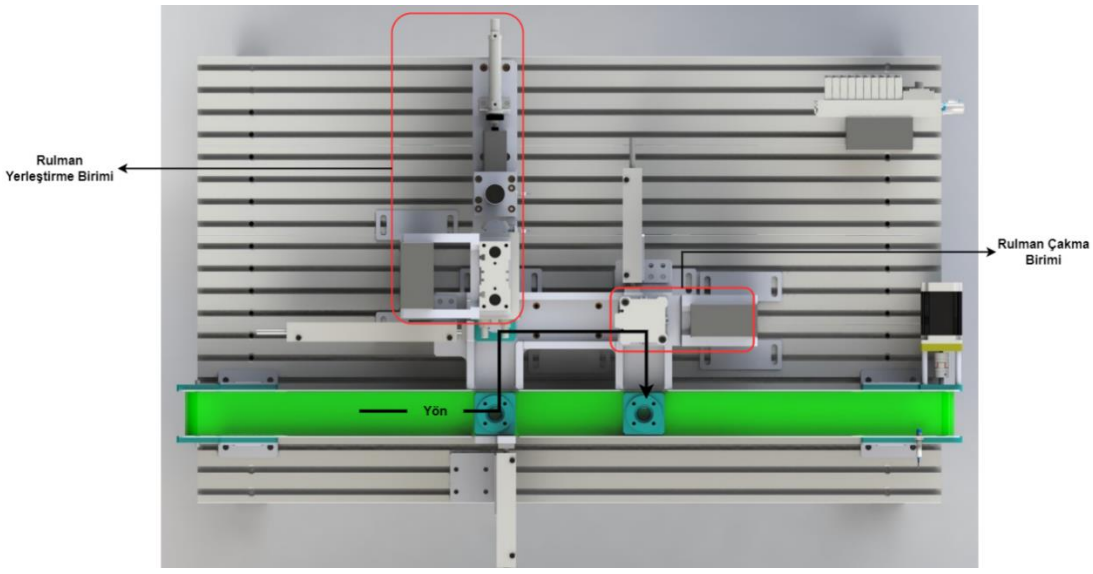

Şekil 10. Rulman çakma istasyonu

2.5. Kapak Yerleştirme İstasyonu

Bu istasyonda konveyör banttan gelen ürünler tespit edilerek kapak yerleştirme işlemi gerçekleştirilmektedir. Her bir çeşit kapak aynı eksende olmak üzere magazine dizilir. Gelen iş parçası tespit edildikten sonra parçaya ait olan kapaklar vakum ile tutulur ve ardından iki eksende

hareket eden elektrikli eyleyici ile pozisyonlanır. Böylece iş parçalarının kapakları yerleştirilerek bir sonraki istasyona transfer edilir. Şekil 11'de kapak yerleştirme istasyonu akış şeması, Şekil 12'de ise istasyon görünümü yer almaktadır.

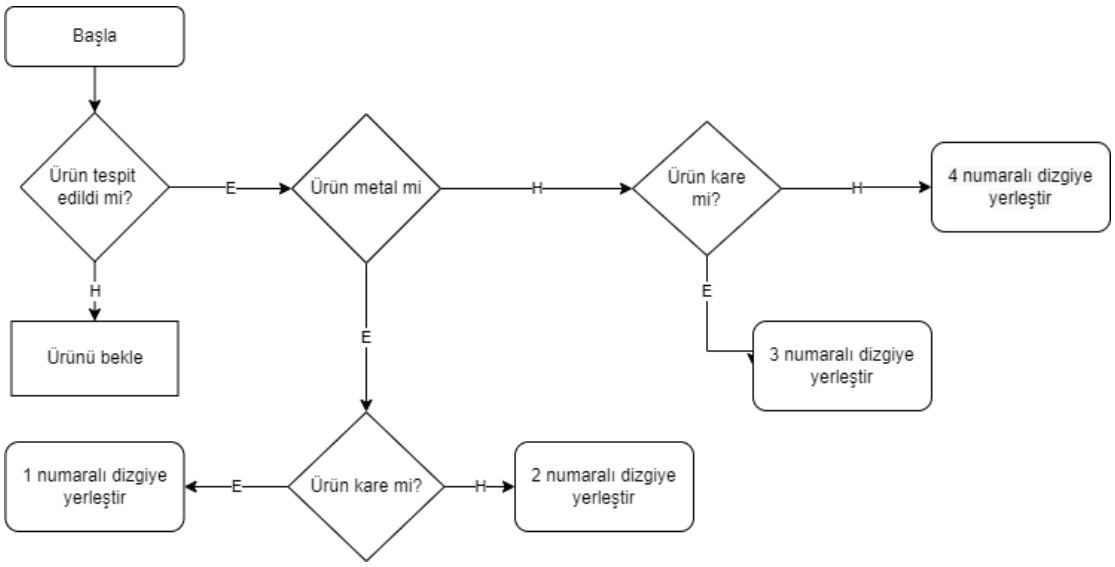

Şekil 11. Kapak yerleştirme istasyonu iş akış şeması

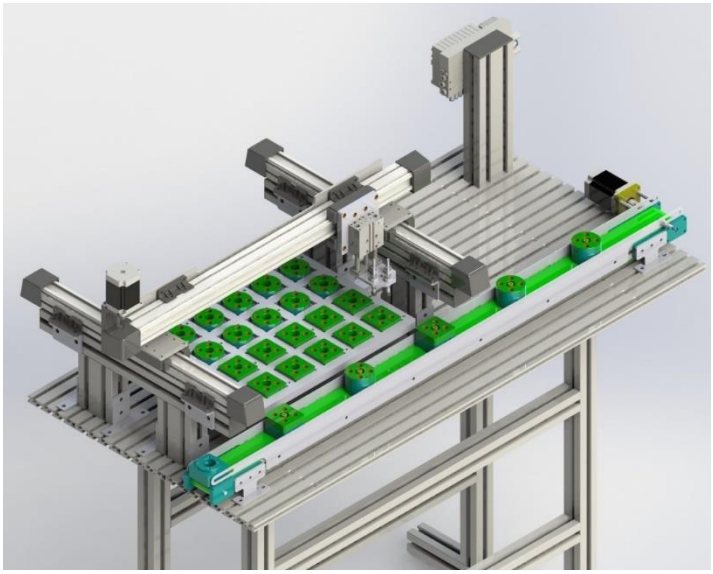

Şekil 12. Kapak yerleştirme istasyonu

2.6. Otomatik Depolama ve Boşaltma İstasyonu

Esnek üretim sistemlerinde anlık değişen isteklere hızlı cevap verebilmek için akıllı depolama sistemleri tercih edilir. Bu sistemler talep ya da üretim durumuna göre fazla malzemeyi depolar ya da gerektiğinde sisteme malzeme desteği sağlar. Otomatik depolama istasyonu, deney setinde bu işlevi yerine getirmektedir. Montajı gerçekleştirilen iş parçaları son ürün olarak bu istasyona ulaşır. Dairesel ve lineer olarak hareket eden eyleyiciler ile pozisyonlama yapılır. Her bir ürün kendisine ait olan dizgide ilgili boş yere yerleştirilir. Böylece işlemi bitmiş ürünlerin otomatik olarak depolanması yapılmış olur. Şekil 13'de istasyonun görseli verilmiştir.

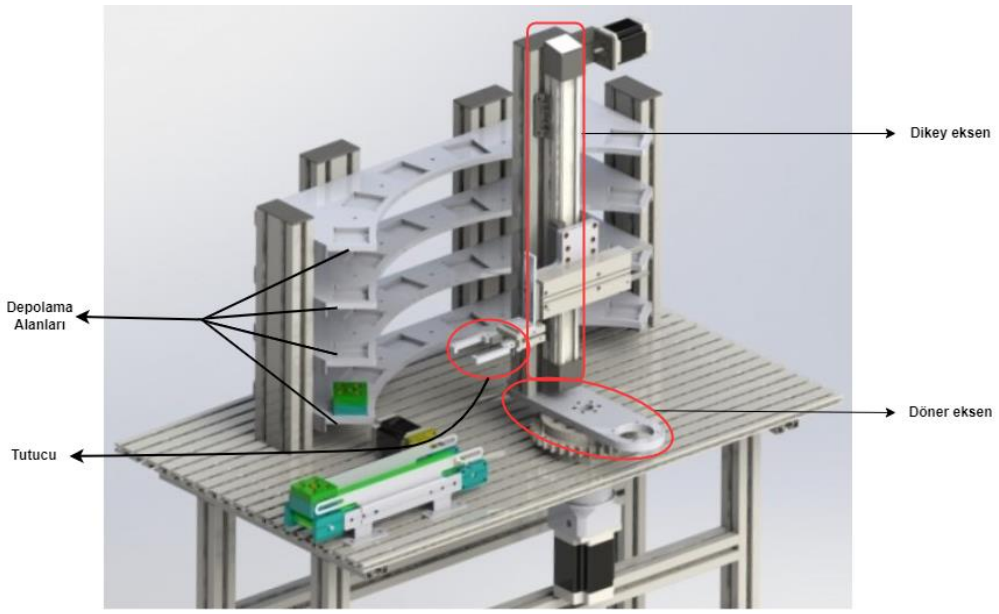

Şekil 13. Otomatik depolama ve boşaltma istasyonu

3. BULGULAR VE TARTIŞMA

3.1. İş Parçalarının Tespiti

İş parçalarının tespitinde ; (i) optik, indüktif ve kapasitif algılayıcılar ve (ii) kamera kullanılarak görüntü işleme yöntemi ile ürün tespiti olmak üzere iki farklı yöntem kullanılmıştır. İş parçaları, istasyonların çeşitli noktalarında tespit ve ayırma işlemine tabi tutulmaktadır. Örnek olarak istasyon 5'te ürünlerin şekli ve yapısı tespit edilerek uygun olan kapakların yerleştirilme işlemi gerçekleştirilmektedir. Ayrıca istasyon 6'da her bir iş parçasının şekli ve yapısı tespit edilerek farklı bir depolama dizgisine yerleştirilmektedir. Böylece her bir ürüne farklı bir işlem uygulanması sağlanmaktadır. Şekil 14'de ürün tespitinde kullanılan yöntemin lojik şeması verilmiştir. Tablo 1'de iş parçasına bağlı olarak çıkış veren algılayıcıların tablosu verilmiştir.

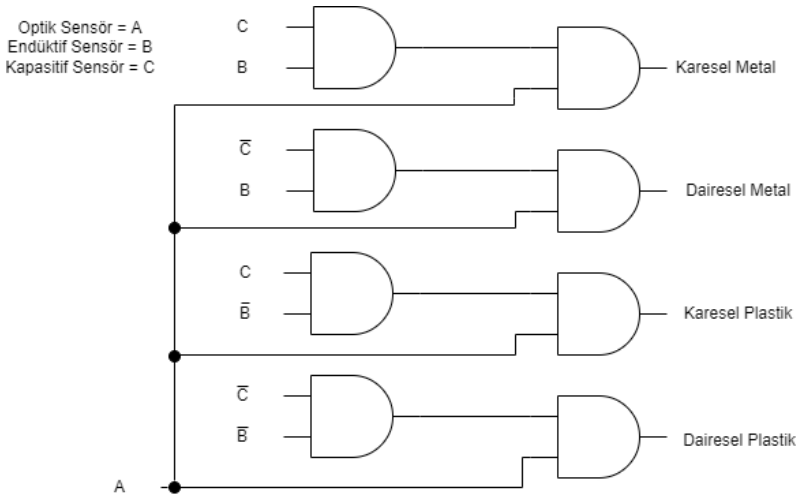

Şekil 14. Ürün tespitinde kullanılan algılayıcıların lojik bağlantı şeması

Tablo 1. Ürünlerin tespiti için algılayıcı çıkış durumları

	Optik Sensör	Indüktif Sensör	Kapasitif Sensör
Kare Metal	✓	✓	✓
Daire Metal	✓	✓	✗ (dairesel yapıdan dolayı cisme uzak olduğundan)
Kare Plastik	✓	✗	✓
Daire Plastik	✓	✗	✗ (dairesel yapıdan dolayı cisme uzak olduğundan)

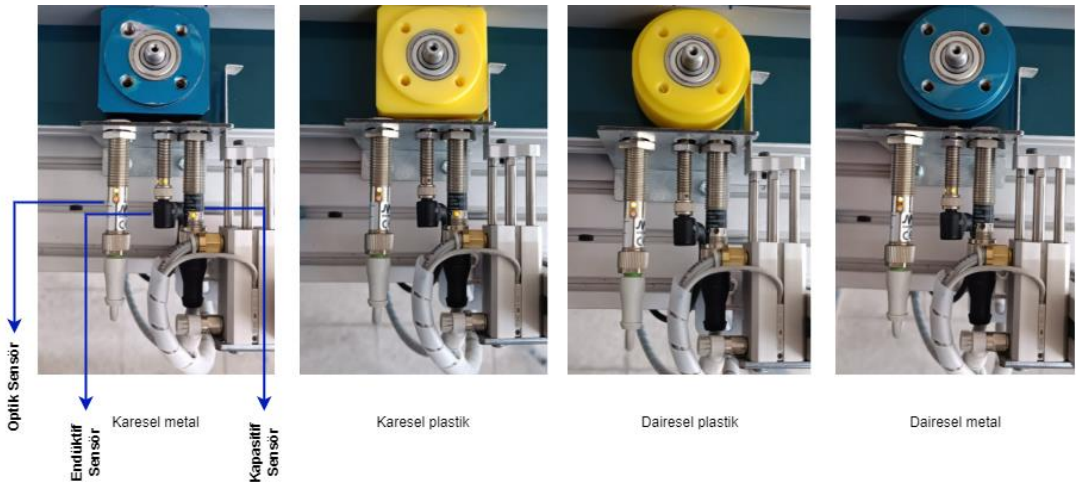

Şekil 15. Ürün tespit noktasında algılayıcılar ve iş parçalarının görüntüsü

Görüntü işleme ile iş parçalarının tespiti üç aşamada yapılmaktadır. İlk olarak kameranın görüntü açısına giren iş parçası optik algılayıcı ile tespit edilmektedir. Aynı zamanda indüktif algılayıcı kullanılarak iş parçasının metal olup olmadığı bilgisi kontrol edilmektedir. Cisimden yansımalı optik algılayıcı üzerinden Raspberry Pi girişine dijital sinyal bilgisi iletilerek iş parçasının geldiği ve tespit için hazır olduğu bilgisi gönderilmektedir. İş parçası tespiti, OpenCV kütüphanesi kullanılarak Python programlama ortamında gerçekleştirilmiştir. Kameradan alınan anlık görüntü üzerinde gerekli maskeleme ve filtreleme işlemlerinden sonra oluşan siyah beyaz görüntü ile kenar tespiti yapılmıştır. 4 adet kenar tespit edilen iş parçaları kare olarak adlandırılırken 4 adetten fazla kenar tespit edilen iş parçaları ise dairesel olarak tanımlanmıştır. Şekil 16'da görüntü işleme yöntemi ile iş parçası tanımlamasına ait bir ekran görüntüsü verilmiştir.

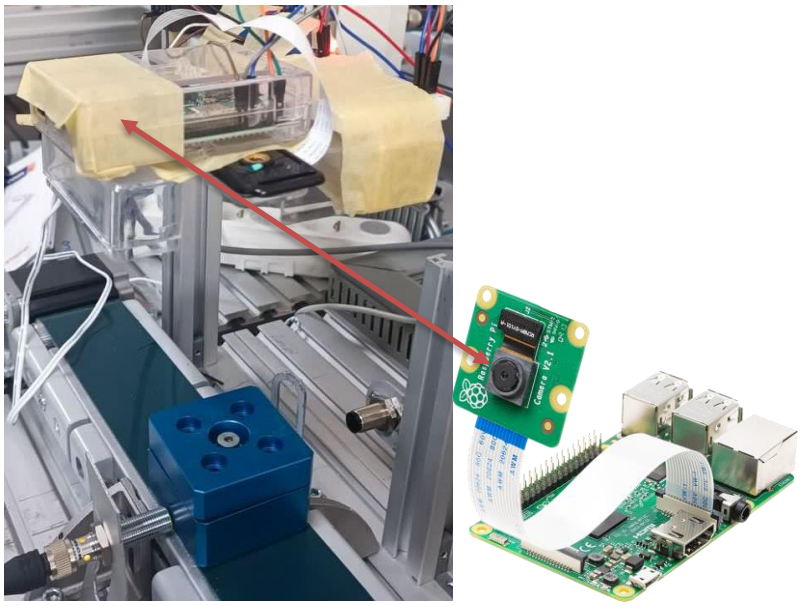

(a) Uygulama Görseli (b) Raspberry Pi ve Kamera

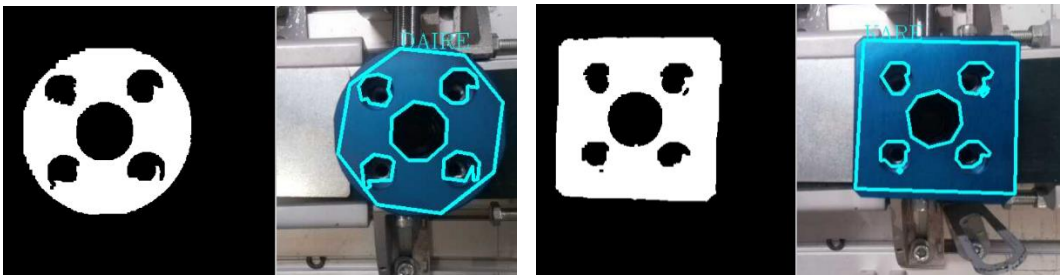

Şekil 16. Deney setinde görüntü işleme yöntemi ile iş parçası tanımlaması

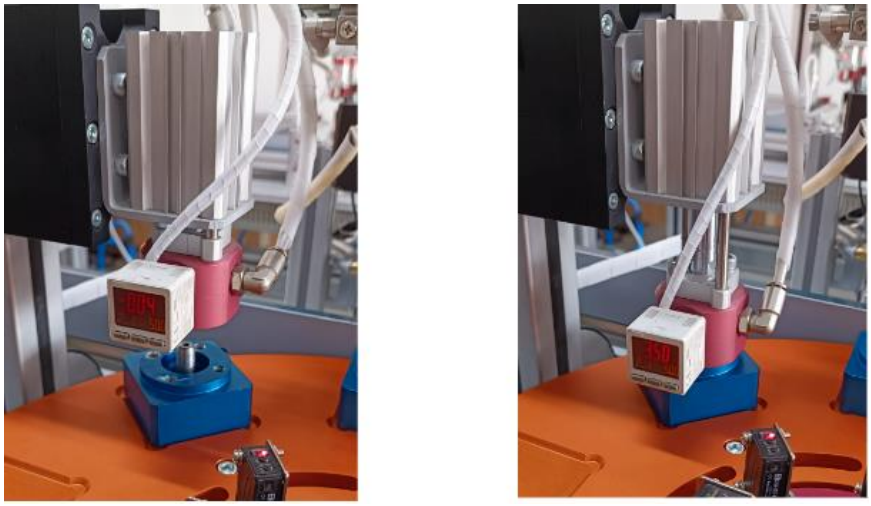

(a) İşlem öncesi (b) İşlem sonrası

Şekil 17. Sızdırmazlık testi görüntüsü

3.2. Basınç ve Sızdırmazlık Testi

Cisimden yansımalı optik algılayıcı ile istenen noktaya ulaşan iş parçasının tespit edilmesiyle basınç ve sızdırmazlık testi başlatılmaktadır. Silindir üzerine yerleştirilmiş olan konum algılayıcıları ile silindirin ileri pozisyonda olduğu tespit edilir ve farklı bir valf tetiklenerek basınçlı hava iş parçasının içine yönlendirilir. Ekran üzerinden belirlenen süre kadar basınç iş parçasına uygulanır.

Belirlenen süre içerisinde istenen basınç değerine ulaşılır ve basınç değeri sabit kalırsa işlem başarılı olarak değerlendirilir. Başarısız olan işlem görsel ve sesli uyarı ile kullanıcıya bildirilir. Şekil 17'de sızdırmazlık testinin uygulama görüntüsü verilmiştir.

3.3. Baskı ve Rulman Çakma İşlemi

Bu istasyonda yer alan yük hücresi (load-cell) ve oransal regülatör Şekil 8'de gösterilen kapalı çevrimli denetim sistemi yapısında çalışmaktadır. Geri besleme elamanı olarak kullanılan yük hücresinden alınan 0-10V bilgisine göre oransal regülatör kontrol edilmektedir. İstenen süre içerisinde başarısız sonuçlanan işlem görsel ve sesli uyarı ile kullanıcıya bildirilmektedir. Şekil 18'de rulman çakma işlemine ait deney seti ekipmanı gösterilmiştir.

Şekil 18. Rulman çakma ünitesi

Deney setinin tüm istasyonlarının birlikte yer aldığı resim Şekil 19'da verilmiştir. Burada tüm istasyonlar ana kontrol ünitesi ile birlikte görülmektedir. Deney setindeki tüm çalışma senaryoları farklı istasyonların bir araya getirilmesi, yerlerinin değiştirilmesi vb. şekilde oluşturularak çeşitli çalışma senaryoları oluşturulabilmektedir.

4. SONUÇLAR

Elektrik, Elektronik, Otomasyon, Makine ve Mekatronik gibi teknik bölümlerde öğrenim gören öğrencilerin dijital dönüşüm süreçlerini içeren ve esnek üretim prosesleri barındıran nitelikli eğitim setlerini kullanarak deneyim kazanmaları sağlanarak endüstriye hazır bulunuşluk düzeylerinin arttırılması günümüzde daha da önemli hale gelmiştir. Bu çalışmada sunulan deney setinde farklı ürünleri temsil etmek için yapı ve şekil itibariyle birbirinden farklı 4 adet iş parçası kullanılarak bir dizi üretim işlemleri benzetimi yapılmıştır. Bu çalışma ile fabrikalarda üretim modelini sembolize eden esnek üretim sistemi tasarlanmıştır.

Şekil 19. Tasarlanan esnek üretim sistemi deney seti

Aşağıda sıralanan konuların uygulamaları bu çalışma kapsamında geliştirilen deney seti kullanılarak gerçekleştirilebilir.

- Dağıtık ve merkezi kontrol uygulamaları,
- Üretim sistemleri arasında veri alışverişi ve haberleşme,
- Arıza tespit tekniklerinin uygulanması ve öğretilmesi,
- Elektrik kumanda ve devre elemanlarının bağlantıları ve kullanımı,
- Üretim biriminin mekanik olarak kurulumu,
- PLC programlama ile dijital ve analog sinyallerin işlenmesi,
- Basınçlı havanın dağıtımı ve kullanıma hazır hale getirilmesi,
- Doğrusal ve döner eksenli pnömatik silindir uygulamaları,

- Vakum teknolojisi ve uygulamaları,
- HMI panel tasarımı ve görsel kullanıcı arayüzü oluşturma,
- Basınç altında sızdırmazlık testi ile üretimde kalite kontrol uygulaması,
- Yük hücresi kullanarak kuvvet testi uygulaması,
- Geri besleme denetim sistemleri ile oransal kontrol uygulamaları,
- Adım motoru sürme ve pozisyon kontrol uygulamaları,
- Optik, indüktif ve kapasitif temassız algılayıcıların kullanımı,
- Dağıtık/Uzak giriş çıkış modüllerinin kullanılması,
- Farklı yapıda üretim senaryoları oluşturma ve PLC programlama.

Deney setinin geliştirilmesi süreçlerinde dijitalleşme, veri analizi, görselleştirme, iş parçaları için izlenebilirlik zincirinin oluşturulması gibi özellikle yazılım süreçlerine yönelik uygulamalar sisteme entegre edilebilir.

6. TEŞEKKÜR

Bu çalışma, sorumlu yazar Yakup Yasin ŞAHİN'in Yüksek Lisans tez çalışması kapsamında ve Modül Modern Eğitim Teknolojileri A.Ş firmasının desteği ile gerçekleştirilmiştir. Bu çalışmada sunulan deney seti için Modül Modern Eğitim Teknolojileri A.Ş firması KOSGEB'ten Ür-Ge desteği almıştır. Katkılarından dolayı KOSGEB Manisa İl Müdürlüğü'ne ve Modül Modern Eğitim Teknolojileri A.Ş'ye teşekkür ederiz.

7. ÇIKAR ÇATIŞMASI

Yazar(lar), bilinen herhangi bir çıkar çatışması veya herhangi bir kurum/kuruluş ya da kişi ile ortak çıkar bulunmadığını onaylamaktadırlar.

8. YAZAR KATKISI

Yakup Yasin ŞAHİN çalışmanın kavramsal ve tasarım süreçlerinin belirlenmesi, Sezai TAŞKIN ve Faruk KARTAL tasarım süreçlerinin geliştirilmesi, genel konseptin doğrulanmasında çalışmaya katkı sağlamışlardır.

9. KAYNAKLAR

Bildstein A., Seidelmann, J., Endüstri 4.0 Üretimine Geçiş, Automatisierung und logistik, Springer Vieweg, Wiesbaden, 2014.

Cronin, C., Awasthi, A., Conway, A., O'Riordan, D., Walsh, J., Design and development of a material handling system for an autonomous ıntelligent vehicle for flexible manufacturing, Procedia Manufacturing, 51, 493-500, 2020.

Erdil A., Manufacturing-Production systems and their ımportance:evaluation of flexible manufacturing systems, European Journal of Science And Technology, 29, 331-342, 2021.

Gönen S., Çelik M., Esnek üretim sistemleri uygulayan işletmelerde üretim maliyetlerinin değerlendirilmesi, Dergipark, 1(4), 133-143, 2004.

Jin X., Wu X., Yu L., Intelligent manufacturing system based on big data and deep learning. Engineering Science, 23(6), 60-68, 2021.

Li Y., Liu X., Wang F., Yang Y., Real-time monitoring and fault diagnosis of production processes in smart manufacturing. Journal of Manufacturing Systems, 64, 408-420, 2022.

Alszer S., Krysrek K. Modular, didactic flexible manufacturing system - case study, 4th International Conference on Control, Automation and Robotics (ICCAR), Auckland, 2018.

Sackey S. M., Bester A., Adams D., Industry 4.0 learning factory didactic design parameters for industrial engineering education in South Africa, South African Journal of Industrial Engineering, 1(28),114-124, 2017.

Taşkın S., MPS modüler üretim sisteminin bilgisayar destekli gerçek zamanlı kontrolü ve teknik eğitime uygulanması, Marmara Üniversitesi Fen Bilimleri Enstitüsü, Doktora Tezi, 2007.

Wang L., Lu Y., Cao W., Hu G., Intelligent manufacturing systems with digital twin in industry 4.0. Robotics and Computer-Integrated Manufacturing, 63, 101921, 2020.

Wang S., Meng J., Xie Y., Jiang L., Ding H., Shao X., Reference training system for ıntelligent manufacturing talent education: platform construction and curriculum development, Journal of Intelligent Manufacturing,1-40, 2021.

Yabanova I., Esnek üretim sisteminin gerçek zamanlı uzaktan erişimli kontrolü ve mekatronik eğitimine uygulanması, Sakarya Üniversitesi Fen Bilimleri Enstitüsü, Doktora Tezi, 2011.

Yeni sanayi devrimi: akıllı üretim sistemleri teknoloji yol haritası, Tübitak, 2016.

Zhang Hu, Xiong Liu, Dong Li, Research and practice of lightweight digital twin speeding up the implementation of flexible manufacturing systems, IEEE 1st International Conference on digital Twins and Parallel Intelligence (DTPI), Beijing, 2021.

JOURNAL of
MATERIALS and MECHATRONICS:A

e-ISSN 2717-8811
JournalMM, 2023, 4(2), 424-445
https://doi.org/10.55546/jmm.1291032

Araştırma Makalesi / Research Article

Improved Tuna Swarm Optimization Algorithm for Engineering Design Problems

Harun GEZİCİ

Kırklareli University, Electronics and Automation Department, Kırklareli, Turkey,
ORCID ID: https://orcid.org/0000-0003-1604-1416, harun.gezici@klu.edu.tr

Geliş/ Received: 02.05.2023; **Kabul / Accepted:** 20.09.2023

ABSTRACT: Tuna Swarm Optimization (TSO) which is developed by being inspired by the hunting strategies of the tuna fish is a metaheuristic optimization algorithm (MHA). TSO is able to solve some optimization problems successfully. However, TSO has the handicap of having premature convergence and being caught by local minimum trap. This study proposes a mathematical model aiming to eliminate these disadvantages and to increase the performance of TSO. The basic philosophy of the proposed method is not to focus on the best solution but on the best ones. The Proposed algorithm has been compared to six current and popular MHAs in the literature. Using classical test functions to have a preliminary evaluation is a frequently preferred method in the field of optimization. Therefore, first, all the algorithms were applied to ten classical test functions and the results were interpreted through the Wilcoxon statistical test. The results indicate that the proposed algorithm is successful. Following that, all the algorithms were applied to three engineering design problems, which is the main purpose of this article. The original TSO has a weak performance on design problems. With optimal costs like 1.74 in welded beam design problem, 1581.47 in speed reducer design problem, and 38.455 in I-beam design problem, the proposed algorithm has been the most successful one. Such a case leads us to the idea that the proposed method of this article is successful for improving the performance of TSO.

Keywords: Tuna Swarm Optimization, Swarm-Based Metaheuristic Algorithm, Engineering Design Problems.

*Sorumlu yazar / Corresponding author: harun.gezici@klu.edu.tr

Bu makaleye atıf yapmak için /To cite this article

Gezici, H. (2023). Improved Tuna Swarm Optimization Algorithm for Engineering Design Problems. Journal of Materials and Mechatronics: A (JournalMM), 4(2), 424-445.

1.INTRODUCTION

Today, real world problems are identified through complex mathematical equations which include many parameters. In the field of optimization, these mathematical equations are named objective functions (Noureddine, 2015). Depending on the kind of the problem, the output of the objective function may be required to be minimum or maximum (Mareli and Twala, 2018). At the same time, these problems have many limitations. These limitations are generally about the interrelation of the parameters in the objective functions. The overall purpose of optimization is to optimally determine the parameters in the objective function under certain limitations (Hashim et al., 2022). In the early stages of optimization studies, gradient descent (GD) methods were used. GD is unlikely to be preferred by researches because of its incapability in solving nonlinear design problems. Besides, for engineering problems with wide search space, computation times are long and they are not able to present optimum solutions (S. Kumar et al., 2023). As a result of such disadvantages of GD, researchers focused on metaheuristic algorithms (MHA) (Feng et al., 2021). Depending on the improvement procedures within their structure, MHAs aim to find the most reasonable result within the most reasonable period of time without scanning the search space. MHAs are classified into four subgroups depending on their source of inspiration. These are

- Evolution-based Algorithms: They are improved by being inspired by the biological behaviours of living creatures. They are based on evolutionary laws like crossover and mutation. Primary evolution-based algorithms are genetic algorithms (Mirjalili, 2019), differential evolution (Deng et al., 2021), genetic programming (F. Zhang et al., 2021), evolutionary strategies (Rosso et al., 2022), and evolutionary programming (Gul et al., 2021).
- Swarm-based Algorithms: They are improved by being inspired by the social behaviours of animals like insects and birds within their group. Particle swarm optimization (PSO) (Gad, 2022), ant colony optimization (Wu et al., 2023), grey wolf optimizer (GWO) (Mirjalili et al., 2014), monarch butterfly optimization (G.-G. Wang et al., 2019), earthworm optimizer (G.-G. Wang et al., 2018), moth search algorithm (G.-G. Wang, 2018), firefly algorithm (V. Kumar and Kumar, 2021), artificial bee colony (Öztürk et al., 2020), bat algorithm (BA) (Y. Wang et al., 2019) and Tuna swarm optimization (Xie et al., 2021) are some examples of MHA in this group.
- Physical-based Algorithms: They are improved through various physic laws. Simulated annealing (Amine, 2019), gravitational search algorithm (Rashedi et al., 2009), nuclear reaction optimization (Wei et al., 2019), water cycle algorithm (Korashy et al., 2019), sine cosine algorithm (SCA) (Abualigah and Diabat, 2021), big bang-big crunch (Mbuli and Ngaha, 2022), black hole (Abdulwahab et al., 2019) and harmony search (Abualigah et al., 2020) are the example of physics-based algorithms.
- Human-based algorithms: They are improved by being inspired by the social behaviours of humans. Teaching-learning-based optimization (Li et al., 2019), social evolution and learning optimization (M. Kumar et al., 2018), group teaching optimizer (Y. Zhang and Jin, 2020), heap-based optimizer (Askari, Saeed, et al., 2020), political optimizer (Askari, Younas, et al., 2020), taboo search (Prajapati et al., 2020), Exchange market algorithm (Jafari et al., 2020) and brain storm optimizer (Xue et al., 2022) are examples of this group.

MHAs are stochastic. They have two search procedures; exploration and exploitation (Raja et al., 2022). During the exploration phase, MHAs determine the promising sections of search space.

During exploitation phase, the determined sections are surveyed in detail. In order to succeed, one of the most significant characteristic of MHAs is the balance between exploitation and exploration (S. Kumar et al., 2023). In some MHAs, this balance is constructed by a probability key that is determined randomly and ranges between 0 and 1 (Ramachandran et al., 2022). Besides, in some MHAs, exploration is performed in early iteration numbers and exploitation is performed in advanced iteration numbers (Xie et al., 2021). Some optimization problems have one local minimum, which is the global minimum at the same time. Some problems have more than one local minimum of which only one is global minimum. Therefore, it is more difficult to solve these problems. Most of the MHAs improved to solve this kind of problems have the disadvantages of premature convergence and being caught by local minimum trap. Moreover, as it is stated by no free lunch theorem, an optimization algorithm cannot solve all optimization problems (Wolpert and Macready, 1997). Hence, researchers tend either to improve new optimizers or to increase the productivity of the available ones.

This study presents an improved version of recently published swarm-based TSO. The proposed algorithm is named Improved TSO (ITSO). It specifically focuses on the premature convergence problem of TSO. In addition to that, local search procedure is improved in order to prevent it from being trapped by local minimum. The improvement is about focusing on the three best points of the search space rather than focusing on the best one. This method eliminates the problems caused by the premature convergence problem by increasing the efficiency of TSO's global search capability. Furthermore, as this method focuses on the three-best solution, it helps to avoid the local minimum trap. The contribution of this study is as follows.

- It introduces a method that allows TSO to escape from premature convergence and local minimum trap.
- It makes betterments in the local search procedure of TSO and presents an improved version of it.
- The proposed algorithm is tested through 10 classical test functions and 3 engineering design problems. The results are evaluated through Wilcoxon test.
- The proposed algorithm is compared to the popular MHAs in the literature.

In earlier studies, TSO is proven to be successful for the solution of optimization problems. However, once it is applied to real world problems, it presents some failures. Hence, researchers conduct works in order to increase its performance. While doing literature review, this study concentrates on works using methods to increase the performance of TSO. In a study on parameter identification of photovoltaic cells, the researchers propose the chaotic variant of TSO (C. Kumar and Magdalin Mary, 2022). In this study, two parameters determined by number of iterations and other randomly determined parameters are assigned through tent chaotic map. The researchers state that the results are more successful than the results of the competitive algorithms. However, this study does not enable us with the information on how other chaotic maps effect the performance of TSO. Besides, no change is made on the mathematical model of TSO. In another study on parameter estimation of photovoltaic batteries, the researchers present a hybrid algorithm made of TSO and differential evolution algorithm (Tan et al., 2022). In order to increase population diversity and convergence efficiency of the proposed algorithm, this study concentrates on strategies such as mutation, crossover factor ranking, and linear reduction of the population. The researchers inform us that the improved algorithm outperforms its competitors. Neither this study makes a change on the mathematical model of TSO. In another study that focuses on estimating the speed of the wind, the modified TSO is hybridized with long short-term memory strategy (Tuerxun et al., 2022). In this

study, in order to increase the diversity of the initial population of TSO, tent chaotic map is used. Moreover, TSO is used for image segmentation as well (J. Wang et al., 2022). Like the previous one, this study too uses tent chaotic map in order to increase the diversity of the initial population of TSO. TSO is also used in another study that deals with path planning of autonomous underwater vehicle (Yan et al., 2023). This study presents TSO based on reinforcement learning. It is emphasized that reinforcement learning improves the weak determination of TSO. In another study that regards the problems of TSO's premature convergence and being caught by local optimum trap, the researchers adapt circle chaotic map and levy flight to TSO (W. Wang and Tian, 2022). The Circle chaotic map is used to increase the diversity of the initial population while Levy flight is integrated to mathematical model of TSO. It is reported that these changes increase the performance of TSO. It is highly common to use PID method for controlling the engine revolution speed. TSO is used to determine the PID coefficient (Guo et al., 2022). The researchers indicate that TSO has a better performance compared to conventional methods (Ashraf et al., 2022; Fu and Zhang, 2022).

Having studied all these methods, it is observed that two methods are used in order to increase the performance of TSO. The first one is using chaotic maps to diversify the initial population. The second one is determining the parameters within the mathematical model of TSO in various ways. On the other hand, in some studies, TSO is used as is. In this study, the mathematical model of TSO is changed. The main objective of such a change is to focus not on the best solution but on the best ones. This approach leads TSO to escape from premature convergence and local minimum trap.

The rest of the study is organized as follows. In the second part, TSO is introduced, and information about the proposed algorithm is given. In the third section, computational results are presented. In the last section, the results of the study are evaluated.

2. MATERIALS AND METHODS

2.1 Tuna Swarm Optimization

Tuna is a carnivorous sea creature (Xie et al., 2021). Thanks to their anatomical structure, they can swim really fast. They also have high manoeuvrability. Compared to their sizes, their preys are smaller. Such a case enables preys to swim and manoeuvre faster. Therefore, Tuna fish hunt in groups. Hunting behaviours of tuna fish have two significant strategies (C. Kumar and Magdalin Mary, 2022). The first strategy is the spiral foraging behaviour that directs prey to shallow waters. The second strategy is that each tuna fish swim following another one and form parabolic shapes (Tuerxun et al., 2022). TSO is a swarm-based MHA improved being inspired by these two hunting strategies of tuna (J. Wang et al., 2022). Like other MHAs, the initial population is given randomly (Equation (1)).

$$X\_i=rand(ub-lb)+lb, \quad i=1,2,...,NP \tag{1}$$

Where, X_i is the initial population, ub,lb is the lower and upper bounds of the search space, and NP is the number of the population.

2.1.1 Spiral foraging

Once small fish packs fish encounter predators such as tuna fish, in order to distract the predators, they continuously change their swimming direction. In order to deal with such a challenge, tuna fish generate a spiral area around their prey. While performing this spiral movement, each Tuna fish follows another one before it. It means that there is an exchange of information between tuna

fish. The mathematical model of the spiral motion of TSO is given in Equation (1). Some parameters in this equation are calculated by Equation (2), (3), (4) and (5).

$$X_i^{t+1} = \begin{cases} \alpha_1 \cdot (X_{best}^t + \beta \cdot |X_{best}^t - X_i^t|) + \alpha_2 \cdot X_i^t, & i = 1 \\ \alpha_1 \cdot (X_{best}^t + \beta \cdot |X_{best}^t - X_i^t|) + \alpha_2 \cdot X_{i-1}^t, & i = 2, \dots, NP \end{cases} \quad (1)$$

$$\alpha_1 = a + (1 - a) \cdot \frac{t}{t_{max}} \quad (2)$$

$$\alpha_2 = (1 - a) - (1 - a) \cdot \frac{t}{t_{max}} \quad (3)$$

$$\beta = e^{bl} \cdot cos(2\pi b) \quad (4)$$

$$l = e^{3\,cos\left(((t_{max}+1/t)-1)\pi\right)} \quad (5)$$

Where, t is the current iteration, t_{max} is the maximum iteration, and b is a random number evenly distributed between 0 and 1. α_1 and α_2 are weight coefficients controlling the tendency of tuna fish to follow each other. The constant a determines the characteristic of this tendency. i^{th} within the X_i^{t+1} $t+1$ is an individual. β is the equation of spiral movement and l is the parameter of this equation. The most important disadvantage of the spiral movement is the hunting failure of the followed Tuna fish. In such a case, tuna fish continue hunting by choosing a random location. This eases each tuna fish to scan a wider area. It also enables TSO to have a more advanced global search capability. The mathematical model of this hunting strategy is given in Equation (6).

$$X_i^{t+1} = \begin{cases} \alpha_1 \cdot (X_{rand}^t + \beta \cdot |X_{rand}^t - X_i^t|) + \alpha_2 \cdot X_i^t, & i = 1 \\ \alpha_1 \cdot (X_{rand}^t + \beta \cdot |X_{rand}^t - X_i^t|) + \alpha_2 \cdot X_{i-1}^t, & i = 2, \dots, NP \end{cases} \quad (6)$$

Here X_{rand}^t is a randomly picked individual from the group. While some MHAs conduct global searches at the early stages of their searching processes, they conduct local searches at the further stages. While improving TSO, this approach is embraced. Hence, as the number of iteration increases, TSO changes the reference point of spiral movement from random individuals to the best one. The final mathematical model of spiral food searching strategy is as follows (Equation (7)).

$$X_i^{t+1} = \begin{cases} \begin{cases} \alpha_1 \cdot (X_{rand}^t + \beta \cdot |X_{rand}^t - X_i^t|) + \alpha_2 \cdot X_i^t, & i = 1 \\ \alpha_1 \cdot (X_{rand}^t + \beta \cdot |X_{rand}^t - X_i^t|) + \alpha_2 \cdot X_{i-1}^t, & i = 2, \dots, NP \end{cases}, rand \geq \frac{t}{t_{max}} \\ \begin{cases} \alpha_1 \cdot (X_{best}^t + \beta \cdot |X_{best}^t - X_i^t|) + \alpha_2 \cdot X_i^t, & i = 1 \\ \alpha_1 \cdot (X_{best}^t + \beta \cdot |X_{best}^t - X_i^t|) + \alpha_2 \cdot X_{i-1}^t, & i = 2, \dots, NP \end{cases}, rand < \frac{t}{t_{max}} \end{cases} \quad (7)$$

2.1.2 Parabolic foraging

Tuna fish hunt also by having parabolic movements around their preys. This movement could be around the prey regarded as the best solution as well as it could be around itself. The probability of picking either of these two moves is equal. The mathematical model of parabolic motion is given in Equation (8) and (9). The pseudo-code of TSO is given in Algorithm 1.

$$X_i^{t+1} = \begin{cases} X_{best}^t + rand \cdot (X_{best}^t - X_i^t) + TF \cdot p^2 \cdot (X_{best}^t - X_i^t), & rand < 0.5 \\ TF \cdot p^2 \cdot X_i^t, & rand \geq 0.5 \end{cases} \quad (8)$$

$$p = \left(1 - \frac{t}{t_{max}}\right)^{(t/t_{max})} \quad (9)$$

where TF is a random number with a value of 1 or -1.

2.2 Improved Tuna Swarm Optimization

In TSO, the best solution is the location of the fish to be caught. Tuna fish try to approach the prey by following each other. This prevents search space from being scanned efficiently. Especially, TSO's focusing only on the best solution at advanced iteration numbers leads it to be caught by local optimum trap. In order to improve the performance of TSO, this study proposes a new local search procedure that is inspired by GWO.

In order to represent the hierarchical order of the wolves in GWO, Alpha, Beta, and Gamma wolves are identified (Mirjalili et al., 2014). Alfa wolf leads the pack. Beta ones are the best Alpha candidates. Besides, Beta wolves enable communication between the pack and the Alpha wolf. Gamma wolves are tertiary wolves and they assist alpha and beta ones to manage the pack. In GWO, the three best solutions are represented by Alpha, Beta, and Gamma wolves. The positions of all other wolves are updated with respect to the positions of these three wolves (A. Kumar et al., 2017).

There is no evidence presenting that tuna fish have a hierarchical order. However, during hunting, the hunting school could make sudden changes in their directions. This occurs especially when the hunters are close to the prey. This act of the hunters leads us to the idea that local search procedure of TSO could be improved. Depending on the position of the prey, the hunting school has countless probability of changing direction. However, since the number of this probability is so high and it will increase the solution time of the algorithm, it should be limited at a reasonable number. In this study, being inspired by GWO, the three best solution vectors are used to update the location of the tuna fish. The new mathematical model of the proposed ITSO is given in Equation (10) and (11).

$$X_i^{t+1} = \begin{cases} \begin{cases} \alpha_1 \cdot (X_{rand}^t + \beta \cdot |X_{rand}^t - X_i^t|) + \alpha_2 \cdot X_i^t, & i = 1 \\ \alpha_1 \cdot (X_{rand}^t + \beta \cdot |X_{rand}^t - X_i^t|) + \alpha_2 \cdot X_{i-1}^t, & i = 2, \dots, NP \end{cases}, rand \geq \dfrac{t}{t_{max}} \\ \begin{cases} X_1 = \alpha_1 \cdot (X_\alpha^t + \beta \cdot |X_\alpha^t - X_i^t|) + \alpha_2 \cdot X_i^t, \\ X_2 = \alpha_1 \cdot \left(X_\beta^t + \beta \cdot \left|X_\beta^t - X_i^t\right|\right) + \alpha_2 \cdot X_i^t, \\ X_3 = \alpha_1 \cdot \left(X_\gamma^t + \beta \cdot \left|X_\gamma^t - X_i^t\right|\right) + \alpha_2 \cdot X_i^t, \\ \dfrac{X_1 + X_2 + X_3}{3}, \end{cases} & i = 1, \dots, NP, rand < \dfrac{t}{t_{max}} \end{cases} \quad (10)$$

$$X_i^{t+1} = \begin{cases} \begin{cases} X_1 = \alpha_1 \cdot (X_\alpha^t + \beta \cdot |X_\alpha^t - X_i^t|) + \alpha_2 \cdot X_i^t, \\ X_2 = \alpha_1 \cdot \left(X_\beta^t + \beta \cdot \left|X_\beta^t - X_i^t\right|\right) + \alpha_2 \cdot X_i^t, \\ X_3 = \alpha_1 \cdot \left(X_\gamma^t + \beta \cdot \left|X_\gamma^t - X_i^t\right|\right) + \alpha_2 \cdot X_i^t, \\ \dfrac{X_1 + X_2 + X_3}{3}, \end{cases} & i = 1, \dots, NP, rand < 0.5 \\ \{TF \cdot p^2 \cdot X_i^t, & i = 1, \dots, NP, rand \geq 0.5 \end{cases} \quad (11)$$

In the equations, X_α, X_β, and X_γ respectively, represent the best, the second best, and the third best solution. X_1, X_2, and X_3 are respectively the location vectors acquired by X_α, X_β, and X_γ. The

new position vector is determined by the mean of X_1, X_2, and X_3. Other parameters in the equations are calculated as in section 2.2. The pseudocode of ITSO is given in Algorithm 1.

Algorithm 1. TSO and ITSO pseudocode

TSO pseudocode	**ITSO pseudocode**
Input: *NP:* Population size, t_{max}: maximum iteration	**Input:** *NP:* Population size, t_{max}: maximum iteration
Output: X_{best}: The best individual, f_{best}: Its fitness value	**Output:** X_α: The best individual, f_α: Its fitness value
Initialize the random population of tunas ($X_i, i = 1,2,\dots,NP$) and assign parameters a and z	Initialize the random population of tunas ($X_i, i = 1,2,\dots,NP$) and assign parameters a and z
While ($t < t_{max}$)	**While** ($t < t_{max}$)
Calculate the fitness values and update X_{best}	Calculate the fitness values and update X_α, X_β ve X_γ
For (each tuna) **do**	**For** (each tuna) **do**
Update α_1, α_2, p using equation (2), (3), (9)	Update α_1, α_2, p using equation (2), (3), (9)
If ($rand < z$) **then**	**If** ($rand < z$) **then**
Update X_i^{t+1} using equation (1)	Update X_i^{t+1} using equation (1)
Else if ($rand \geq z$) **then**	**Else if** ($rand \geq z$) **then**
If ($rand < 0.5$) **then**	**If** ($rand < 0.5$) **then**
If ($t/t_{max} < rand$) **then**	**If** ($t/t_{max} < rand$) **then**
Update X_i^{t+1} using equation (6)	Update X_i^{t+1} using equation (10)
Else if ($t/t_{max} \geq rand$) **then**	**Else if** ($t/t_{max} \geq rand$) **then**
Update X_i^{t+1} using equation (1)	Update X_i^{t+1} using equation (10)
Else if ($rand \geq 0.5$) **then**	**Else if** ($rand \geq 0.5$) **then**
Update X_i^{t+1} using equation (8)	Update X_i^{t+1} using equation (11)
$t = t + 1$	$t = t + 1$
Return: X_{best}, f_{best}	**Return:** X_α, f_α

3. RESULTS AND DISCUSSION

This section provides us with the results that the proposed algorithm and competitor algorithms presents from a series of optimization problems. The results are also interpreted through the Wilcoxon statistical test. All algorithms were first applied to 10 well-known classical test functions. Then it was applied to 3 engineering design problems.

3.1 Compared Algorithms and Experimental Setup

The proposed algorithm is an improved version of TSO. Therefore, TSO was chosen as one of the competing algorithms. The proposed algorithm is inspired by GWO while improving. Therefore, GWO is defined as one of the competing algorithms. Moreover, the proposed algorithm is compared to Cuckoo Search (CS), BAT, SCA, and Covariance Matrix Adaptation Evolution Strategy (CMA-ES). The reason why these MHAs are chosen is that they are popular and validated. Besides, these algorithms have been used for the solutions of many optimization problems in medicine, economy, and engineering. The structure of these algorithms is simple and they generate consistent results. All algorithms are coded in Python language. Tests are conducted on a computer with Windows 10 64-bit Professional and 64GB of RAM. The stopping criteria of the algorithms is the number of iterations. The results of 30 independent runs of all algorithms are recorded at every different population number of all the algorithms. All MHAs are sensitive to initial parameters. Hence, for a just comparison, the parameters of the competing algorithms are adjusted in the way that they are given in their original articles. Table 1 presents information about the parameter settings, iteration and population numbers of all algorithms.

Table 1. Parameter settings for algorithms

Algorithm	Parameters	Iteration	Population
CMA-ES (Hansen et al., 2003)	$m_0 = 0, \sigma_0 = 0.5, C_0 = 1, p_0 = 0, s_0 = 0, k = 0, \mu = \lambda/2$	200	50, 100, 200
SCA (Mirjalili, 2016)	$a = 2, r_1 = rand[0, 2\pi]$		
BAT (Gandomi et al., 2013)	$A = 0.5, r = 0.5, Q_{min} = 0, Q_{max} = 2$		
CS (Rajabioun, 2011)	$p_a = 0.25, \alpha = 0.1, \beta = 1.5$		
GWO (Mirjalili et al., 2014)	$a = 2$		
TSO (Xie et al., 2021)	$z = 0.5, a = 0.7$		
ITSO	$z = 0.5, a = 0.7$		

3.2 Classic Test Functions

In this section, in order to evaluate its performance, the proposed algorithm is tested through 10 well-known functions. 6 of these functions (F1-F6) are unimodal and 4 of them (F7-F10) are multimodal functions. Unimodal functions have one global minimum. Hence, it is used to test the local search capability of MHAs. Multimodal functions have more than one local minimum. Only one of these local minimums is the global minimum. This kind of functions are used to examine the global search capability of MHAs and their ability to avoid the local minimum trap. Descriptive information about classical test functions is given in Table 2.

While performing the first experiment, population is set to be 50. In Table 3, all algorithms' the minimum, average and worst results by the classical test functions are given. In addition, the convergence curves of the algorithms are given in Figure 1. In minimum value metric, the proposed algorithm is the most successful one by generating the most successful results in 7 of 10 functions (F1-F4, F7, F9, F10). On the other hand, CMA-ES generates the best results in 3 functions which leads it to be the second most successful algorithm (F5, F6, F8). In mean value metric, the proposed algorithm generates the best results in 8 of 10 functions (F1-F4, F7, F10) while CMA-ES is successful in 2 functions (F5, F6). In the worst value metric, the proposed algorithm happens to be the most successful one by successfully solving 8 functions (F1-F4, F7-F10) while CMA-ES is successful in 2 functions (F5, F6).

Table 2. Description of benchmark functions

Function	Range	Dim	f_{min}
$F_1(z) = \sum_{i=1}^{dim} z_i^2$	[-100, 100]	30	0
$F_2(z) = \sum_{i=1}^{dim} \lvert z_i \rvert + \prod_{i=1}^{dim} \lvert z_i \rvert$	[-10, 10]	30	0
$F_3(z) = \sum_{i=1}^{dim} \left(\sum_{j=1}^{i} z_j \right)^2$	[-100, 100]	30	0
$F_4(z) = max_i\{\lvert z_i \rvert, 1 \le i \le dim\}$	[-100, 100]	30	0
$F_5(z) = \sum_{i=1}^{dim-1} \left[100\left(z_{i+1} - z_i^2\right)^2 + (z_i - 1)^2 \right]$	[-30, 30]	30	0
$F_6(z) = \sum_{i=1}^{dim} i z_i^4 + rand\ [0,1]$	[-1.28, 1.28]	30	0

$F_7(z) = \sum_{i=1}^{11}\left[a_i - \frac{z_1(b_i^2 + b_i z_2)}{b_i^2 + b_i z_3 + z_4}\right]^2$	[-5, 5]	4	$\approx 0{,}0003075$
$F_8(z) = -\sum_{i=1}^{5}[(X - a_i)(X - a_i)^T + c_i]^{-1}$	[0, 10]	4	$-10{,}1532$
$F_9(z) = -\sum_{i=1}^{7}[(X - a_i)(X - a_i)^T + c_i]^{-1}$	[0, 10]	4	$-10{,}4028$
$F_{10}(z) = -\sum_{i=1}^{10}[(X - a_i)(X - a_i)^T + c_i]^{-1}$	[0, 10]	4	$-10{,}536$

Table 3. Results on benchmark functions (Population: 50)

Obj. Func.		ITSO	TSO	GWO	CMA-ES	CS	BAT	SCA
F1	Min.	***1.68E-46***	2.99E-35	1.12E-13	3.49E-24	1.20E+03	7.60E+03	8.13E+00
	Mean	***3.12E-32***	1.73E-15	1.35E-12	9.77E-12	1.81E+03	1.54E+04	4.20E+02
	Worst	***8.48E-31***	4.57E-14	7.81E-12	1.86E-10	3.21E+03	3.10E+04	1.93E+03
F2	Min.	***1.72E-24***	2.81E-18	1.40E-08	1.17E-15	3.10E+01	3.19E+01	8.59E-02
	Mean	***5.67E-18***	1.61E-08	5.43E-08	6.93E-07	4.67E+01	2.97E+04	6.75E-01
	Worst	***9.24E-17***	2.70E-07	1.34E-07	4.83E-06	6.72E+01	8.03E+05	2.15E+00
F3	Min.	***4.39E-43***	9.48E-41	2.84E-02	5.64E-12	7.54E+03	1.42E+04	6.87E+03
	Mean	***4.34E-23***	4.27E-11	9.12E-01	7.03E-05	1.23E+04	4.78E+04	1.51E+04
	Worst	***1.25E-21***	1.20E-09	3.46E+00	1.17E-03	1.62E+04	8.11E+04	2.71E+04
F4	Min.	***1.28E-23***	3.35E-16	2.58E-03	1.10E-11	2.89E+01	3.13E+01	2.31E+01
	Mean	***3.36E-17***	2.26E-09	1.17E-02	6.92E-06	3.35E+01	4.61E+01	4.51E+01
	Worst	***7.02E-16***	2.87E-08	3.43E-02	5.16E-05	4.02E+01	6.48E+01	7.56E+01
F5	Min.	4.00E-03	2.82E-03	2.60E+01	***1.21E-05***	1.03E+05	2.93E+06	1.14E+04
	Mean	4.49E+00	8.01E-01	2.72E+01	***1.39E-02***	3.92E+05	1.31E+07	7.41E+05
	Worst	2.87E+01	6.25E+00	2.88E+01	***1.01E-01***	8.01E+05	3.17E+07	2.77E+06
F6	Min.	4.78E-06	2.71E-04	1.43E-04	***8.49E-08***	1.01E+03	8.24E+03	1.49E+01
	Mean	9.44E-03	7.10E-03	5.92E-01	***1.70E-04***	1.81E+03	1.56E+04	4.44E+02
	Worst	1.84E-02	6.85E-02	1.30E+00	***7.88E-04***	3.52E+03	2.63E+04	3.02E+03
F7	Min.	***1.88E-05***	3.03E-05	1.24E-03	5.35E-05	2.62E-01	1.35E+00	3.37E-02
	Mean	***2.65E-04***	1.56E-03	4.69E-03	7.47E-04	5.73E-01	7.36E+00	5.56E-01
	Worst	***8.62E-04***	5.07E-03	8.58E-03	3.42E-03	1.16E+00	1.84E+01	3.19E+00
F8	Min.	-1.02E+01	-1.02E+01	-1.02E+01	***-1.02E+01***	-1.02E+01	-1.02E+01	-4.99E+00
	Mean	***-1.02E+01***	-1.01E+01	-8.32E+00	-6.07E+00	-1.01E+01	-5.57E+00	-2.82E+00

	Worst	***-1.01E+01***	-9.77E+00	-2.29E+00	-5.05E+00	-1.01E+01	-2.63E+00	-8.78E-01
F9	Min.	***-1.04E+01***	-1.04E+01	-1.04E+01	-1.04E+01	-1.04E+01	-1.04E+01	-9.42E+00
	Mean	***-1.04E+01***	-1.04E+01	-1.00E+01	-5.43E+00	-1.02E+01	-6.25E+00	-3.73E+00
	Worst	***-1.03E+01***	-9.99E+00	-5.09E+00	-1.84E+00	-5.09E+00	-1.84E+00	-9.02E-01
F10	Min.	***-1.05E+01***	-1.05E+01	-1.05E+01	-5.13E+00	-1.05E+01	-1.05E+01	-9.11E+00
	Mean	***-1.05E+01***	-1.05E+01	-1.03E+01	-5.04E+00	-1.05E+01	-5.90E+00	-4.49E+00
	Worst	***-1.05E+01***	-9.98E+00	-4.92E+00	-2.42E+00	-1.03E+01	-1.68E+00	-2.00E+00

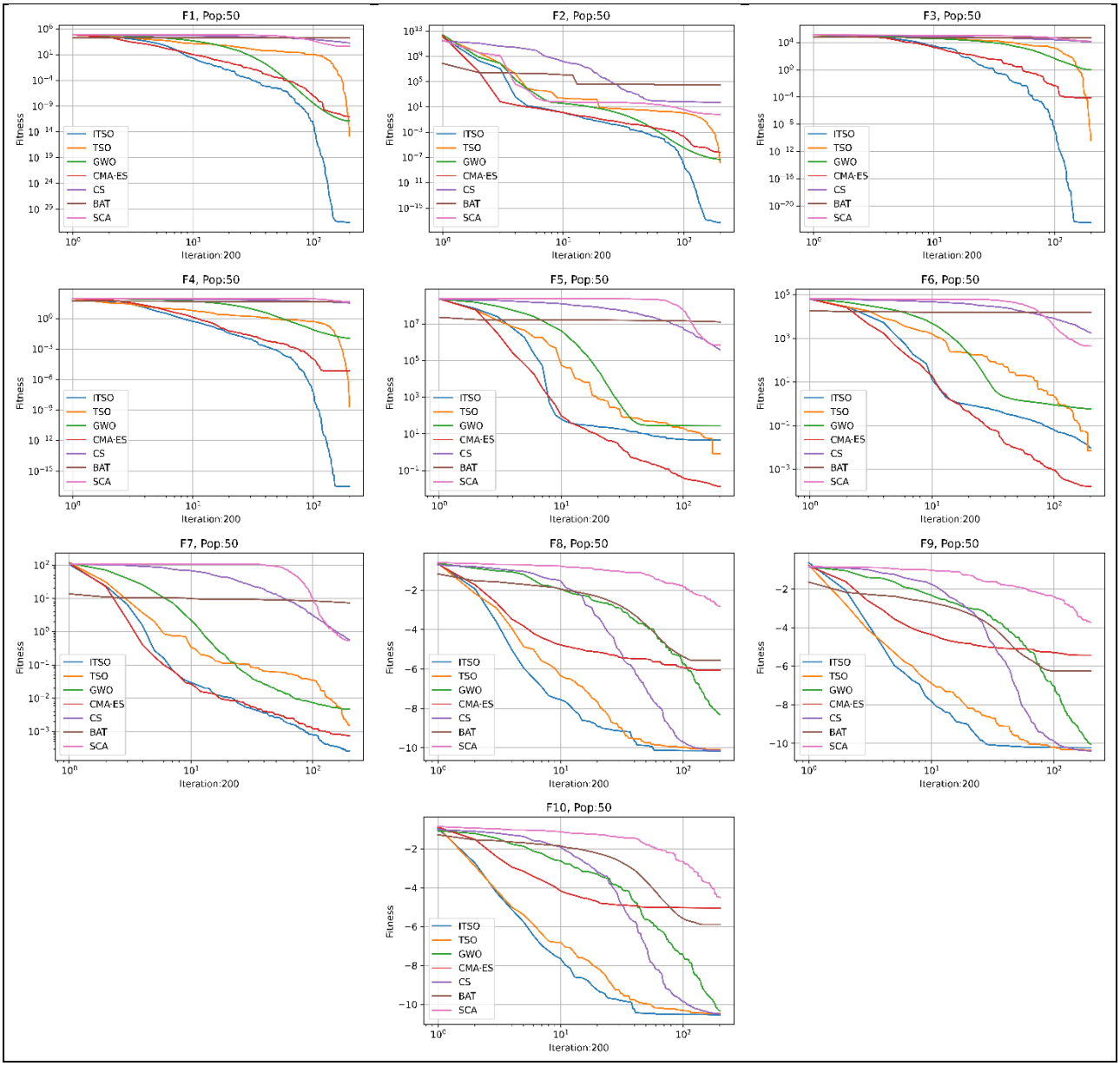

Figure 1. Convergence curve ITSO and other optimizers (Population: 50)

While performing the second experiment, population is set to be 100. In Table 4, all algorithms' the minimum, average and worst results by the classical test functions are given. In addition, the convergence curves of the algorithms are given in Figure 2**.** In minimum value metric, the proposed algorithm is the most successful one in 6 of 10 functions (F1-F4, F6, F7) while BAT is successful in

2 functions (F8-F10). On the other hand, TSO and CMA-ES are successful in one function each (F5, F9). In the mean value metric, the proposed algorithm is the most successful one in 8 out of 10 functions (F1-F4, F7-F10). CMA-ES is successful in two functions (F5, F6). In the worst value metric, the proposed algorithm is the most successful one by successfully solving 8 functions (F1-F4, F7-F10). CMA-ES is successful in two functions (F5, F6).

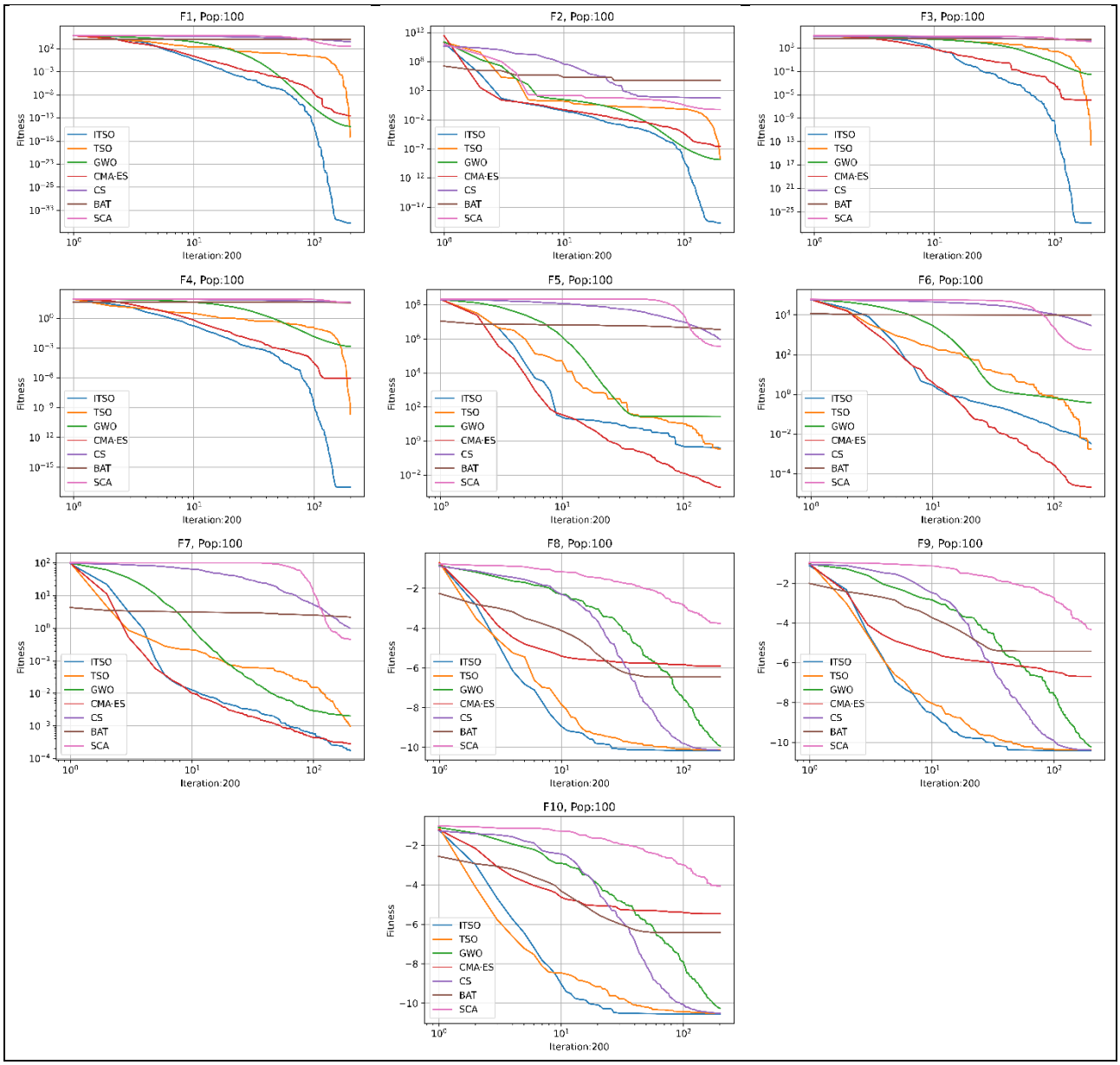

Figure 2. Convergence curve ITSO and other optimizers (Population: 100)

Table 4. Results on benchmark functions (Population: 100)

Obj. Func.		ITSO	TSO	GWO	CMA-ES	CS	BAT	SCA
F1	Min.	***1.32E-50***	4.97E-36	2.13E-16	3.53E-22	1.33E+03	4.74E+03	3.87E+00
	Mean	***2.05E-36***	7.85E-18	1.48E-15	3.06E-13	2.76E+03	8.69E+03	3.24E+02
	Worst	***5.96E-35***	1.33E-16	5.67E-15	5.89E-12	3.96E+03	1.39E+04	3.86E+03
F2	Min.	***2.23E-27***	8.28E-22	3.54E-10	7.99E-20	3.85E+01	1.07E+01	4.57E-02
	Mean	***2.05E-20***	2.23E-09	1.46E-09	2.48E-07	5.42E+01	5.73E+04	5.86E-01
	Worst	***3.40E-19***	3.26E-08	3.81E-09	2.31E-06	7.49E+01	1.71E+06	2.14E+00
F3	Min.	***1.56E-42***	7.71E-37	9.12E-04	2.88E-16	9.99E+03	1.12E+04	3.91E+03
	Mean	***1.51E-27***	2.64E-14	2.96E-02	1.21E-06	1.57E+04	2.77E+04	1.25E+04
	Worst	***2.29E-26***	7.61E-13	2.61E-01	1.61E-05	2.23E+04	7.81E+04	2.80E+04
F4	Min.	***5.55E-26***	6.91E-21	4.11E-04	2.28E-10	3.02E+01	2.78E+01	1.97E+01
	Mean	***1.07E-17***	2.34E-10	1.46E-03	8.66E-07	3.95E+01	3.81E+01	3.90E+01
	Worst	***1.88E-16***	4.99E-09	6.71E-03	5.08E-06	4.48E+01	4.88E+01	6.00E+01
F5	Min.	2.01E-04	***2.02E-09***	2.60E+01	5.04E-07	5.10E+05	6.01E+05	3.91E+03
	Mean	3.79E-01	3.45E-01	2.67E+01	***1.98E-03***	9.41E+05	3.46E+06	3.83E+05
	Worst	1.46E+00	1.18E+00	2.94E+01	***2.16E-02***	1.50E+06	7.29E+06	2.17E+06
F6	Min.	***1.84E-07***	8.53E-05	1.34E-04	2.88E-07	1.82E+03	4.27E+03	1.33E+01
	Mean	3.37E-03	1.71E-03	3.83E-01	***2.14E-05***	2.99E+03	9.56E+03	1.76E+02
	Worst	7.36E-03	3.06E-02	1.01E+00	***2.26E-04***	4.66E+03	1.63E+04	4.96E+02
F7	Min.	***7.01E-07***	6.57E-05	6.00E-04	2.03E-06	3.41E-01	5.45E-01	2.44E-02
	Mean	***1.78E-04***	9.98E-04	2.04E-03	2.82E-04	1.00E+00	2.20E+00	4.60E-01
	Worst	***8.15E-04***	6.53E-03	4.86E-03	2.90E-03	1.60E+00	5.12E+00	2.27E+00
F8	Min.	-1.02E+01	-1.02E+01	-1.02E+01	-1.02E+01	-1.02E+01	***-1.02E+01***	-4.96E+00
	Mean	***-1.02E+01***	-1.01E+01	-9.92E+00	-5.90E+00	-1.01E+01	-6.46E+00	-3.75E+00
	Worst	***-1.02E+01***	-1.01E+01	-3.41E+00	-5.06E+00	-1.01E+01	-2.63E+00	-8.79E-01
F9	Min.	-1.04E+01	-1.04E+01	-1.04E+01	***-1.04E+01***	-1.04E+01	-1.04E+01	-1.03E+01
	Mean	***-1.04E+01***	-1.04E+01	-1.02E+01	-6.68E+00	-1.04E+01	-5.42E+00	-4.32E+00
	Worst	***-1.04E+01***	-1.03E+01	-5.09E+00	-5.09E+00	-1.03E+01	-1.84E+00	-9.08E-01
F10	Min.	-1.05E+01	-1.05E+01	-1.05E+01	-1.05E+01	-1.05E+01	***-1.05E+01***	-6.54E+00
	Mean	***-1.05E+01***	-1.05E+01	-1.03E+01	-5.47E+00	-1.05E+01	-6.41E+00	-4.07E+00
	Worst	***-1.05E+01***	-1.04E+01	-2.42E+00	-2.81E+00	-1.04E+01	-1.68E+00	-9.41E-01

While performing the third experiment, population is set to be 200. In Table 5, all algorithms' the minimum, average and worst results by the classical test functions are given. In addition, the

convergence curves of the algorithms are given in Figure 3**.** In the minimum value metric, the proposed algorithm is the most successful one in 6 out of 10 functions (F1-F5, F7) while CMA-ES is successful in 4 functions (F6, F8-F10). In the mean value metric, the proposed algorithm is the most successful algorithm in 8 out of 10 functions (F1-F4, F7-F10). CMA-ES is successful in two functions (F5, F6). In the worst value metric, the proposed algorithm is the most successful one by presenting the best results in 8 out of 10 functions (F1-F4, F7-F10). CMA-ES solves 2 functions successfully (F5, F6).

Table 5. Results on benchmark functions (Population: 200)

Obj. Func.		ITSO	TSO	GWO	CMA-ES	CS	BAT	SCA
F1	Min.	***2.59E-52***	2.87E-35	2.72E-19	2.27E-24	2.21E+03	1.97E+03	1.87E+00
	Mean	***2.87E-41***	2.21E-19	2.18E-18	1.22E-14	3.81E+03	4.55E+03	1.69E+02
	Worst	***5.87E-40***	6.27E-18	1.00E-17	2.03E-13	5.17E+03	7.27E+03	1.37E+03
F2	Min.	***1.07E-25***	3.02E-20	7.77E-12	7.86E-20	4.66E+01	1.68E+00	6.39E-02
	Mean	***1.32E-21***	5.16E-12	3.03E-11	3.26E-08	6.22E+01	2.76E+02	4.08E-01
	Worst	***1.65E-20***	1.06E-10	1.16E-10	1.21E-07	7.81E+01	5.70E+03	1.14E+00
F3	Min.	***9.02E-44***	1.60E-38	4.05E-06	8.54E-13	1.28E+04	6.01E+03	1.90E+03
	Mean	***1.54E-30***	2.40E-17	3.22E-04	4.45E-08	1.65E+04	1.49E+04	7.33E+03
	Worst	***4.05E-29***	6.77E-16	1.33E-03	7.71E-07	2.04E+04	3.51E+04	1.59E+04
F4	Min.	***6.86E-27***	1.60E-22	2.56E-05	3.13E-11	3.87E+01	2.19E+01	1.65E+01
	Mean	***1.54E-20***	3.44E-12	1.08E-04	1.46E-07	4.36E+01	2.82E+01	3.39E+01
	Worst	***2.54E-19***	6.05E-11	5.03E-04	1.18E-06	4.85E+01	3.78E+01	6.23E+01
F5	Min.	***1.47E-08***	3.97E-05	2.52E+01	1.95E-07	7.83E+05	7.82E+04	7.69E+02
	Mean	9.25E-02	1.74E-01	2.63E+01	***4.56E-04***	1.76E+06	5.60E+05	9.83E+04
	Worst	4.06E-01	1.18E+00	2.79E+01	***9.14E-03***	2.81E+06	2.14E+06	1.33E+06
F6	Min.	1.62E-04	1.19E-07	8.34E-05	***1.29E-08***	2.39E+03	7.31E+02	1.08E+01
	Mean	1.67E-03	4.58E-04	1.27E-01	***1.45E-06***	3.69E+03	4.52E+03	7.92E+01
	Worst	4.20E-03	2.20E-03	5.11E-01	***9.50E-06***	4.88E+03	7.08E+03	2.15E+02
F7	Min.	***8.35E-06***	8.73E-05	4.14E-04	9.61E-06	3.68E-01	4.10E-01	8.97E-03
	Mean	***1.10E-04***	4.47E-04	9.89E-04	1.41E-04	1.42E+00	1.04E+00	1.76E-01
	Worst	***6.21E-04***	1.18E-03	1.84E-03	7.08E-04	2.23E+00	2.27E+00	8.30E-01
F8	Min.	-1.02E+01	-1.02E+01	-1.02E+01	***-1.02E+01***	-1.02E+01	-1.02E+01	-6.67E+00
	Mean	***-1.02E+01***	-1.01E+01	-9.47E+00	-6.92E+00	-1.01E+01	-6.64E+00	-4.38E+00
	Worst	***-1.02E+01***	-1.01E+01	-5.06E+00	-5.06E+00	-1.01E+01	-2.63E+00	-8.79E-01
F9	Min.	-1.04E+01	-1.04E+01	-1.04E+01	***-1.04E+01***	-1.04E+01	-1.04E+01	-8.81E+00
	Mean	***-1.04E+01***	-1.04E+01	-1.02E+01	-6.15E+00	-1.04E+01	-6.90E+00	-4.99E+00

	Worst	***-1.04E+01***	-1.04E+01	-5.12E+00	-5.09E+00	-1.04E+01	-1.84E+00	-9.09E-01
F10	Min.	-1.05E+01	-1.05E+01	-1.05E+01	***-1.05E+01***	-1.05E+01	-1.05E+01	-8.64E+00
	Mean	***-1.05E+01***	-1.05E+01	-1.05E+01	-5.64E+00	-1.05E+01	-6.07E+00	-5.11E+00
	Worst	***-1.05E+01***	-1.05E+01	-1.05E+01	-1.68E+00	-1.05E+01	-2.42E+00	-3.09E+00

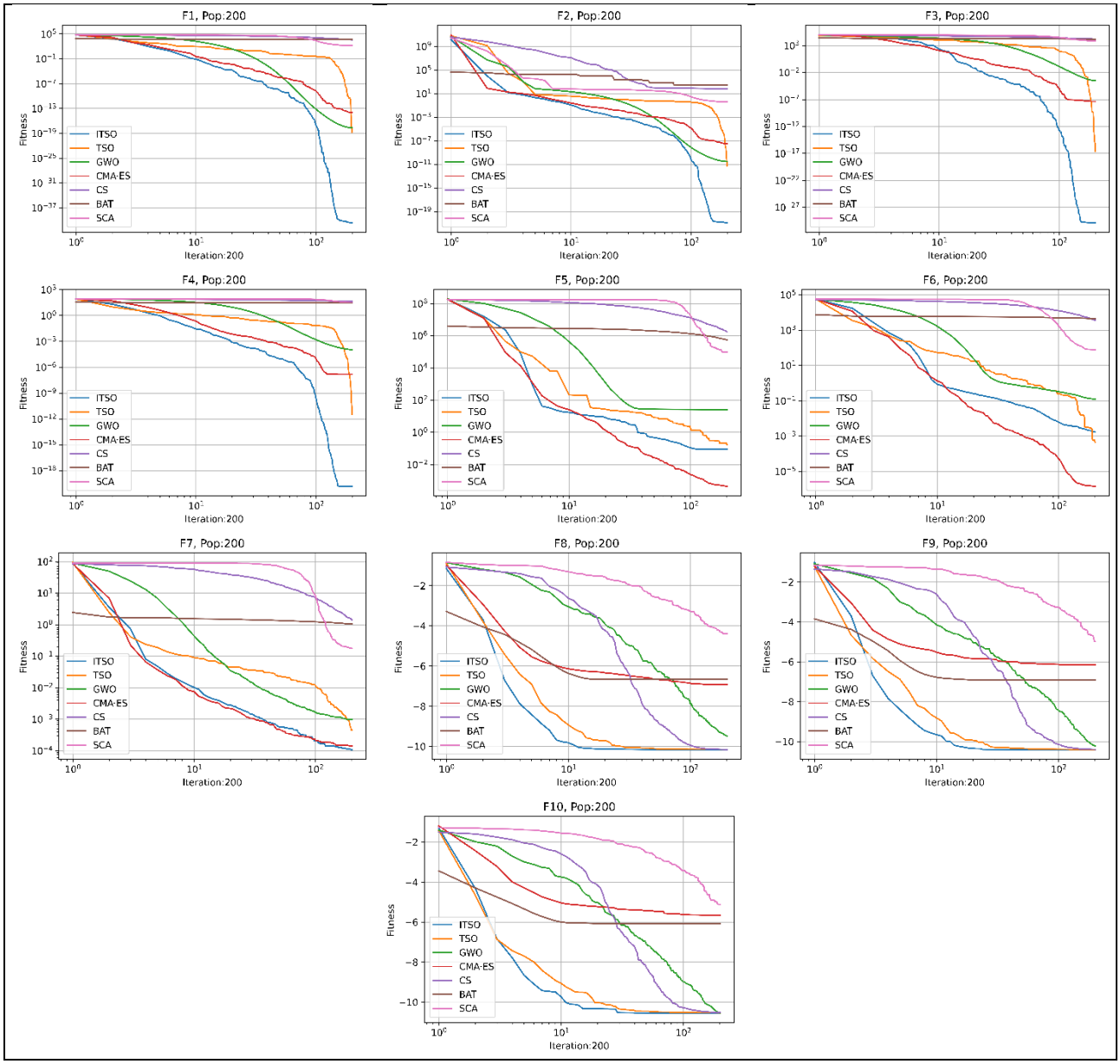

Figure 3. Convergence curve ITSO and other optimizers (Population: 200)

The results of an MHA informs us about its success. However, whether its success is statistically meaningful or not should be indicated. The Wilcoxon test is a non-parametric test that is frequently used for the comparison of optimization algorithms. The significance level of Wilcoxon test is set to be 5%. In Table 6, the results of the proposed algorithm's results of its comparison to its competitors are given. In the tables, "+" symbolizes that the proposed algorithm is better than its competitors while "-" indicates that it is worse.

Table 6. Wilcoxon rank-sum test

	Pop: 50						Pop: 100						Pop: 200					
Fnc.	**TSO**	**GWO**	**CMA-ES**	**CS**	**BAT**	**SCA**	**TSO**	**GWO**	**CMA-ES**	**CS**	**BAT**	**SCA**	**TSO**	**GWO**	**CMA-ES**	**CS**	**BAT**	**SCA**
F1	+	+	+	+	+	+	+	+	+	+	+	+	+	+	+	+	+	+
F2	+	+	+	+	+	+	+	+	+	+	+	+	+	+	+	+	+	+
F3	+	+	+	+	+	+	+	+	+	+	+	+	+	+	+	+	+	+
F4	+	+	+	+	+	+	+	+	+	+	+	+	+	+	+	+	+	+
F5	-	+	-	+	+	+	-	+	-	+	+	+	+	+	-	+	+	+
F6	-	+	-	+	+	+	-	+	-	+	+	+	-	+	-	+	+	+
F7	+	+	+	+	+	+	+	+	+	+	+	+	+	+	+	+	+	+
F8	+	+	+	+	+	+	+	+	+	+	+	+	+	+	+	+	+	+
F9	+	+	+	+	+	+	+	+	+	+	+	+	+	+	+	+	+	+
F10	+	+	+	+	+	+	+	+	+	+	+	+	+	+	+	+	+	+

3.3 Engineering Design Problems

In this section, the proposed algorithm and competitor algorithms are applied to 3 engineering design problems. These problems have more than one local minimum and constraints. Results of 30 independent runs of all algorithms are recorded. Moreover, the population number and the number of iterations are respectively set to be 100 and 200.

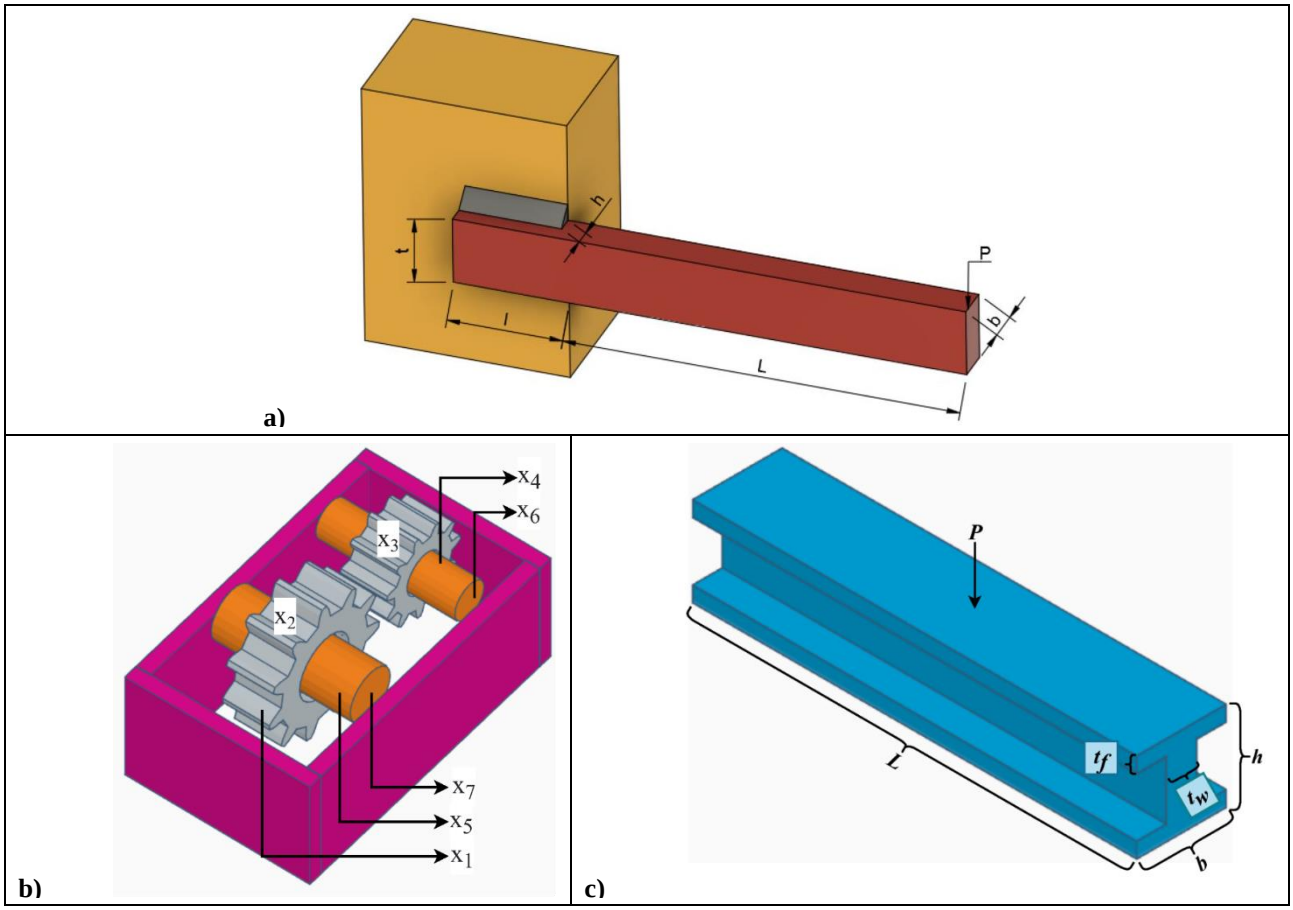

Figure 4. Engineering *d*esign problems a) Welded beam design problem b) Speed reducer design problem c) I-beam design problem

3.3.1 Welded beam design problem

The aim of the welded beam design problem is to minimize the production cost (Xie et al., 2021). The parameters and schematic representation of the problem are given in Figure 4a. The design is expected to stand the P load. The problem has 4 design parameters: welding thickness (h), length of welded joint (l), bar height (t) and bar thickness (b). The parameters (Equation (12)), objective

function (Equation (13)) and constraints (Equation (14), (15), (16)) of the problem are given in the following equations.

Consider: $$\vec{X} = [x_1\ x_2\ x_3\ x_4] = [h\ l\ t\ b] \quad (12)$$

Minimize: $$f_{cost}(\vec{x}) = 1.10471x_1^2x_2 + 0.04811x_3x_4(14.0 + x_2) \quad (13)$$

Subject to: $$g_1(\vec{x}) = \tau(\vec{x}) - \tau_{max} \le 0,\ g_2(\vec{x}) = \sigma(\vec{x}) - \sigma_{max} \le 0,\ g_3(\vec{x}) = \delta(\vec{x}) - \delta_{max} \le 0, g_4(\vec{x}) = x_1 - x_4 \le 0,\ g_5(\vec{x}) = P - P_c(\vec{x}) \le 0,\ g_6(\vec{x}) = 0.125 - x_1 \le 0, g_7(\vec{x}) = 0.11047x_1^2 + 0.04811x_3x_4(14.0 + x_2) - 5.0 \le 0 \quad (14)$$

Range: $$0.1 \le x_1 \le 2,\ 0.1 \le x_2 \le 10, 0.1 \le x_3 \le 10, 0.1 \le x_4 \le 2 \quad (15)$$

Where: $$\tau(\vec{x}) = \sqrt{(\tau')^2 + 2\tau'\tau''\frac{x_2}{2R} + (\tau'')^2}, \tau' = \frac{P}{\sqrt{2}x_1x_2}, \tau = \frac{MR}{J},\ M = P\left(L + \frac{x_2}{2}\right), R = \sqrt{\frac{x_2^2}{4} + \left(\frac{x_1+x_3}{2}\right)^2}, J = 2\left\{\sqrt{2}x_1x_2\left[\frac{x_2^2}{4} + \left(\frac{x_1+x_3}{2}\right)^2\right]\right\}, \sigma(\vec{x}) = \frac{6PL}{x_4x_3^2}, \delta(\vec{x}) = \frac{4PL^3}{Ex_3^3x_4}, P_c(\vec{x}) = \frac{4.013E\sqrt{\frac{x_3^2x_4^6}{36}}}{L^2}\left(1 - \frac{x_3}{2L}\sqrt{\frac{E}{4G}}\right), P = 6{,}000\ lb, L = 14\ in, \delta_{max} = 0.25\ in, E = 30 \times 10^6\ psi, G = 12 \times 10^6\ psi, \tau_{max} = 13{,}600\ psi, \sigma_{max} = 30{,}000\ psi \quad (16)$$

The results of by all algorithms from the welded beam design problem are given in Table *7*. Examining the results, it is observed that with 1.74 optimal cost, the proposed algorithm is the most successful one. GWO is the second and the CMA-ES is the third most successful algorithm with optimal costs like 1.74 and 1.835. With an optimal cost of 2.25, TSO is one of the algorithms having the worst result.

Table 7. Comparison of results for welded beam design problem

Optimizer	Optimal values for variables				Optimal cost
	x_1	x_2	x_3	x_4	
ITSO	**0.204**	**3.520**	**9.110**	**0.205**	**1.740**
TSO	0.100	0.100	0.100	0.100	2.250
GWO	0.185	3.940	9.240	0.205	1.780
CMA-ES	0.200	3.633	9.105	0.206	1.835
CS	0.236	3.200	8.390	0.239	1.860
BAT	0.136	7.540	7.380	0.308	2.510
SCA	0.213	3.610	8.720	0.233	1.900

3.3.2 Speed Reducer Design

The main goal of the speed reducer design problem is to minimize the weight of the design (Ahmadianfar et al., 2020). Speed Reducer Design has 7 design variants which are face width (x_1), module of teeth (x_2), number of teeth on pinion (x_3), length of shaft 1 between bearings (x_4), length of shaft 2 between bearings (x_5), diameter of shaft 1 (x_6), and diameter of shaft 2 (x_7) (Figure 4b). The objective function (Equation (17)) and constraints (Equation (18), (19)) of the problem are given in the following equations.

Minimize: $$f_{cost}(\vec{x}) = 0.7854x_1x_2^2(3.3333x_3^2 + 14.9334x_3 - 43.0934) - 1.508x_1(x_6^2 + x_7^2) + 7.4777(x_6^3 + x_7^3) + 0.7854(x_4x_6^2 + x_5x_7^2) \quad (17)$$

Subject to: $$g_1(\vec{x}) = \frac{27}{x_1x_2^2x_3} - 1 \le 0,\ g_2(\vec{x}) = \frac{397.5}{x_1x_2^2x_3^2} - 1 \le 0,\ g_3(\vec{x}) = \frac{1.93x_4^3}{x_2x_3x_6^4} - 1 \le 0 \quad (18)$$

$$g_4(\vec{x}) = \frac{1.93x_5^3}{x_2x_3x_7^4} - 1 \leq 0,\ g_5(\vec{x}) = \frac{1}{110x_6^3}\sqrt{\left(\frac{745x_4}{x_2x_3}\right)^2 + 16.9 \times 10^6} - 1 \leq 0$$

$$g_6(\vec{x}) = \frac{1}{85x_7^3}\sqrt{\left(\frac{745x_5}{x_2x_3}\right)^2 + 157.5 \times 10^6} - 1 \leq 0,\ g_7(\vec{x}) = \frac{x_2x_3}{40} - 1 \leq 0,$$

$$g_8(\vec{x}) = 5\frac{x_2}{x_1} - 1 \leq 0, g_9(\vec{x}) = \frac{x_1}{12x_2} - 1 \leq 0,\ g_{10}(\vec{x}) = \frac{1.5x_6+1.9}{x_4} - 1 \leq 0,$$

$$g_{11}(\vec{x}) = \frac{1.1x_7 + 1.9}{x_5} - 1 \leq 0$$

Range: $2.6 \leq x_1 \leq 3.6, 0.7 \leq x_2 \leq 0.8, 17 \leq x_3 \leq 28, 7.3 \leq x_4 \leq 8.3,$
$7.3 \leq x_5 \leq 8.3, 2.9 \leq x_6 \leq 3.9, 5 \leq x_7 \leq 5.5$ **(**19**)**

The results of all algorithms from the speed reducer design problem are given in Table 8. With 1581.47 optimal cost, the proposed algorithm is the most successful one while Bat is the second with 1581.494 optimal cost and CS is the third with 1582.539 optimal cost. Having the 1612.18 optimal cost, TSO is the one with the worst result.

Table 8. Comparison of results for speed reducer problem

Optimizer	Optimal values for variables							Optimal cost
	x_1	x_2	x_3	x_4	x_5	x_6	x_7	
ITSO	***3.500***	***0.700***	***17.000***	***8.015***	***8.008***	***3.777***	***5.297***	***1581.470***
TSO	2.605	0.700	17.079	7.293	7.296	2.903	4.994	1612.180
GWO	3.500	0.700	17.000	8.300	8.054	3.900	5.384	1584.598
CMA-ES	3.500	0.700	17.000	7.300	8.300	3.437	5.500	1589.722
CS	3.500	0.700	17.000	8.300	8.300	3.900	5.500	1582.539
BAT	3.500	0.700	17.000	8.300	8.070	3.900	5.413	1581.494
SCA	3.502	0.700	17.000	8.300	8.300	3.900	5.500	1588.522

3.3.3 I-beam design problem

The main purpose of this problem is to minimize the vertical deflection of the I beam (Ahmadianfar et al., 2020). I beam has 4 variants which are length (l), height (h), and two thickness (t_w, t_f) (Figure 4c). The parameters (Equation (20)), objective function (Equation (21)) and constraints (Equation (22), (23)) of the problem are given in the following equations.

Consider: $$\vec{X} = [x_1, x_2, x_3, x_4] = [h, l, t_w, t_f]$$ **(**20**)**

Minimize: $$f_{cost}(\vec{x}) = \frac{5000}{\frac{1}{12}t_w(h-2t_f)^3 + \frac{1}{6}lt_f{}^3 + 2lt_f\left(\frac{h-t_f}{2}\right)^2}$$ **(**21**)**

Subject to: $$g_1(\vec{x}) = 2lt_f + t_w(h-2t_f)^3 \leq 300$$

$$g_2(\vec{x}) = \frac{180000h}{t_w(h-2t_f)^3 + 2lt_f[4t_f{}^2 + 3h(h-2t_f)]} + \frac{15000l}{(h-2t_f)t_w{}^3 + 2t_fl^3} \leq 6$$ **(**22**)**

Range: $$10 \leq h \leq 80, 10 \leq l \leq 50, 0.9 \leq t_w \leq 5, 0.9 \leq t_f \leq 5$$ **(**23**)**

The results of all algorithms from the I-beam design problem are given in Table 9. With 38.455 optimal cost, the proposed algorithm is the most successful one while GWO is the second with 38.61 optimal cost and CMA-ES is the third with 38.668 optimal cost. TSO is algorithm with the worst result as it has 44.777 optimal cost.

Table 9. Comparison of results for I- beam design problem

Optimizer	Optimal values for variables				Optimal cost
	x_1	x_2	x_3	x_4	
ITSO	***13.583***	***25.857***	***0.900***	***5.000***	***38.455***
TSO	10.000	10.000	0.900	0.900	44.777
GWO	13.535	25.998	0.900	5.000	38.610
CMA-ES	13.561	25.934	0.900	5.000	38.668
CS	13.608	25.732	0.900	5.000	38.949
BAT	13.582	25.864	0.900	5.000	41.129
SCA	13.616	25.549	0.900	5.000	39.421

4. CONCLUSION

TSO is a swarm-based MHA that is improved by being inspired by the fishing strategies of tuna fish. The biggest disadvantage of TSO is that it gets caught by the local minimum trap. In order to solve this problem of TSO, this article proposes a new local search procedure. The main philosophy of the proposed approach is not focusing only on the best solution but on the best ones. The new proposed algorithm is applied to 10 classical test functions and welded beam design problem, speed reducer design problem and I-beam design problem. The results indicate the success of the proposed algorithm. The results of this study is as follows.

- Like many other MHAs, TSO focuses on the best results. Focusing not only on the best solution but on the best ones allows it to abstain from local minimum trap.
- The results of the classical test functions indicate that the proposed algorithm is successful at solving unimodal and multimodal functions.
- Besides, statistical results confirm that the improved algorithm's success for the classical test results are meaningful.
- In engineering design problems, TSO is not able to present competitive results. In all design problems, the proposed algorithm is the most successful one though. Such a case indicates that the method proposed in this article to improve the performance of TSO is successful.
- As far as we know, this study is the first one proposing a change in the mathematical model of TSO. Considering the results, it could be suggested that TSO is an algorithm that is open to be improved.

For further studies, the following issues could be considered.

- Redesigning the mathematical model of TSO's spiral and parabolic search strategies. Moreover, TSO could be improved so that it might not need initial parameters.
- Analysing the parameters of TSO in a wide scale by determining them through 2 or 3 dimensional chaotic maps.
- Finding out its weakness by applying it to more real-world problems.
- By integrating TSO into machine learning and artificial intelligence, it could be applied in a field like image processing.
- In the optimization of unmanned air vehicles and the solution of mission planning problems, TSO could generate successful results.

5. CONFLICT OF INTEREST

Author approve that to the best of their knowledge, there is not any conflict of interest or common interest with an institution/organization or a person that may affect the review process of the paper.

6. REFERENCES

Abdulwahab H. A., Noraziah A., Alsewari A. A., Salih S. Q., An Enhanced Version of Black Hole Algorithm via Levy Flight for Optimization and Data Clustering Problems. IEEE Access 7, 142085-142096, 2019.

Abualigah L., Diabat A., Advances in Sine Cosine Algorithm: A comprehensive survey. Artificial Intelligence Review 54(4), 2567-2608, 2021.

Abualigah L., Diabat A., Geem Z. W., A Comprehensive Survey of the Harmony Search Algorithm in Clustering Applications. Applied Sciences 10(11), 3827, 2020.

Ahmadianfar I., Bozorg-Haddad O., Chu X., Gradient-based optimizer: A new metaheuristic optimization algorithm. Information Sciences 540, 131-159, 2020.

Amine K., Multiobjective Simulated Annealing: Principles and Algorithm Variants. Advances in Operations Research 2019, e8134674, 2019.

Ashraf H., Elkholy M. M., Abdellatif S. O., El‐Fergany A. A., Synergy of neuro-fuzzy controller and tuna swarm algorithm for maximizing the overall efficiency of PEM fuel cells stack including dynamic performance. Energy Conversion and Management:X 16, 100301, 2022.

Askari Q., Saeed M., Younas I., Heap-based optimizer inspired by corporate rank hierarchy for global optimization. Expert Systems with Applications 161, 113702, 2020.

Askari Q., Younas I., Saeed M., Political Optimizer: A novel socio-inspired meta-heuristic for global optimization. Knowledge-Based Systems 195, 105709, 2020.

Deng W., Shang S., Cai X., Zhao H., Song Y., Xu J., An improved differential evolution algorithm and its application in optimization problem. Soft Computing 25(7), 5277-5298, 2021.

Feng Y., Deb S., Wang G.-G., Alavi A. H., Monarch butterfly optimization: A comprehensive review. Expert Systems with Applications 168, 114418, 2021.

Fu C., Zhang L., A novel method based on tuna swarm algorithm under complex partial shading conditions in PV system. Solar Energy 248, 28-40, 2022.

Gad A. G., Particle Swarm Optimization Algorithm and Its Applications: A Systematic Review. Archives of Computational Methods in Engineering 29(5), 2531-2561, 2022.

Gandomi A. H., Yang X.-S., Alavi A. H., Talatahari S., Bat algorithm for constrained optimization tasks. Neural Computing and Applications 22(6), 1239-1255, 2013.

Gul F., Rahiman W., Alhady S. S. N., Ali A., Mir I., Jalil A., Meta-heuristic approach for solving multi-objective path planning for autonomous guided robot using PSO–GWO optimization algorithm with evolutionary programming. Journal of Ambient Intelligence and Humanized Computing 12(7), 7873-7890, 2021.

Guo S.-M., Guo J.-K., Gao Y.-G., Guo P.-Y., Fu-Jun a H., Wang S.-C., Lou Z.-C., Zhang X., Research on Engine Speed Control Based on Tuna Swarm Optimization. Journal of Engineering Research and Reports 23(12), 272-280, 2022.

Hansen N., Müller S. D., Koumoutsakos P., Reducing the Time Complexity of the Derandomized Evolution Strategy with Covariance Matrix Adaptation (CMA-ES). Evolutionary Computation 11(1), 1-18, 2003.

Hashim F. A., Houssein E. H., Hussain K., Mabrouk M. S., Al-Atabany W., Honey Badger Algorithm: New metaheuristic algorithm for solving optimization problems. Mathematics and Computers in Simulation 192, 84-110, 2022.

Jafari A., Khalili T., Babaei E., Bidram A., A Hybrid Optimization Technique Using Exchange Market and Genetic Algorithms. IEEE Access 8, 2417-2427, 2020.

Korashy A., Kamel S., Youssef A.-R., Jurado F., Modified water cycle algorithm for optimal direction overcurrent relays coordination. Applied Soft Computing 74, 10-25, 2019.

Kumar A., Pant S., Ram M., System Reliability Optimization Using Gray Wolf Optimizer Algorithm. Quality and Reliability Engineering International 33(7), 1327-1335, 2017.

Kumar C., Magdalin Mary D., A novel chaotic-driven Tuna Swarm Optimizer with Newton-Raphson method for parameter identification of three-diode equivalent circuit model of solar photovoltaic cells/modules. Optik 264, 169379, 2022.

Kumar M., Kulkarni A. J., Satapathy S. C., Socio evolution & learning optimization algorithm: A socio-inspired optimization methodology. Future Generation Computer Systems 81, 252-272, 2018.

Kumar S., Yildiz B. S., Mehta P., Panagant N., Sait S. M., Mirjalili S., Yildiz A. R., Chaotic marine predators algorithm for global optimization of real-world engineering problems. Knowledge-Based Systems 261, 110192, 2023.

Kumar V., Kumar D., A Systematic Review on Firefly Algorithm: Past, Present, and Future. Archives of Computational Methods in Engineering 28(4), 3269-3291, 2021.

Li S., Gong W., Yan X., Hu C., Bai D., Wang L., Gao L., Parameter extraction of photovoltaic models using an improved teaching-learning-based optimization. Energy Conversion and Management 186, 293-305, 2019.

Mareli M., Twala B., An adaptive Cuckoo search algorithm for optimisation. Applied Computing and Informatics 14(2), 107-115, 2018.

Mbuli N., Ngaha W. S., A survey of big bang big crunch optimisation in power systems. Renewable and Sustainable Energy Reviews 155, 111848, 2022.

Mirjalili S., SCA: A Sine Cosine Algorithm for solving optimization problems. Knowledge-Based Systems 96, 120-133, 2016.

Mirjalili S., Evolutionary Algorithms and Neural Networks, Springer International Publishing, First Edition, United States, pp. 43-55, 2019.

Mirjalili S., Mirjalili S. M., Lewis A., Grey Wolf Optimizer. Advances in Engineering Software 69, 46-61, 2014.

Noureddine S., An optimization approach for the satisfiability problem. Applied Computing and Informatics 11(1), 47-59, 2015.

Öztürk Ş., Ahmad R., Akhtar N., Variants of Artificial Bee Colony algorithm and its applications in medical image processing. Applied Soft Computing 97, 106799, 2020.

Prajapati V. K., Jain M., Chouhan L., Tabu Search Algorithm (TSA): A Comprehensive Survey, 3rd International Conference on Emerging Technologies in Computer Engineering: Machine Learning and Internet of Things (ICETCE), Jaipur/India, February 7-8, 2020, pp: 1-8.

Raja B. D., Patel V. K., Yildiz A. R., Kotecha P., Performance of scientific law-inspired optimization algorithms for constrained engineering applications. Engineering Optimization 55(10), 1798-1812, 2023.

Rajabioun R., Cuckoo Optimization Algorithm. Applied Soft Computing 11(8), 5508-5518, 2011.

Ramachandran M., Mirjalili S., Nazari-Heris M., Parvathysankar D. S., Sundaram A., Charles Gnanakkan C. A. R., A hybrid Grasshopper Optimization Algorithm and Harris Hawks Optimizer for Combined Heat and Power Economic Dispatch problem. Engineering Applications of Artificial Intelligence 111, 104753, 2022.

Rashedi E., Nezamabadi-pour, H., Saryazdi S., GSA: A Gravitational Search Algorithm. Information Sciences 179(13), 2232-2248, 2009.

Rosso M. M., Cucuzza R., Aloisio A., Marano G. C., Enhanced Multi-Strategy Particle Swarm Optimization for Constrained Problems with an Evolutionary-Strategies-Based Unfeasible Local Search Operator. Applied Sciences 12(5), 2285, 2022.

Tan M., Li Y., Ding D., Zhou R., Huang C., An Improved JADE Hybridizing with Tuna Swarm Optimization for Numerical Optimization Problems. Mathematical Problems in Engineering 2022, e7726548, 2022.

Tuerxun W., Xu C., Guo H., Guo L., Zeng N., Cheng Z., An ultra-short-term wind speed prediction model using LSTM based on modified tuna swarm optimization and successive variational mode decomposition. Energy Science & Engineering 10(8), 3001-3022, 2022.

Wang G.-G., Moth search algorithm: a bio-inspired metaheuristic algorithm for global optimization problems. Memetic Computing 10(2), 151-164, 2018.

Wang G.-G., Deb S., Coelho L. D. S., Earthworm optimisation algorithm: a bio-inspired metaheuristic algorithm for global optimisation problems. International Journal of Bio-Inspired Computation 12(1), 1-22, 2018.

Wang G.-G., Deb S., Cui Z., Monarch butterfly optimization. Neural Computing and Applications 31(7), 1995-2014, 2019.

Wang J., Zhu L., Wu B., Ryspayev A., Forestry Canopy Image Segmentation Based on Improved Tuna Swarm Optimization. Forests 13(11), 1746, 2022.

Wang W., Tian J., An Improved Nonlinear Tuna Swarm Optimization Algorithm Based on Circle Chaos Map and Levy Flight Operator. Electronics 11(22), 3678, 2022.

Wang Y., Wang P., Zhang J., Cui Z., Cai X., Zhang W., Chen J., A Novel Bat Algorithm with Multiple Strategies Coupling for Numerical Optimization. Mathematics 7(2), 135, 2019.

Wei Z., Huang C., Wang X., Han T., Li Y., Nuclear Reaction Optimization: A Novel and Powerful Physics-Based Algorithm for Global Optimization. IEEE Access 7, 66084-66109, 2019.

Wolpert D. H., Macready W. G., No free lunch theorems for optimization. IEEE Transactions on Evolutionary Computation 1(1), 67-82, 1997.

Wu L., Huang X., Cui J., Liu C., Xiao W., Modified adaptive ant colony optimization algorithm and its application for solving path planning of mobile robot. Expert Systems with Applications 215, 119410, 2023.

Xie L., Han T., Zhou H., Zhang Z.-R., Han B., Tang A., Tuna Swarm Optimization: A Novel Swarm-Based Metaheuristic Algorithm for Global Optimization. Computational Intelligence and Neuroscience 2021, e9210050, 2021.

Xue Y., Zhang Q., Zhao Y., An improved brain storm optimization algorithm with new solution generation strategies for classification. Engineering Applications of Artificial Intelligence 110, 104677, 2022.

Yan Z., Yan J., Wu Y., Cai S., Wang H., A novel reinforcement learning based tuna swarm optimization algorithm for autonomous underwater vehicle path planning. Mathematics and Computers in Simulation 209, 55-86 2023.

Zhang F., Mei Y., Nguyen S., Zhang M., Tan K. C., Surrogate-Assisted Evolutionary Multitask Genetic Programming for Dynamic Flexible Job Shop Scheduling. IEEE Transactions on Evolutionary Computation 25(4), 651-665, 2021.

Zhang Y., Jin Z., Group teaching optimization algorithm: A novel metaheuristic method for solving global optimization problems. Expert Systems with Applications 148, 113246, 2020.

JOURNAL of
MATERIALS and MECHATRONICS:A

e-ISSN 2717-8811
JournalMM, 2023, 4(2), 446-458
https://doi.org/10.55546/jmm.1319818

Araştırma Makalesi / Research Article

Exploring the Effects of Annealing Temperature on Structural and Magnetic Properties of Low-Level Neodymium-Substituted Strontium Hexaferrite Synthesized Via Combustion Method

Esin DEMİR[1], Sefa Emre SÜNBÜL[2], Kürşat İÇİN[3*]

[1] Ondokuz Mayıs Üniversitesi, Teknoloji Transfer Ofisi (TTO), Samsun, Türkiye,
ORCID ID: https://orcid.org/0000-0003-1900-2877, esin.demir@omu.edu.tr
[2] Gaziantep Üniversitesi, Mühendislik Fakültesi, Metalurji ve Malzeme Mühendisliği Bölümü, Gaziantep, Türkiye,
ORCID ID: https://orcid.org/0000-0002-2648-9268, sunbulsefa@ktu.edu.tr
[3] Karadeniz Teknik Üniversitesi, Mühendislik Fakültesi, Metalurji ve Malzeme Mühendisliği Bölümü, Trabzon, Türkiye,
ORCID ID: https://orcid.org/0000-0002-5160-6753, kursaticin@ktu.edu.tr

Geliş/ Received: 25.06.2023; **Kabul / Accepted:** 18.08.2023

ABSTRACT: This study investigates the impact of annealing temperature on the structural and magnetic attributes of Nd-substituted strontium hexaferrite ($Sr_{0.9}Nd_{0.1}Fe_{12}O_{19}$). The research demonstrated that as the annealing temperature increased, diffusion accelerated, thereby inducing a transformation into the $SrFe_{12}O_{19}$ phase and enhancing hard magnetic properties. The annealing process also significantly impacted the bonding structure, specifically affecting the presence of N-O bonds. Peak intensities escalated until 1100°C, subsequently declining due to the emergence of a composite structure ($SrFe_{12}O_{19}$+α-Fe_2O_3) arising from the Nd substitution. Importantly, the coercive field of the compound substantially increased post-annealing, attaining a peak at 1100°C (5.21 kOe) from 0.52 kOe pre-annealing, indicating that annealing amplifies resistance to demagnetization. Furthermore, both remanent magnetization and saturation magnetization values improved, reaching maximum values at 1100°C, measuring 40.2 emu/g and 61.5 emu/g, respectively.

Keywords: Combustion synthesis, Hexaferrite, Magnetic properties, Rare-earth substitution.

*Sorumlu yazar / Corresponding author: kursaticin@ktu.edu.tr

Bu makaleye atıf yapmak için /To cite this article

Demir, E., Sünbül, S.E., İçin, K. (2023). Exploring The Effects Of Annealing Temperature on Structural and Magnetic Properties of Low-Level Neodymium-Substituted Strontium Hexaferrite Synthesized Via Combustion Method. Journal of Materials and Mechatronics: A (JournalMM), 4(2), 446-458.

1. INTRODUCTION

Strontium hexaferrites, also known as $SrFe_{12}O_{19}$, are a class of magnetic materials with unique properties that make them invaluable in numerous applications (Zhang, et al., 2023; Zhivulin, et al., 2023). Derived from the hexagonal ferrite family, these compounds exhibit extraordinary magnetic properties, including high uniaxial magnetic anisotropy and coercivity. They are primarily used in permanent magnets due to their ability to maintain a strong magnetic field (Lim, et al., 2023; Rambabu, et al., 2023; Verma, et al., 2023). Furthermore, strontium hexaferrite have been widely adopted in various sectors, such as electronics, telecommunications, and the automotive industry, because of their high chemical stability, relatively low cost, and ease of production (Gulbadan, et al., 2023; Için, et al., 2022; Kolev, et al., 2022; Serrano, et al., 2021; Zahid, et al., 2021). Lately, extensive research is being directed towards understanding the impact of doping and substitution in strontium hexaferrites in order to enhance their magnetic properties and temperature stability (Elanthamilan, et al., 2023; R. S. Liu, et al., 2023; M. Zhang, et al., 2022; W. H. Zhang, et al., 2022; Wenhao Zhang, et al., 2022).

The unit cells in the crystal structure of strontium hexaferrite magnets are hexagonal and exhibit strong magnetic properties. The dense packing structure of strontium hexaferrite magnets provides a suitable environment for permanent magnet properties. Considering the crystal structure of the magnet, this ferrite magnet has a complex magnetoplumbite-type structure, in which oxygen ions coordinate iron ions in a tetrahedral (FeO_4), trigonal bipyramidal (FeO_5), and octahedral (FeO_6) manner (Li, et al., 2023; Rambabu, et al., 2021; Serrano, et al., 2021; Shariff, et al., 2021). Essentially, studies have been related to the physical properties, characterization, and measurements of strontium hexaferrite magnets. $SrFe_{12}O_{19}$ have shown good electrical properties and a strong anisotropy. M-type strontium hexaferrite magnets crystallize in 64 ions in 11 different symmetry regions in the magnet unit cage. In the densely packed layers, Fe^{3+} ions are distributed in 5 crystallographic interstices. These are; three octahedral (2a, 12k, and 4f2), one tetrahedral (4f1), and one trigonal bipyramidal (2b) site 3 parallel (2a, 12k and 2b) and 2 anti-parallel (4f1 and 4f2) subcages match with O^{2-} ions to form the ferrimagnetic structure (Bohlender, et al., 2019; Gultom, et al., 2020; Oura, et al., 2018; Wenhao Zhang, et al., 2022).

The magnetic moments of ions in crystal structures determine the magnetic behavior of materials. The magnetic properties of these magnetic materials can be altered by doping or impurity incorporation into the crystal structure. Co-doping in $SrFe_{12}O_{19}$ materials causes a change in magnetic properties. This dopant causes changes in the positions of the Fe^{3+} ions, increasing their net magnetic moments and thus enhancing the magnetic behavior of the material. Cobalt provides high-performance magnetic materials by adding high coercive field and excellent magnetic properties to $SrFe_{12}O_{19}$ materials (Granja-Banguera, et al., 2022; Jianfeng, et al., 2022; Ruoshui Liu, et al., 2023). When aluminum (Al) dopant is added to $SrFe_{12}O_{19}$ materials, it becomes more resistant to temperature changes and its magnetic properties become more stable. This dopant causes a decrease in the net magnetic moment created by Fe^{3+} ions in the structure, but the coercive field of the material increases (Gorbachev, et al., 2023; Joshi, and Ruban Kumar, 2023; Manjunatha, et al., 2023). The effect of the Cu dopant or replacement depends on the addition ratio. At low ratios, the Cu dopant improves the remnant magnetization and saturation magnetization properties, while at high ratios, the Cu dopant weakens these properties (Ateia, et al., 2023; Ghimire, et al., 2018; Iqbal, and Ashiq, 2008; Muhammad Javed, et al., 2009; Qiao, et al., 2007).

The use of rare earth elements to modify the magnetic and structural properties of hexaferrites has attracted increasing attention due to the diverse applications that these materials can offer. In

particular, the ability of rare earth elements to induce significant changes in the magnetic and structural characteristics of hexaferrites makes them invaluable tools in the development of advanced magnetic materials (Liu, et al., 2019; Luo, et al., 2015; Singh, et al., 2014; Wang, et al., 2004; Wang, et al., 2005). Hexaferrites, an important class of magnetic materials, have gained prominence due to their unique combination of high magnetic permeability, low cost, and excellent temperature stability. However, their magnetic and structural properties can be tailored to a significant extent using rare earth elements, which can introduce new functionalities to these materials. The ionic radii and the valence state of rare earth elements, which are larger and more varied than those of iron, can significantly affect the crystal structure, leading to a modification of the magnetic properties. For instance, the substitution of rare earth elements, such as Neodymium (Nd) (Bercoff, et al., 2009) and Samarium (Sm) (K, et al., 2020), into the hexaferrite lattice can significantly enhance the magnetic anisotropy and coercivity. This can be extremely beneficial in applications such as permanent magnets, where high coercivity and remanent magnetization are desired. Furthermore, such substitutions can also improve the Curie temperature, making these materials suitable for high-temperature applications. On the structural front, rare earth substitutions can lead to the formation of different types of crystal structures. Depending on the type and concentration of the rare earth element used, one can achieve various types of crystal structures, such as spinel, garnet, or perovskite. This structural versatility enables the design of magnetic materials with desired magnetic properties.

In this study, we investigate the structural and magnetic property changes that occur when rare earth elements (REEs) are substituted for strontium (Sr). Previous research has primarily focused on the substitution of REEs for Sr in Fe-based compounds; however, in this investigation, we extend our analysis to explore the effects of REEs replacing Fe sites. The primary aim of this study is to gain a comprehensive understanding of how these dual substitutions impact the crystal structure and magnetic characteristics of the materials. By delving into this unexplored territory, we aim to contribute valuable insights to the field of materials science, providing a basis for the design and development of novel functional materials with tailored properties for various technological applications. In the context of this research, we've undertaken a comprehensive investigation into the effects of annealing temperature on the structural and magnetic characteristics of a $Sr_{0.9}Nd_{0.1}Fe_{12}O_{19}$ composition, where 0.1 Nd has been substituted for Sr. The main aim of this research is to better comprehend how these characteristics behave when subjected to different annealing temperatures. Additionally, it aims to clarify how substituting Nd impacts the magnetic properties of strontium hexaferrite.

2. MATERIALS AND METHODS

Within the scope of this study, strontium hexaferrite (SrM) powder with a 0.1 Nd additive was produced using the solution combustion synthesis technique (Figure 1). In the $SrFe_{12}O_{19}$ composition that enables the emergence of the hard magnetic phase in strontium hexaferrites, Nd was added in place of Sr. In the production of Nd-doped strontium hexaferrites, the Sr ratio was reduced by 0.1, and Nd was added in its place. Thus, the chemical compound aimed to be formed can be expressed as $Sr_{0.9}Nd_{0.1}Fe_{12}O_{19}$. In the production of the $Sr_{0.9}Nd_{0.1}Fe_{12}O_{19}$ compound, precursor chemicals, i.e. strontium nitrate $Sr(NO_3)_2$, iron nitrate ($Fe(NO_3)_2.9H_2O$), neodymium nitrate ($Nd(NO_3)_3.6H_2O$), were obtained from Sigma Aldrich. These compounds were purity of 99.9%. Citric acid, was also obtained from Sigma Aldrich and used as the necessary fuel for combustion to take place in solution combustion synthesis. The stoichiometric ratio was prepared according to the reaction given in

Equation 1. As a result of previous experimental studies, the stoichiometric ratio between Sr and Fe has been determined as 1:10.

$$Sr(NO_3)_2+Fe(NO_3)_2.9H_2O+Nd(NO_3)_2.6H_2O+C_6H_{10}O_8 \rightarrow SrNdFe_{12}O_{19}+H_2O+CO_2+N_2 \quad (1)$$

As part of the production process for strontium hexaferrite via the auto-combustion method, nitrate compounds and citric acid as a fuel were accurately weighed according to the ratios determined to produce 5 grams of $SrFe_{12}O_{19}$ and added to 30 ml of pure water. The mixture was stirred until a homogeneous solution was formed (approximately 2 hours) at 300 rpm. Ammonia (NH_3) was added to raise the pH of the resulting homogeneous mixture to 7. The solution was further stirred until the pH reached equilibrium (approximately 1 hour). Following this process, the solution was placed on a heating plate at 350 °C, and gel formation was initiated. After the gel formation process was completed, auto-combustion took place due to an exothermic reaction, resulting in the production of strontium hexaferrite precursor powders. The nano-sized powders produced by the exothermic combustion were initially ground in an agate mortar to break up partial agglomerations, and then subjected to high-energy ball milling to completely dissolve the lumps. In a high-energy ball mill, powders were gently milled using a 1:5 ball to powder ratio at 300 rpm in a WC mill with 10mm diameter WC balls. After the mild grinding process, an annealing heat treatment was applied to form the $SrFe_{12}O_{19}$ structure. To study the impact of phase changes occurring at different temperatures on the magnetic properties of strontium hexaferrite powders produced by auto-combustion synthesis from mixtures prepared according to $Sr_{0.9}Nd_{0.1}Fe_{12}O_{19}$ composition, an annealing process was carried out at atmospheric conditions starting from 900 °C, respectively at 1000, 1100, and 1200 °C for 1 hour. Due to the annealing process at high temperatures, a mild grinding process was applied for 5 minutes to break up the partial agglomerations that occurred between the powders. Various methods were employed to examine and analyze strontium hexaferrite magnets in detail. These methods included X-ray diffraction (XRD), Fourier transform infrared spectrophotometer (FTIR), vibration sample magnetometer (VSM). Phase changes in the structure of the produced strontium hexaferrite powders, changes in the crystal structure, were examined with an X-ray diffractometer. These analyses were conducted in the Central Research Laboratory of Karadeniz Technical University on a PANalytical X'pert Powder^3 model XRD device. FTIR analyses were performed in the wave number range of 500-4000 cm^{-1} with a Shimadzu brand IRSprit model FTIR device. The magnetic properties (coercivity, magnetic saturation, remanent magnetization) of strontium hexaferrite powders were measured using a Lakeshore brand 7304 Model vibrating sample magnetometer (VSM) at room temperature.

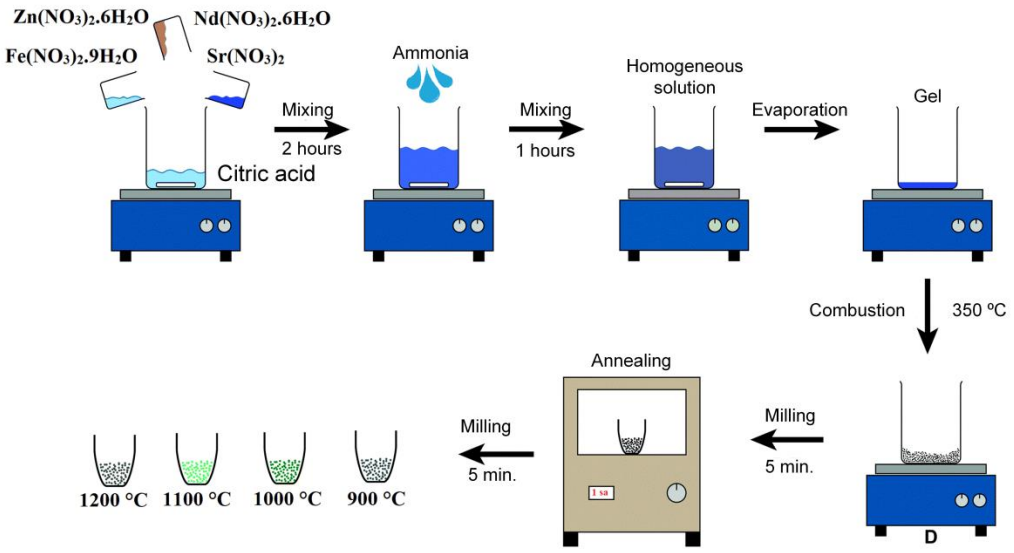

Figure 1. Schematic representation of the process flow diagram used in the study

3. RESULTS AND DISCUSSION

This research investigated the effects of substituting Nd for Sr on the phase structure of strontium hexaferrite, and how these effects evolve with temperature. The first stage of the study was a comprehensive analysis of the $Sr_{0.9}Nd_{0.1}Fe_{12}O_{19}$ composition's phase structure, both pre and post-annealing at temperatures ranging from 900 to 1200 °C, with the heat treatment lasting an hour. This experimental setup enabled the study of the effect of Nd-substitution at elevated temperatures, a critical aspect that affects the phase formation and properties of the material. In Figure 2, the graphical representation of the phase structural changes, it was observed that the initial phase formed in the strontium hexaferrite powders doped with 0.1 Nd, before annealing, is predominantly Fe_3O_4. This finding indicates that Nd substitution initially influences the phase composition by favoring the formation of Fe_3O_4. However, this phase composition does not remain constant. It undergoes dramatic changes with the onset of the annealing process, even at the minimum annealing temperature. The prevalent phase appears to be the $SrFe_{12}O_{19}$ phase, distinguished by its hard magnetic properties and hexagonal crystal lattice structure. This transition reveals the temperature-sensitive nature of the phase transformations, and the pivotal role annealing temperature plays in determining the resultant phase and hence, the magnetic properties of the material. With increasing annealing temperatures, there's a complete transformation of all peaks into $SrFe_{12}O_{19}$, a consequence of enhanced diffusion. The elevated temperature facilitates the mobility of atoms, enabling the formation of the $SrFe_{12}O_{19}$ phase, indicative of Nd's role in enhancing the diffusion process. The α-Fe_2O_3 phase, observed at $2\theta=33°$, persists even after the annealing process at 900 °C for an hour. Despite possessing relatively low magnetic properties, it remains unreacted in the structure, suggesting that the kinetic parameters (temperature and time) for the formation of the $SrFe_{12}O_{19}$ phase were not sufficiently met at this annealing temperature. As the temperature increases to between 1000-1200 °C, the α-Fe_2O_3 phase diminishes but a small impurity peak at $2\theta=36°$ persists in the structure, indicating the tenacity of the phase even at elevated temperatures. Furthermore, the primary diffraction peaks of the $SrFe_{12}O_{19}$ phase at $2\theta=32°$ and 34° show a decrease in width and an increase in intensity with an increase in annealing temperature. These variations in peak intensity and width suggest that the $SrFe_{12}O_{19}$ crystal size experiences growth along with the annealing temperature. The augmentation in crystal size at higher annealing temperatures has been documented in several studies, reinforcing the understanding

of temperature-dependent crystal growth. A study conducted by Urbano-Peña and colleagues suggested (Urbano-Peña, et al., 2019) that at temperatures above the phase temperature, the atomic movement within the structure is accelerated, leading to quicker phase transformations. In scenarios where phase transformation is rapid, grain growth is more likely. These findings are parallel to our observations, strengthening the argument that grain growth accompanies fast phase transformations.

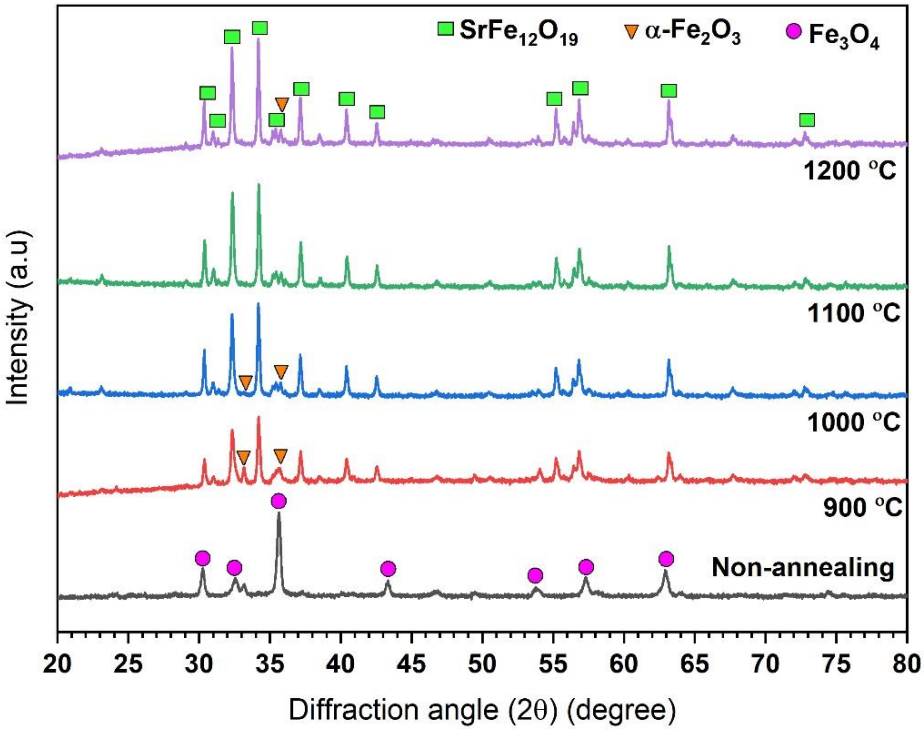

Figure 2. X-ray diffraction pattern of Nd substitution strontium hexaferrite powders

In this study, Fourier Transform Infrared Spectroscopy (FTIR) analyses were used to study the bond changes of neodymium (Nd) substituted strontium hexaferrite powders with respect to the annealing temperature. FTIR is a robust spectroscopic technique that provides valuable insights into the molecular structure and chemical bonding of materials. The results, as depicted in Figure 3, offer a detailed view of the impact of Nd substitution and annealing temperature on the material's bonding. The FTIR analyses were carried out at room temperature, spanning a broad spectral range of 400-1500 cm^{-1}. Room temperature measurements ensure the stability of the sample and prevent additional thermal effects from influencing the results. Since all the FTIR spectra resulted in similar vibrations, each graph was juxtaposed for a comparative analysis. This comparative approach offers a clearer understanding of the subtle differences arising due to Nd substitution and varying annealing temperatures. The $SrNdFe_{12}O_{19}$ compositions containing 0.1 Nd, synthesized using nitrate precursors and citric acid, exhibited absorption peaks of metal oxides within approximately 750-500 cm^{-1} in the FTIR spectrum. These metal oxide peaks are pivotal indicators of the nature of the chemical bonds present within the sample. Moreover, an absorption peak possibly related to N-O was observed at around 1450 cm^{-1}, signifying the potential presence of nitrogen-containing compounds. However, an interesting transformation occurred upon annealing the $Sr_{0.9}Nd_{0.1}Fe_{12}O_{19}$ between 900-1200 °C. The N-O related absorption peak vanishes, revealing a structure dominated by metal-oxygen bonds. This change underscores the importance of the annealing temperature in affecting the bond changes in Nd-substituted strontium hexaferrite powders. The absorption peaks at 566 and 599 cm^{-1} are associated with M-O (Sr-O or Fe-O) lattice vibrations, acting as spectral fingerprints for these metal-oxygen

bonds. The differences in vibrations are due to the dissimilar atomic weights of Sr and Fe, with lower (560 cm^{-1}) and higher (599 cm^{-1}) vibrations corresponding to Sr-O and Fe-O bonds respectively. Furthermore, the intensity of these absorption peaks showed a distinctive pattern based on the annealing temperature. The peak intensity increased until reaching 1100°C, after which it started to decrease. This variation in intensity is attributed to the composite nature of the powders' composition, as a result of Nd substitution, featuring $SrFe_{12}O_{19}$ and α-Fe_2O_3 phases. As the proportion of the α-Fe_2O_3 phase grows with Nd substitution, a new type of Fe-O bond emerges in the structure. An increment in this phase would lead to an increase in vibrations caused by the new Fe-O bond, intensifying the absorption peak seen at 599 cm^{-1}. These findings offer crucial insights into the spectral behavior of the Nd substituted strontium hexaferrite powders, underlining the instrumental role of Nd substitution and annealing temperature in modulating the material's bonding structure.

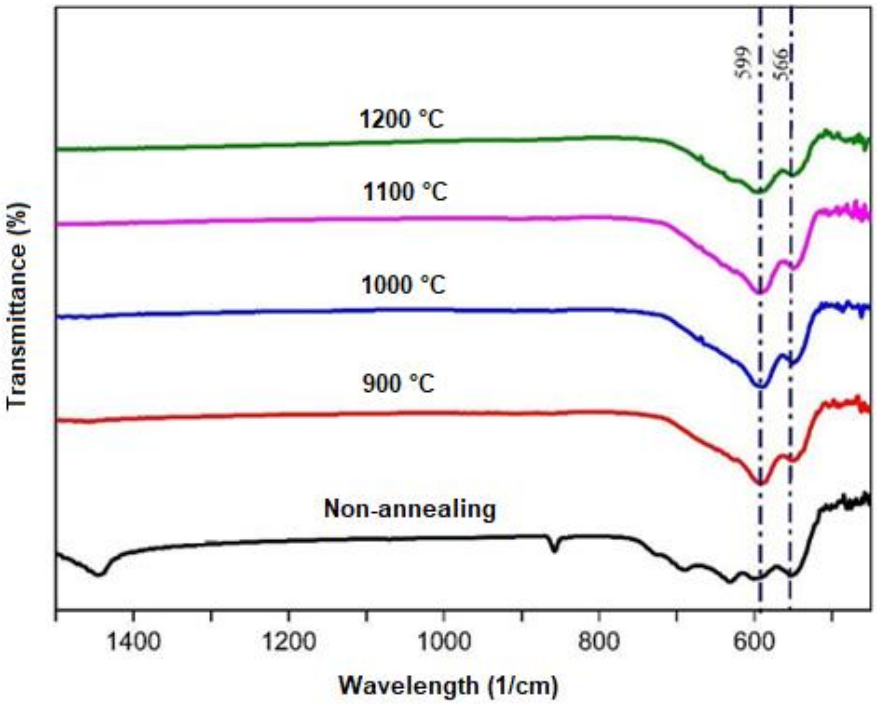

Figure 3. FTIR spectrum of annealed at various temperature Nd substituted strontium hexaferrite powders

This study also provides an in-depth analysis of the magnetic properties of $Sr_{0.9}Nd_{0.1}Fe_{12}O_{19}$, a neodymium (Nd) substituted strontium hexaferrite compound. These properties, which include the coercive field (H_c), remanent magnetization (M_r), and saturation magnetization (M_s), are essential in understanding the behavior of the material under different conditions. The hysteresis loops of the Nd-substituted strontium hexaferrite powders are shown in Figure 4. All magnetic properties of produced magnetic powders are presented in Table 1. Before annealing, the H_c of $Sr_{0.9}Nd_{0.1}Fe_{12}O_{19}$ was recorded to be 0.52 kOe. The coercive field represents the material's resistance to demagnetization. At this initial stage, the remanent magnetization, which indicates the material's magnetization in the absence of an external magnetic field, stood at 18.2 emu/g. Meanwhile, the saturation magnetization, referring to the maximum magnetization that the material can attain, was observed to be 59.5 emu/g. The annealing process, which involves heating the material and allowing it to cool slowly, has significant effects on the magnetic properties of the strontium hexaferrite. As the compound was annealed at various temperatures (900°C, 1000°C, 1100°C, and 1200°C), remarkable changes were observed. At 900°C, the coercivity increased significantly to 5.04 kOe, suggesting improved

resistance to demagnetization. The remanent and saturation magnetization values altered to 32.4 emu/g and 49.7 emu/g, respectively. Further increase in the annealing temperature to 1000°C resulted in a slight decrease in H_c (5.02 kOe), while both M_r and M_s improved (39.1 emu/g and 60.6 emu/g, respectively), suggesting an overall enhancement in magnetic performance. At 1100°C, the coercivity further grew to 5.21 kOe, indicating increased stability in the magnetic state of the material. The remanent and saturation magnetization values followed suit, reaching 40.2 emu/g and 61.5 emu/g, respectively. However, upon reaching an annealing temperature of 1200°C, the coercivity fell to 4.42 kOe, while the remanent and saturation magnetization declined slightly to 38.9 emu/g and 59.2 emu/g, respectively. This points to an optimal annealing temperature range for maximizing the magnetic properties of $Sr_{0.9}Nd_{0.1}Fe_{12}O_{19}$. The observed changes in the magnetic properties of the $Sr_{0.9}Nd_{0.1}Fe_{12}O_{19}$ compound are intrinsically linked to the underlying structural modifications occurring during the annealing process. It is important to highlight that the structure and magnetic properties of a material are closely interconnected. With an increase in annealing temperature up to 1100°C, there is a noticeable enhancement in the compound's H_c, M_r and M_s. This improvement is primarily attributed to the formation and growth of the hard magnetic $SrFe_{12}O_{19}$ phase. As the Nd-substituted strontium hexaferrite is annealed, diffusion processes are enhanced, which leads to the development and enlargement of the $SrFe_{12}O_{19}$ phase. This hard magnetic phase, characterized by a hexagonal crystal lattice structure, is crucial for the elevated magnetic properties observed. The growth of the $SrFe_{12}O_{19}$ phase leads to an increase in the remanent magnetization and the saturation magnetization. This is because the $SrFe_{12}O_{19}$ phase, being a hard magnetic phase, possesses superior magnetic properties compared to the original Nd-substituted ferrite. The increase in coercivity, which indicates better resistance to demagnetization, is also a typical feature of hard magnetic materials. However, when the annealing temperature surpasses the optimal range, around 1200°C in this case, there is a decline in the magnetic properties. This drop can be linked to the occurrence of grain growth induced by the elevated temperatures. With the grain size exceeding the single-domain size, multi-domain particles are formed. The transition from single domain to multi-domain particles usually results in a decline in magnetic properties due to the emergence of demagnetizing fields within the material. Therefore, the slight reduction in coercivity and magnetization at 1200°C is associated with the onset of multi-domain behavior due to grain growth. Thus, the careful control of annealing temperature is critical to balance the beneficial growth of the hard magnetic $SrFe_{12}O_{19}$ phase and mitigate the negative impacts of excessive grain growth, allowing for the optimization of the magnetic properties of the $Sr_{0.9}Nd_{0.1}Fe_{12}O_{19}$ compound.

Table 1. Magnetic properties of strontium hexaferrite powders

	$Sr_{0.9}Nd_{0.1}Fe_{12}O_{19}$		
	H_c kOe	M_r emug^{-1}	M_s emug^{-1}
Non-annealing	0.52	18.2	59.5
900	5.04	32.4	49.7
1000	5.02	39.1	60.6
1100	5.21	40.2	61.5
1200	4.42	38.9	59.2

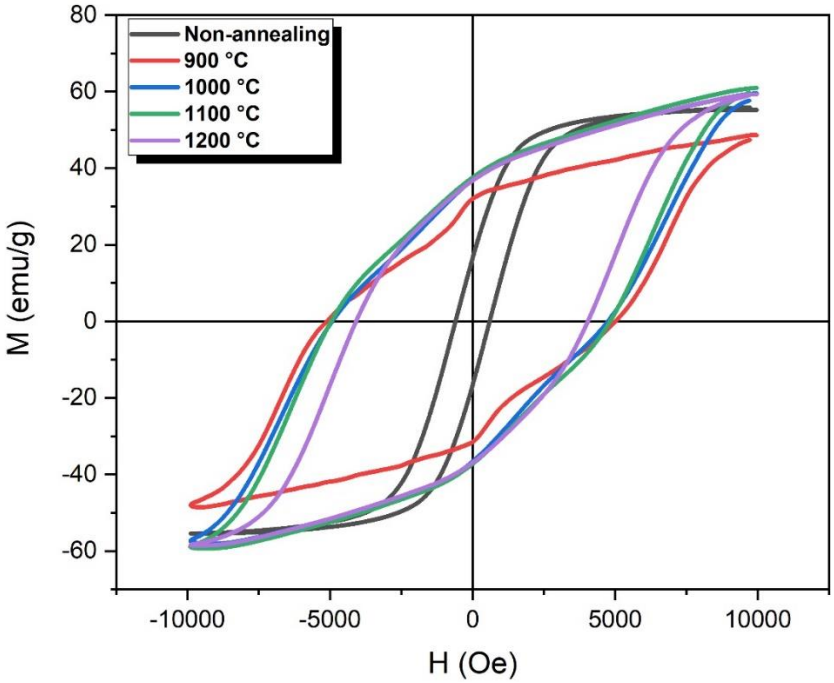

Figure 4. Hysteresis loops of Nd substitution strontium hexaferrite powders

4. CONCLUSION

Building upon the substantial body of research emphasizing the modification of strontium hexaferrites' magnetic properties via ion substitution, this study has endeavored to delve deeper into the nuanced impacts of Nd substitution on the structural, and magnetic characteristics of a $Sr_{0.9}Nd_{0.1}Fe_{12}O_{19}$ composition. A comprehensive exploration of these properties across a range of annealing temperatures has been conducted to elucidate the dynamic interplay between material composition, processing conditions, and resultant properties. Some important observed results were summarized below:

- Increased annealing temperatures expedite diffusion, leading to a transformation into the $SrFe_{12}O_{19}$ phase and enhancement in hard magnetic properties.
- The non-annealed samples displayed absorption peaks related to both metal oxides and N-O, while after the annealing process, the N-O related peak disappeared. This indicates a significant impact of the annealing temperature on the bonding structure, particularly affecting the presence of the N-O bond.
- There was an escalation in peak intensities up to 1100°C annealing temperature, after which a decline was observed due to the composite structure ($SrFe_{12}O_{19}$+α-Fe_2O_3) emerging from the Nd substitution, consequently modifying the Fe-O bond in the structure.
- The coercive field of the $Sr_{0.9}Nd_{0.1}Fe_{12}O_{19}$ compound increased significantly with annealing, reaching its peak at 1100°C (5.21 kOe) from a mere 0.52 kOe before annealing. This indicates that annealing effectively enhances the compound's resistance to demagnetization.
- Annealing also improved the remanent magnetization and saturation magnetization values, demonstrating the highest values at 1100°C with 40.2 emu/g and 61.5 emu/g, respectively.

5. ACKNOWLEDGEMENTS

The project coded FBA-2023-10668 by the Scientific Research Projects Department of KTU and the project numbered 119M111 by TÜBİTAK have played a significant role in carrying out this study. Additionally, we would like to express our profound gratitude to Prof. Dr. Bekir Özçelik for his expertise and contributions in magnetic measurements. Besides, we would like to extend our gratitude to the editors and reviewers for their contributions during the review and evaluation phase of this paper.

6. CONFLICT OF INTEREST

Authors approve that to the best of their knowledge, there is not any conflict of interest or common interest with an institution/organization or a person that may affect the review process of the paper.

7. AUTHOR CONTRIBUTION

In this study, all authors have contributed equally. Esin Demir: Investigation; Sefa Emre Sünbül: Original Draft and software; Kürşat İÇİN: supervisor, analysis, original draft.

8. REFERENCES

Ateia E.E., Rabie O., Mohamed Amira T., Multi-Susceptible Single-Phased Hexaferrite with Significant Magnetic Switching Properties by Selectively Doping, Physica Scripta, 98(6), 065801, 2023.

Bercoff P.G., Herme C., Jacobo S. E., The Influence of Nd–Co Substitution on the Magnetic Properties of Non-Stoichiometric Strontium Hexaferrite Nanoparticles, Journal of Magnetism and Magnetic Materials, 321(14), 2245-50, 2009.

Bohlender C., Kahnes M., Muller R.Topfer J., Phase Formation, Magnetic Properties, and Phase Stability in Reducing Atmosphere of M-Type Strontium Hexaferrite Nanoparticles Synthesized Via a Modified Citrate Process, Journal of Materials Science, 54(2), 1136-46, 2019.

Elanthamilan E., Elizabeth I.B., Wang S.F., Lydia I.S., Strontium Hexaferrite Microspheres: Synthesis, Characterization and Visible-Light-Driven Photocatalytic Activity Towards the Degradation of Methylene Blue Dye, Optical Materials, 137, 41-48, 2023.

Ghimire M., Yoon S., Wang L., Neupane D., Alam J., Mishra S.R., Influence of La Content on Magnetic Properties of Cu Doped M-Type Strontium Hexaferrite: Structural, Magnetic, and Mossbauer Spectroscopy Study, Journal of Magnetism and Magnetic Materials, 454, 110-20, 2018.

Gorbachev Evgeny A., Lebedev Vasily A., Kozlyakova Ekaterina S., Alyabyeva Liudmila N., Ahmed Asmaa, Cervellino A., Trusov Lev A., Tuning the Microstructure, Magnetostatic and Magnetodynamic Properties of Highly Al-Substituted M-Type Sr/Ca Hexaferrites Prepared by Citrate-Nitrate Auto-Combustion Method, Ceramics International, 49(16), 26411-26419, 2023.

Granja-Banguera Claudia P., Silgado-Cortázar Daniel G., Morales-Morales Jimmy A., Transition Metal Substituted Barium Hexaferrite-Modified Electrode: Application as Electrochemical Sensor of Acetaminophen, Molecules, 27(5), 1550, 2022.

Gulbadan S., Khan M. A., Ashraf G. A., Mahmood K., Shahid M., Irfan M.Ahmad A., Insight of Structural, Dielectric and Spectroscopic Characteristics of $Ba_{0.6}Sr_{0.4-Xybx}Fe_{(12-y)}Co_yO_{(19)}$ M-Type Hexaferrite, Ceramics International, 49(4), 6487-99, 2023.

Gultom G., Rianna M., Sebayang P., Ginting M., The Effect of Mg-Al Binary Doped Barium Hexaferrite for Enhanced Microwave Absorption Performance, Case Studies in Thermal Engineering, 18, 100580, 2020.

Için K., Öztürk S., Çakıl D.D., Sünbül S. E., Ergin İ., Özçelik B., Investigation of Nano-Crystaline Strontium Hexaferrite Magnet Powder from Mill Scale Waste by the Mechanochemical Synthesis: Effect of the Annealing Temperature, Materials Chemistry and Physics, 290, 126513, 2022.

Iqbal M. J., Ashiq M.N., Physical and Electrical Properties of Zr–Cu Substituted Strontium Hexaferrite Nanoparticles Synthesized by Co-Precipitation Method, Chemical Engineering Journal, 136(2), 383-89, 2008.

Jianfeng C., Yingli L., isheng Y., Computational and Experimental Study on Cation Distribution of Cobalt Substituted Barium Hexaferrites Bafe12-xCoxO19 (X = 0, 0.3, 0.6, 0.9) for Circulator Applications, Journal of Alloys and Compounds, 891, 161917, 2022.

Joshi H., Ruban K.A., Divalent Cation Substitution Impact on the Properties of Strontium Aluminium Hexaferrite (SrAl2Fe10O19), Physica B: Condensed Matter, 664, 415018, 2023.

Alamelu M., Selvi K.T., Priya M., Effect of Co and Sm Substitutions on the Magnetic Interactions of M-Type Strontium Hexaferrite Nanoparticles, Journal of Superconductivity and Novel Magnetism, 33(3), 713-20, 2020.

Kolev S., Georgieva B., Koutzarova T., Krezhov K., Ghelev C., Kovacheva D., Vertruyen B., Closset R., Tran L. M., Babij M., Zaleski A. J., Magnetic Field Influence on the Microwave Characteristics of Composite Samples Based on Polycrystalline Y-Type Hexaferrite, Polymers, 14(19), 2022.

Li Y. L., Liu Q., Qi M. G., Chen Y. L., C-Axis-Oriented Ba(Znhf)(X)Fe12-Xo19 M-Type Barium Hexaferrite with a High Squareness Ratio, Journal of Electronic Materials, 52(1), 523-29, 2023.

Lim J. P., Kang M. G., Kang Y. M., Development of Multi-Cation-Doped M-Type Hexaferrite Permanent Magnets, Applied Sciences-Basel, 13(1), 2023.

Liu Q., Wu C., Wang Y., You X., Li J., Liu Y., Zhang H., Microstructure and Electromagnetic Properties of Oriented Strontium W-Type Hexaferrite with Rare-Earth Gd3+ Substitution, Ceramics International, 45(9), 12205-10, 2019.

Liu R. S., Wang L. C., Yu X., Xu Z. Y., Gong H. Y., Zhao T. Y., Hu F. X., Shen B. G., Magnetocrystalline Anisotropy Study of Co-Substituted M-Type Strontium Hexaferrite Single Crystals, Ceramics International, 49(2), 1888-95, 2023.

Liu R., Wang L., Yu X., Xu Z., Gong H., Zhao T., Hu F., Shen B., Magnetocrystalline Anisotropy Study of Co-Substituted M-Type Strontium Hexaferrite Single Crystals, Ceramics International, 49(2), 1888-95, 2023.

Luo J., Xu Y., Mao H., Magnetic and Microwave Absorption Properties of Rare Earth Ions (Sm3+, Er3+) Doped Strontium Ferrite and Its Nanocomposites with Polypyrrole, Journal of Magnetism and Magnetic Materials, 381, 365-71, 2015.

Manjunatha B. C., Puneeth Kumar P., Pushpa N., Shankar P.Nagabhushana B. M., Study of Structural and Magnetic Features of Aluminum Substituted Hexaferrites of Calcium Suitable for Memory Storage Application, Materials Today: Proceedings, 89(1), 14-18, 2023.

Muhammad J. I., Muhammad N.A., Pablo H.G., Effect of Annealing Temperature and Substitution of Zr-Cu on Magnetic Properties of Strontium Hexaferrite Nanoparticles, Journal of Physics: Conference Series, 153(1), 012053, 2009.

Oura M., Nagasawa N., Ikeda S., Shimoda A., Waki T., Tabata Y., Nakamura H., Hiraoka N., Kobayashi H., Fe-57 Mossbauer and Co K Beta X-Ray Emission Spectroscopic Investigations of La-Co and La Substituted Strontium Hexaferrite, Journal of Applied Physics, 123(3), 033907, 2018.

Qiao L., You L., Zheng J., Jiang L., Sheng J., The Magnetic Properties of Strontium Hexaferrites with La–Cu Substitution Prepared by Shs Method, Journal of Magnetism and Magnetic Materials, 318(1), 74-78, 2007.

Rambabu C., Sarma K.S., Shivanarayana C., Padmavathi U., Swetha R., Raju K., Batoo K.M., Murali N., Verma R., Lakshminarayana P.V., Effect of La-Cu Co-Substitution on Structural, Microstructural and Magnetic Properties of M-Type Strontium Hexaferrite (Sr1−xLaxFe12−xCuxO19), Inorganic Chemistry Communications, 134, 109053, 2021.

Rambabu C., Uppugalla S., Verma R., Ramakrishna A., Murali N., Shivanarayana C., Parajuli D., Suryanarayana B., Mujasam B.K., Hussain S., Lakshmi Narayana P. V., Effect of La3+and Ni2+ Substitution on $Sr_{1-x}La_xFe_{12-y}Ni_yO_{19}$ Hexaferrite Structural, Magnetic, and Dielectric Properties, Materials Science and Engineering: B, 289, 116257, 2023.

Serrano A., Garcia-Martin E., Granados-Miralles C., Gorni G., Lopez-Sanchez J., Ruiz-Gomez S., Perez L., Quesada A.Fernandez J. F., Hexaferrite-Based Permanent Magnets with Upper Magnetic Properties by Cold Sintering Process Via a Non-Aqueous Solvent, Acta Materialia, 219, 117262, 2021.

Shariff Y.K.R., Choudhary H.K., Khopkar V., Yadav A., Madhusudhana R., Sahoo B., Sol-Gel Auto-Combustion Synthesis of Ba-Sr Hexaferrite Ceramic Powders, Ceramics International, 47(10), 14907-14912, 2021.

Singh T., Batra M.S., Singh I., Katoch A., Composition Dependence of the Magnetic Properties of Strontium Hexaferrite Doped with Rare Earth Ions, Journal of Physics: Conference Series, 534(1), 012013, 2014.

Urbano-Peña M. A., Palomares-Sánchez S. A., Betancourt I., Pérez-Juache T. J.Ruiz F., Effect of Temperature on the Magnetic Properties of Strontium Hexaferrite Synthesized by the Pechini Method, Applied Physics A: Materials Science and Processing, 125(10), 711, 2019.

Verma S., Singh A., Sharma S., Kaur P., Godara S. K., Malhi P. S., Ahmed J., Babu P. D., Singh M., Magnetic and Structural Analysis of $BaZn_xZr_xFe_{12-2}xO_{19}$ (X=0.1-0.7) Hexaferrite Samples for Magnetic Applications, Journal of Alloys and Compounds, 930, 167410, 2023.

Wang J. F., Ponton C. B., Grössinger R., Harris I. R., A Study of La-Substituted Strontium Hexaferrite by Hydrothermal Synthesis, Journal of Alloys and Compounds, 369(1), 170-77, 2004.

Wang J. F., Ponton C. B., Harris I. R., A Study of Pr-Substituted Strontium Hexaferrite by Hydrothermal Synthesis, Journal of Alloys and Compounds, 403(1), 104-09, 2005.

Zahid M., Siddique S., Anum R., Shakir M. F., Nawab Y., Rehan Z. A., M-Type Barium Hexaferrite-Based Nanocomposites for Emi Shielding Application: A Review, Journal of Superconductivity and Novel Magnetism, 34(4), 1019-45, 2021.

Zhang C., Feng S. J., Kan X. C., Zhu Y., Zhang Z. Y., Li Y., Tian H. M., Sun W., Liu X. S., Structure and Magnetic Properties of Al3+ Substituted M-Type Srlaco Hexaferrite, Journal of Solid State Chemistry, 32, 123927, 2023.

Zhang M., Qian C., Zhu R.T., Liu H.M., Zhang Y. X., Liu Q.C., Flower-Like Mos2 Self-Assembled on Multiferroic Z-Type $Sr_3Co_2Fe_{24}O_{41}$ Hexaferrite for Ultra-Wideband Microwave Absorption, Journal of Alloys and Compounds, 926, 166881, 2022.

Zhang W.H., Li J., Li J.W., Guo J., Wang Y. L., Zu P., Li P.W., Structural, Optical, Dielectric, and Magnetic Properties of Sr0.7la0.3zn0.3fe11.7-Xalxo19 Hexaferrite Synthesized by the Solid-State Reaction Method, Journal of Solid State Chemistry, 306, 2022.

Zhang W., Li P., Wang Y., Guo J., Li J., Shan S., Ma S., Suo X., Structure, Spectra, Morphology, and Magnetic Properties of Nb5+ Ion-Substituted Sr Hexaferrites, 8(5), 51, 2022.

Zhivulin V.E., Trofimov E.A., Zaitseva O.V., Sherstyuk DP., Cherkasova N.A., Taskaev S.V., Vinnik D.A., Alekhina Yu A., Perov N.S., Tishkevich D.I., Zubar T.I., Trukhanov A.V., Trukhanov S.V., Effect of Configurational Entropy on Phase Formation, Structure, and Magnetic Properties of Deeply Substituted Strontium Hexaferrites, Ceramics International, 49(1), 1069-84, 2023.

JOURNAL of
MATERIALS and MECHATRONICS:A

e-ISSN 2717-8811
JournalMM, 2023, 4(2), 459-474
https://doi.org/10.55546/jmm.1359453

Araştırma Makalesi / Research Article

Statistical Investigation of the Effect of CO_2 Laser Cutting Parameters on Kerf Width and Heat Affected Zone in Thermoplastic Materials

Oğuzhan DER[1*], Gökhan BAŞAR[2], Muhammed ORDU[3]

[1] Bandırma Onyedi Eylül University, Faculty of Maritime, Department of Marine Vehicles Management Engineering, Balıkesir, Turkey,
ORCID ID: https://orcid.org/0000-0001-5679-2594, oder@bandirma.edu.tr
[2] Osmaniye Korkut Ata University, Faculty of Engineering and Natural Sciences, Department of Industrial Engineering, Osmaniye, Turkey,
ORCID ID: https://orcid.org/0000-0002-9696-7579, gokhanbasar@osmaniye.edu.tr
[3] Osmaniye Korkut Ata University, Faculty of Engineering and Natural Sciences, Department of Industrial Engineering, Osmaniye, Turkey,
ORCID ID: https://orcid.org/0000-0003-4764-9379, muhammedordu@osmaniye.edu.tr

Geliş/ Received: 13.09.2023; **Kabul / Accepted:** 25.10.2023

ABSTRACT: Understanding and optimizing the CO_2 laser cutting process of thermoplastic materials is critical for improving product quality, reducing waste, and achieving efficient manufacturing processes. This study aimed to investigate the effects of a number of input parameters (i.e., material type, power, and cutting speed) on the key output parameters (i.e., kerf width and heat affected zone) in CO_2 laser cutting of thermoplastic materials. The laser cutting process was performed based on the Taguchi L_{18} (2^1x3^2) orthogonal array design. The effects of cutting parameters on the outputs were calculated by using the signal-to-noise (S/N) ratio and analysis of variance (ANOVA) techniques. Furthermore, first and second-degree mathematical models were established by using regression analysis to estimate the values of kerf width and heat affected zone. The optimum laser cutting parameters for kerf width and heat affected zone were determined as and Polyvinyl Chloride (PVC) material type, 80 W power, and 15 mm/s cutting speed. The ANOVA results showed that the most efficient parameter on kerf width was power with 53.99% while the most efficient parameter on heat affected zone was material type with 40.96%. In addition, the coefficient of determination (R^2) values for the regression equations developed for the outputs are significantly high. The R^2 values of the first- and second-degree regression equations for KW are 97.26% and 99.71%, respectively, whereas 93.43% and 98.18% for HAZ.

Keywords: CO_2 Laser Cutting, Kerf Width, Heat Affected Zone, ANOVA, Regression Analysis

*Sorumlu yazar / Corresponding author: oder@bandirma.edu.tr

Bu makaleye atıf yapmak için /To cite this article

Der, O., Başar, G., Ordu, M. (2023). Statistical Investigation of the Effect of CO_2 Laser Cutting Parameters on Kerf Width and Heat Affected Zone in Thermoplastic Materials. Journal of Materials and Mechatronics: A (JournalMM), 4(2), 459-474.

1. INTRODUCTION

Thermoplastic materials, primarily Polyethylene (PE) and Polyvinyl Chloride (PVC), possess a unique combination of properties making them pivotal in numerous applications across diverse industries (Soutis, 2005). PE, characterized by its lightweight, high durability, and resistance to environmental stress, finds broad applications in packaging, agriculture, and the automotive industry (Huda et al., 2008). PVC, on the other hand, stands out for its excellent mechanical strength, chemical resistance, and electrical insulation properties, becoming an essential material in construction, healthcare, and electronics (De Leon et al., 2021). Both PE and PVC are thermoplastics, meaning they can be repeatedly melted and reshaped without losing their material properties, thereby offering extensive reusability and recyclability that contributes significantly to sustainability (Evode et al., 2021).

The application of CO_2 laser cutting for thermoplastics, including PE and PVC, represents a significant advance in manufacturing technology. This technique uses a high-intensity CO_2 laser beam to precisely cut or engrave thermoplastics, resulting in smooth, clean edges with minimal material waste (Der et al., 2022). Due to the non-contact nature of the process, there is significantly reduced mechanical stress on the thermoplastic, preventing deformation and ensuring high-quality finished products. However, process parameters (i.e., laser power, focal position and cutting speed) can significantly influence cutting quality and efficiency, necessitating rigorous process optimization (Der et al., 2019).

Researchers and practitioners focus on two crucial output parameters of CO_2 laser cutting processes: the heat-affected zone (HAZ) and kerf width (KW) (Rajaram et al., 2003). Kerf width, the width of material removed during the cutting process, is an essential factor for precision engineering, as it directly affects the accuracy of the cut and the finish of the product (Jadam et al., 2019). Meanwhile, the HAZ, the area surrounding the cut where the material's properties might have altered due to the heat from the laser, can affect the structural integrity and performance of the final product (You et al., 2020). Therefore, optimizing both kerf width and HAZ through appropriate selection and control of process parameters is of paramount importance in enhancing product quality, reducing material waste, and increasing process efficiency in CO_2 laser cutting of thermoplastics.

There are numerous studies on the machinability of materials, for example, Ordu and Fedai (2021) applied the hybrid MCDM methods to determine the optimum cutting parameters in the milling process of AISI 4140 steel. Fedai et al. (2022) used Gray Relationship Analysis to specify the optimum drilling condition in the drilling process of MWCNTs Reinforced GFRP composites. Ge et al. (2023) aimed to minimize hole damage and increase production efficiency in drilling Carbon-fibre-reinforced-polyetherketonketone (CF/PEKK) composites. Karamimoghadam et al. (2023) investigated the effect of 3D printing and CO_2 laser cutting parameters on the surface morphology of polylactic acid (PLA) material. Petousis et al. (2023) manufactured PLA/CNT (carbon nanotubes) nanocomposites with material extrusion. They increased the shape accuracy and surface quality of nanocomposites by CO_2 laser cutting. Huang et al. (2023) performed fiber laser cutting of glass fiber reinforced plastic (GFRP) materials. They used ANOVA for the effect of cutting parameters on quality characteristics, conducted the regression analysis for the relationship between cutting parameters and quality characteristics, and developed an integrative model to predict and optimize quality characteristics. In a study conducted by Yalçın et al. (2023), the micro-drilling tendencies of Al-PE laminate composites were investigated using the Taguchi L_{16} orthogonal array and ANOVA analyses, focusing on parameters such as thrust force, exit burr height, and hole diameter. Key findings highlighted the significant influence of the tool's point angle on thrust force and burr height,

the role of cutting speed in determining hole diameter, and the identification of the fifth experiment as the optimal cutting condition for minimized thrust, burr height, and diameter change. In fact, multi-objective optimization studies are carried out on thermoplastic materials, and it is a remarkable issue in material selection (Ordu and Der, 2023a; Ordu and Der, 2023b). On the other hand, the effect of cutting parameters of thermoplastic materials on a number of outputs was also investigated. For example, the taper kerf on polymethyl methacrylate (PMMA) obtained after laser cutting was examined by using statistical methods (Varsey and Shaikh, 2019). This research delved into the impact of scanning speed, laser power parameters, and the number of sweeping steps by utilizing variance analysis. In another research, exploring the cutting processes using statistical methods was performed (Haddadi et al., 2019). Taguchi method was employed in order to improve the surface quality of microchannels developed by laser cutting process on PMMA materials. An average roughness of 110 nm was achieved by optimizing a number of output parameters (i.e., power parameters, process duration and scanning speed) (Chen et al., 2017). High-density polyethylene pipes were cut and drilled by a CO_2 laser. The study analyzed the influence of the thickness of the workpiece and the laser power on the KW and HAZ (Saleh et al., 2019). Taguchi method was performed for analyzing the impact of input parameters (i.e., laser speed, power and so on) on the surface quality of polycarbonate gears (Gruescu et al., 2012). The findings of studies focussing on laser cutting of fiber-reinforced polymer composites were compiled. Their review pointed out that most research concentrated on HAZ, KW and the depth of the kerf. The findings recommended to select short pulses, low laser intensity, high speed, and pressure to minimize the HAZ (El-Hofy and El-Hofy, 2019). Algorithms were developed to estimate the count of laser scanning steps in laser cutting process on PMMA materials to obtain a certain kerf depth (Varsi and Shaikh, 2018).

In this study, the Taguchi method was used to determine the optimum processing parameters for CO_2 laser cutting of PE and PVC thermoplastic materials. To do this, an experimental setup was developed for laser cutting of the thermoplastic materials. Then, control factors and levels were determined. Material type, power and cutting speed were selected as control factors. Material type is determined as two levels, power and cutting speed are determined as three levels. Taguchi L_{18} experimental design was chosen in accordance with the control factors and levels. KW and HAZ were determined as quality characteristics. First of all, the optimum experimental condition for minimum KW and HAZ was specified by using the Taguchi method. Analysis of variance was then applied to investigate the effect of control factors on quality characteristics. Finally, regression analysis was used to measure the relationship between quality characteristics and control factors. First and second order regression equations were developed through this analysis. Therefore, the results from this study will contribute to determining the appropriate cutting conditions for thermoplastic materials in CO_2 laser cutting processes, providing valuable insights for practitioners in the field.

The remaining of the paper is organized as follows: the thermoplastic materials are introduced, how to the materials were cut by using CO_2 laser machine, and experimental setup and design are described, and the methods (i.e., S/N ratio, ANOVA and regression analyzes) used in this study are explained in Section 2. After that, the findings of the study are presented and discussed in Section 3. Final section concludes the study, respectively.

2. MATERIALS AND METHODS

2.1 Experimental Procedure

Polyethylene (PE) is a high molecular weight thermoplastic polymer derived from the polymerization of ethylene gas under specific conditions (Yu et al., 2006). It is available in several forms based on its density and branching characteristics, with the two most common forms being high-density polyethylene (HDPE) and low-density polyethylene (LDPE). PE is known for its excellent chemical resistance, low moisture absorption, and high impact resistance. Its flexible and durable nature makes it ideal for a range of applications, from film and sheeting to piping and containers. However, PE also has a relatively low softening point, which necessitates careful handling during laser cutting processes to avoid unnecessary melting or deformation (Choudhury and Shirley, 2010).

Polyvinyl Chloride (PVC), on the other hand, is a thermoplastic composed of 57% chlorine and 43% carbon, obtained from ethylene and chlorine gas (Oberoi and Malik, 2022). PVC is available in two primary forms: rigid and flexible, the latter achieved through the addition of plasticizers (Rahman and Brazel, 2006). Notable for its high tensile strength, flame retardancy, and excellent electrical insulation properties, PVC is a prevalent material in construction, electrical, and healthcare applications. In terms of laser cutting, PVC poses some challenges as it releases hydrochloric acid upon heating, which can corrode equipment and poses health risks. Therefore, handling PVC in laser-cutting processes demands careful consideration of safety measures and protective equipment (Akovali, 2012).

A number of properties (i.e., physical, thermal and mechanical) of materials plays an important role in determining their suitability for laser-cutting operations. Physical properties such as density and melting point can greatly influence the cutting process and the resultant product's quality. Density refers to the mass per unit volume, dictating how much material is present in a given volume, which can affect the material's behavior under the laser. The melting point, the temperature at which a material transitions from a solid to a liquid state, also significantly impacts the laser-cutting process, particularly for thermoplastics. Mechanical properties reflect a material's response to an applied force. For example, Tensile strength is known as the maximum stress which a material is able to resist without failing during pulling or stretching whereas Young's Modulus represents a measure the material's stiffness or its resistance to elastic deformation. Both properties are essential for laser cutting as they influence the material's reaction to stress and deformation. Thermal properties describe how a material responds to temperature changes and its interaction with heat. A material's thermal conductivity, indicating its ability to conduct heat, can greatly affect the precision of the cut and the size of the heat-affected zone (HAZ) in the laser cutting process (Callister, 1991). Table 1 demonstrates the mechanical, physical, and thermal characteristics of PE and PVC.

Tests were performed using a laser setup, which included a 100 W CO_2 laser from the LazerFix LF7010 Laser Cutting Machine. The system was also equipped with a CNC-controlled table that operates on three axes and provides a workspace of 70 cm x 100 cm x 20 cm, as shown in Figure 1.

Before beginning the laser cutting process, the PE and PVC material must be properly prepared. This typically involves cleaning the material surface to remove any dust or contaminants that could potentially interfere with the laser beam. The design to be cut into the thermoplastic is input into the laser cutter's computer system. This design was developed by computer-aided design (CAD) software. The design is then processed and interpreted by the machine's software.

Table 1. The properties of PE and PVC (Fleck et al., 2010)

Property	Unit	PE	PVC
Density	(g/cm³)	0.95	1.45
Thermal Conductivity	(W/m.K)	0.42	0.22
Tensile Strength	(MPa)	33	53
Young's Modulus	(GPa)	0.76	3.1
Elongation at Break	(%)	150	30
Melting Point	(°C)	125	88

Figure 1. LazerFix LF7010 laser cutting machine

Figure 2 presents a comprehensive illustration of a laser-cutting operation on polymeric materials, detailing various geometric patterns. The data derived from these cuttings were scrutinized to quantify the HAZ. In the same figure, to evaluate the kerf width - a critical parameter in cutting - a component was sliced. This procedure entailed making a linear incision on a rectangular plate with dimensions of 10 mm x 100 mm, facilitating the assessment of kerf widths against nine distinct parameters.

Given the specific material properties of PE and PVC, the laser cutter's settings must be properly adjusted. This typically entails setting the laser power, cutting speed, and the focal point of the laser. These settings are pivotal in achieving precision in the cut and minimizing the HAZ. For this purpose, an optimum focal point of 7 mm for the laser was selected. Before the main cut, it is generally advised to conduct a test cut on a small sample piece to verify the suitability of the machine settings for the particular material and thickness. Upon fine-tuning the machine settings, the actual cutting process is initiated. The laser beam follows the path specified by the input design, cutting the material precisely. The high-intensity laser beam rapidly heats the thermoplastic, leading to vaporization and thereby creating a cut. Once the laser cutting process is completed, the cut piece is left to cool down. Any remaining debris from the cutting process can subsequently be removed. The edges of the cut are typically smooth, due to the laser cutting process, but further post-processing (like edge polishing) can be undertaken if necessary. However, since a highly successful cut was achieved in this study, no additional post-processing was required.

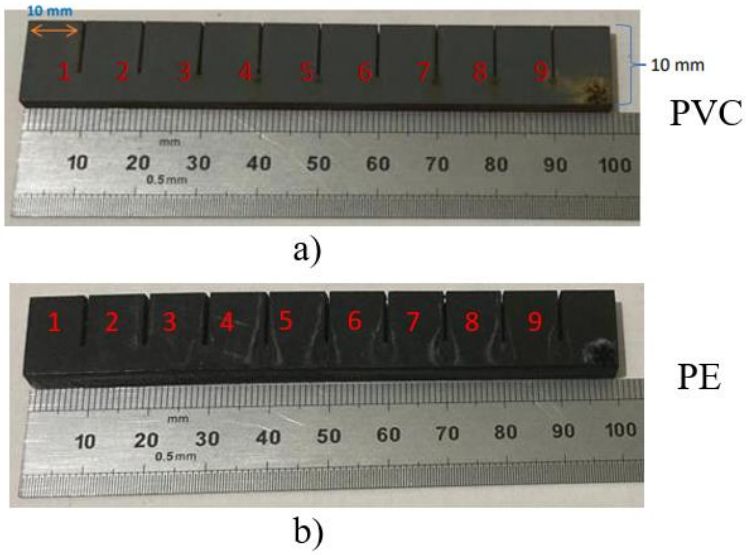

Figure 2. Thermoplastic materials used in the experiments, a) PVC, b) PE

2.2 Kerf Width and Heat-Affected Zone Measurements

The kerf width and heat-affected zone resulting from laser cutting of thermoplastic materials were measured using a computer-connected Dino-Lite AM4113T digital microscope. The measurements were performed using the Dino Capture 2.0 software, and images were captured at a magnification of 55x. The digital microscope and the areas where the measurements were taken are illustrated in Figure 3.

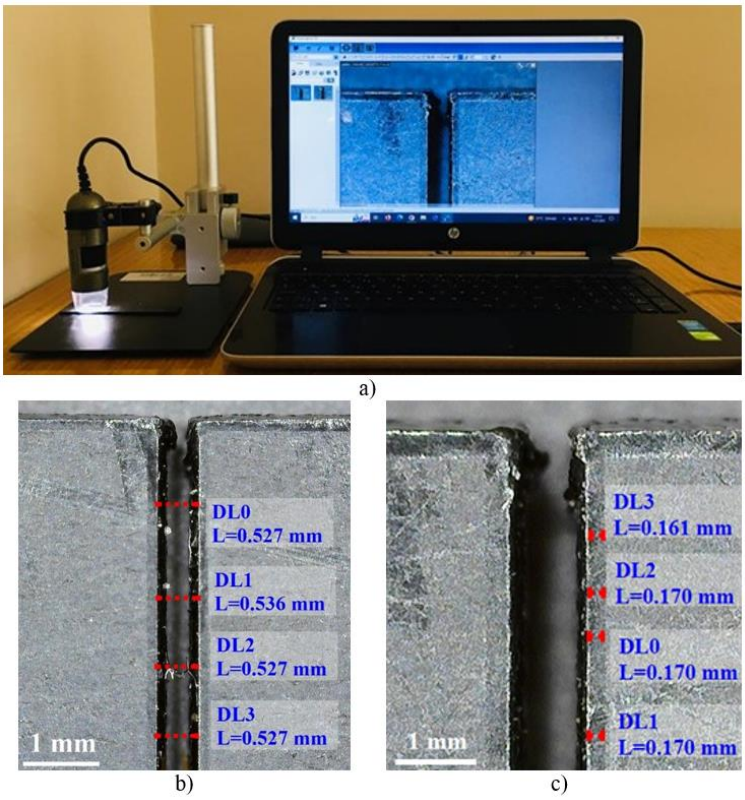

Figure 3. Measurement setup: a) Digital microscope, b) Kerf width measurement, c) Heat Affected Zone measurement.

2.3 Experimental Design Using the Taguchi Method

In the laser cutting of thermoplastic materials, the control factors are selected as cutting speed, material type and power, whereas the quality characteristics are considered as KW and HAZ. The effects of control factors on quality characteristics have been determined using the Taguchi method. In the experiments, the most suitable orthogonal array L_{18} (2^1x3^2) was used, taking into account the total degrees of freedom of the control factors (Roy, 1990). The Taguchi method enables the optimizing the quality characteristics while determining the optimal experimental condition (Roy, 1990; Bilge et al., 2017). Based on the studies carried out in the literature, the appropriate levels of the control factors have been specified and are given in Table 2.

Table 2. Control factors and levels.

Control factors	Symbol	Level 1	Level 2	Level 3
Material type	MT	PE	PVC	-
Power (W)	P	80	90	100
Cutting speed (mm/s)	Vc	5	10	15

In order to achieve low KW and HAZ values in the CO_2 laser cutting of thermoplastic materials, the dependent variable, which is the quality characteristic, was calculated using the signal-to-noise (S/N) ratio in dB according to the "smaller is better" approach, as shown in Equation (1) (Özlü, 2021).

$$S/N_{dB} = -10log\left(\frac{1}{n}\sum_{i=1}^{n} y_i^2\right) \quad (1)$$

n means the number of experiments, and y_i represents the *i*-th observed response for each data point (Motorcu and Ekici, 2016). The effects of each level of the control factors on KW and HAZ were analyzed using the S/N ratios. Additionally, the contribution ratios of the control factors to the quality characteristics were calculated with the help of analysis of variance (ANOVA). The ANOVA tests were conducted at a 95% confidence level. Finally, first and second-degree regression equations were established for estimating KW and HAZ.

3. RESULTS AND DISCUSSION

3.1 Signal-to-Noise (S/N) Ratio Analysis

The cutting process of thermoplastic materials using a CO_2 laser was conducted based on the Taguchi L_{18} orthogonal array. The effects of cutting parameters on output parameters (i.e., KW and HAZ) were investigated. Signal-to-Noise (S/N) analysis was preferred to determine the optimal levels of the control factors. In this study, the "Smaller is better" objective function was selected to achieve higher product quality and lower costs for KW and HAZ. Equation (1) gives the calculation of the S/N ratios for KW and HAZ. The measured KW and HAZ values along with the calculated S/N ratios are given in Table 3 for the laser cutting experiments. The average KW and HAZ values obtained from the laser cutting process are calculated as 0.460 mm and 0.132 mm, respectively. In addition, the average S/N ratios for KW and HAZ values are obtained as 6.812 dB and 17.661 dB, respectively.

An S/N response table was used to analyze the effects of each control factor on KW and HAZ. The calculated S/N ratios for each level of the control factors for KW and HAZ are provided in Table 4. The optimal cutting parameters for the lowest KW and HAZ values are indicated by the levels with the highest S/N ratios in Table 4. From these results, the cutting parameters determined for the lowest

KW and HAZ values are MT (Level 2, S/N=7.320 dB and S/N=7.320 dB), P (Level 1, S/N= 7.934 dB and S/N=18.29 dB), and Vc (Level 3, S/N=7.428 dB and S/N=18.56 dB). The lowest KW and HAZ values were measured as 0.346 mm and 0.097 mm, respectively, under conditions where the material type was PVC, the power was 80 W, and the cutting speed was 15 mm/s. The S/N ratio graphs for the control factors of KW and HAZ in the laser cutting process are shown in Figures 4 and 5, respectively.

Table 3. Experimental results and S/N ratios.

Experiment number	Control factors			KW (mm)	S/N ratio for KW (dB)	HAZ (mm)	S/N ratio for HAZ (dB)
	Material type	Power (W)	Cutting speed (mm/s)				
1	PE	80	5	0.466	6.632	0.156	16.138
2	PE	80	10	0.419	7.556	0.136	17.329
3	PE	80	15	0.402	7.915	0.122	18.273
4	PE	90	5	0.538	5.384	0.164	15.703
5	PE	90	10	0.491	6.178	0.139	17.140
6	PE	90	15	0.462	6.707	0.125	18.062
7	PE	100	5	0.569	4.898	0.167	15.546
8	PE	100	10	0.530	5.514	0.151	16.420
9	PE	100	15	0.504	5.951	0.135	17.393
10	PVC	80	5	0.418	7.576	0.115	18.786
11	PVC	80	10	0.367	8.707	0.113	18.938
12	PVC	80	15	0.346	9.218	0.097	20.265
13	PVC	90	5	0.488	6.232	0.128	17.856
14	PVC	90	10	0.435	7.230	0.125	18.062
15	PVC	90	15	0.413	7.681	0.110	19.172
16	PVC	100	5	0.516	5.747	0.143	16.893
17	PVC	100	10	0.479	6.393	0.130	17.721
18	PVC	100	15	0.442	7.092	0.123	18.202

Table 4. S/N response table for KW and HAZ.

Levels	Control factors					
	KW			HAZ		
	MT	P	Vc	MT	P	Vc
1	6.304	**7.934***	6.078	16.89	**18.29***	16.82
2	**7.320***	6.569	6.930	**18.43***	17.67	17.60
3	-	5.933	**7.428***		17.03	**18.56***
Delta	1.015	2.002	1.349	1.54	1.26	1.74
Rank	3	1	2	2	3	1

***** The significant parameter

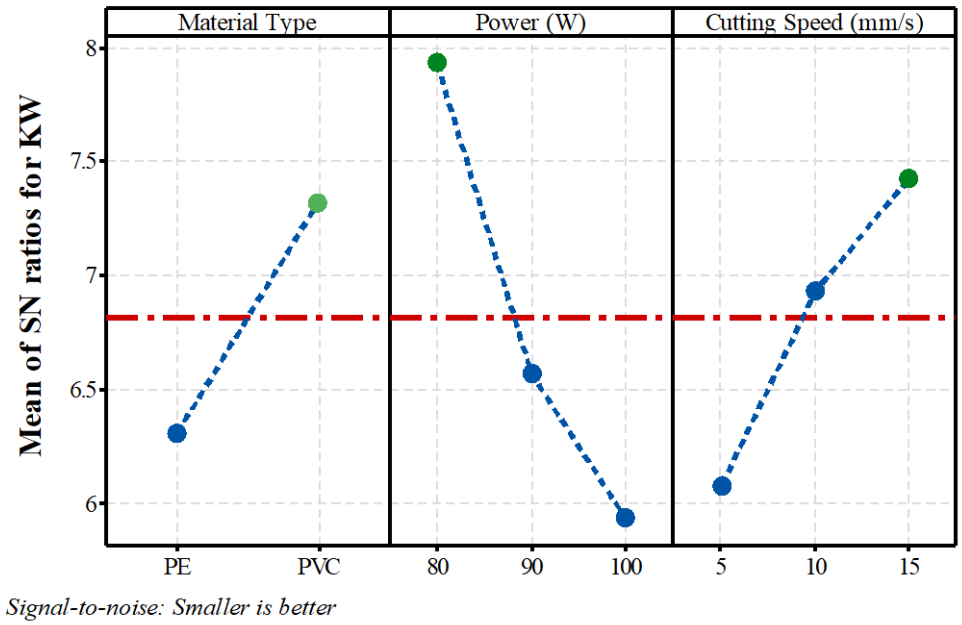

Figure 4. The effects of input parameters on average S/N ratio for KW

The differences in KW and HAZ during CO_2 laser cutting of PVC and PE thermoplastics can be attributed to their unique thermal properties, absorption properties, and melt characteristics. PVC's lower melting point allows for easier cutting, which can potentially result in a narrower KW and smaller HAZ. PVC's ability to absorb CO_2 laser wavelength more effectively than PE due to the presence of chlorine atoms also contributes to more efficient cutting. Lastly, PVC vaporizes rather than melts at its decomposition temperature, leading to cleaner material removal and thus a narrower kerf and lesser HAZ. On the other hand, PE's less efficient absorption of the CO_2 laser wavelength and its tendency to melt rather than vaporize may lead to a wider kerf and larger HAZ.

Our analysis indicated that the minimum KW, referring to the width of the material removed by the laser cut, is obtained under certain conditions - specifically, the minimum laser power and the maximum cutting speed. At low laser power, the heat generated is less intense, hence, inducing less melting and a narrower kerf. Simultaneously, a higher cutting speed guarantees swift movement of the laser, limiting heat accumulation and thereby resulting in a narrower KW (Moradi et al., 2017).

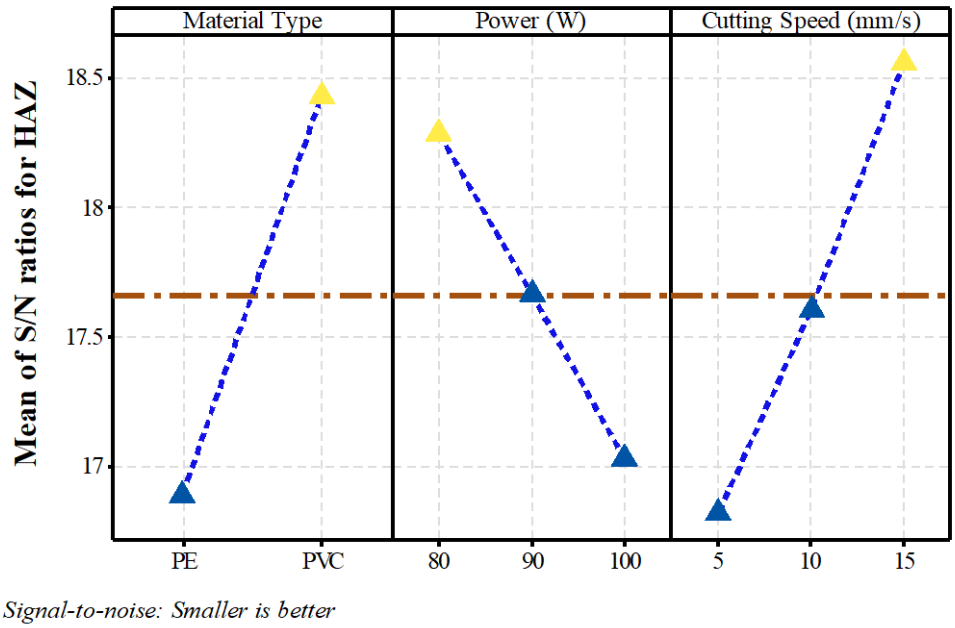

Figure 5. The effects of input parameters on average S/N ratio for HAZ

On the other hand, we discovered a key relationship between the laser power, cutting speed, and the size of the HAZ - an area of material with altered properties due to the heat of the laser. The size of the HAZ and laser power are directly proportional to each other, meaning the greater the laser power, the larger the HAZ. This relationship signifies that an increase in laser power expands the material area affected by heat. However, the HAZ and cutting speed are inversely proportional to each other. This suggests that a faster cutting speed results in a smaller HAZ. A higher cutting speed reduces the dwell time of the laser on the material, leading to less heat spread and subsequently a reduction in the HAZ size (Choudhury and Shirley, 2010; Moradi et al., 2017).

The most advantageous conditions for both minimizing the HAZ and achieving the narrowest KW in our study were determined to be a PVC material type, a laser power of 80 W and a cutting speed of 15 mm/s.

3.2 Analysis of Variance

Analysis of variance (ANOVA) was employed for determining the contribution ratios of the control factors on KW and HAZ in the CO_2 laser cutting experiments. The ANOVA test was performed within a confidence level of 95% and the results are tabulated in Table 5.

In case of the P-value is less than 0.05, it indicates statistical significance, meaning that the control factors are considered statistically significant. Otherwise, it suggests a lack of statistical significance (Akkuş and Yaka, 2018). The control factor that has the greatest impact on the output is determined by considering the largest F-value in the ANOVA test results (Yaka, 2021). The contribution rates (%) obtained from the ANOVA test results illustrated in Figure 6. Accordingly, the percentage contributions of material type, power, and cutting speed on KW were calculated as 20.49%, 53.99%, and 25.18%, respectively. Additionally, the contribution percentages of material type, power, and cutting speed on HAZ were computed as 40.96%, 16.71%, and 35.78%, respectively. According to the ANOVA results, power was found to have the highest influence on KW with a contribution percentage of 53.99%, whereas material type had the highest influence on HAZ with a contribution percentage of 40.96%. Additionally, the low error values for KW and HAZ (i.e., 0.34% and 6.55%, respectively) indicate that the experimental study yielded significant results.

Table 5. ANOVA results for KW and HAZ.

Variance Source	Degree of Freedom	Sum of Squares	Mean Square	F Ratio	P Value
		KW			
MT	1	0.012641	0.012641	725	0
P	2	0.033307	0.016654	955.18	0
Vc	2	0.015536	0.007768	445.55	0
Error	12	0.000209	0.000017		
Total	17	0.061694			
R^2: 99.66					
		HAZ			
MT	1	0.002473	0.002473	75.06	0
P	2	0.001009	0.000505	15.31	0
Vc	2	0.002160	0.001080	32.78	0
Error	12	0.000395	0.000033		
Total	17	0.006039			
R^2: 93.45					

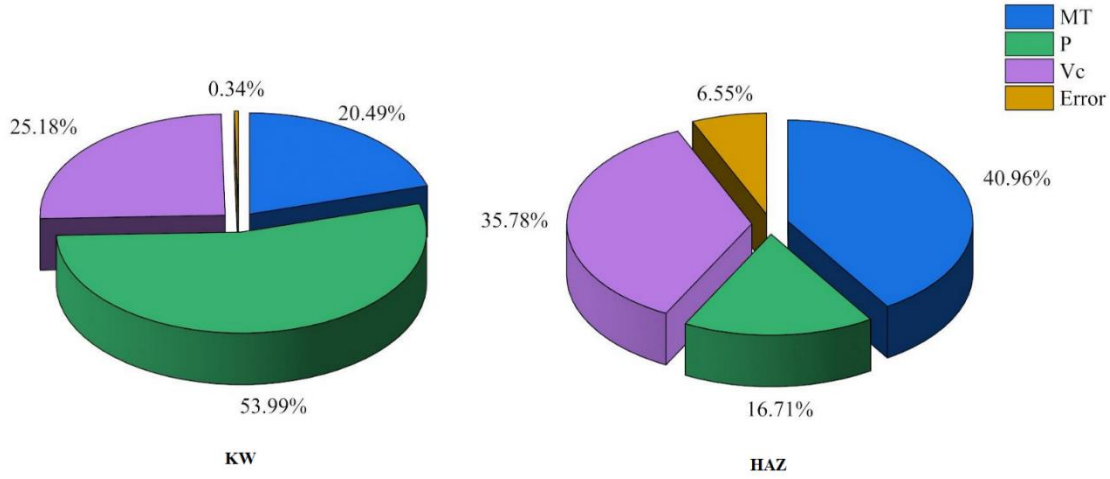

Figure 6. The contribution rates (%)

3.3 Regression Analysis

Regression analysis helps to mathematically express the relationship between dependent and independent variables (Basar et al., 2018). In this study, first and second-degree regression equations were developed for KW and HAZ. In laser cutting process, the independent variables are material type, power, and cutting speed, whearas the dependent variables are KW and HAZ. In Table 6, the first and second-degree regression equations for estimated KW based on the material type are given as Equation (2)-(3) and (4)-(5). In Table 7, the regression equations for estimated HAZ based on the material type are shown as Equation (6)-(7) and (8)-(9), respectively. The determination coefficients (R^2) obtained from the first and second-degree regression equations for KW were calculated as 97.26% and 99.71%. Furthermore, the R^2 obtained from the regression equations for HAZ are determined as 93.43% and 98.18% respectively.

Table 6. Regression equations for KW.

First Degree Regression Equations		
Material Type		
PE	$KW = 0.0913 + 0.005183 \cdot P - 0.0071 \cdot Vc$	(2)
PVC	$KW = 0.0383 + 0.005183 \cdot P - 0.0071 \cdot Vc$	(3)
R^2: 97.26		
Second Degree Regression Equations		
PE	$KW = -1.204 + 0.03474 \cdot P - 0.01429 \cdot Vc - 0.000163 \cdot P^2 + 0.000407 \cdot Vc^2 - 0.000007 \cdot P \cdot Vc$	(4)
PVC	$KW = -1.237 + 0.03458 \cdot P - 0.01483 \cdot Vc - 0.000163 \cdot P^2 + 0.000407 \cdot Vc^2 - 0.000007 \cdot P \cdot Vc$	(5)
R^2: 99.71		

Table 7. Regression equations for HAZ.

First Degree Regression Equations		
Material Type		
PE	$HAZ = 0.0882 + 0.000917 \cdot P - 0.002683 \cdot V_c$	(6)
PVC	$HAZ = 0.0648 + 0.000917 \cdot P - 0.002683 \cdot V_c$	(7)
R^2: 93.43		
Second Degree Regression Equations		
PE	$HAZ = 0.160 - 0.00025 \cdot P - 0.0033 \cdot V_c + 0.000005 \cdot P^2 - 0.00001 \cdot V_C^2$	(8)
PVC	$HAZ = 0.072 - 0.00028 \cdot P - 0.00167 \cdot V_c + 0.000005 \cdot P^2 - 0.00001 \cdot V_C^2$	(9)
R^2: 98.18		

4. CONCLUSION

In this experimental study, the effects of cutting parameters, including material type, cutting speed, and power on the kerf width (KW) and heat-affected zone (HAZ) of 2 mm thick thermoplastic materials using a CO_2 laser were investigated. The aim was to determine the optimum levels of cutting parameters for achieving minimum KW and HAZ. Furthermore, the contribution ratios of the control factors on the quality characteristics were specified by using variance analysis. Finally, mathematical equations for the estimation of KW and HAZ were obtained using regression analysis. The results obtained are presented below:

• According to the experimental results, it was observed that the kerf width ranged from 0.569 mm to 0.346 mm, whereas the heat affected zone ranged from 0.167 mm to 0.097 mm.

• The optimum laser cutting parameters for achieving the lowest KW and HAZ were determined to be PVC material type, 80W power, and 15 mm/s cutting speed.

• The measured values for the KW and HAZ, obtained from the optimum laser cutting parameters, were 0.346 mm and 0.097 mm, respectively.

• The highest values for the KW and HAZ were obtained with the PE material type, 100 W power, and 5 mm/s cutting speed.

• It was determined that the measured values of KW and HAZ for the PVC material were lower than those for the PE material under all experimental conditions.

• It was found that the KW and HAZ decrease with decreasing power and increasing cutting speed.

• According to the ANOVA results, the contribution percentages of the laser cutting parameters on KW were determined as follows: power (53.99%), cutting speed (25.18%), and material type (20.49%).

• In the ANOVA results for HAZ, the contribution percentages of the laser cutting parameters were determined as follows: material type (40.96%), cutting speed (35.78%), and power (16.71%).

• The coefficient of determination (R^2) values for the first and second-degree regression equations for KW were obtained as 97.26% and 99.71%, respectively.

• The R^2 values for the first and second-degree regression equations for HAZ were determined as 93.43% and 98.18%, respectively.

• It was determined that the cutting parameters identified are more suitable for the CO_2 laser cutting of PVC material.

Building on the findings of this study, future research could delve into exploring the effects of other variables such as laser beam diameter, focal point settings, and gas pressure on KW and HAZ. It would also be intriguing to investigate how varying material thicknesses might influence the observed outcomes, and whether other thermoplastic materials exhibit similar or contrasting behaviors under CO_2 laser cutting. Additionally, an extended exploration into the environmental impact of using different cutting parameters and their implications for waste and energy consumption might offer valuable insights for sustainable manufacturing practices. In essence, while this study has unveiled key relationships between certain parameters and laser cutting results, the arena of laser cutting is vast and teeming with myriad opportunities for further exploration.

5. ACKNOWLEDGEMENTS

This work has been supported by Osmaniye Korkut Ata University Scientific Research Projects Coordination Unit under grant number #OKUBAP-2022-PT1-003.

6. CONFLICT OF INTEREST

Authors approve that to the best of their knowledge, there is not any conflict of interest or common interest with an institution/organization or a person that may affect the review process of the paper.

7. AUTHOR CONTRIBUTION

All authors have equal contributions to the study.

8. REFERENCES

Akkuş H., Yaka H. Optimization of Turning Process by Using Taguchi Method. Sakarya Üniversitesi Fen Bilimleri Enstitüsü Dergisi 22 (5), 1444-1448, 2018.

Akovali G. Plastic Materials: Polyvinyl Chloride (PVC). In Toxicity of Building Materials. Woodhead Publishing, Sawston, UK, pp. 23-53, 2012.

Basar G., Kirli Akin H., Kahraman F., Fedai Y. Modeling and Optimization of Face Milling Process Parameters for AISI 4140 Steel. Tehnički Glasnik 12 (1), 5-10, 2018.

Bilge T., Motorcu A.R., Ivanov A. Kompakt Laminat Kompozit Malzemenin Tungsten Karbür Takımlarla Delinmesinde Delaminasyon Faktörünün Değerlendirilmesi. Pamukkale Üniversitesi Mühendislik Bilimleri Dergisi 23 (4), 427-436, 2017.

Callister W.D. Materials Science and Engineering: An Introduction, 2nd Edition, Jr John Wiley & Sons, New York, 1991.

Chen X., Li T., Zhai K., Hu Z., Zhou M. Using Orthogonal Experimental Method Optimizing Surface Quality of CO_2 Laser Cutting Process for PMMA Microchannels. The International Journal of Advanced Manufacturing Technology 88, 2727-2733, 2017.

Choudhury I.A., Shirley S. Laser Cutting of Polymeric Materials: An Experimental Investigation. Optics & Laser Technology 42 (3), 503-508, 2010.

De Leon A.C., Da Silva Í.G., Pangilinan K.D., Chen Q., Caldona E.B., Advincula R.C. High Performance Polymers for Oil and Gas Applications. Reactive and Functional Polymers 162, 104878, 2021.

Der O., Edwardson S., Bertola V. Manufacturing Low-Cost Fluidic and Heat Transfer Devices with Polymer Materials by Selective Transmission Laser Welding. In Encyclopedia of Materials: Plastics and Polymers. Elsevier; 2022.

Der O., Edwardson S., Marengo M., Bertola V. Engineered Composite Polymer Sheets with Enhanced Thermal Conductivity. IOP Conference Series: Materials Science and Engineering 613 (1), 012008, 2019.

El-Hofy M.H., El-Hofy H. Laser Beam Machining of Carbon Fiber Reinforced Composites: A Review. The International Journal of Advanced Manufacturing Technology 101 (9-12), 2965-2975, 2019.

Evode N., Qamar S.A., Bilal M., Barceló D., Iqbal H.M. Plastic Waste and Its Management Strategies for Environmental Sustainability. Case Studies in Chemical and Environmental Engineering 4, 100142, 2021.

Fedai Y., Basar G., Kirli Akin H. Multi-Response Optimization in Drilling of MWCNTs Reinforced GFRP Using Grey Relational Analysis. Tehnički Vjesnik 29 (3), 742-751, 2022.

Fleck N.A., Deshpande V.S., Ashby M.F. Micro-Architectured Materials: Past, Present and Future. Proceedings of the Royal Society A: Mathematical, Physical and Engineering Sciences 466 (2121), 2495-2516, 2010.

Ge J., Zhang W., Luo M., Catalanotti G., Falzon B.G., Higgins C., Zhang D., Jin Y., Sun D. Multi-Objective Optimization of Thermoplastic CF/PEKK Drilling Through a Hybrid Method: An Approach Towards Sustainable Manufacturing. Composites Part A: Applied Science and Manufacturing 167, 107418, 2023.

Gruescu C.M., Ionescu C.L., Nicoara I., Lovasz A. Experimental Optimization of Process Parameters in Laser Cutting of Polycarbonate Gears. Mechanics 18 (2), 233-238, 2012.

Haddadi E., Moradi M., Ghavidel A.K., Ghavidel A.K., Meiabadi S. Experimental and Parametric Evaluation of Cut Quality Characteristics in CO_2 Laser Cutting of Polystyrene. Optik 184, 103-114, 2019.

Huang S., Fu Z., Liu C., Li J. Multi-Objective Optimization of Fiber Laser Cutting Quality Characteristics of Glass Fiber Reinforced Plastic (GFRP) Materials. Optics & Laser Technology 167, 109720, 2023.

Huda M.S., Drzal L.T., Ray D., Mohanty A.K., Mishra M. Natural-Fiber Composites in the Automotive Sector. In Properties and Performance of Natural-Fibre Composites, Woodhead Publishing, Sawston, UK, pp. 221-268, 2008.

Jadam T., Datta S., Masanta M. Study of Surface Integrity and Machining Performance During Main/Rough Cut and Trim/Finish Cut Mode of WEDM on Ti–6Al–4V: Effects of ire Material. Journal of the Brazilian Society of Mechanical Sciences and Engineering 41, 1-23, 2019.

Karamimoghadam M., Dezaki M.L., Zolfagharian A., Bodaghi M. Influence of Post-Processing CO_2 Laser Cutting and FFF 3D Printing Parameters on the Surface Morphology of PLAs: Statistical Modelling and RSM Optimisation. International Journal of Lightweight Materials and Manufacture 6 (2), 285-295, 2023.

Moradi M., Mehrabi O., Azdast T., Benyounis K.Y. Enhancement of Low Power CO_2 Laser Cutting Process for Injection Molded Polycarbonate. Optics & Laser Technology 96, 208-218, 2017.

Motorcu A.R., Ekici E. Al/B4C Kompozitlerin Karbür Matkaplarla Delinmesinin Değerlendirilmesi. Pamukkale Üniversitesi Mühendislik Bilimleri Dergisi 22 (4), 259-66, 2016.

Oberoi S., Malik M. Polyvinyl Chloride (PVC), Chlorinated Polyethylene (CPE), Chlorinated Polyvinyl Chloride (CPVC), Chlorosulfonated Polyethylene (CSPE), Polychloroprene Rubber (CR)—Chemistry, Applications and Ecological Impacts - I. In: Malik, J.A., Marathe, S. (eds) Ecological and Health Effects of Building Materials. Springer, Cham, pp. 33-52, 2022.

Ordu M., Der O. Polymeric Materials Selection for Flexible Pulsating Heat Pipe Manufacturing Using a Comparative Hybrid MCDM Approach. Polymers 15 (13), 2933, 2023a.

Ordu M., Der O. Yeşil Üretim İçin Çevresel Etki Temelli Termoplastik Malzeme Seçimi: Karşılaştırmalı Bir Hibrid ÇKKV Yaklaşımı. Erciyes Üniversitesi Fen Bilimleri Enstitüsü Dergisi 39 (1), 100-115, 2023b.

Ordu M., Fedai Y. A Novel Decision Support System Based on Fuzzy Multi Criteria Decision Making for Optimizing Machining Parameters. Journal of Engineering Research 2021.

Özlü B. St-37 Malzemesinin Lazer Kesiminde İşleme Parametrelerinin Deneysel ve İstatiksel Olarak İncelenmesi. Fırat Üniversitesi Mühendislik Bilimleri Dergisi 33 (1), 161-71, 2021.

Petousis M., Ninikas K., Vidakis N., Mountakis N., Kechagias J.D. Multifunctional PLA/CNTs Nanocomposites Hybrid 3D Printing Integrating Material Extrusion and CO_2 Laser Cutting. Journal of Manufacturing Processes 86, 237-252, 2023.

Rahman M., Brazel C.S. Ionic Liquids: New Generation Stable Plasticizers for Poly (Vinyl Chloride). Polymer Degradation and Stability 91 (12), 3371-3382, 2006.

Rajaram N., Sheikh-Ahmad J., Cheraghi S.H. CO_2 Laser Cut Quality of 4130 Steel. International Journal of Machine Tools and Manufacture 43 (4), 351-358, 2003.

Roy R.K. A Primer on the Taguchi Method. Competitive Manufacturing Series. 1st ed., Van Nostrand Reinhold, New York, USA, 1990.

Saleh S.J., Qaisy A., Karataş C. Laser Cutting of High Density Polyethylene (Hdpe) Pipes Pe100 Using CO_2 Gas Laser. International Journal of Engineering and Advanced Technology (IJEAT) 9 (1), 6193–6199, 2019.

Soutis C. Carbon Fiber Reinforced Plastics in Aircraft Construction. Materials Science and Engineering: A 412 (1-2), 171-176, 2005.

Varsey A.M., Shaikh A.H. Experimental and Statistical Study on Kerf Taper Angle During CO_2 Laser Cutting of Thermoplastic Material. Journal of Laser Applications 31 (3), 032010, 2019.

Varsi A.M., Shaikh A.H. Developing an Algorithm for Predicting Depth as well as Number of Passes During CO_2 Laser Machining on Thermoplastic Material. Journal of Laser Applications 30 (4), 042007, 2018.

Yaka H. Tornalama Sonrası Çıkan Talaşlardan Elde Edilen Alüminyum 5000 Alaşımının Yüzey Pürüzlülüğünün Taguchi Yöntemi ile Analizi. Iğdır Üniversitesi Fen Bilimleri Enstitüsü Dergisi 11 (1), 464-473, 2021.

Yalçın B., Yüksel A., Aslantaş K., Der O., Ercetin A. Optimization of Micro-Drilling of Laminated Aluminum Composite Panel (Al–PE) Using Taguchi Orthogonal Array Design. Materials 16 (13), 4528, 2023.

You K., Yan G., Luo X., Gilchrist M.D., Fang F. Advances in Laser Assisted Machining of Hard and Brittle Materials. Journal of Manufacturing Processes 58, 677-692, 2020.

Yu L., Dean K., Li L. Polymer Blends and Composites from Renewable Resources. Progress in Polymer Science 31 (6), 576-602, 2006.

JOURNAL of
MATERIALS and MECHATRONICS:A

e-ISSN 2717-8811
JournalMM, 2023, 4(2), 475-491
https://doi.org/10.55546/jmm.1358963

Araştırma Makalesi / Research Article

Comparison of Mechanical Properties of Samples Fabricated by Stereolithography and Fused Deposition Modelling

M. Said BAYRAKLILAR[1], Abdulkadir BULDU[2], M. Tayyip KOCAK[3], Osman ULKIR[4*], Melih KUNCAN[5]

[1]Department of Civil Engineering, Faculty of Engineering, Siirt University, Siirt, Turkey,
ORCID ID: https://orcid.org/0000-0002-5365-4441, said.bayraklilar@siirt.edu.tr
[2]Department of Electrical and Electronics Engineering, Faculty of Engineering, Siirt University, Siirt, Turkey
ORCID ID: https://orcid.org/0000-0002-9161-4862, abdulkadir.buldu@siirt.edu.tr
[3]Department of Software Engineering, Istanbul Health and Technology University, Istanbul, Turkey,
ORCID ID: https://orcid.org/0000-0003-2276-2658, muhammedtayyipkocak@gmail.com
[4]Department of Electric and Energy, Technical Sciences Vocational School, Mus Alparslan University, Mus, Turkey,
ORCID ID: https://orcid.org/0000-0002-1095-0160, o.ulkir@alparslan.edu.tr
[5]Department of Electrical and Electronics Engineering, Faculty of Engineering, Siirt University, Siirt, Turkey,
ORCID ID: https://orcid.org/0000-0002-9749-0418, melihkuncan@siirt.edu.tr

Geliş/ Received: 13.09.2023; **Kabul / Accepted:** 31.10.2023

ABSTRACT: Additive manufacturing (AM) technology has attracted significant attention with the rapid fabrication of 3D parts for various applications. The two most popular techniques in this technology, Fused Deposition Modelling (FDM) and Stereolithography (SLA), make it possible to produce functional parts with complex shapes quickly and cheaply. Determining the mechanical properties of the parts fabricated by these methods is important in terms of efficient operation in the relevant fields. In this study, forty-five test specimens were fabricated using three different polymer materials (UVR, PLA, and ABS) in SLA and FDM type 3D printers, including tensile, compression, and 3-point bending tests. Samples are printed at a 75% fill rate according to ASTM standards. Experimental studies were carried out to determine the mechanical properties of the samples. Among the samples, the highest strength values in tensile, compression and bending test samples made of UVR material were 60.39 MPa, 127.74 MPa and 118.35 MPa, respectively. In addition to mechanical properties, hardness, and SEM analyses were performed to examine the surface roughness, surface topography, and composition of the samples.

Keywords: Additive manufacturing, Compression test, Fused deposition modelling, Stereolithography, Tensile test, 3-point bending test.

*Sorumlu yazar / Corresponding author: o.ulkir@alparslan.edu.tr

Bu makaleye atıf yapmak için /To cite this article

Bayraklılar, M.S., Buldu, A., Kocak M.T., Ulkir, O., Kuncan, M. (2023). Comparison of Mechanical Properties of Samples Fabricated by Stereolithography and Fused Deposition Modelling Additive Manufacturing Methods. Journal of Materials and Mechatronics: A (JournalMM), 4(2), 475-491.

1. INTRODUCTION

Additive manufacturing (AM) produces objects directly from three-dimensional (3D) models by combining materials layer by layer. Appropriate application of AM can help to save fabrication time and cost, shorten the product development cycle, and increase fabrication capability and complexity (Singh et al., 2017). Thanks to its unique fabrication technique, AM is adopted in many industrial applications such as aerospace, automobile, automation, food, and pharmaceutical (Haleem and Javaid, 2019; Böcking and Tillman, 2019; Ble-Bail et al., 2020). The main additive manufacturing applications include rapid prototyping, rapid tooling, and rapid manufacturing. Much research is being done to improve the AM process by developing new fabrication technologies, evaluating environmental sustainability performance by performing cost analysis and evaluation, and improving printing accuracy and quality (Cheeser et al., 2019; Uludag et al., 2023). AM technologies are primarily applied for fit and function prototyping and tooling in the design and modeling phase. In such cases, the mechanical properties of prototypes or tools are very important (Shassere et al., 2019; Du Plessis et al., 2020). Because products must withstand high pressure from the rig or injection molding testing. It is important to determine these pressure data in tension, compression, and bending conditions before the product is used.

The distinguishing features of AM are often presented in the context of comparison with traditional manufacturing processes. The term "additive manufacturing" is ultimately defined by the American Testing and Materials Corporation (ASTM) F42 committee as a technique. AM techniques can be divided into seven categories according to the ASTM standard (Kawalkar et al., 2022): material extrusion, powder bed fusion, vat photopolymerization, material sputtering, binder sputtering, sheet lamination, and directed energy deposition (Li et al., 2020; Duman and Ozsoy, 2022). These processes include stereolithography (SLA) (Ertugrul et al., 2023), electron beam melting (EBM) (Galati et al., 2018) selective laser melting (SLM) (Cheng et al., 2016), fused deposition modelling (FDM) (Ozsoy et al., 2022), polyjet (Patpatiya et al., 2022), two photon polymerization (2PP) (Nguyen and Karayan, 2017) and digital light processing (DLP) (Chaudry et al., 2023) are also widely used in AM. In the current study, FDM, a material extrusion process, and SLA, a photo polymerization-based method, were preferred. These methods are the most preferred and researched technologies in the 3D printing process.

While various methods exist for the 3D printing process, FDM is a widely used methodology. In the FDM technique, the 3D printers used a thermoplastic type filament, which is heated until it reaches its melting temperature, then extruded layer by layer (Shi et al., 2021). The uninterrupted usability of the given material is made by using printing pieces in a layered manner. The heating element in the liquefier head is used to bring the filament to a semi-liquid phase, which is then extruded from the nozzle into the printing area to print the actual component. The most important task in this process is to melt the next layer before it solidifies since solidification before fusing can have a greater impact on other properties of the component. The most used raw materials in the FDM fabrication process are Acrylonitrile Butadiene Styrene (ABS), Polylactic Acid (PLA), Polycarbonate (PC), Polyethylene Terephthalate Glycol (PETG), and Thermoplastic Polyurethane (TPU) (De Leon et al., 2019; Yadav et al., 2020). Parts fabricated with FDM are suitable for detailed functional prototypes, durable fabrication tools, and low-volume fabrication. FDM is used in aviation, medicine, consumer goods, architecture, and automotive (Chohan et al., 2017; Kempin et al., 2017).

SLA is the first AM technology in which a liquid photosensitive resin is converted into a solid by selectively exposing it to an ultraviolet (UV) light (Prabhakar et al., 2021). The liquid-based materials used in the SLA process are complex chemical compounds specially designed for each SLA

printer. Both solid and powder-based materials used in SLA are polymers such as photopolymer resin, PLA, and ABS (Miedzinska et al., 2020). While SLA materials are fragile, toxic, or vulnerable to light exposure, recent developments gradually reduce these limitations. During the process, a thin layer of liquid in contact with UV light is solidified into the fabrication bed. When the process is complete, the fabrication bed is removed with the fabricated object attached to it; then, it is un-breakable and cleaned with alcohol-based chemicals. Depending on the material selection, the part is either post-treated with other chemicals or cured briefly under intense UV light (Kafle et al., 2021). SLA is widely used in the fabrication of medical prototypes and prosthetics, small and sensitive prototypes, optical parts and transparent fabrications, and dental fields (Dehurtevent et al., 2017; Mukhtarkhanov et al., 2020).

Many studies are carried out to determine and develop various properties of products fabricated with SLA and FDM methods (Heidari-Rarani et al., 2019; Camargo et al., 2019; Marsavina et al., 2022) Mercado-Colmenero et al., (Mercado-Colmenero et al., 2020) present numerical and experimental analysis of polymeric material PETG fabricated by FDM technology, aiming to obtain its mechanical characterization under uniaxial compression loads. Yadav et al., (Yadav et al., 2020) discussed the effects of material density, filler density, and extrusion temperature on the tensile strength of ABS, PETG, and multi-material test pieces. The multi-material is fabricated by layer-by-layer bonding of 50% ABS and 50% PETG in an FDM 3D printer. A total of 30 test pieces were printed according to ASTM D638-(IV) standard with different fill densities, extrusion temperatures, and material densities. In addition, the fill density and extrusion temperature are optimized to increase the tensile strength of the FDM fabrication units. Özsoy et al., (Özsoy et al., 2021) fabricated 36 test specimens, including two different polymer materials (PLA and ABS), tensile, compression tests, and 3-point bending tests, in the FDM-type printer. Chacón et al. (Chacón et al., 2017) aimed to characterize the effect of structure direction, layer thickness, and feed rate on the mechanical performance of PLA samples fabricated with a low-cost 3D printer.

Tensile and three-point bending tests were performed to determine the mechanical response of the printed samples. Due to the layer-by-layer fabrication, it was observed that the samples exhibited anisotropic behaviour, and vertical orientation showed the lowest mechanical properties. Regarding layer thickness and feed rate, it was determined that ductility decreased as the layer thickness and feed rate increased. The current study is aimed to compare the mechanical properties of the samples by producing tensile, compression, and bending tests with these three types of materials in SLA and FDM-based 3D printers. Thus, innovation will be added to the literature.

In this study, test samples were fabricated using three different polymer materials (UVR, PLA, and ABS) to examine the material properties of SLA and FDM 3D printing methods, which are AM methods. Test specimens were prepared according to ASTM standards for plastic materials. While UVR material was used in the SLA to produce the samples, PLA and ABS materials were used in the FDM. Forty-five test specimens were fabricated for each process parameter, including fifteen tensile, fifteen compressions, and fifteen bending tests.

2. MATERIALS AND METHODS

2.1 Materials

This section presents the types of 3D printers and materials used in the additive manufacturing process of the test samples whose mechanical properties will be examined. Since the samples will be fabricated by Stereolithography (SLA) and Fused Deposition Modelling (FDM) methods, two types

of printers were used. FDM-based 3D printing can be obtained from these printers with the printer in Figure 1a. Creality Ender 6 brand printer has a large print volume of 250x250x400 mm. In addition, the printing speed can reach 150 mm/s with 0.1 mm resolution. Printing with PLA, ABS, TPU, Nylon, HIPS, and conductive filament types is possible with the Creality printer. The slicing program named Cura was used for the printing process with this printer. SLA-based 3D printing is possible with the printer in Figure 1b. The FlashForge Foto 6.0 brand printer has a low print volume of 130x78x155 mm. However, finely detailed prints can be obtained in small volumes with high efficiency and precision. The printer has a pixel resolution of 2560x1620 and offers a print speed of 30 mm/h. The slicing program called Chitubox was used for the printing process with the printer. Ultraviolet light-sensitive fluid resin was used as the printing material in the Flashforge Photo 6.0 printer.

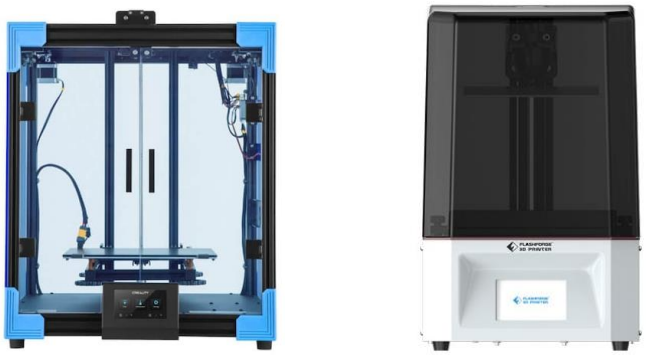

(a) (b)

Figure 1. FDM and SLA type printers used in 3D fabrication (a) Creality Ender 6 (b) Flashforge Foto 6.0

Three materials were used to produce test samples: ABS, PLA, and UVR. PLA and ABS were used in filament form, while UVR was used in fluid form. ABS is a common thermoplastic polymer typically used for injection moulding applications. This engineering plastic is popular for its low cost of manufacture and ease of processing by the material's plastic manufacturers. ABS material is advantageous in various industries due to its properties such as structural strength and rigidity, chemical resistance, and excellent electrical insulation. However, it also brings restrictions due to its properties such as being damaged by sunlight and being dangerous when burned. PLA is a completely biodegradable thermoplastic polymer composed of renewable raw materials. Another advantage of using PLA filament is its environmentally friendly properties (Morão and De, 2019).

Table 1. Properties of ABS, PLA and UVR materials

	Compression Temperature (°C)	**Density (g/cm^3)**	**Tensile Strength (MPa)**	**Elongation at Break (%)**	**Bending Strength (MPa)**	**Impact Strength (kJ/m^2)**
PLA	180-215	1.24	65	28	92	6.8
ABS	210-230	1.04	40	40	75	7.6
	Viscosity (mPa.s)	**Density (g/cm^3)**	**Tensile Strength (MPa)**	**Elongation at Break (%)**	**Wavelength (nm)**	**Hardness (D)**
UVR	150-200	1.25	52	20	405	84

As a biodegradable material made from renewable resources, it produces fewer emissions during the printing process compared to other materials. Among all 3D printing materials, PLA is part of the most popular materials used for additive manufacturing for filament fabrication. The UV resin material is viscous and is fabricated for 3D printing devices. The photopolymer-based resin

material has fast-drying properties after exposure to UV light. After curing, UV resin is non-stick, clear, yellowing, and scratch resistant. Recently, it has been used frequently in industrial applications and biomedical fields. Some technical specifications of ABS, PLA and UVR materials are given in Table 1 (Aloyaydi and Sivasankaran, 2020; Kim et al., 2007; Turan et al., 2022).

ASTM standard was preferred for sizing test samples. The technical drawing and dimensions of the samples are shown in Figure 2. ASTM D638-14, ASTM D695, and ASTM D790 standards were used for tensile, compression, and 3-point bending tests, respectively (Laureto and Pearce, 2018; Salman et al., 2015; Ishak et al., 2010). The samples were fabricated in the dimensions shown in Figure 2 and with a thickness of 3.20 mm. Solid models of the samples were made in 3D with SolidWorks software within the framework of the specified dimensions.

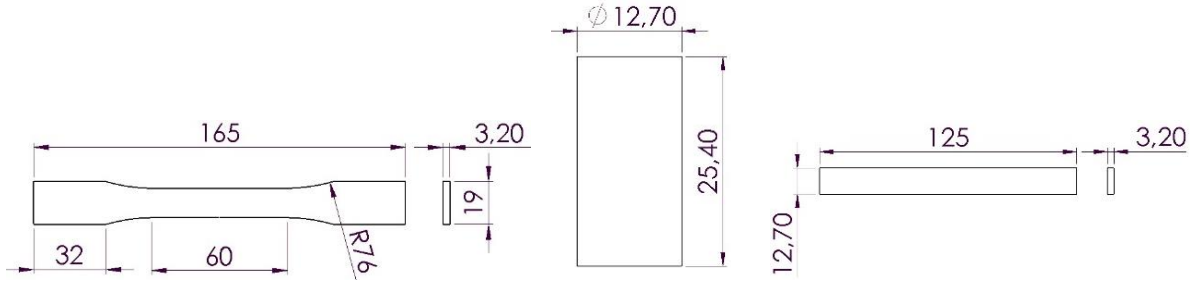

Figure 2. Dimensions of test specimens in ASTM standards (mm) (a) Tensile specimen (b) Compression specimen (c) 3-point bending specimen

2.2 Methods

In this section, the fabrication process of tensile, compression and bending test samples is given. The printing parameters of SLA and FDM-based printers must be adjusted for fabrication with 3D printers. The printing parameters selected for ABS, PLA, and UVR materials. Although the occupancy rate was chosen as fixed in both printers, other parameters had to be selected differently because there were different types of printers. In addition, since the printing temperature values materials are different in FDM technique, two nozzle and table temperatures were determined.

The parameters in Table 2 are defined in the slicing program of the 3D printer to generate the G-codes of the solid modelled samples. This code defines settings such as the position and angle of the part to be printed on the printer table. The G-codes fabricated in the program are transferred to the 3D printer with the help of a USB, and the part is made ready for printing. The printer table needs to be calibrated manually for both 3D printers. After this process, the necessary material is attached to the printer or poured, and fabrication is started. Before starting the manufacturing process, a thin film of adhesive was applied to the print bed in the FDM method to ensure better adhesion of the first layer of the sample to the glass print bed during fabrication.

Table 2. 3D printing parameters used in FDM and SLA methods.

	Fill Rate (%)	**Layer Thickness (mm)**	**Wall Thickness (mm)**	**Print Speed (mm/s)**	**Nozzle Temperature (°C)**	**Table Temperature (°C)**
FDM	75	0.15	0.9	50	200/220	70/80
	Fill Rate (%)	**Layer Thickness (mm)**	**Number of Base Layers**	**Print Speed (mm/s)**	**Number of Transition Layers**	**Exposure Time (s)**
SLA	75	0.03	15	1.8	10	80

Calibration settings were made on the FDM 3D printer, and the red color Creality, brand PLA material, was attached to the printer for the fabrication of tensile test specimens. The samples were fabricated according to the parameters in Table 2 as in Figure 3a. The same print settings were repeated, and the fabrication was made with yellow Creality brand ABS material. Ten tensile specimens were fabricated by the FDM method, five for each material type. Finally, the tensile samples in Figure 3a were fabricated on an SLA-based printer using transparent Anycubic brand UVR material. Thus, fifteen tensile test specimens were fabricated following ASTM D638-14 standards with three materials and two different fabrication techniques. Using the same printing parameters and material types, fifteen 3-point bending test specimens were fabricated in ASTM D790 standards as in Figure 3b. Finally, fifteen compression test samples were fabricated in accordance with ASTM D695 standards as in Figure 4.

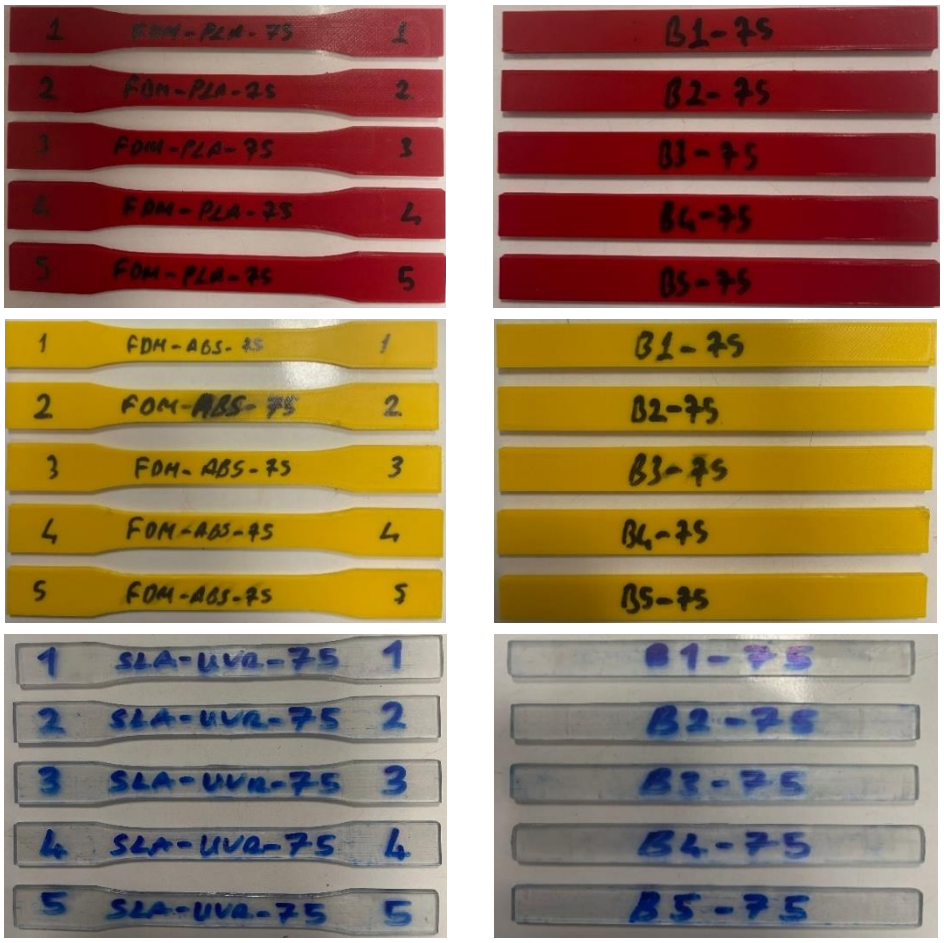

(a) (b)

Figure 3. Tensile and 3-point bending test specimens fabricated on a 3D printer using PLA, ABS and UVR materials: (a) Tensile test specimens (b) 3-point bending test specimens

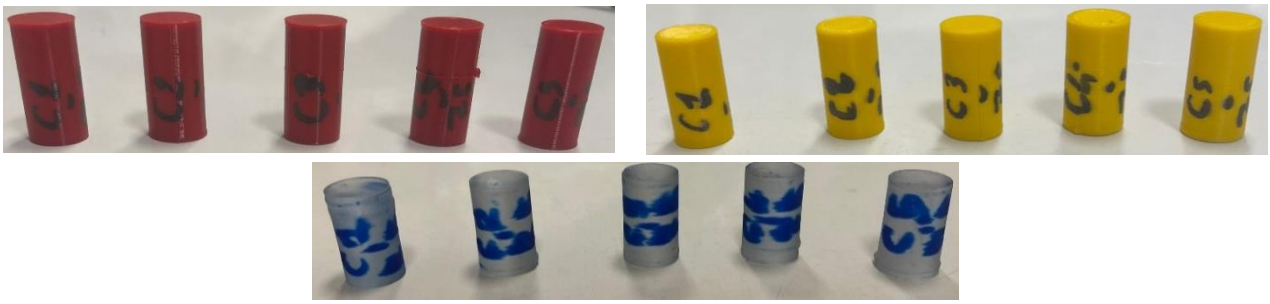

Figure 4. Compression test samples fabricated on a 3D printer using PLA, ABS and UVR materials

3. RESULTS AND DISCUSSION

Mechanical test sample groups fabricated by FDM and SLA additive manufacturing methods are named according to the mechanical tests to be applied. The tensile test sample group is named the letter 'T', the compression test sample group is named the letter 'C', and the 3-point bending test sample group is named 'B'. The results are given both graphically and in tabular form.

3.1 Tensile Strength Tests Results

Tensile experimental studies were performed on a 50 kN capacity test device (AG-X, Shimadzu) using the ASTM D638-14 standard. The device has a reading range of ±0.1% between 50kN and 50N according to ISO 7500/1, ASTM E4, and DIN51221 standards. The test speed range is 0.0005mm/min-1000mm/min. Experimental studies were carried out at a tensile speed of 1 mm/s. The stress-strain diagrams resulting from the tensile test of the samples fabricated with PLA, ABS, and UVR materials are shown in Figure 5. The stress, percent elongation, and modulus of elasticity calculated according to the applied force and elongation are given in Table 3.

Table 3. Tensile test results of PLA, ABS and UVR materials

PLA	Strength (MPa)	Strain (%)	Elasticity Module (GPa)	**ABS**	Strength (MPa)	Strain (%)	Elasticity Module (GPa)	**UVR**	Strength (MPa)	Strain (%)	Elasticity Module (GPa)
T1	36.12	2.48	1.452	**T1**	25.75	2.37	1.084	**T1**	61.75	4.39	1.403
T2	36.42	2.26	1.592	**T2**	27.74	2.42	1.114	**T2**	54.42	3.72	1.627
T3	36.51	2.19	1.716	**T3**	28.72	2.44	1.117	**T3**	61.31	4.48	1.366
T4	36.21	2.35	1.552	**T4**	31.65	2.43	1.319	**T4**	62.36	4.47	1.391
T5	36.73	2.49	1.478	**T5**	32.81	2.44	1.332	**T5**	62.14	4.27	1.453
Average	36.39	2.35	1.558		29.33	2.42	1.193		60.39	4.26	1.448

The highest tensile strength value occurs in the samples fabricated with the SLA technique using UVR material. When Figure 5 is examined, it can be said that the strength-strain curves of the samples fabricated using different materials coincide. When the strength-strain curves of the products fabricated with UVR and ABS materials are compared, the tensile strength values of the products fabricated with UVR material are approximately 90% higher than those fabricated with ABS material. The elongation at break values of the products fabricated with ABS material is 60% higher than those fabricated with UVR material. This is because the bond structure between the layers in the 3D printing process is better in UVR material samples than in PLA and ABS materials. The average elongation amounts of PLA, ABS, and UVR samples were determined as 2.35 mm, 2.42 mm, and 4.26 mm, respectively. The mean modulus of elasticity values of PLA, ABS, and UVR material samples was calculated as 1.558 GPa, 1.193 GPa, and 1.448 GPa, respectively.

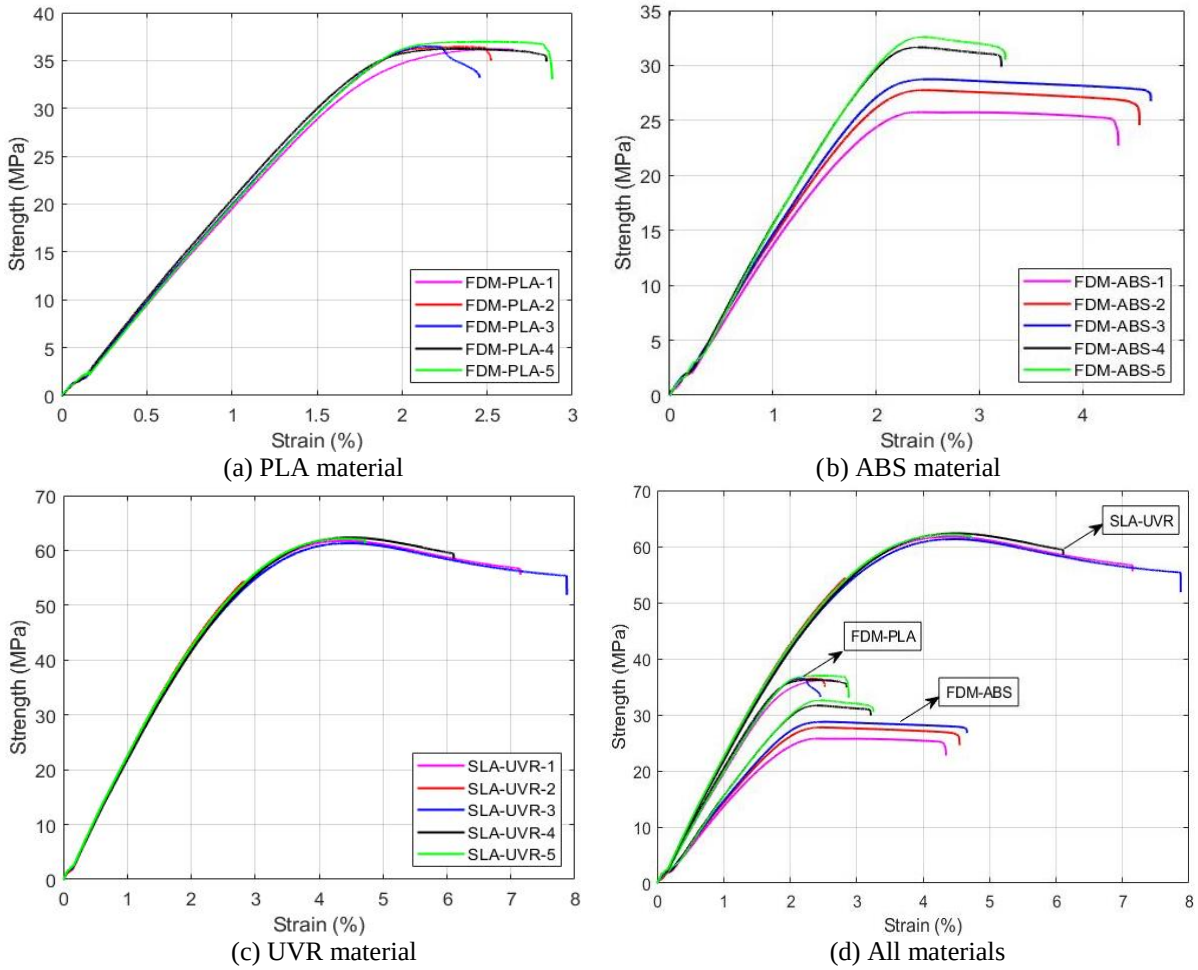

Figure 5. Strength-strain diagrams of tensile tests for tensile specimens made of different materials (a) PLA materials (b) ABS materials (c) UVR materials (d) All materials

The tensile strength of the samples fabricated by the SLA method is higher than FDM because they have isotropic properties. With this feature, SLA-type specimens have the same force value in all directions. When the tensile and elasticity modulus data obtained as a result of the tensile test and the existing studies in the literature are examined, it is seen that there is a similarity in terms of material properties. Zhao et al. (Zhao et al., 2019) investigated the effect of compression angle and layer thickness on the tensile strength and Young's modulus of PLA materials fabricated with FDM. According to the results, the printing material with a 90° compression angle and 0.1 mm layer thickness had the highest tensile strength with 49.66 MPa. In contrast, the printing material with 0° compression angle and 0.3 mm layer thickness had the highest tensile strength with 19.16 MPa. Grabowik et al. (Grabowik et al., 2017) presented tensile test results for samples from ABS, PLA, PET, PMMA, ASA, and wood material groups. The peak stress value for ABS material is between 34.6 and 35 MPa.

3.2 Compression Tests Results

Compression test experimental studies were performed on a 50 kN capacity test device (AG-X, Shimadzu) using the ASTM D695 standard. The study applied a constantly increasing compression load to PLA, ABS, and UVR material samples placed between two jaws. The stress-strain diagrams resulting from the compression test applied to the specimens are given in Figure 6. The stress, percent elongation, and modulus of elasticity calculated according to the applied force and elongation are given in Table 4.

Table 4. Compression test results of PLA, ABS and UVR materials

PLA	Strength (MPa)	Strain (%)	Elasticity Module (GPa)	**ABS**	Strength (MPa)	Strain (%)	Elasticity Module (GPa)	**UVR**	Strength (MPa)	Strain (%)	Elasticity Module (GPa)
C1	94.63	6.63	0.601	**C1**	86.56	6.51	0.531	**C1**	130.02	2.90	1.752
C2	93.57	6.51	0.602	**C2**	88.66	6.44	0.538	**C2**	131.42	3.06	1.685
C3	93.82	6.74	0.603	**C3**	88.52	6.68	0.528	**C3**	116.12	2.35	1.945
C4	94.12	6.52	0.592	**C4**	88.42	6.64	0.529	**C4**	127.54	2.93	1.712
C5	95.15	6.73	0.598	**C5**	88.75	6.56	0.536	**C5**	133.62	3.02	1.743
Average	94.25	6.62	0.599		88.18	6.56	0.532		127.74	2.85	1.767

The UVR material samples have higher compressive strength values than ABS and PLA samples (Figure 6). The most important factor affecting compressive strength is the material's molecular structure. The differences in the molecular structures of the materials used in the test processes, the chemical composition, metallographic structure, and the number of functional groups of the polymers affected the compressive strength. The UVR material structure consists of resin + photoinitiators. Photoinitiators absorb light of different wavelengths and form free radicals that initiate crosslinking and curing of a formula. Among the process parameters, the elastic range of ABS material is minimal and visible for UVR and PLA. Taking the average of the experimental studies, the compressive strengths for PLA, ABS, and UVR were calculated as 94.25 MPa, 88.18 MPa, and 127.74 MPa, respectively. The mean modulus of elasticity values of PLA, ABS, and UVR material samples was calculated as 0.599 GPa, 0.532 GPa, and 1.767 GPa, respectively.

When the strength data obtained as a result of the compression test and the existing studies in the literature are examined, it is seen that there is a similarity in terms of material properties. Kholil et al. (Kholil et al., 2022) aimed to determine the compressive strength of FDM with parameters. The sample fabrication process includes ABS and PLA materials. The highest compressive strength was found in PLA material with a yield strength value of 66.78 MPa and a layer thickness of 0.15 mm. The lowest compressive strength was found in ABS material, with a yield strength value of 33.41 MPa and a layer thickness of 0.35 mm. Miedzińska et al. (Miedzińska et al., 2020) present the results of durability tests on selected materials used for printing with SLA technology. To determine the properties of these materials, two types of tests differing in strain rate were used: the quasistatic test on the Zwick & Roell Kappa 50DS strength machine and the dynamic test on the Hopkinson bar. As a result of the experimental studies performed with Tough and Clear type resins, the average values of the maximum compressive strength were found to be 189.5 MPa and 231.2 MPa, respectively. The strain ratios at these values were measured as 4.568 and 5.994. Based on the results obtained, the tested Tough and Clear light-curable resins revealed that the strain rate significantly affected the compressive behaviour, yield strength, material weakening, and strain hardening. Static compression tests revealed the elastic-plastic behaviour of the material. The 50% of strains obtained in the tests did not cause cracking in the samples. The samples were deformed but remained consistent.

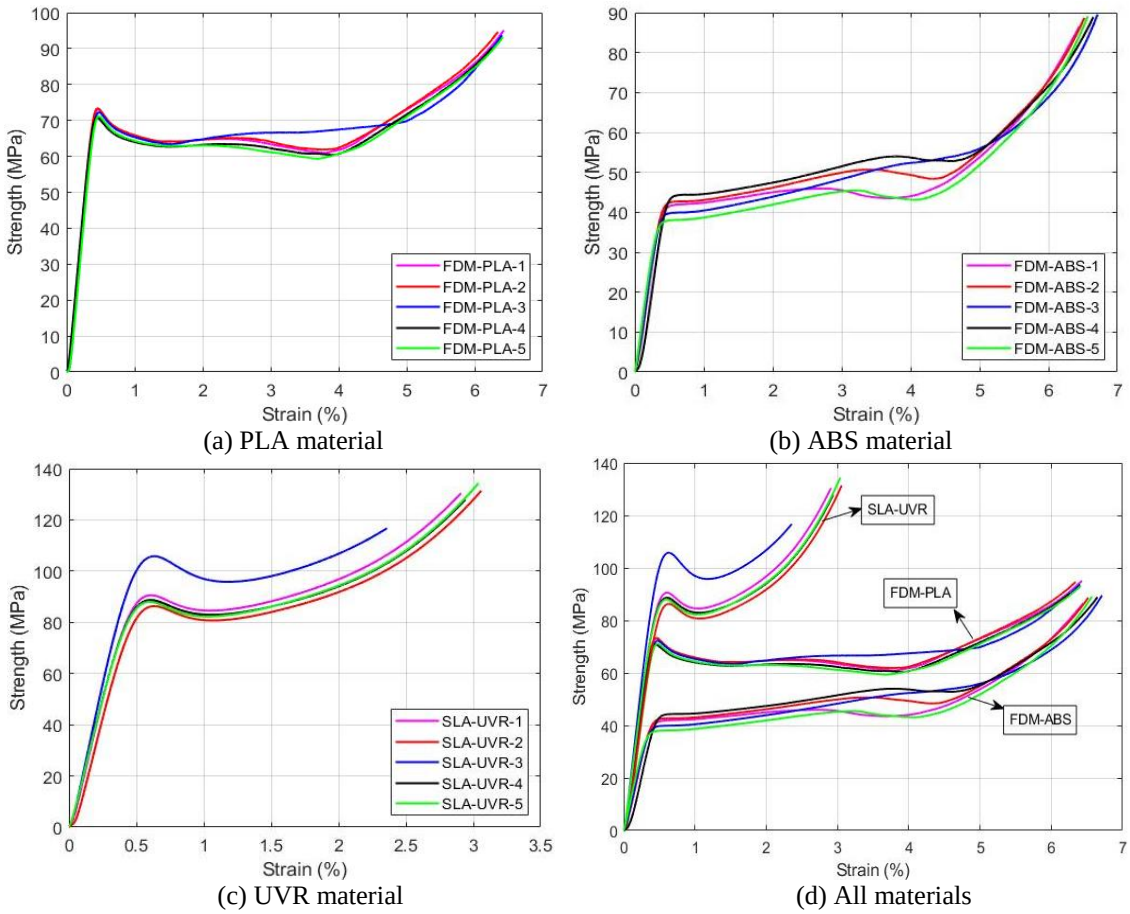

(a) PLA material (b) ABS material

(c) UVR material (d) All materials

Figure 6. Strength-strain diagrams of compression tests for compression specimens made of different materials (a) PLA materials (b) ABS materials (c) UVR materials (d) All materials

3.3 3-Point Bending Tests Results

The 3-point bending test is usually performed on brittle materials rather than a tensile test. For this reason, the 3-point bending test gives more meaningful results in brittle materials. Bend test studies were performed on a 50 kN force transducer capacity machine (AGS-X, Shimadzu) using the ASTM D790 standard. The mandrel's diameter and the supports' diameter were fixed in accordance with the standard. After the assemblies were fixed, both PLA, ABS, and UVR materials were placed on the supports for the test specimens, and the specimens were bent with the help of a mandrel by applying the load. The strength-strain diagrams resulting from the 3-point bending test of the samples are shown in Figure 7. The stress, percent elongation, and modulus of elasticity calculated according to the applied force and elongation are given in Table 5.

Table 5. 3-point bending test results of PLA, ABS and UVR materials

PLA	Strength (MPa)	Strain (%)	Elasticity Module (GPa)	**ABS**	Strength (MPa)	Strain (%)	Elasticity Module (GPa)	**UVR**	Strength (MPa)	Strain (%)	Elasticity Module (GPa)
B1	78.35	3.26	0.913	**B1**	37.57	3.44	0.406	**B1**	117.91	2.72	1.205
B2	80.60	3.12	0.881	**B2**	56.72	3.43	0.621	**B2**	120.22	3.03	1.214
B3	80.28	2.87	0.901	**B3**	44.82	3.42	0.493	**B3**	121.34	3.32	1.195
B4	80.68	3.44	0.865	**B4**	54.18	3.39	0.598	**B4**	118.38	2.95	1.186
B5	80.01	3.15	0.910	**B5**	53.45	3.44	0.615	**B5**	113.92	3.43	1.198
Average	79.98	3.16	0.894		49.34	3.42	0.546		118.35	3.09	1.199

The highest bending strength was observed in the samples made of UVR material. The lowest bending moment was found in ABS materials. The average bending strength values for PLA, ABS, and UVR samples were 79.98 MPa, 49.34 MPa, and 118.35 MPa, respectively. It can be seen that results similar to the compression test were obtained. The most important reason for this is the difference between the molecular structure of the materials. In addition, the high bending strength of the UVR material led to higher bending strength values.

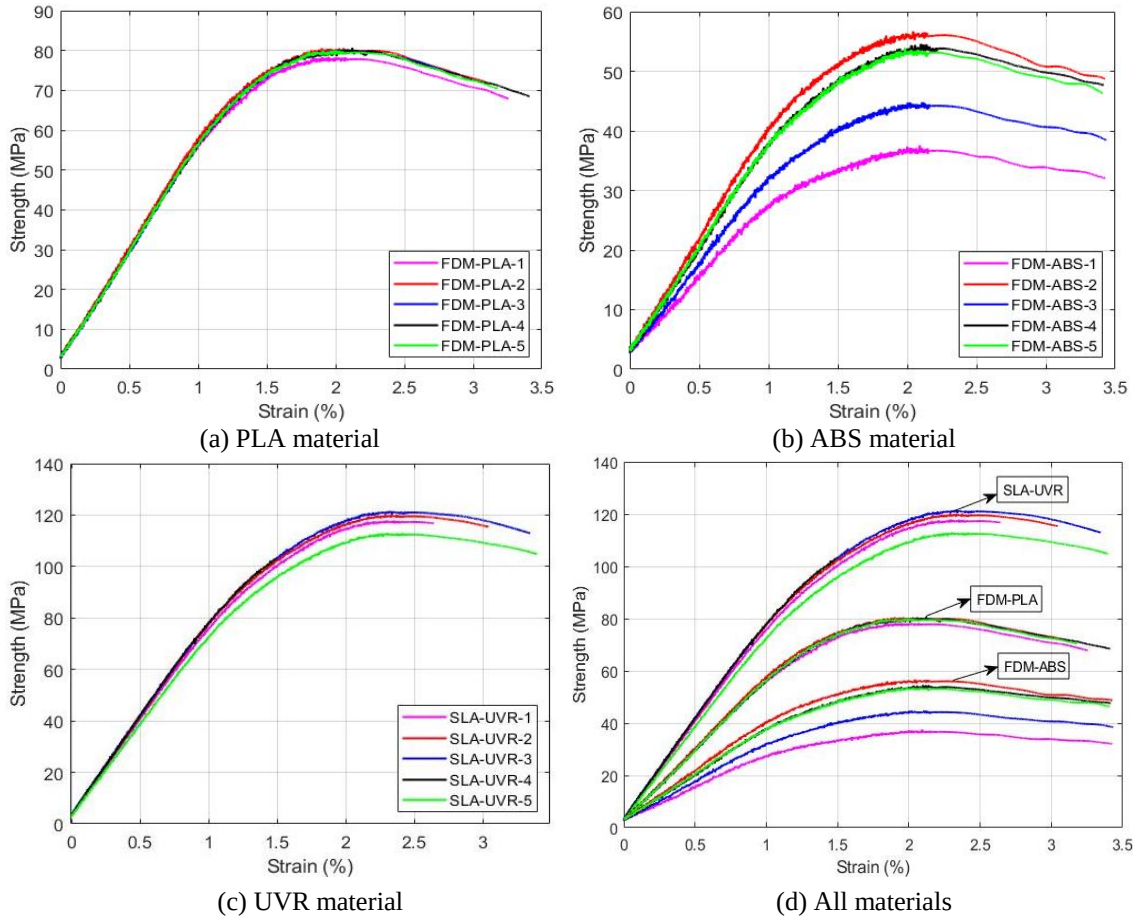

Figure 7. Strength-strain diagrams of 3-point bending tests for 3-point bending specimens made of different materials (a) PLA materials (b) ABS materials (c) UVR materials (d) All materials

This bending strength was followed by PLA and ABS materials, respectively. While the bending strength values of UVR and PLA samples were close to each other for five tests; there are 25% differences in ABS materials. The elastic range is visible for all materials. When the average of the experimental studies is taken, the percent elongation values for PLA, ABS, and UVR materials were calculated as 3.16%, 3.42%, and 3.09%, respectively. The mean modulus of elasticity values of PLA, ABS, and UVR material samples was calculated as 0.894 GPa, 0.546 GPa, and 1.199 GPa, respectively.

When the data obtained as a result of the 3-point bending test and the existing studies in the literature are examined, it is seen that there is a similarity in terms of material properties. Atakok et al. (Atakok et al., 2022) used the Taguchi methodology to investigate the effects of FDM fabrication parameters (tensile strength, three-point flexural strength, and 3D-printed PLA and Re-PLA) on impact strength. Filaments (PLA, Re-PLA), three different layer thicknesses, filling ratios, and filling structure were determined as FDM process parameters.

3.4 Hardness Measurement Results

Hardness measurements of the test sample were made with the TRONIC PD-801 Analog Shoremeter device in SHORE D. The Shoremeter device is suitable for measuring hard rubber, synthetic materials, thermoplastics, vinyl sheets, cellulose acetates and MDF. Tensile test sample was used for hardness measurements. Hardness measurements were made from 5 different points on the upper and lower surfaces of each sample and calculations were made by taking the average values. The measured hardness values are given in Table 6. When the test samples fabricated with PLA, ABS and UVR materials are compared among themselves, it is seen that the hardness values of the products fabricated with UVR material are higher than the products. Made from PLA and ABS. The reason for this is that the void structure in products fabricated with UVR is quite low compared to other materials. When the upper and lower zone hardness values are examined, it is seen that the lower surface hardness is higher than the upper surface hardness. It is thought that the adhesives applied to ensure the adhesion of the sample to the glass table in the manufacturing made with the FDM technique cause the hardness of the lower surfaces of the samples to increase. For this reason, the substrate hardness of ABS and PLA samples was higher. Similarly, the hardness of the sample fabricated with the SLA technique was higher on the surface that first adhered to the table, that is, the lower surface.

Table 6. Hardness values of PLA, ABS and UVR materials

	Shore D Hardness Values	
	Top Surface Average	Bottom Surface Average
PLA	62.15	75.13
ABS	69.77	80.35
UVR	72.54	84.76

3.5. Surface Analysis Results

Surface image analysis was performed with a scanning electron micro-scope (SEM) device to examine the surface morphology of the tensile test specimens fabricated from PLA, ABS, and UVR materials after breaking within the scope of experimental studies. With SEM, besides taking surface images at high magnifications, information about the chemical composition of the material can also be obtained. Images of the fractured areas of the specimens broken in the tensile tests were taken with the ZEISS Gemini 500 FESEM.

After the tensile test was applied to PLA, ABS, and UVR materials, pictures of the fractured areas of the fracture test specimens were taken in the SEM device with 40x, 100x, 2000x, and 5000x magnifications and are given in Figure 8. SEM analysis of the UVR test sample shows that the material interface is better compared to ABS and PLA samples. It is seen in Figure 8f that there is almost no gap in each layer of the sample fabricated with UVR material. The gaps between the 3D printed fibers in each layer of the fabricated samples are higher in ABS samples (Figure 8g). In the 5000x magnified images of the fracture areas of the fabricated samples in SEM, it is seen that the interlayer gaps in the ABS sample are much larger. The sample's hardening and strength are reduced by its extensive void structure. When the samples fabricated with ABS and PLA are examined, it is seen that the 3D-printed fibres in each layer are in linear contact with each other (Figure 8a and Figure 8b).

It can be said that the ABS material test sample behaves like a ductile material because the interlayer bonds are weaker. Surface fractures of PLA and UVR materials indicate a brittle fracture.

Although it seems to be a partially brittle fracture in ABS material, it exhibited a slightly different fracture behaviour as it has a hollower structure. In the SEM image of the PLA sample in Figure 8e, up to half of the material is where the fracture starts and where the fracture is very rapid and brittle. Later, as the shrinkage continued, the lower part of the material was catastrophically broken, and a wavy structure was formed. The UVR material also appears to have a very brittle fracture.

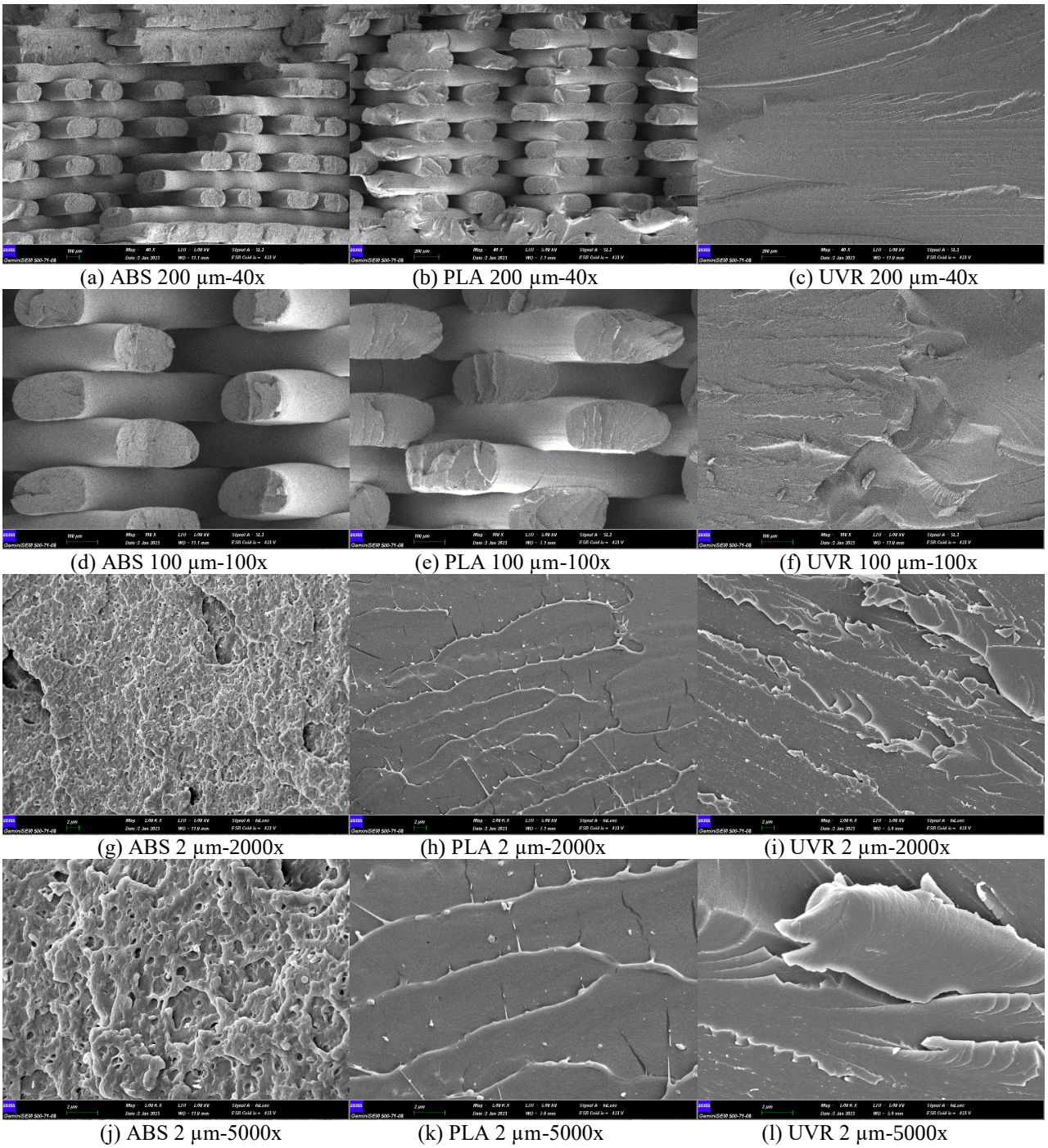

(a) ABS 200 µm-40x (b) PLA 200 µm-40x (c) UVR 200 µm-40x

(d) ABS 100 µm-100x (e) PLA 100 µm-100x (f) UVR 100 µm-100x

(g) ABS 2 µm-2000x (h) PLA 2 µm-2000x (i) UVR 2 µm-2000x

(j) ABS 2 µm-5000x (k) PLA 2 µm-5000x (l) UVR 2 µm-5000x

Figure 8. 40x, 100x, 2000x and 5000x magnified images taken from SEM of the broken parts of the samples as a result of the tensile test (a) ABS 200 µm-40x (b) PLA 200 µm-40x (c) UVR 200 µm-40x (d) ABS 100 µm-100x (e) PLA 100 µm-100x (f) UVR 100 µm-100x (g) ABS 2 µm-2000x (h) PLA 2 µm-2000x (i) UVR 2 µm-2000x (j) ABS 2 µm-5000x (k) PLA 2 µm-5000x (l) UVR 2 µm-5000x

4. CONCLUSION

This study fabricated tensile, compression, and 3-point bending test specimens following the standards using PLA, ABS, and UVR-type materials with FDM and SLA-based additive manufacturing methods. The mechanical properties of these materials were examined and compared with the tests performed. For each material type, fifteen test specimens were fabricated. ASTM standard was used for sizing forty-five test samples fabricated with a 3D printer. PLA, ABS, and UVR is important for efficient parts operation and the widespread use of the fabrication technique. The best mechanical properties were observed in the test specimens made of UVR material. The highest tensile, compressive, and bending strengths were measured in these samples. These values are, on average, 60.39 MPa, 127.74 MPa, and 118.35 MPa, respectively. After the UVR material, the highest strength values were observed in the PLA sample, while the lowest values were measured in the ABS samples. When the test samples fabricated with PLA, ABS, and UVR materials are compared among themselves, it is seen that the hardness values of the products fabricated with UVR material are higher than the products fabricated with PLA and ABS. This is because the void structure inside the UVR samples is very small compared to other materials. Finally, surface image analysis was performed with the SEM device to examine the surface morphology fabricated from PLA, ABS, and UVR materials after breaking. As a result of the analysis, the excess of the void structure and the bond weakness in the ABS samples were observed.

5. ACKNOWLEDGEMENTS

This work is supported by the Scientific Research Projects Coordination Unit of Siirt University as a project with the number 2022-SİÜMÜH-009. This study was carried out in the Additive Manufacturing and Seismic Isolator Laboratory of the Siirt University Faculty of Engineering. The author of this article would like to thank the staff of the Additive Manufacturing and Seismic Isolator Laboratory for their support.

6. CONFLICT OF INTEREST

Authors approve that to the best of their knowledge, there is not any conflict of interest or common interest with an institution/organization or a person that may affect the review process of the paper.

7. AUTHOR CONTRIBUTION

Conceptualization, M. Said Bayraklilar and Melih Kuncan; Methodology, Osman Ulkir and Melih Kuncan; Formal analysis, M. Said Bayraklilar and Abdulkadir Buldu; Investigation, M. Tayyip Kocak and Osman Ulkir; Validation, M. Tayyip Kocak and Melih Kuncan; Software, Abdulkadir Buldu, M. Tayyip Kocak and Osman Ulkir; Data curation, M. Said Bayraklilar and Melih Kuncan; Writing-original draft and review & editing, M. Said Bayraklilar, Abdulkadir Buldu and Osman Ulkir.

8. REFERENCES

Aloyaydi B. A., Sivasankaran S., Low-velocity impact characteristics of 3D-printed poly-lactic acid thermoplastic processed by fused deposition modeling. Transactions of the Indian Institute of Metals 73, 1669-1677, 2020

Atakok G., Kam, M., Koc H.B., Tensile, three-point bending and impact strength of 3D printed parts using PLA and recycled PLA filaments: A statistical investigation. Journal of Materials Research and Technology 18, 1542-1554, 2022.

Ble-Bail A., Maniglia B.C., Le-Bail P., Recent advances and future perspective in additive manufacturing of foods based on 3D printing. Current Opinion in Food Science 35, 54-64, 2020.

Böckin D., Tillman A.M., Environmental assessment of additive manufacturing in the automotive industry. Journal of cleaner production, 226, 977-987, 2019.

Camargo J.C., Machado Á.R., Almeida E.C., Silva E.F.M.S., Mechanical properties of PLA-graphene filament for FDM 3D printing. The International Journal of Advanced Manufacturing Technology 103, 2423-2443, 2019.

Chacón J.M., Caminero M.A., García-Plaza E., Núnez P.J., Additive manufacturing of PLA structures using fused deposition modelling: Effect of process parameters on mechanical properties and their optimal selection. Materials & Design 124, 143-157.

Chaudhary R., Fabbri P., Leoni E., Mazzanti F., Akbari R., Antonini C., Additive manufacturing by digital light processing: a review. Progress in Additive Manufacturing 8, 331-351, 2023.

Cheng B., Shrestha S., Chou, K., Stress and deformation evaluations of scanning strategy effect in selective laser melting. Additive Manufacturing 12, 240-251, 2016.

Chesser P., Post B., Roschli A., Carnal C., Lind R., Borish M., Love L., Extrusion control for high quality printing on Big Area Additive Manufacturing (BAAM) systems. Additive Manufacturing 28, 445-455, 2019.

Chohan J.S., Singh R., Pre and post processing techniques to improve surface characteristics of FDM parts: a state of art review and future applications. Rapid Prototyping Journal 23, 495-513, 2017.

De León A.S., Domínguez-Calvo A., Molina S.I., Materials with enhanced adhesive properties based on acrylonitrile-butadiene-styrene (ABS)/thermoplastic polyurethane (TPU) blends for fused filament fabrication (FFF). Materials & Design 182, 108044, 2019.

Dehurtevent M., Robberecht L., Hornez J.C., Thuault A., Deveaux E., Béhin P., Stereolithography: A new method for processing dental ceramics by additive computer-aided manufacturing. Dental materials 33, 477-485, 2017.

Du Plessis A., Yadroitsava I., Yadroitsev I., Effects of defects on mechanical properties in metal additive manufacturing: A review focusing on X-ray tomography insights 2020, Materials & Design 187, 108385, 2020.

Duman B., Özsoy K., A deep learning-based approach for defect detection in powder bed fusion additive manufacturing using transfer learning. Journal of the Faculty of Engineering and Architecture of Gazi University 37, 361-375, 2022.

Ertugrul I., Ulkir O., Ersoy S., Ragulskis M., Additive Manufactured Strain Sensor Using Stereolithography Method with Photo-polymer Material. Polymers 15, 991, 2023.

Galati M., Iuliano L., A literature review of powder-based electron beam melting focusing on numerical simulations. Additive Manufacturing 19, 1-20, 2018.

Grabowik C., Kalinowski K., Ćwikła G., Paprocka I., Kogut P., Tensile tests of specimens made of selected group of the filament materials manufactured with FDM method. In MATEC Web of Conferences 112, 04017, 2017.

Haleem A., Javaid M., Additive manufacturing applications in industry 4.0: a review. Journal of Industrial Integration and Management 4, 1930001, 2019.

Heidari-Rarani M., Rafiee-Afarani M., Zahedi A.M., Mechanical characterization of FDM 3D printing of continuous carbon fiber reinforced PLA composites. Composites Part B: Engineering 175, 107147, 2019.

Ishak M. R., Leman Z., Sapuan S. M., Edeerozey A. M. M., Othman I. S., Mechanical properties of kenaf bast and core fibre reinforced unsaturated polyester composites. In IOP Conference Series: Materials Science and Engineering 11 (1), 012006, 2010.

Kafle A., Luis E., Silwal R., Pan H.M., Shrestha P.L., Bastola A.K., 3D/4D Printing of polymers: Fused deposition modelling (FDM), selective laser sintering (SLS), and stereolithography (SLA). Polymers 13, 3101, 2021.

Kawalkar R., Dubey H.K., Lokhande S.P., A review for advancements in standardization for additive manufacturing. Materials Today: Proceedings 50, 1983-1990, 2022.

Kempin W., Franz C., Koster L.C., Schneider F., Bogdahn M., Weitschies W., Seidlitz A., Assessment of different polymers and drug loads for fused deposition modeling of drug loaded implants. European Journal of Pharmaceutics and Biopharmaceutics 115, 84-93, 2017.

Kholil A., Asyaefudin E., Pinto N., Syaripuddin S., Compression Strength Characteristics of ABS and PLA Materials Affected by Layer Thickness on FDM. In Journal of Physics: Conference Series 2377, 012008, 2022.

Kim Y., Choi E. S., Kwak W., Shin Y., Analysis of the thermal distribution by using laser-beam irradiation. Journal of the Korean Physical Society 51, 503-508, 2007.

Laureto J. J., Pearce J. M., Anisotropic mechanical property variance between ASTM D638-14 type i and type iv fused filament fabricated specimens. Polymer Testing, 68, 294-301, 2018.

Li W., Mille L.S., Robledo J.A., Uribe T., Huerta V., Zhang Y.S., Recent advances in formulating and processing biomaterial inks for vat polymerization-based 3D printing. Advanced healthcare materials 9, 2000156, 2020.

Marșavina L., Vălean C., Mărghitaș M., Linul E., Razavi N., Berto F., Brighenti R., Effect of the manufacturing parameters on the tensile and fracture properties of FDM 3D-printed PLA specimens. Engineering Fracture Mechanics 274, 108766, 2022.

Mercado-Colmenero J.M., La Rubia M.D., Mata-Garcia E., Rodriguez-Santiago M., Martin-Doñate C., Experimental and numerical analysis for the mechanical characterization of petg polymers manufactured with FDM technology under pure uniaxial compression stress states for architectural applications. Polymers 12, 2202, 2020.

Miedzińska D., Gielet R., Małek E., Experimental study of strength properties of SLA resins under low and high strain rates. Mechanics of Materials 141, 103245, 2020.

Morão A., De Bie, F., Life cycle impact assessment of polylactic acid (PLA) produced from sugarcane in Thailand. Journal of Polymers and the Environment, 27(11), 2523-2539, 2019.

Mukhtarkhanov M., Perveen A., Talamona D., Application of stereolithography based 3D printing technology in investment casting. Micromachines 11, 946, 2020.

Nguyen A.K., Narayan, R.J., Two-photon polymerization for biological applications. Materials Today 20, 314-322, 2017.

Özsoy K., Aksoy B., Bayrakçı H.C., Optimization of thermal modeling using machine learning techniques in fused deposition modeling 3-D printing. Journal of Testing and Evaluation 50, 613-628, 2022.

Özsoy K., Erçetin A., Çevik Z.A., Comparison of mechanical properties of PLA and ABS based structures fabricated by fused deposition modelling additive manufacturing. Avrupa Bilim ve Teknoloji Dergisi 27, 802-809, 2021.

Patpatiy P., Chaudhary K., Shastri A., Sharma S., A review on polyjet 3D printing of polymers and multi-material structures. Proceedings of the Institution of Mechanical Engineers, Part C: Journal of Mechanical Engineering Science 236, 7899-7926, 2022.

Prabhakar M.M., Saravanan A.K., Lenin A.H., Mayandi K., Ramalingam P.S., A short review on 3D printing methods, process parameters and materials. Materials Today: Proceedings 45, 6108-6114, 2021.

Salman S. D., Hassimb W. W., Leman Z, Experimental comparison between two types of hybrid composite materials in compression test. Carbon, 3, 119-23, 2015.

Shassere B., Nycz A., Noakes M.W., Masuo C., Sridharan N., Correlation of microstructure and mechanical properties of metal big area additive manufacturing. Applied Sciences 9, 787, 2019.

Shi K., Salvage J.P., Maniruzzaman M., Nokhodchi A., Role of release modifiers to modulate drug release from fused deposition modelling (FDM) 3D printed tablets. International journal of pharmaceutics 597, 120315, 2021.

Singh S., Ramakrishna S., Singh R., Material issues in additive manufacturing: A review. Journal of Manufacturing Processes 25, 185-200, 2017.

Turan S. R., Ülkir O., Kuncan M., Buldu A., Stereolithografi eklemeli imalat yöntemiyle farklı doluluk oranlarında üretilen numunelerin mekanik özelliklerinin incelenmesi. International Journal of 3D Printing Technologies and Digital Industry 6(3), 399-407.

Uludag M., Ulkir O., Ertugrul, I., Kaplanoglu E., Design, fabrication, and experiments of a soft pneumatic gripper with closed-loop position control. Journal of Testing and Evaluation 51, 2023.

Yadav D., Chhabra D., Garg R.K., Ahlawat A., Phogat A., Optimization of FDM 3D printing process parameters for multi-material using artificial neural network. Materials Today: Proceedings 21, 1583-1591, 2020.

Yadav D.K., Srivastava R., Dev S., Design & fabrication of ABS part by FDM for automobile application. Materials Today: Proceedings 26, 2089-2093, 2020.

Yang Y., Li L., Zhao J., Mechanical property modeling of photosensitive liquid resin in stereolithography additive manufacturing: Bridging degree of cure with tensile strength and hardness. Materials & Design 162, 418-428, 2019.

Zhao Y., Chen Y., Zhou Y., Novel mechanical models of tensile strength and elastic property of FDM AM PLA materials: Experimental and theoretical analyses. Materials & Design 181, 108089, 2019.

JOURNAL of
MATERIALS and MECHATRONICS:A

e-ISSN 2717-8811
JournalMM, 2023, 4(2), 492-503
https://doi.org/10.55546/jmm.1363808

Araştırma Makalesi / Research Article

A Numerical Study on the Large Displacement in Functionally Graded Beam under Thermal Effect

Ersin DEMİR

Pamukkale University, Faculty of Technology, Department of Mechatronics Engineering, Denizli, Turkey,
ORCID ID: https://orcid.org/0000-0001-8222-5358, edemir@pau.edu.tr

Geliş/ Received: 21.09.2023; **Kabul / Accepted:** 02.11.2023

ABSTRACT: The large displacement behavior of a Functionally Graded (FG) beam under uniform thermal load is investigated numerically. Six different effects are taken into consideration when examining the large displacement behavior of the beam. These are the effects of temperature, material, geometry, slenderness, force, and boundary conditions. The nonlinear numerical analysis is carried out by using the Simulation mode of SolidWorks, which is a finite element-based commercial program. It is obtained from the results that the displacement of the end of the beam increases with increasing temperature, slenderness ratio, and force. It is also found that it decreases with increase in the ratio of ceramic in Functionally Graded Material (FGM). Moreover, the displacement of the end of the beam decreases with increasing the width of the beam. Furthermore, as expected, the maximum and minimum displacements are obtained in the beams with Clamped-Free and Clamped-Clamped boundary conditions, respectively.

Keywords: Large displacement, Beam, FGM, Thermal load

*Sorumlu yazar / Corresponding author: edemir@pau.edu.tr

Bu makaleye atıf yapmak için /To cite this article

Demir, E. (2023). A Numerical Study on the Large Displacement in Functionally Graded Beam under Thermal Effect. Journal of Materials and Mechatronics: A (JournalMM), 4(2), 492-503.

1. INTRODUCTION

Some structural elements can be exposed to large displacement without exceeding their yield stress. Therefore, the large displacement problem in a structural element, especially in a beam, under force effect has attracted the attention of many researchers. Many studies have been done on this subject in the last decade. Some of these studies published in recent years are mentioned below. Khosravi and Jani (2018) proposed two novel numerical techniques to solve large displacements of cantilever beams with mixed boundary conditions. They compared their proposed mathematical model results with the results obtained from the experiment. Li and Li (2019) considered the three-point bending study of a Timoshenko beam. They analyzed the large displacement and rotation of the beam. Moreover, they compared calculated results with experimental data. Tari et al. (2015), overcame the large displacement problems of Euler-Bernoulli cantilever beams under a force and moment. They presented the solutions for different loading in cartesian coordinates. Furthermore, they developed piecewise parametric large displacement solutions. Kimiaeifar et al. (2014), overcame a solution of the large displacement of a cantilever beam. They used the Homotopy Analysis Method (HAM) in their analysis. Mohyeddin and Fereidoon (2014) examined the large displacements of a shear-deformable beam under a point load. They obtained an equation system based on Timoshenko's theory. Kimiaeifar et al. (2012) studied the large displacement of a Euler-Bernoulli beam which has variable flexural rigidity. They solved the problem by HAM. They found the characteristics of the displacement of a beam under a follower force. Kimiaeifar et al. (2011) studied the large displacement and rotation of a beam subjected to static loading. They solved the governing equation of this problem by HAM. They compared their results with the results obtained from the Range Kutta method. Chen (2010) proposed an approach to solve the large displacement of a cantilever beam.

Although there have been many studies on composites (Ünal et al., 2022) or FGMs (Demir et al., 2022) in recent years, there are relatively few studies on the large displacement of beams made by FGM in the literature. Some of them, encountered in the open literature, are given below. Zhou et al. (2018) presented a study on the large defection of a FG beam subjected to transverse loading. They obtained a yield criterion for a FG beam. They formulated analytical solutions for the large displacements of beams using proposed criteria and compared their solution with numerical solutions. Horibe and Mori (2018) investigated a bending problem for axially FG tapered beam under transverse load by using the Runge-Kutta method. Using a finite element method, Gan and Kien (2014) overcame the large displacement behavior of FG beams resting on an elastic foundation. They used a method that combined the arc-length control method with the incremental iterative method. Sitar et al. (2014) solved the equation of large displacements of a non-homogeneous beam. They solved equations numerically and tested on some examples. Mien and Gan (2014) analyzed the large displacements of tapered FG beams. They solved the large displacement problem by using the arc-length control algorithm. Davoodinik and Rahimi (2011) studied the bending problem of a tapered FG beam under inclined end and intermediate loadings. They introduced a curvilinear coordinate system to obtain the governing equations for large deformation. They used semi-analytical methods in their study and compared their results with the existing solution. Kang and Li (2010) investigated the large deformation of a FG beam. They obtained an expression for rotation and displacement in a FG beam under the end moment. They investigated the effects of variations in the Elasticity modulus and the material property on the bending of the FG beam. Rahimi and Davoodinik (2010) studied the large displacement behavior of a FG beam under inclined end loading by using the analytical and Adomian Decomposition Method (ADM). They also used a solver based on finite element analysis to solve the equation. They showed that the ADM is useful in solving such problems.

As the literature is surveyed, it can be seen that the problem of large displacement of beam subjected to the thermal effect, is quite limited. Li and Song (2006) determined the non-linear deformation of beams under mechanical and thermal loads. They solved the equation by using the Shooting Method. They analyzed the thermal large displacements of Timoshenko beams with fixed-fixed and pinned-pinned ends. Yin and Wang (2004) obtained the results of the large displacement of the beam under temperature loads numerically. He investigated the effect of different temperature distributions, loads, and stiffness on displacement.

In the study, the large displacement behavior of FG beam with variable cross-section under uniform thermal load is studied numerically. The effects of the temperature, material, geometry, slenderness, force, and boundary condition on the displacement of the end FG beam are investigated. From the open literature research, no similar study could be found.

2. MODEL

In Figure 1, a FG beam with variable cross-section is shown. The dimensions of the beam are given as follows: The width at the clamped end (b_o) is 20 mm, while the width at the free end (b_L) is 5 mm. h is the thickness and equal to 1 mm and L is the length of the beam and equal to 200 mm. Moreover, F is transverse force and is equal to 5N.

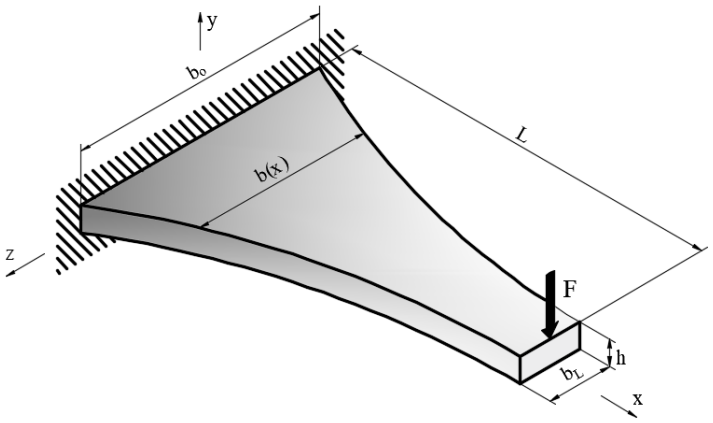

Figure 1. FG beam with variable cross-section

As can be seen from the figure, the beam exhibits varying width along its length and the width is given by the formula below.

$$b(x) = (b_L - b_o)\left(\frac{x}{L}\right)^k + b_o \tag{1}$$

In Equation 1, x is the distance from the clamped end along the x direction and k is geometric index. When k is equal to zero, the beam's width is equal to 5 mm and constant. When k approaches infinity, the width of the beam is also constant and equal to 20 mm. The k is taken as 0.5, 1, and 2. The variation of beam width by geometric index is represented in Figure 2. From the figure, it can be observed that the width of the beam decreases linearly when k is equal to 1. However, when k is equal to 0.5 and 2, the decrease in beam width is curved and these curves are convex and concave, respectively.

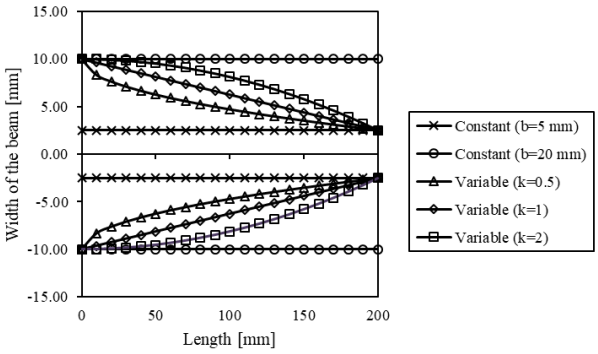

Figure 2. Variation of beam width by geometric index

3. MATERIAL

The beam is made of FGMs, which is obtained by volumetric mixing of Stainless Steel (SUS304) and Aluminum Oxide (Al_2O_3). As known, the material properties vary with change in the temperature. Shen (2009) gave the following equation. This equation gives the temperature-dependent material properties.

$$P_j = P_0(P_{-1}T^{-1} + 1 + P_1T + P_2T^2 + P_3T^3) \quad (2)$$

where T is the temperature in Kelvin (K) and P_i (i = -1, 0, 1, 2, 3) is the coefficient listed in Table 1. P_j is material properties. E is the elasticity modulus in Pascal (Pa), ν is Poisson's ratio, α is *the* thermal expansion coefficient per Kelvin (K^{-1}), and κ is thermal conductivity in Watts per meter Kelvin (W/mK) of the steel and ceramic.

Table 1. Coefficients of material properties (Shen, 2009)

	E [Pa]		***ν***		***α [K^{-1}]***		***κ [W/mK]***	
	SUS304	**Al_2O_3**	**SUS304**	**Al_2O_3**	**SUS304**	**Al_2O_3**	**SUS304**	**Al_2O_3**
P₀	201.04e+9	349.55e+9	0.3262	0.2600	12.330e-6	6.8269e-6	15.379	-14.087
P₋₁	0	0	0	0	0	0	0	-1123.6
P₁	3.079e-4	-3.853e-4	-2.002e-4	0	8.086e-4	1.838e-4	-1.264e-3	-6.227e-3
P₂	-6.534e-7	4.027e-7	3.797e-7	0	0	0	2.092e-6	0
P₃	0	-1.673e-10	0	0	0	0	-7.223e-10	0

To see the temperature effect, the temperature of the beam is increased from 22 °C to 400 °C. The temperature is increased by interval of 100 °C between 100 °C and 400 °C. The material properties of steel and ceramic are calculated from Equation 2 and Table 1 for each temperature. The densities of the steel and ceramic are assumed as constant due to the minor change in temperature increase. The densities of the steel and ceramic are taken as 8166 kg/m^3 and 3750 kg/m^3, respectively (Shen, 2009).

The material characteristics of the FG beam vary from one end to the other. The following equation is used to determine the material properties of the beam in the study,

$$MP = (MP_s - MP_c)\left(\frac{x}{L}\right)^n + MP_c \quad (3)$$

where MP is the material properties of the whole beam. MP_s and MP_c are material properties of steel and ceramic, respectively. As abovementioned, the material properties are E, ν, α, or κ. x is the distance along the length from one end of the beam and n is material index. This equation is similar to the equation given (Shen, 2009). According to Equation 3, the effects of the variations in the T

[°C] and *n* on the abovementioned material properties along the beam length are shown as follows, respectively.

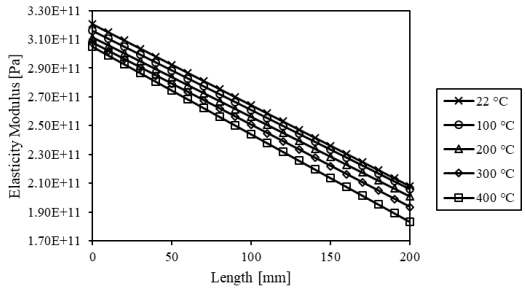

(a) with temperature

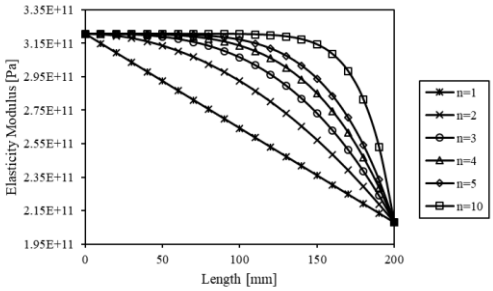

(b) with material index

Figure 3. Variation in elasticity modulus

Figures 3(a) and (b) depict the changes in the elasticity modulus along the beam's length with respect to temperature and material index *n*, respectively. It can be seen from the above two figures that the beam's leftmost end is Stainless Steel and the rightmost end is Aluminum Oxide. It is seen in Figure 3(a) that the Elasticity Modulus decreases gradually with increasing temperature. However as depicted in Figure 3(b), the elasticity modulus exhibits a hyperbolic increase along the length of the beam as the material index rises.

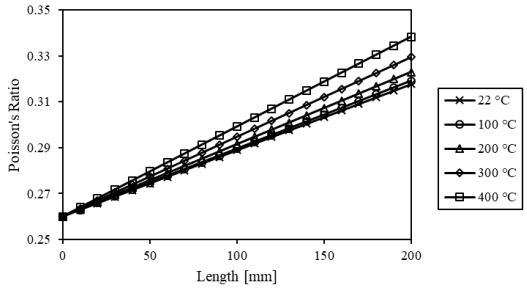

(a) with temperature

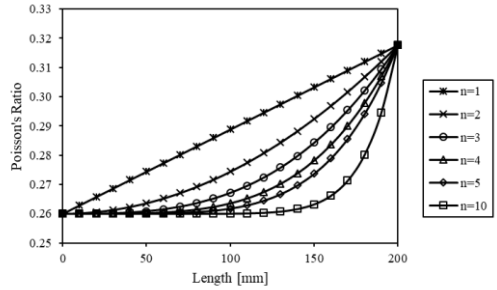

(b) with material index

Figure 4. Variation in Poisson's ratio

The variation in Poisson's ratio is depicted in Figure 4. Figure 4(a) indicates that as the temperature increases, Poisson's ratio also increases. As depicted in Figure 4(a), the increase in displacement is greater at the free end of the beam in comparison to the clamped end. Moreover, the difference at the free end is quite low at low temperatures. Figure 4(b) shows the Poisson's ratio decreases throughout the beam's span with increasing the material index *n*.

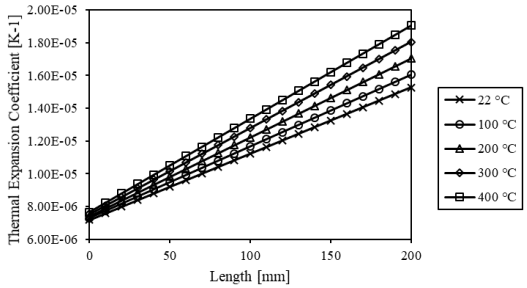

(a) with temperature

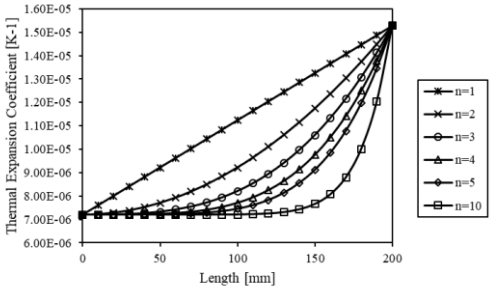

(b) with material index

Figure 5. Variation in the thermal expansion coefficient

The change in the coefficient of thermal expansion is shown in Figure 5. It is seen from Figures 5(a) and 4(a) that the figure obtained for the thermal expansion coefficient is similar to the figure obtained for Poisson's ratio. But, contrary the Figure 4(a), the differences at the free end are almost the same here. Figure 5(b) represents the thermal expansion coefficient decreases across the longitudinal axis of the beam with increasing the material index *n*.

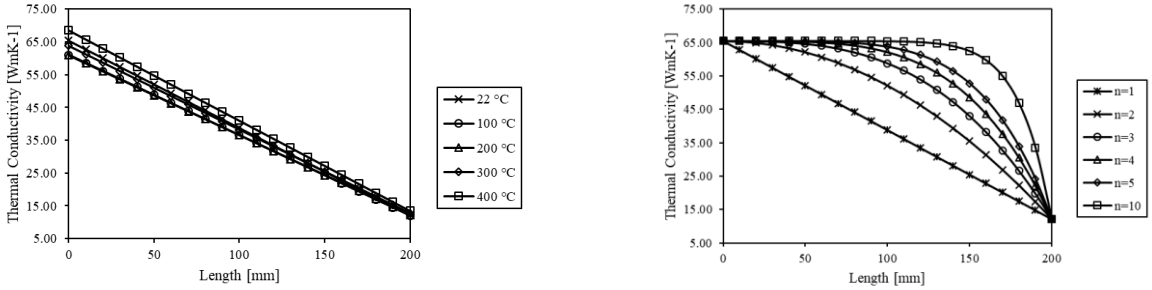

(a) with temperature **(b)** with material index

Figure 6. Variation in thermal conductivity

The thermal conductivity variation is shown in Figure 6. Unlike the coefficient of thermal expansion, the thermal conductivity decreases with increasing temperature, as seen in Fig 6(a). Figure 6(b) shows the thermal conductivity increases over the entire length of the beam with increasing the material index *n*.

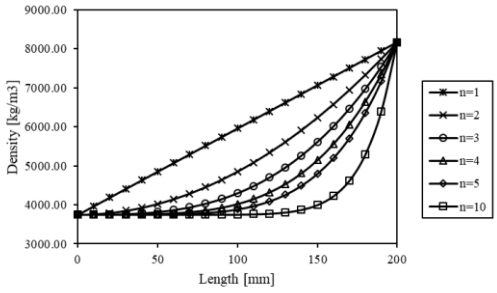

Figure 7. Variation in density with material index

In this study, it is assumed that the density does not change with temperature. Figure 7 shows the variation in density with material index *n*. As can be seen, the density decreases along the length of the beam with increasing *n* index.

4. NUMERICAL SOLUTION

The numerical thermal large displacement behavior of the beam is overcome by the SolidWorks program. SolidWorks is a program that can perform both drawing and analysis of engineering structures. So, this program is used for both drawing and large displacement analysis. Firstly, the wireframe model of the beam is drawn. The program allows curve drawing with equation. Therefore, wireframe of a beam with variable width according to Equation 1 is drawn easily. The resulting wireframe model is then converted to a planer surface model. The beam material is defined separately as a special material given in Section 3. After the model is completed, the Simulation mode of the SolidWorks program is launched for the analysis. In the Simulation mode of the program, both thermal and static analyses are performed on the beam. Intel Direct Sparse is used as a solver in both analyses. The thickness of the beam is defined in the Simulation mode of the program. Moreover,

after thermal loads are defined, the beam is meshed and the thermal analysis is executed. The data obtained from thermal analysis are transferred to static analysis. Again, after the supports and loads are defined, the beam is meshed and the nonlinear static analysis is executed. The meshed model and the case after analysis of the beam with k=1 are shown in Figures 8(a) and (b), respectively. The mean node number and the mean element number are obtained 2737 and 1260 respectively for the beam with k=1 as a result of the meshed process. As a result of both analyses, large displacement values at the end of the beam are obtained.

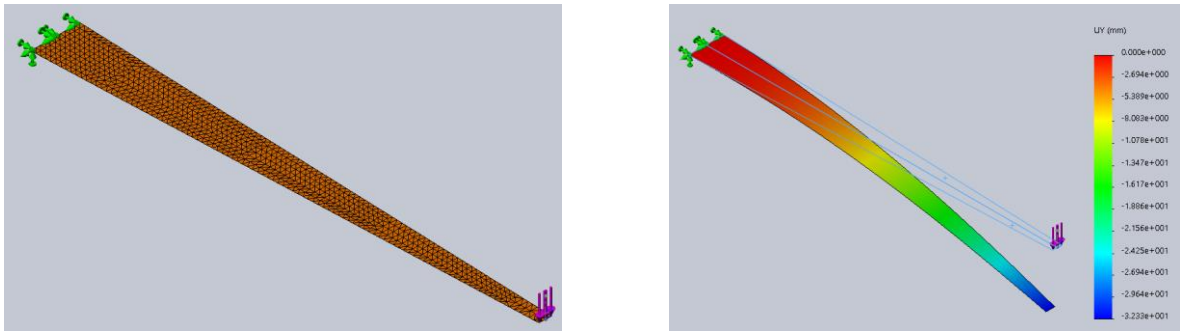

(a) before analysis **(b)** after analysis

Figure 8. Simulation model of the variable beam

5. RESULTS AND DISCUSSION

The numerical thermal large displacement behavior of the FG beam with variable cross-section is done in the analysis. The effects of temperature, material, geometry, slenderness, force, and boundary conditions are examined in the following subsections, respectively.

5.1 Effects of Temperature

Some assumptions are made only to see the temperature effect. The beam edge condition is taken as Clamped-Free (C-F). The beam's longitudinal, transverse, and thickness dimensions are taken as constant and they are 200 mm, 20 mm, and 1 mm, respectively. Since the material index n is taken 1, the beam material is FGM. The force is applied at the free end of the beam and the value of the force is taken 5 N. The temperature is raised in increments of 100°C, starting from 100°C and reaching 400°C. The room temperature (22 °C) is also taken into consideration in the analysis.

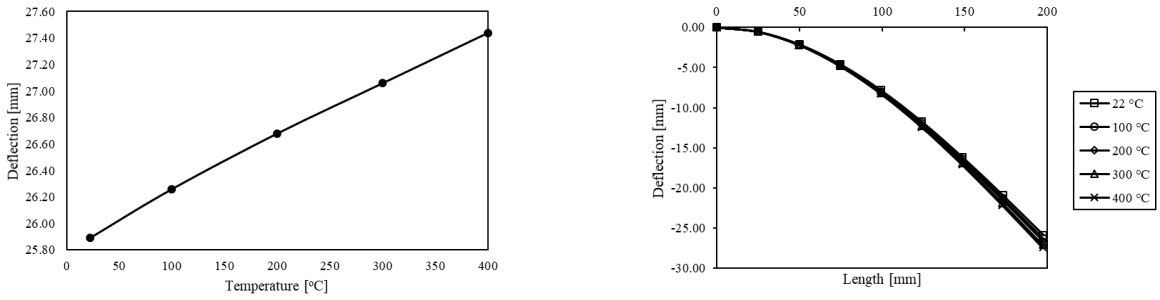

(a) Variation of displacement with temperature **(b)** Large displacement profiles of the beam

Figure 9. Effect of temperature

Figures 9(a) and (b) show the variations of the large displacement values at the beam's endpoint and the large displacement profiles of the beam with temperature, respectively. The figures show that the displacement of the free end of the beam rises with the rising temperature. As compared to the

displacement at 400 °C and 22 °C, there is a difference of about 1.5 mm. Therefore, it can be said that the increase in temperature does not affect the amount of displacement excessively.

5.2 Effects of Material Index (*n*)

To see the effect of the material, the material index is chosen between 0 and 4 by 1 increment. The material of the beam is pure steel according to Equation 3 when n=0. Pure ceramic material is also taken into account in the analysis. Increase in material index converts the beam material from steel to ceramic. So, when n is equal to infinity, the beam material is pure ceramic. The boundary condition of the beam is taken as C-F. The beam is assumed to have constant dimensions: a length of 200 mm, a width of 20 mm, and a thickness of 1 mm. The temperature is accepted 22 °C. The force value is chosen 5 N.

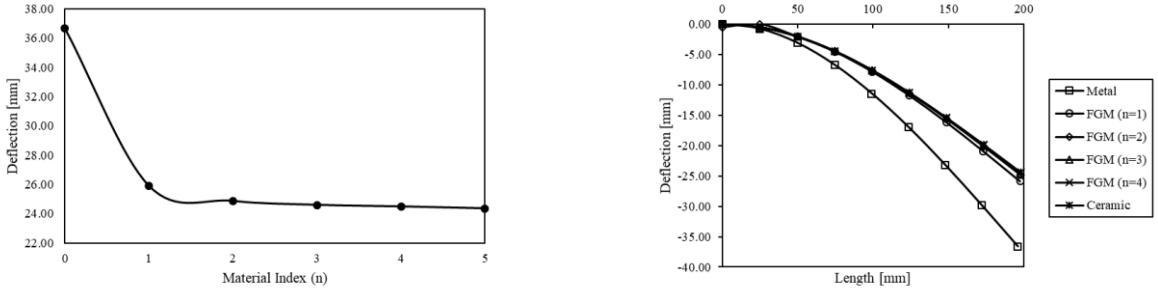

(a) Variation of displacement with n **(b)** Large displacement profiles of the beam

Figure 10. Effect of material index

Figures 10(a) and (b) depicted the variations of the large displacement of the end of the beam and the large displacement profiles of the beam with material index, respectively. Figures 10(a) and (b) show that displacement at the free end of the steel beam is much greater than the FGM and ceramic beam. The difference appears to be approximately 10 mm. Furthermore, it is also seen from the figures that the displacement of the free end of the beam decreases with increasing the ratio of ceramic in FGM but, the decrease is quite low. Therefore, it can be said that the use of FGM significantly reduces displacement as compared with the use of steel.

5.3 Effects of Geometric Index (*k*)

To examine the effect of the geometry, the geometric index is taken as 0, 0.5, 1, and 2. The width of the beam is constant and equal to 5 mm according to Equation 1 when k=0. Increase in the geometric index changes the width of the beam from 5 mm to 20 mm. So, when k is equal to infinity, the width of the beam is equal to 20 mm. The boundary condition of the beam is taken C-F. The length and thickness of the beam are taken constant and 200 mm and 1 mm, respectively. The material index n is taken 1 so that the beam material is FGM. The temperature and the force are chosen 22 °C and 5 N, respectively.

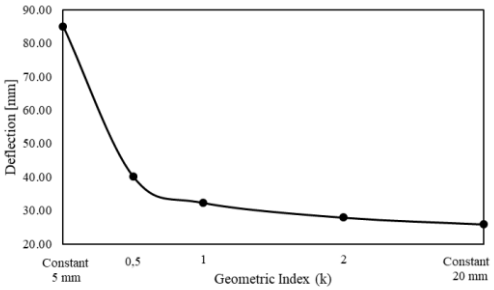

(a) Variation of displacement with k

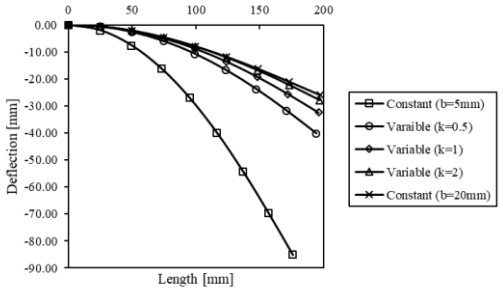

(b) Large displacement profiles of the beam

Figure 11. Effect of geometric index

The variations of the large displacement at the free end of the beam and the large displacement profiles of the beam with geometric index are represented in Figures 11(a) and (b), respectively. The figures show that the displacement at the end of the beam decreases with increasing the geometric index. The figures clearly indicate a considerable variation between the beams having widths of 5 mm and 20 mm. The results show that the displacement in the convex-shaped tapered beam (k=0.5) is more than that of the concave-shaped tapered beam (k=2).

5.4 Effects of Slenderness Ratio

To see the effect of the slenderness ratio (b/L), the width and the thickness of the beam are taken constant and equal to 20 mm and 1 mm, respectively. Meanwhile, the beam's length is incrementally raised from 200 mm to 600 mm, with increments of 100 mm. The boundary condition of the beam is taken C-F. The temperature, force, and material index n are again taken 22 °C, 5 N, and 1, respectively.

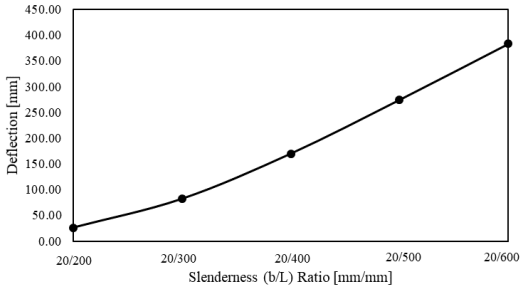

(a) Variation of displacement with slenderness ratio

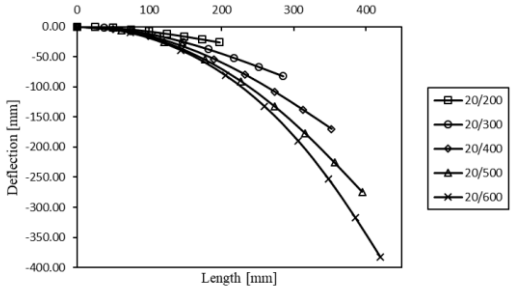

(b) Large displacement profiles of the beam

Figure 12. Effect of slenderness ratio

Figures 12(a) and (b) depict the variations of the large displacement at the free end of the beam and the large displacement profiles of the beam with slenderness ratio, respectively. It is seen from the figures that the displacement of the free end of the beam increases gradually with increasing slenderness ratio. According to the figures, the end-point displacement of the beam increases almost fifteen times when the length of the beam increases threefold.

5.5 Effects of Force

The material of the beam is chosen as pure steel to see the effect of force on the large displacement. Hence, the material index is equal to zero. The temperature is taken 22 °C. The width, thickness, and length of the beam are taken 20 mm, 1 mm, and 200 mm, respectively. The force is exerted on the free end of the beam. The force is increased from 1 N to 20 N. The beam is assumed to have a C-F boundary condition.

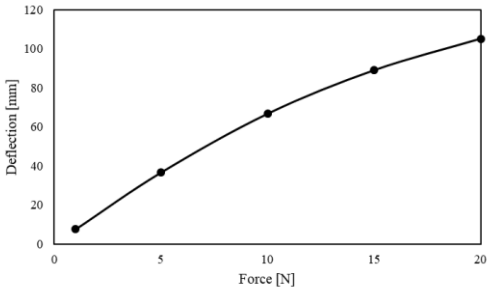

(a) Variation of displacement with force

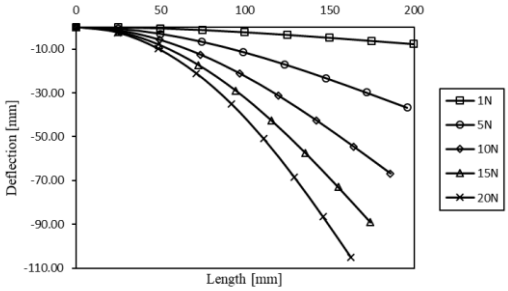

(b) Large displacement profiles of the beam

Figure 13. Effect of force

Figures 13(a) and (b) represent the variations of the large displacement at the free end of the beam and the large displacement profiles of the beam with forces, respectively. The figures show that the displacement increases with increasing force, as expected. According to the results, there is a direct proportional relationship between the applied force and the displacement at the beam's end.

5.6 Effects of Boundary Conditions

In order to see the effect of boundary conditions, four types of boundary conditions are taken into account. They are Clamped-Free (C-F) boundary condition, Clamped-Clamped (C-C) boundary condition, Clamped-Simply Supported (C-SS) boundary condition, and Simply Supported-Simply Supported (SS-SS) boundary condition. Since the material index n is taken 1, the beam material is FGM. The length, width, and thickness of the beam are taken constant and 200 mm, 20 mm, and 1 mm, respectively. The temperature is taken 22 °C. To ensure consistent comparisons among various boundary conditions, the force is exerted at the midpoint of the beam. Moreover, the force is chosen 20 N. This is because, when 5 N is applied to the beam with C-C boundary conditions, the displacement value is quite small.

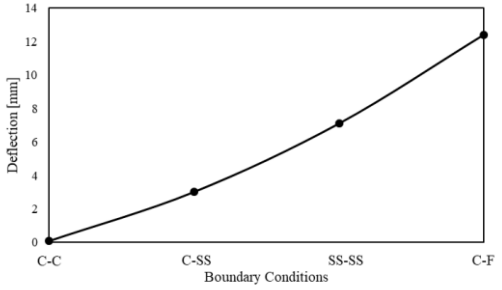

(a) Variation of displacement with boundary conditions

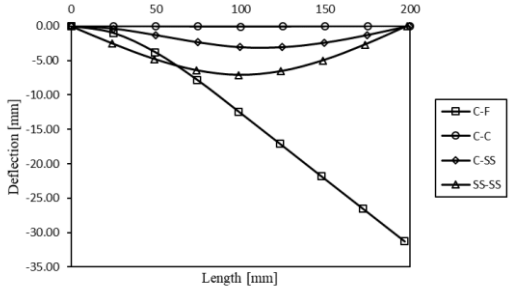

(b) Large displacement profiles of the beam

Figure 14. Effect of boundary conditions

From Figures 14(a) and (b), one can observe the changes in large displacement at the midpoint of the beam and the corresponding large displacement profiles across various boundary conditions. It is seen from the figures that, the beam with C-F boundary condition exhibits the maximum displacement at its midpoint. It can be also seen from Figure 14(b) that the displacement after the midpoint of the beam with the C-F boundary condition is linear, not curvilinear, as expected. Because the force is applied at the midpoint of the beam. It can be seen from Figure 14(a) that displacement increases gradually as the boundary condition changes from C-C to C-F.

6. CONCLUSION

This study aims to examine the large displacement behavior of a FG beam with a variable cross-section subjected to uniform thermal loading. The following results are obtained from the study:

- The displacement at the free end of the beam under the force increases with increasing temperature. But this is relatively small.
- The addition of ceramic powder to the beam material significantly reduces the displacement at the free end of the beam. However, the increase in the volume fraction ratio of ceramic in FGM does not affect the displacement at the free end of the beam too much.
- The displacement at the end of the beam decreases with increasing the beam width. In addition, the displacement at the end of the convex-shaped tapered beam (k=0.5) is more than that of the concave-shaped tapered beam (k=2).
- The displacement at the beam's free end increases gradually with increasing slenderness ratio.
- The displacement at the end of the beam increases with increasing force.
- The minimum displacement in the midpoint of the beam is obtained in the beam with the C-C boundary condition.

7. CONFLICT OF INTEREST

Author approve that to the best of their knowledge, there is not any conflict of interest or common interest with an institution/organization or a person that may affect the review process of the paper.

8. AUTHOR CONTRIBUTION

The entire responsibility for the research lies with Ersin Demir, encompassing the acquisition of the theoretical framework through a review of relevant literature, conducting numerical analyses for data collection, ensuring the overall harmony of the text during the writing process, and making corrections and revisions.

9. REFERENCES

Chen L., An integral approach for large deflection cantilever beams. International Journal of Non-Linear Mechanics 45(3), 301-305, 2010.

Davoodinik A.R., Rahimi G.H., Large deflection of flexible tapered functionally graded beam. Acta Mechanica Sinica 27(5), 767-777, 2011.

Demir E., Sayer M., Callioglu M., An approach for predicting longitudinal free vibration of axially functionally graded bar by artificial neural network. Proceedings of the Institution of Mechanical Engineers, Part C: Journal of Mechanical Engineering Science DOI: 10.1177/09544062221141246, 2022.

Gan B.S., Kien N.D., Large Deflection Analysis of Functionally Graded Beams Resting on a Two-Parameter Elastic Foundation. Journal of Asian Architecture and Building Engineering 13(3), 649-656, 2014.

Horibe T., Mori K., Large deflections of tapered cantilever beams made of axially functionally graded material. Mechanical Engineering Journal 5(1), DOI: 10.1299/mej.17-00268, 2018.

Kang Y.A., Li X.F., Large Deflections of a Non-linear Cantilever Functionally Graded Beam, Journal of Reinforced Plastics and Composites, 29(12), 1761-1774, 2010.

Khosravi M., Jani M., Numerical resolution of large deflections in cantilever beams by Bernstein spectral method and a convolution quadrature. International Journal of Nonlinear Analysis and Applications 9(1), 117-127, 2018.

Kimiaeifar A., Domairry G., Mohebpour S.R., Sohouli A.R., Davodi A.G., Analytical Solution for Large Deflections of a Cantilever Beam Under Nonconservative Load Based on Homotopy Analysis Method. Numerical Methods for Partial Differential Equations 27(3), 541-553, 2011.

Kimiaeifar A., Lund E., Thomsen O.T., Series solution for large deflections of a cantilever beam with variable flexural rigidity. Meccanica 47(7), 1787-1796, 2012.

Kimiaeifar A., Tolou N., Barari A., Herder, J.L., Large deflection analysis of cantilever beam under end point and distributed loads. Journal of the Chinese Institute of Engineers 37(4), 438-445, 2014.

Li D.K., Li X.F., Large deflection and rotation of Timoshenko beams with frictional end supports under three-point bending. Comptes Rendus Mecanique 344(8), 556-568, 2019.

Li S.R., Song X., Large thermal deflections of Timoshenko beams under transversely non-uniform temperature rise. Mechanics Research Communications 33(1), 84-92, 2006.

Mien N.D., Gan B.S., Large deflections of tapered functionally graded beams subjected to end forces. Applied Mathematical Modelling 38(11-12), 3054-3066, 2014.

Mohyeddin A., Fereidoon A., An analytical solution for the large deflection problem of Timoshenko beams under three-point bending. International Journal of Mechanical Sciences 78, 135-139, 2014.

Rahimi G.H., Davoodinik A.R., Large Deflection of Functionally Graded Cantilever Flexible Beam with Geometric Non-Linearity: Analytical and Numerical Approaches. Scientia Iranica Transaction B-Mechanical Engineering 17(1), 25-40, 2010.

Shen H.S., Functionally Graded Materials Nonlinear Analysis of Plates and Shells. CRC Press Taylor & Francis Group, Boca Raton, Florida, USA, 2009.

Sitar M., Kosel F., Brojan M., Large deflections of nonlinearly elastic functionally graded composite beams. Archives of Civil and Mechanical Engineering 14(4), 700-709, 2014.

Tari H., Kinzel G.L., Mendelsohn D.A., Cartesian and piecewise parametric large deflection solutions of tip point loaded Euler-Bernoulli cantilever beams. International Journal of Mechanical Sciences 100, 216-225, 2015.

Ünal H., Ermiş K., Demirtaş Ş., Investigation of mechanical and microstructural properties of polyolefin rubber and glass beads filled polypropylene composites. Journal of Materials and Mechatronics: A 3(1), 91-105, 2022.

Yin Y.Z., Wang Y.C., A numerical study of large deflection behaviour of restrained steel beams at elevated temperatures. Journal of Constructional Steel Research 60(7), 1029-1047, 2004.

Zhou P., Liu Y., Liang X.Y., Analytical solutions for large deflections of functionally graded beams based on layer-graded beam model. International Journal of Applied Mechanics 10(9), DOI: 10.1142/S1758825118500989, 2018.

JOURNAL of
MATERIALS and MECHATRONICS:A

e-ISSN 2717-8811
JournalMM, 2023, 4(2), 504-517
https://doi.org/10.55546/jmm.1349825

Araştırma Makalesi / Research Article

Production of Vehicle Brake Lining with Andesite Powder Additives at Different Pressing Pressures and Determination of Their Effects on Braking Performance

Muhammet Ziya GÜVEN[1], Hüseyin BAYRAKÇEKEN[2*], Hicri YAVUZ[3]

[1]MAN Türkiye A.Ş., Ankara, Türkiye,
ORCID ID: https://orcid.org/0009-0002-6359-9893, m.ziya.guven@hotmail.com
[2]Automotive Engineering, Faculty of Technology, Afyon Kocatepe University, Afyon, Türkiye,
ORCID ID: https://orcid.org/0000-0002-1572-4859 , bceken@aku.edu.tr
[3]Department of Engine Vehicles and Transportation Technology, Vocational School of Afyon, Afyon Kocatepe University, Afyon, Türkiye,
ORCID ID: https://orcid.org/0000-0001-8427-5164, hicriyavuz@aku.edu.tr

Geliş/ Received: 25.08.2023; **Kabul / Accepted:** 13.11.2023

ABSTRACT: The purpose of braking systems is to stop or slow down the moving vehicle. Braking is achieved by converting kinetic energy into heat energy due to the friction created by the brake pads. Today, it is common to use disc brake systems on both front and rear wheels. Recently, serious studies have been carried out in different sectors to utilize industrial wastes, and it is aimed at bringing these waste products into the economy. For this purpose, using different materials in the brake pad contents is common. This study aims to utilize the waste powders resulting from the processing of andesite stone. The materials used in the brake pad samples were developed by the hot-pressing method at pressing pressures of 15, 20, 25, 30, 35, and 40 MPa. Friction coefficient, wear rate, density, hardness, and SEM analysis of the samples were performed. As a result of the study, the density and hardness of the lining samples increased with the increase in pressing pressure. The maximum friction coefficient was obtained in the 40 MPa sample, and the minimum wear rate was obtained in the 25 MPa sample. It was determined that the coefficient of friction and wear rate performances of the lining samples meet the desired properties for the lining. Using andesite dust waste material in the brake lining sector will contribute to the environment and economy.

Keywords: Brake Lining, Coefficient of Friction, Wear, Andesite, Vehicle Technology.

*Sorumlu yazar / Corresponding author: bceken@aku.edu.tr

Bu makaleye atıf yapmak için /To cite this article

Güven, M.Z., Bayrakçeken, H., Yavuz, H. (2023). Production of Vehicle Brake Lining with Andesite Powder Additives at Different Pressing Pressures and Determination of Their Effects on Braking Performance. Journal of Materials and Mechatronics: A (JournalMM), 4(2), 504-517.

1. INTRODUCTION

With recent technological developments, vehicle speeds have also increased due to the increase in engine power in vehicles. Vehicles can reach high speeds in a very short time. The system that ensures safe control of the vehicle at these high speeds is the brake system. The essential parts of the brake system are elements such as a pad, disc, caliper and hydraulic, etc. Braking occurs by converting kinetic energy into heat energy. In the brake system, operations such as stopping or slowing down vehicles are carried out by providing friction force between the disk caliper and the brake pad. Today, disc brakes are widely used in vehicles. During braking, friction-induced heat energy is released. This temperature increase adversely affects braking. There are various studies in the literature on lining content, tribological properties, service life, and production parameters to bring braking performance to desired levels. Some studies are given below.

In recent years, there has been much work on alternative friction materials to control friction, reduce the wear rate, and increase braking safety in studies on brake pads (Xiao et al., 2016). In the study by Boz, ceramic-based brake pads were produced at a sintering temperature of 820 °C at a pressure of 350 MPA. The density of the samples decreased as the amount of ceramic increased. The lead used in the content settled into the voids in the lining with the sintering temperature and caused a decrease in the volumetric area of the samples (Boz, 2003). In the study by Kurt and Boz, bronze material was used as a friction regulator. Bronze material increased the density value and contributed to the decrease in wear rate. It was stated that the friction coefficient increased with the amount of tin (Kurt and Boz, 2005). Yawas et al. investigated the effect of using periwinkle instead of asbestos material, which is harmful to health, in brake linings. 125 μm particle size sea shell was used with 35% resin. As a result of the test, it was determined that the desired performance values were met in the friction test with a decrease in wear rate (Yawas et al., 2016). In the study by Timur and Kılıç, a study was carried out to utilize marble wastes in brake pads. Marble powder was used as filler instead of barite. A friction coefficient between 0.30-0.53 was obtained in the samples. As a result, it was stated that marble dust wastes could be used as filler (Timur and Kılıç, 2013). Öktem et al. produced lining specimens with pet coke powder, readily available cheaply. As a result of the experiments, it was reported that pet coke material gave a stabilizing coefficient of friction, and specific wear rates improved (Öktem et al., 2021). In the study conducted by Ünaldı and Kuş, ecological brake pad samples were produced with miscanthus material as reinforcement material. The results obtained, it was stated that density values were affected by the mixing ratio factor while curing time and curing temperature were effective on porosity (Ünaldı and Kuş, 2018). Brake pad specimens were developed by Malak et al. with 5, 10, and 15% carbon fiber material. The maximum friction coefficient was obtained in the 15% carbon fiber sample. In addition, it was stated that carbon fiber can be used in brake pads as an alternative as the density and wear values decrease and surface roughness increases as the carbon fiber ratio increases (Malak et al., 2015). Sugözü et al. prepared three brake lining samples containing 4%, 8%, and 12% of ulexite and borax. The experimental studies determined that the frictional stability increased as the amount of ulexite and borax increased by mass (Sugözü et al., 2018). Başar et al. developed brake lining samples with 4%, 8%, and 12% colemanite and borax additives by hot pressing. They stated that the materials they developed are suitable for lining materials (Başar et al., 2018). Surajo et al. determined the effect of phenolic resin and fly ash on brake linings. As a result of the experiment, they determined that the coefficient of friction decreased with increasing the amount of phenolic resin in the sample content. In contrast, the friction coefficient increased with the amount of fly ash (Suojo et al., 2014). Pujari and Srikiran stated that 0-50% palm kernel, 0-15% Nile rose, and 0-10% wheat powder could be a substitute alternative for asbestos

material. Using the Nile rose to increase the coefficient of friction and wheat powder to reduce the wear rate, and positive contributions were made to the coefficient of friction, noise pollution, and wear rates. It was stated that palm kernel, Nile rose, and wheat powder could be used as a substitute for asbestos (Pujari and Srikiran, 2019). In the study conducted by Yılmaz, in the investigation of the tribological efficiency of fly ash, it was stated that fly ash is generally a waste and can be found in abundance because it is obtained from the burning of coal and can be used as an alternative material in brake linings. According to the experimental results, it was stated that fly ash could be used instead of aluminum powder in the lining content and increases the coefficient of friction (Yılmaz, 2022). The study conducted by Güney and Mutlu aimed to comply with the standard by applying brake system tests according to the vehicles' usage and environmental conditions. TSE 555 and SAE J866 standards are used to determine the brake system's friction coefficient values at the disc/drum and lining interface. Thus, it was stated that the brake system parts evaluated within the framework of the standards directly affect the production methods (Güney and Mutlu, 2015).

The brake pad is one of the essential parts of the brake system used to slow down or stop a moving vehicle. The industry's demand for the brake pad, a part that wears due to friction, is relatively high. Due to the number of manufacturers and differences in demand, product diversity in this sector is increasing daily. Brake pads of varying specifications are preferred according to the vehicle. Nowadays, especially in the direction of utilization of industrial wastes, there are many studies in brake lining and different sectors. In this study, samples with different pressure parameters were developed to contribute to the industry and scientific studies of the waste dust released due to andesite processing, which is used for various purposes, such as interior or exterior building cladding. In the developed samples, microscopic analyses of the worn surfaces and parameters that directly affect braking performance, such as friction coefficient and wear rate, were carried out. Instead of a material taken from nature directly to the production stage, industrial wastes generated by andesite processing were evaluated. Andesite is a material obtained by cooling underground lava above the ground, which has very high strength and can be used as a wear and friction regulator. While preparing the sample contents, care was taken to ensure that the other raw materials in the brake pads were harmless to biological life forms and the environment.

2. MATERIAL METHODS

2.1 Development of the samples

This study developed lining samples by applying the hot-pressing method at different pressure values of 15, 20, 25, 30, 35, and 40 MPa. In the developed samples, phenolic resin 20%, steel fiber 15%, alumina 6%, graphite 3%, cashew powder 6%, calcite 40%, and andesite powder 10% were used as a constant percentage by weight. The products were weighed on a precision balance of 0.001 g and then collected in a mixing container. They were mixed homogeneously in a mechanical mixer for 60 1/min for 15 minutes. In order to proceed to the next step in the production process, hot pressing, the mixture was added to each mold compartment shown in Figure 1.

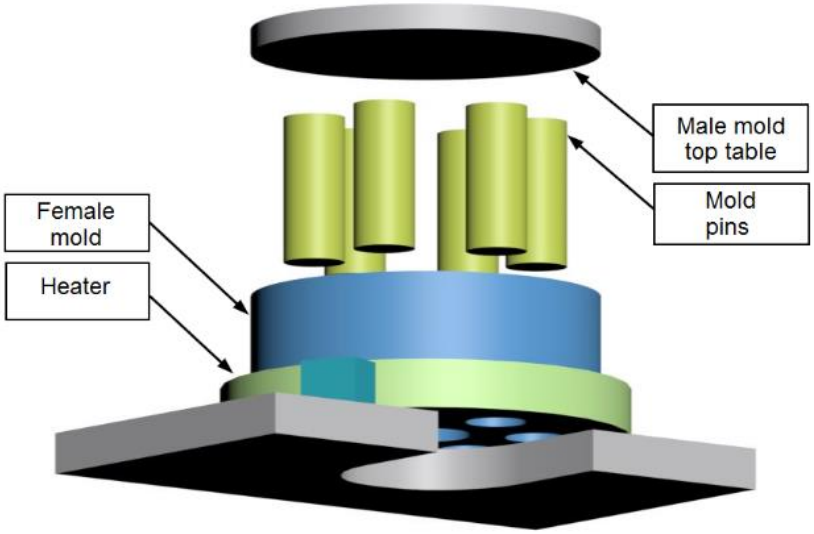

Figure 1. View of mold design.

The materials placed in the mold were shaped at 15, 20, 25, 30, 35, and 40 MPa pressing pressure at 150 °C for the time specified in Figure 2.

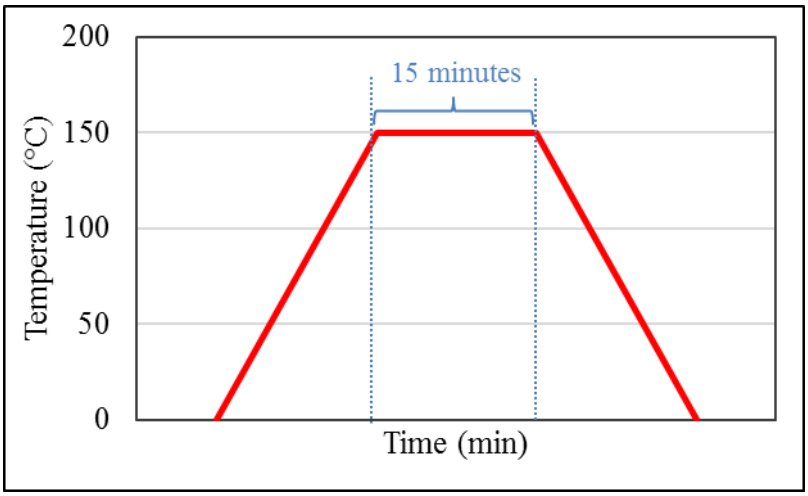

Figure 2. Temperature-duration graph under production conditions.

The production method was developed based on the studies in the literature (Yavuz, 2023; Yavuz and Bayrakceken, 2022). In order to apply an initial pressure value of 15 MPa, the ceramic resistance heater in Figure 1 around the mold was activated until it reached a temperature of 150 °C. A hydraulic press kept the pressure values stable during the heating period. When the mold temperature reached 150 °C, it waited for 15 minutes. The heating process of the resistance was stopped by keeping the pressure constant. The mold temperature was allowed to drop to 75 °C. Brake pad samples were carefully removed from the mold.

2.2 Density and Hardness Measurement

According to Archimedes' principle, density values were calculated according to Equation 1 with a density measurement kit on a precision balance. According to Archimedes' principle, weight measurements of 3 samples in each series were performed in air and water. The density value was obtained by using the average values of the samples whose measurements were completed.

$$\rho_b = \frac{g_h}{g_h - g_s}\rho_s \quad (1)$$

In the above equation;
ρ_b= Density of the lining sample (g/cm^3)
g_h= Weight of the pad sample in air (g)
g_s= Weight of the pad sample in water (g)
ρ_s= Density of pure water (g/cm^3)

Hardness measurements were performed with the Shore D device that is used for composite, resin, and plastic materials in accordance with ASTM D2240 (ASTM D2240-15 2021) standard. The average values of five points on three pad surfaces in each series gave hardness results (Figure 3).

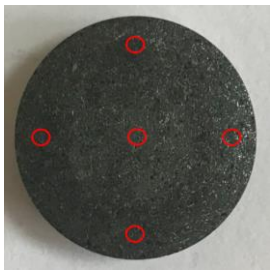

Figure 3. Hardness measurement points.

2.3 Coefficient of friction and wear rate

The specimens were tested by the brake pad tester shown in Figure 4. The brake pad tester uses a vertically positioned electric motor. The brake disc used in vehicles is used in the device, and the brake disc can be moved in the desired speed ranges. Load cells are used for friction force and applied load measurement. The brake pads apply load to the load cells by friction.

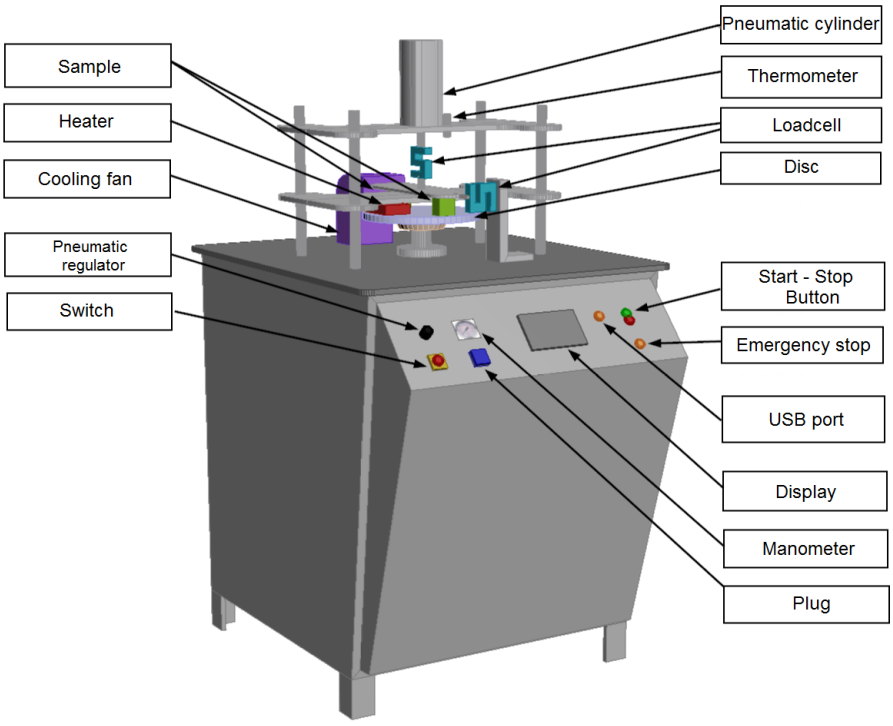

Figure 4. Test device design view.

With the other load cell located between the pneumatic cylinder and the pad samples, the loads applied to the pads were recorded on the control panel. The temperature value formed on the disk surface is recorded with a non-contact thermometer. According to the measurement results, the coefficient of friction was calculated by Equation 2.

$$\mu = \frac{f}{F} \quad (2)$$

In the equation above;
μ: Coefficient of friction
f: Friction force read on a dynamometer
F: Compressive force applied to test specimen

The specimen surfaces were sanded with 320-grit sandpaper, and the specimens were prepared for the test. The brake pad standard states that the sliding speed should be between 6 m/s and 8 m/s, and the compression pressure should be 1 ± 0.02 MPa (*TS555*, 2019). In this study, the disk speed was 6 m/s, and the pressure applied to the specimen was 1 ± 0.02 MPa. In the lining tester, experiments were carried out at a sliding distance of 8 km after a 2.8 km run to acclimatize the specimen surfaces to the disk surface. The coefficient of friction temperature plots were generated to cover the operating period after the break-in run.

Before and after the experiment, the weight of the samples was weighed on a precision balance and was used to calculate the wear rate which was determined according to Equation 3.

$$W_a = \frac{\Delta G}{SMd} \quad (3)$$

In the equation above;
W_a: Wear rate
ΔG: Weight loss
S: Sliding distance
M: Loading weight
d: Density of the abrasion material

2.4 Sem analysis

Before SEM analysis, the sample surfaces were coated with a carbon using a flash coating device. SEM analysis was performed on the LEO brand 1430 VP model scanning electron microscope (SEM) device attached with RÖNTEC QX2 (EDX – Energy Dispersive X-ray Spectroscopy) detector.

3. RESULTS AND DISCUSSION

3.1 Density measurements

Figure 5 shows the density values of the lining samples produced in this study. The densities of the specimens increased proportionally as the molding pressures were increased. The lowest density value in the lining samples was produced under 15 MPa pressure whereas the most dense lining was produced at 40 MPa compaction pressure. With the increase in molding pressure, the distance between the compacted powders is reduced and hence the sizes of the voids between the powders decrease dramatically, therefore, the density of the lining samples increases accordingly.

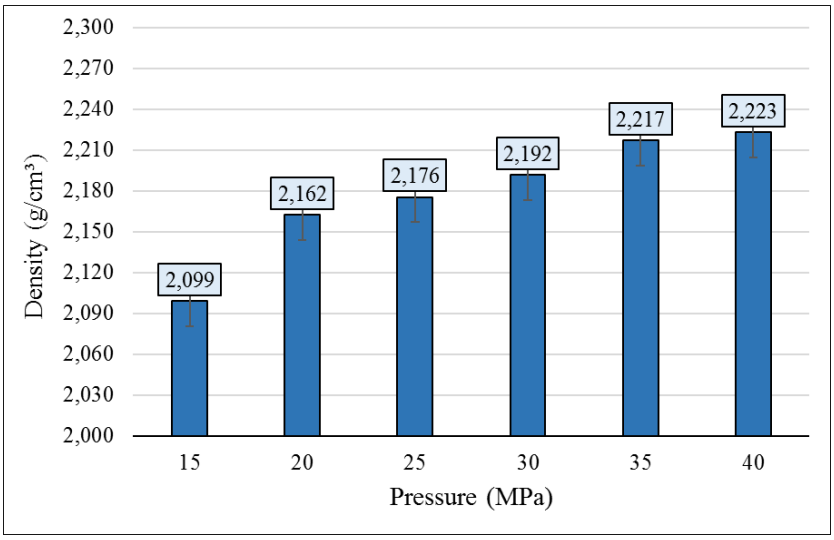

Figure 5. Density values.

3.2 Coefficient of Friction

Friction coefficient graphs and explanations for all specimens are given under this heading. When the graphs are examined, it is determined that the temperature values increase with increasing sliding distance and remain partially constant after the 7000 m sliding distance. This is an expected behavior from friction pairs. This study reached a point where heat equilibrium was reached after almost a 7000 m sliding distance. In the experiments carried out, temperature values were above 100 °C towards the last stage of the experiment. Rising temperature values are an essential variable in friction coefficient performance. In the experiments conducted for all samples, performance was not negatively affected, even at very high temperatures. Figure 6 shows the friction curve of the lining sample produced under 15 MPa pressure. As a result of the experiment, the average coefficient of friction is 0.34, and the maximum temperature of the disc friction surface is 135.9 °C.

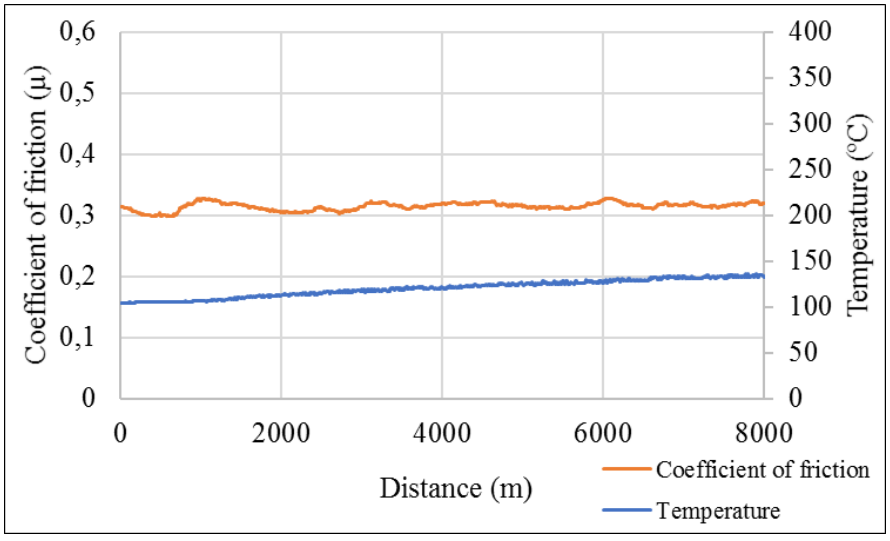

Figure 6. 15 MPa friction coefficient and temperature graph.

Figure 7 shows the friction graph of the lining sample produced under 20 MPa pressure. As a result of the experiment, the average coefficient of friction is 0.34, and the maximum temperature of the disc friction surface is 189.8°C.

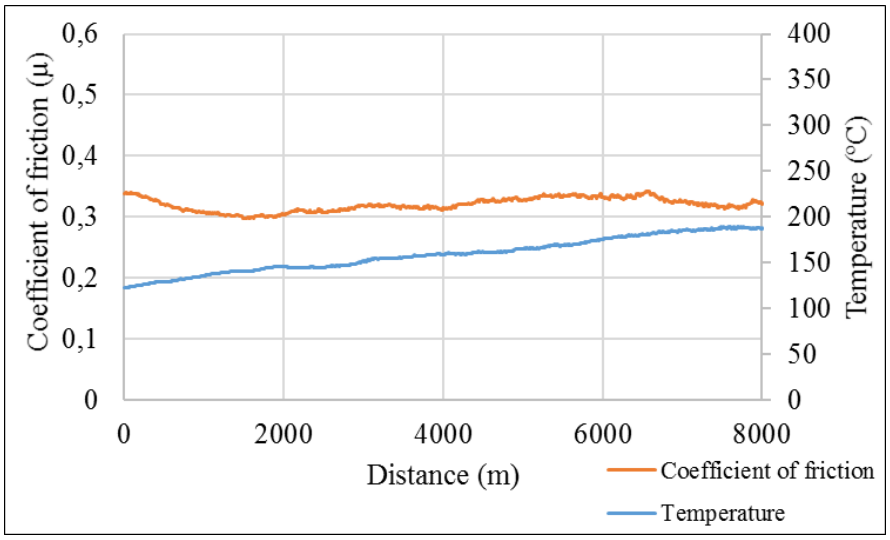

Figure 7. 20 MPa friction coefficient and temperature graph.

Figure 8 shows the friction graph of the lining sample produced under 25 MPa pressure. As a result of the experiment, the average coefficient of friction is 0.35, and the maximum temperature of the disc friction surface is 167.1°C.

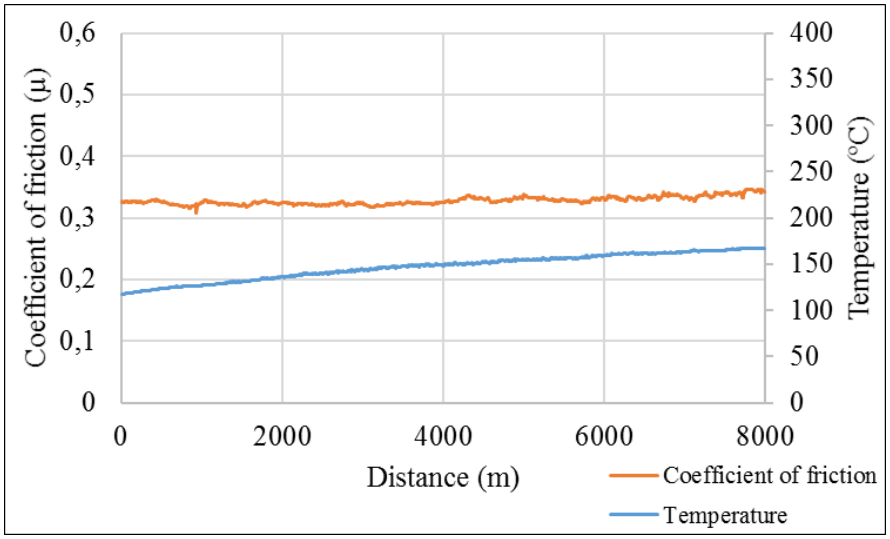

Figure 8. 25 MPa friction coefficient and temperature graph.

The friction graph of the lining sample produced under 30 MPa pressure is shown in Figure 9. As a result of the experiment, the average coefficient of friction is 0.35, and the maximum temperature of the disc friction surface is 189.7°C.

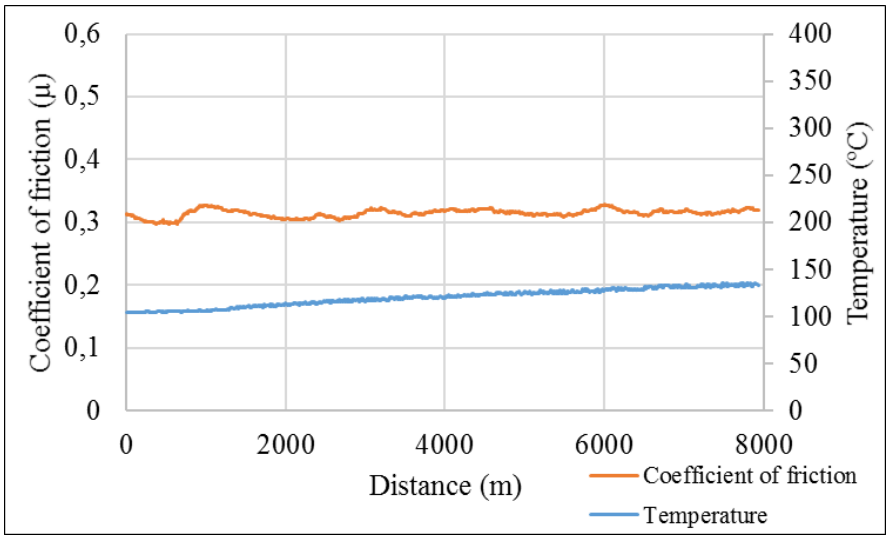

Figure 9. 30 MPa friction coefficient and temperature graph.

Figure 10 shows the friction graph of the lining sample produced under 35 MPa pressure. As a result of the experiment, the average coefficient of friction is 0.33, and the maximum temperature of the disc friction surface is 218.1°C.

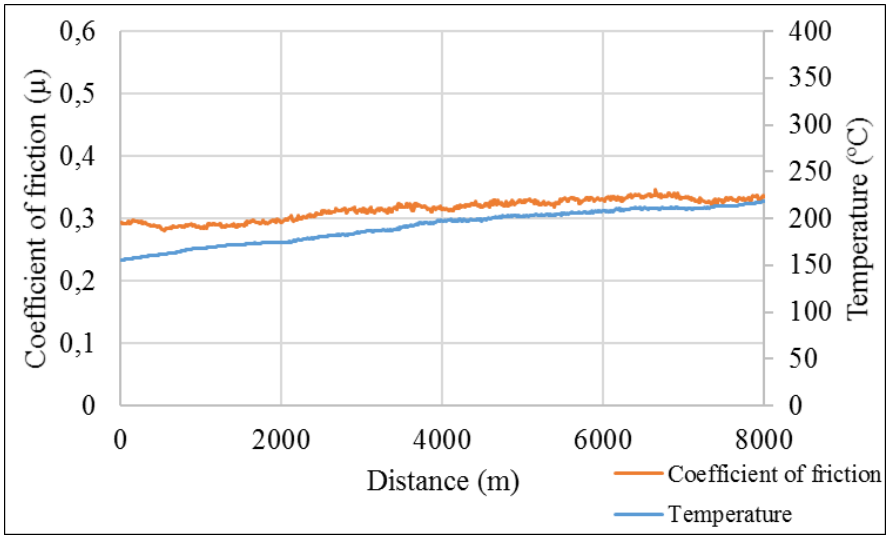

Figure 10. 35 MPa friction coefficient and temperature graph.

Figure 11 shows the friction graph of the lining sample produced under 40 MPa pressure. As a result of the experiment, the average coefficient of friction is 0.37, and the maximum temperature of the disc friction surface is 206.7°C.

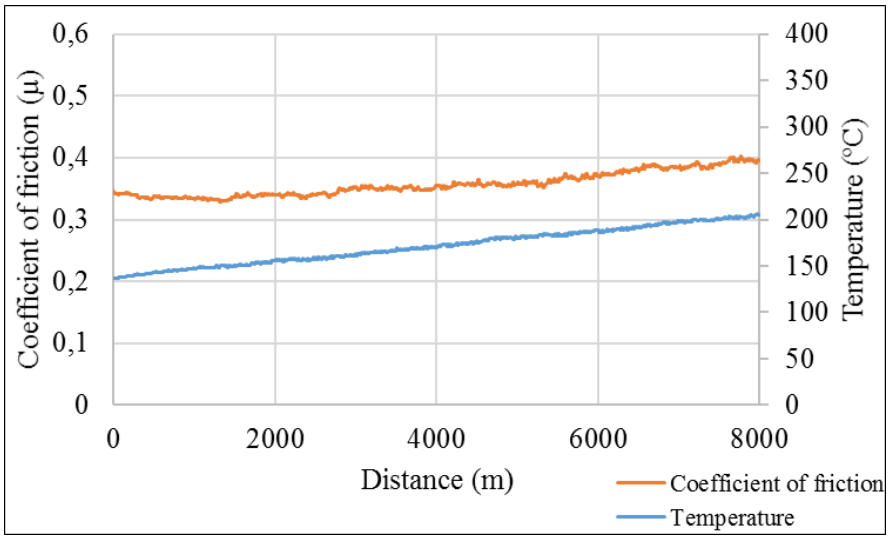

Figure 11. 40 MPa friction coefficient and temperature graph.

Table 1 shows the average coefficient of friction values of the brake pads. The average friction coefficients of the samples between 15-35 MPa varied between 0.33 and 0.35, and the values were very close to each other. The maximum coefficient of friction is desired for brake pads, and the highest value was obtained in the sample produced at 40 MPa. In the brake pad standard (*TS555*, 2019), the friction coefficient range for disc brakes is between 0.20-0.70, depending on the temperature. The coefficient of friction of all specimens is within these values.

Table 1. Average coefficients of friction.

Pressure	15	20	25	30	35	40
Coefficient of friction	0,34	0,34	0,35	0,35	0,33	0,37

3.3 Wear Rates

The wear rates measured in all samples were similar to studies conducted in the literature (Sugözü et al., 2018). The wear phenomenon in brake pads is very complex, and the wear rate values of the developed pads were measured as 0.18 - 0.28 X 10^{-7} cm^3/Nm. According to the brake pad standard (TS555, 2019), the wear rate should be 1X10^{-7} cm^3/Nm at 200°C and 1.5X10^{-7} cm^3/Nm at 250°C. The maximum temperature obtained in the samples varies depending on the coefficient of friction increase and between 135.9 and 218.1 °C. According to brake pad standards, the wear rate values suit brake pads.

Table 2. Wear Rates

Pressure	15	20	25	30	35	40
Wear rate (X$10^{-7}$$cm^3$/Nm)	0,28	0,25	0,18	0,28	0,25	0,24

3.4 Hardness measurements

Shore D hardness measurement values are shown in Figure 12. It is observed that the hardness values of the pads produced under 15 and 40 MPa pressure are close to each other. The sample produced at 40 MPa pressure had the highest hardness value, while the sample produced at 15 MPa pressure had the lowest. As the pressure values increased, the gap between the particles of the

materials forming the specimens decreased, which increased hardness values. Hardness values were similar to studies conducted in the literature (Yavuz and Bayrakceken, 2022).

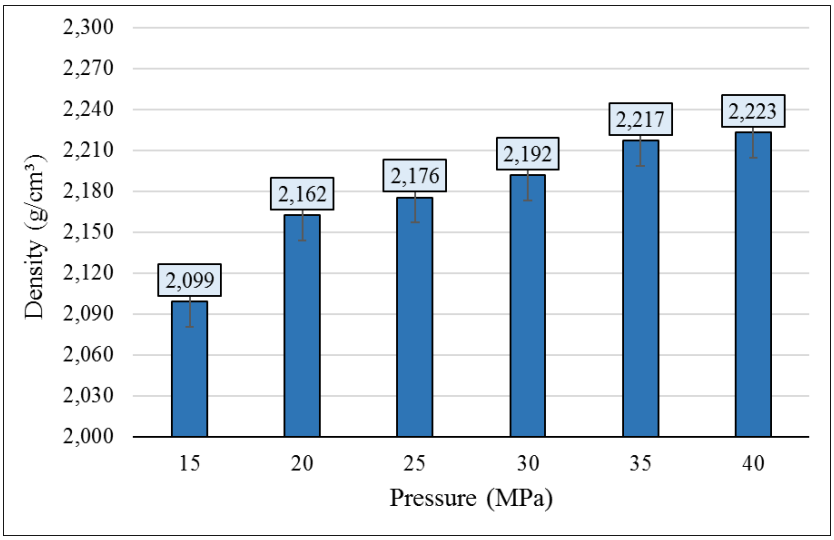

Figure 12. Shore D hardness measurements.

3.5 SEM analysis

When the SEM images obtained on the wear surfaces of the samples as a result of 1000X magnification in Figure 13 are examined, the friction layers formed after the test are identified. It is desirable that the friction layers have a large area in brake pads and the friction surface has a large area in all brake pad samples. The 30 MPa brake pad specimen in Figure 8 shows intense scratches in the friction layer. The intense scratches in this specimen are considered to be caused by abrasive hard particles.

4. CONCLUSIONS

This study prepared a recipe consisting of powdered materials from the processing of andesite stone and other materials that make up the brake pad structure. With these materials forming the samples, lining samples were produced at different pressure parameters of 15, 20, 25, 30, 35, and 40 MPa. The lining samples were analyzed for wear rate, friction coefficient, density, hardness, and SEM analysis. As a result of the measurements and tests, the following results were determined.

- When the post-test density values are examined, the density and pressure values were measured in direct proportion to the lowest 15 MPa and the highest 40 MPa pressure in the lining samples.
- According to the results of hardness values, the average Shore D value was determined as 96.07. According to the samples, the hardness value increased in direct proportion to the increase in production pressure and density.
- A stable coefficient of friction is desirable for braking performance. In all of the samples, a stable situation was observed in the friction coefficient graphs.
- The maximum coefficient of friction was obtained as 0.37 for the 40 MPa sample, and the average friction coefficient for all samples is within the desired limits. Wear rate value differences are close and within the desired values.

In this study, brake lining samples were developed from andesite powder, considered industrial waste, and results were obtained at the desired performance values. Using this material as industrial waste will contribute to recycling and material costs.

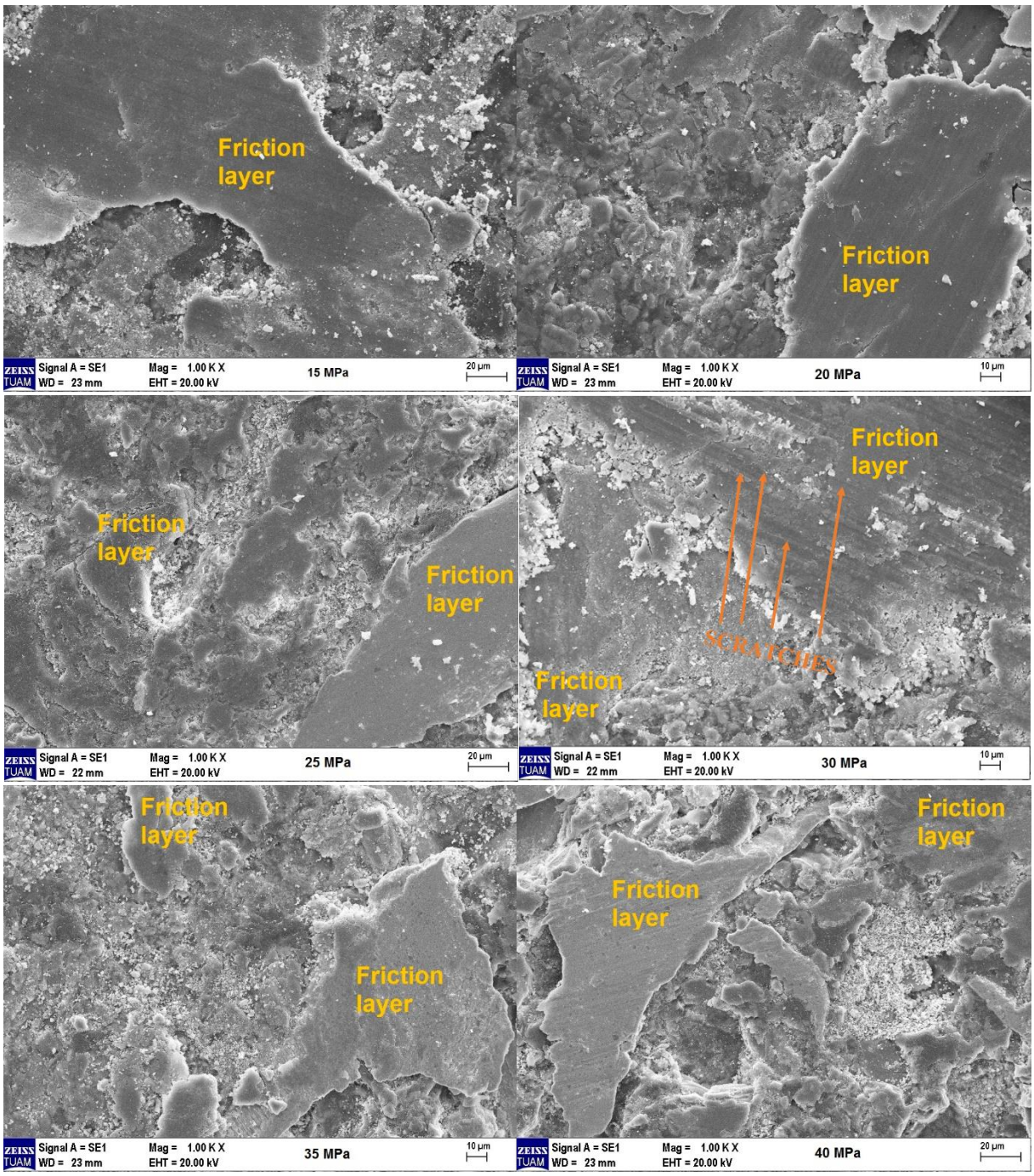

Figure 13. SEM images.

5. ACKNOWLEDGEMENTS

This article was created using the data and graphics from Muhammet Ziya GÜVEN's master's thesis titled "Investigation of pressure change effect in brake lining production" at Afyon Kocatepe University, Institute of Science, Department of Automotive Engineering.

6. CONFLICT OF INTEREST

Authors approve that to the best of their knowledge, there is not any conflict of interest or common interest with an institution/organization or a person that may affect the review process of the paper.

7. AUTHOR CONTRIBUTION

Hüseyin Bayrakçeken, Muhammet Ziya Güven, and Hicri Yavuz contributed to the Determination of the Conceptual Design Processes of the Study, Data Analysis and Interpretation, and the Creation of the Article Draft. In addition, Critical Review of Intellectual Content Hüseyin Bayrakçeken and Hicri Yavuz Data Analysis and Interpretation Muhammet Ziya Güven contributed. Final Approval and Full Responsibility belong to Muhammet Ziya Güven.

8. REFERENCES

ASTM D2240-15. (2021). In standard test method for rubber property-durometer hardness. standard test method for rubber property-durometer hardness. https://www.astm.org/d2240-15r21.html

Başar G., Buldum B. B., Sugözü İ. Friction performance of brake pads reinforced colemanite and borax. El-Cezerî Journal of Science and Engineering, 5(2), 635–644. 2018. www.dergipark.gov.tr

Boz M. Seramik takviyeli bronz esaslı toz metal fren balata üretimi ve sürtünme-aşınma özelliklerinin araştırılması [Doktora tezi]. Gazi Üniversitesi, Fen Bilimleri Enstitüsü. 2003.

Güney B., Mutlu İ. Investigation of vehicle brake testing standards applied in the EU and the USA. Afyon Kocatepe University Journal of Sciences and Engineering, 15, 7–16. 2015. https://doi.org/10.5578/fmbd.8524

Kurt A., Boz M.. Wear behaviour of organic asbestos based and bronze based powder metal brake linings. Materials and Design, 26(8), 717–721. 2005. https://doi.org/10.1016/j.matdes.2004.09.006

Malak A., Mutlu İ., Aysal F. E., Bayrakçeken H., Özgören Y. Ö., Yavuz İ. The effect of carbon fiber additive in automotive friction materials. ISITES2015, Valencia, Spain, 998–1005. 2015.

Öktem H., Akıncıoğlu S., Uygur İ., Akıncıoğlu G. A novel study of hybrid brake pad composites: new formulation, tribological behaviour and characterisation of microstructure. Plastics, Rubber and Composites, 50(5), 249–261. 2021. https://doi.org/10.1080/14658011.2021.1898881

Pujari S., Srikiran S. Experimental investigations on wear properties of Palm kernel reinforced composites for brake pad applications. Defence Technology, 15(3), 295–299. 2019. https://doi.org/10.1016/j.dt.2018.11.006

Sugözü B., Buldum B. B., Sugözü İ. Tribological properties of brake friction materials containing ulexite and borax. Journal of Boron, 3(2), 125–131. 2018. https://doi.org/10.30728/boron.365196

Suojo E., Jamasri J., Malau V., Ilman M. N. Effects of phenolic resin and fly ash on coefficient of friction of brake shoe composite. ARPN Journal of Engineering and Applied Sciences, 9(11), 2234–2240. 2014. www.arpnjournals.com

Timur M., Kılıç H. Marble waste using produced of automotive brake pad of friction coefficient different pad brake pads with comprasion. Pamukkale University Journal of Engineering Sciences, 19(1), 10–14. 2013. https://doi.org/10.5505/pajes.2013.55264

TS555 (555). Road vehicles - Brake linings and pads for friction type brakes. 2019.

Ünaldı M., Kuş R. The determination of the effect of mixture proportions and production parameters on density and porosity features of Miscanthus reinforced brake pads by Taguchi method. International Journal of Automotive Engineering and Technologies, 7(1), 48–57. 2018. http://ijaet.academicpaper.org

Xiao X., Yin Y., Bao J., Lu L., Feng X. Review on the friction and wear of brake materials. Advances in Mechanical Engineering, 8(5), 1–10. 2016. https://doi.org/10.1177/1687814016647300

Yavuz H. Evoluation of blue cupressus arizone cone in automotive brake pad biocomposite. Bioresources, 18(3), 5182–5197. 2023.

Yavuz H., Bayrakceken, H. Friction and wear characteristics of brake friction materials obtained from fiber and huntite blends. Industrial Lubrication and Tribology, 74(7), 844–852. 2022. https://doi.org/10.1108/ILT-03-2022-0079

Yawas D. S., Aku S. Y., Amaren, S. G. Morphology and properties of periwinkle shell asbestos-free brake pad. Journal of King Saud University - Engineering Sciences, 28(1), 103–109. 2016. https://doi.org/10.1016/j.jksues.2013.11.002

Yılmaz A. C. Effects of fly ash introduction on friction and wear characteristics of brake pads. International Journal of Automotive Engineering and Technologies, 11(3), 96–103. 2022. https://doi.org/10.18245/ijaet.1108124

JOURNAL of
MATERIALS and MECHATRONICS:A

e-ISSN 2717-8811
JournalMM, 2023, 4(2), 518-541
https://doi.org/10.55546/jmm.1354113

Araştırma Makalesi / Research Article

Experimental Investigation of Ballistic Performance of Free Particle Armor Systems

Emre AYTAV[1]*, A. Mahir IŞIK[2]

[1]Milli Savunma Üniversitesi, Kara Harp Okulu Dekanlığı, Makine Mühendisliği Bölümü, Ankara, Türkiye,
ORCID ID: https://orcid.org/0000-0003-4296-6703, emreaytav@gmail.com
[2]Milli Savunma Üniversitesi, Kara Harp Okulu Dekanlığı, Makine Mühendisliği Bölümü, Ankara, Türkiye,
ORCID ID: https://orcid.org/0000-0003-2454-5219, bymahir64@gmail.com

Geliş / Received: 01.09.2023; **Kabul / Accepted:** 30.11.2023

ABSTRACT: Recent armor studies generally rely on improving the single-shot capabilities of ceramic armors. In multi-shot studies, ballistics tests assume that there is a certain distribution, so these successive shots were not made from exact same point. With these shots, thus, the armor completely loses its effectiveness. In this study, the ballistic performance of damaged and undamaged free particle armor system in multiple hits from exact same and different points was experimentally investigated. The new armor system, consisting Al2O3 free ceramic balls, tested with 9 mm FMJ and 7.62 mm API ammunition. This armor system prevented perforation in multi-hits from the same point, and the depth of depression in ballistic clay was 9.42 mm and bullet deviation in trajectory was 27 mm. In the shots with dispersion, depression depth was limited to 3.52 mm and deviation increased with each shot. As a result, it has been found that the free particle armor system performs more ballistic efficiency than conventional armors even in the most challenging conditions. The ceramic balls, being more irregularly and densely spaced with each shot, increase the likelihood of the bullet hitting at larger angles and increase ricochet in direct proportion.

Keywords: Ceramic Armor, Al_2O_3, Free Spherical Particles, Terminal Ballistic, Multi-hits, Aramids, Ballistic Clay

*Sorumlu yazar / Corresponding author: emreaytav@gmail.com

Bu makaleye atıf yapmak için /To cite this article

Aytav, E., Işık, A.M. (2023). Experimental Investigation of Ballistic Performance of Free Particle Armor Systems. Journal of Materials and Mechatronics: A (JournalMM), 4(2), 518-541.

1. INTRODUCTION

The requirement for lighter armor materials for the purpose of using in military applications has given increasing value to the use of ceramic armor materials. Ceramic armors have greatly progressed over the decades as the mechanical properties have been optimized along with advancing technology (Crouch, 2016; Hazell, 2015). The seeking for enhancing the ballistic performance/areal density ratio and the need for protective and containment materials that can provide maximum ballistic resistance have led to the development of different armor combinations using ceramics (Bracamonte et al., 2016a). Ceramic armors, having high hardness and compressive strength together with the lightness advantage brought by their low density, have been developed for a high level of bullet resistance. Ceramics offer a great advantage over steel in weight reduction and over all metals in absorbing the impact energy. Therefore, they are considered as one of the most important materials for light armor applications with their high compressive strength, high hardness value and low densities (Gadow and Kern, 2014; Yang and Qiao, 2010).

Of primary importance are ceramic types such as Al_2O_3, B_4C, SiC and ceramic matrix composites (CMC) which are the most preferred and used in ballistic armor applications (Carter and Norton, 2007; Karandikar et al., 2009). Al_2O_3 has the best cost effectiveness among high-performance ceramics due to its easier manufacturing, lower cost, high elastic modulus, high refractoriness and high hardness compared to boron carbide and silicon carbide, which are highly covalent ceramics with high melting temperature (Biçer, 2022). However, Al_2O_3 has lower fracture toughness and flexural strength compared to SiC and B_4C in ballistic performance (Tressler, 2002). In addition, the ballistic performance of the ceramic materials can be improved by adding ceramic fiber to obtain CMCs or by adding tetragonal zirconia particles (Heimann, 2010; Orange et al., 1986).

Swab et al. compared ceramic armor designs with metal-based armor resistant to the same type of ammunition and showed that bullet mass can be significantly reduced using ceramic (Swab et al., 2005). Klement et al. have found that B_4C, Al_2O_3, Si_3N_4, SiC, TiB_2, Si and SiC (SiC – Si) etc. are prominent in ceramics for armor application. (Klement et al., 2008). Dresch et al., on the other hand, compared Al_2O_3, SiC and B_4C in terms of ballistic performance in their research. They reported that Al_2O_3 and B_4C gave similar results in performance against 7.62 mm caliber AP rounds. There is also an relationship between hardness and fracture toughness; They found that hardness causes the bullet to wear and break, while fracture toughness helps the ceramic withstand multiple impacts (Dresch et al., 2021). Both hardness and fracture are important in light armor applications. However, deciding which to improve and maintaining the balance between the two has always been a problem for designers of ceramic armor (Goh et al., 2017). Composite armor systems, which have different armor complications by showing different properties according to different reinforcement materials, are divided into three main groups as metallic reinforced, ceramic reinforced and fiber reinforced according to the type of reinforcement element used (Chi et al., 2013; Zaera and Sánchez-Gálvez, 1998). Fiber-reinforced polymer composites have been found to further reduce the weight of body armor and facilitate personnel movement compared to metallic materials (Guo et al., 2020). Materials with high strength, component integrity and high modulus of elasticity, such as Kevlar, have become a natural candidate for reinforcement material due to their lightweight structure, and have found widespread use in the development of "Soft Armor" armor systems (Cheng et al., 2004; Guo et al., 2021).

The ballistic performance of an armor system is determined by several parameters such as material properties, sample sizes, projectile geometry, projectile velocities and boundary conditions (Grujicic et al., 2012). It is often difficult to optimize these factors simultaneously. Most studies have

generally relied on improving single-shot capabilities of ceramic armors rather than multi-hit performance. (Bhat et al., 2021; Wadley et al., 2013; Yungwirth et al., 2011). When an armor system is hit by a projectile, it easily breaks and fragments beyond the impact area, significantly reducing its multi-hit capability (Guo et al., 2020). One of the most important ways to increase multi-hit ability on is to be able to limit damage within a specific area. Hence, ceramics began to be used as tiles instead of a monoblock design (Medvedovski, 2010a). Nevertheless, in order to further increase the multi-hit performance, Medvedovski conducted tests using Al_2O_3 spherical ceramic particles on the front and inside of the armor and compared the results with a normal Al_2O_3 plate. As a result of this study, he showed that the ceramic spheres, which are stationary in the system, can provide protection against multiple hits (Medvedovski, 2010b). In the study by Zahraee and Sabet in which they compared traditional ceramic armor plate and hybrid armor that ceramic particles were embedded in a polymer matrix, it was reported that while there was no significant difference in ballistic limiting velocities for the two types of ceramic targets at impact, the results were at the same ballistic level for both. On the second impact, plates with ceramic particles showed a significant ballistic performance in terms of higher energy absorption, and it was reported that the armor could be easily repaired thanks to the ability of ceramic embedded plates to be replaced later (Zahraee ve Sabet, 2014). As a result of these developments, the "Free Particle Modular Armor", which is believed to show high performance on multi-hits (IŞIK, 2021). It was inspired by the sandbag and transformed into a more complex ballistic structure by placing free ceramic balls inside it, has been the research subject of this study.

Ballistic testing assumes that there is a certain dispersion in successive shots, so shots do not come from the exact same point. With these shots, the armor largely loses its effectiveness. In this study, an attempt was made to uncover the effect of repeated shots fired from the exact same point, which is rare in the literature, on the ballistic performance of the free particle armor system and its behavior on multiple hits with a specific dispersion. Within this framework, the armor system designed with Al_2O_3 free ceramic balls was tested according to the NIJ-0101.04 Level 2 (9 mm FMJ) and STANAG 4569 Level II (7.62 x 39 mm API BZ) standards, as well as with real-time shots. As a result of the tests, an attempt was made to explain the performance of the armor system with free spherical particles with repeated shots at the same and various points, how it minimizes the energy of the projectile, and the condition of the armor materials after the shots using SEM and optical microscope images.

2. MATERIALS AND METHODS

In the study, shots were fired with 9 mm FMJ rounds to investigate the effects of armor system design factors on ballistic performance, based on the NIJ-0101.04 standard II. protection level. In addition, the performance evaluation was carried out on multi-hit capability based on the penetration depths formed on the ballistic clay at the rear of the armor system. In the experimental setup, a marking was made with the help of the laser, the entry position of the projectiles from the front plate and the exit from the back plate were observed during firing, and the extent of the deflection in bullet trajectory was measured. Al_2O_3 ceramic balls with diameter of 10 mm were used in the armor system. First shots were fired at a thickness of 90 mm, the thickness was reduced until data was obtained on the rear surface of the armor configuration. Having obtained the data at a thickness of 40 mm, the experiments were carried out at this thickness. Using the data recorded on the ballistic clay, the energy absorption and the amount of deflection of the shots fired from the exact same point were studied.

Though, the system's reactions to shots arriving at different points of the same armor system were examined. In addition, additional tests were conducted using ceramic balls with diameter of 6 mm to check if larger diameter bullets that would hit the system were used to check, if there was ball flow from armor through the system would come the deformation of the front cover.

Moreover, the new concept of armor, developed using the example of layered armor systems, was studied and with the increase in the level of protection, the armor-piercing bullet 7.62 mm x39 API BZ according to STANAG 4569 Level II was used in the tests. Shots were fired from 30 m at a speed of 695 m/s and conclusions were drawn about its ballistic performance.

2.1. Alumina Ceramic Balls

The desire to produce ceramic balls with equivalent and homogeneous properties in ceramic products requires the use of more complex systems. One of the techniques currently used is the production of spherical ceramic beads of reproducible size and homogeneous properties using ceramic spherical bead forming equipment (Buaki-Sogo et al., 2013). As shown in Figure 1, the system includes a slurry mixer, slurry transport pump, intravenous tubing for ethanol, multi-nozzle system, nozzle position controller, 700 mm dripping column, metallic filter net, manual valve and collection container. The upper containers contain ceramic slurry and ethanol, which are two liquids.

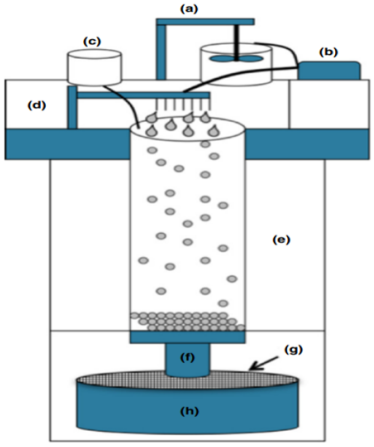

a	Slurry Mixer
b	Slurry Transport Pump
c	Intravenous Tubing for Ethanol
d	Nozzle And Nozzle Position Controller
e	Drip Column
f	Manual Valve
g	Metallic Filter Mesh
h	Collection Cup

Figure 1. Diagram of Ceramic Spherical Bead Forming Equipment (Santos et al., 2013).

In this study, 99% pure Al_2O_3 ceramic balls manufactured by this method and supplied by "Civelek Porcelain" were used. Figure 2 shows the appearance and mechanical values of Al_2O_3 ceramic balls are given.

%99 Al_2O_3 Balls - Hardness (Rockwell 45N): 82 Density (kg/m3): 3,72		
Size (radius) (mm)	**Crush Strength (kg) (min.)**	**Surface Area (m^2/m^3)**
6	105	420
10	200	390

Figure 2. Mechanical Properties of %99 Al_2O_3 Balls

The ceramic balls used in the test procedure are 6 mm and 10 mm in diameter. The reason for choosing the diameters in this way is that the aim of the tests is to use larger and smaller diameter

bullets than the 9mm and 7.62mm bullets. Therefore, it is planned to check whether smaller-diameter bullets flow out of the large-diameter bullet holes formed in the case of deformation in the front plates.

2.2. Armor System Configurations

The armor system, whose frame is formed by welding 20 x 20 mm square steel profiles, has a height of 200 mm, a width of 200 mm and a depth of 90 mm. A review of the literature and examination of the STANAG 4569 Level II one-piece ceramic armor currently on the market shows that their thickness varies between 40 and 50 mm. However, these models are manufactured as a whole. Since the armor model used in this study consists of free spherical particles, its density decreases. In order to be able to draw clearer conclusions when comparing the two armor models, the thickness of the armor model in question was calculated to be the same in density, using the ceramic density per m^3, and the armor thickness was adjusted to 90 mm for the first experiment. An image of the armor system design filled with ceramic bullets is shown in Figure 3.

Figure 3. Armor System Configuration

For the front and back covers of the armor design, Plexiglass® (Acrylic) sheet is used, since it does not require any specific properties except ductility, it is easy to find in the market, it is light and easy to process, and it allows observing the inside of the armor. Polymethyl methacrylate (PMMA), also known by the trade names and brands of Crylux, Plexiglass, Acrylic, Astariglas, Lucite, Perclax and Perspex, is a transparent thermoplastic developed as an alternative to glass with its lightweight and shatter resistant structure, and is generally in sheet form used (Gent, 2009).

Table 1. Mechanical Properties of Acrylic

Parameters	Value
Density (g/cm^3)	1.19
Hardness (Rockwell)	94-105
Tensile Strength (MPa)	75
Compressive Strength (MPa)	110-124

In the study, acrylic sheets were attached using screws through the holes drilled in the steel frame. The mechanical properties of acrylic material are listed in Table 1.

2.3. Experimental Setup

Due to the limited sharing of test setup images performed in CES Advanced Composites and Defense Technologies INC's ballistics laboratory, in accordance with the company's confidentiality

policy, Figure 4 uses equivalent test setup images. The devices and setups in these images match the experimental setups in the laboratory where the experiments were carried out exactly.

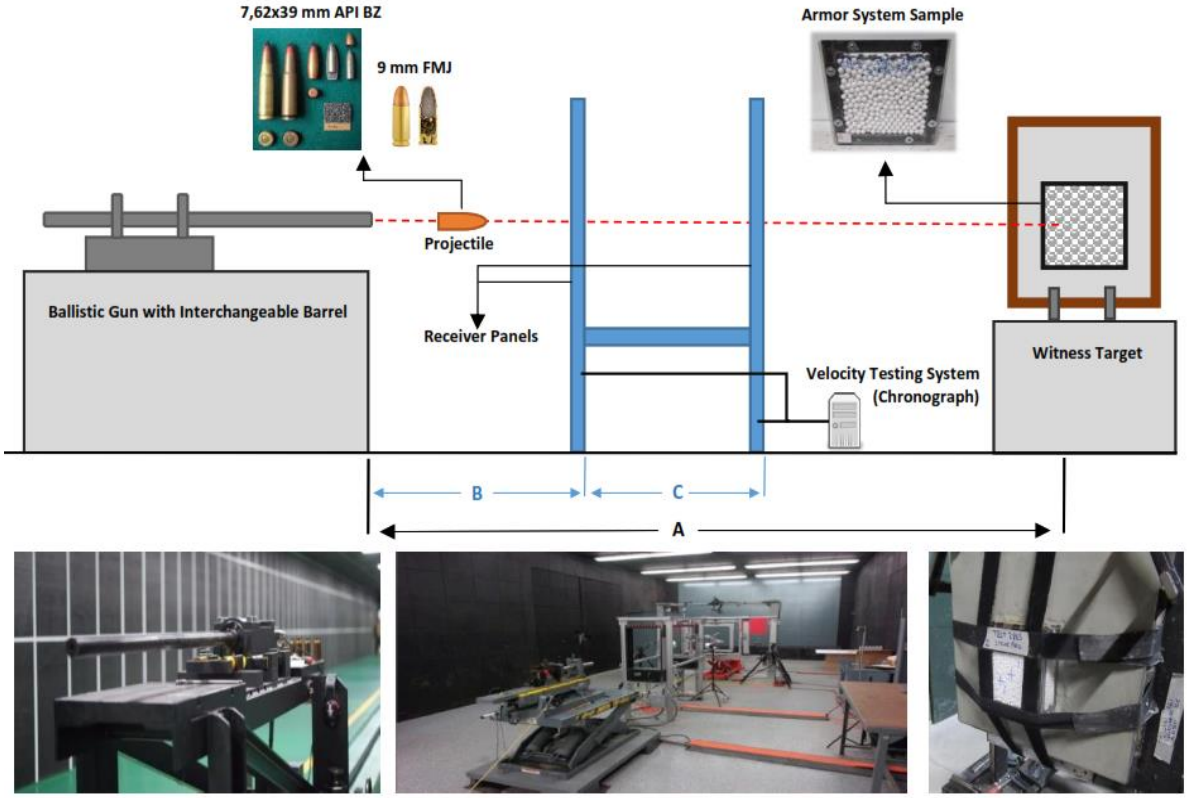

Figure 4. Schematic Illustration of Ballistic Experimental Setup

Different types of bullets are loaded in the fixed barrel shown in Figure 4, and the barrel and bullets are interchanged to achieve different muzzle velocities. In addition, the barrel-to-target distance can be adjusted according to different ballistic testing standards. Bullet velocity is measured between the panels to ensure full calibration during firing. The length A, the distance between the sample and the barrel, is fixed at 5 m for armor levels I, II, II-A and III-A. For level III and IV armors, it is increased to 15 m. The length B, the distance between the barrel and the first receiver, must be fixes at a minimum length of 2 m for armor levels I, II, II-A and III-A, and at least 12 m for armors levels III and IV. Length C, is the distance between the receivers, is adjusted between 0.5 m and 1.5 m.

The speed of the bullet passing the first and last receiver panels is measured by chronographs with each shot. This velocity measurement is made by dividing the distance between the panels by the time between the wave produced by the bullet on the oscilloscope when passing through the first receiving panel and the wave formed when passing through the last receiving panel. If the bullet velocity is not at the desired level, the shot is considered invalid. The distance between the receivers varies depending on different levels. Besides, the receiver panels must be covered with a protective layer due to fragments that will break from the armor and bullet. As can be seen in Figure 4, the sample, which is small in size and difficult to fix, was buried in ballistic clay by opening a pit with armor dimensions and a depth of 50 mm. In addition, the armor system has been tightened in such a way that it remains completely stable during the shootings, by connecting with the Velcro straps used as standard in the experiments. The same procedure was repeated for each sample. The distance between the barrel and the target was fixed at 5 m, the distance between the first receiver and the

barrel to 2 m, and the distance between the receiver panels to 1 m, in accordance with the NIJ 0101.04 level II standard, and the system was made ready for testing.

2.4. Ballistic Clay

During the testing phase, ballistic clay was used to determine the damage to the armor backplate caused by the bullets. In order for the ballistic clay, which is "Sculpture House-Roma Plastilina No:1" and has a gray color, to be ready for use, it must be kept at a temperature of 29 ^{o}C and above for at least 3 hours. Figure 5 provides a visual of the ballistic clay preparation process.

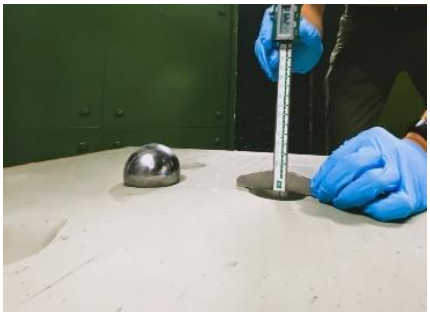

Figure 5. Free Fall Test with Steel Shots and Measurement of Pit Depths

To measure that the ballistic clay is ready for the testing process and can provide stable values, steel balls weighing 1043 ±5 grams and having a diameter of 63.5 ±0.05 mm are dropped onto the clay by free fall (Bozdoğan et al., 2015). From the holes of the 2 m high and previously prepared upper platform, 5 steel balls are dropped onto the clay in free fall and then the arithmetic mean of the depths of the formed pits is determined. If the arithmetic mean is 20 ±3 mm, it is understood that the ballistic clay is ready for the test. Additively, according to the NIJ-0101.04 standard, the net criterion of the level of ballistic protection is that the depth of deformation formed on the clay, taking the human body as an example, and is positioned behind the armor, should be less than 44 mm.

2.5. A Change of Concept Against Armor Piercing Bullet

A layered armor design has been developed to recognize the ballistic protective properties of free-particle ceramic balls against superior ammunition and to minimize the fragmentation and scattering that occurs with explosive ammunition working with the shaped charge principle. Accordingly, the armor system was divided into two parts with aramid fabric and filled with 10 mm Al_2O_3 balls on one side and 6 mm Al_2O_3 ceramic balls on the other. The new concept is schematized in Figure 6.

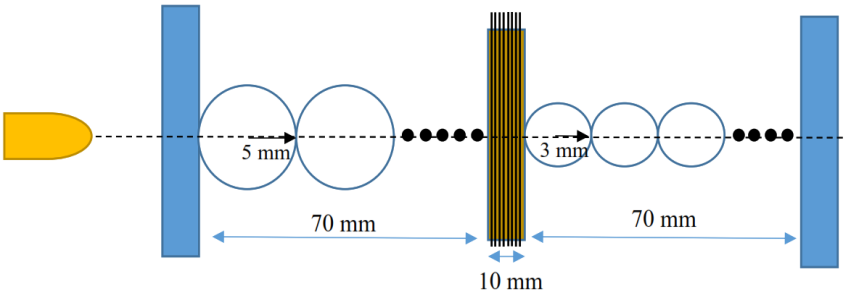

Figure 6. Schematic Illustration of the New Armor Concept

The first part of the armor system encountering the bullet was filled with 10 mm balls and adjusted to 70 mm thickness. A 10 mm thick aramid fiber fabric was then used. The second part of

the armor was adjusted to a thickness of 70 mm and filled with 6 mm diameter ceramic balls. Thus, a new armor concept with an inner thickness of 150 mm was obtained. The purpose of this layered armor system is to increase the level of protection by taking the layered sandwich armor as an example and making a difference in concept. Hereby, two free layers are obtained, the interior of which is filled with balls in a dynamic and free state. It is assumed that the projectile, hitting balls with different diameters, will increase the angle of deflection and dwell time in the armor when it reaches the second part. It is also envisaged that bullet will lose its effectiveness as it penetrates the fabric. The thickness of an aramid (Kevlar®) fabric used as an intermediate layer is about 0.34 mm. A total of 30 layers of aramid fabric were used to achieve a thickness of 10 mm. The mechanical properties of aramid fabric are given in Table 2.

Table 2. Mechanical Properties of Aramid Fabric

Features	Values
Fiber Type	Aramid
Density	1.4 g/cm^3
Tensile Strength	2926 MPa
Elasticity Module	110 GPa
Thermal Degradation	>450 ^{o}C

Along with the increase in the level of protection, the armor-piercing bullet 7.62 mm API BZ was used during the test in accordance with the STANAG 4569 Level II format. The bullet was fired from 30 m at a speed of 695 m/s.

2.6. Types of Ammunition

The tests used 9 mm FMJ 124-gram bullets conforming to NIJ 0101.04 standard level II and 7.62 mm x 39 API BZ bullets conforming to STANAG 4569 standard level 2. While 9 mm FMJ bullets reach a speed of 358 m/s, 7.62 mm x 39 API BZ bullets reach a speed of 695 m/s. Armor-piercing 7.62mm x 39 API BZ bullets consist of a hardened steel core surrounded by a copper jacket, while 9mm FMJ bullets consist of a soft lead core surrounded by a 70% copper and 30% zinc alloy brass jacket.

2.7. Scanning Electron Microscope (SEM)

A Jeol Neoscpae JCM-6000 brand SEM device located in the Mechanical Engineering Laboratory of the National Defense University was used (Figure 7) in this experiment. Even if Al_2O_3 ceramic spheres show fragmentation, they form a denser structure by filling the voids. In addition, these differently shaped pieces increase the irregularity and increase the probability of the bullet deviating from the trajectory in the armor. The shattered bullets were examined with the relevant device and evaluations were made after fragmentation.

Figure 7. Jeol Neoscpae JCM-6000 SEM Device

The images obtained with the device, as well as the crack propagation and surface images seen on the ceramic balls after the shots, were examined and the images obtained are presented in the following section.

2.8. International Test Standards

NATO AEP-55 STANAG 4569 is a NATO Standardization Agreement covering the levels of protection for occupation in logistics and light armored vehicles standards. Standard covers attacks from kinetic energy, artillery and IED explosions (Craig, 2009). In this study, shots were made based on level 2. Table 3 shows the levels of this standard.

Table 3. STANAG 4569 Test Standards

Level	Ammunition	Velocity	Range
1	5.56mm x 45 M193	937 m/s	30 m
1	5.56mm x 45 NATO SS109	900 m/s	30 m
1	7.62mm x 51 NATO	833 m/s	30 m
2	7.62mm x 39 API BZ	695 m/s	30 m
3	7.62mm x 51 AP	930 m/s	30 m
3	7.62mm x 54R B32 API	854 m/s	30 m
4	14.5mm x 114 API/B32	911 m/s	200 m
5	25mm x 137 APDS-T, PMB 073	1258 m/s	500 m

In this study, 9 mm FMJ bullets were fired according to the NIJ 0101.04 level II standard, which is used to evaluate the performance of armor systems, and the shots are set at 5 m. The scope of the standard is limited to ballistic resistance only and does not address different types of threats, such as knives and cutting tools (Craig, 2009). Additionally, these standards must be considered for the use of ballistic clay. Table 4 shows the levels in this standard.

Table 4. NIJ 0101.04 Test Standards

Level	Ammunition	Required Min. Velocity	Max. Deformation
I	38 Special RN Lead	259 m/s	44 mm
I	22 LRHV Lead	320 m/s	44 mm
II-A	357 Magnum JSP	381 m/s	44 mm
II-A	9 mm FMJ	332 m/s	44 mm
II	357 Magnum JSP	425 m/s	44 mm
II	9 mm FMJ	358 m/s	44 mm
III-A	44 Magnum Lead SWC Gas Checked	426 m/s	44 mm
III-A	9 mm FMJ	426 m/s	44 mm
III	7.62 mm (308 Winchester) FMJ	838 m/s	44 mm
IV	30-06 AP	868 m/s	44 mm

3. RESULTS AND DISCUSSION

3.1. Experiments on the Armor System Using Al_2O_3 Balls with a Diameter of 10 mm

In the first test setup, after determining the ballistic limit value as the thickness of the armor system, the goal was to observe the reactions of the armor system and the change in resistance to multiple shots fired on the same armor system through the depressions formed on the ballistic clay. Because of this, the armor thickness was gradually reduced with each shot until the result was

obtained on ballistic clay. 9 mm FMJ bullets were fired at a speed of 358 m/s from a total distance of 5 m, on the armor filled with 10 mm ceramic balls and measuring 200 mm x 200 mm x 90 mm in these tests. The visuals obtained as a result of the test shots are shown in Figure 8.

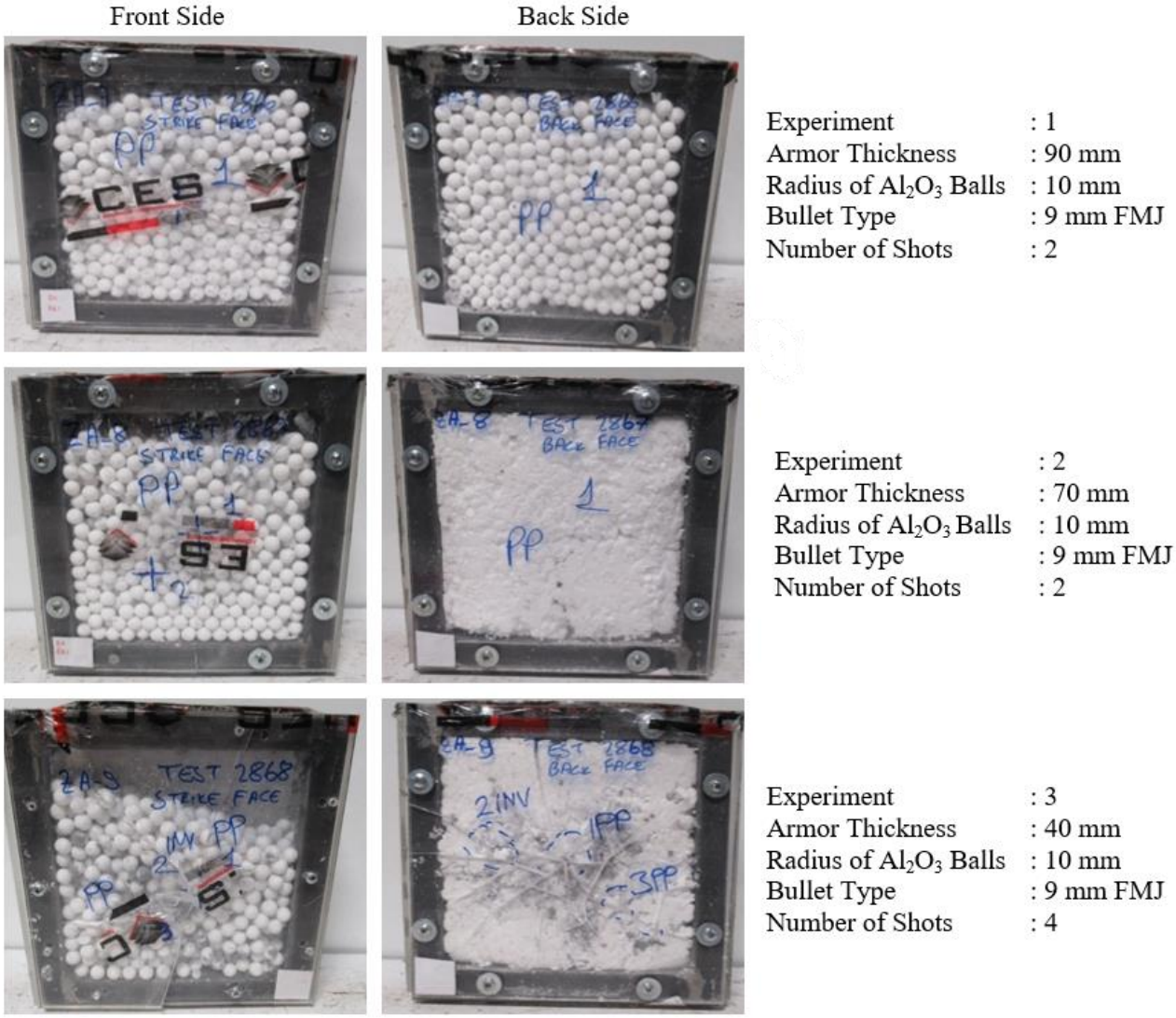

Figure 8. Experiments on the Armor System Using Al_2O_3 Balls

No damage was observed on the back cover as a result of the shots fired in Experiment 1, which used the 90 mm armor system, and no deformation could be observed on the ballistic clay. Therefore, shots were fired by reducing the thickness of the armor system to 70 mm and 40 mm, respectively, by laying Styrofoam (10 and 20 mm thick) in front of the back cover until a depression formed on the ballistic clay. After each decrease in thickness, the front and back covers, as well as Al_2O_3 balls, were replaced with new ones. After any deformation is observed on ballistic clay, Experiment 3 was launched with an armor thickness of 40 mm.

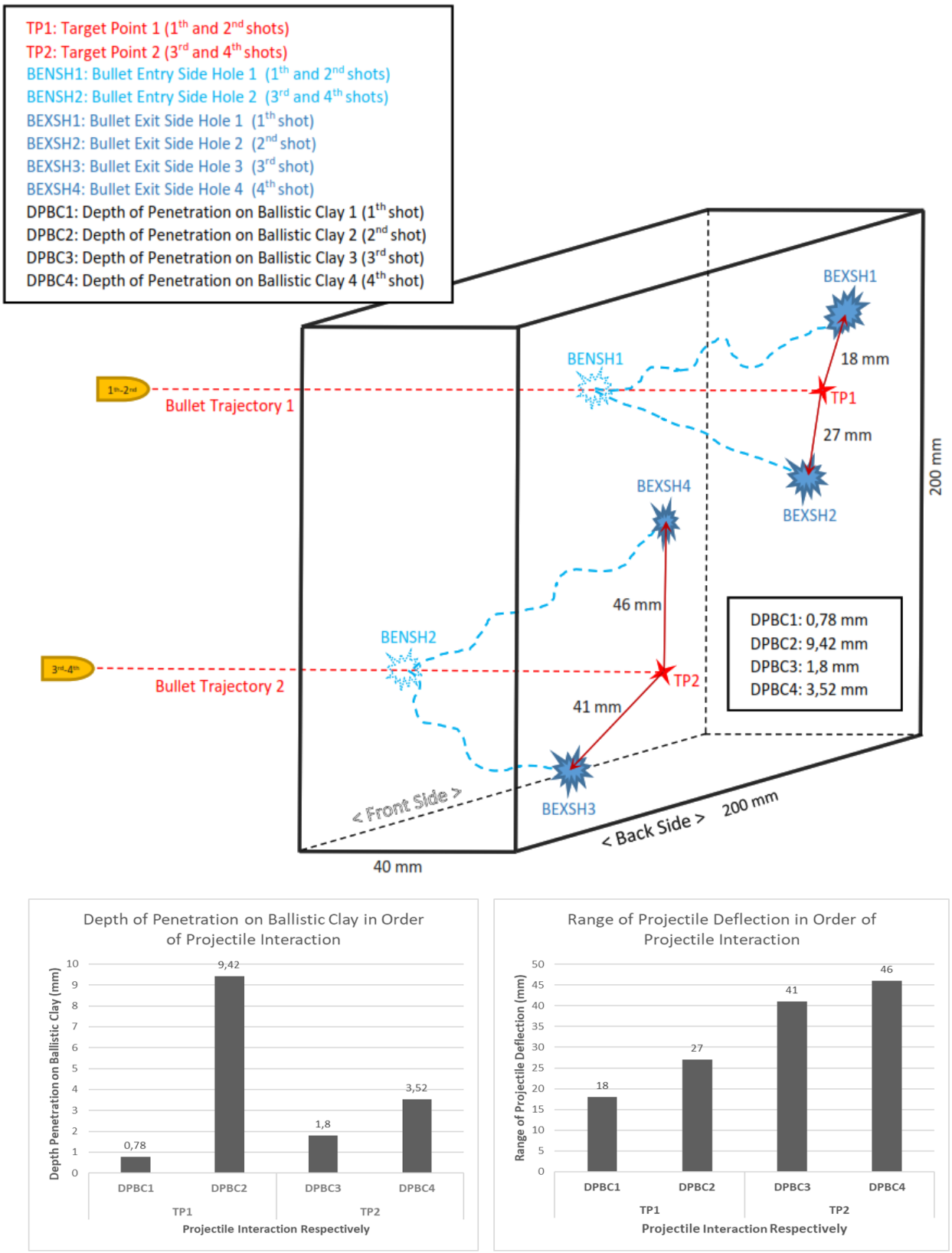

Figure 9. Detail of Experiment 3

In Experiment 3, shown schematically in Figure 9, the back side of the armor was damaged in the 1st shot aimed at the targeted point (TP1), and a small penetration deformation was formed on the ballistic clay. While the bullet entered the armor system from the BENSH1 point and was defeated

within the armor system, it was determined that there was a deviation between the TP1 and the damage caused by the bullet on the back side of the armor system (BEXSH1).

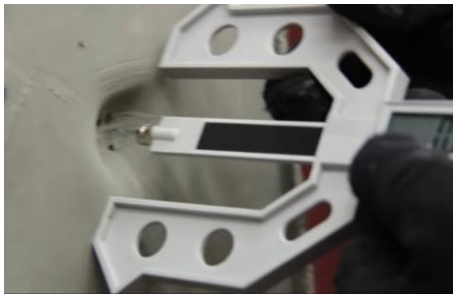

Figure 10. Measuring Depth of Penetration on Ballistic Clay

As a result of the 1st shot, the depth of penetration into the ballistic clay (DPBC1) was measured with a digital depth caliper as seen in Figure 10 and was 0.78 mm. In addition, the deviation between TP1 and BEXSH1 was measured at 18 mm by looking at the red laser pointer, which indicated the projectile motion and the firing point on the armor. After data acquisition on ballistic clay, TP1 was re-targeted, and the 2nd shot was fired. Therewith, while the DPBC2 value was 9.42 mm, the deviation between TP1 and BEXSH2 was found the increase to 27 mm. It is aimed to measure the response of the armor system with these two shots targeted TP1 (multiple shots fired from the same point on the armor system), which do not appear in the literature.

To determine the reaction of the "damaged armor system" in multiple shots from the same point, 3rd and 4th shots were fired at the TP2. The TP2 point is randomly positioned according to international standards, with a distance distribution of 40 mm between it and TP1. Although the depth of penetration was expected to increase as a result of the 3rd shot, it was determined that DPBC3 decreased to 1.8 mm and the amount of deviation between BEXSH3 and TP2 increased to 41 mm. In the 4th shot, where the TP2 was again aimed, the DPBC4 increased slightly to 3.52 mm, while deviation between BEXSH4 and TP2 increased to 46 mm.

Consequently, it is considered that the main reason for the high rate of increase between DPBC1 and DPBC2 is that the balls that first encounter the bullet after firing cannot be filled in exactly the same order by other balls after fragmentation. Because the ceramic balls, which are in a tight order in the first shots, disperse after the interaction and are randomly positioned on the same route with the effect of the deformed particles, reducing the armor density. Thus, it is seen that the depth of depression on the clay increases in shots made from exactly the same point. In the 3rd and 4th shots to the TP2, the depth of penetration DPBC4 increased approximately twice that of DPBC3. It is thought that the reason for obtaining different values from the shots fired at the TP1 is due to the irregular breaks in the balls and the fact that the bullet becomes much more unstable due to the irregular structures formed as a result of spallation.

Previous studies have almost exclusively focused on firing from different points on the armor not exactly the same point. The reason for this is that the bullet distribution seen on the target in a possible conflict is always irregular and the probability of hitting the armor system over exactly the same point is low. In addition, armor systems greatly lose their effectiveness when hit from the same point. In this study, it was observed that from ballistic point of view, the protection of the free particle armor system persists and prevents the formation of the perforation mechanism, even in the conditions where the protection of the free particle armor system is the lowest from exactly the same point. At

the same time, it is believed that it can form a scientific basis in the literature by obtaining original test results from multi hits at the same point.

The deviation increases regularly for all shots fired at TP1 and TP2. If one compares the deviation in the 1st and 2nd shots to TP1, an increase of 50% can be observed. There was also a 50% increase between the 2nd shot in TP1 and the 3rd shot in TP2. An increase in the deviation of 12% was determined for the 4th shot. Although armor performance decreased as expected, it was found that this decrease was not as great as in conventional armors and continued to provide protection. The deviation increased with each shot, so the time it took the bullet to penetrate the armor naturally increased. In conventional metal armors, hydrodynamic behavior is observed in the contact area with the ammunition due to the sudden heat and high pressure, and the armor permeability increases. In addition, mechanical properties change in a certain interaction area after contact. Radial crack propagation, conoid fracture and comminution are observed in monoblock ceramic armors; performance on multi-hits drops significantly. In the armor system of this study, while the hardness of the ceramic armors was exploited, the fragmentation situation was turned from a disadvantage to an advantage. By utilizing the spherical geometry of the ceramic, the movement of the bullet in the armor is deflected and aggravated. Even though Al_2O_3 ceramic spheres exhibits fragmentation, they form a denser structure by filling the voids, similar to the carbon atoms that fill the interatomic spaces in the steel alloy and give steel strength. In addition, differently shaped ceramic pieces increase the irregularity and increase the probability of the bullet deviating from the trajectory in the armor.

Comparing the data obtained with the literature shows that it is seen that they are consistent with the experimental study by Grujicic et al. (2012). This study shows that for 4 shots fired at different locations on the transparent armor, bullet dwell time in the armor increases by about 60% with each shot. In the same study, it was reported that the data from two bullet types fired at 893 m/s and 682 m/s achieved approximately the same rate of increase. Correspondingly, the propagation of cracks and their irregularities in the fragile armor system prolong the dwell time of the bullets in the armor (Grujicic et al., 2012).

3.2. Experiments on the Armor System Using Al_2O_3 Balls with a Diameter of 6 mm

In the second experimental setup, an armor system filled with 6 mm diameter Al_2O_3 ceramic balls was used as a sample. It is aimed to determine whether the balls will flow from the deformation area that will be created on the front plate by bullets with a larger diameter than ceramic balls and to see the reaction of the front plate made of ductile material.

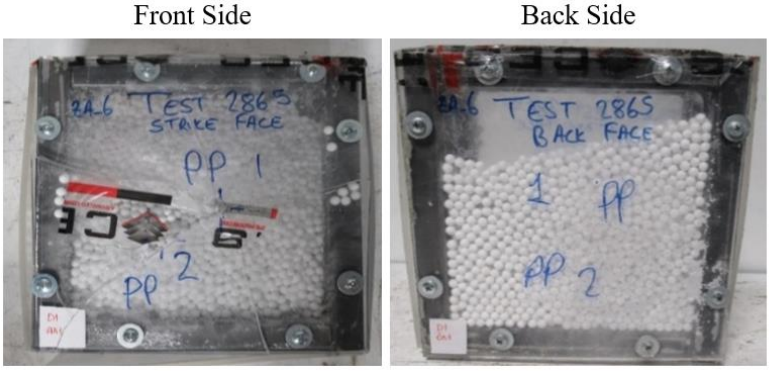

Figure 11. Experiments on the Armor System Using Al_2O_3 Balls

Two shots were fired at 358 m/s with 9 mm FMJ bullets from a distance of 5 m on the armor, which is 200 mm x 200 mm x 90 mm in size and contains 6 mm ceramic balls, as seen in Figure 11.

These shots were made with a dispersion margin of 4 cm between each shot. As a result of the experiment, the armor was not fully penetrated, and no damage occurred on the back cover. In addition, due to the inward bending of the plexiglass plate after the shot, the ceramic balls did not spill through the holes drilled on the plates and the armor continued to protect effectively. Hereby, it is also evaluated that the surface roughness of the ceramic balls is high and thus it is difficult to slide and move between the balls.

3.3. Ballistic Behavior of Free Particle and Layered Armor against Armor Piercing Bullet

In the experiment on the new armor concept with an internal thickness of 150 mm, armor-piercing 7.62 mm API BZ bullets according to STANAG 4569 Level II format were used. The shots were fired at a speed of 695 m/s from a distance of 30 m. The first part of the armor system to resist the bullet was filled with 10 mm balls and adjusted to 70 mm thickness. A 10 mm thick aramid fiber fabric was then used. The second part of the armor was adjusted to thickness 70 mm and filled with 6 mm diameter ceramic balls. This resulted in a new armor concept with an internal thickness of 150 mm. The changes in the armor system after firing are shown in Figure 12.

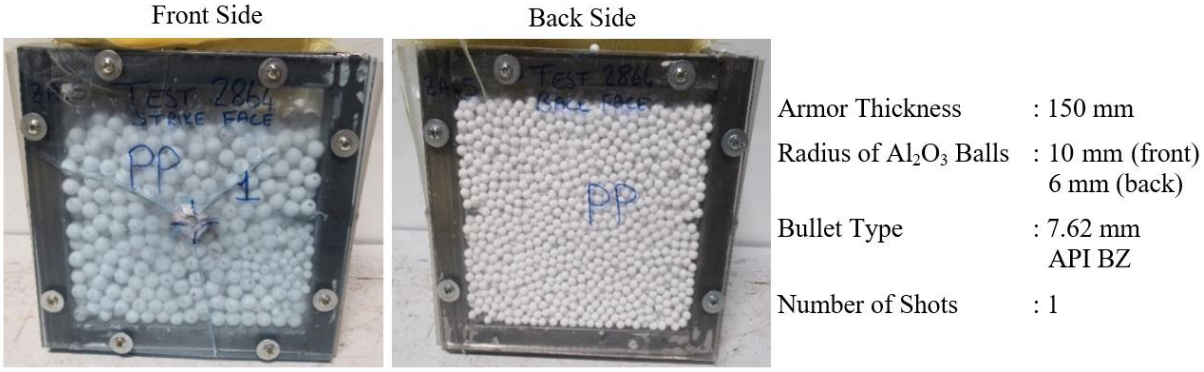

Figure 12. Deformation of Front and Back Covers After Shooting

As a result of the experiment, it was found that the bullet, which could not pass the first layer of 70 mm thickness, was mostly defeated within the first layer (containing 10 mm balls). It was observed that the last part of the energy remaining on the bullet reached the aramid fiber fabric, and the bullet fragments hit the first 5 layers of the aramid fabric and were completely stopped. No deformation or traces of contact were found in the 6th layer of the aramid fiber fabric. No matter how ballistic effective the aramid fabric was, due to its soft structure, it flexed inward at the end of the first shot and led to a deterioration in the armor system's structure. For this reason, further recordings were not carried out because stable results could not be obtained. The images and amounts of deformation obtained as a result of the examination made by separating the layers of the subject aramid fiber fabric are shown in Figure 13.

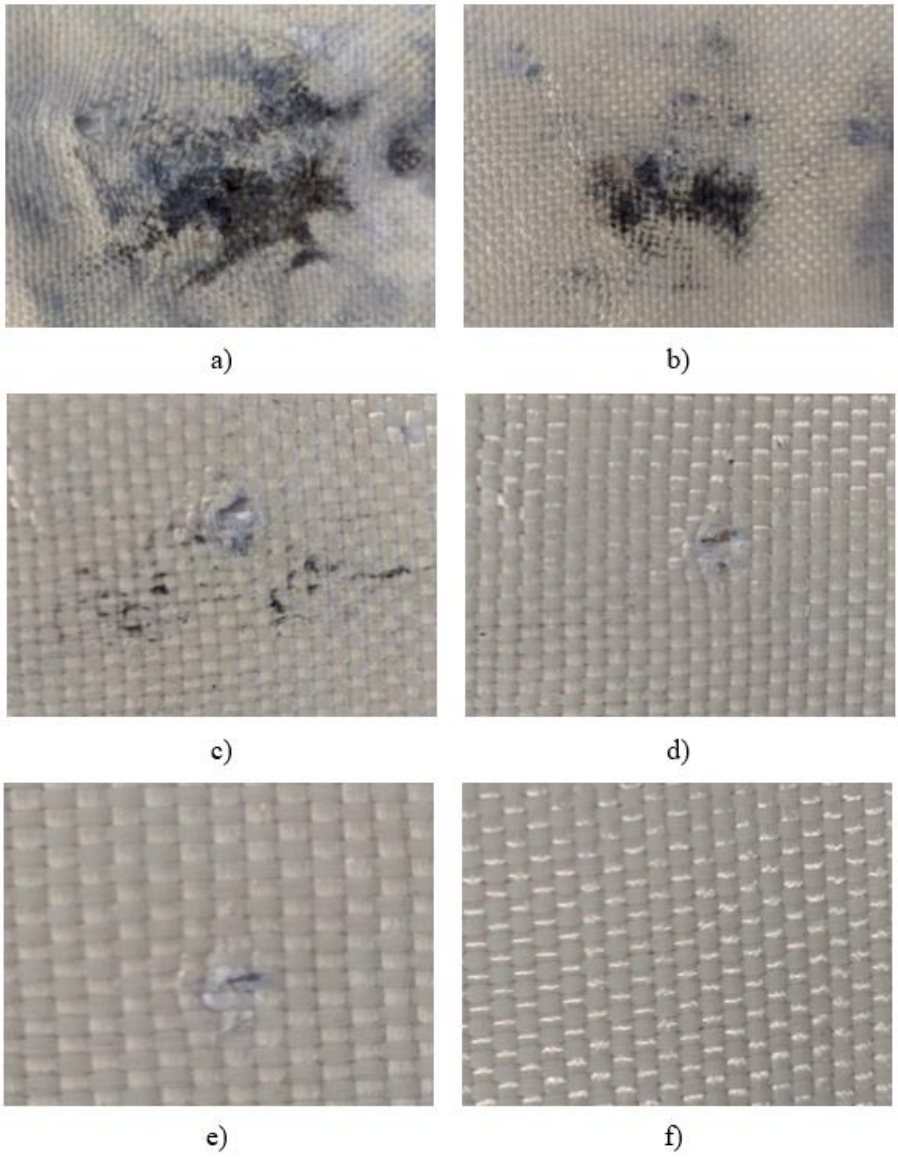

Figure 13. Aramid Fiber a) Layer 1 b) Layer 2 c) Layer 3 d) Layer 4 e) Layer 5 f) Layer 6

Figure 13 shows that the first layer is irregularly deformed. It is believed that the main reason for the deterioration of this irregular deformation in several places is that the armor-piercing bullet, which began to disintegrate by absorbing its energy in the armor, loses its integrity and impacts the aramid fabric from different points in the form of smaller particles. It can be seen that the similar penetration mechanism, albeit decreasing, also occurs in the aramid fabric layers in b and c. It was observed that the majority of the armor piercing bullet fragments were repelled in the first three layers of the aramid fiber fabric, and only attempted to penetrate as a single particle in the fourth and fifth fabric layers. It was found that the damping is completed with the tearing of the fibers in the fifth layer, which is seen in minimal size.

As can be seen, the energy of the armor-piercing bullet, which does not fully penetrate the layers, is absorbed, and prevented from entering to the second part of the armor system. Aramid fabric with a high modulus of elasticity also overlaps with the study by Guo et al. [19]. Accordingly, thanks to this property, aramid fabric, which has a high modulus of elasticity, greatly absorbs the energy of the bullet at the moment of interaction with the bullet.

Aramid fabric deforms vertically and horizontally under ballistic impact. If the bullet velocity stays within the ballistic limits of the aramid fabric, the deformation in the fabric propagates outward. When the bullet velocity exceeds the ballistic limit, the bullet perforates the fabric (Karahan et al., 2008). The layers of aramid fabric have a limited energy absorption capacity. The propagation speed of the shock wave formed in the ballistic plane during the ballistic interaction is related to the energy absorbing ability of the fabric layers. The ability of the fabric layers to absorb energy and prevent the propagation of shock waves depends on the tensile modulus of the fibers and yarns.

The aramid fabric used in the study was flexed inward after interaction, which degraded the configuration of the armor system. In future studies, it is evaluated that using harder materials such as carbon fiber blocks instead of aramid fabric will make free particle ceramic balls more stable. Thus, the damaged blocks can be easily replaced later, and their shape will not be deformed during the shots, which will ensure the protection of the layered structure of the armor.

3.4. Investigation of Ceramic Ball and Bullet Deformation

Structural changes in the ceramic balls as a result of the tests were examined. Accordingly, it has been observed that ceramics, depending on the different deflection angles of projectile, fractionate in different forms and lose their integrity. The images obtained as a result of the collecting and examining of the parts are given in Figure 14.

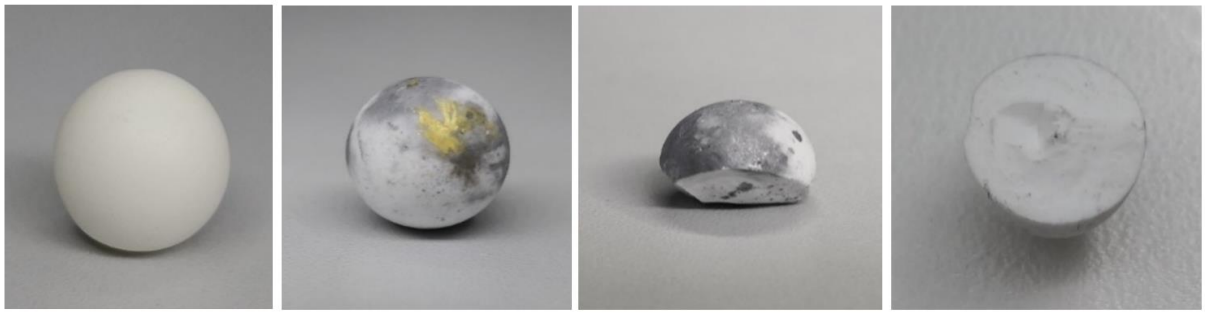

Figure 14. a) Undamaged Ceramic Ball b) Non-Fractured Ball Smeared on its Surface c) Fractured Ball d) Broken Ball (Inner surface)

The high temperature created by the high-velocity interaction of the bullet cores with the armor particles causes the core to exhibit hydrodynamic behavior. Because of this hydrodynamic behavior, it was observed that the bullet core material was plastered on the surface of the ceramic balls and this plastering/smearing occurred in almost all the balls in contact with the bullet. It is expected that the energy of the penetrator mass is not only absorbed by the fracture seen in the ceramic balls, but that some of the energy may also be absorbed due to the mass reduction with this plastering process. The fact that this plastering event affected a large number of balls was considered as an indicator of the distribution of the bullets hitting at different angles by liquefaction from the interstices of the ceramic balls and dispersed to different points. SEM and optical microscope images of damaged ceramic balls are shown in Figure 15.

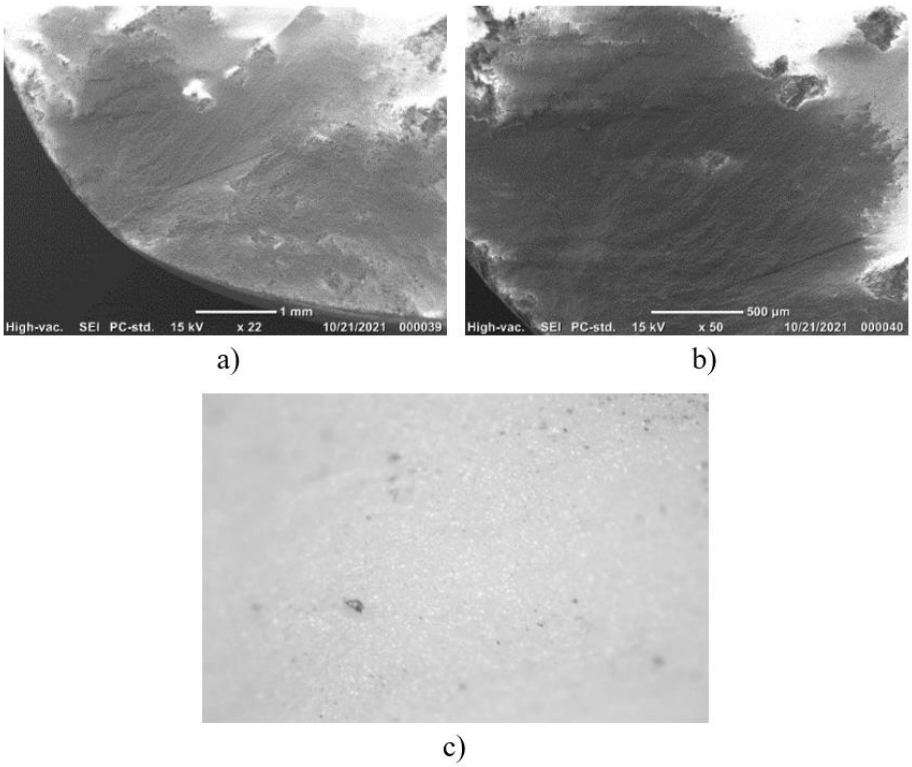

Figure 15. Ceramic Surface with Radial Crack (SEM) b) Ceramic Surface with Radial Crack (SEM) c) Ceramic Surface with Radial Crack (Optical Microscope)

Ceramic balls that interacted with the bullet generally showed a regular crack path in two dimensions, starting from the point of interaction, resulting in well-shaped ceramic fractures. Radial cracks running in the direction of the bullet cut the ceramic balls by a plane. As cab be seen in Figure 15 parts a and b, almost crack-free surfaces were obtained. Thus, these cleanly formed ceramic parts demonstrate that they can continue to provide protection against multiple hits, allowing for longer-term protection than expected.

There have been numerous studies to investigate the continuation of protection of ceramic pieces that have broken and disintegrated. In their study, Goh et al. covered the Al_2O_3 ceramic plate with AISI 4340 steel from all sides. Even when the covered ceramic plate exhibited fragmentation and comminution from multiple hits, it continued to provide protection as it was confined to a specific area (Goh et al., 2019). Bracamonte et al. found in their study that the protection of an environmentally covered ceramic plate remained almost constant in multiple hits. They explained that the main reason for this is that, there is no loss in ballistic performance after interaction by preventing the covered ceramic plates from disintegrating (Bracamonte et al., 2016b).

As a result of the tests, an attempt was made to evaluate the deformation characteristics of the ammunition after interaction. Accordingly, images of deformed bullets (9 mm FMJ and armor-piercing 7.62 mm API BZ) and their finds are sown in Figure 16.

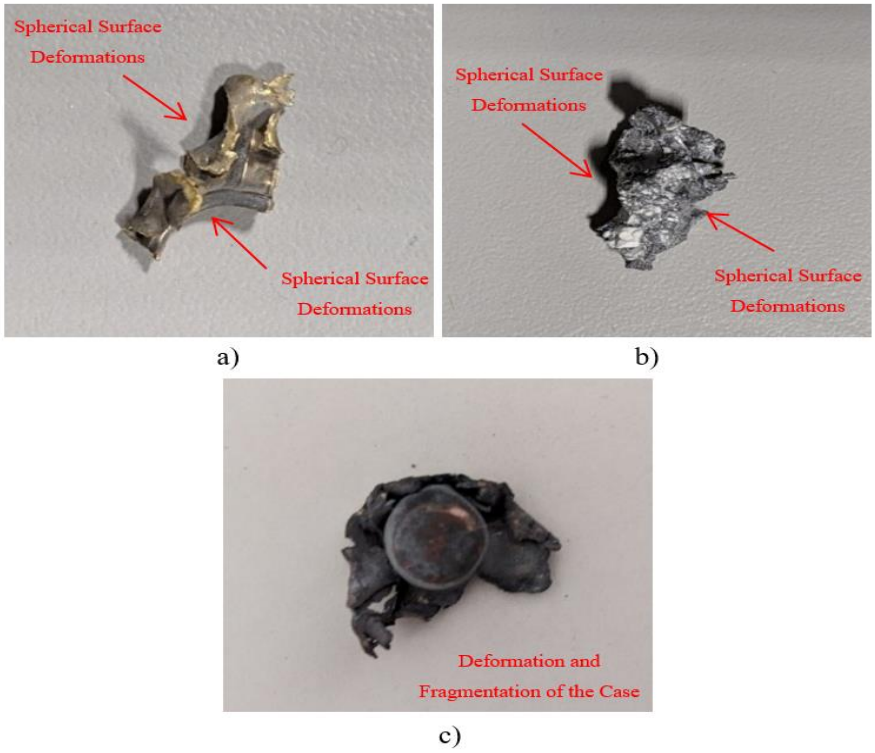

Figure 16. a) 9 mm Bullet Core Outer Shell (Jacket) b) 7.62 Bullet Inner Core c) 7.62 Bullet Outer Shell (Jacket)

As can be seen in the figure, all types of ammunition have their inner core and outer casing separated and fragmented. It has been observed that the ammunition cores lose mass by plastering on ceramic surfaces due to the thermal effect created by the high pressure and the resulting collision energy. Spherical tracks are observed to form in the core that have been deformed by hitting more than one spherical surface (Figure 16).

In his study, Helliker says that jacketed bullets like the 9mm FMJ and 7.62mm API exhibit deformation when interacting with the target. Accordingly, the amount of deformation increases according to the deceleration of the bullet seen in the target armor. The possibility of deformation and fragmentation increases with the effect of rapid deceleration, in the high hardness materials. He also explains that with the deformation of the bullet, extrusion can occur along the bullet shell and often the inner core can be thrown out by splitting of the jacket (Helliker, 2016). In the images obtained as a result of the experiments, it is judged that a same mechanism, seen in the previous studies, occurs and that the processes of same penetration and deformation occur.

3.5. Comparison of Mass Efficiency of Free Particle Armor System with Conventional Armor Systems

The fact that armor systems do not have sufficient hardness and metal-structured armors in particular behave like a liquid by exhibiting hydrodynamic characteristics under high temperature and pressure, allowing high-temperature airflow to pass through the armor with the bullet, and having a high weight due to high density create weakness. In Table 5, a comparison of conventional armor systems is made based on the density/volume/mass values of the free particle armor system.

Table 5. Mass Comparison of Conventional Armor Systems (MIL-A-12560:H "Armor Plate, Steel, Wrought, Homogeneous (For Use in Combat-Vehicles and for Ammunition Testing)", 2009; Patnaik, 2002)

Material	**Density**	**Volume**	**Mass**
MIL-A-12560 Armor Steel	7.8 g/cm^3	1600 cm^3	12.48 kg
Aluminum Plate (5083)	2.56 g/cm^3	1600 cm^3	4.096 kg
Al_2O_3 Ceramic Plate	3.72 g/cm^3	1600 cm^3	5.952 kg
Al_2O_3 Free Particle Armor System (*Ball Diameter: 10 mm, Armor Frame Weight Not Included*)	3.72 g/cm^3	1600 cm^3	2.3-2.9 kg

Metal armors are widely used in vehicle armors owing to their ready availability and machinability. However, when the density factor comes into play, it boasts higher weight ratings compared to its alternatives. Comparing the masses of armor systems in the same volume in Table 5, an average armor steel reaches about 3 times the weight of aluminum plates, while it corresponds to about 2 times that of Al_2O_3 ceramic plates. Although aluminum plates are preferred due to their lightness, they have inferior mechanical and ballistic properties. This situation causes it to lose its effectiveness especially against kinetic energy ammunition. Metal-based armors such as steel and aluminum can exhibit different ballistic behaviors under different conditions. These are brittle fracture, ductile hole enlargement, radial cracking, plugging, fragmentation and petalling (Backman, 1976). This behavior of metal armor under different conditions affects a specific area and causes a significant reduction in ballistic performance in multiple shots, especially getting into this area.

Ceramic, on the other hand, shows effective performance against kinetic energy ammunition due to its high hardness. These brittle materials absorb a large part of projectile's energy as the crack propagation. The fracture mechanism of ceramics under impact shows different physical properties compared to other armor steel materials due to the brittleness caused by the hardness of the ceramics. Particularly, comminution, fragmentation and many cracks cause the need to be supported by other materials (Swab et al., 2005).

Although ceramic plates are almost 50% lighter compared to armor steels, they are 31% heavier than aluminum plates. In terms of ballistic performance, they offer better protection than other type of armors. Nevertheless, it can be clearly seen that the weight of Al_2O_3 ceramics, which is very preferred in armor systems, is high enough even with small volumes such as 1600 cm^3. This situation increases the need to research various armor designs, including body armor. Thanks to the free-particle armor system with the advantages of the design, almost the same performance is achieved with particles with the same hardness as the ceramic plate, with up to 50% lower weights, and there is no performance loss with multiple shots. The design offers comfort to the user due to its wide range of use and modularity.

4. CONCLUSION

In this study, the ballistic performance of the free particle modular armor system was investigated. Findings obtained as a result of the experimental study are presented below;

- Ballistics tests assumes that there is a certain distribution in successive shots, so shots are not made from exactly the same point. With these shots, thus, the armor completely loses its

effectiveness. In this study, in contrast to recent studies, it has been revealed that the armor system maintains its protection even though the ballistic performance decreases in multiple hits from exact the same point. In addition, it was noted that when moving through the armor system, the bullet deviated from its trajectory in these multiple shots fired at the same and different points. It was observed that the ceramic balls placed in a certain order before the test, the damaged ball particles during the shots were gathered in a more dispersed order each time with the effect of the energy from the bullet, and the armor system became denser as random-sized small particles filled in the gaps. It has been found that these ceramic balls, being more irregularly and densely spaced with each shot, increase the likelihood of the bullet hitting at larger angles and increase the risk of ricochet in direct proportion, also minimizing the drop in performance by multiple shots. This shows that the ballistic performance of the free particle modular armor system is higher than conventional armor systems.

- Penetration time of an armor is important in increasing ballistic efficiency. Sometimes, to increase the duration, the armor is positioned at an oblique angle, and sometimes the method of increasing the thickness of the armor is applied. The free particle armor system, on the other hand, exploits the spherical nature of the ceramic balls in the armor system without increasing the thickness and therefore the weight, causing the bullet to deviate from its natural axis. Penetration time of the armor thereby increases
- It has been found that even when larger diameter ammunition is used than ceramic balls in the armor system, the ductile cover materials are deformed inward along the bullet interaction area, preventing escape of smaller diameter balls. In addition, since ceramic balls provide sufficient protection, there is no need for ballistic resistance on the front and back cover. Instead of reacting to the bullet, it is desired to pass the bullet as much as possible and not disperse in the meantime.
- It has been revealed that upon impact to high-hardness material at high-velocity, the bullet's core smears on the bullet's surface, significantly reducing the bullet's mass and facilitating energy absorption.
- As a result of the weight comparison, it has been appointed that the free particle armor system is both lighter and outperforms conventional metal-based armors.
- Although the thickness of this armor system affects the level of protection linearly, it tends to disperse and loses its effectiveness against area-of-effect weapons such as Barrett and RPG. For this reason, this vulnerability can be prevented by creating an armor system with 2 or more layers and panels arranged one behind the other. It is believed that the number of layers can be increased to prevent armor spallation, especially against RPG ammunition.

Although further investigations are needed, the present study contributes to a better characterization of free particles which is used in armor systems. Future studies will evaluate that by using harder materials such as carbon fiber blocks instead of aramid fabric, more stable layered armor can be achieved. In addition, the damaged blocks can be easily replaced later, the system is not be disrupted during the interaction, and the disintegration of the armored layered structure will be prevented.

Table 6. List of symbols and abbreviations

Symbol/ Abbreviation	Meaning	Symbol/ Abbreviation	Meaning
Al_2O_3	Alumina	BENSH1	Bullet Entry Side Hole 1
B_4C	Boron Carbide	BEXSH1	Bullet Exit Side Hole 1
SiC	Silicon Carbide	TP1	Target Point 1
ZrO_2	Zirconium Oxide	BENSH2	Bullet Entry Side Hole 2
Si_3N_4	Silicon Nitride	BEXSH2	Bullet Exit Side Hole 2
TiB_2	Titanium Diboride	TP2	Target Point 2
CMC	Ceramic Matrix Composites	DPBC1	Depth of Penetration on Ballistic Clay 1
PMMA	Polimethyl Methacrylate	DPBC2	Depth of Penetration on Ballistic Clay 2
FMJ	Full Metal Jacket	DPBC3	Depth of Penetration on Ballistic Clay 3
API BZ	Armor Piercing Incendiary	DPBC4	Depth of Penetration on Ballistic Clay 4
		SEM	Scanning Electron Microscope

5. ACKNOWLEDGEMENTS

This study is derived from the master's thesis titled "The Effect of Free Particle Modular Armor System Design on Ballistic Performance". We thank CES Advanced Composites and Defense Techonologies INC (Ankara/Turkey) for ballistic testing laboratory facilities.

6. CONFLICT OF INTEREST

Author(s) approve that to the best of their knowledge, there is not any conflict of interest or common interest with an institution/organization or a person that may affect the review process of the paper.

7. AUTHOR CONTRIBUTION

Emre AYTAV contributed to the determination and execution of the conceptual and experimental design processes of the study, the execution of shooting tests in accordance with international standards, the design and writing of the article and the interpretation of the data. Abdullah Mahir IŞIK contributed to the preparation of the samples, execution of the shooting tests, writing of the article and interpretation of the data.

8. REFERENCES

Backman, M. E., Terminal Ballistics, Naval Weapons Center China Lake CA, 1976.

Bhat, A., Naveen, J., Jawaid, M., Norrrahim, M. N. F., Rashedi, A. and Khan, A., Advancement in Fiber Reinforced Polymer, Metal Alloys and Multi-Layered Armour Systems for Ballistic

Applications – A Review, Journal of Materials Research and Technology, 15, 1300–1317, 2021. DOI: 10.1016/j.jmrt.2021.08.150

Biçer, H., Reactive Sintering of Boron Carbide Based Ceramics by SPS, Journal of Materials and Mechatronics: A 3(1), 129–36, 2022. DOI: 10.55546/jmm.1072466

Bozdoğan, F., Üngün, S., Temel, E. and Mengüç, G. S., Textile Materials Used for Ballistic Protection, Properties and Ballistic Performance Tests, 2015.

Bracamonte, L., Loutfy, R., Yilmazcoban, I. K. and Rajan, S. D., 12 - Design, Manufacture, and Analysis of Ceramic-Composite Armor, in Lightweight Ballistic Composites (Second Edition), A. Bhatnagar, Ed., Woodhead Publishing, 349–67, 2016.

Bracamonte, L., Loutfy, R., Yilmazcoban, I. K. and Rajan, S. D., 12 - Design, Manufacture, and Analysis of Ceramic-Composite Armor, in Lightweight Ballistic Composites (Second Edition), A. Bhatnagar, Ed., Woodhead Publishing, 349–67, 2016.

Buaki-Sogo, M., Serra, M., Primo, A., Alvaro, M. and Garcia, H., Alginate as Template in the Preparation of Active Titania Photocatalysts, ChemCatChem 5(2), 513–18, 2013. DOI: 10.1002/cctc.201200386

Carter, C. B. and Norton, M. G., Ceramic Materials: Science and Engineering, Springer Science & Business Media, 727, 2007.

Cheng, M., Chen, W. and Weerasooriya, T., Experimental Investigation of the Transverse Mechanical Properties of a Single Kevlar® KM2 Fiber, International Journal of Solids and Structures 41(22), 6215–32, 2004. DOI: 10.1016/j.ijsolstr.2004.05.016

Chi, R., Serjouei, A., Sridhar, I. and Tan, G. E. B., Ballistic Impact on Bi-Layer Alumina/Aluminium Armor: A Semi-Analytical Approach, International Journal of Impact Engineering, 52, 37–46, 2013. DOI: 10.1016/j.ijimpeng.2012.10.001

Craig, Industry Ballistic and Stab Resistant Standards, Craig International Ballistics (blog), 2009.

Crouch, I. Ed., The Science of Armour Materials, Waltham, MA: Woodhead Publishing, 754, 2016.

Dresch, A. B., Venturini, J., Arcaro, S., Montedo, O. R. K. and Bergmann, C. P., Ballistic Ceramics and Analysis of Their Mechanical Properties for Armour Applications: A Review, Ceramics International 47(7), 8743–61, 2021. DOI: 10.1016/j.ceramint.2020.12.095

Gadow, R. and Kern, F., 2.06 - Advanced Manufacturing of Hard Ceramics, in Comprehensive Hard Materials, V. K. Sarin, Ed., Oxford: Elsevier, 207–30, 2014.

Gent, A., Major Industrial Polymers, Encyclopedia Britannica, 2009.

Goh, W. L., Zheng, Y., Yuan, J. and Ng, K. W., Effects of Hardness of Steel on Ceramic Armour Module against Long Rod Impact, International Journal of Impact Engineering, 109, 419–26, 2017. DOI: 10.1016/j.ijimpeng.2017.08.004

Goh, Wei Liang, Luo, B., Zeng, Z., Jianming, Y. and Ng, K. W., Effects of Hardness and Toughness of Ceramic in a Ceramic Armour Module Against Long Rod Impacts: Ceramic Engineering and Science Proceedings 39(2), 185–98, 2019.

Grujicic, M., Pandurangan, B. and Entremont, B. d', The Role of Adhesive in the Ballistic/Structural Performance of Ceramic/Polymer–Matrix Composite Hybrid Armor, Materials & Design, 41, 380–93, 2012. DOI: 10.1016/j.matdes.2012.05.023

Guo, G., Alam, S. and Peel, L. D., An Investigation of the Effect of a Kevlar-29 Composite Cover Layer on the Penetration Behavior of a Ceramic Armor System against 7.62 Mm APM2 Projectiles, International Journal of Impact Engineering, 157, 2021. DOI: 10.1016/j.ijimpeng.2021.104000

Guo, G., Alam, S. and Peel, L. D., Numerical Analysis of Ballistic Impact Performance of Two Ceramic-Based Armor Structures, Composites Part C 3, 2020. DOI: 10.1016/j.jcomc.2020.100061

Hazell, P. J., Armour: Materials, Theory, and Design, CRC Press, 2015.

Heimann, R. B., Classic and Advanced Ceramics: From Fundamentals to Applications, John Wiley & Sons, 576, 2010.

Helliker, A., 4 - Ballistic Threats: Bullets and Fragments, in Lightweight Ballistic Composites (Second Edition), A. Bhatnagar, Ed., Woodhead Publishing, 87–114, 2016.

Işık, A., The Effect of Free Particle Modular Armor System Design on Ballistic Performance (Serbest Parçacık İçeren Modüler Zırh Sistemi Tasarımının Balistik Performansa Etkisi), Alparslan Defence Sciences and National Security Institute, 2021.

Karahan, M., Kus, A. and Eren, R., An Investigation into Ballistic Performance and Energy Absorption Capabilities of Woven Aramid Fabrics, International Journal of Impact Engineering, 35, 499–510, 2008. DOI: 10.1016/j.ijimpeng.2007.04.003

Karandikar, P., Evans, G., Wong, S., Aghajanian, M. and Sennett, M., A Review of Ceramics For Armor Applications, in Ceramic Engineering and Science Proceedings, 163–75, 2009.

Klement, R., Rolc, S., Mikulikova, R. and Krestan, J., Transparent Armour Materials, Journal of the European Ceramic Society 5(28), 1091–95, 2008. DOI: 10.1016/j.jeurceramsoc.2007.09.036

Medvedovski, E., Ballistic Performance of Armour Ceramics: Influence of Design and Structure. Part 1, Ceramics International 36(7), 2103–15, 2010a. DOI: 10.1016/j.ceramint.2010.05.021

Medvedovski, E., Ballistic Performance of Armour Ceramics: Influence of Design and Structure. Part 2, Ceramics International, 36, 2117–27, 2010b. DOI: 10.1016/j.ceramint.2010.05.022

Orange, G., Fantozzi, G., Bigay, Y. and TORRE, J. P., Transformation Toughening in Ceramics : Mechanical Properties and Temperature Dependence of Tetragonal Polycrystalline Zirconia (TZP), Http://Dx.Doi.Org/10.1051/Jphyscol:19861100, 1986. DOI: 10.1051/jphyscol:19861100

Santos, C. J. E., Wei, T.-S., Cho, B. and Kriven, W. M., A Forming Technique to Produce Spherical Ceramic Beads Using Sodium Alginate as a Precursor Binder Phase, Journal of the American Ceramic Society 96(11), 3379–88, 2013. DOI: 10.1111/jace.12584

Swab, J. J., Zhu, D. and Kriven, W. M., Advances in Ceramic Armor: A Collection of Papers Presented at the 29th International Conference on Advanced Ceramics and Composites, 2005, Cocoa Beach, FL, Wiley, 300, 2005.

Tressler, R. E., An Assessment of Low Cost Manufacturing Technology for Advanced Structural Ceramics and Its Impact on Ceramic Armor, Ceramic Transactions, 134, 451–62, 2002.

Wadley, H. N. G., O'Masta, M. R., Dharmasena, K. P., Compton, B. G., Gamble, E. A. and Zok, F. W., Effect of Core Topology on Projectile Penetration in Hybrid Aluminum/Alumina Sandwich Structures, International Journal of Impact Engineering, 62, 99–113, 2013. DOI: 10.1016/j.ijimpeng.2013.05.008

Yang, M. and Qiao, P., 4 - High Energy Absorbing Materials for Blast Resistant Design, in Blast Protection of Civil Infrastructures and Vehicles Using Composites, N. Uddin, Ed., Woodhead Publishing, 88–119, 2010.

Yungwirth, C. J., O'Connor, J., Zakraysek, A., Deshpande, V. S. and Wadley, H. N. G., Explorations of Hybrid Sandwich Panel Concepts for Projectile Impact Mitigation: Explorations of Hybrid Sandwich Panel Concepts for Projectile Impact Mitigation, Journal of the American Ceramic Society, 94, 62–75, 2011. DOI: 10.1111/j.1551-2916.2011.04501.x

Zaera, R. and Sánchez-Gálvez, V., Analytical Modelling of Normal and Oblique Ballistic Impact on Ceramic/Metal Lightweight Armours, International Journal of Impact Engineering 21(3), 133–48, 1998. DOI: 10.1016/S0734-743X(97)00035-3

Zahraee, S. M. and Sabet, A. R., Ballistic Performance of Hybrid Armor with Ceramic Inserts and Polymeric Matrix for Different Threat Levels (TECHNICAL NOTE), International Journal of Engineering 27(6), 945–50, 2014.

JOURNAL of
MATERIALS and MECHATRONICS:A

e-ISSN 2717-8811
JournalMM, 2023, 4(2), 542-560
https://doi.org/10.55546/jmm.1326482

Araştırma Makalesi / Research Article

Preparation of Diatomite-Chitosan Composites for Loading and Release of Diphenhydramine HCl

Zeynep ÖZKAN[1], Muhammet Davut ARPA[2*], Melih ÖZÇATAL[3], Hakan ÇİFTÇİ[4**]

[1]Afyon Kocatepe University, Graduate School of Natural and Applied Sciences, Department of Nanoscience and Nanotechnology, Afyonkarahisar, Türkiye,
ORCID ID: https://orcid.org/0000-0003-2793-157X, zeyyozkan26@gmail.com
[2]Istanbul Medipol University, School of Pharmacy, Department of Pharmaceutical Technology, Istanbul, Türkiye,
ORCID ID: https://orcid.org/0000-0001-9290-2404, mdarpa@medipol.edu.tr
[3]Afyon Kocatepe University, Faculty of Technology, Department of Mechatronics Engineering, Afyonkarahisar, Türkiye,
ORCID ID: https://orcid.org/0000-0002-0831-9038, mozcatal@aku.edu.tr
[4]Afyon Kocatepe University, Faculty of Engineering, Department of Mining Engineering, Afyonkarahisar, Türkiye,
ORCID ID: https://orcid.org/0000-0001-7910-7350, hakanciftci86@gmail.com

Geliş/ Received: 12.07.2023; **Kabul / Accepted:** 03.12.2023

ABSTRACT: Diatomite ores have great potential as an adsorbent and drug carrier system due to their natural abundance, biocompatible, and high surface area. In the first stage of this study, raw diatomite ore was enriched by grinding and calcination processes. As a result of the enrichment process, the surface area was found to be 21.7 m^2/g for raw diatomite and 75.1 m^2/g for calcined diatomite. Subsequently, a series of diatomite-chitosan composites with different composition ratios were produced. Then, the loading (adsorption) performances of diphenhydramine hydrochloride (DPH), an antihistaminic agent, were investigated on the prepared composites. The highest loading capacity was 91.1 mg/g, and the lowest loading capacity was 48.8 mg/g in the prepared DPH-loaded formulations. After DPH loading studies, DPH release profiles (desorption) and release kinetics from composites were investigated. As a result of *in vitro* release studies, it was observed that formulations containing chitosan polymer had slower release than chitosan free formulations. It was determined that the formulations had a cumulative release in the 70-90% range, and the release processes were completed between 45-90 minutes. *In vitro* release profiles of the prepared formulations were compatible with Higuchi kinetics.

Keywords: Diatomite, Chitosan, Diphenhydramine, Release kinetic.

*Sorumlu yazar / Corresponding author: *mdarpa@medipol.edu.tr **hakanciftci86@gmail.com

Bu makaleye atıf yapmak için /To cite this article

Özkan, Z., Arpa, M.D., Özçatal, M., Çiftçi, H. (2023). Preparation of Diatomite-Chitosan Composites for Loading and Release of Diphenhydramine HCl. Journal of Materials and Mechatronics: A (JournalMM), 4(2), 542-560.

1. INTRODUCTION

For the active substance released in drug delivery systems to be beneficial, it must remain within the therapeutic range. In classical drug delivery methods, repeat doses are needed to ensure the therapeutic dose. Controlled release systems can reduce these dose repetitions and side and toxic effects. The selection of an appropriate and effective drug delivery system depends on its biocompatibility, loading capacity, release rate, safety, and cost of production (Ibrahim et al., 2021). One of the popular examples of materials with these properties is natural or synthetic silica and silicate-based materials. In the last decade, porous and micro-nano-sized silicates have attracted significant attention in pharmaceutical applications due to their excellent biocompatibility, high surface area, thermal stability, chemical inertness, and diffusion-controlled drug release mechanisms. In the last decade, porous and micro-nano-sized silicates have attracted much attention in pharmaceutical applications, especially as drug delivery systems. Because these substances have a high surface area, are chemically and physically stable, and are also biocompatible. For example, natural nanoporous silicates such as diatomite and natural zeolite are more cost-effective than synthetic porous silica-based materials (Zhang et al., 2013; Ibrahim et al., 2021). Micro- and nano-scale drug delivery systems have significantly affected the pharmaceutical industry by minimizing the disadvantages of drugs, such as short half-life, poor stability, and side effects (Çiftçi et al., 2020).

Diatomaceous earth, also known as diatomite, is a fossil material of sedimentary origin, formed over centuries by the siliceous skeleton (frustule) of single-celled micro-algae in water, deposited at the bottom of lakes or found in marine environments. Diatomite morphology consists of particles of sizes ranging from 2 μm to 2 mm. Particle size distributions may vary according to the type and size of diatoms, their shells, and clay and sand inclusions. The bulk density of diatomite is between 0.51-0.55 g/cm^3) and the specific gravity of 2.55 g/cm^3 (Reka et al., 2021). Diatomite frustules can have a large surface area of up to 200 m^2/g (Wang et al., 2013; Rea et al., 2014). Diatomite, whose main component is amorphous silica, may contain organic compounds from the environment and impurities such as metal oxides (MgO, Al_2O_3, Fe_2O_3). Therefore, raw diatomite may need to be purified first. For this, processes such as thermal calcination and washing with HCl are used (M Rosenholm et al., 2011; Taş and Çetin, 2012). Physical (gravity methods, separation according to particle size, sedimentation) and chemical enrichment (acid leaching, calcination) methods can be used in diatomite enrichment. Physical enrichment methods are suitable for some diatomite ores and are ineffective in increasing the specific surface area. In this case, chemical enrichment methods can be used. Organic impurities accumulated in the pores of diatomite can only be removed by chemical methods. The leaching method can remove Organic substances by dissolving them, but this method is costly. The calcination process is the cheapest and most efficient method to enrich ores such as diatomite and increase the surface area. It is known that the total potential diatomite reserve in the world is 2 billion tons, and it is approximately 125 million tons in Turkey (Ruggiero et al., 2014). Due to its widespread availability in many parts of the world, its high thermochemical stability, low density, high adsorption capacity, non-toxicity, and excellent biocompatibility, it interests researchers in many areas. Diatomite is a promising adsorbent material thanks to the pores on the frustule surface and the pores between the frustules (Wang et al., 2013). In a study the removal of some heavy metal ions such as Al^{+3}, Ba^{+2}, Cd^{+2}, Cr^{+3}, Cu^{+2} by taking advantage of the excellent adsorption capacity of diatomite was investigated. It is observed that the maximum removal percentage of many heavy metal ions at pH 4 (M Rosenholm et al., 2011). At the same time, diatomite is of interest as a potential drug carrier in pure or modified form. For example, in a study diclofenac sodium was adsorbed on a modified diatomite sample and the formulation showed a release over 8 h, further indicating the

potential safety of diatomite in their *in vivo* toxicity test results on mice (Taş and Çetin, 2012). In another study, different concentrations of chemically modified diatomite nanoparticles were incubated in cancer cells and homogeneous distribution of nanoparticles in the cytoplasm and nucleus in imaging analysis was observed (Ruggiero et al., 2014). Diatom microalgae drug carrier systems was developed for topical delivery of naproxen. In cytotoxicity studies, it has been shown that both the diatom and the carrier system are not cytotoxic (Vona et al., 2023). In a study, a diatomite-based sponge was developed to prevent excessive bleeding. With the biocompatibility studies performed, the blood compatibility, cytocompatibility, and histocompatibility of the system were tested separately by in vitro or in vivo studies. It was determined that these diatomite-based carrier systems were highly biocompatible due to a 5% of hemolysis rate, and 90% of cell viability, as well as not affecting the proliferation and the growth of tissue cells, and not causing any inflammation (Yang et al., 2021). Studies showed that phase transformations in diatomite occur from 600 to 1200°C, however, critical changes in the opal phase were reported to be observed between 1000 and 1200°C (Reka et al., 2021).

Polymers play an essential role as carriers in the design of efficient drug delivery systems due to their stability, high drug-loading capacity, and providing controlled drug release (Vilar et al., 2012; Abdel-Bary et al., 2020). Natural chitosan shows promising results in drug delivery systems among the available polymers. Chitosan, obtained by deacetylation of chitin, mainly found in shellfish, is the second most abundant polymer after cellulose. Chitosan technically have high reactivity, high stability, high biocompatibility, non-toxicity, and high biodegradability (Tian et al., 2020; Arpa et al., 2023). All these properties are helpful for the production of chitosan as a potential carrier with various types of silica and silicate-based structures. Thanks to this integration, the physicochemical properties of chitosan combined with diatomaceous earth improve (Burkhanova et al., 2000; Akyuz et al., 2017). According to a reported study, curcumin loaded on chitosan-silica nanoparticles and 48-hour release was observed. It is stated that it promises as a pH-dependent drug-releasing molecule (Gaware et al., 2019).

Histamine is a chemical mediator that mediates allergic and inflammatory reactions, gastric acid secretion, and neurotransmission in specific brain regions. Various drugs, such as dimenhydrinate, thyroxine, pheniramine, and diphenhydramine, have been used to abolish the effects of histamine by blocking histamine receptors. Diphenhydramine hydrochloride (DPH) is a potent antihistamine active ingredient (H_1 receptor blocker) with antiemetic, sedative, and anticholinergic effects. DPH causes strong side effects such as dry mouth and throat, tachycardia, pupillary dilation, urinary retention, constipation, motor impairment, hallucinations, and delirium at high doses. The controlled release has been proposed as a promising method to reduce the reported side effects of the active ingredient using innovative carriers. Various methods have been developed to minimize these side effects and provide a controlled release of DPH (Ghebaur et al., 2012; Rezaeifar et al., 2016).

In this study, raw diatomite was first enriched by calcining and then characterized. Later, drug carrier systems were obtained using calcined diatomite and chitosan. A total of six different formulations were produced from different diatomite and chitosan composition ratios and different DPH loading amounts. The effect of delivery systems on DPH release characteristics was evaluated by examining their drug release profiles. Release data were analyzed using Zero order, First order, Higuchi, Hixson-Crowell, and Korsmeyer Peppas kinetics.

2. MATERIALS and METHODS

2.1 Materials

Raw diatomite samples were collected from Afyonkarahisar Seydiler District, diphenhydramine HCl, hydrochloric acid, potassium dihydrogen phosphate, o-phosphoric acid, and acetonitrile were purchased from Sigma-Aldrich, chitosan (low molecular weight, deacetylation degree >90) was purchased BBI Life Scineces, sodium hydroxide was purchased from Merck, and acetic acid (glacial) was purchased from Carlo Erba. All used chemicals were pharmaceutical grade.

2.2 Methods

2.2.1 Purification of diatomite

The purification process was carried out to increase the diatomite's surface area and purify it from its impurities. For this, three stages of crushing and grinding were carried out to reduce the diatomite's particle size. The large-grained diatomite was first fed into the laboratory jaw crusher, the primary crusher, and then the roller crusher, the secondary crusher. The crushed diatomite was then ground in a ring mill for 2 min. After that, the ground diatomite was subjected to drying and calcination processes. It was kept in an oven at 105°C for 24 h for the drying process. Then, it was held in a laboratory-type ash oven at 550°C for 4 h to be calcined. Temperatures between 500-600 ºC are generally used to remove organic substances. While it may not be fully effective at lower temperatures, structural deterioration may occur in the inorganic material at higher temperatures.

2.2.2 Characterization studies of raw and purified diatomite

The raw and purified diatomite samples were dried at 105ºC for 24 hours and ground in a ring mill for 2 minutes. Then, X-ray diffraction (XRD) spectra were obtained with the Shimadzu XRD-6000 instrument with Cu-Ka radiation at a wavelength of λ: 1.54184 Å. The samples were scanned in the 2-70º angle range. The chemical composition of the samples, which were subjected to the same pre-treatment, was also determined elementally with the XRF (Rigaku ZXS Primus II) device. LEO 1430 VP model SEM device was used to determine the topographic features of the dried and ground samples. The specific surface areas of the raw and calcined diatomite samples were calculated by the Brunauner-Emmett-Teller (BET) equation, which is based on the calculation of the amount of gas required to cover the sample surface with a single molecular layer. The size distribution of the pores was obtained from the desorption isotherm data using the Barrett, Joyner, and Halenda (BJH) method. To this end, Micromeritics brand Gemini VII 2390t model device based on nitrogen gas adsorption technique in a liquid nitrogen environment at -196ºC was used. Particle size distributions were determined using the Malvern Mastersizer 2000 instrument, and the procedures in our previous work were followed for the analysis (Çiftçi et al., 2020). For zeta potential (ζ) analysis, Malvern brand Nano-Z model zeta-meter device was used, and the procedure in our previous studies was followed for the analysis (Çiftçi et al., 2020).

2.2.3 Preparation of DPH loaded diatomite-chitosan composites

First, a 2% aqueous acetic acid solution containing 1 mg/mL of active ingredient (DPH) was prepared. 250 mL of this prepared stock solution was used to prepare each formulation. A certain amount of diatomite was added to 250 mL of stock solution and stirred for 1 h at 55°C in a magnetic stirrer. Then, the amount of chitosan determined in the formulations was added to the solution. Chitosan-containing solutions were stirred on a magnetic stirrer at 55°C for 24 h. The product obtained at the end of the process was dried in an oven at 55°C for 24 h. The same procedures were repeated for all formulations. A temperature value of 55oC was used to increase the solubility of

chitosan, to avoid damaging the drug molecules at higher temperatures, and to also dry the formulation. The composition ratios of the prepared formulations (Table 1) were determined according to the general literature review.

Table 1. The composition ratios of the prepared formulations.

Formulation	DPH/Carrier material	Amount of diatomite (mg)	Chitosan ratio (%) (according to the total amount of carrier)	1000 mg/L DPH solution (mL)
F1	1/10	2500	0	250
F2	1/10	1625	35	250
F3	1/10	1875	25	250
F4	1/7.5	1875	0	250
F5	1/7.5	1218.75	35	250
F6	1/7.5	1406.25	25	250

2.2.4 FT-IR analysis

The functional groups and FT-IR spectra of the purified diatomite, chitosan, DPH and the composite formulations were examined in a Perkin Elmer device in the 400-4000 cm^{-1} range.

2.2.5 Quantification of DPH and loading capacity

Eight different DPH solutions at specific concentrations were prepared from 100 mcg/mL of DPH stock solution by diluting them with distilled water, and their measurements were performed using a HPLC (Agilent 1100) device. The calibration equation and determination coefficient (r^2) were determined by drawing the calibration graph with the data obtained (Figure 1). To determine the maximum loading capacities, 60 mg of powder formulations was dispersed in 200 mL of distilled water and after 12 h the samples were taken, filtered and analyzed by HPLC device.

An Agilent 1100 HPLC device was used in the HPLC method developed to determine diphenhydramine HCl (DPH). Validation parameters such as linearity, reproducibility, precision, limit of quantification (LOQ), and limit of detection (LOD) were evaluated. A C18 column (GC Sciences, InterSustain C18, 150*4.6 mm, 5 µm) was used for analysis. 35% aqueous acetonitrile phosphate buffer solution (pH: 3) was used as the mobile phase. The flow rate was 1.2 mL/min, the wavelength was 227 nm, the injection volume was 20 µL, and the column temperature was 25°C. A stock solution was prepared by dissolving DPH in 35% aqueous acetonitrile at a 100 µg/mL concentration. Samples were prepared from this stock solution by making dilutions with 35% aqueous acetonitrile solution in the 1-30 µg/mL range. All samples were filtered using a membrane filter (pore size of 0.2 µm).

2.2.6 In vitro release studies

The release study of drug-loaded formulations was performed using UPS apparatus I - basket method (Figure 1). *In vitro* release profiles of the composites were determined in simulated gastric fluid (80 mL of 1.0 N HCl, 2.0 g NaCl, q.s. 500 mL purified water: pH: 1.2) release media. First, the formulations containing 25 mg of diphenhydramine HCl (DPH) were weighed. It was filled into hard gelatin capsules numbered 0, as suitable for the bulk density and amount of the material. The weights of the filled capsules were recorded. The speed of the dissolution device was set to 50 rpm and the temperature to 37±1°C. Vessels were filled with 900 mL of the simulated gastric fluid. At the specified time intervals (5, 15, 30, 45, 60, 75, 90, 120, 150, and 180 min), 1 mL sample was taken

and filtered through a membrane filter (pore size of 0.2 μm) and transferred to vials. The same amount of fresh medium was added to the vessels. Samples were analyzed in the HPLC device at 227 nm. The study was performed in triplicate for each formulation, and the mean values of the results were recorded.

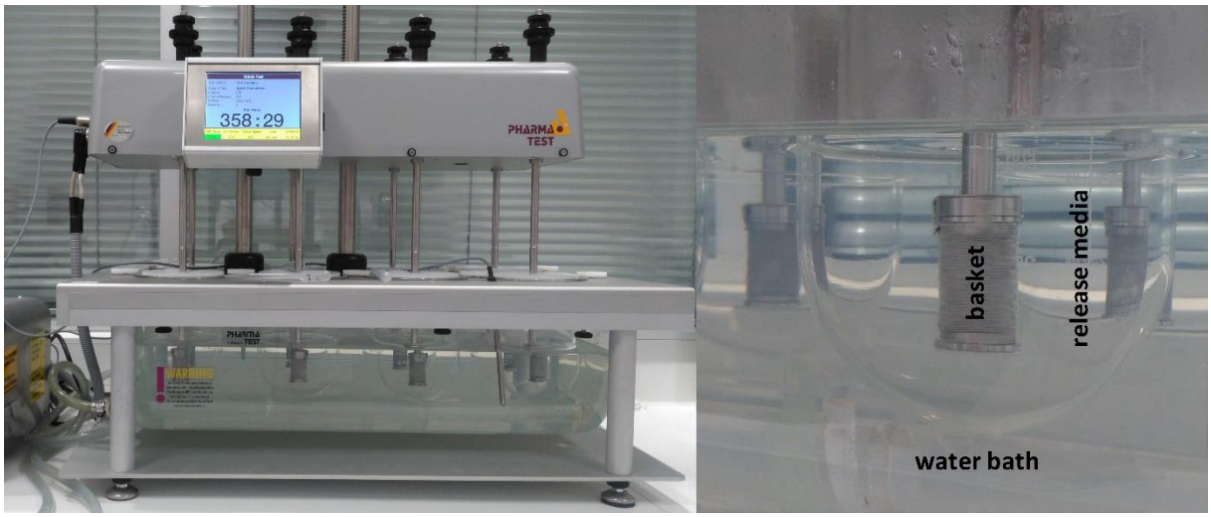

Figure 1. Dissolution device and release medium used in release studies.

In order to explain the kinetics of DPH release from chitosan-diatomite composites, the results of the release studies were analyzed using kinetic models. Equations of the models used (Equations 1-5) are given below. In addition, whether there was a similarity between the release characteristics of the formulations was determined by the f2 similarity factor. f2>50 was evaluated being similarity of the DPH release profiles (Arpa et al., 2021).

Zero order equation

$$M_t/M_\infty = k_0.t \quad (1)$$

First order equation

$$\ln(1-(M_t/M_\infty)) = -k_1.t \quad (2)$$

Higuchi equation

$$M_t/M_\infty = k_H.t^{1/2} \quad (3)$$

Hixson-Crowell equation

$$1-(1- M_t/M_\infty)^{1/3} = -k_{HC}.t \quad (4)$$

Korsmeyer-Peppas equation

$$M_t/M_\infty = k_{KP}(t)^n \quad (5)$$

where M_t and M_∞ are drug release at "t" and equilibrium time, respectively. k_0, k_1, k_H, k_{HC}, k_{KP} are the respective release rate constants. n is a constant describing the release mechanism.

Mechanisms corresponding to the "n" value have been determined for polymeric-controlled release systems. Dissolution of the drug delivery system when n>1, controlled release through

diffusion from the polymer matrix when n<0.5, and drug diffusion and dissolution of the carrier system at the same time when 0.5<n<1 are in question (Kevadiya et al., 2012; Luo et al., 2016).

2.2.7. Statistical analyzes

For the evaluation of the data obtained, statistical analyzes were made by applying Student's t-test. $p<0.05$ was accepted as statistically significant.

3. RESULTS and DISCUSSION

3.1 Characterization Studies

The XRD spectrum showing the crystal structure of diatomite is given in Figure 2. The broad band observed at 2θ=22° in the spectrum indicates the presence of amorphous silica, forming the diatomite's characteristic structure. Apart from the peak showing the presence of amorphous silica, a sharp peak indicating the presence of another mineral could not be detected in the spectrum.

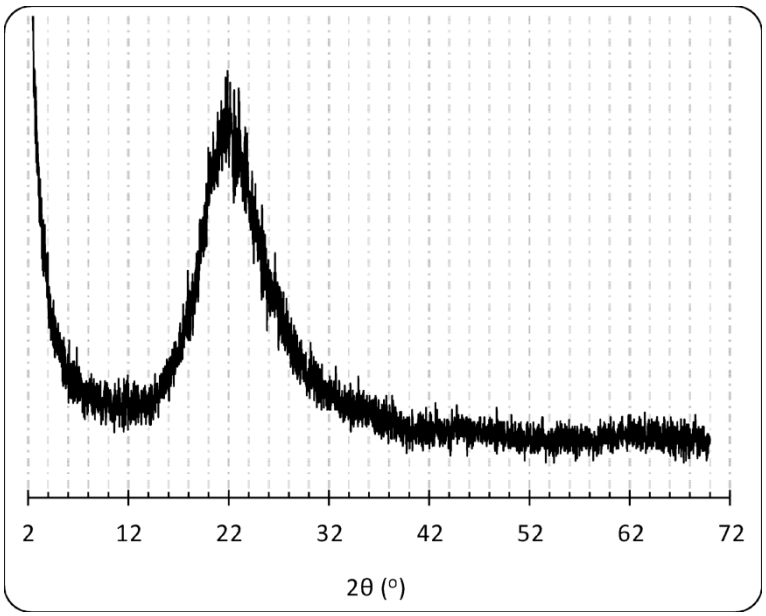

Figure 2. XRD spectrum of the diatomite sample.

Diatomites'chemical composition and crystal structure play an essential role in drug release. In the XRF analysis of the diatomite, the results of which are given in Table 2, SiO_2 was observed as the primary component with a ratio of 94.5%. This result is in agreement with the XRD data (Moradi and Yıldız, 2021). The 3.3% increase in glow loss can be attributed to organic impurities precipitated in the diatomite pores.

Table 2. Chemical analysis (XRF) results of diatomite sample.

Component	SiO_2	Al_2O_3	CaO	Fe_2O_3	K_2O	Na_2O	MgO	LOI
Amount (wt. %)	94.51	0.98	0.42	0.30	0.17	0.08	0.08	3.3

LOI: Loss of ignition

The surface morphology of the diatomite was investigated based on SEM images (Figure 3). Diatomite, which has a highly porous structure, also appears to contain large volumes of voids after calcination. Having these properties makes diatomite a potential material in drug release applications. Diatomite grains were found to be circular, elliptical, and elongated. There was a heterogeneous

population of structures that differ in both size and shape. It can be seen from Figure 3(a,b) that the micro and submicron pores and crevices in the form of the raw diatomite are primarily open and are not closed much by organic materials. A 3.3% mass loss in XRF analysis also supported this. Figure 3(c,d) showed that the submicron pores were open in some grains after calcination; that is, the organic structures in these pores were removed by calcination.

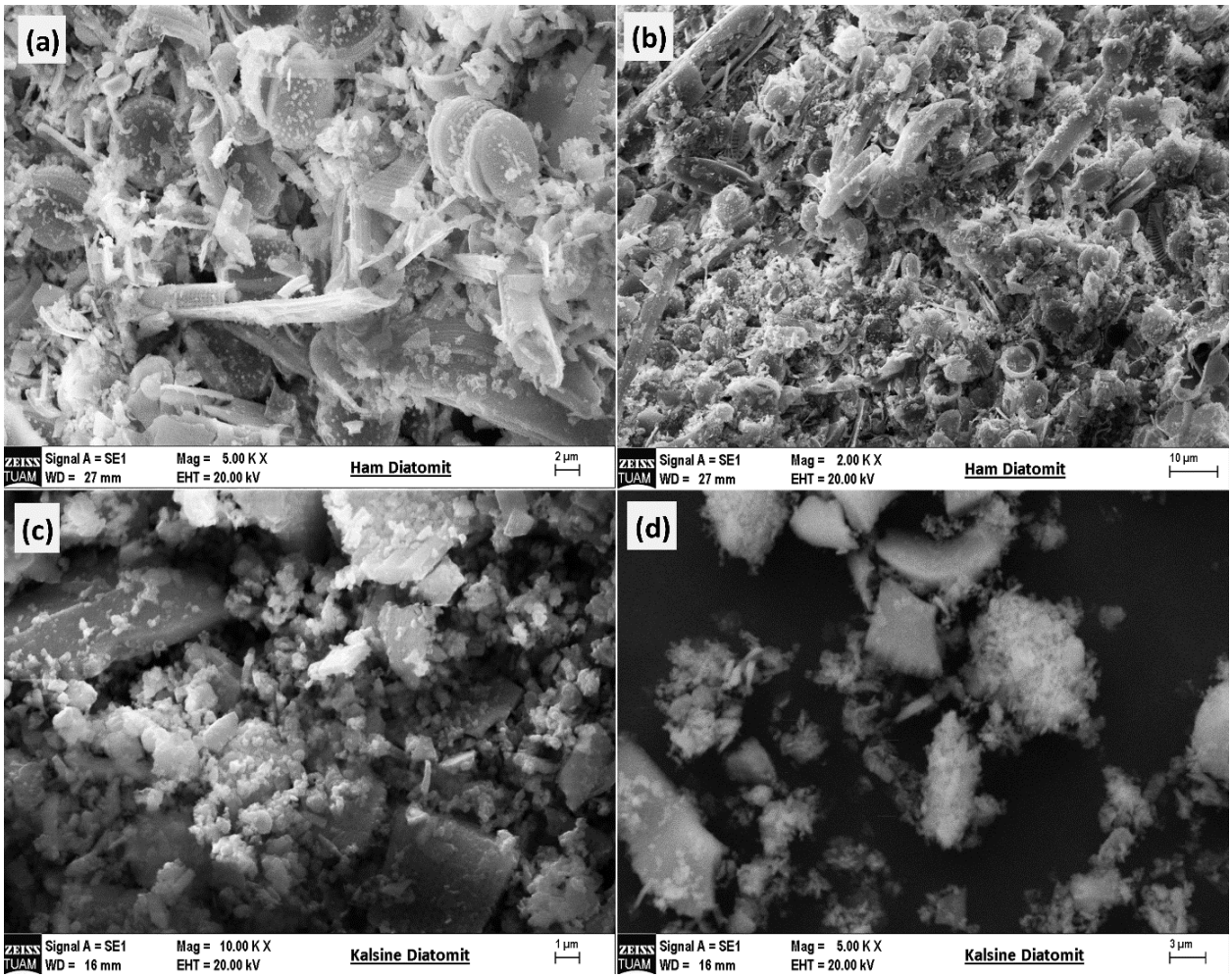

Figure 3. SEM images of raw (a,b) and calcined (c,d) diatomite.

Table 3 gives the raw and calcined diatomite properties determined by the N_2 sorption method. After the calcination process, the morphological structure of the diatomite did not fundamentally change, but it was observed that the surface area increased significantly as a result of the opening of Si-O-Si bridges on the diatomite spine surface and the removal of organic impurities (Fowler et al., 2007). The literature has reported that temperatures above 1600°C close the siloxane bridges (Yusan et al., 2012). In this study, due to the calcination carried out at 550°C, an almost 3-fold increase was observed in the pore volume determined by the BJH method, from 0.24 cm^3/g to 0.76 cm^3/g. It was concluded that the calcination processes performed at low temperatures increased the surface area and pore volume. Additionally, the pore size of the diatomite sample was around 50 nm, that is, it was mesoporous. It is known that the mesoporous structure is a useful feature for controlled drug release systems as it slows down the release (Çiftçi et al., 2020).

Table 3. Textural properties of the diatomite samples.

Sample	BET surface area (m^2/g)	Total volume of pores, with BJH ads. (cm^3/g)	Average pore diameter, with BJH ads. (nm)
Raw diatomite	21.69	0.24	52.18
Calcined diatomite	75.11	0.76	49.0

N_2 adsorption-desorption isotherms of raw and calcined diatomite are given in Figure 4(a). As can be seen in the graph, the isotherm of calcined diatomite belongs to type III with an H_3 hysteresis loop according to the International Union of Pure and Applied Chemistry (IUPAC) classification, which corresponds to the characteristic curves of mesoporous and macroporous materials (Yusan et al., 2014; Zheng et al., 2019). Such isotherms are associated with the formation of aggregates with plate-like fragments. When P/P_0 is close to 1, it shows that the adsorption in the macropores occurs at the maximum level (Tsai et al., 2006; Gârea et al., 2016; Silvestri et al., 2017). The BJH pore size distributions of raw and calcined diatomite are given in Figure 4(b). It can be said that the diatomite samples have a macroporous (pore diameter > 50 nm) structure according to the classification according the size of the pores recommended by the International Union of Pure and Applied Chemistry (IUPAC). Both diatomite samples have a heterogeneous pore diameter distribution with pore distributions below 125 nm. However, the increase in the pore volume of the calcined diatomite is seen. From this, it is understood that the macro and mesopores are opened after the calcination process. BJH pore size distributions also overlap with the data obtained by BET analyses (Table 3).
Zeta potential (ζ) measurements were performed in 10^{-3} M NaCl solution with 0.01% solid ratio. The ζ values of the diatomite surface at different pH values are given in Figure 4(c). It is seen that the ζ changed according to the pH value of the environment. As is known, the ζ of diatomite particles is negative over a wide pH range. Therefore, the surface of diatomite particles is naturally negatively charged (Gao et al., 2005). While the ζ value was -14.4 mV at the lowest pH value (1.9), the ζ value was measured as -33.8 mV when the pH value was 12. It is understood from the graph that the negative charge decreases with increasing pH.

The particle size distributions of the raw and calcined diatomite are given in Figure 4(d). As seen in the graph, it was determined that the particle sizes of raw and calcined diatomite samples were between 1.5-50 μm, and they had a homogeneous size distribution. However, it was observed that there was a slight increase in the particle size distribution after the calcination process. The reason for this can be explained by the fact that tiny particles physically adhere to each other and agglomerate after the calcination process (Ediz et al., 2010). When the d_{10}, d_{50}, and d_{90} values of diatomite samples were compared, the d_{50} value of natural diatomite was 7.7 μm, while the d_{50} value of calcined diatomite was 8.9 μm. Similarly, the d_{90} value of natural diatomite was determined as 20.3 μm, and the d_{90} value of calcined diatomite was 21.3 μm by grain size analysis (Table 4). This means the diatom structure shrinks and agglomerates due to removing organic matter and moisture after calcination, as expressed in the particle size distribution graphs.

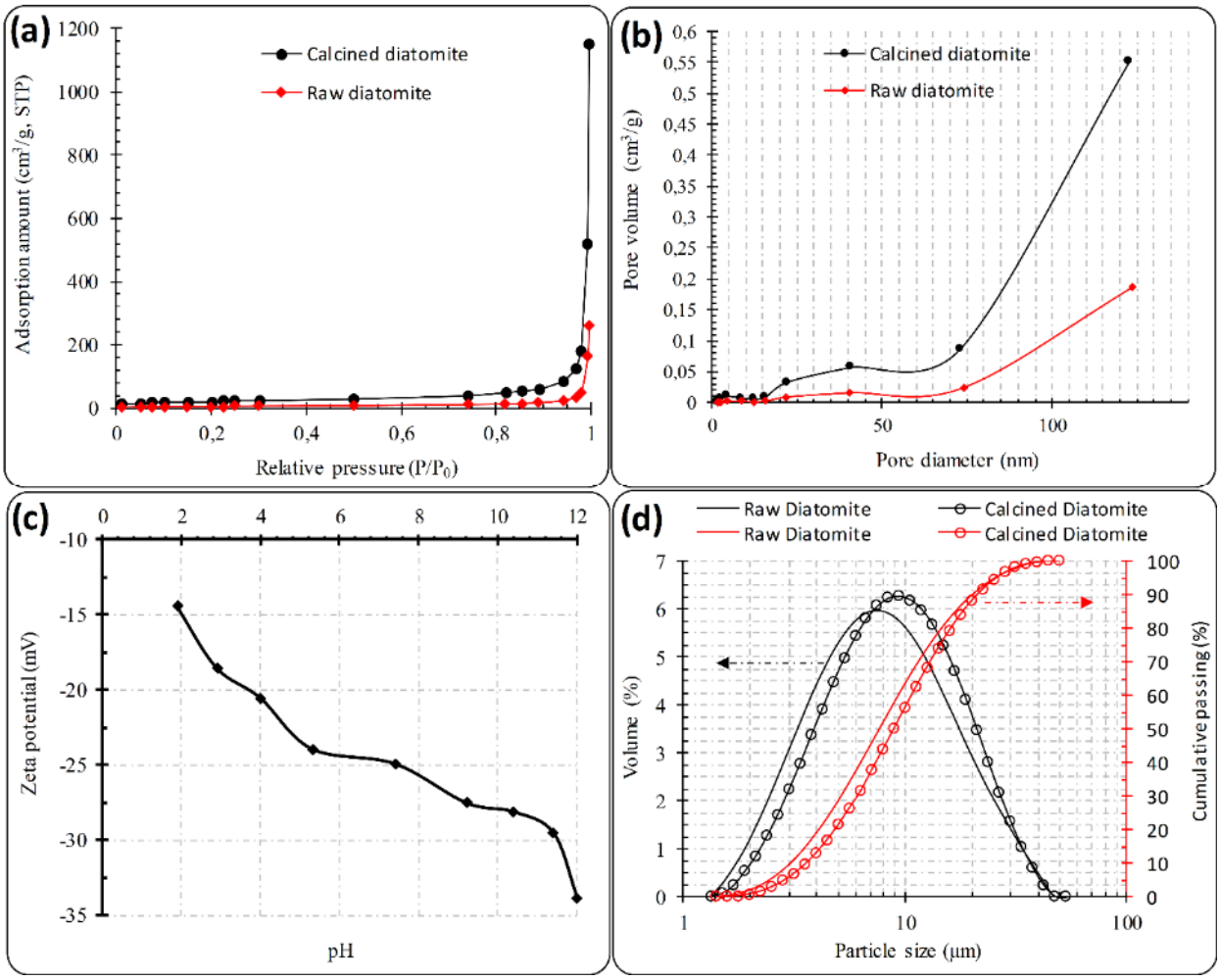

Figure 4. (a); N_2 sorption isotherms, (b); pore size distributions, (c); zeta potential with respect to pH, and (d); particle size distributions of the diatomite samples.

Table 4. Particle size distributions of the raw and calcined diatomite samples.

	Raw diatomite	Calcined diatomite
d_{10} (µm)	3.1	3.6
d_{50} (µm)	7.7	8.9
d_{90} (µm)	20.3	21.3

3.2 FT-IR Analysis

The functional groups of the composite components and all formulations were determined by FT-IR spectra (Figure 5). It is seen that the calcined diatomite revealed three characteristic broad bands: 1065 cm^{-1}, 797 cm^{-1}, 454 cm^{-1}. These peaks are assigned to the symmetric stretching vibration of the Si-O-Si group, the Si-OH bending vibration and the characteristic band of the Si-O-Si bond, respectively. The peak at 1624 cm^{-1} wavelength can be assigned to the H-OH bend, which is a weak bend (Gültürk and Güden, 2011). The band between 3600-3000 cm^{-1} seen in the chitosan FT-IR spectrum corresponds to the stretching of the hydroxyl (OH) groups and was a wide band due to hydrogen bonds (Zheng and Wang, 2009). The 2948 cm^{-1} and 2861 cm^{-1} absorption bands represent C-H symmetrical and asymmetrical stresses, respectively. 1645 cm^{-1} C=O stretching (Amine I), 1636 cm^{-1} and 1318 cm^{-1} C-N stretching (Amine III), 1582 cm^{-1} NH bending, 1377 cm^{-1} CH bending, 1028

cm^{-1} C-O stretching (Queiroz et al., 2014; Thakur et al., 2016). The peak at a wavelength of 891 cm^{-1} represents the saccharide groups in chitosan (Thakur et al., 2016). In the spectrum of diphenhydramine, aromatic C-H stretching, amine C-N stretching and ether C-O stretching were observed in the absorption bands of 3033 cm^{-1}, 1172 cm^{-1} and 1108 cm^{-1}, respectively (Abbas et al., 2020). In addition, the peaks corresponding to wavelengths of 2953 cm^{-1} and 1455 cm^{-1} represent stretching vibrations of the CH bond in CH_2 groups (Zargarian et al., 2015). Vibrations at 756 cm^{-1}, 714 cm^{-1} represent the C-H deformation of phenyl outside the aromatic benzene ring (Ly et al., 2017).

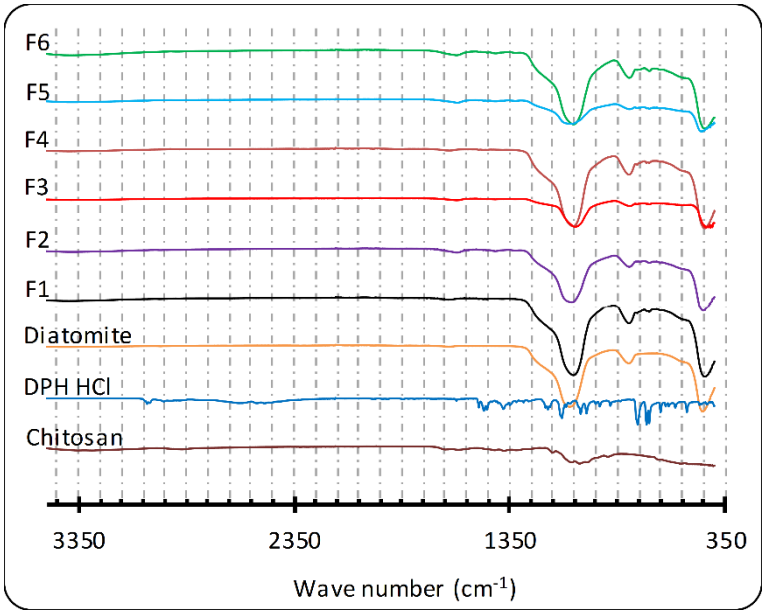

Figure 5. FT-IR spectra of the samples.

The bands around 1582 cm^{-1} belonging to chitosan disappeared in the formulations. This indicates that the peaks of the weaker amide and amine groups of chitosan compared to diatomite are absorbed by the dominant peaks of the diatomite (Wu et al., 2016). Dominant peaks of DPH molecules were also detected in the formulations. This proves that DPH molecules are adsorbed on the carrier composite. It was observed that the Si-O stretching vibration intensity in the 1065 cm^{-1} band of the diatomite and the Si-OH bending vibration intensity in the 797 cm^{-1} band decreased due to the addition of chitosan.

3.3 Calibration Curve and Srug (DPH) Loading Capacities

The correlation coefficient was found to be 0.99 according to the HPLC method developed (Figure 6). The high reproducibility and precision of the DPH assay method were demonstrated by the obtained coefficients of variation of less than 2% (data not shown). The formulations with the highest and the lowest loading capacity were determined as F1 and F5, respectively (Table 5). It was observed that the presence of chitosan in the prepared formulations caused a decrease in the DPH loading capacity.

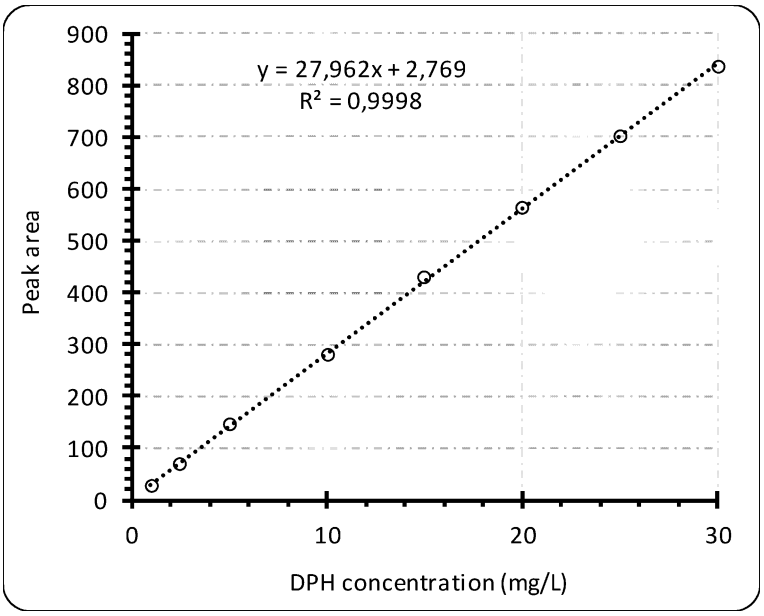

Figure 6. Calibration curve of DPH active ingredient.

Table 5. DPH loading capacities of all formulations.

Formulation	F1	F2	F3	F4	F5	F6
DPH loading capacity (mg/g)	97.1±7.7	56.2±1.1	54.8±2.4	85.5±3.8	48.8±1.8	51.3±5.6

3.4 In vitro DPH Release Profiles of the Formulations

The drug-loaded composite was added to the hard gelatin capsule to make the prepared product easier for the patient compliance. Orally used capsule formulations have high patient compatibility, ease of use, and low cost (Hadi et al., 2013). The *in vitro* release profiles of the DPH active ingredient were examined in gastric medium (pH 1.2) versus time with all formulations (Figure 7).

The basket method (USP Apparatus I) was used in the release studies of formulations filled into capsules. This method is a frequently used dissolution for capsule formulations (Kumar et al., 2012; Lo et al., 2013; Damian et al., 2021). As shown in Figure 7, with the disintegration of the capsule wall depending on the temperature and medium, the DPH passed into the release medium from the 5^{th} minute. This indicated that the capsule wall began to break down within 5 min. At the same time, this situation was observed observationally during the study.

The rapid release of the DPH from the carrier system to the release medium is related to the fact that DPH is an active ingredient with high solubility in water (Wang et al., 2017). Formulations without chitosan polymer (F1 and F4) showed faster and higher drug release from the 5^{th} minute than the other formulations. During the first 45 min, 50% or more of all formulations diffused rapidly to the release medium, followed by a slower release.

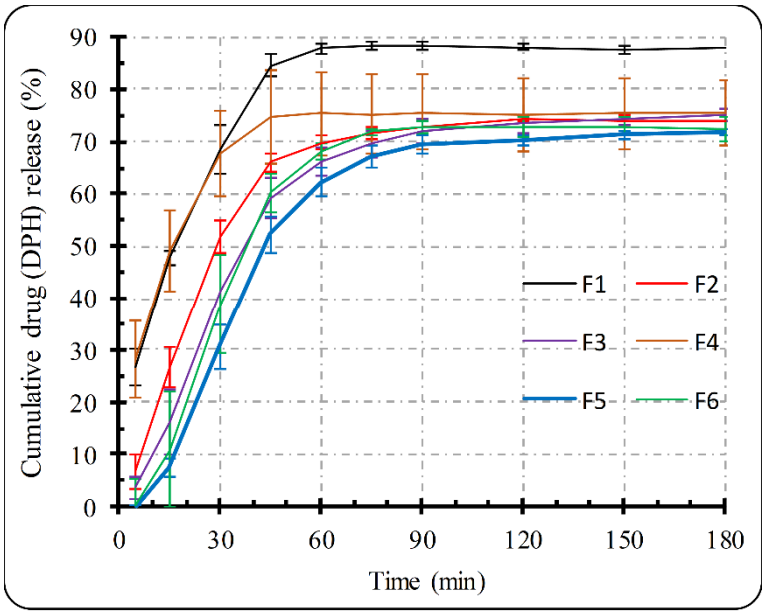

Figure 7. DPH release profiles of all composite formulations at pH 1.2.

F1 formulation showed statistically higher drug release at all-time points than chitosan-containing formulations (F2, F3, F5, F6) ($p<0.05$). The chitosan with bio-adhesive (Arpa et al., 2023) and binding properties (Tang et al., 2017) adsorbed on the surface and pores of the diatomite particles, causing the drug release to be slower than in other formulations.

When the chitosan-free F1 and F4 formulations were evaluated among themselves, a proportionally higher release amount was observed in F1 than in F4. This is related to the fact that there is a higher amount of carrier material (1/10 = DPH/Diatomide) in the F1 formulation than the active ingredient. In other words, while the amount of DPH in the environment during drug loading was the same, there was more diatomite in the F1 formulation. Thus, there was not enough driving force for DPH molecules to be adsorbed on micro and mesopores, and DPH molecules concentrated more rapidly in macropores. This facilitated the release of DPH molecules, allowing it to occur at a higher rate. In the F4 formulation, however, since there was less diatomite and relatively more driving force was provided, DPH molecules were allowed to move toward the micro and mesopores. This resulted in the inability of DPH molecules concentrated in the micropores and crevices to pass into the release medium completely. The same situation is seen in the F2 and F5 formulations.

As a result, the expression of repulsive force is the force that pushes the adsorbate toward the adsorbent surface and pores. A high level causes high adsorption and more adsorbate concentration in micropores/slits. High adsorbate (DPH) concentration in the environment or low adsorbent (diatomite) concentration provides the elevated driving force. However, no significant difference was observed between F3 and F6 in this respect ($p > 0.05$). The F5 formulation with less diatomite released less DPH in the first 60 min than the others. As a result of this situation, it can be understood that DPH accumulated in the inner pores at a higher rate, and the high speed of chitosan, however, caused the release to be less and slower. There was no significant difference between F3 and F6 formulations regarding release percentage and kinetics. From the 90th minute, the DPH release from all formulations finished.

3.5 In vitro Release Kinetics

Several different kinetic models were used to explain the DPH active ingredient release kinetics of the products of all formulations. Kinetic models were evaluated with the data obtained from drug release studies. The correlation coefficients (r^2) and "n" values obtained from the kinetic models are given in Table 6.

Table 6. The kinetic models used and the *in vitro* drug release parameters obtained.

Kinetic model / Formulation	Zero order (r^2)	First order (r^2)	Higuchi (r^2)	Hixson-Crowell (r^2)	Korsmeyer-Peppas (r^2)	Korsmeyer-Peppas n
F1	0.9261	0.8436	0.9997	0.8756	0.9922	0.4983
F2	0.9219	0.7654	0.9963	0.8307	0.9696	0.9611
F3	0.9653	0.8132	0.9734	0.8867	0.9853	1.2136
F4	0.9228	0.7634	0.9991	0.7896	0.9679	0.4137
F5	0.9823	0.7272	0.9634	0.8888	0.9902	1.6581
F6	0.9705	0.7204	0.9734	0.8779	0.9787	1.6813

As shown in Table 6, the kinetic with the highest r^2 values of the equations obtained from the release data was evaluated as the most appropriate. According to the findings, the model with the highest r^2 value was Higuchi kinetics in general. Higuchi is a mathematical kinetics determining the release rates of active ingredients dispersed in drug delivery systems which show controlled release. The findings and the prepared system's data showed that it was compatible with this kinetic. On the other hand, in Korsmeyer Peppas kinetics, where the data up to the point where the drug release reaches 70%, the slope of the equation, the "n" value, was used to interpret the release profiles. It indicates Fickian diffusion when $n \leq 0.5$ and non-Fickian diffusion when $0.5 < n$. In non-Fickian diffusion, the release of the active ingredient from the formulation occurs as a combination of both diffusion and erosion-controlled release (Coneac et al., 2015; Laxmi et al., 2015; Arpa et al., 2022). Therefore, the fact that the n value was less than 0.5 in F1 and F4 formulations that did not contain chitosan indicated that drug release occured by the Fickian mechanism. Adding chitosan to the formulations caused a change in the release characteristics. Formulations containing chitosan, $n>1$, indicated non-Fickian diffusion and zero-order kinetics. The fact that the zero-order kinetics have the highest r^2 values after the Higuchi kinetics means that the release of the active ingredient was time-independent. When the release data obtained were examined over the f2 similarity factor, the formulations that did not contain chitosan polymer (F1 and F4) did not show similarity both among themselves and in pairwise pairings with other formulations ($f2<50$). While the release data were similar in all pairwise comparisons of the four formulations containing chitosan ($f2>50$), only the F2 and F5 formulations had a similarity factor of 48.13 (dissimilar).

4. CONCLUSIONS

As a result of preliminary characterization tests (XRD, XRF) of the raw diatomite, it was determined that it mainly consisted of silicon dioxide. The broad flat peak detected in the XRD analysis proved that the raw diatomite sample was composed of amorphous silica. However, since it is known that organic impurities exist in raw diatomite ores, purification was carried out by the calcination process. Thus, both purer diatomite with higher surface area was successfully obtained.

It was determined that the presence of chitosan in the prepared DPH-loaded formulations caused a decrease in the DPH-loading capacity. The formulation with the highest DPH loading capacity was F1 (97.13 mg/g), and the formulation with the lowest loading capacity was F5 formulation (48.75 mg/g).

As a result of *in vitro* release studies, it was observed that formulations containing chitosan polymer (F2, F3, F5, F6) had slower release than other formulations. At the same time, it was determined that the F5 formulation, which has less diatomite content than other formulations, released less and slower DPH than other formulations. In this case, it was concluded that for the F5 formulation, the DPH active ingredient accumulated in the diatomite inner pores at a higher rate, and with the presence of chitosan, the release was both less and slower.

Drug release profiles of the prepared formulations were compatible with Higuchi kinetics. The n value in Korsmeyer Peppas kinetics was $n<0.5$ for formulations F1 and F4 (chitosan free), which was associated with the Fickian mechanism. In other formulations, this indicated non-Fickian diffusion and zero-order kinetics as $n>1$.

In conclusion, the study showed that diatomite-chitosan composites can have controlled release ability and be used as potential drug carrier systems. Formulations with a slower release profile can be obtained with more detailed studies, incredibly when enriching the diatomite and making it composite with chitosan. More effective drug formulations can be obtained by trying the compositions of other polymeric materials, either alone or together, with diatomite at different composition ratios.

5. ACKNOWLEDGEMENTS

This study was financially supported by Afyon Kocatepe University, Scientific Research Project (BAP), Project No: 23.FEN.BIL.05.

6. CONFLICT OF INTEREST

The authors declare that they have no known competing financial interests or personal relationships that could have appeared to influence the work reported in this paper.

7. AUTHOR CONTRIBUTION

Zeynep Özkan: investigation, writing, methodology, original draft. Muhammet Davut Arpa: original draft, methodology, writing, conceptualization. Melih Özçatal: methodology, editing, conceptualization. Hakan Çiftçi: supervision**,** writing, methodology, editing, conceptualization.

8. REFERENCES

Abbas H.K., AbdulRazzaq I.F., Salal Y.A., Shaheed D.Q., Preparation and evaluation of proniosomal gel containing diphenhydramine HCl, Drug Invention Today, 13(2), 2020.

Abdel-Bary A.S., Tolan D.A., Nassar M.Y., Taketsugu T., El-Nahas A.M., Chitosan, magnetite, silicon dioxide, and graphene oxide nanocomposites: Synthesis, characterization, efficiency as cisplatin drug delivery, and DFT calculations, International Journal of Biological Macromolecules, 154, 621-633, 2020.

Akyuz L., Kaya M., Koc B., Mujtaba M., Ilk S., Labidi J., Yildiz A., Diatomite as a novel composite ingredient for chitosan film with enhanced physicochemical properties, International journal of biological macromolecules, 105, 1401-1411, 2017.

Arpa M.D., Okur N.Ü., Gök M.K., Özgümüş S., Cevher E., Chitosan-based buccal mucoadhesive patches to enhance the systemic bioavailability of tizanidine, International Journal of Pharmaceutics, 123168, 2023.

Arpa M.D., Seçen İ.M., Erim Ü.C., Hoş A., Üstündağ Okur N., Azelaic acid loaded chitosan and HPMC based hydrogels for treatment of acne: formulation, characterization, in vitro-ex vivo evaluation, Pharmaceutical Development and Technology, 27(3), 268-281, 2022.

Arpa M.D., Ünükür M.Z., Erim Ü.C., Formulation, characterization and in vitro release studies of terbinafine hydrochloride loaded buccal films, Journal of Research in Pharmacy, 25(5): 667-680, 2021.

Arpa M.D., Yağcılar A.P., Biltekin S.N., Novel benzydamine hydrochloride and chlorhexidine gluconate loaded bioadhesive films for local treatment of buccal infections, Journal of Drug Delivery Science and Technology, 84, 104497, 2023.

Burkhanova N.D., Yugai S.M., Pulatova K.P., Nikononvich G.V., Milusheva R.Y., Voropaeva N.L., Rashidova S.S., Structural investigations of chitin and its deacetylation products, Chemistry of Natural Compounds, 36, 352-355, 2000.

Çiftçi H., Arpa M.D., Gülaçar İ.M., Özcan L., Ersoy B., Development and evaluation of mesoporous montmorillonite/magnetite nanocomposites loaded with 5-Fluorouracil, Microporous and Mesoporous Materials, 303, 110253, 2020.

Çiftçi H., Arpa M.D., Gülaçar İ.M., Özcan L., Ersoy B., Development and evaluation of mesoporous montmorillonite/magnetite nanocomposites loaded with 5-Fluorouracil, Microporous and Mesoporous Materials, 303, 110253, 2020.

Çiftçi H., Ersoy B., Evcin A., Purification of Turkish bentonites and investigation of the contact angle, surface free energy and zeta potential profiles of organo-bentonites as a function of CTAB concentration, Clays and Clay Minerals, 68, 250-261, 2020.

Coneac G., Vlaia V., Olariu I., Muţ A.M., Anghel D.F. Ilie C., Vlaia L., Development and evaluation of new microemulsion-based hydrogel formulations for topical delivery of fluconazole, Aaps Pharmscitech, 16, 889-904, 2015.

Damian F., Harati M., Schwartzenhauer J., Van Cauwenberghe O., Wettig S.D., Challenges of dissolution methods development for soft gelatin capsules, Pharmaceutics, 13(2), 214, 2021.

Ediz N., Bentli İ., Tatar İ., Improvement in filtration characteristics of diatomite by calcination, International Journal of Mineral Processing, 94(3-4), 129-134, 2010.

Fowler C.E., Buchber C., Lebeau B., Patarin J., Delacôte C., Walcarius A., An aqueous route to organically functionalized silica diatom skeletons, Applied surface science, 253(12), 5485-5493, 2007.

Gao B., Jiang P., An F., Zhao S., Ge Z., Studies on the surface modification of diatomite with polyethyleneimine and trapping effect of the modified diatomite for phenol, Applied surface science, 250(1-4), 273-279, 2005.

Gârea S.A., Mihai A.I., Vasile E., Nistor C., Sârbu A., Mitran R., Synthesis of new porous clay heterostructures: The influence of co-surfactant type, Materials Chemistry and Physics, 179, 17-26, 2016.

Gaware S.A., Rokade K.A., Kale S.N., Silica-chitosan nanocomposite mediated pH-sensitive drug delivery, Journal of Drug Delivery Science and Technology, 49, 345-351, 2019.

Ghebaur A., Garea S.A., Iovu H., New polymer–halloysite hybrid materials—potential controlled drug release system, International journal of pharmaceutics, 436(1-2), 568-573, 2012.

Gültürk E., Güden M., Thermal and acid treatment of diatom frustules, Journal of Achievements in Materials and Manufacturing Engineering, 46(2), 196-203, 2011.

Hadi A., Rao N.G., Rao A.S., Shiva G., Akram J.W., Impact of capsules as a carrier for multiple unit drug delivery and the importance of HPMC capsules, Research Journal of Pharmacy and Technology, 6(1), 34-43, 2013.

Ibrahim S.M., Bin Jumah M.N., Othman S.I., Alruhaimi R.S., Al-Khalawi N., Salama Y.F., Abukhadra M.R., Synthesis of chitosan/diatomite composite as an advanced delivery system for ibuprofen drug; equilibrium studies and the release profile, Acs Omega, 6(20), 13406-13416, 2021.

Kevadiya B.D., Patel T.A., Jhala D.D., Thumbar R.P., Brahmbhatt H., Pandya M.P., Bajaj H.C., Layered inorganic nanocomposites: a promising carrier for 5-fluorouracil (5-FU), European Journal of Pharmaceutics and Biopharmaceutics, 81(1), 91-101, 2012.

Kumar N., Sangeetha D., Sunil Reddy P., Malleswara Reddy A., Development and validation of a dissolution test for delayed release capsule formulation of duloxetine hydrochloride, Current Pharmaceutical Analysis, 8(3), 236-246, 2012.

Laxmi M., Bhardwaj A., Mehta S., Mehta A., Development and characterization of nanoemulsion as carrier for the enhancement of bioavailability of artemether, Artificial cells, nanomedicine, and biotechnology, 43(5), 334-344, 2015.

Lo L., Lu X., Lloyd D., Dissolution testing of a controlled-release capsule formulation: Challenges and solutions using a semi-automated dissolution system, Dissolut. Technol, 20(2), 6-12, 2013.

Luo H., Ji D., Li C., Zhu Y., Xiong G., Wan Y., Layered nanohydroxyapatite as a novel nanocarrier for controlled delivery of 5-fluorouracil, International Journal of Pharmaceutics, 513(1-2), 17-25, 2016.

Lv G., Chang P.H., Xing X., Jiang W.T., Jean J.S., Li Z., Investigation of intercalation of diphenhydramine into the interlayer of smectite by XRD, FTIR, TG-DTG analyses and molecular simulation, Arabian Journal of Chemistry, 10(6), 855-861, 2017.

M Rosenholm J., Sahlgren C., Linden M., Multifunctional mesoporous silica nanoparticles for combined therapeutic, diagnostic and targeted action in cancer treatment, Current drug targets, 12(8), 1166-1186, 2011.

Moradı A.N., Yıldız A., Seydiler (Afyonkarahisar) diyatomitleri ile modifiye edilmiş bitümlerin reolojik özelliklerinin araştırılması, Afyon Kocatepe University Graduate School of Natural and Applied Sciences, Master Thesis (Printed), 2021.

Queiroz M.F., Teodosio Melo K.R., Sabry D.A., Sassaki G.L., Rocha H.A.O., Does the use of chitosan contribute to oxalate kidney stone formation?, Marine drugs, 13(1), 141-158, 2014.

Rea I., Martucci N.M., De Stefano L., Ruggiero I., Terracciano M., Dardano P., Lamberti A., Diatomite biosilica nanocarriers for siRNA transport inside cancer cells, Biochimica et Biophysica Acta (BBA)-General Subjects, 1840(12), 3393-3403, 2014.

Reka, A.A., Pavlovski, B., Fazlija, E., Berisha, A., Pacarizi, M., Daghmehchi, M., & Oral, A., Diatomaceous Earth: Characterization, thermal modification, and application, Open Chemistry, 19(1), 451-461, 2021.

Rezaeifar M., Mahmoudvand H., Amiria M., Formulation and evaluation of diphenhydramine gel using different gelling agents, Der Pharma Chemica, 8(5), 243-9, 2016.

Ruggiero I., Terracciano M., Martucci N.M., De Stefano L., Migliaccio N., Tatè R., Rea I., Diatomite silica nanoparticles for drug delivery, Nanoscale research letters, 9, 1-7, 2014.

Silvestri S., Foletto E.L., Preparation and characterization of Fe2O3/TiO2/clay plates and their use as photocatalysts, Ceramics International, 43(16), 14057-14062, 2017.

Tang C., Hu D., Cao Q., Yan W., Xing B., Silver nanoparticles-loaded activated carbon fibers using chitosan as binding agent: Preparation, mechanism, and their antibacterial activity, Applied Surface Science, 394, 457-465, 2017.

Taş B., Çetin M., Biyolojik orijinli tek doğal mineral: diyatomit, Tübav Bilim Dergisi, 5(2), 28-46, 2012.

Thakur G., Singh A., Singh I., Formulation and evaluation of transdermal composite films of chitosan-montmorillonite for the delivery of curcumin, International journal of pharmaceutical investigation, 6(1), 23, 2016.

Tian L., Abukhadra M.R., Mohamed A.S., Nadeem A., Ahmad S.F., Ibrahim K.E., Insight into the loading and release properties of an exfoliated kaolinite/cellulose fiber (EXK/CF) composite as a carrier for oxaliplatin drug: cytotoxicity and release kinetics, ACS omega, 5(30), 19165-19173, 2020.

Tsai W.T., Lai C.W., Hsien, K.J., Characterization and adsorption properties of diatomaceous earth modified by hydrofluoric acid etching, Journal of Colloid and Interface Science, 297(2), 749-754, 2006.

Vilar G., Tulla-Puche J., Albericio F., Polymers and drug delivery systems, Current drug delivery, 9(4), 367-394, 2012.

Vona, D., Flemma, A., Piccapane, F., Cotugno, P., Cicco, S.R., Armenise, V., & Ragni, R., Drug delivery through epidermal tissue cells by functionalized biosilica from diatom microalgae, Marine Drugs, 21(8), 438, 2023.

Wang C., Hu S., Sun C.C., Expedited development of diphenhydramine orally disintegrating tablet through integrated crystal and particle engineering, Molecular pharmaceutics, 14(10), 3399-3408, 2017.

Wang Y., Cai J., Jiang Y., Jiang X., Zhang D., Preparation of biosilica structures from frustules of diatoms and their applications: current state and perspectives, Applied microbiology and biotechnology, 97, 453-460, 2013.

Wu X.J., Wang J.D., Cao L.Q., Characterization and adsorption performance of chitosan/diatomite membranes for Orange G removal, e-Polymers, 16(2), 99-109, 2016.

Yang, H., Ma, Z., Guan, X., Xiang, Z., Ke, Y., Xia, Y., & Yin, J, Facile fabrication of diatomite-based sponge with high biocompatibility and rapid hemostasis, Journal of Applied Polymer Science, 138(46), 51360, 2021.

Yusan S., Gok C., Erenturk S., Aytas, S., Adsorptive removal of thorium (IV) using calcined and flux calcined diatomite from Turkey: Evaluation of equilibrium, kinetic and thermodynamic data, Applied Clay Science, 67, 106-116, 2012.

Yusan S., Korzhynbayeva K., Aytas S., Tazhibayeva S., Musabekov K., Preparation and investigation of structural properties of magnetic diatomite nanocomposites formed with different iron content, Journal of Alloys and Compounds, 608, 8-13, 2014.

Zargarian S.S., Haddadi-Asl V., Hematpour H., Carboxylic acid functionalization of halloysite nanotubes for sustained release of diphenhydramine hydrochloride, Journal of Nanoparticle Research, 17, 1-13, 2015.

Zhang H., Shahbazi M.A., Mäkilä E.M., da Silva T.H., Reis R.L., Salonen J.J., Santos H.A., Diatom silica microparticles for sustained release and permeation enhancement following oral delivery of prednisone and mesalamine, Biomaterials, 34(36), 9210-9219, 2013.

Zheng Y., Fang H., Wang F., Huang H., Yang J., Zuo, G., Fabrication and characterization of mesoporous Si/SiC derived from diatomite via magnesiothermic reduction, Journal of Solid State Chemistry, 277, 654-657, 2019.

Zheng Y., Wang A., Enhanced adsorption of ammonium using hydrogel composites based on chitosan and halloysite, Journal of Macromolecular Science, Part A, 47(1), 33-38, 2009.

JOURNAL of
MATERIALS and MECHATRONICS:A

e-ISSN 2717-8811
JournalMM, 2023, 4(2), 561-570
https://doi.org/10.55546/jmm.1357217

Araştırma Makalesi / Research Article

Effect of Lattice Design and Process Parameters on the Properties of PLA, ABS AND PETG Polymers Produced by Fused Deposition Modelling

Cem GÜDÜR[1], Türker TÜRKOĞLU[2*], İlker EREN[3]

[1] Balıkesir University, Engineering Faculty, Mechanical Engineering Department, Balıkesir, Türkiye, ORCID ID: https://orcid.org/0000-0002-6836-7656, cemgudur12@gmail.com
[2] Balıkesir University, Engineering Faculty, Mechanical Engineering Department, Balıkesir, Türkiye, ORCID ID: https://orcid.org/0000-0002-0499-9363, turker.turkoglu@balikesir.edu.tr
[3] Balıkesir University, Engineering Faculty, Mechanical Engineering Department, Balıkesir, Türkiye, ORCID ID: https://orcid.org/0000-0003-4326-0294, ieren@balikesir.edu.tr

Geliş/ Received: 11.09.2023; **Kabul / Accepted:** 13.12.2023

ABSTRACT: In this study, tensile strengths of different polymer-based materials PLA (Polylactic Acid), ABS (Acrylonitrile Butadiene Styrene), and PETG (Polyethylene Terephthalate Glycol) were investigated by applying BCC (Body-Centered Cubic), FCC (Face-Centered Cubic) and Gyroid lattice designs with FDM (Fused Deposition Modeling) method which one of the additive manufacturing methods. In addition, weight reduction was performed in the materials with the lattice designs applied. After the mechanical tests, it was determined that the lattice structure has an important role in tensile strengths. Especially in the gyroid lattice structure, which is one of the TPMS (Triply Periodic Minimal Surface) lattice types, it was determined that the maximum strength was obtained in PLA material. In terms of % deformation, the maximum elongation was obtained for PETG material in the gyroid lattice structure. In addition, weight reduction was aimed by using lattice structure patterns, and the maximum weight reduction was found in the BCC lattice structure.

Keywords: Additive manufacturing, Lattice designs, Fused deposition modelling, PLA, ABS, PETG

*Sorumlu yazar / Corresponding author: turker.turkoglu@balikesir.edu.tr

Bu makaleye atıf yapmak için /To cite this article

Güdür, C., Türkoğlu, T., Eren İ. (2023). Effect of Lattice Design and Process Parameters on the Properties of PLA, ABS AND PETG Polymers Produced by Fused Deposition Modelling. Journal of Materials and Mechatronics: A (JournalMM), 4(2), 561-570.

1. INTRODUCTION

Additive manufacturing technology is the process of creating the desired part by adding the material used in general terms layer by layer on top of each other (Sezer et al., 2016 and Özer, 2020). The machines that perform this process are called 3D printers (3D). 3D printers, which have become widespread in recent years, were first included in our lives as a device designed and patented by Charles Hull in the 80s (Srinivasan et al., 2020). Thanks to 3D printers, it is possible to produce parts with complex structures from many materials such as plastic, metal, etc., which are difficult to produce with classical production methods. 3D printers can be used in many different fields from aviation to the automotive industry, from medicine to architecture (Kaygusuz and Özerinç, 2018; Kamer et al., 2022).

3D printers can be classified into 3 main groups according to the material to be used: liquid-based, solid-based, and powder-based (Çelik et al., 2013). In today's market, FDM (Fused Deposition Modelling) technology, which is one of the solid-based additive manufacturing technologies, is widely used. The low cost of the materials used in FDM technology, the variety of materials to be used, and easy accessibility have made this technology more widespread than other Technologies (Evlen, 2019; Başçı and Yamanoğlu, 2021). In 3D printers working with FDM technology, materials called filaments are used as production materials. Filaments are materials that are made suitable for use in 3D printers. Today, Polylactic Acid (PLA), Acrylonitrile Butadiene Styrene (ABS), and Polyethylene Terephthalate Glycol (PETG) are among the filaments used (Zhao et al., 2019; Cano-Vicent et al., 2021).

PLA filament is one of the most widely used filaments because it is easy to work with at low temperatures and in many 3D printers. The printing temperature (on average) is around 190 °C-215 °C. It is easier to print than ABS and PETG filament. Since it has a natural structure, it has no negative effect on human health. It is compatible with open-frame printers. ABS filament is another type of filament that is frequently used today. ABS filament has high heat and impact resistance. However, ABS filament is a petroleum-based filament type. The printing temperature is higher than PLA and PETG filaments and is between 240°C-260°C on average. It is not compatible with open-case printers, a closed-case printer is required. PETG filament is among the most durable filaments. It has high hardness and is impact-resistant. It can be printed more easily than ABS filament. The Printing temperature is between 235°C-255°C on average. It is also compatible with open-frame printers (Awasthi and Banerjee, 2021; Corvi et al., 2023; Jimanez-Martinez et al., 2023).

In their study, Srinivasan et al. (Srinivasan et al., 2020) preferred PETG as filament material, and, parameters such as layer thickness, filler shape, and nozzle diameter were kept constant. However, the filler percentage varied between 20% and 100% with an increment of 10%. In total, 9 samples with different filling percentages were printed in accordance with ASTM D638 Standard. Ender 3 Pro, an FDM printer, was preferred for printing. Firstly, the surface roughnesses of the 9 samples were measured, and then mechanical properties were tested by tensile test. As a result, the sample with a 100 % fill percentage gives the highest result. Alarifi et al. focused on PETG material reinforced with carbon fiber. The filamentised composite mixture was produced in different lattice designs by FDM. Tensile, flexural, and compression tests were carried out. Experimental tests were supported by numerical studies, and it was proved that significant increases in flexural and tensile strength were obtained for PETG-Carbon fiber composite (Alarifi et al., 2023).

ABS material was preferred in the study of Dwiyati et al. (Dwiyati et al., 2019). In this study, there are 6 samples produced with ABS material. These specimens were adjusted so that the layer thickness was 0.1-0.2-0.3 mm. At the same time, all specimens were printed both axially and laterally.

All specimens were printed one by one. As a result, the axial specimen with a layer thickness of 0.3 mm has the largest force and the highest tensile strength. When the axial and lateral directions are compared, the axial specimens have greater force and tensile strength. Similarly, specimens with a layer thickness of 0.3 mm had greater strength and tensile strength. When the images of axial 0.3 and lateral 0.3 specimens were evaluated under SEM, the axial specimens were less dense and consisted of many voids. Srinivasan et al. optimized the production parameters of ABS material through fused deposition modeling. Infill density, infill pattern, and layer thickness values were determined as inputs. The effectiveness of the inputs on the mechanical properties was analyzed using a central composite design. It was determined that the most effective production parameters were infill density and layer thickness (Srinivasan et al., 2020).

PLA material was preferred in the research paper of Rismila et al. (Rismilia et al., 2019). In this study, the effect of the filling pattern and filling density on the results was investigated. Filling densities of 25%, 50%, and 75% were preferred, and grid, tri-hexagon, and concentric were preferred as filling patterns. Parameters such as printing temperature, layer thickness, and printing speed of the samples were kept constant. As a result, the sample with the concentric filling pattern with 75% filling had the highest stress. In the study of Cetin et al. on the mechanical testing of the bonding process of PLA material under hydrothermal conditions; Taguchi orthogonal array optimization was used to determine the optimum set parameters for unaged samples of 45°, 0° surface patterns (Cetin et al., 2023). Tunay et al. focused on the design of auxetic structures from PLA material by fused deposition modeling method. It was stated that auxetic structures have a serious effect on improving properties such as lightness, energy absorption capability, and impact resistance. In addition, the analysis of the variance ANOVA method was also utilized in the study. It was reported that the strut thickness parameter is the most effective parameter on mechanical properties in auxetic samples produced from PLA material. This parameter was followed by strut angle and strut orientation in order of effectiveness.

Lattice structures are three-dimensional structures consisting of one or more repeating unit cells. Each cell consists of uprights connected to each other at nodes within it. Lattice structures can be named as periodic or stochastic lattice structures according to the regular or irregular repetition of the unit cell. On the other hand, lattice structures can be categorised into three different categories according to their shapes; strut-based lattice structures, triple periodic minimum surface lattice structures and shell lattice structures. FCC and BCC belong to the group of strut-based lattice structures, while Gyroid belongs to the group of Triply Periodic Minimum Surface. Sokullu et al. produced Ti6Al4V material in FCC, BCC, Gyroid, Primitive and Diamond lattice structure designs. According to the tensile test results, they reported that the maximum tensile strength was obtained from the TPMS-based lattice structure and the minimum tensile strength was obtained from the strut-based BCC lattice structure (Sokullu et al., 2022)

Weight reduction processes in machine parts constitute one of the objectives of industrial manufacturing operations. The use of different lattice structure patterns in the design of the manufacturing part without compromising mechanical properties and the production of parts by additive manufacturing method stands out as one of the important advantages of FDM technology. In this study, the effect of using different lattice types in the design of 3 different materials on the

mechanical properties was investigated. The lattice productions carried out in the design are considered material-oriented and the results are presented comparatively.

2. MATERIALS AND METHODS

2.1 Materials

In this study, specimens with FCC, BCC, and Gyroid structures were produced using FDM device (Figure 1). PLA, PETG, and ABS filaments were used as filler materials in the production of these samples. All filaments used during the study were purchased from the same supplier and the diameter of these filaments was 1.75 mm.

2.2 Method

The specimens were first designed in Topology software, in accordance with the ISO 527/2 standards. Ultimaker Cura, an open-source slicing program, was preferred for creating G-Codes of the designed samples. In Ultimaker Cura Programme, many parameters such as the position of the sample to be produced on the printing table, printing speed, printing temperature, table temperature, layer height, and fan speed were determined. Among these parameters, nozzle diameter (0.4 mm), support status (no support), the diameter of filaments used (1.75 mm), layer height (0.2 mm), and printing speed (50 mm/s) were kept constant. Production parameters are given in Table 1.

Figure 1. 3D Printer used for his study

Table 1. Production parameters

Material	Production Temperature (°C)	Table Temperature (°C)
PLA	210	60
PETG	230	75
ABS	245	95

The printing temperature and table temperature as variable values were determined according to the filament properties, and the most suitable values were preferred. Variable parameters are shown in the table above. All adjusted samples were printed on Creality Cr5 ProH 3D printer. The same 3D printer was preferred for all samples. The preferred 3D printer can print all 3 filaments used. Tensile tests were carried out in a LABOMAK brand test machine with a capacity of 20 kN (Figure 2.). Tests

were carried out at a speed of 5 mm/s. Tensile tests of PLA, ABS, and PETG materials produced by additive manufacturing were performed according to ISO 527/2 standard.

Figure 2. Tensile test device used for testing specimens (Labomak)

3. RESULTS AND DISCUSSION

The designed lattice structure patterns are shown in Figure 3. In the study, three productions of each design were carried out and the graphs given are the results of the samples where average values were obtained. Images of the specimens after the tensile test were added to the study. In Figure 4; it is determined that lattice structure patterns have a significant effect on strength. It can be seen that the strength and deformation levels change as the types of lattice structure patterns change on the material. It was determined that PLA was the material with the highest strength among materials with the BCC lattice type. In addition, when evaluated within the scope of the percentage deformation, it was determined that PLA was the material that showed the maximum shape change before deformation. For BCC lattice type pattern, PETG material was also found to show high strength after PLA. It was determined that the results for the BCC lattice type pattern of ABS material were relatively low.

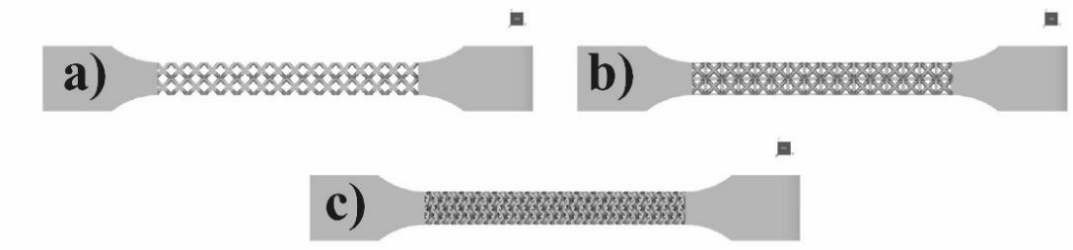

Figure 3. Lattice designs a) BCC b) FCC c) Gyroid

The 3-dimensional tensile test results of the specimens produced with the FCC lattice type using the FDM method are shown in Figure 5. While the highest strength was obtained in the materials produced with PLA material and FCC lattice types, it was observed that the maximum ductility was obtained from PETG material in terms of percentage deformation. In ABS material, it was determined that the lowest mechanical results were obtained as in the BCC lattice type.

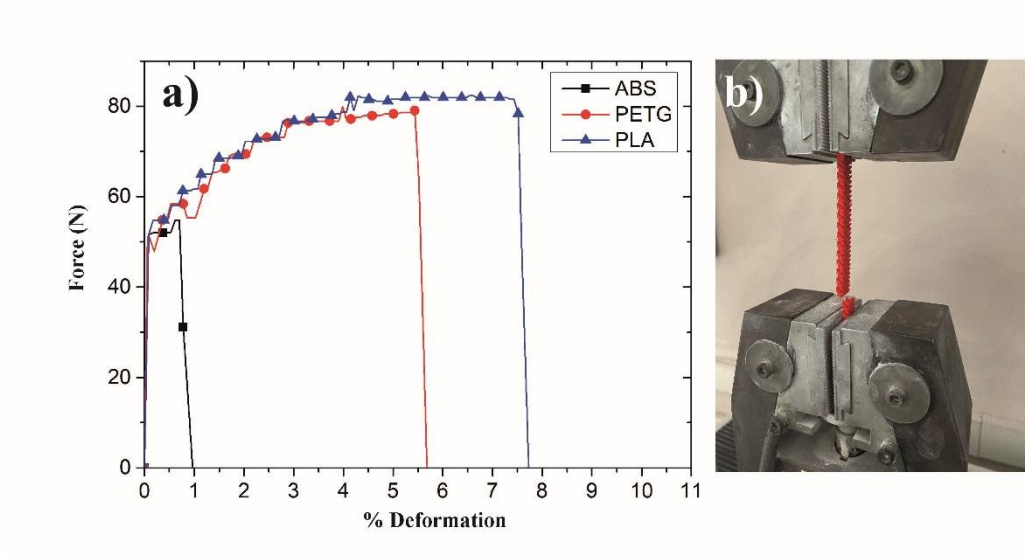

Figure 4. Tensile test results of BCC lattice designs

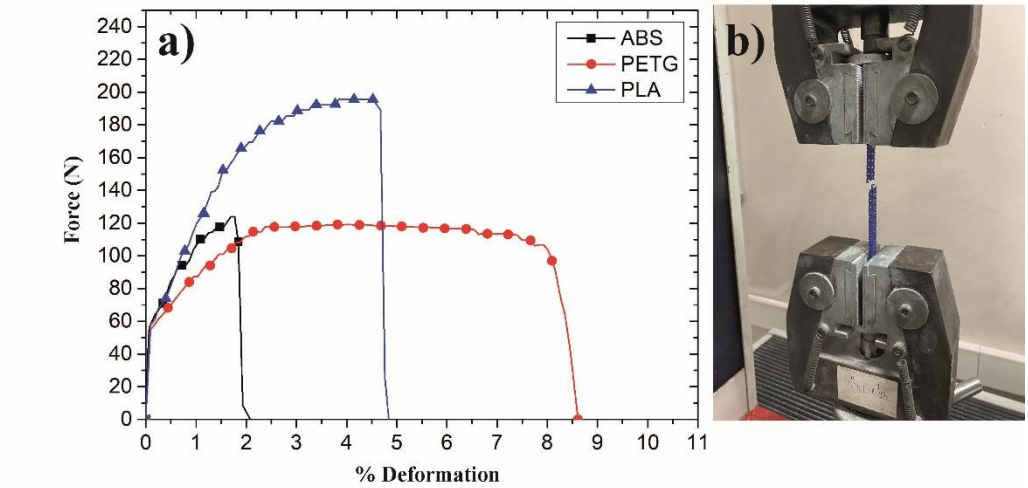

Figure 5. Tensile test results of FCC lattice designs

In all specimens subjected to tensile tests, it was determined that the deformation occurred at the midpoints. In addition, while the BCC and FCC lattice types are specified as Strut-Based, the Gyroid lattice structure is specified in the literature as the TPMS (Triply Periodic Minimum Surface) structure created using surface formations obtained from mathematical formulas (Zhao et al., 2019). Because of the designed gyroid structure, the strength was significantly increased for all materials used in the study. While the maximum strength for the gyroid structure was obtained from PLA material, it was determined that the strength increased considerably in ABS material, unlike the BCC and FCC lattice design (Figure 6). It was also determined that significant progress was made in the percentage deformation for PETG material. The reason for these high mechanical properties is based on the fact that gyroid structures have stretch-dominated behavior. This situation was explained by

the two primary characteristics of TPMS lattices: their increased stability in failure mechanisms and their ability to reduce stress concentrations by doing away with joints.

Lattice structure patterns contribute to weight reduction as well as the mechanical properties they provide to material design. They have potential use, especially in sectors such as the automotive and aerospace industries that require weight reduction. In this study, weights were significantly reduced with BCC, FCC, and gyroid lattice structure patterns compared with the fully filled specimen.

The weight of fully filled tensile test specimens for PLA, ABS, and PETG were calculated as 10.04 g, 8.4 g, and 10.32 g, respectively. Because of the lattice structure patterns applied to the specimens, weight change percentages were determined in BCC, FCC, and gyroid structures for PLA, ABS, and PETG specimens. For PLA material produced with different lattice types by the FDM method, 31.92%, 29.87%, and 26.33% weight reductions were achieved in BCC, FCC, and gyroid lattice types, respectively. After the application of BCC, FCC, and gyroid lattice design to ABS material, 29.50%, 26.37%, and 21.75% weight reductions were achieved, respectively. For PETG material, 33.33%, 31.01%, and 27.58% weight reduction were achieved after the application of BCC, FCC, and gyroid lattice design, respectively. To achieve a better strength-to-weight ratio, some novel attempts have recently been made to design lightweight structures based on porous TPMS. The strength of intricate structures can be increased with the aid of this technique, while the consumption of materials can be reduced.

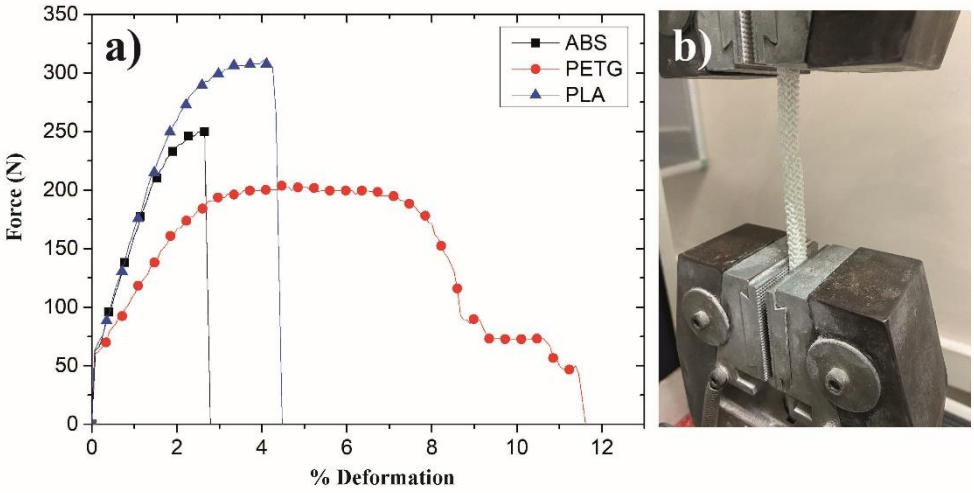

Figure 6. Tensile test results of gyroid lattice designs

Lattice structures are designed for weight reduction in the part. In addition to the weight reduction process, the mechanical properties of the lattice structured parts must be at an acceptable level. The tensile strength values of solid samples were determined as 60.14 MPa, 44.85 MPa and 58.46 MPa for PLA, ABS and PETG, respectively.

In Table 2, tensile test results of specimens produced from different lattices and different plastics are compared.

Table 2. Tensile test results of lattice specimens

	ABS		PETG		PLA	
	Force (N)	**%Def**	**Force (N)**	**%Def**	**Force (N)**	**%Def**
BCC	i)56.26	i)1.20	i)77.53	i)5.09	i)85.12	i)8.36
	ii)54.80	ii)0.96	ii)80.27	ii)5.91	ii)80.85	ii)7.68
	iii)50.12	iii)0.94	iii)79.24	iii)5.68	iii)82.34	iii)7.72
FCC	i)122.12	i)2.02	i)119.19	i)8.61	i)201.83	i)5.23
	ii)123.95	ii)2.07	ii)122.07	ii)8.98	ii)195.55	ii)4.83
	iii)126.18	iii)2.93	iii)117.6	iii)8.21	iii)194.16	iii)4.79
Gyroid	i)249.66	i)2.78	i)202.72	i)11.61	i)290.18	i)5.01
	ii)252.28	ii)3.02	ii)201.66	ii)10.95	ii)285.64	ii)4.33
	iii)249.09	iii)2.66	iii)205.01	iii)12.07	iii)289.49	iii)4.67

Figure 7 shows the deformation images of the specimens after the tensile test. Red colour represents PLA material, white colour represents ABS material and blue colour represents PETG material.

Figure 7. Deformation images after tensile test

4. CONCLUSION

In this study, the FDM technology was used to successfully create PLA, ABS, and PETG materials in BCC, FCC, and gyroid lattice structure patterns.

- The PLA material demonstrated the highest strength for the BCC lattice type and failed under a maximum force of 82.3 N, according to the tensile test findings. Additionally, it was found that the same material (7.7%) shows the high percentage of elongation.
- As a result of the tensile test performed by applying the FCC lattice structure pattern to the sample, it was reported for PLA material that was observed under a maximum percentage elongation was obtained from PETG material (8.6%).

- In a gyroid lattice structure pattern, the PLA material showed the greatest strain at a maximum force of 310.9 N, whereas the PETG material showed the greatest percentage deformation (11.6%).
- The BCC lattice design was found to achieve the greatest weight reduction. For PLA, ABS, and PETG materials, a highest weight decrease of 31.9%, 29.5%, and 33.3% was attained.

5. ACKNOWLEDGEMENTS

No financial support was received for this study.

6. CONFLICT OF INTEREST

Authors approve that to the best of their knowledge, there is not any conflict of interest or common interest with an institution/organization or a person that may affect the review process of the paper.

7. AUTHOR CONTRIBUTION

Cem GÜDÜR conceived and designed the study. Türker TÜRKOĞLU collected data and wrote the manuscript. İlker EREN interpreted the results of this study.

8. REFERENCES

Alarifi I., Mechanical Properties and Numerical Simulation of FDM 3D Printed PETG/carbon Composite Unit Structures, Journal of Materials Research and Technology, 23, 656-669, 2023.

Awasthi P., Banerjee S., Fused Deposition Modeling of Thermoplastic Elastomeric Materials: Challenges and Opportunities, Additive Manufacturing, 46, 1-18, 2021.

Başçı Ü.G., Yamanoğlu R., New Generation Production Technology: Additive Manufacturing via FDM, International Journal of 3D Printing Technologies and Digital Industry, 5, 339-352, 2021.

Cano-Vicent A., Tambuwala M., Hassan S., Barh, D., Aljabali A., Birkett M., Arjunan A., Serrano-Aroca A., Fused Deposition Modeling: Current Status, Methodology, Applications and Future Prospects, 47, 1-19, 2021.

Çelik İ., Karakoç İ., Çakır C., Duysak A., Hızlı Prototipleme Teknolojileri ve Uygulama Alanları, Dumlupınar Üniversitesi Fen Bilimleri Enstitüsü Dergisi, 31, 53-70, 2013.

Cetin E., Fossi, C., Experimental Investigation on Mechanical Strength of Adhesively Bonded 3D-Printed Joints Under Hygrothermal Conditions Using Taguchi Method, International Journal of Adhesion and Adhesives, 126, 103472, 2023.

Corvi A., Collini L., Sciancalepore C., Kumar A., Analysis and Modeling of Damage Mechanism in FDM 3D-Printed Lattice Structure Under Compression Loading, Journal of Mechanical Science and Technology, 37, 1089-1095, 2023.

Dwiyati S., Kholil A., Riyadi R., Putra S., Influence of Layer Thickness and 3D Printing Direction on Tensile Properties of ABS Material, Journal of Physics: Conference Series, 1042, 1-7, 2019.

Evlen H., Investigation of the Effect of Infill Rate on Mechanical Properties of TPU and TPE Specimens Produced in 3D Printer, Dokuz Eylül University Faculty of Engineering Journal of Science and Engineering, 21, 793-804, 2019.

Jimanez-Martinez M., Varela-Soriano J., Carreon J., Mechanical Fatigue of PLA in Additive Manufacturing, Engineering Failure Analysis, 149, 1-19, 2023.

Kamer M., Temiz Ş., Yaykaşlı H., Kaya A., Akay O., Comparison of Mechanical Properties of Tensile Test Specimens Produced with ABS and PLA Material at Different Printing Speeds in 3D Printer, Journal of the Faculty of Engineering and Architecture of Gazi University, 37, 1197-1211, 2022.

Kaygusuz B., Özerinç S., 3 Boyutlu Yazıcı ile Üretilen PLA Bazlı Yapıların Mekanik Özelliklerinin İncelenmesi, Makina Tasarım ve İmalat Dergisi, 16, 1-16, 2018.

Özer G., Eklemeli Üretim Teknolojileri Üzerine Bir Derleme, Nigde Omer Halisdemir University Journal of Engineering Sciences, 9, 606-621, 2020.

Rismilia M., Hidajat S.C., Permana I.G.R, Hadisujoto B., Muslimin M., Triawan F., Infill Pattern and Density Effects on the Tensile Properties of 3D Printed PLA Material, Journal of Physics: Conference Series, 1402, 1-7, 2019.

Sezer H.K., Eren O., Börklü H.R., Karbon Fiber Takviyeli ABS Filamanet Üretimi ve Mekanik Özelliklerinin Araştırılması, 1. 3B Baskı Teknolojileri Uluslararası Sempozyumu, İstanbul/Türkiye, May 5-7, 2016, pp:1-12.

Sokullu B., Gulcan O., Konukseven E., Mechanical Properties Comparison of Strut-Based and Triply Periodic Minimal Surface Lattice Structures Produced by Electron Beam Melting, Additive Manufacturing, 60, 103199, 2022.

Srinivasan R., Pridhar T., Ramprasath L., Charan N., Ruban W., Prediction of Tensile Strength in FDM Printed ABS Parts Using Response Surface Methodology (RSM), Materials Today: Proceedings, 27, 1827-1832, 2020.

Srinivasan R., Ruban W., Deepanraj A., Bhuvanesh R., Bhuvanesh T., Effect on Infill Density on Mechanical Properties of PETG Part Fabricated by Fused Deposition Modeling, Materials Today: Proceedings, 27, 1838-1842, 2020.

Tunay M., Cetin E., Energy Absorption of 2D Auxetic Structures Fabricated by Fused Deposition Modeling, Journal of the Brazilian Society of Mechanical Sciences and Engineering, 45, 500, 2023.

Zhao Y., Chen Y., Zhou Y., Novel Mechanical Models of Tensile Strength and Elastic Property of FDM AM PLA Materials: Experimental and Theoretical Analyses, Materials and Design, 181, 1-10, 2019.

JOURNAL of
MATERIALS and MECHATRONICS:A

e-ISSN 2717-8811
JournalMM, 2023, 4(2), 571-587
https://doi.org/10.55546/jmm.1375777

Araştırma Makalesi / Research Article

Response Surface Modeling of Material Removal and Tool Wear Rate in Powder Mixed Electrical Discharge Machining of CoCrMo Alloy

Faruk ÇAVDAR[1*], CAN YILDIZ[2], Erdoğan KANCA[3]

[1] Osmaniye Korkutata University, Osmaniye Vocational School, Department of Machinery and Metal Technologies, Osmaniye, Turkey,
ORCID ID: https://orcid.org/0000-0002-4981-6428, farukcavdar@osmaniye.edu.tr
[2] Iskenderun Technical University, Institute of Graduate Studies, Hatay, Turkey,
ORCID ID: https://orcid.org/0000-0001-5289-2520, canyildiz33@gmail.com
[3] Iskenderun Technical University, Faculty of Engineering and Natural Sciences, Department of Mechanical Engineering, Hatay, Turkey,
ORCID ID: https://orcid.org/0000-0002-7997-9631, erdogan.kanca@iste.edu.tr

Geliş/ Received: 13.09.2023; **Kabul / Accepted:** 13.12.2023

ABSTRACT: Electric discharge machining (EDM) is commonly used in implant manufacturing due to the challenge of machining materials that are widely employed in these applications. The study applies response surface methodology to model the impact of powder concentration and machining parameters in powder mixed EDM of CoCrMo alloys, a prevalent material for implantation. AISI 316L stainless steel was selected as the electrode material, while Ti6V4Al was chosen as the additive powder based on their biocompatibility properties. An experimental design was created using a Taguchi L_{16} array, which involved selecting 4 levels for each parameter of additive ratio, discharge current, pulse on time, and pulse off time. Regression models were developed for material removal rate (MRR) add tool wear rate (TWR) with satisfactory coefficients of determinations (0.87). Effect of the process parameters on MRR and TWR were analysed by means of 3D response surface plots. As a result of the modeling, it was revealed that discharge current, puls on time positively affected MRR, powder concentrations and puls off time negatively affected it. On the other hand, all of the considered process parameters have increasing effect on TWR.

Keywords: Electric Discharge Machining, CoCrMo, Powder Mixed EDM, MRR, TWR, RSM

*Sorumlu yazar / Corresponding author: farukcavdar@osmaniye.edu.tr

Bu makaleye atıf yapmak için /To cite this article

Çavdar, F., Yıldız, C., Kanca, E. (2023). Response Surface Modeling of Material Removal and Tool Wear Rate in Powder Mixed Electrical Discharge Machining of CoCrMo Alloy. Journal of Materials and Mechatronics: A (JournalMM), 4(2), 571-587.

1. INTRODUCTION

Electric Discharge Machining (EDM) is regarded as the more efficient approach due to its implementation of thermal energy rather than mechanical energy for shaping of electrically conductive substances (Ceritbinmez and Kanca, 2021). In EDM, workpiece machinability is not dependent on the mechanical strength and the temperature resistance. In addition, in EDM, no intimate contact exists between the electrode and the workpiece, eliminating mechanical stresses, vibrations, and noise. EDM is widely used, especially in industries such as mold making, casting, automotive, aerospace, and surgical components, where high mechanical and thermal resistance materials and complex-shaped parts are employed (Ho and Newman, 2003; Sharma and Singh, 2014; Ceritbinmez and Kanca, 2022; Srivastava et al., 2023).

Despite its mentioned advantages, the industrial use of EDM has been limited due to disadvantages such as low processing efficiency and poor surface quality (Ceritbinmez et al., 2023). Extensive research has been conducted to overcome these disadvantages, better understand processing parameters, and improve processing performance (Mujumdar et al., 2015; Abdudeen et al., 2020). In this context, one of the methods developed in recent years to enhance the capabilities of EDM and eliminate its drawbacks is the powder mixed electro-discharge machining (PM-EDM) process. This new method, addresses the drawbacks of EDM and enhances its processing capabilities (Abbas et al., 2020).

In this method, conductive particles such as copper, graphite, tungsten, aluminum, and chromium are added to the dielectric fluid used in conventional EDM. The introduction of these particles weakens the electrical insulation properties of the dielectric fluid, which in turn reduces the spark gap between the electrode and the workpiece, thus making the EDM process more stable. This results in an increase in material removal rate (*MRR*) and surface quality of the workpiece. Additionally, some studies have found that surfaces obtained with PM-EDM exhibit high resistance to corrosion (Sharma and Singh, 2014; Rajkumar and Vishwakamra, 2018; Jawahar et al., 2019).

In recent times, the use of PM-EDM in the field of biomedicine has gained significant attention. PM-EDM is one of the most prominent shaping techniques in this sector (Rajkumar and Vishwakamra, 2018; Erdem and Kiliç, 2020; S. S. Kumar et al., 2020). The use of PM-EDM processing has been found to increase the material's corrosion and wear resistance, as well as enhance the mechanical strength and fatigue life of implants (Al-Amin et al., 2021; Zhang et al., 2022). Additionally, there have been recent reports regarding the use of PM-EDM for applying a nano-porous and bio-mimetic layer to the processed implant surface (Peng et al., 2010; Yang and Huang, 2010; Bains et al., 2020;). This coating layer promotes a strong bone-implant connection (Al-Amin et al., 2020).

CoCrMo alloy is a preferred material for orthopedic implants (Öztürk et al., 2006; Long and Rack, 1998;). This alloy is chosen for its compatibility with bone and other tissues, biocompatibility, and mechanical durability. Furthermore, CoCrMo alloy is suitable for use in corrosive environments such as bodily fluids due to its high corrosion resistance (Jakobsen et al., 2010; Onderka et al., 2014; Bahçe et al., 2019).

The electro-erosion machining method offers advantages in processing CoCrMo alloys due to its flexibility and its ability to overcome challenges associated with traditional machining methods (Kumar 2018; Cakiroglu, 2022; TRAJER, 2023). There is a substantial quantity of literature on the machining of CoCrMo alloy using EDM, both with and without the inclusion of powder in dielectric fluid. In these studies, the classic EDM processing of CoCrMo material has been examined to determine the effects of various processing parameters, electrode types, and dielectric fluids on

surface properties, biological responses, corrosion resistance, in vitro compatibility, electrochemical properties, and surface cytocompatibility of the workpiece. Graphite, W, Cu, Cu-W, and Ti have been used as electrode materials in some of these studies (Iranmanesh et al., 2017; Mahajan et al., 2019; Mahajan and Sidhu, 2019a; Mahajan and Sidhu, 2019b; Chakmakchi et al., 2021). Additionally, in other research, the impact of adding Fe2O3 and γ-Fe2O3 nano powders to the dielectric fluid at different concentrations on the MRR has been investigated (Elsiti et al., 2017; Elsiti and Noordin, 2017).

In this study, the main focus has been on ensuring that there are no residues that can be harmful to the living body on the workpiece when processing CoCrMo material using PM-EDM, especially for implant applications. Therefore, 316L, commonly used in implant fabrication, was selected as the electrode material, and Ti6V4Al, also used in implants, was chosen as the dielectric additive powder (Kayalı and Yalçın, 2020). In a previous study, the effects of powder concentration and EDM parameters on the surface quality of workpieces were investigated when processing CoCrMo with PM-EDM (Yildiz et al., 2023). Furthermore, the use of 316L and Ti6V4Al materials as both electrodes and additive powders has not been found in the literature surveys conducted by the authors.

In this study, the effects of powder concentration (w), discharge current (I), pulse duration (T_{on}), and off time (T_{off}) parameters on the material removal rate (MRR) and tool wear rate (TWR) in the processing of CoCrMo workpieces with a 316L electrode have been analyzed by modeling using the response surface methodology. A Taguchi L_{16} experimental design was conducted using four independent variables at four different levels. Through experimental procedures conducted with the specified experimental set values, wear rates on the workpiece and tool were determined. Regression models were established using the obtained data through the response surface methodology, and the results were analyzed.

2. MATERIALS AND METHODS

The impacts of powder ratio and electric discharge parameters such as discharge current, pulse duration, and off time on the material removal rate and tool wear rate in powder-mixed electro-erosion machining were investigated in this study.

To ensure that the data obtained from a limited number of experiments adequately represent the design space, a Taguchi L_{16} orthogonal experimental design was used, with each of the four independent variables having four different levels.

In this study, ASTM F1537-11 grade CoCr28Mo6 round bar was used as the workpiece, AISI 316L was employed as the electrode material, and Dielektrikum 358 EDM oil was mixed with Ti6V4Al powder in various ratios as the dielectric fluid. Experimental samples were prepared by cutting in 10 mm thickness from a 30 mm diameter round bar then polishing the surfaces. Then processed using the experimental setup detailed in reference (Yıldız et al., 2023) with the Best-3000S ZNC EDM machine.

The parameter sets used in each experiment and the corresponding MRR and TWR values are listed in Table 1. Since the number of independent variables considered in the study is relatively large, regression models were established by using the response surface methodology to better analyze the relationships among these variables and to predict the values of dependent variables for sets of variable values for which experiments were not conducted.

2.1 Determination of *MRR* and *TWR*

To determine the material removal rate, workpiece samples were processed for 10 minutes using the EDM machine, following the specified parameters. After machining, the eroded areas of the workpieces were scanned over the diameter using a Hommel Etamic C8000 profilometer with a TKU300 model probe, as shown in Figure 1, to obtain wear profiles. For each specimen 3 scans have been performed on different diameters of machined area at equal angles, thus 3 wear profile have been obtained. Subsequently, after calculating the area of the wear profile, the adapted *a*, machining depth, as shown in Figure 2, was determined by using Equation 1. Here, A_p represents the area of the wear profile, *a* denotes the equivalent height, and l represents the length of the wear profile. This equivalent machining depth was used to calculate the volume (*V*) of material removed from the workpiece. The wear volume values were then divided by the processing time to determine the *MRR*. Table 2 lists the corresponding heights, wear volumes, and *MRR* values for each experimental sample.

$$h = \frac{A_p}{a} \tag{1}$$

$$V = \frac{\pi l^2}{4} h \tag{2}$$

Table 1. Set values of independent variables used in the experiments and corresponding *MRR* and *TWR* values.

Exp. No	Powder Concentration (g/l)	Current (A)	T_{on} (µs)	T_{of} (µs)	*MRR* (mm³/min)	*TWR* (mm³/min)
E1	0	9	180	18	0.027	0.000
E2	0	12	240	24	0.105	0.253
E3	0	15	300	30	0.304	0.759
E4	0	18	360	36	0.506	1.266
E5	2	9	240	30	0.102	0.158
E6	2	12	180	36	0.165	0.380
E7	2	15	360	18	0.513	0.886
E8	2	18	300	24	0.586	1.138
E9	5	9	300	36	0.017	0.759
E10	5	12	360	30	0.241	1.139
E11	5	15	180	24	0.311	1.266
E12	5	18	240	18	0.350	1.425
E13	8	9	360	24	0.020	0.506
E14	8	12	300	18	0.110	1.013
E15	8	15	240	36	0.215	1.139
E16	8	18	180	30	0.223	1.899

To determine *TWR*, the electrodes to be used in each experimental process were weighed using a precision scale after which the processing was carried out for 10 minutes using the powder ratio and EDM parameters specified in Table 1. Subsequently, each electrode was re-weighed using the same scale to find their mass losses. Equation 3 was used to calculate the volume loss from the mass loss, and this value was divided by the processing time to calculate *TWR*. In Equation 3, *V* represents the volume loss, *m* stands for the mass loss, and φ represents the specific mass of the electrode. The mass

before and after each experiment, mass and volume losses, and *TWR* values for each experimental sample are listed in Table 2.

$$V = \frac{m}{\varphi} \tag{3}$$

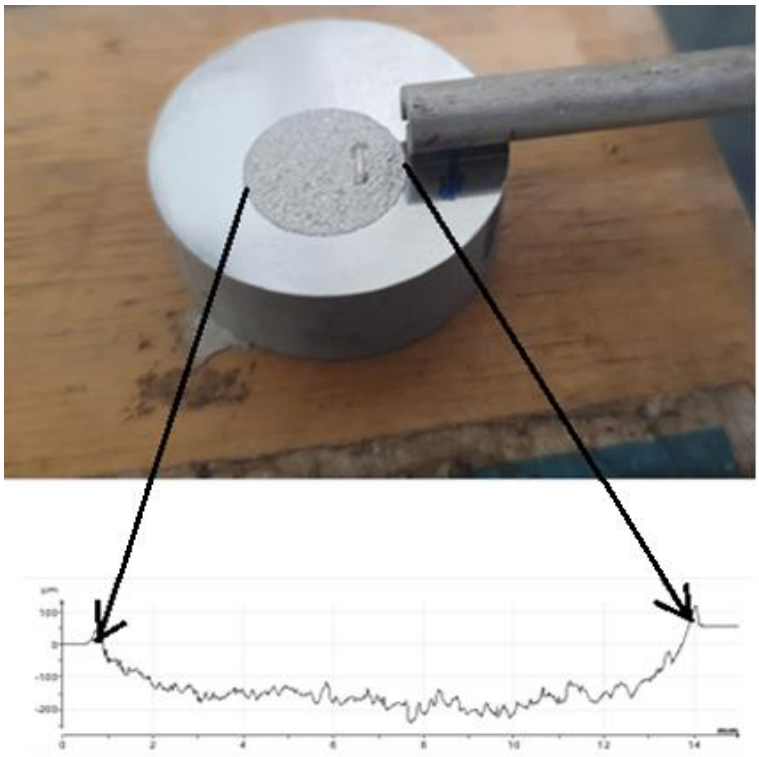

Figure 1. Obtaining wear profiles

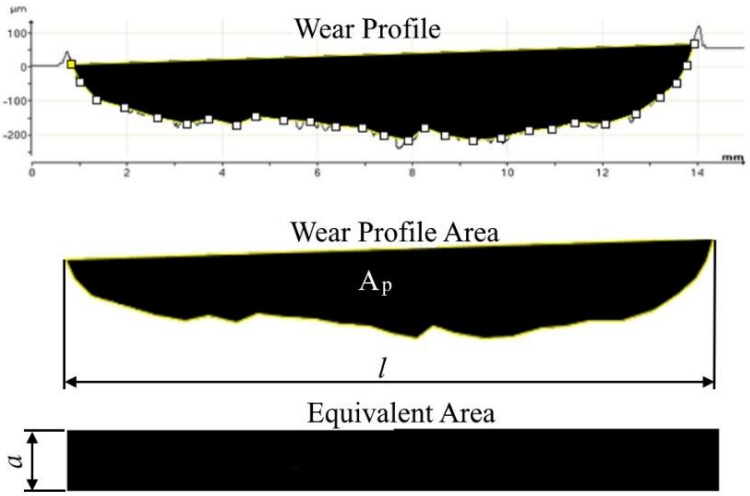

Figure 2. Calculation of equivalent height (h)

2.2 Development of Response Surfaces

In this study, the response surface methodology, which comprises statistical and mathematical operations commonly used to obtain regression models, was employed. Independent variables were set as *w*, *I*, T_{on}, and T_{off}, while the values presented in Table 1 were used to predict the dependent variables, *MRR* and *TWR*.

The Design Expert commercial software was employed in creating the response surfaces. Linear regression models were established for both *MRR* and *TWR*.

Table 2. Data to calculate *MRR* and *TWR* for each experiment sample

	Workpiece			Electrode				
Exp. No	**Equivalent Depth (µm)**	**Wear Volume (mm^3)**	***MRR* (mm^3/min)**	**Mass before process (g)**	**Mass after process (g)**	**Mass loss (g)**	**Wear volume (mm^3)**	***TWR* (mm^3/min)**
E1	23.94	0.271	0.027±0,002	121.320	121.320	0.000	0.000	0.000
E2	92.87	1.050	0.105±0,006	118.790	118.770	0.02	2.532	0.253
E3	118.31	1.337	0.134±0,009	118.560	118.500	0.06	7.595	0.759
E4	447.92	5.063	0.506±0,021	120.100	120.000	0.1	12.658	1.266
E5	90.37	1.022	0.102±0,004	121.580	121.568	0.012	1.575	0.158
E6	146.34	1.654	0.165±0,011	115.080	115.050	0.03	3.797	0.380
E7	783.04	8.851	0.885±0,041	122.430	122.360	0.07	8.861	0.886
E8	943.30	10.663	1.066±0,047	122.600	122.510	0.090	11.384	1.138
E9	15.29	0.173	0.017±0,003	120.940	120.880	0.06	7.595	0.759
E10	213.12	2.409	0.241±0,017	118.490	118.400	0.09	11.392	1.139
E11	274.8	3.106	0.311±0,015	118.160	118.060	0.1	12.658	1.266
E12	309.65	3.500	0.350±0,021	119.650	119.537	0.113	14.251	1.425
E13	17.49	0.198	0.020±0,001	121.300	121.260	0.04	5.063	0.506
E14	97.42	1.101	0.110±0,006	114.630	114.550	0.08	10.127	1.013
E15	189.91	2.147	0.215±0,013	122.110	122.020	0.09	11.392	1.139
E16	197.10	2.228	0.223±0,010	122.190	122.040	0.15	18.987	1.899

3. RESULTS AND DISCUSSION

3.1 ANOVA Results

The results of the analysis of variance (ANOVA) conducted for *MRR* and *TWR* regression models are presented in Table 3. In the table, having an F-value of around 18 for both *MRR* and *TWR*, along with model P-values of 0.0001, indicates that the models are statistically significant. Furthermore, the correlation coefficient (R2) for the *MRR* and *TWR* models is 0.8713 and 0.8697, respectively. This suggests that both models have a good level of predictive capability.

Table 3. ANOVA table for *MRR* and *TWR* models

Response	***MRR* (mm3/min)**	***TWR* (mm3/min)**
Model Type	Linear	Linear
Model Degree of Freedom	4	4
Model F-value	18,62	18,36
Model p-value	<0.0001	<0.0001
R^2	0.8713	0.8697
R^2_{adj}	0.8245	0.8224

Additionally, the adjusted R^2 (R^2_{adj}) values in the table show that the difference between R^2 and R^2_{adj} in the respective models is less than 20%. This indicates that there are no unnecessary terms in the models.

In Table 4, the coded and actual coefficients of terms for the *MRR* regression model are listed. The coded coefficients indicate the degree of influence of the terms on the dependent variables. From Table 4, it can be observed that the term *I* has the most significant impact on *MRR*, while the influence of T_{off} is relatively low. Furthermore, it is evident that *I* and *Ton* have a positive effect on *MRR*, while *w* and T_{off} have a negative impact.

Using the actual coefficients of the terms in Table 4, the *MRR* regression model is constructed as shown in Equation 4.

Table 1. Regression coefficients of coded and actual terms of *MRR* model

Terms	**Coefficients of coded terms**	**Coefficients of actuals terms**
Constant	0.2289	-0.456422
w	-0.0397	-0.016684
I	0.1163	0.04348
T_{on}	0.0425	0.000795
T_{off}	-0.0098	-0.001833

$$TWR = -4564 - 0.016684w + 0.04348I + 0.000795T_{on} - 0.001833T_{off} \quad (4)$$

The experimental values of *MRR* and the corresponding predictions from the regression model are visualized in Figure 3. It is evident from the figure that the predictions from the regression model closely match the actual values, indicating a good fit of the model to the experimental data.

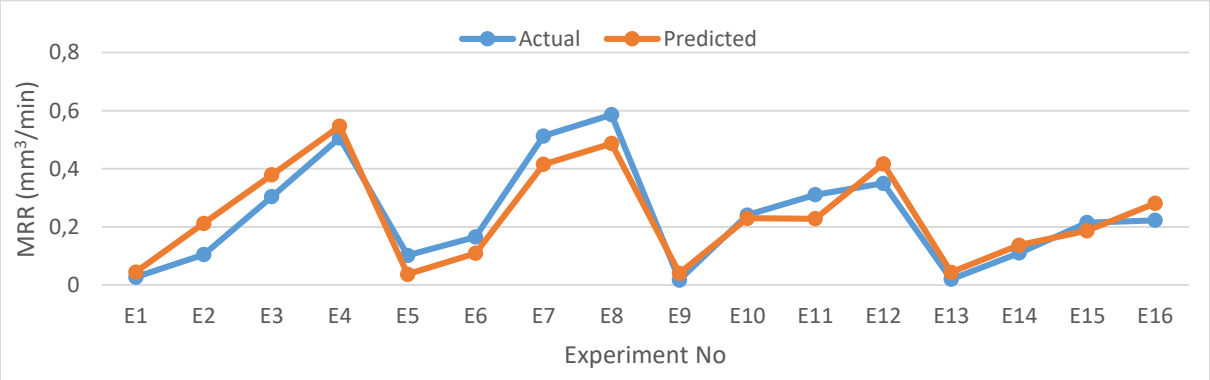

Figure 3. Measured *MRR* values and corresponding predicted values by regression model

The coded and actual coefficients of terms for the *TWR* regression model are provided in Table 5. From the coded coefficients in the table, it can be understood that all terms have a positive influence on *TWR*. Additionally, it is observed that the factor with the highest impact on *TWR* is *I*, and unlike *MRR*, the contribution of T_{off} is higher than *Ton*.

Table 5. Regression coefficients of coded and actual terms of *TWR* model

Terms	Coefficients of coded terms	Coefficients of actuals terms
Constant	0.916	-1.33361
w	0.1854	0.077966
I	0.3192	0.119312
T_{on}	0.0335	0.000625
T_{off}	0.0314	0.005862

The *TWR* regression model equation, created using the actual coefficients from Table 5, is provided in Equation 5.

$$TWR = -1.3336 + 0.07797w + 0.119312I + 0.000625T_{on} + 0.005862T_{off} \quad (5)$$

The experimental values of *TWR* and the predictions from the regression model are depicted in Figure 4. From the graph, it is evident that the model predictions closely align with the experimental results, indicating a strong agreement between the model and the actual data.

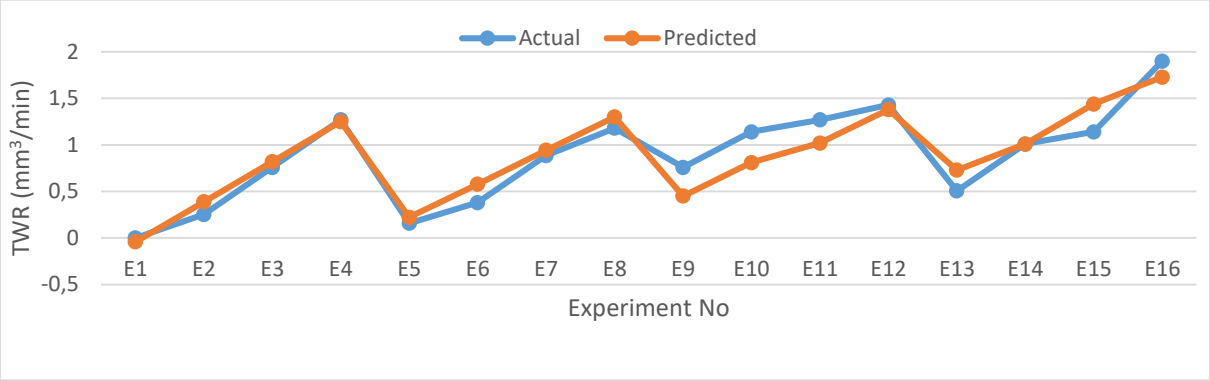

Figure 4. Measured *TWR* values and corresponding predicted values by regression model

3.2 Discussions

To gain a better understanding of how material removal rate and tool wear rate change depending on four different factors, regression models were employed to create three-dimensional surface plots. In three-dimensional plots, only one dependent variable can be represented against two independent variables at a time. Therefore, in each drawing, the values of two variables were held constant.

In Figure 5, we can observe how variations in powder ratio and discharge current relate to different constant values of *Ton* and T_{off}. In Figure 5a, when *Ton* and T_{off} are held at 210 µs and 21 µs, respectively, a linear increase in *MRR* is evident as the current is raised from 10 A to 18 A. This change is notable in the region where the powder ratio is zero, going from 0.11 mm³/min to 0.45 mm³/min, and in the region with a powder ratio of 8 g/l, where it increases from 0 to 0.32 mm³/min. As the discharge current increases, the flow of electrons between the electrode and the workpiece is expected to increase, leading to an anticipated rise in spark frequency and energy. This, in turn, will result in an increased amount of material removed from the workpiece per unit time (Elsiti & Noordin, 2017; Long, Phan, Cuong, & Jatti, 2016; Long, Phan, Cuong, & Toan, 2016; Rehman et al., 2022). Conversely, as the powder ratio increases from 0 to 8 g/l, *MRR* shows a linear decrease. This decline is noticeable, dropping from 0.11 mm³/min to 0 mm³/min when *I* is at 10 A, and from 0.45 mm³/min to 0.32 mm³/min when *I* is at 18 A. The negative impact of the powder ratio on MRR does not align

with the results in the literatüre (Banh et al., 2016; Jahan et al., 2010; Jailani et al., 2020; Majid & Issa, 2014; Razak et al., 2015; Rehman et al., 2022; Singh et al., 2015; Zain et al., 2012). This discrepancy suggests that an increase in the powder ratio may enhance wear on the electrode and that detached particles could potentially adhere to the workpiece. When we consider these changes together, it becomes apparent that the increase in *w* diminishes the positive impact of *I* on *MRR*.

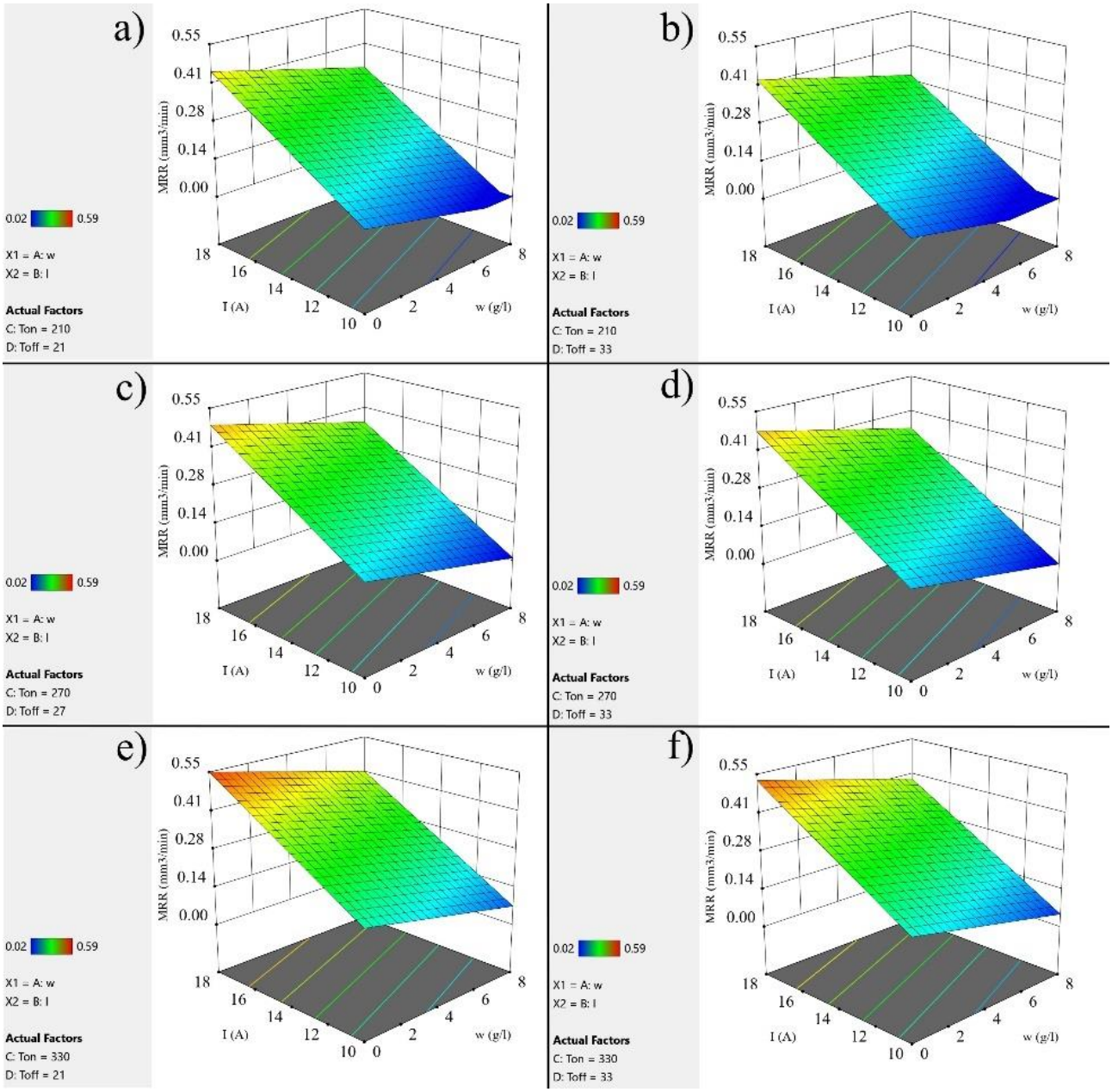

Figure 1. Change in *MRR* according to *w* and *I* for the constant values of a) T_{on} =210 µs, T_{off}=21 µs; b) T_{on} =210 µs, T_{off} =33 µs; c) T_{on} =270 µs, T_{off} =27 µs; d) T_{on} =270 µs, T_{off} =33 µs; e) T_{on} =330 µs, T_{off} =21 µs; f) T_{on} =330 µs, T_{off} =33 µs

In Figure 5b, with *Ton* and T_{off} held at fixed values of 210 ms and 33 ms, respectively, we observe a behavior closely resembling that of Figure 5a. In this graphical representation, it becomes evident that an increase in the value of T_{off} has a discernible negative impact on *MRR* across various values of *w* and *I*. These findings are consistent with those in the literature (Cuong et al., 2020; Long, Phan, Cuong, & Toan, 2016; Nguyen et al., 2021). Furthermore, at elevated *w* values, the influence of *I* appears to slightly weaken, while conversely, at higher *I* values, the effect of *w* also exhibits a marginal increase.

When *Ton* and T_{off} values are increased to their average values for the region of the study, which are 270 and 27 µs, respectively (Figure 5c), the graph exhibits a structure similar to the previous ones, and *MRR* continues to increase for all data points. Furthermore, at low *w* values, the influence of *I* appears to persistently intensify, while at high *I* values, the effect of *w* also continues to increase.

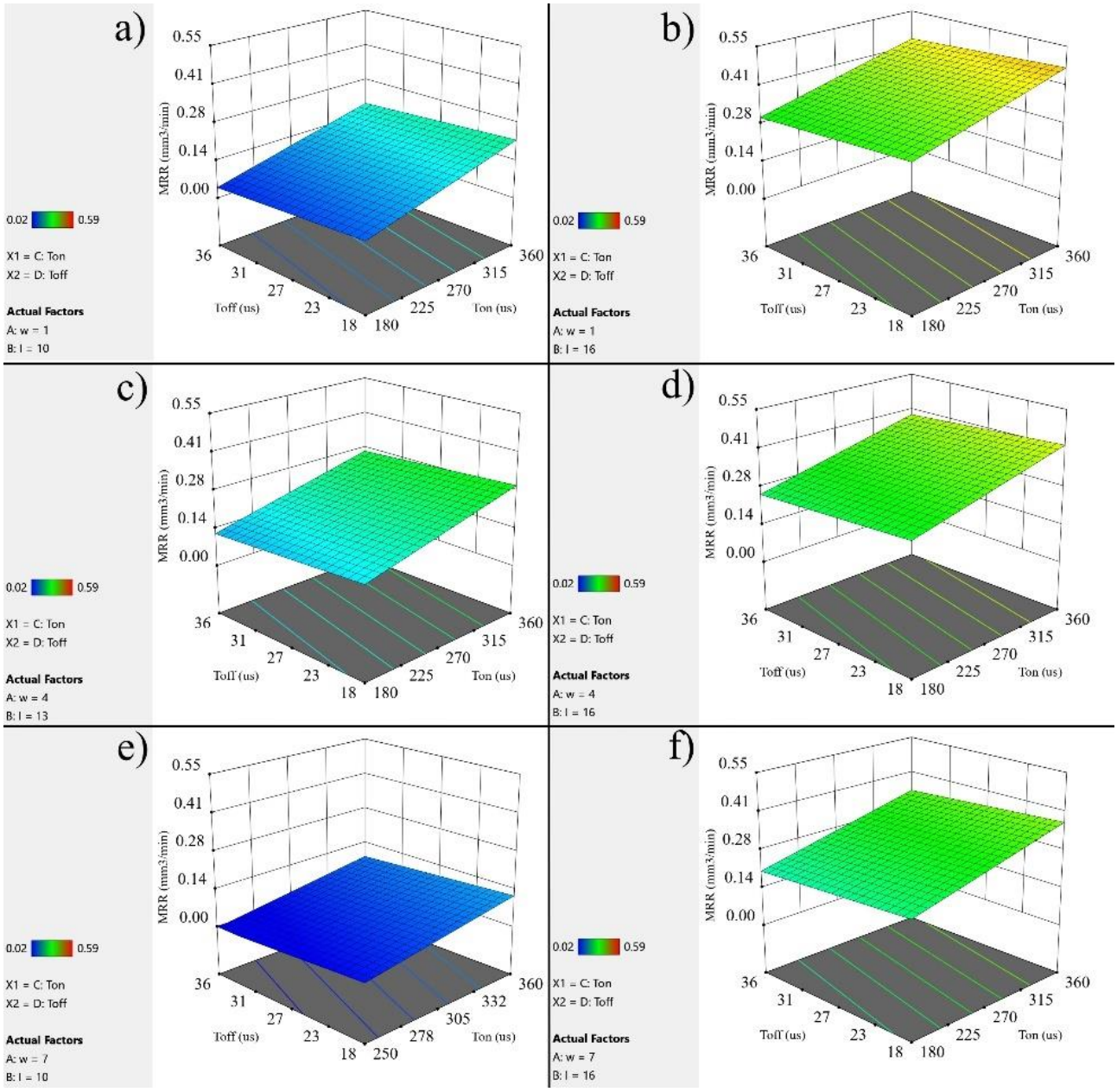

Figure 6. Change in *MRR* according to T_{on} and T_{off} for the constant values of a) *w*=1 g/l, *I*=10 A; b) *w*=1 g/l, *I*=19 A; c) *w*= 4 g/l, *I*=13 A; d) *w*=4 g/l, *I*=16 A; e) *w*=7 g/l, *I*=10 A; f) *w*=7 g/l, *I*=16 A

Figure 5c illustrates the ongoing effect of increasing T_{off} values. Beyond this point, in Figure 5d (*Ton* = 270 and T_{off} = 33 µs), the situation begins to reverse, and *MRR* is observed to decrease indistinctly across the entire graph.

In Figure 5e, at fixed values of *Ton* and T_{off}, 330 and 21 µs, respectively, *MRR* reaches its highest value at 0.548 mm³/min. Figure 5f (*Ton* = 330 and T_{off} = 33 µs) shows a slight decrease in *MRR* across the entire graph due to a slight increase in T_{off}.

The graphs illustrating the variation of *MRR* with respect to *Ton* and T_{off} for constant powder ratio and current values are presented in Figure 6. In Figure 6a, with *w* and *I* fixed at 1 g/l and 10 A,

respectively, *MRR* linearly increases from 0.072 mm³/min to 0.214 mm³/min as *Ton* increases from 180 to 360 µs when T_{off} is 18 µs. In the region where T_{off} is 36 µs, *MRR* similarly rises from 0.039 mm³/min to 0.181 mm³/min within the same *Ton* range. This suggests that the rate of change remains constant for the same T_{off} values.

Upon comprehensive examination of Figure 6a, b, c, d, e, and f, it becomes evident that the increases in current lead to an augmentation of *MRR* across all areas covered by the graphs. Conversely, an increase in the powder ratio is discerned to reduce *MRR* across the entire dataset. Furthermore, with an increase in current (*I*), the slope of *MRR* concerning *Ton* at constant T_{off} values also escalates.

In Figure 7, variation graphs of *TWR* with respect to powder ratio and discharge current for different fixed values of *Ton* and T_{off} are depicted. In Figure 7a, the alterations in *TWR* with respect to *w* and *I* at values of *Ton* and T_{off}, namely, 210 µs and 21 µs, are presented in three dimensions. The graph illustrates that, in the region where *w* equals 0 and *I* ranges from 9 to 18 A, *MRR* linearly increases from 0 to 1.07 mm³/min. When the powder ratio reaches 8 g/l, the change in *MRR* within the *I* range of 9 to 18 A is observed to elevate from 0.77 mm³/min to 1.83 mm³/min. The increase in energy resulting from the rise in discharge current will lead to an increase in temperature not only on the workpiece surface but also on the tool surface, consequently causing an escalation in tool wear (Joshi & Joshi, 2021; Oskueyan et al., 2022; S. et al., 2018).

Conversely, in the region where *I* is 9 A, when *w* increases from 0 to 8 g/l, *TWR* has risen from 0.14 mm³/min to 0.76 mm³/min. This change is observed to occur as an increase from 1.21 mm³/min to 1.84 mm³/min when *I* reaches 18 A. The increase in the powder ratio leading to the rise in TWR is in line with the influence of graphite powder observed in Çogun et al.'s study (Çogun et al., 2006; Jahan et al., 2010).

Upon examining all the graphs in Figure 7 collectively, it becomes apparent that they share a remarkably similar pattern, with *TWR* values exhibiting a gradual and indistinct rise with the increase of *Ton* and T_{off}.

The variation of *MRR* with *Ton* and T_{off} at different fixed values of powder ratio and discharge current is illustrated in Figure 8 through three-dimensional graphs.

In Figure 8a, the variations of *TWR* with respect to *Ton* and T_{off} are depicted with *w* fixed at 1 g/l and *I* at 10 A. In the region where T_{off} is 18 ms, an increase in *Ton* from 180 ms to 360 ms results in a linear rise of *MRR* from its lowest value of 0.16 mm³/min to 0.27 mm³/min. In the same region of T_{off} at 18 ms, this change takes place as an elevation from 0.26 mm³/min to the highest value in the graph, which is 0.37 mm³/min.

The changes in *TWR* in the other graphs closely resemble that of Figure 8a. In each graph, while the values of *TWR* vary with *w* and *I*, the slopes remain consistent. In Figure 8a, with *w* at 1 g/l and *I* at 10 A, the minimum and maximum *TWR* values are 0.17 and 0.37 mm³/min, respectively. In Figure 8c, with *w* at 7 g/l and *I* at 10 A, these values increase to 0.62 and 0.84 as *I* increases. On the other hand, with *I* fixed at 16 A, while *w* varies at 1 g/l (Figure 8b), 4 g/l (Figure 8d), and 7 g/l (Figure 8c), the minimum and maximum *TWR* values are determined as 0.87 and 1.08; 1.11 and 1.32; and 1.34 and 1.45, respectively. From this, it can be inferred that the influence of *I* on *TWR* is significantly higher than that of *w*.

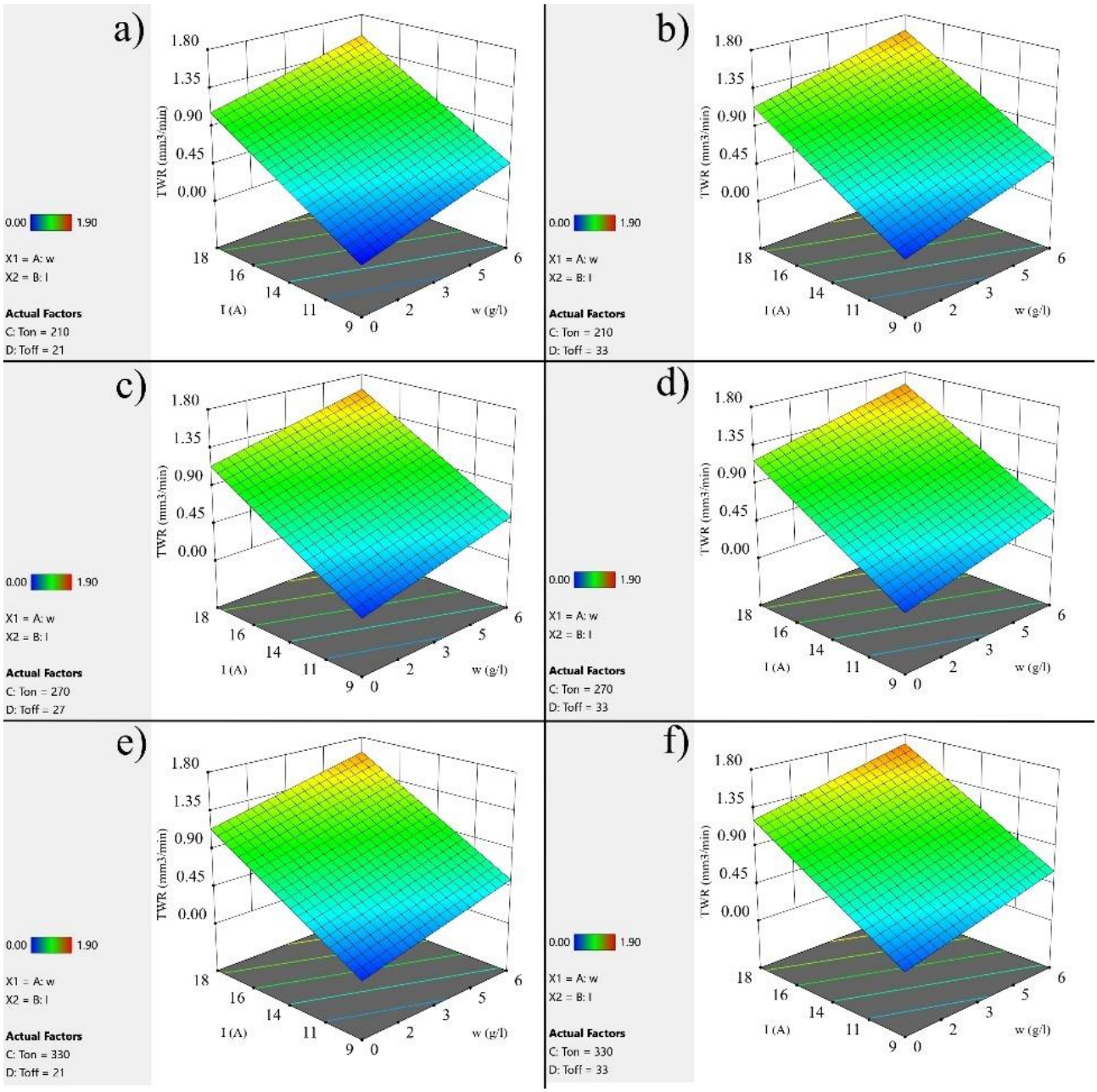

Figure 7. Change in *TWR* according to *w* and *I* for the constant values of a) T_{on} =210 µs, T_{off} =21 µs; b) T_{on} =210 µs, T_{off} =33 µs; c) T_{on} =270 µs, T_{off} =27 µs; d) T_{on} =270 µs, T_{off} =33 µs; e) T_{on} =330 µs, T_{off} =21 µs; f) T_{on} =330 µs, T_{off} =33 µs

4. CONCLUSION

In the present study, RSM was used to model the effect of EDM parameters on *MRR* and *TWR* during the machining of a CoCr28Mo6 workpiece with an AISI 316L electrode and a Ti6V4Al dielectric liquid additive at different ratios. Linear response surfaces constructed by using experimental results of experimental machining of the sample with variable set values of the variables.

Linear regression models developed for *MRR* and *TWR* with R^2 of 0.8713 and 0.8697 respectively. Significances of the models are also verified by p-values smaller than 0.0001.

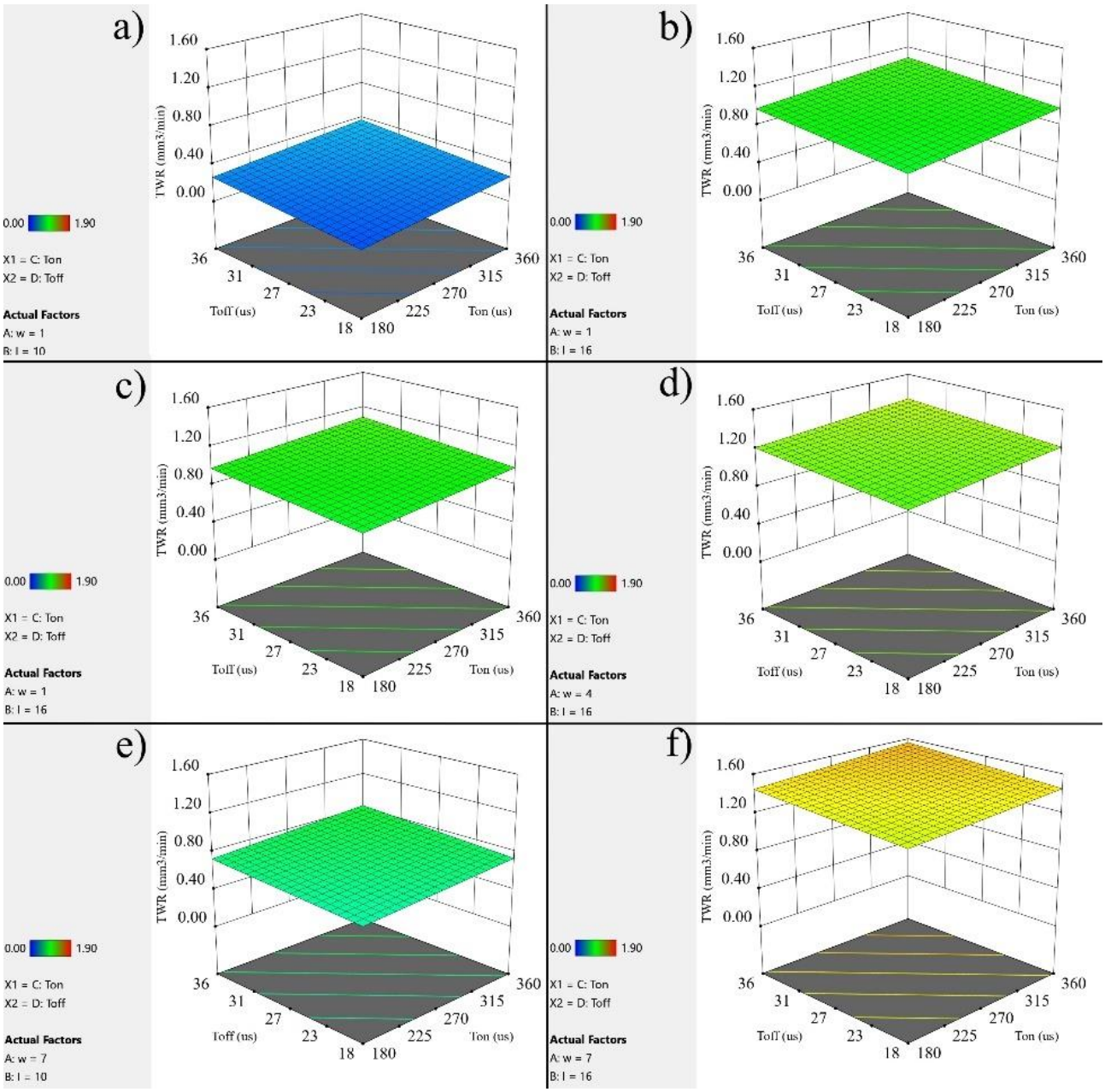

Figure 8. Change in *MRR* according to T_{on} and T_{off} for the constant values of a) *w*=1 g/l, *I*=10 A; b) *w*=1 g/l, *I*=10 A; c) *w*=1 g/l, *I*=10 A; d) *w*=1 g/l, *I*=10 A; e) *w*=1 g/l, *I*=10 A; f) *w*=1 g/l, *I*=10 A

Response surfaces plotted in 3-D according to the mathematical models of *MRR* and *TWR* and following items have been concluded from these plots.

- The most effective factor on *MRR* is *I*. The order of significance of the other factors is as follows: *Ton*, *w*, and T_{off}.
- Impact of *I* and *Ton* on *MRR* is positive, while that of *w* and T_{off} is negative.
- At high dust concentrations, the impact of *I* on *MRR* slightly decreases.
- Effect of *w* on *MRR* increases at higher *I* values.
- *I* is the most influential factor on *MRR*. Additionally, *w* also has a significant effect. However, the influence of *Ton* and T_{off} on *TWR* is quite limited.
- All of the factors have positive impact on *TWR*.

5. ACKNOWLEDGEMENTS

We would like to thank the Payas Vocational and Technical Anatolian High School Directorate for their support.

6. CONFLICT OF INTEREST

Authors approve that to the best of their knowledge, there is not any conflict of interest or common interest with an institution/organization or a person that may affect the review process of the paper.

7. AUTHOR CONTRIBUTION

Faruk ÇAVDAR performed experiment design, constructed response surface models, constructed and interpreted of *MRR* and *TWR* plots, prepared the manuscript. Can YILDIZ manufactured of experiment set up, prepared workpiece samples and electrodes, conducted of experimental machining, made critical analysis of the manuscript. Erdoğan KANCA determined the concept, designed process of the research, and managed the research, obtained of surface profiles, determined of *MRR* and *TWR* values, made critical analysis of the manuscript.

8. REFERENCES

Abbas M.A., Lajis M.A., Abbas D.R., Merzah O.M., Kadhim M.H., Shamran A.A., Influence of additive materials on the roughness of AISI D2 steel in electrical discharge machining (EDM) environment. Materialwissenschaft Und Werkstofftechnik 51(6), 719–724, 2020.

Abdudeen A., Abu Qudeiri J.E., Kareem A., Ahammed T., Ziout A., Recent Advances and Perceptive Insights into Powder-Mixed Dielectric Fluid of EDM. Micromachines 11(8), 754, 2020.

Al-Amin M., Abdul-Rani A.M., Aliyu A.A., Bryant M., Danish M., Ahmad A., Bio-ceramic coatings adhesion and roughness of biomaterials through PM-EDM: a comprehensive review. Materials and Manufacturing Processes 35(11), 1157-1180, 2020.

Al-Amin M., Abdul-Rani A.M., Danish M., Rubaiee S., Mahfouz A.bin, Thompson H.M., Ali S., Unune D.R., Sulaiman M.H., Investigation of Coatings, Corrosion and Wear Characteristics of Machined Biomaterials through Hydroxyapatite Mixed-EDM Process: A Review. Materials 14(13), 3597, 2021.

Bahçe E., Aslan A.K., Çakır N., Güler M.S., CoCrMo Alaşımı Üzerine TaN Esaslı İnce Film Kaplamaların Yüzey Özelliklerinin İncelenilmesi. Karadeniz Fen Bilimleri Dergisi 9(2), 223–237, 2019.

Bains P.S., Bahraminasab M., Sidhu S.S., Singh G., On the machinability and properties of Ti–6Al–4V biomaterial with n-HAp powder–mixed ED machining. Proceedings of the Institution of Mechanical Engineers, Part H: Journal of Engineering in Medicine 234(2), 232–242, 2020.

Banh L.T., Nguyen P.H., Ngo C., Tool wear rate optimization in PMEDM using titanium powder by Taguchi method for die steels. Science and Technology Development Journal 19(2), 88–97, 2016.

Cakıroglu R., Investigation of The Effects of Processing Parameters on Measuring Accuracy in Electro Erosion Machining of Ti-6Al-4V Alloy. Gazi Üniversitesi Fen Bilimleri Dergisi Part C: Tasarım ve Teknoloji, 10(1), 77–85, 2022.

Ceritbinmez F., Günen A., Gürol U., Çam G. A comparative study on drillability of Inconel 625 alloy fabricated by wire arc additive manufacturing. Journal of Manufacturing Processes 89, 150–169, 2023.

Ceritbinmez F., Kanca E., The Effects of Cutting Parameters on the Kerf and Surface Roughness on the Electrode in Electro Erosion Process. Gazi Üniversitesi Fen Bilimleri Dergisi Part C: Tasarım ve Teknoloji 9(2), 335–346, 2021.

Ceritbinmez F., Kanca E., The Effects of Using Brass and Copper Wires on the Cutting Quality of Sleipner Cold Work Steel Cut by WEDM. Journal of Materials and Mechatronics: A 3(2), 163–178, 2022.

Chakmakchi M., Ntasi A., Mueller W.D., Zinelis S., Effect of Cu and Ti electrodes on surface and electrochemical properties of Electro Discharge Machined (EDMed) structures made of Co-Cr and Ti dental alloys. Dental Materials 37(4), 588–596, 2021.

Cuong N.M., Tung L.A., Danh B.T., Cuong N., Van, Hong T.T., Linh N.H., Quy L.T., Pi V.N., Influence of Input Factors on Material Removal Rate in PMEDM Cylindrical Shaped Parts with Silicon Carbide Powder Suspended Dielectric. Key Engineering Materials 861, 129–135, 2020.

Çogun C., Özerkan B., Karaçay T., An experimental investigation on the effect of powder mixed dielectric on machining performance in electric discharge machining. Proceedings of the Institution of Mechanical Engineers, Part B: Journal of Engineering Manufacture 220(7), 1035–1050, 2006.

Elsiti N., Mohd Yusof N., Idris A., Effect of maghemite (γ-Fe2O3) nano-powder mixed dielectric medium on tool wear rate (*TWR*) during micro-EDM of CO-Cr-MO. Pertanika Journal of Science and Technology 25, 847–858, 2017.

Elsiti N.M., Noordin M.Y., Experimental Investigations into the Effect of Process Parameters and Nano-Powder (Fe2O3) on Material Removal Rate during Micro-EDM of Co-Cr-Mo. Key Engineering Materials 740, 125–132, 2017.

Erdem O., Kılıç S., TiO2 Katkılı Çevre Dostu Dielektrik Sıvının Elektro Erozyon Delik Delme Performanslarının Araştırılması. Bilecik Şeyh Edebali Üniversitesi Fen Bilimleri Dergisi 7 (2), 863-885, 2020.

Ho K.H., Newman S.T., State of the art electrical discharge machining (EDM). International Journal of Machine Tools and Manufacture 43(13), 1287–1300, 2003.

Iranmanesh S., Esmaeilzadeh A., Razavykia A., Optimization of Electrical Discharge Machining Parameters of Co-Cr-Mo Using Central Composite Design. Campana, G., Howlett, R., Setchi, R., Cimatti, B. (eds) Sustainable Design and Manufacturing 2017. SDM 2017. Smart Innovation, Systems and Technologies, vol 68. Springer, 48–57, 2017.

Jahan M.P., Rahman M., Wong Y.S., Modelling and experimental investigation on the effect of nanopowder-mixed dielectric in micro-electrodischarge machining of tungsten carbide. Proceedings of the Institution of Mechanical Engineers, Part B: Journal of Engineering Manufacture 224(11), 1725–1739, 2010.

Jailani H.S., Murugan M., Jeavudeen S., Powder additives influence on dielectric strength of EDM fluid and material removal. International Journal of Machining and Machinability of Materials 22(1), 47, 2020.

Jakobsen S.S., Baas J., Jakobsen T., Soballe K., Acid Etching does not Improve CoCrMo Implant Osseointegration in a Canine Implant Model. HIP International 20(2), 171–178, 2010.

Jawahar M., Sridhar Reddy Ch., Srinivas Ch., A review of performance optimization and current research in PMEDM. Materials Today: Proceedings 19, 742–747, 2019.

Joshi A.Y., Joshi A.Y., Multi response optimization of PMEDM of Ti6Al4V using Al2O3 and SiC powder added de-ionized water as dielectric medium using grey relational analysis. SN Applied Sciences 3(7), 718, 2021.

Kayalı Y., Yalçın, Y., Borlanmış AISI 316 L Paslanmaz Çeliğin Difüzyon Kinetiğinin İncelenmesi . Journal of Materials and Mechatronics: A 1(1), 12–21, 2020.

Kumar S., Multi Objective Optimization of Process Parameters of EDM on EN 31 Alloy Steel by Using Grey-Taguchi Method. International Journal for Research in Applied Science and Engineering Technology 6(4), 4771–4778, 2018.

Kumar S.S., Erdemir F., Varol T., Kumaran S.T., Uthayakumar M., Canakci A., Investigation of WEDM process parameters of Al–SiC–B4C composites using response surface methodology. International Journal of Lightweight Materials and Manufacture 3(2), 127–135, 2020.

Long B.T., Phan N.H., Cuong N., Jatti V.S., Optimization of PMEDM process parameter for maximizing material removal rate by Taguchi's method. The International Journal of Advanced Manufacturing Technology 87(5–8), 1929–1939, 2016.

Long B.T., Phan N.H., Cuong N., Toan N.D., Surface quality analysis of die steels in powder-mixed electrical discharge machining using titan powder in fine machining. Advances in Mechanical Engineering 8(7), 168781401665773, 2016.

Long M., Rack H.J., Titanium alloys in total joint replacement—a materials science perspective. Biomaterials 19(18), 1621–1639, 1998.

Mahajan A., Sidhu S. S., Ablyaz T., EDM Surface Treatment: An Enhanced Biocompatible Interface. In P. S. Bains, S. S. Sidhu, M. Bahraminasab C. Prakash (Eds.), Biomaterials in Orthopaedics and Bone Regeneration: Design and Synthesis, Springer Singapore, 33–40, 2019.

Mahajan A., Sidhu S.S., Potential of electrical discharge treatment to enhance the in vitro cytocompatibility and tribological performance of Co–Cr implant. Journal of Materials Research 34(16), 2837–2847, 2019b.

Mahajan A., Sidhu, S.S., In vitro corrosion and hemocompatibility evaluation of electrical discharge treated cobalt–chromium implant. Journal of Materials Research, 34(8), 1363–1370, (2019a).

Majid M.A., Issa A.M., Effect of electric discharge machining of die steel DIN 1.2714 and DIN 1.2343 on surface characteristics and performance measures, 565–577, 2014.

Mujumdar S.S., Curreli D., Kapoor S.G., Ruzic D. Modeling of Melt-Pool Formation and Material Removal in Micro-Electrodischarge Machining. Journal of Manufacturing Science and Engineering 137(3), 2015.

Nguyen A.T., Le X.H., Nguyen V.T., Phan D.P., Tran Q.H., Nguyen D.N., Nguyen M.C., Vu N.P., Optimizing Main Process Parameters When Conducting Powder-Mixed Electrical Discharge Machining of Hardened 90CrSi. Machines, 9(12), 375, 2021.

Onderka F., Volodarskaja A., Kadlec J., Dobrocký D., Klanica O., Electrochemical Deposition of Hydroxyapatite Coatings on CoCrMo Alloy. ECS Transactions 63(1), 277–289, 2014.

Oskueyan S., Abedini V., Hajialimohammadi A., Effects of hybrid Al2O3 - SiO2 nanoparticles in deionized water on the removal rate and surface roughness during electrical discharge machining of Ti-6Al-4V. Proceedings of the Institution of Mechanical Engineers, Part E: Journal of Process Mechanical Engineering 236(3), 1122–1133, 2022.

Öztürk O., Türkan U., Eroglu, A.E., Metal ion release from nitrogen ion implanted CoCrMo orthopedic implant material. Surface and Coatings Technology 200(20–21), 5687–5697, 2006.

Peng P.W., Ou K.L., Lin H.C., Pan Y.N., Wang C.H. Effect of electrical-discharging on formation of nanoporous biocompatible layer on titanium. Journal of Alloys and Compounds, 492(1–2), 625–630, 2010.

Rajkumar H., Vishwakamra M., Performance Parameters Characteristics of PMEDM: A Review. International Journal of Applied Engineering Research 13(7), 5281-5290, 2018.

Razak M.A., Abdul-Rani A.M., Nanimina A.M., Improving EDM Efficiency with Silicon Carbide Powder-Mixed Dielectric Fluid. International Journal of Materials, Mechanics and Manufacturing 3(1), 40–43, 2015.

Rehman A.U., Arif W., Hussain M.I., Miran S., Hussain S., Lee G.H., Analysis of Particle Size and Concentration in Die Sinking Electric Discharge Machining. Materials 15(14), 4932, 2022.

S. R., Jenarthanan M.P., A.S., B.K., Experimental investigation of powder-mixed electric discharge machining of AISI P20 steel using different powders and tool materials. Multidiscipline Modeling in Materials and Structures 14(3), 549–566, 2018.

Sharma R., Singh J., Effect of Powder Mixed Electrical Discharge Machining (PMEDM) on Difficult-to-machine Materials – a Systematic Literature Review 14(4), 233–255, 2014.

Singh B., Kumar J., Kumar S., Influences of Process Parameters on MRR Improvement in Simple and Powder-Mixed EDM of AA6061/10%SiC Composite. Materials and Manufacturing Processes 30(3), 303–312, 2015.

Srivastava S., Vishnoi M., Gangadhar M.T., Kukshal, V., An insight on Powder Mixed Electric Discharge Machining: A state of the art review. Proceedings of the Institution of Mechanical Engineers, Part B: Journal of Engineering Manufacture, 237(5), 657–690, 2023.

Trajer M., Analysis of the relationship between the properties of selected materials and the parameters of the EDD process. Materials Research Proceedings 28, 1747–1758, 2023.

Yang W.E., Huang, H.H., Improving the biocompatibility of titanium surface through formation of a TiO2 nano-mesh layer. Thin Solid Films 518(24), 7545–7550, 2010.

Yıldız C., Çavdar F., Kanca E., A Response Surface Modeling Study on Effects of Powder Rate and Machining Parameters on Surface Quality of CoCrMo Processed by Powder Mixed Electrical Discharge Machining. Karadeniz Fen Bilimleri Dergisi 13(2), 415–433, 2023.

Zain Z.M., Ndaliman M.B., Khan A.A., Ali M.Y., Electro-Discharge Machining of SUS 304 Stainless Steel with TaC Powder-Mixed Dielectric. Advanced Materials Research, 576, 72–75, 2012.

Zhang W., Li L., Wang N., Meng J., Ren J., Surface modification of Ti-6Al-4 V by gas–liquid mixed EDM. The International Journal of Advanced Manufacturing Technology, 119(5–6), 3833–3844, 2022.

JOURNAL of
MATERIALS and MECHATRONICS:A

e-ISSN 2717-8811
JournalMM, 2023, 4(2), 588-597
https://doi.org/10.55546/jmm.1388504

Araştırma Makalesi / Research Article

Effect of Welding Methods and Compound Reinforcement Used in Joining Natural Gas Pipes on Weld Strength

Rıza KARA[1*], Fatih ÇOLAK[2], Gökhan YILDIRIM[3], Hakan Furkan AKSU[4]

[1] Uşak Üniversitesi, Teknik Bilimler Meslek Yüksekokulu, Makine ve Metal Teknolojileri Bölümü, Uşak, Türkiye,
ORCID ID: https://orcid.org/0000-0002-0820-2577, riza.kara@usak.edu.tr
[2] Uşak Üniversitesi, Teknik Bilimler Meslek Yüksekokulu, Makine ve Metal Teknolojileri Bölümü, Uşak, Türkiye,
ORCID ID: https://orcid.org/0000-0002-1161-9875, fatih.colak@usak.edu.tr
[3] Uşak Üniversitesi, Teknik Bilimler Meslek Yüksekokulu, Makine ve Metal Teknolojileri Bölümü, Uşak, Türkiye,
ORCID ID: https://orcid.org/0000-0002-6863-171X, gokhan.yildirim@usak.edu.tr
[4] Nuri Şeker Uşak Şeker Fabrikası, Uşak, Türkiye,
ORCID ID: https://orcid.org/0009-0006-1521-2702, hakanfurkan_123@hotmail.com

Geliş/ Received: 09.11.2023; **Kabul / Accepted:** 21.12.2023

ABSTRACT: In this study, API 5L X52 steel pipe with a diameter of 1/2 inch and a thickness of 2.8 mm was cut into a 100 mm length and the weld grooves were machined for the weldability with different welding processes using SiC additions. The steel pipes were welded with welding methods of oxy-gas, electric arc and MAG. The specimens were welded in two ways: with and without silicon carbide (SiC) reinforcement. The welded samples were prepared for microstructure, tensile, fatigue and hardness tests in accordance with the standards and mechanical tests were applied. The highest yield strength was obtained with the electric arc welded sample using a rutile electrode with SiC reinforcement. It was observed that the mechanical properties of API 5L X52 steel welds were improved with the addition of SiC reinforced.

Keywords: API 5L X52 steel, Welding methods, Mechanical properties, SiC

*Sorumlu yazar / Corresponding author: riza.kara@usak.edu.tr

Bu makaleye atıf yapmak için /To cite this article

Kara, R., Çolak, F., Yıldırım, G., Aksu, H.F. (2023). Effect of Welding Methods and Compound Reinforcement Used in Joining Natural Gas Pipes on Weld Strength. Journal of Materials and Mechatronics: A (JournalMM), 4(2), 588-597.

1. INTRODUCTION

Natural gas, which has a wide area of use in the world, is the most consumed fuel (Biresselioglu et al., 2015). Safety and economy should be taken into consideration in the selection of natural gas pipes to be used for transporting the natural gas from its source (Capelle et al., 2013). Pipelines are the most common method in the world to transport high-consumption and constantly used liquids and gases over long distances, such as oil, water, and natural gas (Abedi et al., 2007; Baek et al., 2010; Javidi et al., 2014). Today, these pipes are preferred because they are easy to join by welding, are safe and economical (Mulder et al., 2007).

X52 type steel pipes are one of the preferred materials used for the transmission of liquid and gaseous fuels (Ju et al., 2003). X52 type steels constitute an important steel group preferred due to their high yield strength and high toughness properties. Conventional arc welding methods are widely used in joining of structural steels including stainless grades (Ezer & Cam, 2022; Senol & Cam, 2023; Serindag & Cam, 2021; Serindag & Cam, 2022; Serindag & Cam, 2023; Serindag et al., 2022a; Serindag et al., 2022b). However, the most obvious problem encountered during welding in these steels is the tendency for hardening that occurs in the heat affected zone (HAZ) (Seyedrezai et al., 2014). Micro islands consisting of martensite and austenite containing high carbon may form in the HAZ of these steels (Bhadeshia et al., 2004; Bohemen et al., 2017; Hossain et al., 2017). The amount of this micro-sized island is directly affected by the cooling rate. The effect of microalloying elements such as titanium (Ti) and boron (B) on the toughness of HAZ is related to the carbon equivalent value of X52 type steels. The carbon equivalence of X52 type steels is in the appropriate range for good toughness in the HAZ (Handoko et al., 2019). High amounts of silicon (Si) are harmful for welding. However, when the manganese rate is increased, the amount of Si can also be increased. In fusion welds of steels containing more than 0.7% Si, if necessary, precautions are not taken, it occurs as a pore and crack defect in the silicon oxide welded area (Ghosh et al., 2013; Jonas et al., 2013). The presence of Mg in the filler metal can provide useful properties through alloying (Jayashree et al., 2020).

However, in traditional welding processes, differences occur in the physical properties of the weld metal and the reinforcement phase due to welding defects such as slag, porosity and recovery of SiC particles in the melting weld zone. Thus, a brittle phase forms due to chemical reactions occurring at high temperatures between the weld metal and the reinforcement phase, making high-quality weld joint difficult (Jayashree et al., 2021). Therefore, lower Si content in SiC reinforced composites negatively affects the desired results after welding (Iseki et al., 1984).

In this study, the welding of API 5L X52 steel were investigated using oxy-gas, electric arc welding, MAG welding methods with and without SiC reinforcement. These welding processes were performed using different welding methods, and as a result, tensile and fatigue strengths and hardness distributions were calculated. The microstructure-mechanical property relationship of welded samples was determined through tensile, fatigue and hardness testing.

2. MATERIALS AND METHODS

The materials and methods used in the experimental methods for experimental studies are given below. The chemical composition analysis (% weight) of X52 steel pipe used for welding is given in Table 1, and its mechanical properties are given in Table 2. At the same time, the ferrite and perlite ratios of the X52 steel pipe are given in Table 3.

Table 1. Chemical Composition Analysis (% Weight) Results of X52 Steel Pipe

	C	Mn	Si	Cu	Al	Nb	S	P	V	Cr
X52	0,106	0,91	0,24	0,021	0,039	0,02	0,007	0,013	0,002	0,017

Table 2. Mechanical Properties of X52 Steel Pipe (API specification 5L, 2018)

	0.2% offset yield strength, MPa	Tensile strength, MPa
X52	360 (min)	460 (min)

Table 3. Ferrite to Perlite Ratios of X52 Steel Type (Tobón et al., 2014)

Steel Type	Ferrite Ratio	Perlite Ratio
X52	86,64	13,35

In this study, X52 pipes of 1/2 inch diameter, 2.8 mm thick and 100 mm long were welded using Oxy-gas, Electric Arc and MAG welding methods. Table 4 shows the weld parameters of all four weld methods and conditions for SiC reinforcement used for the welding of X52 pipe steels.

Table 4. Prepared Samples and Welding Conditions

	Weld	Addition	Comp.	Current(A)		Weld	Addition	Compound	Current(A)
1	Oxy-gas	∅ 2 mm AISI 1020 Steel	---	---	**5**	Oxy-gas	∅ 2 mm AISI 1020 Steel	2gr Cellulosic Varnish + 2 gr SiC	---
2	EAW	∅ 3,25 Rutile (E-6013)		115	**6**	EAW	∅ 3,25 Rutile (E-6013)		115
3	EAW	∅ 3,25 Cellulosic (E8010-G)		115	**7**	EAW	∅ 3,25 Cellulosic (E8010-G)		115
4	MAG	∅ 1 mm Steel (SG2)		125	**8**	MAG	∅ 1 mm Steel (SG2)		125

Samples 1 and 5 were welded in a single pass with oxy-gas (Oxy-Acetylene) welding (Fig. 1a). Samples 2, 3, 6 and 7 were tack welded from four different locations and then welded in a single pass using electric arc welding at 115 A. MAG welding of samples 4 and 8 was done with pure CO_2 (100%) gas (Fig. 1b). First, the samples were tack welded from four different locations and then welded in a single pass with 125 A and 1.5 m/s wire feed speed. For samples 5, 6, 7 and 8, a mixture of cellulosic varnish (2 g) and SiC (2 g) was prepared and applied to the weld joints.

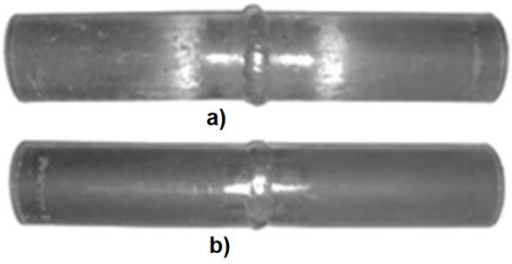

Figure 1. Welded X52 steel pipe

Transverse tensile samples were prepared from the welded samples according to TS EN ISO 4136 standard. Tensile test results were obtained with 3 test samples at room temperature and under each condition, by selecting 2 mm/min as the tensile speed. Hardness values from the welding areas of the samples welded by different welding methods were measured in Rockwell A (HRA). In metallographic examinations, the welded parts were cut and ground perpendicular to the direction of welding progress. The polished samples were etched with 3% Nital + alcohol mixture. During metallographic examinations, images were taken with a microscope at 100X and 200X magnifications.

3. RESULTS AND DISCUSSION

The results of the tensile tests of the welded samples with and without SiC addition are shown in Figure 2. As can be seen, the highest yield strength of 380 MPa was measured in the samples welded with electric arc welding using rutile and electrode with an addition of SiC. It is seen that SiC reinforcement has an effect on the yield strength and maximum tensile strength when the welds made with all welding methods are compared. In welding processes without SiC reinforcement, the yield strength was obtained as 90 MPa in samples welded with oxy-gas, 95 MPa in EAW samples made with rutile electrode, and 70 MPa in samples welded using cellulosic electrode. The yield strength of the samples welded with the MAG welding method was obtained as 160 MPa. In the samples welded using oxy-gas, electric arc and MAG welding methods without SiC reinforcement, the highest tensile strength was obtained as 313 MPa in the sample joined by the MAG welding method. The lowest tensile strength was obtained at 215 MPa in the sample welded with oxy-gas welding. The highest % elongation value was obtained as 14.7% in the SiC unreinforced welded sample joined by the EAW method with rutile electrodes. The lowest % elongation was obtained as 3.5% in the sample joined with MAG welding without SiC reinforcement. The difference in these two tensile strength and % elongation amounts is due to the difference in the amount of ferrite formed in the microstructure of the welded joints.

The yield strength of SiC reinforced welds was obtained as 340 MPa in samples welded with oxy-gas welding method, 380 MPa in samples welded with EAW, and 200 MPa in samples welded with MAG welding method. Vargas-Arista et al., 2012, in their study, stated that the yield strength was 420-520 MPa in samples joined using submerged arc welding. In another study (Candan et al., 2006), it was stated that the highest values were obtained in the welding of X52 steel pipes with the MAG welding method.

The maximum % elongation in welded specimens were 15.5% in samples welded with oxy-gas with SiC reinforcement, 16% in samples welded with EAW with rutile electrode, 17.5% with cellulosic electrode and 4.25% in MAG welding. When the tensile test results are examined, the values closest to the yield limit of the main material, which is approximately 360 MPa (Table 2), were obtained in SiC reinforced samples. The yield stress in the SiC reinforced EAW sample was obtained higher than that of the main material (380 MPa). The yield strength of the samples joined by welding without the use of reinforcement was lower than the yield strength of the base material. Regarding the tensile strength of the samples welded by SiC reinforced oxy-gas, electric arc and MAG welding methods, the highest tensile strength was obtained as 544 MPa in the sample joined by the rutile electrode EAW method, and the lowest tensile strength was obtained as 329 MPa in the sample joined by the MAG welding method. The highest average % elongation of the SiC reinforced welded samples was obtained as 17.5% in the sample joined by the cellulose electrode EAW method. The

lowest % elongation value was obtained as 4.25% in the sample joined with SiC reinforced MAG welding. The results of the fatigue test performed are given in Table 5.

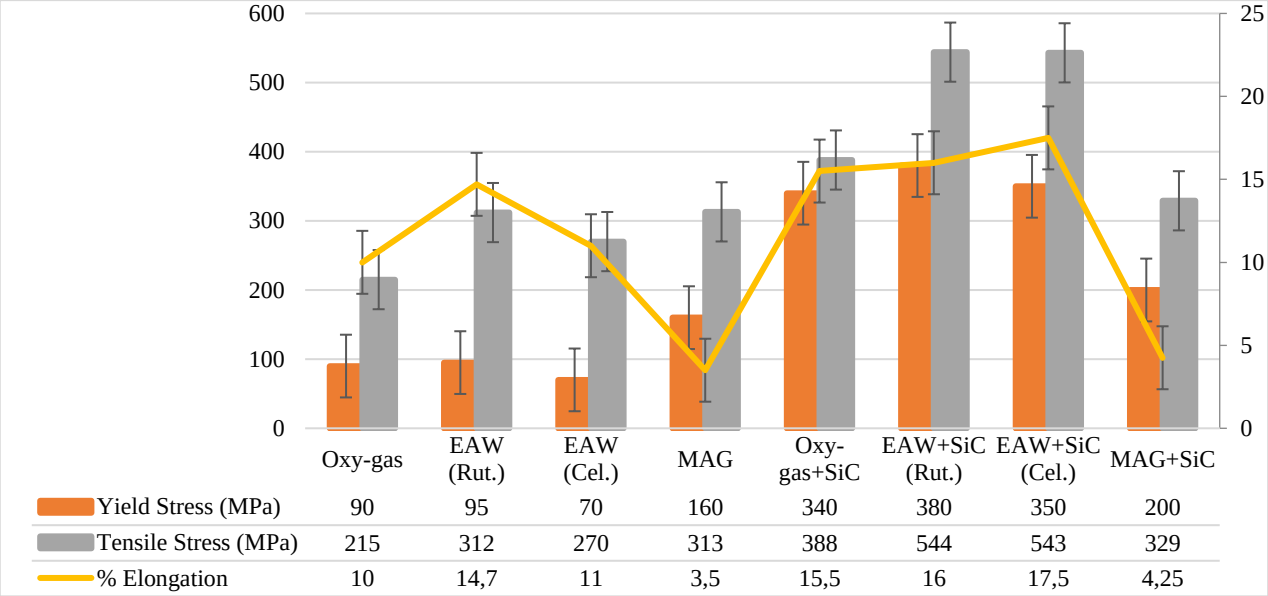

Figure 2. Tensile test results graph

Table 5. Fatigue Test Results

No	1	2	3	4	5	6	7	8
Number of Cycles	1000	1291	3700	26298	60000	52000	27648	27740
Fracture Zone	W.Z.	W.Z.	W.Z.	HAZ	B.M.	W.Z.	W.Z.	HAZ

When the fatigue test results of welds without SiC reinforcement were examined, the longest number of cycles was seen in the sample 4 that was joined using MAG welding method. The lowest number of cycles was obtained in the oxy-gas welded sample. Except for the sample joined with the MAG welding method, it was observed that there were ruptures in the weld area in the samples welded with other welding methods.

However, the rupture occurred in the HAZ region of the sample welded with the MAG welding method. The Mn and C content of the additional wire used here affected the tensile and fatigue test results in the welded samples. This effect was observed clearly in the MAG welding method. In microstructure studies, changes in the properties of the electrodes used have led to changes in the weld microstructures.

When the fatigue results were examined, the longest number of cycles in the samples welded with SiC reinforcement was obtained in the welding process with oxy-gas welding (sample no. 5). The lowest number of cycles was seen in sample number 8, which was welded by the MAG welding method with SiC reinforcement. The hardness of the weld areas of the welds was also measured. To compare the hardness results of each weld, first the hardness of the base material and then the welded samples were measured. The hardness values obtained here are given in Table 6.

In a study (Candan et al., 2006), micro hardness values of X52 steel pipes were obtained as 155-160 HV5 in samples welded in horizontal groove position with the MAG welding method. The hardness value was higher as a result of welding with the MAG welding method compared to the main material and oxy-gas welding method. It was observed that the 66.2 HRA value obtained in

experimental studies was approximately 318 HV from the hardness conversion table. This can be explained by the fact that the SiC reinforcement breaks down due to the high temperature generated by welding electrode during the welding process, creating carbon-rich regions in the weld metal structure.

Table 6. Hardness Values

No	B.M.	1	2	3	4	5	6	7	8
Hardness (HRA)	23,2	22,5	40,6	41,8	40,7	43,3	44,7	56,4	66,2

The samples were examined metallographically to determine the microstructure-mechanical property relationship. The microstructure of the base material is given in Figure 3. Separate optical microstructure images were taken from the HAZ and weld metal of the welded samples. When the overall microstructures were examined, it was observed that the needle structures seen were acicular ferrite. The rapid solidification of the samples after welding explains the reason for the formation of this acicular ferrite structure.

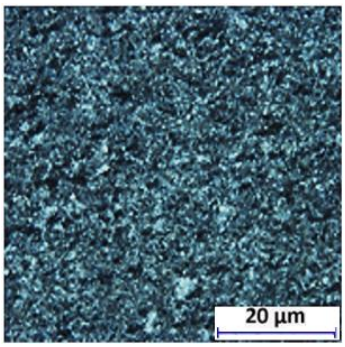

Figure 3. Microstructure of base material

The microstructure of the samples welded with oxy-gas welding method is given in Figure 4 (a), the weld metal without SiC reinforcement, the HAZ with SiC reinforcement in Figure 4 (b), and the weld metal with SiC reinforcement in Figure 4 (c). Here, it is observed that after the oxy-gas welding, the grain size of the sample becomes larger compared to the base metal.

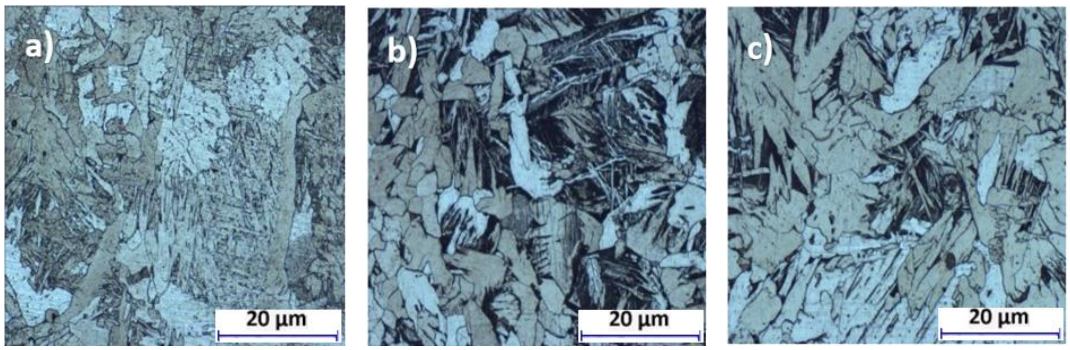

Figure 4. Microstructure of samples welded by oxy-gas welding method (100X) (a) SiC without, weld metal, (b) SiC reinforced, HAZ, (c) SiC reinforced weld metal microstructure

The SiC-reinforced weld metal of the sample welded using EAW with a rutile electrode is shown in Figure 5 (a), the SiC reinforced HAZ is shown in Figure 5 (b), and the microstructure of the

SiC reinforced weld metal is shown in Figure 5 (c). The microstructure obtained with the SiC reinforcement appears to be coarsened. The phases in the intergranular region also appers darker due to refinement of local microstructure. It is also possible that the decomposition of SiC and hence the addition of Si and C into weld metal increased the amount of residual phase that appear as dark region due to increased activity of alloying elements insoluble in ferrite phase. Thus, with slow cooling, both the grains and the carbides in the intergranular region became larger. The SiC-reinforced weld metal of the sample welded using EAW with cellulosic coated electrode is shown in Figure 6 (a) and (b), the SiC reinforced HAZ, and the microstructure of the SiC reinforced weld metal is shown in Figure 6 (c).

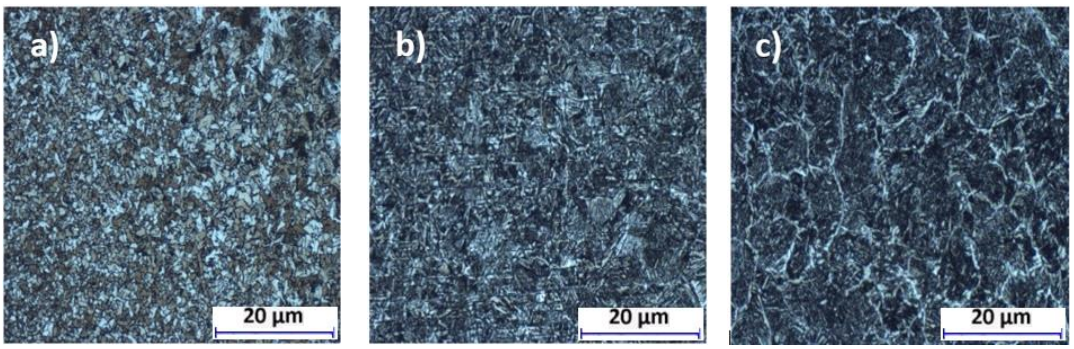

Figure 5. Microstructure of the sample welded using rutile electrode by electric arc welding method (100X) (a) SiC without, weld metal, (b) SiC reinforced, HAZ, (c) SiC reinforced weld metal microstructure

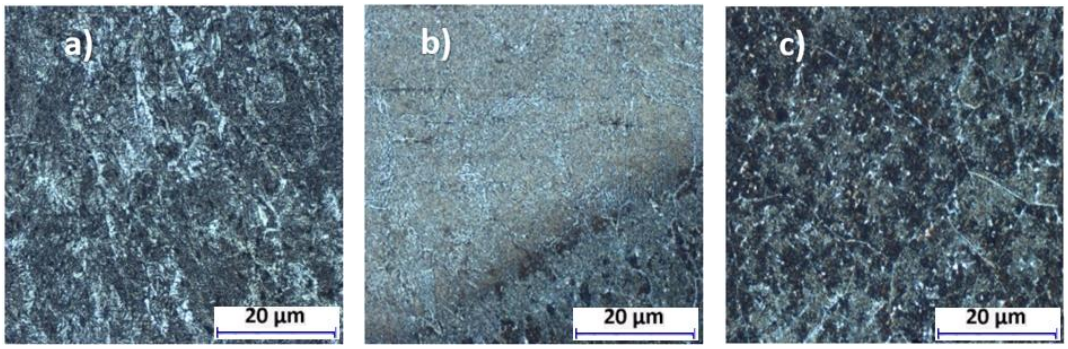

Figure 6. Microstructure of the sample welded using cellulosic electrode by electric arc welding method (100X) (a) SiC without, weld metal, (b) SiC reinforced, HAZ, (c) SiC reinforced weld metal microstructure

In the microstructure of the MAG welded sample, it can be seen that as the ratio of elements such as C and Mn in the welding filler wire increases, the perlite ratio in the microstructure increases and the grains become quite coarse (Figure 7). The intragranular microstructure consists of very fine acicular ferrite. In MAG welding without SiC reinforcement, the desired microstructure is approximately 95% acicular ferrite.

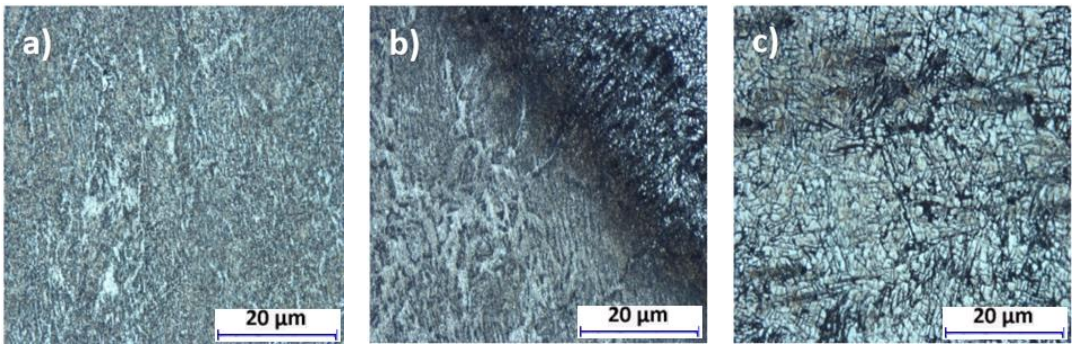

Figure 7. Microstructure of the sample welded by MAG welding method (100X) (a) SiC without, weld metal, (b) SiC reinforced, HAZ, (c) SiC reinforced weld metal microstructure

4. CONCLUSION

In this study, it was observed that the cooling time in the welding area and the carbon and other alloying elements in the additional wire content affected the phase amounts and grain structure change, and also affected the mechanical test results. A needle and oriented epitaxial microstructure was formed in the suddenly cooled region. It was observed that the mechanical properties of samples welded with oxy-gas were the lowest compared to other applied welding methods. When EAW, which is performed with lower heat input, is compared to welds made using the oxy-gas welding method, it is seen that the intragranular structures become thinner.

It was observed that the mechanical properties of SiC reinforced samples improved compared to the samples without SiC reinforcement. It has been determined that SiC reinforcement significantly increases the hardness values of the weld zone.

5. CONFLICT OF INTEREST

Authors approve that to the best of their knowledge, there is not any conflict of interest or common interest with an institution/organization or a person that may affect the review process of the paper.

6. AUTHOR CONTRIBUTION

Rıza KARA, Fatih ÇOLAK and Gökhan YILDIRIM determining the concept and design process of the research and research management, Hakan Furkan AKSU data collection and analysis, Rıza KARA and Fatih ÇOLAK data analysis and interpretation of results.

7. REFERENCES

Abedi S. S., Abdolmaleki A., Adibi N., Failure analysis of SCC and SRB induced cracking of a transmission oil products pipeline. Engineering Failure Analysis, 14(1), 250–261, 2007.

API specification 5L, Specification for line pipe, 46th Edition, USA, 2018.

Baek J., Hyun K., Pyo Y., Kim C., Man K., W. Sik S., Sung C., Effects of pre-strain on the mechanical properties of API 5L X65 pipe. Materials Science and Engineering A, 527(6), 1473–1479, 2010.

Bhadeshia H. K. D. H., Developments in martensitic and bainitic steels: role of the shape deformation. Materials Science and Engineering: A, 378(1–2), 34–39, 2004.

Biresselioglu M. E., Yelkenci T., Oz I. O., Investigating the natural gas supply security: A new

perspective. Energy, 80, 168–176, 2015.

Bohemen S. M.,Van C., Morsdorf L., Acta Materialia Predicting the M s temperature of steels with a thermodynamic based model including the effect of the prior austenite grain size. Acta Materialia, 125, 401–415, 2017.

Candan İ., Durgutlu A., Kahraman N., Gülenç B., Farklı Pozisyonlarda MAG Kaynağı ile Birleştirilen Boruların Kaynak Dikişlerinin Ultrasonik ve Mekanik Muayenesi. Politeknik Dergisi, 2006.

Capelle J., Dmytrakh I., Azari Z., Pluvinage G., Evaluation of electrochemical hydrogen absorption in welded pipe with steel API X52. International Journal of Hydrogen Energy, 38(33), 14356–14363, 2013.

Ezer M., Cam, G., A Study on microstructure and mechanical performance of gas metal arc welded AISI 304L joints. Materialwissenschaft und Werkstofftechnik, 53 (9), 1043-1052, 2022.

Ghosh C., Basabe V. V., Jonas J. J., Kim Y., Jung I.-H., Yue S., The dynamic transformation of deformed austenite at temperatures above the Ae 3. Acta Materialia, 61(7), 2348–2362, 2013.

Handoko W., Pahlevani F., Hossain R., Sahajwalla V., Stress-induced phase transformation and its correlation with corrosion properties of dual-phase high carbon steel. Journal of Manufacturing and Materials Processing, 3(3), 2019.

Hossain R., Pahlevani F., Sahajwalla V., Effect of small addition of Cr on stability of retained austenite in high carbon steel. Materials Characterization, 125, 114–122, 2017.

Hossain R., Pahlevani F., Sahajwalla V., Stability of retained austenite in high carbon steel – Effect of post-tempering heat treatment. Materials Characterization, 149(November 2018), 239–247, 2019.

Iseki T., Kameda T., Maruyama T., Interfacial reactions between SiC and aluminium during joining. Journal of Materials Science, 19, 1984.

Javidi M., Bahalaou H. S., Investigating the mechanism of stress corrosion cracking in near-neutral and high pH environments for API 5L X52 steel. Corrosion Science, 80, 213–220, 2014.

Jayashree P. K., Gowrishankar M. C., Sharma S., Shetty R., Shettar M., Hiremath P., Influence of homogenization and aging on tensile strength and fracture behavior of TIG welded Al6061-SiC composites. Journal of Materials Research and Technology, 9(3), 3598–3613, 2020.

Jonas J. J., Ghosh C., Role of mechanical activation in the dynamic transformation of austenite. Acta Materialia, 61(16), 6125–6131, 2013.

Ju J. B., Lee J. S., Jang J. I., Kim W. S., Kwon D., Determination of welding residual stress distribution in API X65 pipeline using a modified magnetic Barkhausen noise method. International Journal of Pressure Vessels and Piping, 80(9), 641–646, 2003.

Mulder G., Hetland J., Lenaers G., Towards a sustainable hydrogen economy: Hydrogen pathways and infrastructure. International Journal of Hydrogen Energy, 32(10–11), 1324–1331, 2007.

Pk J., Gowrishankar M. C., Sharma S., Shetty R., Hiremath P., Shettar M., The effect of SiC content in aluminum-based metal matrix composites on the microstructure and mechanical properties of welded joints. Journal of Materials Research and Technology, 12, 2325–2339, 2021.

Senol M., Cam G., Investigation into microstructures and properties of AISI 430 ferritic steel butt joints fabricated by GMAW. International Journal of Pressure Vessels and Piping, 202, 104926, 2023.

Serindag H.T., Cam G., Microstructure and mechanical properties of gas metal arc welded AISI 430/AISI 304 dissimilar stainless steels butt joints. Journal of Physics: Conference Series, 1777, 012047, 2021.

Serindag H.T., Cam G., Multi-pass butt welding of thick AISI 316L plates by gas tungsten arc welding: Microstructural and mechanical characterization. International Journal of Pressure Vessels and Piping, 200, 104842, 2022.

Serindag H.T., Tardu C., Kircicek I.O, Cam G., A study on microstructural and mechanical properties of gas tungsten arc welded thick cryogenic 9% Ni alloy steel butt joint. CIRP Journal of Manufacturing Science and Technology, 37, 1-10, 2022.

Serindag H.T., Kircicek I.O, Tardu C., Cam G., Determination of microstructural and mechanical properties of gas tungsten arc welded 9Ni cryogenic steel joint, Mühendis ve Makine (Engineer and Machinery), 63(706), 117-137, 2022.

Serindag H.T., Cam G., Characterizations of microstructure and properties of dissimilar AISI 316L/9Ni low alloy cryogenic steel joints fabricated by GTAW. Journal of Materials Engineering and Performance, 32, 7039-7049, 2023.

Seyedrezai H., Pilkey A. K., Boyd J. D., Effect of pre-IC annealing treatments on the final microstructure and work hardening behavior of a dual-phase steel. Materials Science and Engineering A, 594, 178–188,2014.

Tobón C., Cruz A. M. D., Velázquez J. L. G., Salcedo J. G. G., Salinas R. M., Comparative study on rate of flow accelerated corrosion (FAC) of API 5L X-52-65-70 steels in a brine added with H2S at 60°C by using a rotating cylinder electrode (RCE). International Journal of Electrochemical Science 9 (12): 6781–92, 2014.

Vargas-Arista B., Balvantin A., Baltazar A., García-Vázquez F., On the use of ultrasonic spectral analysis for the characterization of artificially degraded API 5L X52 steel pipeline welded joints. Materials Science and Engineering A, 550, 227–234, 2012.

JOURNAL of
MATERIALS and MECHATRONICS:A

e-ISSN 2717-8811
JournalMM, 2023, 4(2), 598-607
https://doi.org/10.55546/jmm.1390664

Araştırma Makalesi / Research Article

Investigation on the Effect of Coating Temperature on the Properties of NbC Layer Coated with Pack Cementation Technique on GGG70 Nodular Graphite Cast Iron Surface

Serkan DAL

Nevşehir Hacı Bektaş Veli University, Faculty of Engineering and Architecture, Department of Metallurgical and Materials Engineering, Nevşehir, Türkiye,
ORCID ID: https://orcid.org/0000-0002-0197-7943, serkandal@nevsehir.edu.tr

Geliş/ Received: 14.11.2023; **Kabul / Accepted:** 20.12.2023

ABSTRACT: Nodular Graphite Cast Irons stand out with their high castability, high strength, vibration damping and high loading capacity. With today's technologies, the surface properties of materials can be improved by coating them with various methods and high-performance engineering materials can be obtained. Pack Cementation Technique is preferred among coating methods due to its relatively lower cost and applicability. In this study, it was aimed to coat NbC on the surface of GGG70 Nodular Graphite Cast Iron using the Pack Cementation Technique at 900 °C, 1000 °C and 1100 °C for 6 hours. The effect of temperature on the properties of the resulting coating layers was investigated. For this purpose, the surface morphologies of the samples were examined and their fracture toughness and hardness values were obtained. Coating morphologies were examined by XRD, optical microscope and SEM analysis and changes in coating structure and thickness were obtained. When the results were examined, it was determined that the coating thickness increased with the increase in coating temperature. Accordingly, it was observed that the fracture toughness value of the coatings first increased and then decreased slightly. Microhardness values increased approximately 5 times in the coating areas.

Keywords: Nodular Graphite Cast Iron, NbC Coating, Fracture Toughness, Microhardness.

*Sorumlu yazar / Corresponding author: serkandal@nevsehir.edu.tr

Bu makaleye atıf yapmak için /To cite this article

Dal, S. (2023). Investigation on the Effect of Coating Temperature on the Properties of NbC Layer Coated with Pack Cementation Technique on GGG70 Nodular Graphite Cast Iron Surface. Journal of Materials and Mechatronics: A (JournalMM), 4(2), 598-607.

1. INTRODUCTION

Increasing technological needs and their corresponding developments lead to important discoveries in the field of materials (Fernandes et al., 2018). In the industry, efforts are being made to increase the service life of materials by improving their surface properties, wear resistance, corrosion and oxidation resistance and friction properties (Kan et al., 2018; Chen et al., 2021a, 2021b; Erdoğan, 2019; Okay et al., 2010; Günen et al., 2023a, 2023b, 2023c). For this purpose, creating a hard and thin film coating on the surface is a good option (Karamış and Yıldızlı, 2010; Okay et al., 2010). Carbides such as niobium carbide, vanadium carbide etc. are obtained on metal material surfaces by forming thin films through various processes such as pack cementation technique, laser coating and reactive spraying etc. (Cai and Xu, 2017; Chen et al., 2021). The pack cementation technique is relatively less complex and less costly than other methods (Cai and Xu, 2017).

Nodular graphite cast irons are used as an alternative to steels in the industry and are preferred due to their properties close to steels (Fernandes et al., 2018; Okay et al., 2010). In addition, its ability to be produced more economically compared to steels and its high castability properties provide an additional advantage (Karaca and Şimşir 2019). Nodular graphite cast irons are obtained by adding elements such as magnesium and cerium to the molten metal and the graphite solidifying into spheroids. Thus, an alloy with superior strength, fatigue resistance, toughness, ductility and vibration damping properties is obtained compared to other alloys. With these properties, Nodular graphite cast irons are used in many areas such as hot rolling rolls, aluminium melting crucibles, molds for the glass industry, gears and hydraulic presses. In addition, although they are used in many areas, their wear resistance is not sufficient in places where wear resistance is required. Therefore, in order to increase the wear resistance of nodular graphite cast iron material surfaces, the surfaces have been tried to be improved by methods such as thermal spray, laser, pack cementation technique, etc. and various heat treatments (Megahed et al. 2019), and positive results have been reported (Günen et al.,2022).

Owing to their important physical and chemical properties, carbides of transition metals have found a place in cutting tool coatings, aerospace, and many industrial applications (Peng at al.,2021).The pack cementation technique is based on the principle that the carbon atom spreads to the surface with high temperature and forms carbides on the surface with elements such as Cr, Nb, V. Thanks to this method, depending on the structure of the carbide layer formed, very hard layers can be obtained on the surface without any deterioration in the main structure of the material. Thus, while the wear and hardness values of the material are increased, its toughness properties are preserved against external impacts (Günen et al., 2022). It has been stated that in this method, transition metal carbide coatings cannot be obtained in alloys with C concentration below 0.3% (Günen et al., 2023c).

Niobium carbide (NbC), is considered an ideal candidate as a coating material thanks to its resistance to corrosion and wear (Zhong et al., 2020; Peng et al.,2021). NbC, which has high hardness (35GPa) and high melting point (3600 °C)(Cai et al., 2015a), can be deposited from the surface to the depths of Fe-based materials, and the hardness and elastic modulus values of the material are increased (Zhong et al., 2020). Various studies have been carried out on the formation mechanism and microstructure of the NbC coating layer. With the improvement of the morphology of the coating layer, the surface properties will change significantly (Cai et al., 2015b).

A few studies have been conducted in the literature involving the coating of NbC coatings on steel materials (Günen et al., 2023b.). A small number of NbC coating studies on cast irons with the TRD method have been encountered. In their study, Mariani et al. (Mariani et al., 2020) obtained 3

different coatings, namely NbC, VC and NbVC, on the surface of lamellar graphite cast iron in a salt bath at 1000 °C for 2 hours with the thermoreactive diffusion method. It has been reported that the hardness of the coating was obtained above 2300, 2500 and 3050 Hv, respectively. Cai et al. In their study, (Cai et al., 2016) formed NbC coatings on the gray cast iron surface using the in-situ method. It was reported that the coating thickness was approximately 21μm and the coating hardness was 21 GPa.

In this study, NbC layer was formed on GGG70 nodular graphite cast iron surfaces at 900 °C, 1000 °C and 1100 °C for 6 hours. The effects of coating temperature on the properties of the formed NbC layers were examined. For this purpose, the changes in coating morphology, fracture toughness and hardness values were observed and the results were compared.

2. MATERIALS AND METHODS

In this study, GGG70 spheroidal graphite cast iron samples, whose elemental content is given in Table 1, were cut into 15x15x10 mm dimensions and used as the substrate material to be coated. All surfaces of the samples to be coated were first sanded with 120-400-800 sandpaper and then washed with soap and water to remove oil and dirt.

Table 1. Elemental content of GGG70 nodular graphite cast iron samples.

	Wt%								
Material	**C**	**Si**	**Mn**	**Cu**	**Cr**	**S**	**P**	**Mg**	**Fe**
GGG70	3.47	2.41	0.17	0.07	0.03	0.01	0.02	0.05	Balance

The samples, whose surface water was removed with alcohol, were placed in steel crucibles with coating powder consisting of a powder mixture of 45% Fe-Nb + 45% Al_2O_3 + 10% NH_4Cl. In order to minimize contact with air, activated carbon powder was added to the mixture and then the mouth of the crucible was covered with ceramic clay pastes. The prepared crucibles were kept in a high temperature furnace (Carbolite CWF1200) for 6 hours at 900 °C, 1000 °C and 1100 °C, respectively. The heating rate was 15 °C/min from room temperature to coating temperatures, and then the samples were cooled in an open air environment. The samples, which had a coating layer on their surface, were cleaned of dust and dirt, their surfaces were sanded with 120-400-800-1200 mesh sandpaper, and then they were polished and etched with 3% Nital solution. The fracture toughness (K_C) of the NbC coating layer formed on the surface was estimated using Equations 1 and 2, taking into account the crack lengths developing from the corners of the micro hardness trace taken from 3 different regions (Kulka et al., 2017). Future-Tech (FM 700) microhardness device was used for fracture toughness and microhardness measurements. Nikon (MA 100) microscope and Clemex (image analysis system) image analysis system were used to determine the phase structure, crack lengths and coating thicknesses. The following equations were used for fracture toughness calculation.

$$K_C = A.P/c^{3/2} \quad (1)$$

$$A = 0.028\ (E/H)^{1/2} \quad (2)$$

where A is the residual indentation coefficient, P is the load, c is half the notch crack length, H is the hardness, and E is the Young's modulus. The obtained E_{NbC} values are approximately 435 GPa. (Zhao et al., 2017)

3. RESULTS AND DISCUSSION

3.1 Characterization of the Coating Layer

SEM microstructure photographs of samples coated with NbC by the pack cementation method at 900 °C, 1000 °C and 1100 °C for 6 hours are given in Figure 1. The NbC layer formed on the surface has a homogeneous and flat morphology. The layer/matrix interface appears quite flat. It is seen that the layer thickness increases with the increase of the coating temperature. However, in the sample coated at 1100 °C, the coating thickness reached the highest values and pore-like pits were formed. Günen et al. (2023a) observed similar pore-like pits on the coating surface due to the diffusion process when they applied niobizing process to AISI D3 steel at 1000 °C for 6 hours in their study. As a result of point EDS analysis, they determined that the pit regions had lower Nb and C ratios than other regions. (Günen et al., 2023). When the coating temperature was 1100 °C and 6h, due to the high diffusion time and temperature, it caused an indentation to grow towards the substrate material in the coating line and the formation of pore-like structures in the coating morphology (Figure 1-c).

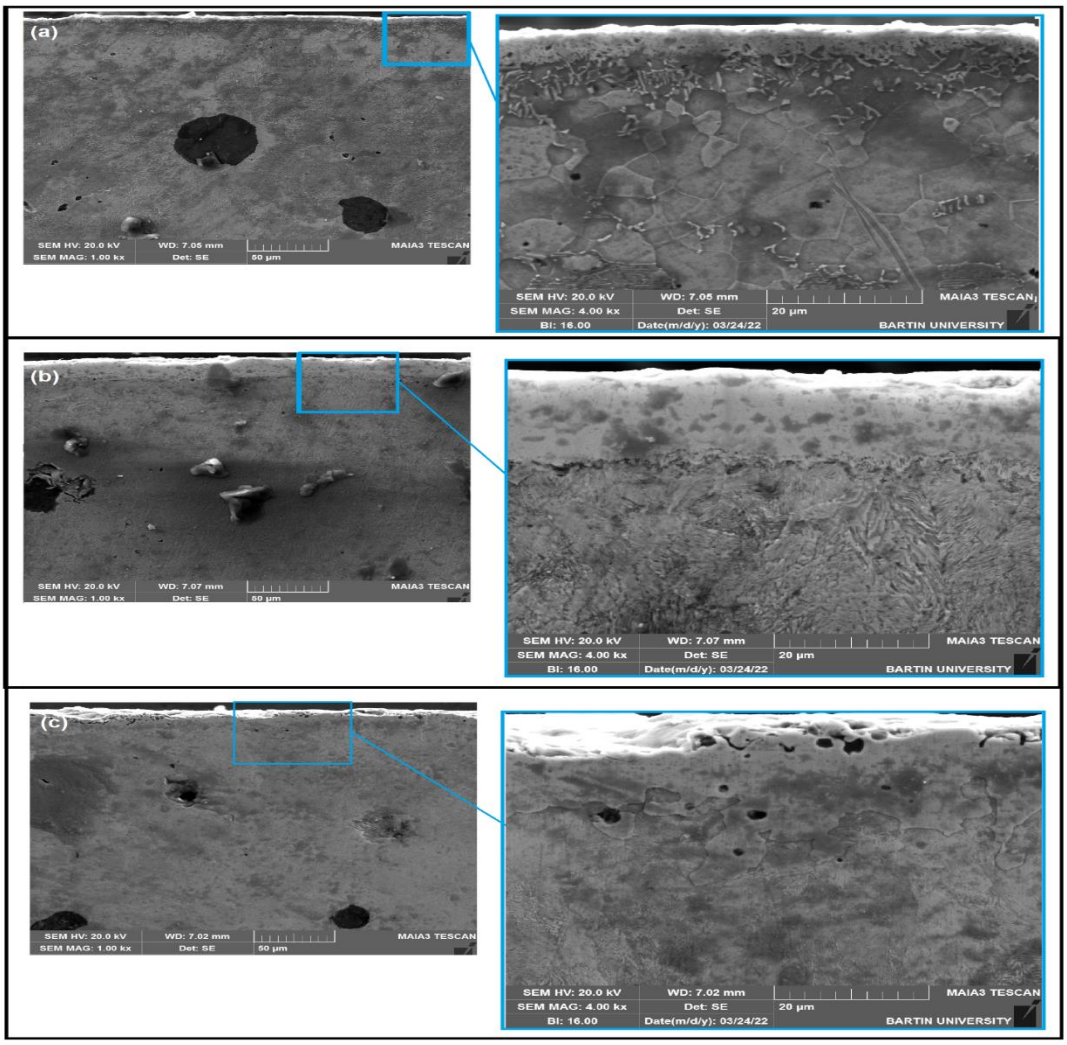

Figure 1. SEM images of NbC coated samples at a) 900 °C, b) 1000 °C and c) 1100 °C for 6 hours.

XRD analysis results taken from the surfaces of the obtained NbC coated samples are given in Figure 2. The diffraction peaks of the samples show that a layer consisting of NbC (ICDD card No. 00-038-1364) phase and α-Fe (ICDD card No. 01-087-0721) is formed, in accordance with the literature (Mariani et al., 2020; Günen et al., 2023a). In all samples, the most dominant peaks were observed between 2θ=30° and 60°. In the sample coated at 900 °C, the most dominant phase was the (111) plane NbC phase and the second dominant phase was the (110) plane α-Fe phase (Figure.2-a). In the sample coated at 1000 °C, the most dominant phase was the (111) plane NbC phase and the second dominant phase was the (200) plane NbC phase, and the (110) plane a-Fe phase intensity decreased slightly (Figure.2-b). In the sample coated at 1100 °C, the most dominant phase was the (110) plane α-Fe phase and the second dominant phase was the (200) plane NbC phase, and the intensity of the (111) plane NbC phase decreased slightly (Figure 2-c). As the coating temperature increased from 900 °C to 1000 °C, the intensity of the (110) plane α-Fe phase first decreased, but in the sample coated at 1100 °C, it increased and became the most dominant peak.

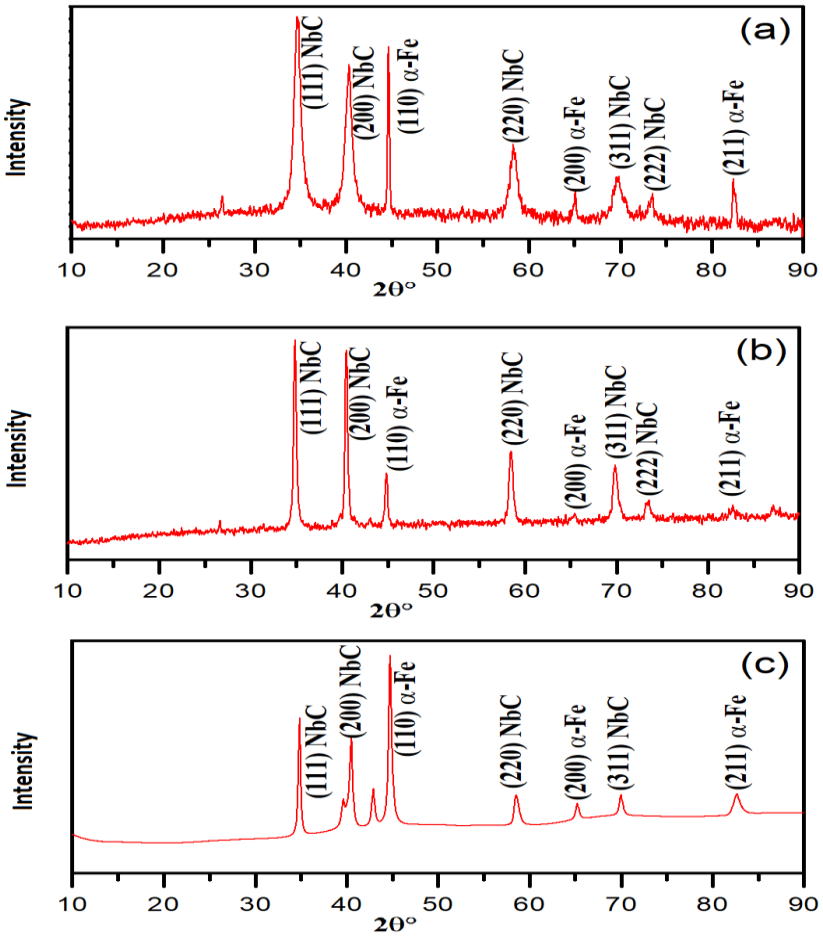

Figure 2. XRD analysis graphs taken from the coating surface of samples coated at a) 900 °C, b) 1000 °C c)1100 °C for 6 hours.

Linear elemental analysis graphs taken from the surface of the coating samples to the substrate material are shown in Figure 3. In the sample coated at 900 °C (Figure.3-a), it is seen that wt% Nb decreases from the coating to the substrate material and wt% Fe suddenly increases in the substrate material. A similar situation is observed in the sample coated at 1000 °C (Figure 3-b). However, it is observed that the wt% Nb and C ratio in the coating layer in the sample coated at 1000°C is higher than in the sample coated at 900°C. In the sample coated at 1100 °C (Figure.3-c), it is seen that wt%

Nb decreases from the coating to the substrate material and wt% Fe suddenly increases in the substrate material. However, in the sample coated at 1100 °C, it is seen that the wt% Nb ratio is lower and the wt% Fe ratio is higher at the coating line compared to the samples coated at 900 °C and 1000 °C. This is compatible with the XRD results.

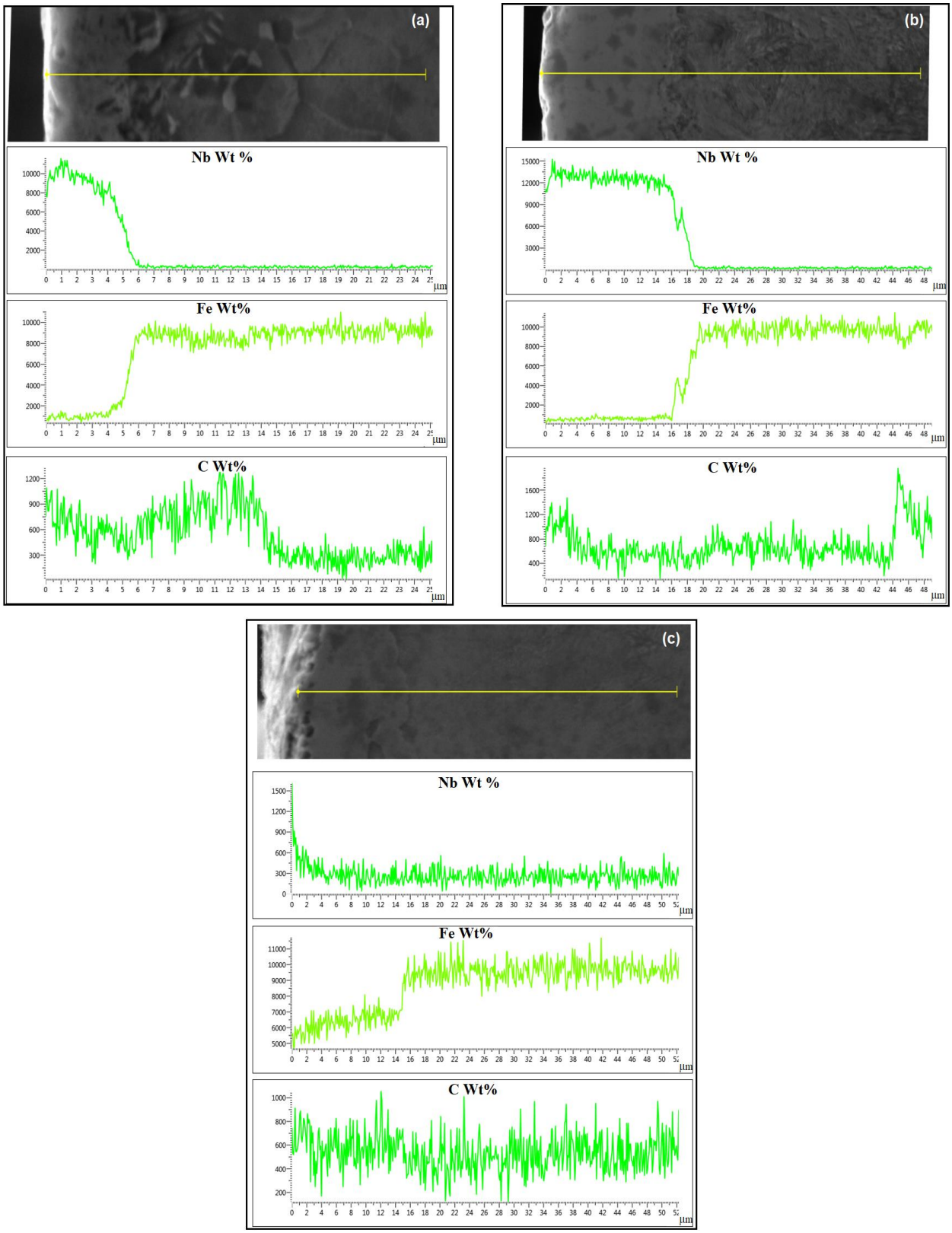

Figure 3. Linear elemental analysis images taken from samples coated with NbC at a) 900 °C, b) 1000 °C c)1100 °C.

3.2 Thickness, Fracture Toughness and Hardness of NbC Layer

NbC layer thickness values and Fracture toughness values of steel coated with pack cementation technique at different temperatures are given in Table 2. Additionally, the optical microstructures of NbC layer thicknesses are shown in Figure 4. The fracture toughness (K_C) of the NbC coating layer formed on the surface was estimated by taking into account the crack lengths developing from the corners of the microhardness trace.

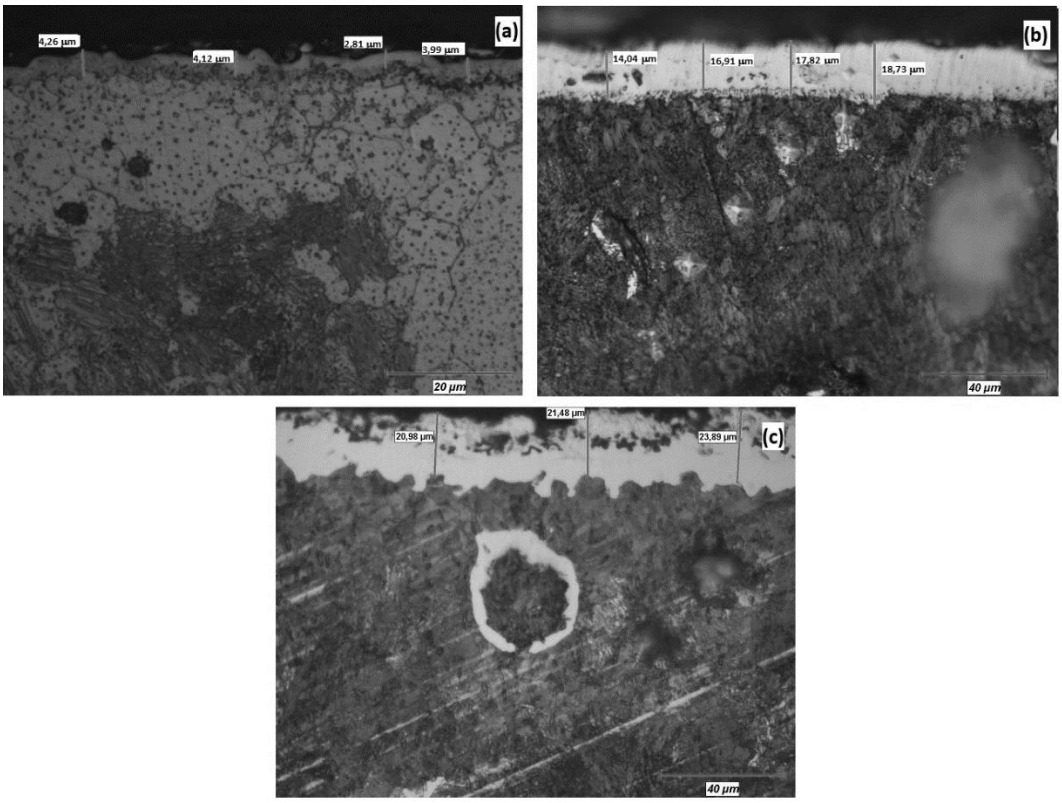

Figure 4. Optical microstructure images taken from samples coated with NbC at a) 900 °C, b) 1000 °C c)1100 °C.

With the increase in coating temperature, coating thicknesses increased and were obtained as an average of 3.79 µm, 16.87µm and 22.12 µm at 900 °C, 1000 °C and 1100 °C, respectively. In addition, fracture toughness values increased from 1.47 MPa $m^{1/2}$ to 2.61 MPa $m^{1/2}$ as the coating temperature increased from 900 °C to 1000 °C. However, even though the coating thickness increased in the sample coated at 1100 °C, the fracture toughness decreased to 2.25 MPa $m^{1/2}$.

Table 2. Thickness and fracture toughness values of GGG70 nodular cast iron coated with NbC at different temperatures.

Coating Temperature (°C)	Coating Thickness (µm)	Fracture Toughness (K_C (MPa $m^{1/2}$)
900	3.79±0.67	1.47±0.2
1000	16.87±2.03	2.61±0.3
1100	22.12±1.56	2.25±0.2

Microhardness measurements were made under a 25 gf load from the cross-sectional surface of the coated samples to a certain depth and the hardness of the NbC layer and matrix regions was

determined. The microhardness measurements were determined by taking the order of hardness from the substrate material to the coating surface (Figure 5).

By coating the GGG70 nodular cast iron surface with NbC using the pack cementation method, the surface hardness increased approximately 5 times. As seen in Figure 5, the hardness distribution of GGG70 nodular cast iron towards the coating surface can be seen. In the hardness distribution of the formed NbC layer from the surface, a high hardness value is obtained throughout the NbC layer and a sudden decrease is observed when it reaches the matrix. Depending on the thickness of the coating layer, the hardness values are seen to be higher than the substrate material. It has been reported in the literature that microhardness values will increase with increasing coating temperature (Günen et al., 2023a). It was observed that the microhardness values increased as the coating temperature increased from 900° to 1000°C and 1100°C in the NbC coating layers formed on the GGG70 nodular graphite cast iron surface. Although the hardness values of the coating obtained at 1100 °C are close to the hardness value of the coating layer obtained at 1000 °C, it is seen that it decreases slightly. It can be said that this is due to pore-like pits that are poorer in Nb and C.

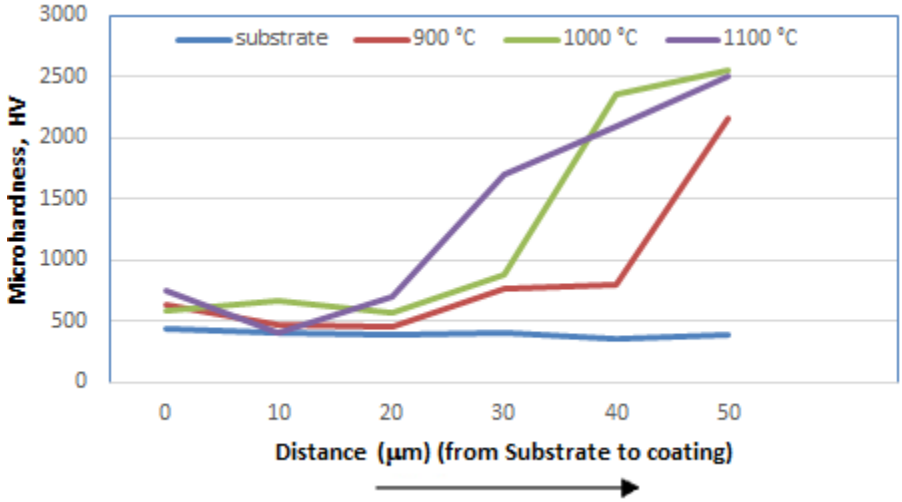

Figure 5. Microhardness change of NbC layers in the obtained samples.

4. CONCLUSION

In this study, an NbC layer was obtained on the surface of GGG70 nodular graphite cast iron using the pack cementation technique at temperatures of 900°C, 1000°C, 1100°C for 6 hours, and the effects of the coating temperature on the coating properties were investigated. In conclusion;

- NbC layer with a homogeneous and flat morphology was obtained on the surface. The layer/matrix interface appears quite flat. It is seen that the layer thickness increases with the increase of the coating temperature. However, although the coating thickness reached the highest values in the sample coated at 1100 °C, a pore-like coating layer poor in Nb and C was obtained. The most homogeneous and smooth coatings were obtained on sample surfaces coated at 1000 °C for 6 hours.
- As a result of XRD analysis, the desired NbC phase was obtained. It was observed that the intensity of the α-Fe phase increased and the intensity of the NbC phase decreased in the sample coated at 1100 °C.

- The hardness values of the coating layer increased approximately 5 times compared to the substrate material.
- When the fracture toughness values of the coatings were examined, the highest value was reached in the coating obtained at 1000 °C and this value decreased slightly in the samples coated at 1100 °C.

5. CONFLICT OF INTEREST

Author approve that to the best of their knowledge, there is not any conflict of interest or common interest with an institution/organization or a person that may affect the review process of the paper.

6. AUTHOR CONTRIBUTION

Serkan Dal: Determining the research and research method, conducting experiments, collecting and analyzing data, interpreting the analysis results.

7. REFERENCES

Cai X., Xu Y., Microstructure, friction and wear of NbC coatings on a Fe substrate fabricated via an in situ reaction, Surface & Coatings Technology, 322, 202–210, 2017.

Cai X., Xu Y., Zhao N, Zhong L., Zhao Z., Wang J., Investigation of the adhesion strength and deformation behaviour of in situ fabricated NbC coatings by scratch testing, Surface & Coatings Technology, 299, 135–142, 2016.

Cai X., Xu Y., Zhong L., Zhao N., Yan Y., Kinetics of niobium carbide reinforced composite coating produced in situ, Vacuum, 119, 239-244, 2015b.

Cai X., Zhong L., Wang J., Shao T., Zhao N., Xu Y., Microstructure and Hardness of NbC Coating Produced in situ, Advanced Materials Research, 1120-1121, 745-745, 2015a

Chen L., Li Y., Zhao Z., Zheng Q., Yi D., Li X., Peng J., Sun L., First-principles calculation of the adhesion work, fracture toughness and tensile behavior of the Fe/MCs (M = Nb and Ta) interfaces by two different optimization methods, Chemical Physics, 547, 111193, 2021a.

Chen L., Yu T., Xu P., Zhang B., in situ NbC reinforced Fe-based coating by laser cladding: Simulation and experiment, Surface & Coatings Technology 412,127027, 2021b.

Erdoğan A., Investigation of high temperature dry sliding behavior of borided H13 hot work tool steel with nanoboron powder, Surface & Coatings Technology 357, 886–895, 2019.

Fernandes L.M., Lopes J.C., Volpato R. S., Diniz A.E., Oliveira R.F.M., Aguiar P. R., Mello H. J., Bianchi E.C., Comparative analysis of two CBN grinding wheels performance in nodular cast iron plunge grinding, The International Journal of Advanced Manufacturing Technology, 98, 237–249, 2018.

Günen A., Açıkgöz H. H., Çavdar F, Karahan İ. H., A Response Surface Study on The Grown Behavior and Some Mechanıcal Properties of Niobium Carbide Coatings, Surface Review and Letters, 30(9), 2350058(1-15), 2023a.

Günen A., Açıkgöz H. H., Karahan İ. H., Niobium Carbide Coatings Grown on Cold Work Tool Steel AISI D3 by Thermomechanical Processing: Characterization, Wear and Corrosion Behaviors, Protection of Metals and Physical Chemistry of Surfaces, 59: 4, 648–670. Pleiades Publishing, Ltd., 2023c.

Günen A., Açıkgöz H. H., Keddam M., Karahan İ. H., Characterizations and Kinetics of Refractory Niobium Carbide Coatings on AISI D3 Steel, JMEPEG, 32:8972–8980, 2023b.

Günen A., Soylu B., Karakaş Ö., Titanium carbide coating to improve surface characteristic, wear and corrosion resistance of spheroidal graphite cast irons, Surface & Coatings Technology, 437, 128280, 2022.

Kan W. H., Albino C, Dias-da-Costa D. Dolman K., Lucey T., Tang X., Chang L., Proust G., Cairney J., Microstructure characterisation and mechanical properties of a functionally-graded NbC/high chromium white cast iron composite, Materials Characterization 136, 196–205, 2018.

Karaca B. and Şimşir M., The Effects of Heat Treatment on the Tensile Properties of Camshaft made of GGG70 Series Spherical Graphite Cast Iron, Acta Physica Polonica A, 135(4), 811-818, 2019.

Karamış M.B., Yıldızlı K., Surface modification of nodular cast iron: A comparative study on graphite elimination, Materials Science and Engineering A, 527, 5225–5229, 2010.

Kulka M., Makuch N., Piasecki A., Nanomechanical characterization and fracture toughness of FeB and Fe_2B iron borides produced by gas boriding of Armco iron, Surf. Coat. Technol. 325, 515–532, 2017.

Mariani F. E., Rego G. C., Bonella P. G., Neto A. L., Totten G. E., Casteletti L. C., Wear Resistance of Niobium Carbide Layers Produced on Gray Cast Iron by Thermoreactive Treatments JMEPEG, 29:3516–3522, 2020.

Megahed H., El-Kashif E., Shash A. Y., Essam M. A., Effect of holding time, thickness and heat treatment on microstructure and mechanical properties of compacted graphite cast iron, jmaterrestechnol. 8(1),1188–1196, 2019.

Okay F., Sert H., Habalı K., Gül F., Effect of TiN Coating by Physical Vapour Deposition on the Wear Behaviour of Austempered Ductile Iron, J. Fac. Eng. Arch. Gazi Univ. 25(4), 787-794, 2010.

Peng S., Xu J., Li Z., Jiang S., Xie Z.H., Munroe P., Electrochemical noise analysis of cavitation erosion corrosion resistance of NbC nanocrystalline coating in a 3.5 wt% NaCl solution, Surface & Coatings Technology 415, 127133, 2021

Zhao N., Xua Y., Fu Y., Mechanical properties of one-step in situ synthesized NbC-Fe composite coating, Surface & Coatings Technology 309, 1105–1110, 2017.

Zhong L., Wei J., Bai H., Zhu J., Xu Y., Effects of soaking time on the microstructure and mechanical properties of Nb-NbC/Fe core–shell rod-reinforced cast-iron-matrix composite fabricated through two-step in situ solid-phase diffusion, jmaterrestechnol, 9(6):12308–12317, 2020.